Macromolecules
EDITORIAL

DOI: 10.1021/ma102855k

Editorial

Happy new year to all our readers, authors, and reviewers, and thank you for contributing to another very successful year for the journal. We have experienced very positive response to the convenience of the American Chemical Society's Web-based platform, Paragon Plus, for both submitting and reviewing manuscripts. As always, we welcome your feedback and suggestions for ways in which we can make these processes even better. The *Macromolecules* Home Page (http://pubs.acs.org/journal/mamobx) also undergoes continual enhancements in functionality, which we hope you enjoy. The past year also saw continued growth in the journal impact factor (4.539) and total citations (88 896), confirming our preeminent position in both quality and quantity. We encourage you to continue to suggest possible topics and authors for Perspectives, as the positive response of the community demonstrates that this series of topical reviews is proving very useful. Indeed, the 16 Perspectives published in 2010 have already been widely read and cited.[1−16]



Karen I. Winey



Timothy M. Swager

Almost every new year is marked by changes within our distinguished team of Associate Editors, and this year is no exception. After many years of exceptional service, Jerry Schultz (University of Delaware, Associate Editor since 1999) and Chris Ober (Cornell University, Associate Editor since 1996) have decided to set their red pens aside and devote their energies to other endeavors. Also, Jim Moore (RPI, Associate Editor since 1998) stepped down one year ago. We appreciate all their hard work, good judgment, and leadership that have contributed so much to the growth of the journal and to its enviable reputation in the field. At the same time we are delighted to acknowledge two new Associate Editors, Dr. Timothy M. Swager and Dr. Karen Winey, who began handing papers in July of last year.

Tim is the John D. MacArthur Professor of Chemistry at MIT, where he has been since 1996. Prior to that, he was on the faculty at the University of Pennsylvania from 1990. He earned his Ph.D. in Chemistry 1988 at Caltech under the guidance of Professor Bob Grubbs and followed that with a postdoctoral fellowship at MIT with Professor Mark Wrighton. Tim's current research interests include electronic and optical polymers, chemical sensors, supramolecular chemistry, and molecular recognition. Tim has received many awards and recognitions, including an Alfred P. Sloan Research Fellowship, a Camille Dreyfus Teacher-Scholar Award, Cope Scholar (ACS), NSF Young Investigator, and the Carl Marvel Creative Polymer Chemistry Award from the Polymer Division of the ACS. In 1998 Tim was elected to membership in the National Academy of Sciences.

Dr. Karen I. Winey is a Professor of Materials Science and Engineering and Chemical and Biomolecular Engineering at the University of Pennsylvania. Her group designs and fabricates polymer nanocomposites containing carbon nanotubes and metal nanowires with the aim of understanding how to improve their mechanical, thermal, and especially electrical properties. More recently, this work has expanded to include simulations of electrical conductivity and polymer dynamics in the presence of nanoparticles. Karen earned her B.S. in Materials Science and Engineering from Cornell University and her M.S. and Ph.D. in Polymer Science and Engineering from the University of Massachusetts, Amherst. Her honors and awards include an NSF Young Investigator Award (1994−1999), Fellow of the American Physical Society (2003), and NSF Special Creativity Award (2009−2011). In addition to serving on various advisory boards, Winey chaired the 2010 Polymer Physics Gordon Research Conference.

We are delighted to have Tim and Karen join the *Macromolecules* team, and we look forward to the benefit of their insight and wisdom for years to come.

References and Notes

(1) Shoichet, M. S. Polymer Scaffolds for Biomaterials Applications. *Macromolecules* **2010**, *43*, 581–591; DOI: 10.1021/ma901530r.
(2) Sumerlin, B. S.; Vogt, A. P. Macromolecular Engineering through Click Chemistry and Other Efficient Transformations. *Macromolecules* **2010**, *43*, 1–13; DOI: 10.1021/ma901447e.
(3) Monteiro, M. J. Nanoreactors for Polymerizations and Organic Reactions. *Macromolecules* **2010**, *43*, 1159–1168; DOI: 10.1021/ma902348r.
(4) Jinnai, H.; Spontak, R. J.; Nishi, T. Transmission Electron Microtomography and Polymer Nanostructures. *Macromolecules* **2101**, *43*, 1675–1688; DOI: 10.1021/ma902035p.

© 2011 American Chemical Society
Published on Web 01/18/2011

(5) Kiesewetter, M. K.; Shin, E. J.; Hedrick, J. L.; Waymouth, R. M. Organocatalysis: Opportunities and Challenges for Polymer Synthesis. *Macromolecules* **2010**, *43*, 2093–2107; DOI: 10.1021/ma9025948.
(6) Kloxin, C. J.; Scott, T. F.; Adzima, B. J.; Bowman, C. N. Covalent Adaptable Networks (CANs): A Unique Paradigm in Cross-Linked Polymers. *Macromolecules* **2010**, *43*, 2643–2653; DOI: 10.1021/ma902596.
(7) Hayward, R. C.; Pochan, D. J. Tailored Assemblies of Block Copolymers in Solution: It Is All about the Process. *Macromolecules* **2010**, *43*, 3577–3584; DOI: 10.1021/ma9026806.
(8) McKeown, N. B.; Budd, P. M. Exploitation of Intrinsic Microporosity in Polymer-Based Materials. *Macromolecules* **2010**, *43*, 5163–5176; DOI: 10.1021/ma1006396.
(9) Spiess, H. W. Interplay of Structure and Dynamics in Macromolecular and Supramolecular Systems. *Macromolecules* **2010**, *43*, 5479–5491; DOI: 10.1021/ma1005952.
(10) Yagci, Y.; Jockusch, S.; Turro, N. J. Photoinitiated Polymerization: Advances, Challenges, and Opportunities. *Macromolecules* **2010**, *43*, 6245–6260; DOI: 10.1021/ma1007545.
(11) Kim, H.; Abdala, A. A.; Macosko, C. W. Graphene/Polymer Nanocomposites. *Macromolecules* **2010**, *43*, 6515–6530; DOI: 10.1021/ma100572e.
(12) Tennyson, A. G.; Norris, B.; Bielawski, C. W. Structurally Dynamic Conjugated Polymers. *Macromolecules* **2010**, *43*, 6923–6935; DOI: 10.1021/ma101198z.
(13) Roland, C. M. Relaxation Phenomena in Vitrifying Polymers and Molecular Liquids. *Macromolecules* **2010**, *43*, 7875–7890; DOI: 10.1021/ma101649u.
(14) Hu, J.; Liu, S. Responsive Polymers for Detection and Sensing Applications: Current Status and Future Developments. *Macromolecules* **2010**, *43*, 8315–8330; DOI: 10.1021/ma1005815.
(15) Qin, A.; Lam, J. W. Y.; Tang, B. Z. Click Polymerization: Progresses, Challenges, and Opportunities. *Macromolecules* **2010**, *43*, 8693–8702; DOI: 10.1021/ma101064u.
(16) Stone, D. A.; Korley, L. T. J. Bioinspired Polymeric Nanocomposites. *Macromolecules* **2010**, *43*, 9217–9226; DOI: 10.1021/ma101661p.

Timothy P. Lodge
Editor

Macromolecules
PERSPECTIVE

Macromolecules **2011**, *44*, 183–190 **183**
DOI: 10.1021/ma101223q

Homogeneous Shear, Wall Slip, and Shear Banding of Entangled Polymeric Liquids in Simple-Shear Rheometry: A Roadmap of Nonlinear Rheology

Shi-Qing Wang,* S. Ravindranath,† and P. E. Boukany‡

Department of Polymer Science, University of Akron, Akron, Ohio 44325, United States.
†Current affiliation: Celanese/Ticona. ‡Current affiliation: The Ohio State University

Received June 1, 2010; Revised Manuscript Received December 3, 2010

ABSTRACT: The recent particle-tracking velocimetric (PTV) observations revealed that well-entangled polymer solutions and melts tend to either exhibit wall slip or assume an inhomogeneous state of deformation and flow during nonlinear rheological measurements in simple-shear rheometric setups. Many material parameters and external conditions have been explored since 2006, and a new phenomenological picture has emerged. In this Perspective, we not only point out the challenges to perform reliable rheometric measurements but also discuss the relation between wall slip and internal (bulk) cohesive breakdown and summarize all available findings in terms of a phase diagram. This map specifies the conditions under which shear homogeneity, interfacial slip, and bulk shear inhomogeneity would prevail. The paper is closed by enumerating a number of unresolved questions for future studies.

1. Introduction

Rheometry is a widely used experimental technique in polymer science and engineering. The polymer scientist often makes rheometric measurements to characterize the linear viscoelastic properties of his polymer samples. Frequently, linear viscoelastic characteristics have been thought to yield unique information about such molecular information as the molecular weight distribution of a linear polymer melt.[1,2] The rheometric measurements usually follow the standard analysis that is based on three key assumptions: (1) no-slip boundary conditions and (2) homogeneous velocity profile during shear as shown in Figure 1a and (3) relaxation upon shear cessation occurring without emergence of macroscopic motions. These assumptions about the state of deformation hold true by definition for linear viscoelastic measurements and have been the basis of most rheometric studies in the literature. The most common rheometric setup[3] is a rotational shear device involving either cone−plate (see the middle figure in TOC graphic) or parallel-plate (disk) shear cell, where the typical sample thickness H is macroscopic, in the range 0.1−1 mm.

Polymer scientists and engineers have also performed nonlinear rheological studies[4] to learn more about the molecular structures including chain architecture.[5] In studies involving simple shear, the dominant nonlinearity is strain softening: both the relaxation modulus and steady-shear viscosity of entangled polymers are lower than their values in the linear response regime. In absence of any direct evidence to contradict, in the past we assumed that such strain softening had occurred in a homogeneous manner.

To verify whether this is the case, we have recently developed an *in situ* particle-tracking velocimetric (PTV) method as shown in the middle figure of the TOC graphic.[6] The combination of rheometric and PTV measurements revealed a clear violation of each of the three basic assumptions listed in the first paragraph. In other words, shear inhomogeneity was found to take place cone−plate shear cell during startup shear[7−10] and large-amplitude oscillatory shear.[11] Entangled solutions[12] and melts[13] were not quiescent upon shear cessation from a large step strain. Thus, the nonlinear responses of entangled polymers appear far more complicated than previously revealed. In other words, when using any commercial rheometer for simple shear, we could no longer assume *a priori* that the states of deformation and flow are homogeneous.

In this Perspective, we indicate some guidance for future rheological experiments by showing when, how, and why the three basic assumptions in polymer rheology may be invalid. We first briefly review a primary type of shear inhomogeneity, i.e., wall slip, as schematically illustrated in Figure 1b. We then describe when nonlinear rheological measurements might be complicated by such effects as edge fracture. Subsequently, we enumerate the situations where shear homogeneity prevails before discussing a relation between wall slip and shear banding. We summarize the available results in terms a phase diagram to map out the parameter space and to show where shear homogeneity, wall slip, and shear banding (schematically illustrated in Figure 1c) are "located". We conclude by indicating what we still do not know and the theoretical implications of the emerging PTV observations.

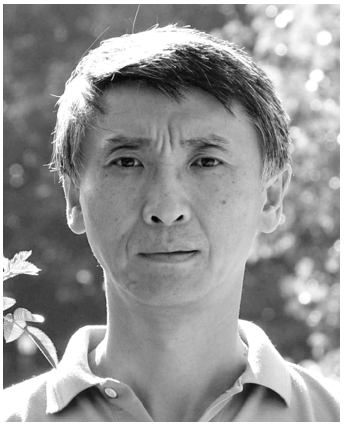
2. Wall Slip: Primary Example of Shear Inhomogeneity and How To Minimize

Entangled linear polymeric liquids can display one unique property that nonentangled liquids do not possess: They are capable of macroscopically measurable wall slip. Phenomena involving polymer wall slip have been reported since the 1950s.[14−20] De Gennes[21] offered in 1979 the first understanding of why entangled polymers have the ability to display observable wall slip on macroscopic scales. According to de Gennes, slip can be quantified by the extrapolation length b defined in Figure 1b and can be macroscopically large due to the high shear viscosity η originating from chain entanglement. Specifically, it can be

*Corresponding author. E-mail: swang@uakron.edu.

© 2011 American Chemical Society

Published on Web 01/18/2011



Shi-Qing Wang is Professor of Polymer Science at the University of Akron. He obtained a BS in Physics from Wuhan University in China before receiving his Ph.D. in Physics from the University of Chicago in 1987 and did postdoctoral studies in the Department of Chemistry at UCLA before joining the Department of Macromolecular Science and Engineering at Case Western Reserve University in Fall 1989. Dr. Wang was elected an APS Fellow in 1997. Since Fall 2000, he has been in his current position. His research interests are in polymer physics, particularly interfaces, dynamics, and rheology of entangled polymeric materials. Since summer 2006, Dr. Wang has made at least one visit each year to different academic institutions in China, where he has been made a guest professor in Beijing University of Chemical Technology, Nanjing University, University of Science and Technology of China, and Changchun Institute of Applied Chemistry of the Chinese Academy of Sciences.

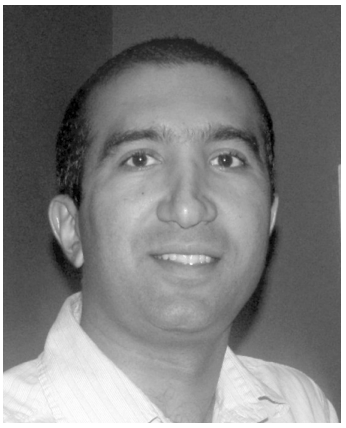


Sham Ravindranath obtained his B.E. in Polymer Science and Technology from Sri Jayachamarajendra College of Engineering, Visvesvaraya Technological University, India. He received his Ph.D in Polymer Science from University of Akron. His doctoral work focused on understanding the nonlinear rheology of entangled polymer solutions in Professor Shi-Qing Wang's group. He is currently working as Analytical Scientist in Celanese/Ticona.

readily shown that[21,22]

$$b = (\eta/\eta_i)a \tag{1}$$

where η is the shear viscosity in the bulk, η_i is a local viscosity at the polymer/wall interface, and a is the interfacial slip-layer thickness of a molecular dimension. This viscosity ratio can be exceedingly large, allowing b to attain a macroscopic magnitude when the value of η_i diminishes as a consequence of either chain desorption or disengagement of adsorbed chain from the bulk entanglement network.[22] Subsequent to de Gennes' analysis,[21] a number of studies were devoted to theoretical[23−25] and experimental accounts[26−34] of steady-state wall slip.[22,35] Since wall slip is such an important rheological character of entangled polymers, we describe it in some detail in Appendix A. In particular, we illustrate in Appendix A why both entangled solutions and melts could exhibit significant wall slip. In Appendix B, we present a list of nomenclatures to ease the reading of this paper.



Pouyan E. Boukany obtained his B.S and M.S degree in Textile Engineering with major in Textile Chemistry and Fiber Science from the Isfahan University of Technology, Iran. He received his Ph.D in Polymer Science from University of Akron. His doctoral work explored various aspects of nonlinear responses of entangled liquids ranging from DNA fluids to entangled polymer melts in Professor Shi-Qing Wang's group. He is currently a Postdoctoral Research Associate working with Professor L. James Lee in the Center for Affordable Nanoengineering of Polymeric Biomedical Devices at The Ohio State University.

Because polymeric materials, particularly entangled polymers, are prone to wall slip, rheometric measurements of nonlinear behavior can be difficult to interpret. Many of the nonlinear rheological measurements of entangled polymer solutions and melts in the literature might have involved wall slip. This may be particularly true in the large step strain studies[36−41] of well-entangled polymer solutions made with small organic liquids as solvents. In other words, wall slip[42] is likely the cause[28] for the observed ultra strain softening[37−40] in stress relaxation from step strain that deviated from the prediction[43] of the Doi−Edwards tube model.[44] Even when the experimental data agree with the model calculation,[38] interfacial failure can be present after shear cessation as revealed recently in a PTV study.[12] More discussion on the development of the tube theory in the context of continuous shear is provided in Appendix C.

For entangled solutions, eq A.4 in Appendix A explains why wall slip could be present in previous studies of entangled polymer solutions in both step shear[36−40] and continuous shear[45] due to use of small molecular organic solvents with a water-like viscosity η_s. Because of the low η_s in the dominator of eq A.4, b_{max} can be comparable to or larger than the sample thickness H. Solutions with higher concentration c or polymer molecular weight M_w are more affected by wall slip in their nonlinear rheological measurements. This explains why there is more strain softening in a step strain test when cM_w is higher.[37−40]

For entangled polymer solutions that show significant wall slip,[46,47] we have confirmed two ways to minimize slip. An effective way to get rid of wall slip stems from our understanding of what parameters control the magnitude of wall slip. It has been shown that the degree of wall slip can be reduced by using an entangled polymeric solvent.[12,48] In other words, eq A.4 for b_{max} not only explains why polymer solutions can undergo strong wall slip but also points to an effective way to minimize wall slip. According to a previous study,[49] the solution viscosity η does not increase proportionally with the solvent viscosity η_s when the polymeric solvent's molecular weight increases. Thus, b_{max} of eq A.4 can be considerably reduced by using a polymeric

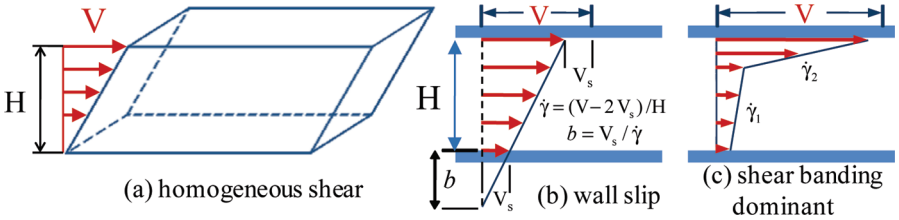


Figure 1. (a) 3-D view of homogeneous shear at an apparent shear rate $\dot{\gamma}_{app} = V/H$ in absence of wall slip. (b) Side view: velocity profile in presence of wall slip on two identical shearing surfaces, when $\dot{\gamma}_{app}\tau > 1$, with τ being the dominant chain relaxation time. When a slip velocity V_s is present, the amount of slip can be quantified by the extrapolation length b defined in the figure involving the bulk shear rate $\dot{\gamma}$. (c) Side view: bulk shear banding along with a small amount of wall slip is a characteristic response of well-entangled linear polymer solutions during startup shear at high rates when wall slip alone can no longer prevent the sample bulk from shearing at rates higher than the dominant relaxation rate $1/\tau$.

solvent of sufficiently high molecular weight.[12] Surface roughness has been demonstrated to be effective in reducing wall slip.[32] We have also used sandpapers as the shear surfaces to produce shear banding in a solution that would only exhibit interfacial failure on smooth surfaces.[48,50]

Well-entangled melts undergo even greater amount of wall slip:[21,22,34,51] The maximum value b_{max} is inherently dictated by the degree of chain entanglement, as expressed in eq A.1. Thus, for well-entangled linear polybutadiene melts with a large b_{max}, large step strain tests could only demonstrate ultra strain softening,[52] resulting from wall slip. We must have some means for the shear surfaces to grab polymer melts so that sufficient shear deformation can be exerted on the sample to probe its intrinsic nonlinear rheological responses. For certain melts such as styrene−butadiene rubber (SBR) with high vinyl content, we have demonstrated that various superglues can effectively fix the samples onto solid surfaces so that simple shear can take place in sliding plate without wall slip.[13]

3. Meniscus Instability or Edge Fracture

Simple shear in rotational device, e.g., cone−plate or parallel-disk or circular Couette (coconcentric cylinders), can in principle reach a steady rheological state. In reality, such geometries leave a rim of meniscus exposed to the ambient air. Since the free surface is cohesively weaker, highly viscoelastic materials such as strongly entangled polymer melts and solutions are often found to undergo edge or meniscus instability upon significant strains. This finite size effect severely constrains rheometric studies of large deformation behavior.

The intrinsic difficulty of meniscus instability in rotational rheometry can be successfully dealt with by using a cone-partitioned plate (CPP) setup to decouple rheometric measurements from any disturbance due to the edge fracture. In CCP, there is a rotating cone as in a conventional cone−plate setup, and the stationary surface is made of two pieces: an inner disk linked to the torque transducer and an outer ring unattached to the inner disk. Because the inner disk and the ring are not physically connected, any edge fracture or instability occurring over the ring region would not affect the rheometric measurements. Figure 1 of ref 10 depicted such a CPP device coupled with particle-tracking velocimetric (PTV) capability. For entangled polymer solutions, CPP appears to ensure reliable characterization during (a) steady-state continuous shear,[10] (b) large-amplitude oscillatory shear of linear polymer melts,[53] and (c) nonquiescent relaxation after a large step shear.[54]

4. Particle-Tracking Velocimetry: A Necessary Tool in Nonlinear Rheometry

In complicated setups such as channel flow, particle tracking has been applied to visualize the state of polymer flow since 1950s.[55−57] In most cases, capillary flow in the entrance and channel flow in die land have been observed using either particle-tracking[55−59] or laser Doppler velocimetry.[60,61] Such visualization is informative and necessary because the flow field is unknown *a priori*. Particle tracking velocimetry has been applied to visualize complex flow behavior of other fluids.[62−66]

In simple-shear rheometry we have often conveniently assumed that the state of deformation or flow would be homogeneous independent of the constitutive properties of entangled polymers. Typically, rheometric studies of entangled polymers have been carried out on the basis of shear homogeneity, and no commercial rheometers have been designed to directly probe the velocity field in such shear cells as cone−plate or parallel disk. We have recently recognized the need to independently measure the states of deformation and flow during startup shear, large-amplitude oscillatory shear, and step shear. Specifically, an effective PTV method[6] has been implemented to determine whether entangled polymer solutions (made with polymeric solvents) would undergo inhomogeneous shear instead of, or in addition, to wall slip. Because of the revelation of wall slip and shear banding through the PTV observations,[6] the PTV measurements should now be regarded as an indispensable part of any nonlinear rheological study of highly viscoelastic materials including entangled polymers. It is worth noting in passing that the time resolution of our PTV method is only limited by the camera speed, whereas the previous attempts placed a CCD camera along the velocity gradient direction and could only image the shear−vorticity plane one layer at a time.[28,67] In fact, because of the poor vertical resolution, this arrangement may only be effective to monitor wall slip behavior at the sample/plate interface.

5. The Roadmap for Nonlinear Rheology of Entangled Polymers

In this section we begin by indicating the situations where rapid external shearing fields would not result in inhomogeneous deformation and flow. Then we discuss the relation between wall slip and shear banding. We close by presenting a phase diagram to summarize what can be expected in startup continuous shear.

5.1. Homogeneous Shear with $Wi_{app} > 1$ and Quiescent Relaxation after Step Shear. We enumerate several conditions, under which homogeneous shear and quiescent relaxation prevail so that rheometric measurements may receive straightforward interpretation. When the apparent Weissenberg number $Wi_{app} = \dot{\gamma}_{app}\tau > 1$, shear homogeneity can still prevail under the following circumstances.

(a) When an entangled polymer solution is not strongly entangled, we have $b_{max}/H \ll 1$. Consequently, neither wall slip nor shear banding is observable. In other words, the steady-state profile tends to be homogeneous although transient shear inhomogeneity may occur.[9,68,69]

(b) Even when the entanglement level is high, shear inhomogeneity can be suppressed[10,48] during startup shear by reducing the extrapolation length b_{max} using a polymeric solvent of sufficiently high molecular weight to produce a large η_s in eq A.4.

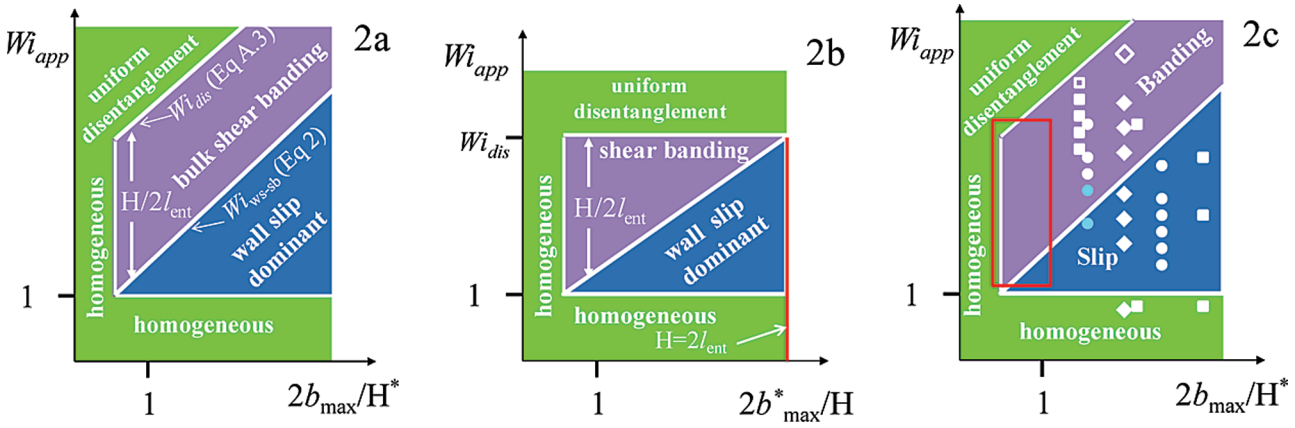


Figure 2. Phase diagrams in the parameter space of Wi_{app} vs $2b_{max}/H$ (double log scales) to map out the different responses in terms of the state of deformation for (a) a fixed sample thickness so that b_{max}/H^* simply denotes the level of chain entanglement and (b) a given sample so that b^*_{max}/H increases with lowering H until the upper bound is reached at $H = 2l_{ent}$ when only wall slip is possible, moving along the red vertical line. (c) Regions of the phase diagram where PTV studies have been carried out, including the small b_{max}/H regime inside the rectangle, and six solutions of different $2b_{max}/H$ equal to 22, 26, 136, 140, 259, and 1470. The open symbols indicate approximate shear homogeneity.

Table 1. Five PTV Studies of Entangled Solutions of Different Ability To Undergo Slip[a]

references	samples	solution viscosity (kPa)	solvent viscosity (Pa)	$2b_{max}/H$	Wi_{app}	PTV observations of steady state
ref 9	0.7M(5%)-2K	21	97	0.01	10−150	no slip, no banding
	0.7M(10%)-9K	57	10	0.2	15−50	only transient banding
	1M(15%)-9K	510	10	1.5	45−400	banding
ref 10	1M(10%)-1.5K	50	0.7	3	16−110	slip, banding
	1M(10%)-15K	250	36	0.27	14−140	no slip, no banding
ref 72 (diamond symbols in Figure 2c)	1% DNA solution water based	190	0.001	136	14−14000	slip, banding
ref 50 (square symbols in Figure 2)	water based	5.8	0.001	1470	0.5−220	slip
	ethylene glycol based	13	0.023	142	0.9, 750	banding
	glycerol based	58	0.7	22	950−22800	banding
ref 75 at a low gap of $H = 50\ \mu$m (circle symbols in Figure 2c)	1M(13%)-1.5K	130	0.7	259	12−240	slip
	1M(13%)-10K	600	14	26	20−390	slip, banding

[a] $H = 800-900\ \mu$m for the first four papers. The last column indicates available PTV results.

(c) When $b/H \ll 1$, macroscopic motions after a large step strain may not be observable. In other words, with $b/H \ll 1$, no macroscopic motions take place during the relaxation.[48]

(d) Preliminary evidence based on both entangled DNA[70] and polymer[71] solutions indicates that shear banding observed upon sudden startup shear can be avoided if the shear rate is gradually approached from the Newtonian regime.

(e) Shear homogeneity has been observed to return at sufficiently high rates where no entanglement network structure could survive.[9,69] This condition corresponding to a Weissenberg number Wi_{dis} is discussed in some detail in Appendix A.

5.2. Relationship between Wall Slip and Bulk Shear Banding. Wall slip usually precedes any bulk inhomogeneous response to an external shearing field because polymer/wall interface typically has weaker adhesion than the cohesion of entangled polymers. Because of wall slip sketched in Figure 1b, the sample bulk can avoid high shear and stay in the Newtonian regime ($Wi_{app} < 1$) until an apparent rate $\dot{\gamma}_{app}$, corresponding to a critical Weissenberg number[50,72]

$$Wi_{ws\text{-}sb} = 1 + 2b_{max}/H \qquad (2)$$

where the subscript "ws-sb" denotes this critical shearing condition for the transition from wall slip to (bulk) shear banding. To estimate this critical condition, we have equated the bulk shear rate $\dot{\gamma}_c$ at the borderline between the Newtonian and shear thinning regimes to the reciprocal relaxation time $1/\tau$, i.e., $\dot{\gamma}_c\tau = 1$. The expression b_{max} is given by eq A.1 for entangled melts and by eq A.4 for entangled solutions in Appendix A. According to eq 2, the higher the value of b_{max}/H, the wider range of the apparent rate is for the wall slip to be the dominant response. A more recent study involved only this slip regime because $Wi_{app} \ll Wi_{ws\text{-}sb}$ in their experiments.[73] When $Wi_{app} > Wi_{ws\text{-}sb}$, shear banding may be expected to emerge for well-entangled polymers. Moreover, bulk shear banding could emerge at a much lower value of Wi_{app} than $Wi_{ws\text{-}sb}$ when rough shearing surfaces are used to remove wall slip. For example, surfaces made of sandpaper can effectively reduce wall slip so that shear banding takes its place.[48,50]

5.3. The "Phase Diagram". Clearly, b_{max}/H is the key parameter to control the nonlinear rheology of entangled polymers, dictating when and what type of shear inhomogeneity may occur for a given apparent Weissenberg number Wi_{app}. Here we summarize what we know about the nonlinear rheological responses to startup shear in terms of a phase diagram as shown in Figure 2a, where for a fixed gap distance H^* the X axis of $2b_{max}/H^*$ is controlled by b_{max}. For linear-chain melts, eq A.1 shows how the molecular weight dictates the magnitude of b_{max}. For entangled solutions made with polymeric solvents, besides the molecular weight of the solute, the solvent viscosity η_s can also alter b_{max} according to eq A.4. For a given polymeric system, i.e., for a fixed b^*_{max}, varying H would have the consequence shown in Figure 2b.

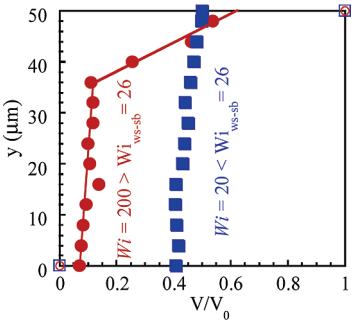


Figure 3. PTV observations of steady-state shear in a gap of $H = 50\,\mu$m at two different rates of 0.3 and 3.0 s^{-1} for an entangled solution of 13 wt % polybutadiene ($M_w \sim 10^3$ kg/mol) in a polybutadiene solvent ($M_w \sim 10$ kg/mol).

In both (a) and (b) of Figure 2, at small values of b_{max}/H, we have the vertical "homogeneous" strips to the left of the vertical white lines. The inclined white borderline between wall slip and shear banding is given by eq 2. The boundary between "uniform disentanglement" and "shear banding" is depicted by eq A.3 or eq A.6, which is inclined in Figure 2a and horizontal in Figure 2b. Actually, Figure 2a is somewhat analogous to Figure 6 of ref 6. Both (a) and (b) of Figure 2 serve as a roadmap for the steady-state behavior of well-entangled polymers in startup shear.

We can summarize the available results from the literature[74] in Figure 2c as well as in Table 1 that lists five PTV-based studies[9,10,50,72,75] on 11 entangled solutions. Here the specification of the various 1,4-polybutadiene (PB) solutions follows the following convention: 0.7M(5%)-2K means 5 wt % of 1,4-PB with molecular weight equal to 0.7×10^6 g/mol in a PB solvent of molecular weight equal to 2 kg/mol. The first two papers in Table 1 focused on the phase space circled by the (red) rectangle in Figure 2c in the region of $2b_{max}/H < 1$. We specifically mark the other regions corresponding to the other six solutions listed at the bottom of Table 1, having respectively $2b_{max}/H$ equal to 136, 1470, 142, 22, 259 and 26. Here both axes, i.e., Wi and $2b/H$, are implicitly on logarithmic scales. Particularly worth mentioning is the system with $2b_{max}/H = 26$ represented by the five circles that shows both slip dominant and shear banding prevailing features as the applied shear rate increases.

Also special about this study[75] is the significantly reduced sample thickness from a conventional rheometric dimension of ca. 1000 to 50 μm. Reducing H broadens the window for wall-slip-dominated rheological responses, leading some to suggest[76] that wall slip would be the only characteristic rheological response of entangled polymers. Indeed, when we reduce H from 1 mm to 50 μm, a sample that would not show significant wall slip "suddenly" does. However, Figure 3 shows that the wall-slip dominant response switches to bulk shear banding behavior as the applied rate crosses the predicted borderline given by eq 2, represented by the two (light blue) circles in Figure 2c. This switch would always occur unless the sample thickness H becomes comparable to the entanglement spacing l_{ent}. Figure 2b shows that the shear banding regime shrinks to zero only at the red vertical line at $H = l_{ent}/2$. The window for shear banding is given by $Wi_{dis}/Wi_{ws\text{-}sb} = H/2l_{ent}$, as indicated in Figure 2a,b.

6. Unresolved Questions in Both Shear and Extensional Rheometry

We close by listing a number of important issues that we have either not resolved or only obtained partial, preliminary answers. Our PTV method has its natural constraints. In particular, startup continuous shear over a large amount of strain units always requires wrapping a film around the meniscus to prevent sample loss. Sometimes, air bubbles are trapped during sample loading. Small bubbles are difficult to remove under vacuum. The role of bubbles remains to be clarified.

Moreover, many questions remain as listed in no particular order that future studies must deal with:

(1) Shear banding appears not to be a steady-state property for entangled polymers. At least for solutions, we were able to achieve homogeneous shear by very gradual rate ramp-up instead of a sudden startup shear.[70,71] It remains to be seen whether the same is true for entangled melts.

(2) Only a handful of studies exist in the literature on transient rheological behavior of *melts* during startup shear.[13,77,78] Rheological measurements along with PTV observations of *steady shear* behavior of *entangled melts* remain to be carried out.

(3) During startup shear, shear banding emerges after the shear stress maximum where the high shear band is usually adjacent to the moving surface and low shear band stays next to the stationary surface. The origin of this *symmetry breaking* is elusive and could be related to the presence of polymer/wall interfaces although the initial elastic deformation is homogeneous.

(4) The cohesive breakdown, i.e., *elastic yielding* after a large step shear, appears to occur within the sample thickness at unpredictable locations for entangled solutions although styrene−butadiene rubbers show failure in the midplane when they are well adhered to the shear surfaces by superglue.[13] More data are required to show whether the failure location is truly random.

(5) Macroscopic shear inhomogeneity has been observed in various entangled polymeric liquids. However, the PTV technique cannot detect any *microscopic structural inhomogeneity* on micrometer to submicrometer length scales. Systematic small-angle neutron scattering experiments should be carried out during shear banding to probe any microscopic structural inhomogeneity as a consequence of chain disentanglement. Preliminary experiments found some submicrometer structural development during shear.[79]

(6) Other complementary methods including optical birefringence and small-angle X-ray scattering along the vorticity direction would help gathering more information in a spatial-resolved manner about the nature of the shear inhomogeneity.

(7) So far, most studies focused on monodisperse samples. It remains to be demonstrated how shear inhomogeneity weakens with increasing *polydispersity* in the molecular weight distribution.[8] PTV studies have yet to be carried out for miscible and immiscible blends in the nonlinear response regimes.

7. Summary: Localized Yielding in Entangled Polymers

In such standard rheometric tests as startup shear and step shear, the PTV observations offer fresh insight into the nature of rheological responses of entangled polymers. A sudden startup simple-shear produces the well-known stress overshoot, which is an indication of yielding[80] with universal scaling characteristics:[81,82] At the shear stress maximum, the system reaches a force imbalance between the growing elastic (intrachain) retraction force and intermolecular gripping force,[83] beyond which further deformation of the entanglement network is no longer possible and chains mutually slide past one another to approach a state of flow.[84] This transformation is a cohesive failure that can occur in a spatially localized manner in simple-shear apparatuses. In a large step strain test, instead of quiescent relaxation as perceived in previous experimental and theoretical studies, macroscopic motions were observed after shear cessation.[12,13] For systems with a sizeable b_{max}/H, quiescent relaxation only occurs when the amplitude of step strain is below one strain unity, implying that the entanglement network has a characteristic level of cohesion on shorter time scales than the terminal relaxation

time τ. The nonquiescent relaxation indicates that sufficient residual elastic retraction force can overcome the network's cohesion, locally transforming this elastically strained "solid" into a liquid. When this elastic yielding occurs inhomogeneously in space, macroscopic motions naturally arise: a solid region can sustain stress but a liquid region cannot. This elastic yielding upon step strain[83] is a unique nonlinear rheological response of entangled polymers and can be most straightforwardly demonstrated using PTV without any experimental difficulty such as edge fracture because of the small amount of strain involved.

Finally, a word is due about the theoretical situation. Is there any theory to account for the observed shear banding? If shear banding exists in steady state, then one needs a constitutive theory that allows the shear rate to be double-valued for a given stress. But if this shear banding can be avoided by a slow rate ramp-up, then we have to resort to a different theory that prescribes a one-to-one correspondence between stress and rate simple shear. However, such a monotonic constitutive theory would not permit any shear banding to prevail upon a sudden startup shear. Thus, if the conclusions of refs 70 and 71 are true, we would not be able to resort to any version of the tube model for a proper theoretical description of the experimental observations.

Acknowledgment. This work is supported, in part, by a grant (DMR-0821697) from the US National Science Foundation.

Appendix A. Account of Wall Slip and Ultimate Homogeneous Shear

When the apparent shear rate V/H indicated in Figure 1a is below the slowest relaxation rate $1/\tau$ of an entangled polymer, i.e., $(V/H)\tau < 1$, the amount of external shear deformation is lower than unity within the relaxation time τ. As a consequence, the entanglement network does not deform sufficiently to break up elastically. In other words, under this condition, there is no chain disentanglement at either the polymer/wall interface or in the bulk. Homogeneous shear prevails as shown in Figure 1a. The viscosity ratio in eq 1 is on the order of unity, and b is only molecularly small.

When the apparent Weissenberg number $Wi_{app} = (V/H)\tau$ is much higher than unity, the adsorbed chains cannot remain engaged with the bulk chain entanglement network indefinitely during startup simple shear. Such interfacial yielding[34] produces an interfacial layer (of thickness a) with a greatly reduced viscosity η_i. Consequently, b can be millions of times a, i.e., macroscopically large according to eq 1. For an entangled linear polymer melt with (weight-average) molecular weight M_w, the maximum value of b can be estimated,[22] upon complete interfacial chain disengagement by conducting a controlled-stress experiment to produce a stick−slip transition (that occurs near the end of the Newtonian regime),[51] to be related to the Newtonian viscosity η_0

$$b_{max} = (\eta_0/\eta_e)l_{ent} = (M_w/M_e)^{3.4}l_{ent}, \quad \text{for entangled melts} \tag{A.1}$$

when η_i in eq 1 turns into η_e, which is that of a melt with entanglement molecular weight M_e. Equation A.1 assumes the slip layer thickness to be the entanglement spacing l_{ent}, related to M_e as[85,86] $(M_e/\rho N_A p)^{1/2}$, where ρ is the polymer mass density, p is the packing length, and N_A is the Avogadro constant. Here we adopted the empirical exponent 3.4 to depict the molecular weight dependence of η_0. The viscosity ratio in eq A.1 can readily approach 10^6, making b_{max} macroscopically large, for polymer melts, especially polyethylene, polybutadiene, and polyisoprene that are usually highly entangled.

Industrial polymer processing always occurs in the shear thinning regime. Under a typical processing condition the limit of homogeneous shear at Wi_{dis}, which is discussed in eq A.3, is not accessible for well-entangled polymers. Even for a sample with $M_w \sim 10M_e$, it requires $Wi_{dis} \sim 10^{3.4} = 2512$ to reach this regime. On the other hand, since wall slip occurs whenever the Weissenberg number Wi is greater than unity, wall slip is highly relevant for processing. However, the magnitude of wall slip, as characterized by b_{max} of eq A.1, is usually not large for polymers such as polystyrene (PS) because the processable PS typically only have 10−20 entanglements per chain, corresponding to a molecular weight range of 130−260 kg/mol; i.e., b_{max} would not exceed $7.7 \times 20^{3.4} = 0.2$ mm, where the entanglement spacing is 7.7 nm for PS. This value is smaller than the typical dimensions of processing equipment. On the other hand, polymers such as linear polyethylenes (PE) of both high and low density and polybutadiene (PB) suffer significant wall slip because the number of entanglement per chain readily exceeds 100 in these polymers, with the entanglement molecular weight being as low as 0.9 and 1.6 kg/mol for PE and 1,4-PB, respectively. Thus, the magnitude of b_{max} can easily exceed 10 mm.

For monodisperse well-entangled polymer, there may exist a rather broad stress plateau whose width, depicted in terms of the range of the apparent rate, is bounded on the low end by $\dot\gamma_c \sim 1/\tau$ and the on the high end, we assert, by the local shear rate $\dot\gamma_{dis}$ found in the entanglement-free slip layer upon maximum slip. At the onset of shear thinning, we have shear stress $\eta_0\dot\gamma_c$ in the bulk and $\eta_e\dot\gamma_{dis}$ in the slip layer. Thus, we arrive at

$$\dot\gamma_{dis} = (\eta_0/\eta_e)\dot\gamma_c = (\dot\gamma_c\tau)/\tau_e \sim 1/\tau_e \tag{A.2}$$

where $\eta_0/\eta_e = \tau/\tau_e$ follows from the tube model,[44] with the confinement time τ_e is related to the dominant relaxation (i.e., reptation) time τ as $\tau_e = \tau(M_e/M_w)^{3.4}$. The corresponding Weissenberg number Wi_{dis} is given by

$$Wi_{dis} = \dot\gamma_{dis}\tau = \tau/\tau_e = b_{max}/l_{ent} \tag{A.3}$$

which is given by $(M_w/M_e)^{3.4}$ for melts according eq A.1, where the last equality follows from eq A.1.

For an entangled polymer solution with polymer weight fraction ϕ, complete slip corresponds to having η_i in eq 1 reduced to the solvent viscosity η_s, where a may also be thought of as the enlarged entanglement spacing[49,87] $l_{ent}(\phi) = l_{ent}\phi^{-0.6}$, so that we rewrite eq 1 as

$$b_{max}(\phi) = [\eta_0(\phi)/\eta_s]l_{ent}(\phi), \quad \text{for entangled polymer solutions} \tag{A.4}$$

Since η_s can be as low as 10^{-3} Pa·s (i.e., that of water), entangled solutions could also display significant wall slip. Similar to eq A.2, the local shear rate in the slip layer upon complete slip is given by

$$\dot\gamma_{dis} = [\eta_0(\phi)/\eta_s]\dot\gamma_c \tag{A.5}$$

which can be rewritten in terms of the corresponding Weissenberg number Wi_{dis} as

$$Wi_{dis} = \dot\gamma_{dis}\tau(\phi) = [\dot\gamma_c\tau(\phi)][\eta_0(\phi)/\eta_s] \sim \eta(\phi)/\eta_s = b_{max}(\phi)/l_{ent}(\phi) \tag{A.6}$$

where the last equality follows from eq A.4, and the product $\dot\gamma_c\tau$ is on the order of unity. Note that eq A.6 is of the same form as eq A.3.

Homogeneous shear should occur upon complete chain disentanglement when the imposed rate is as high as the local shear rate $\dot\gamma_{dis}$ in the slip layer during maximum wall slip. This critical shear rate is given by eq A.2 for melts and by eq A.5 for solutions corresponding to a Weissenberg number Wi_{dis} that is related to the maximum slip length b_{max} as $Wi_{dis} = b_{max}/l_{ent}$ as shown in eqs A.3 and A.6.

Appendix B. Nomenclature

Glossary

a	interfacial slip layer thickness
b, b_{max}	extrapolation length or slip length, and its maximum value, for melts and solutions
ϕ	polymer concentration in terms of the weight fraction
$\dot{\gamma}_{app}$	apparent shear rate or nominal shear rate
$\dot{\gamma}_{dis}$	shear rate to reach homogeneous fully disentangled state
$\dot{\gamma}_c$	onset shear rate for shear thinning, equal to $1/\tau$
$l_{ent}(\phi)$	entanglement spacing of solution at concentration ϕ
l_{ent}	entanglement spacing of melt
V_s	slip velocity
τ	dominant or overall relaxation time of polymer melt
$\tau(\phi)$	longest relaxation time of solution at ϕ
τ_e	entanglement confinement time
H	typical dimension of a rheometric setup such as the gap distance
η_0	zero-shear melt viscosity
$\eta_0(\phi)$	zero-shear solution viscosity at polymer concentration ϕ
η_i	viscosity at the polymer/wall interface
η_e	zero-shear viscosity of a Rouse melt at M_e
η_s	solvent viscosity
Wi_{app}	Weissenberg number equal to $\dot{\gamma}_{app}\tau$
Wi_{dis}	Weissenberg number corresponding to $\dot{\gamma}_{dis}$
$Wi_{ws\text{-}sb}$	critical Weissenberg number, beyond which wall slip is expected to evolve to bulk shear banding

Appendix C. Brief Survey of the Tube Theory Concerning Shear Banding

The original 1978–1979 tube model[44] of Doi and Edwards revealed a nonmonotonic constitutive relation in its calculation. The nonmonotonicity occurs because of excessive chain alignment in the shearing direction. It has the same physical origin as the shear stress overshoot that the tube theory is able to produce.[88] They and subsequently others related such a feature to a flow instability (known as the stick−slip transition[22,51]) observed in capillary rheometry.[89,90] Subsequently, it was proposed in a 1993 theoretical study[91] that shear banding could occur in entangled polymer solutions under simple shear. The experimental report for shear banding, inspired by this theoretical analysis, was made in 1996 for wormlike micellar solutions.[92,93] Because the wormlike micelles are capable of adjusting their sizes in shear and may even suffer breakage by shear,[100,101,102] shear banding in wormlike micellar solutions[94−103] was not taken to imply that conventional noncharged, nonassociative polymers would also shear inhomogeneously. In the decade between 1996 and 2005, a couple of studies reported a hint of shear banding in semidilute polyacrylamide/water solutions where chain−chain associations occur through hydrogen bonding.[104,105] Apart from this special case, the important premise of shear homogeneity had never been observed to break down for entangled polymer liquids. In absence of a perfect stress plateau in the steady state flow curve and any direct evidence of shear inhomogeneity, major modifications[106,107] including the introduction of convective constraint release[108] were made to make sure that the tube model does not prescribe a nonmonotonic constitutive relation for entangled polymers.

References and Notes

(1) Wasserman, S. H.; Graessley, W. W. *J. Rheol.* **1992**, *36*, 543.
(2) Mead, D. W. *J. Rheol.* **1994**, *38*, 1797.
(3) Macosko, C. W. *Rheology: Principles, Measurements and Applications*; VCH: New York, 1994.
(4) Nonlinear rheological responses occur in (a) continuous shear, (b) large-amplitude oscillatory shear, and (c) large step shear. In (a), one finds the steady-state shear stress is no longer linearly proportional to the shear rate $\dot{\gamma}_{app}$ when $\dot{\gamma}_{app}\tau > 1$, where τ is the dominant chain relaxation time. In (b), the measured time-dependent shear stress is no longer linearly proportional to the strain amplitude γ_0 when γ_0 exceeds a critical value (which is on the order of unity for monodisperse entangled linear polymers) and the oscillatory frequency ω is higher than $1/\tau$. In (c), the resulting shear stress after a step strain relaxes in a quantitatively different way (from its relaxation behavior after a small step shear) when the amplitude of the step shear is large.
(5) For some recent publications invoking nonlinear rheological measurements to characterize polymer materials, see: (a) Tezel, A. K.; Oberhauser, J. P.; Graham, R. S.; et al. *J. Rheol.* **2009**, *53*, 1193. (b) Hoyle, D. M.; Harlen, O. G.; Auhl, D.; et al. *J. Rheol.* **2009**, *53*, 917. (c) Kapnistos, M.; Kirkwood, K. M.; Ramirez, J.; et al. *J. Rheol.* **2009**, *53*, 1133. (d) Lee, J. H.; Driva, P.; Hadjichristidis, N.; et al. *Macromolecules* **2009**, *42*, 1392. (e) Lee, J. H.; Orfanou, K.; Driva, P.; et al. *Macromolecules* **2008**, *41*, 9165.
(6) Wang, S. Q. *Macromol. Mater. Eng.* **2007**, *292*, 15.
(7) Tapadia, P.; Wang, S. Q. *Phys. Rev. Lett.* **2006**, *96*, 016001.
(8) Boukany, P. E.; Wang, S. Q. *J. Rheol.* **2007**, *51*, 217.
(9) Ravindranath, S.; et al. *Macromolecules* **2008**, *41*, 2663.
(10) Ravindranath, S.; Wang, S. Q. *J. Rheol.* **2008**, *52*, 957.
(11) Ravindranath, S.; Wang, S. Q. *J. Rheol.* **2008**, *52*, 341.
(12) Ravindranath, S.; Wang, S. Q. *Macromolecules* **2007**, *40*, 8031. This important PTV study of step strain pointed out that only a subset of experimental data happened to agree with the tube model calculation that assumes quiescent relaxation. Actually, Osaki et al. first found the disagreement in 1980 (i.e., ref 37) before reporting the far better known agreement in ref 38 in 1982. We showed in this paper that the agreement between the stress relaxation data and the tube model prediction was completely fortuitous because the simultaneous PTV observations revealed significant macroscopic motions after shear cessation, and yet the calculation was only valid for quiescent stress relaxation.
(13) Boukany, P. E.; Wang, S. Q. *Macromolecules* **2009**, *43*, 6261.
(14) (a) Tordella, J. P. *J. Appl. Phys.* **1956**, *27*, 454. (b) Tordella, J. P. *J. Appl. Polym. Sci.* **1963**, *7*, 215.
(15) Bagley, E. B.; Cabott, I. M.; West, D. C. *J. Appl. Phys.* **1958**, *29*, 109.
(16) Rielly, F. J.; Price, W. L. *SPE J.* **1961**, 1097.
(17) Benbow, J. J.; Lamb, P. *SPE Trans.* **1963**, *3*, 7.
(18) Blyler, L. L.; Hart, A. C. *Polym. Eng. Sci.* **1970**, *10*, 193.
(19) Bergem, N. *Proc. Int. Congr. Rheol., 7th, Gothenburg, Sweden* **1976**, 50.
(20) (a) Vinogradov, G. V. *J. Polym. Sci., Part A-2* **1972**, *10*, 1061. (b) Vinogradov, G. V.; Malkin, A. Y. *Rheology of Polymers - Viscoelasticity and Flow of Polymers*; Springer-Verlag: Berlin, 1980. Apparently, the view that wall slip in spurt flow is related to the sample undergoing a "fluid-to-rubber transition" has persisted to this date:(c) Malkin, A. Y.; Semakov, A. V.; Kulichikhin, V. G. *Adv. Colloid Interface Sci.* **2010**, *157*, 75.
(21) (a) De Gennes, P. G. *C. R. Acad. Sci.* **1979**, *288B*, 219. Here de Gennes contemplated a case where a melt was perceived to flow by a nonadsorbing wall and rediscovered Navier's account of wall slip: (b) Navier, C.-L. *Mémo Acad. R. Sci. Inst. France* **1823**, *6*, 414. This reference originates from:(c) Goldstein, S. *Modern Developments in Fluid Mechanics*; Oxford University Press: London, 1938; Vol. *2*, pp 676−680.
(22) Wang, S. Q. *Adv. Polym. Sci.* **1999**, *138*, 227. This review summarized the research carried out in the 1990s and mentioned key publications in the period from 1950 to 1990.
(23) Brochard, F.; de Gennes, P. G. *Langmuir* **1992**, *8*, 3033.
(24) Joshi, Y. M.; Lele, A. K.; Mashelkar, R. A. *J. Non-Newton. Fluid Mech.* **2000**, *89*, 103.
(25) Brochard-Wyart, F.; Gay, C.; deGennes, P. G. *Macromolecules* **1996**, *29*, 377.
(26) Hatzikiriakos, S. G.; Dealy, J. M. *J. Rheol.* **1992**, *36*, 703.
(27) Migler, K. B.; Hervet, H.; Leger, L. *Phys. Rev. Lett.* **1993**, *70*, 287.
(28) Archer, L. A.; Chen, Y. L.; Larson, R. G. *J. Rheol.* **1995**, *39*, 519.
(29) Wang, S. Q.; Drda, P. A. *Macromolecules* **1996**, *29*, 2627.
(30) Mhetar, V.; Archer, L. A. *Macromolecules* **1998**, *31*, 6639.
(31) Leger, L.; Raphael, E.; Hervet, H. *Adv. Polym. Sci.* **1999**, *138*, 185.
(32) Sanchez-Reyes, J.; Archer, L. A. *J. Rheol.* **2002**, *46*, 1239.
(33) Sanchez-Reyes, J.; Archer, L. A. *Langmuir* **2003**, *19*, 3304.
(34) Boukany, P. E.; Wang, S. Q. *Macromolecules* **2009**, *42*, 2222.

(35) Denn, M. M. *Ann. Rev. Fluid Mech.* **2001**, *33*, 265.
(36) Fukuda, M.; Osaki, K.; Kurata, M. *J. Polym. Sci., Polym. Phys.* **1975**, *13*, 1563.
(37) Osaki, K.; Kurata, M. *Macromolecules* **1980**, *13*, 671.
(38) Osaki, K.; Nishizawa, K.; Kurata, M. *Macromolecules* **1982**, *15*, 1068.
(39) Larson, R. G.; Khan, S. A.; Raju, V. R. *J. Rheol.* **1988**, *32*, 145.
(40) Morrison, F. A.; Larson, R. G. *J. Polym. Sci., Polym. Phys. Ed.* **1992**, *30*, 943.
(41) Archer, L. A.; Sanchez-Reyes, J. *Macromolecules* **2002**, *35*, 10216.
(42) Osaki, K. *Rheol. Acta* **1993**, *32*, 429. Although Osaki speculated about the possibility of wall slip, he was actually inclined toward a different explanation given by Marrucci, G. *J. Rheol.* **1983**, *27*, 433, which was prompted by the ultrastrain softening data of ref 52 on step strain of polybutadiene melts that could readily experience massive wall slip.
(43) Doi, M. *J. Polym. Sci.* **1980**, *18*, 1005.
(44) Doi, M.; Edwards, S. F. *The Theory of Polymer Dynamics*, 2nd ed.; Clarendon Press: Oxford, 1988.
(45) Menezes, E. V.; Graessley, W. W. *J. Polym. Sci., Polym. Phys. Ed.* **1982**, *20*, 1817.
(46) Mhetar, V.; Archer, L. A. *Macromolecules* **1998**, *31*, 6639.
(47) Plucktaveesak, N.; Wang, S. Q.; Halasa, A. *Macromolecules* **1999**, *32*, 3045.
(48) Ravindranath, S.; Wang, S. Q. *Rheol. Acta* **2010**, in press.
(49) (a) Wang, S. F.; Wang, S. Q.; Halasa, A.; Hsu, W.-L. *Macromolecules* **2003**, *36*, 5355. The conclusion of this paper disagrees with:(b) Struglinksi, M. J.; Graessley, W. W. *Macromolecules* **1985**, *18*, 2630.
(50) Boukany, P. E.; Wang, S. Q. *Soft Matter* **2009**, *5*, 780.
(51) Boukany, P. E.; Wang, S. Q. *J. Rheol.* **2006**, *50*, 641.
(52) Vrentas; Graessley, W. W. *J. Rheol.* **1982**, *26*, 359.
(53) Li, X.; Wang, S. Q.; Wang, X. R. *J. Rheol.* **2009**, *57*, 1255.
(54) Li, X.; Wang, S. Q. *Rheol. Acta* **2010**, *49*, 985.
(55) Tordella, J. P. *J. Rheol.* **1957**, *1*, 203.
(56) Galt, J. C.; Maxwell, B. *Mod. Plast.* **1964**, *42*, 115.
(57) White, J. L. US-Japan Seminar on Polymer Processing and Rheology. *Appl. Polym. Symp.* **1973**, *20*, 155.
(58) Rodriguez-Gonzalez, F.; Perez-Gonzalez, J.; Marin-Santibanez, B. M.; et al. *Chem. Eng. Sci.* **2009**, *64*, 4675.
(59) Ramamurthy, A. V. *Trans. Soc. Rheol.* **1974**, *18*, 431.
(60) Munstedt, H.; Schmidt, M.; Wassner, E. *J. Rheol.* **2000**, *44*, 413.
(61) Schwetz, M.; Munstedt, H.; Heindl, M.; et al. *J. Rheol.* **2002**, *46*, 797.
(62) Adrian, R. J. *Annu. Rev. Fluid Mech.* **1991**, *23*, 261.
(63) Maas, H. G.; Gruen, A.; Papantoniou, D. *Exp. Fluids* **1993**, *15*, 133.
(64) Cowen, E. A.; Monismith, S. G. *Exp. Fluids* **1997**, *22*, 199.
(65) Melling, A. *Meas. Sci. Technol.* **1997**, *8*, 1406.
(66) Adrian, R. J. *Exp. Fluids* **2005**, *39*, 159.
(67) Archer, L. A.; Larson, R. G.; Chen, Y. L. *J. Fluid Mech.* **1995**, *301*, 133.
(68) Hu, Y. T.; et al. *J. Rheol.* **2007**, *51*, 275. This rheometric setup is a circular Couette that has a finite shear stress gradient across the sample thickness. Sharp shear banding may not survive in presence of such a stress gradient for the moderately entangled polymer solutions under study.
(69) Boukany, P. E.; Wang, S. Q. *J. Rheol.* **2009**, *53*, 73.
(70) Boukany, P. E.; Wang, S. Q. *Macromolecules* **2010**, *43*, 6950.
(71) Cheng, S. W.; Ravindranath, S.; Chavan, V. S.; Quirk, R. P. To be submitted.
(72) Boukany, P. E.; Hu, Y. T.; Wang, S. Q. *Macromolecules* **2008**, *41*, 2644.
(73) Hayes, K. A.; et al. *Macromolecules* **2010**, *43*, 4412.
(74) We omit here the only other available data from ref 68 because we do not have the explicit information on the extrapolation lengths.
(75) Boukany, P. E.; Ravindranath, S.; Wang, S. Q.; Lee, L. J. To be submitted.
(76) Hayes, K. A.; et al. *Phys. Rev. Lett.* **2008**, *101*, 218301.
(77) Schweizer, T.; van Meerveld, J.; Öttinger, H. C. *J. Rheol.* **2004**, *48*, 1345.
(78) Auhl, D.; et al. *J. Rheol.* **2008**, *52*, 801.
(79) Wang, H.; Tapadia, P.; Wang, S. Q. Unpublished, **2005**.
(80) "In engineering, the transition from elastic behavior to plastic behavior is yield" according to Wikipedia http://en.wikipedia.org/wiki/Plasticity_%28physics%29. The flow is possible only after the underlying structure has yielded. This yielding concept is not very different from "yield" in the concept of yield-stress that describes mechanical response to external stress of materials such as ketchup and yogurt. In such yield-stress materials, the viscosity is very high and abruptly drops greatly over a narrow range of shear stress due to some stress-induced structure rearrangements; i.e., the structure that survives at low stresses yields to a new state of flow beyond a particular stress level. Yield-stress materials are usually amorphous and noncrystalline. Evans (Evans, I. D. *J. Rheol.* **1992**, *36*, 1313) settled the controversy brought up by Barnes and Walters (Barnes; Walters *Rheol. Acta* **1985**, *24*, 323).
(81) Ravindranath, S.; Wang, S. Q. *J. Rheol.* **2008**, *52*, 681.
(82) Boukany, P. E.; Wang, S. Q. *J. Rheol.* **2009**, *53*, 617.
(83) Wang, S. Q.; Ravindranath, S.; Wang., Y. Y.; Boukany, P. E. *J. Chem. Phys.* **2007**, *127*, 064903.
(84) Wang, Y. Y.; Wang, S. Q. *J. Rheol.* **2009**, *53*, 1389.
(85) Fetters.; et al. *Macromolecules* **1994**, *27*, 4639.
(86) Wang, S. Q. *Macromolecules* **2007**, *40*, 8684.
(87) Colby, R. H.; Rubinstein, M. *Macromolecules* **1990**, *23*, 2753.
(88) The physics of the stress overshoot is rich and has to do with yielding of the entanglement network and cannot be readily captured by the tube model calculation where the shear stress is calculated from the intrachain force of a single chain.
(89) Doi, M.; Edwards, S. F. *J. Chem. Soc., Faraday Trans. 2* **1979**, *75*, 38.
(90) McLeish, T. C. B.; Ball, R. C. *J. Polym. Sci., Polym. Phys.* **1986**, *24*, 1735.
(91) Cates, M. E.; McLeish, T. C. B.; Marrucci, G. *Europhys. Lett.* **1993**, *21*, 451.
(92) Callaghan, P. T.; et al. *J. Phys. II* **1996**, *6*, 375.
(93) Mair, R. W.; Callaghan, P. T. *Europhys. Lett.* **1996**, *36*, 719.
(94) Britton, M. M.; Callaghan, P. T. *Phys. Rev. Lett.* **1997**, *30*, 4930.
(95) Britton, M. M.; Mair, R. W.; Lambert, R. K.; Callaghan, P. T. *J. Rheol.* **1999**, *43*, 897.
(96) Fischer, E.; Callaghan, P. T. *Europhys. Lett.* **2000**, *50*, 803.
(97) Salmon, J. B.; Colin, A.; Manneville, S.; Molino, F. *Phys. Rev. Lett.* **2003**, *90*, 228303.
(98) Salmon, J. B.; Manneville, S.; Colin, A. *Phys. Rev. E* **2003**, *68*, 051503.
(99) Becu, L.; Manneville, S.; Colin, A. *Phys. Rev. Lett.* **2004**, *93*, 018301.
(100) Hu, Y. T.; Lips, A. *J. Rheol.* **2005**, *49*, 1001.
(101) Lopez-Gonzalez, M. R.; Holmes, W. M.; Callaghan, P. T. *Soft Matter* **2006**, *2*, 855.
(102) Boukany, P. E.; Wang, S. Q. *Macromolecules* **2008**, *41*, 1455.
(103) Ballesta, P.; Manneville, S. *J. Non-Newtonian Fluid Mech.* **2007**, *147*, 23.
(104) Britton, M. M.; Callaghan, P. T. *J. Rheol.* **1997**, *41*, 1365.
(105) Callaghan, P. T.; Gil, A. M. *Macromolecules* **2000**, *33*, 4116. It was concluded that "the origin of shear banding in (relatively polydisperse) polyacrylamide solutions is associated with hydrogen bond breakage above a critical shear rate". Such a conclusion was reached because other polymer (PS and PEO) solutions and poly(dimethylsiloxane) melt were found to display no shear banding: private communication with Paul T. Callaghan. PDMS is naturally polydisperse and consequently does not show shear banding, see:Li, X.; Wang, S. Q. *Rheol. Acta* **2010**, *49*, 89. We can indeed find a more recent example where hydrogen bonding seems to play a dominant role. See:van der Gucht, J.; et al. *Phys. Rev. Lett.* **2006**, *97*, 108301.
(106) Mead, D. W.; Larson, R. G.; Doi, M. *Macromolecules* **1998**, *31*, 7895.
(107) Graham, R. S.; Likhtman, A. E.; McLeish, T. C. B.; Milner, S. T. *J. Rheol.* **2003**, *47*, 1171.
(108) Marrucci, G. *J. Non-Newtonian Fluid Mech.* **1996**, *62*, 279.

Macromolecules
COMMUNICATION TO THE EDITOR

Macromolecules **2011**, *44*, 191–193 **191**
DOI: 10.1021/ma1019818

Polymer Tracer Diffusion Exhibits a Minimum in Nanocomposites Containing Spherical Nanoparticles

Minfang Mu,[†] Michelle E. Seitz,[†] Nigel Clarke,[‡] Russell J. Composto,[†] and Karen I. Winey*,[†]

[†]*Department of Materials Science and Engineering, University of Pennsylvania, Philadelphia, Pennsylvania 19104-6272, United States, and* [‡]*Department of Chemistry, Durham University, Durham DH1 3LE, England*

Received August 26, 2010
Revised Manuscript Received October 25, 2010

Introduction. In previous work,[1,2] we reported that a minimum in tracer diffusion coefficient with nanotube loading is observed in polystyrene (PS) composites with single wall carbon nanotubes (SWCNT) and multiwall carbon nanotubes (MWCNT) if the radius of gyration (R_g) of the tracer is larger than the radius of the nanotube bundles.[1] Here we extend this work to include C_{60}/PS composites to determine if the minimum in diffusion coefficient will be observed for spherical nanoparticles or if it arises from the cylindrical geometry of the nanotube bundles. Comparing PS composites with SWCNT, MWCNT, and C_{60} allows particle geometry and size to vary while minimizing differences in enthalphic interactions between the particles and the matrix.

Experimental Details. Fullerene C_{60} was purchased from SES Research. Polystyrene and deuterated polystyrene with molecular weights of 76.9 and 478.7 kg/mol were purchased from Polymer Source and Pressure Chemical and will be denoted 75k dPS and 480k PS, respectively. Both polymers have PDIs of 1.03 and were used as received.

Composites were prepared by first stirring 10 wt % 480k PS in toluene overnight. The C_{60} was dissolved in toluene at a concentration of 3 mg/mL by sonicating for 3 h. The C_{60} solution is purple and transparent indicating that no aggregates were observed. The C_{60} diameter in solution as measured with a Malvern Nano S particle size analyzer is 0.7 nm, and this agrees with reported C_{60} molecule size,[3] indicating that it is fully dispersed. The C_{60} and PS solutions were combined to achieve the desired C_{60} concentrations of 0.01−2 wt % C_{60} in the dried films ($C_{60}/(C_{60} + PS)$). To convert to volume fractions, densities of 1.05 and 1.65 g/cm^3 were used for PS and C_{60}, respectively. The resulting solutions were spin-coated at 1000 rpm for 60 s onto cleaned silicon wafers. Previous work has suggested that C_{60} may segregate to the silicon substrates during spin-casting.[4−7] However, the solutions used in this work have high solids loadings ($(C_{60} + PS)/(C_{60} + PS + toluene)$ = 6−10 wt % versus 2 wt %[4]) and the PS molecular weight is large (480k versus 1.8k[4] or 76k[7]), both of which will lead to increased solution viscosity and mitigation of C_{60} segregation. Additionally, this work focuses on very low C_{60} loadings. Estimates from the literature indicate C_{60} to be stable against aggregation in bulk PS to concentrations of ∼1−2 wt % (0.64−1.27 vol %).[8,9] Spin-coating was selected as the sample preparation method because quiescent solvent evaporation led to C_{60} crystallization (as detected by X-ray scattering).

*Corresponding author. E-mail: winey@seas.upenn.edu.

Five or fewer spin-coated films were floated and stacked (keeping their original orientation) to obtain thick nanocomposite films ($> 1\ \mu$m) which were then dried in a hood for 3 days. For a sample with 1.3 vol % C_{60}, no C_{60} crystalline reflections were detected with wide-angle X-ray scattering even after thermal annealing for 18 h at 150 °C (twice the annealing time used in our diffusion experiments). This suggests that C_{60} does not aggregate and form crystals (which due to its monodisperse size and shape C_{60} readily forms when aggregated) either during spin-casting or throughout the diffusion anneal. No evidence of dewetting (e.g., changes in sample appearance) was observed after annealing.

Diffusion bilayers were made by picking up a floated ∼20 nm spin-cast film of 75k dPS with the C_{60}/480k PS nanocomposite films. The bilayers were dried before annealing for 9 h in vacuum at 150 °C. Concentration profiles for 75k dPS in the C_{60}/480k PS nanocomposites were measured by elastic recoil detection[10] using a 3 MeV He^{2+} beam at 15° glancing angle with a spot size of $\sim 5 \times 5$ mm^2. The sampling depth is ∼800 nm with a resolution of ∼80 nm. Diffusion coefficients were obtained by fitting the dPS volume fraction profiles to the solution to Fick's second law convoluted with instrument resolution.[10] Additionally, excellent agreement between the experimental diffusion data and the fits to Fick's second law was obtained, suggesting diffusion into a homogeneous medium; stable layers of interfacially segregated C60 would lead to deviation from Fick's second law solution.

Results and Discussion. Figure 1 shows the measured 75k dPS volume fraction as a function of depth for a composite with 1.3 vol % C_{60} after annealing for 9 h at 150 °C. It is in good agreement with Fick's second law[10] using a diffusion coefficient of 8.85×10^{-15} cm^2/s. These data are representative of results for other C_{60} concentrations. Figure 2 shows the tracer diffusion coefficients, D, for 75k dPS as a function of C_{60} concentration in C_{60}/480k PS nanocomposites. The diffusion coefficient initially decreases rapidly with increasing C_{60} concentration followed by a slower increase at concentrations above a critical volume fraction, ϕ_{crit}, where the minimum D is observed. This behavior is qualitatively similar to the behavior of 480k PS nanocomposites with either SWCNTs[2] or MWCNTs[1] when the tracer $2R_g$ is larger than the diameter of the nanotube bundles. For C_{60}/480k PS composites, the diffusion coefficient is reduced by ∼80% at the critical C_{60} loading of 0.064 vol %. This critical C_{60} loading is much smaller than the percolation threshold (∼30 vol % C_{60} as determined by electrical conductivity[11]); thus, percolation of the filler is not required for a diffusion coefficient minimum to be observed. Neat 480k PS and C_{60}/480k PS with critical C_{60} loading of 0.064 vol % have indistinguishable glass transition temperatures (107 °C, determined via second heat DSC). This is consistent with the literature[8] that suggests at most a few degree increase in T_g with C_{60} loadings below 1.3 vol % for well dispersed composites. Therefore, the dramatic decrease in diffusion cannot be attributed to a shift in T_g. Additionally, C_{60} loadings below 0.63 vol % have been shown to be stable against agglomeration even after high-temperature annealing,[8] indicating that the minimum in diffusion is not related to a change in the spatial distribution of the nanoparticles.

Figure 3 compares the reduced diffusion (D/D_0 where D_0 is the diffusion coefficient in pure PS) coefficient of 75k dPS in

© 2010 American Chemical Society
Published on Web 12/20/2010

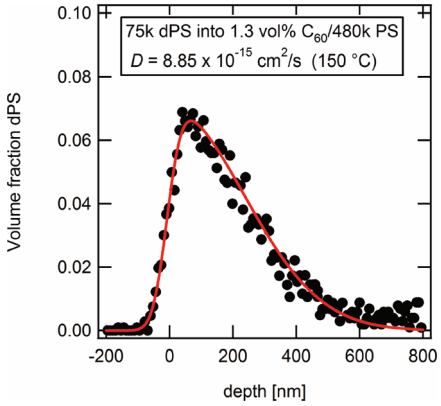


Figure 1. Volume fraction of 75k dPS as a function of depth in a 1.3 vol % C_{60}/480k PS nanocomposite after annealing for 9 h at 150 °C. The red line is the model fit using Fick's second law with $D = 8.85 \times 10^{-15}$ cm^2/s.

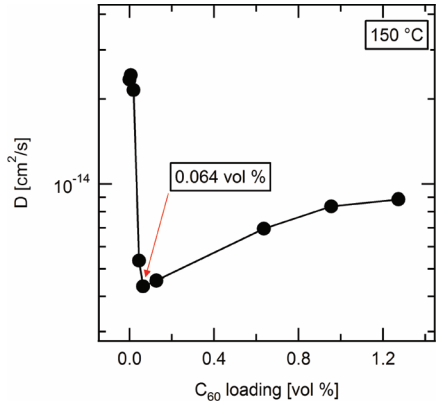


Figure 2. Tracer diffusion coefficient for 75k dPS in C_{60}/480k PS nanocomposites as a function of C_{60} loading.

480k PS nanocomposites containing SWCNTs or C_{60} as a function of the particle volume fraction normalized by the critical volume fraction. The SWCNT/PS composites contain nanotube bundles with a mean diameter of ~9.6 nm and a mean aspect ratio of ~35, and the minimum in D occurs at 0.4 vol % SWCNT. It should be noted that both the tracer and matrix polymers are identical in these samples; they differ only in nanoparticle type and loading. The magnitude of reduction in tracer diffusion is comparable for both systems. However, the diffusion coefficient recovers differently for the two systems as the particle loading increases. In SWCNT nanocomposites, D increases above ϕ_{crit} until its value becomes similar to that in pure 480k PS at a nanoparticle concentration of $\sim 10\phi_{crit}$. In contrast, D recovers more slowly in C_{60} nanocomposites and does not regain the D observed in the neat matrix even at $\phi > 20\phi_{crit}$.

That PS nanocomposites with vastly different particle geometry and size should show such similar diffusion behavior is striking. The nanotube network within the CNT/PS nanocomposites is assumed to be relatively immobile during the diffusion experiments compared to the diffusing polymer chains. In comparison to nanotube bundles, C_{60} is more mobile, and this could complicate the interpretation of our results. As a first approximation, we use the equation for Brownian motion to estimate the diffusion coefficient of the C_{60} in the matrix ($D_{C_{60}} = k_B T/6\pi\eta r$) where r is the particle radius of the diffusing particle and η is the viscosity of the matrix. Using $r = 0.35$ nm for C_{60}, that is assuming no aggregation, and $\eta = 8 \times 10^4$ Pa s for the 480k PS matrix

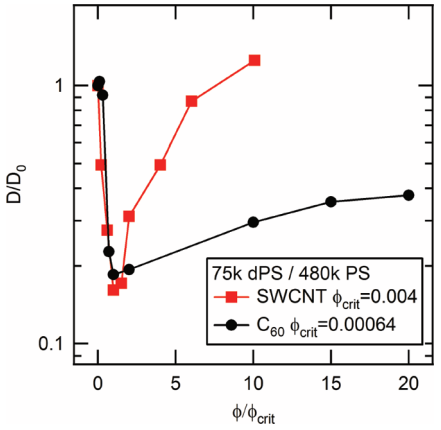


Figure 3. Reduced diffusion coefficients (D/D_0 where D_0 is the diffusion coefficient in pure PS) of 75k dPS in 480k PS nanocomposites containing SWCNTs (from ref 2) and C_{60} as a function of normalized nanoparticle loading. The diffusion coefficient recovery in nanocomposites with C_{60} is much slower for those with SWCNTs.

(determined from oscillatory shear rheology at 200 °C and shifted to 150 °C using the WLF equation with parameters $c_1 = -6.8$, $c_2 = 98$) yields $D_{C_{60}} = 5.6 \times 10^{-16}$ cm^2/s at 150 °C. Thus, even the slowest diffusing tracer molecules are still diffusing nearly an order of magnitude faster than the C_{60}. Moreover, there have been reports that the addition of C_{60} to PS reduces the nanocomposite viscosity relative to the neat PS;[12] this implies that we have overestimated η. In order for C_{60} to have a diffusion coefficient that is comparable to the slowest tracer polymers, the viscosity would have to be reduced by a factor of ~9. However, at loadings of 1 wt % C_{60} the reported viscosity reduction[12] is only a factor of 3, indicating that the tracer molecules are the most rapidly moving component in our study. Any aggregation or clustering of the C_{60} would presumably decrease its mobility. Thus, we conclude that although C_{60} is more mobile during the diffusion experiments than SWCNT and MWCNT bundles, the dPS tracer molecules are still the faster species. Assuming that the mobility of C_{60} can be tuned by the matrix molecular weight, an intriguing future study would be tracer diffusion in C_{60}/PS nanocomposites as a function of matrix molecular weight.

Our previous work demonstrated that the tracer molecule must be larger than the diameter of the nanotube bundles (e.g., $2R_g > d$) for a diffusion minimum to occur. This study demonstrates that cylindrical fillers are not required for a minimum in tracer diffusion to be observed. The minimum in the tracer diffusion coefficient that we observed arises, at least in part, from accessing the new size regime made available by the synthesis of particles that are smaller than the polymer radius of gyration and provides a new challenge for the fundamental understanding of polymer melt diffusion. Further studies using a variety of nanofillers, polymers, and temperature to better understand how enthalpic interactions and geometric considerations contribute to the origin of the diffusion minimum are underway. While the effect of C_{60} on glass formation in PS has received attention recently,[8,13,14] this study highlights that very small nanoparticle loadings can also significantly alter polymer dynamics at longer time scales which has implications for permeability and mechanical properties.

Acknowledgment. This research was funded by the National Science Foundation Materials World Network DMR-0908449 (K.I.W., R.J.C., N.C.), MRSEC-DMR05-20020 (K.I.W., R.J.C.), and Polymer Programs DMR05-49307 (R.J.C.). N.C. gratefully acknowledges the award of an EPSRC Overseas Travel Grant,

EP/E050794/1. We thank Prof. Shu Yang at the University of Pennsylvania for use of the size exclusion chromatograph.

References and Notes

(1) Mu, M. F.; Composto, R. J.; Clarke, N.; Winey, K. I. *Macromolecules* **2009**, *42* (21), 8365–8369.
(2) Mu, M. F.; Clarke, N.; Composto, R. J.; Winey, K. I. *Macromolecules* **2009**, *42* (18), 7091–7097.
(3) Hedberg, K.; Hedberg, L.; Bethune, D. S.; Brown, C. A.; Dorn, H. C.; Johnson, R. D.; Devries, M. *Science* **1991**, *254* (5030), 410–412.
(4) Barnes, K. A.; Karim, A.; Douglas, J. F.; Nakatani, A. I.; Gruell, H.; Amis, E. J. *Macromolecules* **2000**, *33* (11), 4177–4185.
(5) Han, J. T.; Lee, G. W.; Kim, S.; Lee, H. J.; Douglas, J. F.; Karim, A. *Nanotechnology* **2009**, *20* (10), 105705.
(6) Holmes, M. A.; Mackay, M. E.; Giunta, R. K. *J. Nanopart. Res.* **2007**, *9* (5), 753–763.
(7) Yaklin, M. A.; Duxbury, P. M.; Mackay, M. E. *Soft Matter* **2008**, *4* (12), 2441–2447.
(8) Wong, H. C.; Sanz, A.; Douglas, J. F.; Cabral, J. T. *J. Mol. Liq.* **2010**, *153* (1), 79–87.
(9) Mackay, M. E.; Tuteja, A.; Duxbury, P. M.; Hawker, C. J.; Van Horn, B.; Guan, Z. B.; Chen, G. H.; Krishnan, R. S. *Science* **2006**, *311* (5768), 1740–1743.
(10) Composto, R. J.; Walters, R. M.; Genzer, J. *Mater. Sci. Eng., R* **2002**, *38* (3−4), 107–180.
(11) Ltaief, A.; Bouazizi, A.; Davenas, J.; Alcouffe, P.; Chaabane, R. B. *Thin Solid Films* **2006**, *511−512*, 498.
(12) Tuteja, A.; Duxbury, P. M.; Mackay, M. E. *Macromolecules* **2007**, *40* (26), 9427–9434.
(13) Sanz, A.; Ruppel, M.; Douglas, J. F.; Cabral, J. T. *J. Phys.: Condens. Matter* **2008**, *20* (10), 104209.
(14) Kropka, J. M.; Garcia Sakai, V.; Green, P. F. *Nano Lett.* **2008**, *8* (4), 1061–1065.

194 *Macromolecules* **2011**, *44*, 194–202
DOI: 10.1021/ma102267f

Macromolecules
ARTICLE

Dramatic Enhancement of Superacid-Catalyzed Polyhydroxyalkylation Reactions

Maria T. Guzmán-Gutiérrez,[†] Daniel R. Nieto,[†] Serguei Fomine,[†] Salvador L. Morales,[†] Mikhail G. Zolotukhin,*[,†] M. Carmen G. Hernandez,[‡] Hans Kricheldorf,[§,⊥] and Edward S. Wilks[∥]

[†]*Instituto de Investigaciones en Materiales, Universidad Nacional Autonoma de Mexico, Apartado Postal 70-360, CU, Coyoacan 04510, Mexico D.F., Mexico,* [‡]*Institut für Werkstoffforschung, Helmholtz-Zentrum Geesthacht, Max-Planck-Strasse 1, 21502 Geesthacht, Germany,* [§]*Institut fur Technische und Makromolekulare Chemie, Bundesstrasse 45, D-20146 Hamburg, Germany,* [⊥]*BAM, Unter den Eichen 87, D-12205 Berlin, Germany, and* [∥]*113 Meriden Drive, Hockessin, Delaware 19707, United States*

Received October 1, 2010; Revised Manuscript Received November 23, 2010

ABSTRACT: Complementary theoretical and experimental studies of the consecutive steps of superacid catalyzed polyhydroxyalkylation reactions have been carried out. Calculations for the superacid catalyzed polyhydroxyalkylation of trifluoroacetone and trifluoroacetophenone with aromatic hydrocarbons explained a number of experimental facts within a single theoretical framework of monoprotonation. The principal factors affecting kinetics of superacid mediated hydroxyalkylation were shown to be as follows: (i) the acidity of the superacid affecting protonation energy of carbonyl components; (ii) the electrophilicity of carbonyl components; and (iii) the nucleophilicity of aromatic components. The modification of those factors allows for tuning of the reactivity of carbonyl and aromatic components; thereby, reaction kinetics are controlled. The conclusions were confirmed by the experiments. Theoretically predicted stoichiometrically imbalanced polymerizations of trifluoroacetone, trifluoroacetophenone, octafluoroacetophenone, and isatin with nonactivated, aromatic hydrocarbons gave high-molecular-weight polymers with a very small excess of the carbonyl compound. The main reasons contributing to the polymerization accelerations were found to be an increase of the first, rate-determining step reaction, and a high efficiency of the superacid catalyzed polyhydroxyalkylations. The present work has thus opened a new route to preparations of polymers of linear, hyperbranched, or hybrid (e.g., linear−hyperbranched) architecture by operating on structural parameters and reaction conditions.

1. Introduction

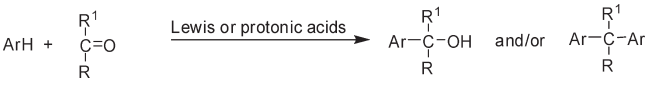
The classical theory of step-growth polymerization is based on two concepts.[1−3] The first is an assumption of equal reactivity of both functional groups in a bifunctional reactant. It is also assumed that at any given stage of the polymerization all functional groups are equally reactive regardless of the size of the molecule to which they are attached (and that no intramolecular cyclization occurs). The molecular weight distribution consequently predicted is known as the "most probable" distribution.

The second concept is that stoichiometric imbalance in monomer feed ratio decreases degree of polymerization. The highest molecular weight of linear polymer is obtained when exactly stoichiometric amount of the monomers are present.

There are many examples of polymerizations involving reactants where the equal reactivity of functional groups assumption is not valid. For example, this occurs with unsymmetrical reactants, such as toluene-2,4-diisocyanate, propane-1,2-diol, and butane-1,3-diol,[4] when the more reactive functional groups react first. Generally, the first reaction rate of a bifunctional monomer is faster than the second one. The opposite situation, when the first reaction enhances the reactivity of the second one, has received very little attention.

In 1999, T. Endo in the course of study of polycondensation of 2,2-dichloro-1,3-benzodioxole and 4,4′-isopropylidenediphenol reported on the rate enhancement of the second reaction by the first one in the case when two functional groups are present on the same atom.[5] But more important was the finding that the degree of polymerization is enhanced by stoichiometric imbalance if the first condensation of bifunctional monomer enhances the second condensation of the remaining functional group. The highest molecular weight of polyorthocarbonate (M_n 120 000) was obtained when ca. 0.7 equiv. excess of 2,2-dichloro-1,3-benzodioxole was used. A kinetic analysis of the polycondensation was described. It is worth mentioning that a positive effect of the stoichiometric imbalance was also observed in the polycondensation of dichlobenzene with sodium sulfide[6] and in the reactions of methylene bromide with bisphenol salts[7] and 4,4′-thiobis(benzenethiol).[8] In all these cases one of the monomers has the functional groups connected to the same atom.

Another synthesis type with two consecutive reactions is the acid-catalyzed condensation of ketones and aldehydes with aromatic compounds, known as the hydroxyalkylation reaction[9,10]



where R and R^1 are H, alkyl, aryl.

Depending on the monomer structures and reaction conditions, an alcohol, a diaryl-compound or a mixture of these can be obtained. The acid-catalyzed addition reactions of aldehydes and ketones have been known for a long time. For instance, the condensation of chloral with benzene in the presence of sulfuric

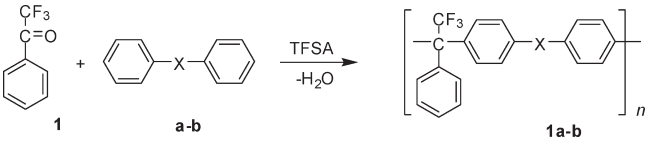
*Corresponding author. E-mail: zolotukhin@iim.unam.mx.

 Published on Web 12/21/2010 © 2010 American Chemical Society

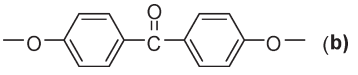
acid was reported by A. Bayer as early as 1872.[11] Nevertheless, these Friedel−Crafts-type reactions have not been studied to the same extent as the corresponding reactions involving alcohols, alkyl halides or aryl halides. Probably, the main reason for such neglect is the generally lower yields and the formation of oligomeric byproducts.

The concept of superelectrophilic activation proposed by Olah and co-workers to explain the high reactivities of electrophilic species in superacidic media[12,13] and its application for hydroxyalkylation reactions turned out to be remarkably successful.[14] Numerous reactions have been carried out using superacids as a reaction medium (mostly trifluoromethanesulfonic acid (TFSA), which has been often acclaimed as one of the strongest of all known monoprotic organic acids.[15,16]

Recently, for the first time, superacid-catalyzed polyhydroxylakylation reactions of carbonyl compounds with nonactivated aromatic hydrocarbons to produce high-molecular-weight linear[17−24] or hyperbranched[25−28] dendrons and dendrimers[29] were reported. In these reactions, the intermediate alcohol reacts with another aromatic compound to give a diarylation product. Thus, reactions 2,2,2-trifluoroacetophenone (**1**) with biphenyl and 4,4′-diphenoxybenzophenone in the presence of TFSA gave linear, film-forming polymers with *para*-substitution in the main chain[18]

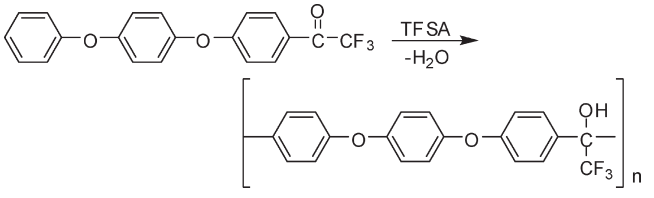


where −X− is nil (**a**) or



It is worth mentioning that trifluoromethyl groups in carbonyl compounds eventually become substituents in polymer chains, which affords new polymer structures and properties.

More recently, M. Ueda reported an interesting case of the TFSA-catalyzed self-polymerization of 2,2,2-trifluoro-1-[4-(4-phenoxyphenoxy)phenyl]ethanone, which led to a linear polyether instead of the expected hyperbranched polymer:[30]



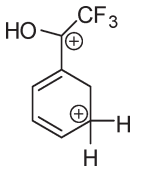
It was also demonstrated[31] that the reactivities of the monomer and the intermediate (the rate constants of the first and the second reactions) can be different and depend on the acidity of the reaction medium.

Taking into account cheaper, more readily available monomers and the promising properties of polymers that might be obtained from possessing large synthetic potential polyhydroxylations, the objectives of this present article deal with (i) a mechanistic analysis of the consecutive electrophilic substitution reactions in superacid-catalyzed polyhydroxylation, and (ii) an increase of the efficiency of polyhydroxyalkylation by means of nonstoichiometric chemistry.

2. Results and Discussion

2.1. Theoretical Aspects. *2.1.1. Reaction of 2,2,2-Trifluoracetophenone with Anisole.* It was found that only the diarylation product, 4,4′-(2,2,2-trifluoro-1-phenylethane-1,1-diyl)bis(methoxybenzene) (**7**), was selectively obtained in methanesulfonic acid (MSA) after the reaction of an equimolar amount of anisole with **1**, whereas a hydroxyalkylation product, 2,2,2-trifluoro-1-(4-methoxyphenyl)-1-phenylethanol (**3**), was formed quantitatively in TFSA (Scheme 1). When two equiv of anisole to **1** were used only diarylation products were isolated in the cases of both MSA and TFSA.[30]

It has been also suggested that in TFSA a very reactive dicationic intermediate is generated:[30]



To verify this hypothesis the reaction of 2,2,2-trifluoroacetophenone (**1**) with anisole has been studied theoretically in both MSA and TFSA media. The inner solvation sphere was represented by two explicit MSA or TFSA molecules (Figure 1).

Figure 1 shows the PBE0/6-311+G(d,p) optimized geometries of **1** in TFSA (**1-TFSA**) and MSA (**1-MSA**), transition state structures for the first reaction step between **1** and anisole in TFSA (**TS1-TSFA**) and MSA (**TS1-MSA**), optimized structures of **2** in TSFA and the corresponding transition state in TFSA (**TS2**).

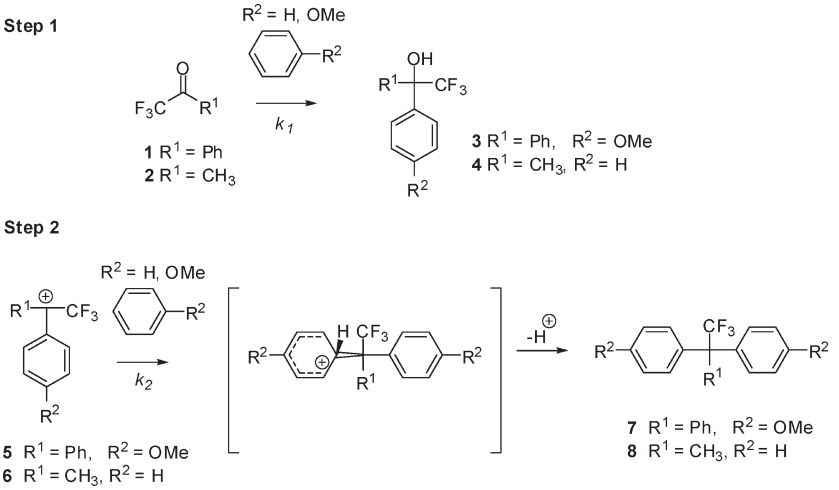
For the outer solvation sphere, the SMD continuous model was used as implemented in Gaussian 09.[32] (Dielectric constant of 77.4 and solvent radius of 2.60 was applied for TFSA. For MSA dielectric constant of 70.0 and solvent radius of 2.34 Å were used (Scheme 1). All geometries were optimized with the PBE0 functional[33] in combination with the /6-311+G-(d,p) basis set. This is the slightly modified computational model described in ref 34, which reproduces pK_a of selected acids within 1 pK_a unit.

Our model rationalizes different reactivity of **1** in two reaction media without the need to involve the diprotonated carbonyl group. The free Gibbs activation energy of the first step in TFSA (22.51 kcal/mol) is lower than that of the second step (25.98 kcal/mol), in agreement with experimental findings.

However, no diprotonation of the carbonyl group takes place (Figure 1). The proton transfer occurs only during nucleophilic attack of anisole at the carbonyl group and at any given moment only one proton is transferred to the carbonyl oxygen, while the other one forms a hydrogen bond with the carbonyl group at all stages of σ-complex formation. The MSA mediated reaction between anisole and **1** (Figure 1 and Table 1) result in the formation of a monoprotonated transition state (**TS1-MSA**) and a monoprotonated σ-complex similar to that formed in the TFSA catalyzed reaction.

However, the free Gibbs activation energy of the first step increases by 3.5 kcal/mol (Table 1), while the second step has a similar activation energy in both MSA and TFSA. The increase of activation energy in MSA compared to TFSA for the first reaction step is due to more positive protonation energy for MSA (weaker acid), which contributes to the total activation energy for the first reaction step. Therefore, it is possible to change the relative rates of the first and second steps using less a reactive aromatic component to avoid excessive stabilization of the carbocation to decrease the activation energy of the second reactive step. A good model on which to test this hypothesis is the reaction between trifluoracetone (**2**) and benzene.

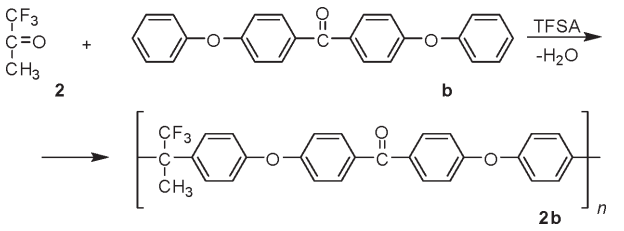
Scheme 1. Reaction between Carbonyl Compounds and Aromatics



2.1.2. Reaction of 2,2,2-Trifluoracetone with Benzene. Theoretical studies suggested that monoprotonated species are the active electrophiles in this reaction.[34] Calculations demonstrated that the free Gibbs activation energy (G_a) of the first reaction step (27.57 kcal/mol) is higher than that of the second (22.09 kcal/mol) (Table 1). The carbonyl group of **2** forms only hydrogen bonds with protons of TFSA (Figure 1). The proton transfer occurs only during the nucleophilic attack of benzene at carbonyl group and at any given moment only one proton is transferred to the carbonyl oxygen, while the other one forms a hydrogen bond with carbonyl group at all stages of σ-complex formation. Therefore, those data suggest the presence of monoprotonated electrophilic species in this reaction. Since G_a of the first step is higher than that of the second, the first step is slower than the second according to calculations. High and positive protonation energies of the electronically deficient carbonyl group of **2** contribute to the high activation energy of the first step and favor low k_1.

Since the rate constants (k) are related to G_a through the Eyring equation $k = (k_bT/h)\exp(-G_a/RT)$, where k_b, T, h, and R are the Boltzmann constant, absolute temperature, Plank's constant and gas constant, it is possible to calculate k_1/k_2 ratio (Scheme 1)..The calculated k_1/k_2 ratio in TFSA for the reaction of **2** with anisole is 350, while for the reaction of **1** with benzene this ratio is only 10^{-4}. The rate constant ratio in MSA for the reaction of **2** with anisole is close to 1. Therefore, high protonation energy of the carbonyl component favors low k_1 ($k_1 < k_2$). Low protonation energy and high reactivity of aromatic component favors high k_1 ($k_1 > k_2$). Generally the k_1/k_2 ratio depends on three factors: the first is the carbonyl group protonation energy. The protonation energy depends on the basidity of a carbonyl group and acid strength. The second one is the electrophilicity of carbonyl component.[35] Those two factors are interconnected since higher electrophilicity implies a lower activation energy of σ-complex formation but higher protonation energy. The third factor is the nucleophilicity of the aromatic component.[36] A less nucleophilic aromatic component decreases k_1 but decreases k_2 with respect to k_1 due to destabilization of carbocation, the reactive intermediate of the second reaction step. The increase of the acidity of the media (all other things being equal) decreases k_1 at the expense of protonation energy but leaves k_2 intact. Therefore, it is possible to adjust the k_1/k_2 value by modifying either the reaction conditions or the monomer structure. As a result, a monoarylated carbinol or diarylated derivative can be obtained selectively in super-acid-catalyzed hydroxyalkylation. Application of this methodology for the polymer syntheses allows for nonstoichiometric accelerations and for polymers of different topology such as linear, hyperbranched, or linear−hyperbranched hybrids to be obtained.

2.2. Polymer Syntheses. *2.2.1. Polycondensation of Trifluoroacetone with 4,4′-Diphenoxybenzophenone.* Calculations demonstrated that in the reactions of trifluoroacetone with non nonactivated aromatic hydrocarbons, Gibbs activation energy (G_a) of the first step is higher than that of the second; therefore, the first step is slower than the second one, which should allow for nonstoichiometric polycondensations to occur. To evaluate the effect of the stoichiometric imbalance (excess amount of the carbonyl compound), further experiments were carried out with polycondensations of trifluoroacetone with 4,4′-diphenoxybenzophenone. The polycondensations were carried out according to the following scheme



with variation of molar ratio of comonomers in TFSA medium at room temperature. Figure 2 illustrates the dependence of viscosity $\eta_{inh.}$ of the polymers on the stoichiometric imbalance.

It is quite remarkable that even a 15% excess of **2** significantly increases polymer viscosity. Further increase of stoichiometric imbalance results in a dramatic increase in molecular weight of the polymers. The viscosity of the reaction mixture very rapidly increased, and the reactions were complete in several minutes. However, a large excess of trifluoroacetone led to extensive cross-linking. The analytical data (IR, ^{1}H and ^{13}NMR) of the polymers from the nonstoichiometric syntheses were identical to those from the stoichiometric ones, except for the viscosity. As an example, the NMR spectra of polymer **2b** obtained with 20% excess of trifluoroacetone is given in Figure 3.

Yields of the polymers obtained were close to quantitative (96−97%). Therefore, neither purity nor decomposition of **2**

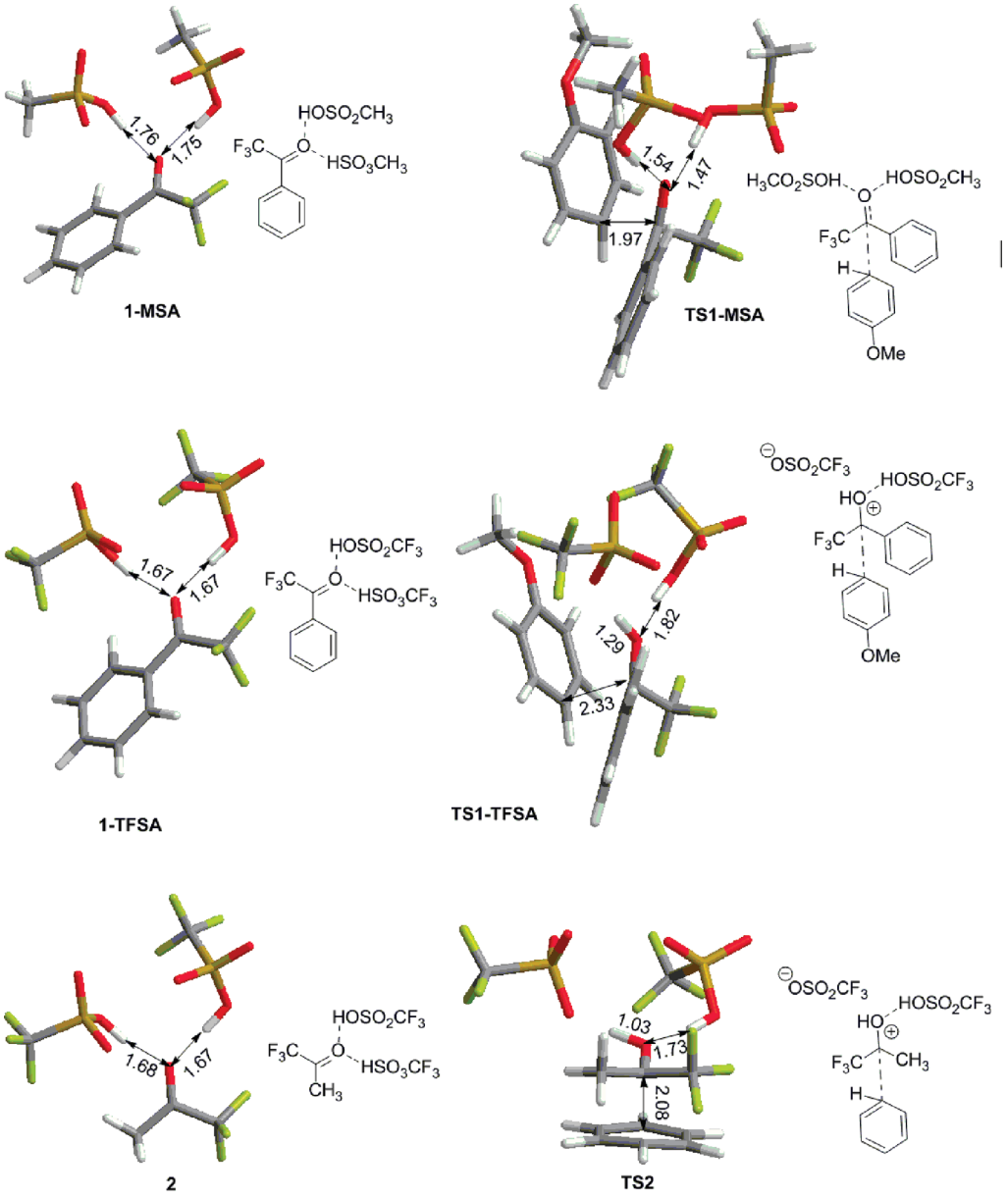


Figure 1. Optimized geometries of the reaction intermediates.

Table 1. Free Gibbs Activation Energies G_a (kcal/mol) of Studied Reaction, Calculated at the PBE0/6-311+Gd,p Level in TFSA and MSA, Respectively

reaction	G_a (kcal/mol)
TFSA	
1 + anisole → **3**	22.51
5 + anisole → **7**	25.98
2 + benzene → **4**	27.57
6 + benzene → **8**	22.09
MSA	
1 + anisole → **3**	26.00
5 + anisole → **7**	25.89

could be the reason for the most effective polycondensation. Table 2 shows the effect of stoichiometric imbalance on the viscosity and weight- and number-averaged molecular weights and polydispersity of **3**.

The results clearly indicate that the polymers with higher molecular weight are obtained under nonstoichiometric conditions. As can be seen from the table, the molecular weight and polydispersity of the resulting polymer increased with the increase in stoichiometric imbalance.

The high polydispersity of the polymers obtained with a large excess of trifluoroacetone points to the occurrence of side reactions. Structural studies of the polymers by means of ^{1}H and ^{13}C NMR spectroscopy revealed *para*-substituted phenylene fragments in the main chain of the polymers. There are, however, small broad multiplets around the main signals. It is very likely that the signals are due to products of some reactions of diphenyl ether fragments.[37]

During the past 10 years, H. Kricheldorf and co-workers have shown that in kinetically controlled stoichiometric polycondensation of linear monomers ring closure competes with propagation at any concentration and at any stage of the polycondensations.[38] Besides, any optimization of the reaction conditions toward high molecular weights also raises the fraction of cyclic molecules at the expense of all linear chains. As a result, all reaction products are necessarily macrocycles at 100% conversion when side reactions are absent. Obviously, suppression of macrocycle formation would

give result in very high molecular weight linear polymers. One may assume that the decrease in the macrocyclic content could contribute to the efficiency of nonstoichiometric polyhydroxyalkylations.

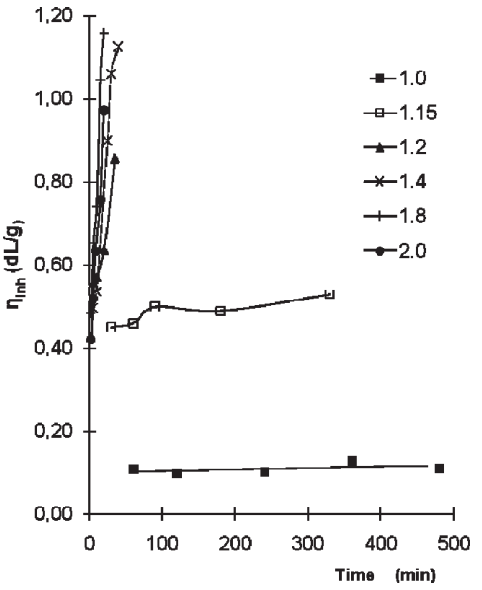


Figure 2. Relationship between the monomer feed ratio and the inherent viscosity of the polymers.

In this connection, two polymer samples obtained from stoichiometric (**2bs**, $M_w = 15\,400$, $M_n = 9860$) and non**s**toichiometric (**2bns**, $M_w = 299\,000$, $M_n = 108\,000$) syntheses were characterized. The MALDI−TOF mass spectra (Figure 4) revealed the existence of macrocycles in both samples.

An interesting and important result is the observation that the sample from stoichiometric synthesis contains also linear chains having diphenoxybenzophenone end groups. This is additional evidence that the second reaction is faster than the first one. Although only mass peaks of cycles (**M2**−**M5**), were detectable in the sample **2bns**, it is obvious that high molecular weight cycles and linear structures are also present in these samples. It is well-known that high molar mass polymers are discriminated in MALDI−TOF measurements, and the low signal-to-noise ratio of **M2**−**M5** in the B-spectrum indicates that only a small fraction of cyclic oligomers appears in this mass spectrum. See Figure 5 for structures of **M** and **L**.

On the whole, one may conclude that in the structural aspect the nonstoichiometric polyhydroxyalkyaltion is in line with modern theory of step-growth polymerizations.[38,39] If so, the main reason for the nonstoichiometric acceleration should be increase of the first reaction as the concentration of **2** and k_2/k_1 value are increased.[40] Since the rate-determining

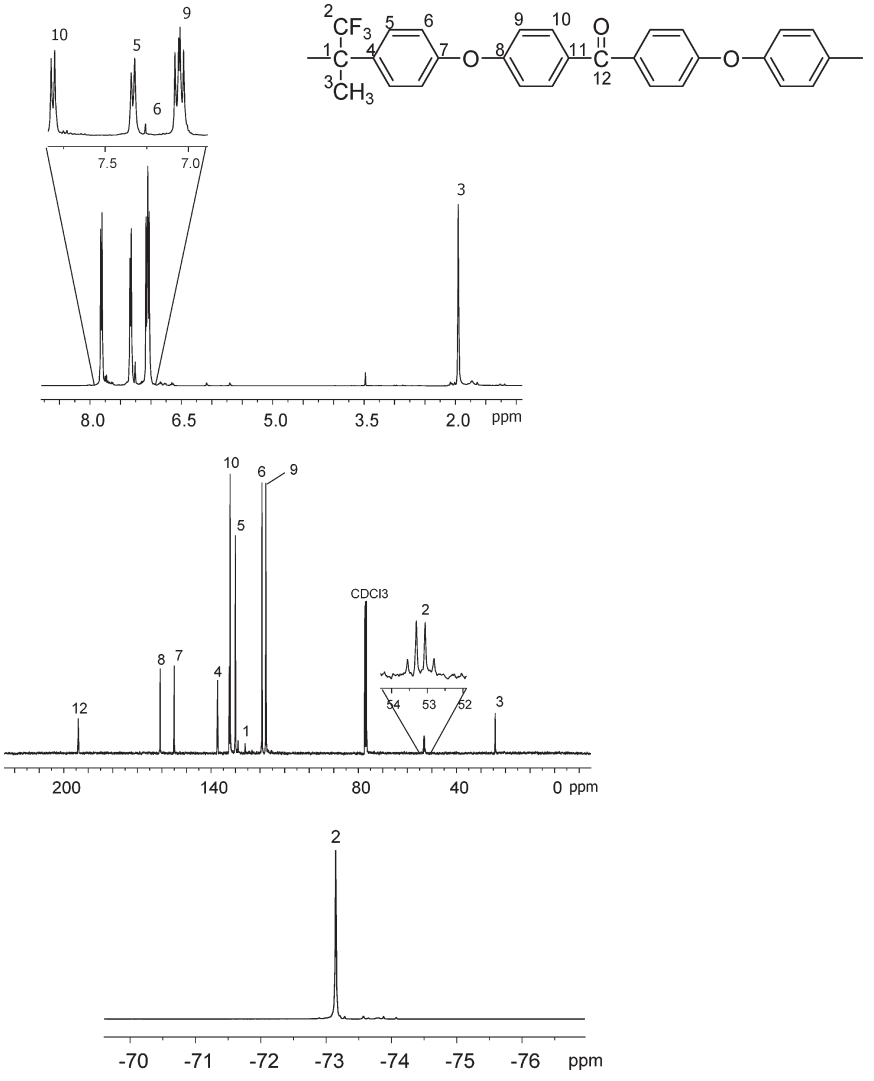


Figure 3. The ^{1}H (top), ^{13}C (middle), and ^{19}F (bottom) spectra of polymer **2b** (solution in $CDCl_3$).

Table 2. Effect of feed ratio on the polycondensation of trifluoroacetone (2) with 4,4′-diphenoxybenzophenone (b)

2:**b** (mol/mol)	reaction time, min	inherent viscosity $\eta_{inh.}$, dL g^{-1} (NMP)	molecular weight, (g/mol), $M_w \times 10^4$	molecular weight, (g/mol), $M_n \times 10^4$	M_w/M_n
1	60	0.22	1.843	1.112	1.66
	360	0.27	15.82	8.040	1.96
1:2	5	0.56	25.09	12.63	1.98
	35	0.86	36.26	12.77	2.84
1:4	5	0.49	17.79	8.04	2.21
	30	1.06	61.70	16.27	3.79
1:8	5	0.65	18.15	5.71	3.17
	20	1.16	117.50	25.32	4.65

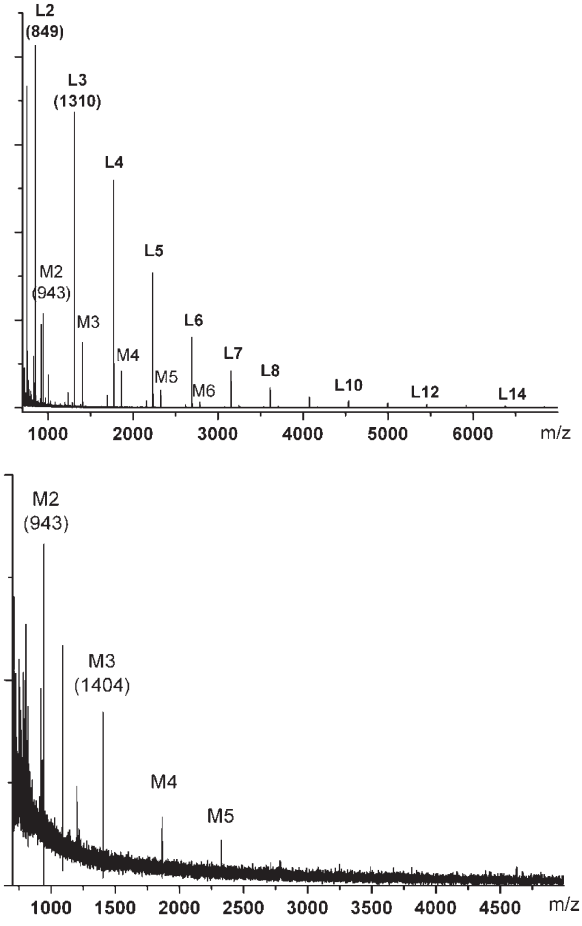
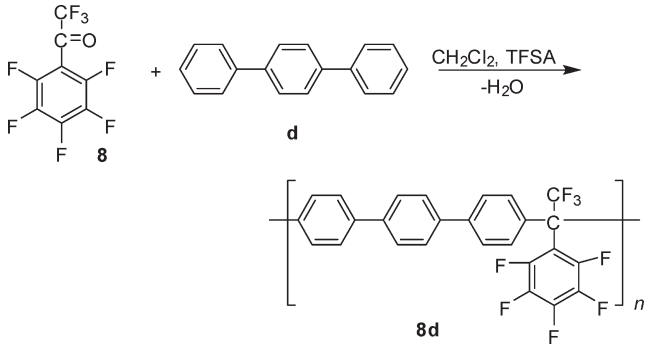


Figure 4. MALDI−TOF spectra of polymer **2bs** (top) and **2bns** (bottom).

step k_1 governs the net rate of the polymerization, the net rate of the polymerization also increases, and a high molecular weight polymer would be obtained.

2.2.2. Polycondensations of Trifluoroacetophenone, Octafluoroacetophenone, and Isatin with Aromatic Hydrocarbons. According to calculations, in TFSA catalyzed hydroxyalkylations involving 2,2,2-trifluoroacetophenone (**1**) and an aromatic hydrocarbon less reactive than anisole, the rate of the second reaction can be faster than that of the first one. Therefore, one can expect that polycondensation of **1** with diphenyl ether (**c**) would be enhanced by stoichiometric imbalance. Indeed, the high molecular weight polymer was obtained in 3 h when 0.4 equiv excess of **1** was used (Table 3). Biphenyl (**a**), an aromatic hydrocarbon less nucleophilic than diphenyl ether in aromatic electrophilic substitution reactions, still reacts with **1** to give a polymer with an inherent viscosity 0.59 dL/g. Remarkably, nonstoichiometric polycondensation of biphenyl with an excess of **1** gave in 7.5 h a polymer **1a** with $\eta_{inh.}$= 1.19 dL/g.

Octafluoroacetophenone (**8**) is significantly less reactive (electrophilic) than **1**. Polycondensation of octafluoroacetophenone with terphenyl proceeds very slowly to give in 24 days a film-forming polymer with an inherent viscosity 0.47 dL/g



It is very likely that the low basicity (which means high protonation energy) of octafluoroacetophenone (which favors low rate constant of the first reaction) is the main reason for its low reactivity. Therefore, it seemes plausible that the degree of polymerization can be elevated by a stoichiometric imbalance. Polycondensation of terphenyl (**d**) with 0.4 equiv excess of octafluoroacetophenone (**8**) gave in 2 days a polymer **8d** with an inherent viscosity 0.71 dL/g (Table 3, entry 5 and 6).

The ^{1}H NMR and ^{13}C NMR spectra of the polymer **8d** (Figure 6) are well resolved, and all signals related to the *para*-substituted terphenylene and pentafluorophenyl fragments are evident. Detail analysis of these spectra revealed no essential indications of structural irregularities

It is worthy of mention that the reaction medium in the course of the polycondensation of phenyl ether with **1** was homogeneous, whereas the reactions involving biphenyl and terphenyl proceeded as 'precipitation polycondensations', when the polymer formed precipitated from the initially homogeneous solution. It is generally accepted that premature polymer formation in polycondensation syntheses prevents further macromolecular chain growth reactions. However, it has been found that under certain conditions polymer-forming reactions can occur in the precipitate, i.e., after phase separation, to yield high-molecular-weight polymers.[41,42] The precipitate formed during the course of polymerizations that involve fluorinated carbonyl compounds and biphenyl or terphenyl, appear as a colored elastic mass ("reactive gel"). After completion of the reaction, the precipitates formed are isolated from the reaction medium, shredded, washed thoroughly with methanol, and dried overnight in air. After reprecipitation from chloroform into methanol, followed by filtration and extraction with refluxing methanol before drying at 100 °C under vacuum, white fibrous polymers were obtained.

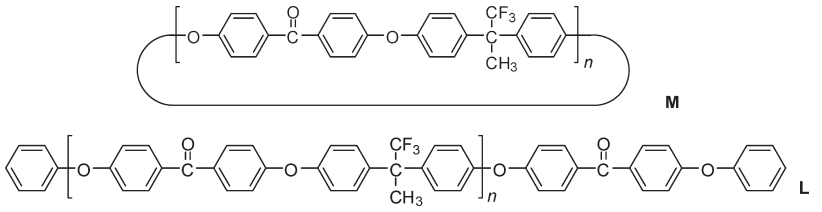


Figure 5. Chemical compositions of cyclic (**M**) and linear (**L**) products.

Table 3. Effect of Feed Ratio on the Inherent Viscosities

entry	carbonyl compound	aromatic hydrocarbon	ketone/aromatic (mol/mol)	reaction time	inherent viscosity $\eta_{inh.}$ dL/g, (NMP)
1	trifluoroacetophenone (**1**)	diphenyl ether (**c**)	1.0	3 h	0.14
2			1.4	3 h	0.60
3		biphenyl (**a**)	1.0	24 h	0.59
4			1.4	7.5 h	1.20
5	octafluoroacetophenone(**8**)	terphenyl (**d**)	1.0	24 days	0.47
6			1.4	2 days	0.71
7	isatin (**9**)	biphenyl (**a**)	1.0	6 h	0.39
			1.1	6 h	2.37
8		terphenyl (**d**)	1.0	6 h	0.45
			1.3	3 h	2.29
			1.5	2 h 50 m	4.40

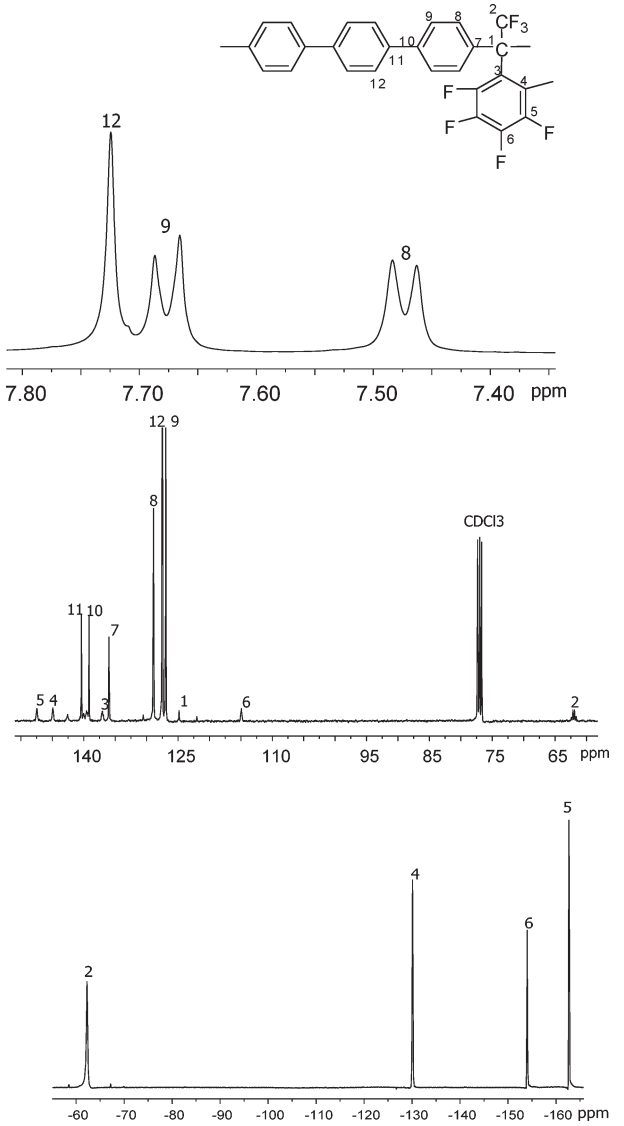
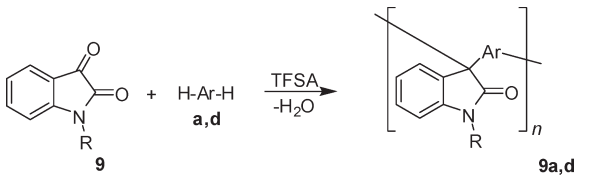


Figure 6. The ^{1}H (top), ^{13}C (middle), and ^{19}F (bottom) spectra of polymer **8d** (solution in $CDCl_3$).

As seen in Table 3, despite the heterogeneous reaction medium the stoichiometric imbalance enhances above-mentioned polycondensations.

Finally, stoichiometric and nonstoiciometric polymerizations of isatin with aromatic hydrocarbons were carried out according to the following scheme:



To decrease reactivity of isatin the reactions were performed in a mixture of TFSA with trifluoroacetic acid (TFA). Nevertheless, the effect of stoichiometric imbalance in these reactions is even more pronounced (Table 3, entries 7, 8). Remarkably, all the polymers obtained are completely soluble. Recently, we reported on highly efficient reactions of isatin with linear, nonactivated, multiring aromatic hydrocarbons.[24] We found that isatin based polymerizations meet the criteria needed for "click" polymer chemistry. Therefore, another factor contributing to the nonstoichiometric acceleration could be efficiency of the polymerization.

3. Conclusions

The calculations for the consecutive superacid catalyzed electrophilic aromatic substitution reactions of trifluoroacetone and trifluoroacetophenone with aromatic hydrocarbons explained a number of experimental facts within one theoretical framework of monoprotonation. They also revealed principal factors affecting kinetics of superacid mediated hydroxyalkylation, such as (i) the acidity of superacid affecting protonation energy of carbonyl component, (ii) electrophilicity, and (iii) nucleophilicity of carbonyl and aromatic components, respectively. The modification of those factors allows for tuning of the reactivity of carbonyl and aromatic components; thereby, reaction kinetics are controlled. Thus, an increase of acid strength and electrophilicity of the carbonyl component increase k_1, while the decrease of nucleophilicity of aromatic monomer increases k_2 with respect to k_1.

A proper relationship between the electrophilicity of the carbonyl group, the nucleophilicity of the aromatic hydrocarbon, and the acidity of the reaction medium allows for the selection of favorable conditions for the nonstoichiometric polymerizations.

The conclusions were confirmed by the experiments. Theoretically predicted stoichiometrically imbalanced polymerizations of trifluoroacetone, trifluoroacetophenone, octafluoroacetophenone and isatin with nonactivated, aromatic hydrocarbons gave high molecular weight polymers with a very small excess of the carbonyl compound. The acceleration of nonstoichiometric polymerizations does not depend on the phase state (heterogeneity) of the reaction medium.

The main reasons contributing to the polymerization accelerations were found to be an increase of the first reaction, the rate-determining step reaction, and a high efficiency of the superacid catalyzed polyhydroxyalkylations.

The present work has thus opened a new route to preparations of polymers of linear, hyperbranched or hybrid (e.g., linear-hyperbranched) architecture by operating on structural parameters and reactions conditions. Cheaper, commercially available monomers and the promising properties of polymers that might be obtained from them would stimulate interest in that field.

4. Experimental Part

4.1. Characterization. NMR spectra were recorded on Bruker Avance 400 Spectrometer, operating at 400.13 and 100 MHz for ^{1}H and ^{13}C respectively. Chloroform-*d* ($CDCl_3$) was used as solvent. Infrared (IR) spectra were measured on a Nicolet FT-IR-ATR spectrometrer. The inherent viscosities of 0.2% polymer solutions in 1-methyl-2-pyrrolidinone (NMP) were measured at 25 °C using an Ubbelohde viscometer. Molecular weights were determined by gel permeation chromatography (GPC−MALLS) according to the published method.[40] Thermogravimetric analyses (TGA) were carried out in air and under nitrogen at a heating rate of 10 °C/min on a DuPont 951 thermogravimetric analyzer. The T_g was evaluated by differential scanning calorimetry (DSC) measured at 10 °C/min on DuPont 910. An Autoflex III MALDI−TOF mass spectrometer (Bruker Daltonik, Germany) was used. The system is equipped with a "Smartbeam" laser working at 355 nm. Samples were dissolved in chloroform (1−2 mg/mL) and mixed with (2-[(2*E*)-3-(4-*tert*-butylphenyl)-2-methylprop-2-enyliden] malononitril) (DCTB) matrix solution (10 mg/mL in tetrahydrofuran) and sodium trifluoroactate (NaTFA, 2 mg/mL in tetrahydrofuran) in a ratio of 20/50/2 (v/v/v). A 1 μL sample of this solution was dropped on the target and inserted in the mass spectrometer after evaporation of the solvent. A total of 2000 single laser shots were accumulated for one spectrum.

4.2. Materials. All starting materials were obtained from Aldrich. Biphenyl, phenyl ether, and *p*-terphenyl were used as received. Methylene chloride, TFSA, trifluoroacetone, trifluoroacetophenone, and octafluoroacetophenone were distilled before use. Isatin was purified by recrystallization with charcoal from ethanol.

4.3. Polymer Syntheses. *Preparation of Poly*[*oxy-1,4-phenylenecarbonyl-1,4-phenyleneoxy-1,4-phenylene*(*2,2,2-trifluoro-1-methylethylidene*)*-1,4-phenylene*] (***2b***). 1,1,1-Trifluoroacetone (0.313 g 2.8 mmol), diphenoxybenzophenone (1.027 g 2.8 mmol) and TFSA (5 mL) were stirred at room temperature for 8 h and the resulting clear, viscous red solution was then poured slowly into methanol (100 mL). The white fiber formed was filtered off and extracted with hot methanol. After drying 1.333 g (99% yield) of white fiber polymer was obtained. The polymer had an inherent viscosity (η_{inh}) of 0.27 dL g^{-1} in NMP.

Nonstoichiometric Synthesis of of Poly[*oxy-1,4-phenylenecarbonyl-1,4-phenyleneoxy-1,4-phenylene*(*2,2,2-trifluoro-1-methylethylidene*)*-1,4-phenylene*] (***2b***). 1,1,1-Trifluoroacetone (0.375 g 3.36 mmol), diphenoxybenzophenone (1.027 g 2.8 mmol) and TFSA (5 mL) were stirred at room temperature for 5 min and the resulting viscous red solution was then poured slowly into methanol (100 mL). The white fiber formed was filtered off and extracted with hot methanol. After drying 1.303 g (97% yield) of white fiber polymer was obtained. The polymer had an inherent viscosity (η_{inh}) of 0.42 dL g^{-1} in NMP.

Poly[[*1,1′-biphenyl*]*-4,4′-diyl*(*2,2,2-trifluoro-1-phenylethylidene*)] (***1a***). TFSA (41.3 mL) was added to a mixture of 2,2,2 trifluoroacetophenone (8.42 g 48.3 mmol), biphenyl (7 g 48.3 mmol), and CH_2Cl_2 (33.7 mL). The reaction mixture was stirred with magnetic stirrer at room temperature for 4 days and the resulting viscous, green solution was then poured slowly into methanol (500 mL). The white fiber polymer was filtered off and extracted with refluxing methanol for 12 h. The resulting polymer (15 g 98%) had an inherent viscosity (η_{inh}) of 0.59 dL g^{-1} in NMP.

Poly[*oxy-1,4-phenylene*(*2,2,2-trifluoromethyl-1-phenylethylidene*)*-1,4-phenylene*] (***1c***). Polymer synthesis was conducted in single necked 15 mL flask equipped with magnetic stirrer. 2,2,2 -Ttrifluoroacetophenone (0.992 g 5.7 mmol), diphenyl ether (0.9705 g 5.7 mmol), CH_2Cl_2 (3.2 mL) and TFSA (0.8 mL) were stirred at room temperature for 3 h and the resulting clear, viscous orange solution was then poured slowly into methanol (200 mL). The white fiber formed was filtered off and extracted with hot methanol. After drying, 1.769 g (95% yield) of white fiber polymer was obtained. The polymer had an inherent viscosity η_{inh} of 0.14 dL g^{-1} in NMP.

Poly[*1,1′:4′,1″-terphenyl-4,4″-diyl*[*2,2,2-trifluoro-1-*(*2,3,4,5,6-pentafluorophenyl*)*ethylidene*]] (***8d***). TFSA (4.5 mL) was added to a mixture of octafluoroacetophenone (1.264 g 4.8 mmol), terphenyl (1.102 g 4.8 mmol), and CH_2Cl_2 (3.9 mL). The reaction mixture was stirred at room temperature for 30 days and the resulting viscous green solution was then poured slowly into methanol (400 mL). The white fiber formed was filtered off and extracted with hot methanol. After drying, 2.2 g (96% yield) of white fiber polymer was obtained. The polymer had an inherent viscosity η_{inh} of 0.46 dL g^{-1} in NMP.

Preparation of Poly[(*2,3-dihydro-2-oxo-1H-indole-3,3-diyl*)-[*1,1′-biphenyl*]*-4,4′-diyl*] (***9a***). A typical example of polymer preparation is as follows. TFA acid (1.2 mL) and TFSA (1.8 mL) were added to a mixture of isatin (0.066 g, 0.45 mmol) and biphenyl (0.069 g, 0.45 mmol). The reaction mixture was stirred at room temperature for 6 h and precipitated into methanol. The slightly yellow fiber formed was filtered off and washed with hot methanol. After drying, 0.1234 g (97%) of white fiber like polymer (**9a**) was obtained. The inherent viscosity $\eta_{inh.}$ of the 0.2% solution of the polymer in NMP was found to be 0.39 dL g^{-1}.

Synthesis of poly[(*2,3-dihydro-2-oxo-1H-indole-3,3-diyl*)-[*1,1′:4′,1″-terphenyl*]*-4,4″-diyl*] (***9d***). Isatin (0.066 g, 0.45 mmol), *p*-terphenyl (0.104 g, 0.45 mmol), methylene chloride (1.7 mL), TFA (1.0 mL), and TFSA (0.3 mL) were stirred at room temperature for 6 h and precipitated into methanol. The slightly yellow fiber formed was filtered off and washed with hot methanol. After drying, 0.155 g (96. %) of white polymer **9d** with an inherent viscosity $\eta_{inh.}$ of 0.45 dL g^{-1} (NMP) was obtained.

Acknowledgment. The authors acknowledge the financial support from CONACYT Mexico (Grant 60942) and from DGAPA-UNAM (PAPIIT IN 104211). Thanks are due to Dr. M. I. Chavez, G. Cedillo, and E. Fregoso-Israel for assistance with thermal and spectroscopic analysis. The authors also thank Dr. Steffen Weidner (Federal Institute for Materials Research and Testing, Germany) for his help in MALDI−TOF measurements.

References and Notes

(1) Carothers, W. H. *Chem. Rev.* **1931**, *8*, 353–426.
(2) Flory, P. J. *Principles of polymer chemistry*; Cornell University Press: Ithaca, NY, 1953, Chapter II.

(3) Odian, G. *Principles of Polymerization*, 4th ed.; John Wiley and Sons: New York, 2004, Chapter 2.
(4) Ozizmir, E.; Odian, G. *J. Polym. Sci.: Polym. Chem. Ed.* **1980**, *18*, 1089–1097.
(5) Kihara, N.; Komatsu, S.; Takata, T.; Endo, T. *Macromolecules* **1999**, *32*, 4776–4783.
(6) Lenz, R. W.; Handlovits, C. E.; Smith, H. A. *Polym. Sci.* **1962**, *58*, 351–367.
(7) Miyatake, K.; Hlil, A. R.; Hay, A. S. *Macromolecules* **2001**, *34*, 4288–4290.
(8) Iimori, H.; Shibasaki, Y.; Ando, Sh.; Ueda, M. *Macromol. Symp.* **2003**, *199*, 23–35.
(9) March, J. *Advanced Organic Chemistry*, 4th ed.; Wiley: New York, 1992; p 548.
(10) Hofmann, J. E.; Schriesheim, A. Alkylation of Aromatics with Aldehydes and Ketones. In *Friedel−Crafts and Related Reactions*; Olah, G. A., Ed.; John Wiley & Sons: New York, 1964, Vol. *II*, pp 597−640.
(11) Bayer, A. *Ber. Dtsch. Chem. Ges.* **1872**, *5*, 1094–1100.
(12) Olah, G. A. *Angew. Chem., Int. Ed. Engl.* **1993**, *32*, 767–922.
(13) Olah, G. A.; Klumpp, D. A. *Superelectrophiles and Their Chemistry*; Wiley & Sons: New York, 2008.
(14) Olah, G. A.; Surya Prakash, G. K.; Molnar, A.; Sommer, J. *Superacid Chemistry*, 2nd ed.; Wiley & Sons: Hoboken, NJ, 2009.
(15) Howells, R. D.; McCown, J. D. *Chem. Rev.* **1977**, *77*, 69–92.
(16) Stang, P. J.; White, M. R. *Aldrichimica Acta* **1983**, *16*, 15–23.
(17) Colquhoun, H. M.; Zolotukhin, M. G.; Khalilov, L. M.; Dzhemilev, U. M. *Macromolecules* **2001**, *34*, 1122–1124.
(18) Zolotukhin, M. G.; Fomine, S.; Salcedo, R.; Khalilov, L. M. *Chem. Commun.* **2004**, *N 8*, 1030–1031.
(19) Zolotukhin, M. G.; Fomina, L.; Salcedo, R.; Sansores, L. E.; Colquhoun, H. M.; Khalilov, L. M. *Macromolecules* **2004**, *37*, 5140–5141.
(20) Zolotukhin, M. G.; Fomine, S.; Lazo, L. M.; Salcedo, R.; Sansores, L. E.; Cedillo, G.; Colquhoun, H. M.; Fernandez, J. M.; Khalizov, A. *Macromolecules* **2005**, *38*, 6005–6014.
(21) Diaz, A. M.; Zolotukhin, M. G.; Fomine, S.; Salcedo, R.; Manero, O.; Cedillo, G.; Velasco, V. M.; Fritsch, D.; Khalizov, A. F. *Macromol. Rapid Commun.* **2007**, *28*, 183–187.
(22) Cruz, A. R.; Zolotukhin, M. G.; Morales, S. L.; Cardenas, J.; Cedillo, G.; Fomine, S.; Salmon, M.; Carreón-Castro, M. P. *Chem. Commun.* **2009**, *N 29*, 4408–4410.
(23) Carmen, G.; Hernandez, M.; Zolotukhin, M. G.; Maldonado, J. L.; Rehmann, N.; Meerholz, K.; King, S.; Monkman, A. P.; Fröhlich, N.; Kudla, C. J.; Scherf, U. *Macromolecules* **2009**, *42*, 9225–9230.
(24) Carmen, G.; Hernandez, M.; Zolotukhin, M. G.; Fomine, S.; Cedillo, G.; Morales, S. L.; Fröhlich, N.; Preis, E.; Scherf, U.; Salmón, M.; Chávez, M. I.; Cárdenas, J.; Ruiz-Trevino, A. *Macromolecules* **2010**, *43*, 6968–6978.
(25) Smet, M.; Schacht, E. H.; Dehaen, W. *Angew. Chem., Int. Ed.* **2002**, *41*, 4547–4550.
(26) Smet, M.; Fu, Y.; Zhang, X.; Schacht, E. H.; Dehaen, W. *Macromol. Rapid Commun.* **2005**, *26*, 1458–1463.
(27) Fu, Y.; Van Oosterwijck, C.; Vandendriessche, A.; Kowalczuk-Bleja, A.; Zhang, X.; Dworak, A.; Dehaen, W.; Smet, M. *Macromolecules* **2008**, *41*, 2388–2393.
(28) Kowalczuk, A.; Vandendriessche, A.; Trzebicka, B.; Mendrek, B.; Szeluga, U.; Cholewinski, G.; Dehaen, W.; Dworak, A.; Smet, M. *J. Polym. Sci., Part A: Polym. Chem.* **2009**, *47*, 1120–1135.
(29) Vandendriessche, A.; Thomas, J.; Oosterwijck, C. V.; Huybrechts, J.; Dervaux, B.; D'hollander, S.; Du Prez, F.; Dehaen, W.; Smet, M. *Eur. Polym. J.* **2009**, *45*, 3196–3209.
(30) Segawa, Y.; Sinananwanich, W.; Ueda, M. *Macromolecules* **2008**, *41*, 8309–831.
(31) Segawa, Y.; Higashihara, T.; Ueda, M. *J. Am. Chem. Soc.* **2010**, *132*, 11000–11001.
(32) Frisch, M. J.; Trucks, G. W.; Schlegel, H. B.; Scuseria, G. E.; Robb, M. A.; Cheeseman, J. R.; Montgomery, J. A., Jr.; Vreven, T.; Kudin, K. N.; Burant, J. C.; Millam, J. M.; Iyengar, S. S.; Tomasi, J.; Barone, V.; Mennucci, B.; Cossi, M.; Scalmani, G.; Rega, N.; Petersson, G. A.; Nakatsuji, H.; Hada, M.; Ehara, M.; Toyota, K.; Fukuda, R.; Hasegawa, J.; Ishida, M.; Nakajima, T.; Honda, Y.; Kitao, O.; Nakai, H.; Klene, M.; Li, X.; Knox, J. E.; Hratchian, H. P.; Cross, J. B.; Bakken, V.; Adamo, C.; Jaramillo, J.; Gomperts, R.; Stratmann, R. E.; Yazyev, O.; Austin, A. J.; Cammi, R.; Pomelli, C.; Ochterski, J. W.; Ayala, P. Y.; Morokuma, K.; Voth, G. A.; Salvador, P.; Dannenberg, J. J.; Zakrzewski, V. G.; Dapprich, S.; Daniels, A. D.; Strain, M. C.; Farkas, O.; Malick, D. K.; Rabuck, A. D.; Raghavachari, K.; Foresman, J. B.; Ortiz, J. V.; Cui, Q.; Baboul, A. G.; Clifford, S.; Cioslowski, J.; Stefanov, B. B.; Liu, G.; Liashenko, A.; Piskorz, P.; Komaromi, I.; Martin, R. L.; Fox, D. J.; Keith, T.; Al Laham, M. A.; Peng, C. Y.; Nanayakkara, A.; Challacombe, M.; Gill, P. M. W.; Johnson, B.; Chen, W.; Wong, M. W.; Gonzalez, C.; Pople, J. A. Gaussian 09, revision A.02; Gaussian, Inc.: Wallingford, CT, **2009**.
(33) Adamo, C.; Barone, V. J. *Chem. Phys.* **1999**, *110*, 6158–6163.
(34) Lira, A. L.; Zolotukhin, M. G.; Fomina, L.; Fomine, S. *Macromol. Theory Simul.* **2007**, *16*, 227–239.
(35) Parr, R. G.; Szentpály, L. V.; Liu, S. *J. Am. Chem. Soc.* **1999**, *121*, 1922–1924.
(36) Contreras, R.; Andres, J.; Safont, V. S.; Campodonico, P.; Santos, J. G. *J. Phys. Chem. A* **2003**, *107*, 5588–5593.
(37) Zolotukhin, M. G.; Rueda, D. R.; Balta Calleja, F. J.; Cagiao, M. E.; Bruix, M.; Sedova, E. A.; Gileva, N. G. *Polymer* **1997**, *38*, 3441–3453.
(38) Kricheldorf, H. R. *Macromol. Rapid Commun.* **2008**, *29*, 1695–1704.
(39) Kricheldorf, H. R. *J. Polym. Sci., Part A: Polym. Chem.* **2010**, *48*, 251–284.
(40) Oiwa, M. *Hannou Sokudo Keisanhou* (*Calculation of the Rate of the Reaction*); Asakura: Tokyo, 1962; p 206.
(41) Zolotukhin, M. G.; Dosiere, M.; Fougnies, C.; Villers, D.; Gileva, N. G. *Polymer* **1995**, *36*, 3575–3583.
(42) Zolotukhin, M. G.; Rueda, D. R.; Balta Calleja, F. J.; Cagiao, M. E.; Bruix, M.; Sedova, E. A.; Gileva, N. G. *Polymer* **1997**, *38*, 1471–1476.

Macromolecules
ARTICLE

Macromolecules **2011**, *44*, 203–207 **203**
DOI: 10.1021/ma1025797

Synthesis of a Polymeric Electron Acceptor Based on Perylenediimide-Bridged Ladder Polysiloxane

Wenxin Fu,[†] Chang He,[†] Shidong Jiang,[‡] Zhize Chen,[†] Jintao Zhang,[†] Zhibo Li,*[,†] Shouke Yan,*[,‡] and Rongben Zhang*[,†]

[†]*Beijing National Laboratory for Molecular Sciences (BNLMS), Institute of Chemistry, Chinese Academy of Sciences, Beijing 100190, China, and* [‡]*State Key laboratory of Chemical Resource Engineering, Beijing University of Chemical Technology, Beijing 100029, China*

Received November 14, 2010; Revised Manuscript Received December 8, 2010

ABSTRACT: A soluble perylenediimide (PDI) bridged ladder polysiloxane (PDI-LPS) was prepared using ladder superstructure (LS) directed dehydration polycondensation. LS was first assembled via synergistic interactions of hydrogen-bonding and $\pi-\pi$ stacking of tetrasilanol monomers (**M2**s) as verified from XRD, ^{29}Si NMR, and VPO characterizations. The ladder regularity of PDI-LPS was confirmed by a narrow half-peak width (Δ) of <1 ppm for $SiO_{2/2}$ unit in the ^{29}Si NMR spectra. The alignment of ladder chains was also demonstrated from high-resolution transmission electronic microscopy (HR-TEM) observations. We successfully used ladderlike structure to chemically confine PDI cores within one-dimensional polymeric semiconductor. The resulting PDI-LPS not only retained PDI's optoelectronic properties but also gained enhanced solubility in common organic solvents and improved thermal stability.

Introduction

Polymer solar cells (PSCs) are being extensively studied because of their great potential application. Compared with inorganic materials based solar cells, PSCs can be easily fabricated via spin-coating, enabling the manufacture of large area, flexible, light-weight, inexpensive, and renewable devices.[1−3] Generally, all of the solar cell devices require both hole-transporting (p-type) and electron-transporting (n-type) materials, which are desirable to have a good combination of physical, chemical, electrical, and photochemical properties.[4−7] In particular, fullerene derivatives, e.g. [6,6]-phenyl-C61-butyric acid methyl ester (PCBM), were extensively used as acceptor material. However, the absorption of PCBM in the visible region is relatively weak. Thus, development of new n-type substitutes for PCBM has attracted intensive research activities.[8−10] Perylenediimide (PDI) and its derivatives were well-known n-type organic semiconductors with high electron mobility.[11,12] However, their poor solubility made them difficult to form flexible films in common organic solvents. Herein, to solve the above-mentioned problems, we proposed an alternative strategy of using a PDI derivative as the central bridge to form ladder polymer. Through chemically incorporating PDI into ladder polymer backbone, we hope to minimize the conglomeration of PDI and improve materials' thermostability and solubility while retaining its optoelectronic properties.

It was known that polysiloxane-based materials generally had good solubility in common organic solvents and good film-forming ability.[13,14] Compared to the single-chain counterpart, the ladder polysiloxanes (LPSs) were found to have greater resistance to irradiation as well as thermal and chemical degradation.[15,16] These features inspired us to think of combining organic semiconductor compounds such as PDIs and ladder architecture together to create intramolecularly ordered polymeric semiconductors. Toward this goal, Würthner took the advantage of the supramolecular forces to synthesize polymer containing PDIs.[17] Herein, we adopted a different approach based on the "supramolecular architecture-directed stepwise coupling and polymerization" (SCP) strategy.[16] In this method, tetrafunctional precursor first self-assembled into ladder superstructure (LS) via H-bonding and $\pi-\pi$ stacking. The supramolecular LS acted as both polymerization precursor and template to form LPS.[18] Considering the encountered insolubility issue of PDI, we used tetra-*tert*-butylphenoxy-substituted PDI as the bridges for LPS shown in Scheme 1.

Experimental Section

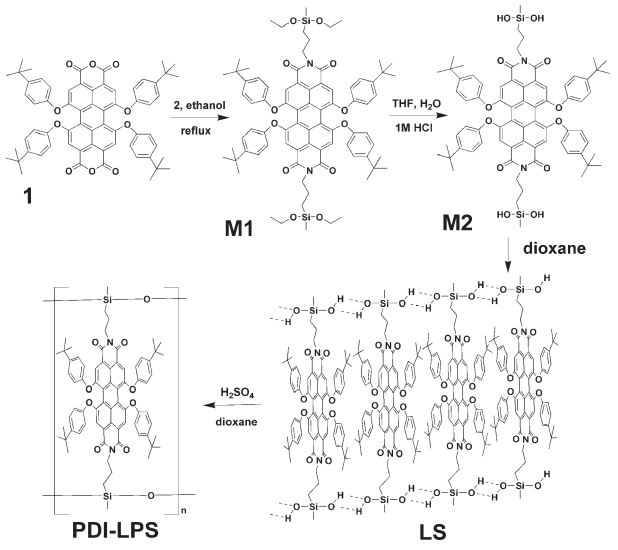
Materials and Characterizations. 1,6,7,12-Tetra-*tert*-butylphenoxyperylene-3,4,9,10-tetracarboxylic dianhydride (**1**) was purchased from Beijing Wenhaiyang Industry and Trading Co. Ltd. 3-Aminopropylmethyldiethoxysilane (**2**) was purchased from Alfa Aesar. Tetrahydrofuran (THF) and 1,4-dioxane were distilled over sodium benzophenone complex. Number-averaged molecular weight (M_n) was determined from the vapor pressure osmometry (VPO) method using a Knauer VPO instrument (Germany) in THF or dioxane at 40−50 °C. FT-IR measurement was performed using a Perkin-Elmer 80 spectrometer, and the samples were prepared by casting solution sample on KBr flake. UV−vis spectra were obtained on a Shimadzu UV−vis spectrometer (UV-1601PC). Fluorescence spectra were recorded on a Hitachi F-4500. ^{1}H and ^{29}Si NMR spectra were obtained on a Bruker Advance DPS-400 (400 MHz) spectrometer. For HR-TEM observation, 1 mg/mL solution of PDI-LPS in ethanol was dropped onto the carbon-coated mica surface. After evaporation of the solvent, the carbon film together with the sample was then floated onto the surface of distilled water and subsequently transferred onto 400 mesh copper grids for TEM observation. JEOL JEM-2100F TEM operated at 200 kV was used. X-ray diffraction (XRD) analysis was performed on a Rigaku D/MAX 2400 diffractometer. Cyclic voltammetry was performed on CHI660D voltammetric analyzer (CH Instruments)

*To whom all correspondence should be addressed: e-mail zbli@iccas.ac.cn (Z.L.), skyan@mail.buct.edu.cn (S.Y.), zhangrb@iccas.ac.cn (R.Z.); Tel +86-10-62565612; Fax +86-10-62565612.

© 2010 American Chemical Society

Published on Web 12/28/2010

Scheme 1. Synthetic Route to Target PDI-LPS



with a standard three-electrode electrochemical cell in a 0.1 M tetrabutylammonium tetrafluoroborate solution in CH_2Cl_2 at room temperature (rt) under a nitrogen atmosphere. The scanning rate is 0.1 V/s. A glassy carbon working electrode, a Pt wire counter electrode, and a silver wire as a quasi-reference electrode were used. The experiments were calibrated with the internal standard ferrocene/ferrocenium (Fc) redox system.

Synthesis. *Preparation of 1,6,7,12-Tetra-tert-butylphenoxyperylene-N,N′-bis(3-aminopropylmethyldiethoxysilane)-3,4,9,10-tetracarboxylic Dianhydride* (***M1***). 2.44 g of **1** (2.48 mmol) was added into a three-necked flask with magnetic stirring bar. The flask was then evacuated and purged with argon three times. 200 mL of dry ethanol was added under an argon atmosphere. The reaction mixture was heated to reflux prior to addition of 4.75 g (24.8 mmol) of **2** as one portion. The reaction mixture was then refluxed for 10 h under argon before cooled to rt. Then the reaction mixture was filtrated to give a fluffy cake, which was subsequently washed with cold ethanol. 1.95 g of dark red product was obtained using flash chromatography on a silica gel column (CH_2Cl_2/petroleum ether = 2/1) in 60% yield; R_f = 0.4 (CH_2Cl_2/petroleum ether = 2/1).[19] ^{1}H NMR ($CDCl_3$, 400 MHz, δ, ppm): 0.094 (s, 6H, Si−CH_3), 0.65−0.7 (t, J = 8 Hz, 4H, Si−CH_2), 1.15−1.19 (t, 12H, J = 6.94 Hz, Si−OCHH_2CH_3), 1.29 (s, 36H, −C(CH_3)$_3$), 1.74 (s, 4H, Si−CH$_2$CH_2), 3.69−3.75 (q, 8H, J = 6.96 Hz, Si−OCH_2CH$_3$), 4.07−4.11 (t, 4H, J = 7.28 Hz, Si−CH$_2$CH$_2$CH_2), 6.81−6.83 (d, 8H, J = 8.32 Hz, H-3 of *tert*-butylphenoxy), 7.22−7.24 (d, 8H, J = 8.44 Hz, H-2 of *tert*-butylphenoxy), 8.22 (s, 4H, H-2 of perylenediimide). ^{29}Si NMR (59.6 MHz, δ, ppm): −6.97 with half-peak width Δ of < 1 ppm. MALDI-TOF MS (m/z) Calcd: for $C_{80}H_{94}N_2O_{12}Si_2$, 1330.63. Found: 1330.8 M^+.

Preparation of 1,6,7,12-Tetra-tert-butylphenoxyperylene-N,N′-bis(3-aminopropylmethyldihydroxylsilane)-3,4,9,10-tetracarboxylic Dianhydride (***M2***). 1 g of **M1** (0.75 mmol) was first dissolved in a mixture of 300 mL of THF and 4 mL of water. To this solution, three drops of 1 M HCl were added with stirring at 0 °C. The reaction was monitored by TLC (methanol/CH_2Cl_2 = 1/20). After 6 h, 100 mL of diethyl ether and 80 mL of water were added. The ether layer was separated and washed with 40 mL of water three times. The organic layer was then dried over sodium sulfate and filtered. The filtrate was condensed to ~40 mL and precipitated using 100 mL of hexane, followed by filtration to give a cakelike dark red product. The product was dried under vacuum at rt, and 800 mg of dark red powder was obtained in 87.5% yield. ^{1}H NMR ($CDCl_3$, 400 MHz, δ, ppm): 0.094 (s, 6H, Si−CH_3), 0.66−0.7 (t, J = 7.17 Hz, 4H, Si−CH_2), 1.29 (s, 36H, −C(CH_3)$_3$), 1.82−1.85 (t, 4H, J = 6.92 Hz, Si−CH$_2$CH_2), 3.01−3.05 (br d, 4H, Si−OH), 4.11−4.14 (t, 4H, J = 6.8 Hz, Si−CH$_2$CH$_2$CH_2), 6.80−6.82 (d, 8H, J = 8.28 Hz, H-3 of *tert*-butylphenoxy), 7.22−7.24 (d, 8H, J = 8.4 Hz, H-2 of *tert*-butylphenoxy), 8.20 (s, 4H, H-2 of perylenediimide). ^{29}Si NMR (59.6 MHz, δ, ppm): −8.51 with half-peak width Δ of < 1 ppm. MALDI-TOF MS (m/z) Calcd: for $C_{72}H_{78}N_2O_{12}Si_2$, 1218.5. Found: 1218.9 M^+.

Preparation of the Target PDI-LPS. 1.00 g of **M2** (0.82 mmol) was dissolved in 50 mL of dioxane, and then two drops of concentrated H_2SO_4 were added to the mixture to catalyze the condensation reaction. After 72 h, the reaction mixture was concentrated to about 20 mL under reduced pressure at 45 °C, and the concentrated mixture was stirred for another 72 h to complete the condensation reaction. To end-cap the terminal silanol groups of the polymer, 0.83 g of triethylamine (8 mmol) and 0.88 g of trimethylchlorosilane (8 mmol) dissolved in 5 mL of dioxane were added drop by drop into the flask under stirring. The mixture was stirred at rt for another 24 h. Filtration was performed to remove the small amount of gel generated during the condensation process. Adding 50 mL of methanol to the filtrate caused instantaneous precipitation of a dark red solid, which was further purified by Soxhlet extraction with methanol, *n*-hexane, and THF in turn and then eluted by THF and CH_2Cl_2 on silica gel columns. Finally, 0.87 g of PDI-LPS was obtained in 89.6% yield after being dried in a vacuum oven at 100 °C for 24 h. FT-IR (KBr, thin film, cm^{-1}): 1259 (Si−CH$_3$), 1012−1078 (Si−O−Si). ^{1}H NMR ($CDCl_3$, 400 MHz, δ, ppm): 0.07 (br s, 6H, Si−CH$_3$), 0.23−0.61 (br s, 4H, Si−CH$_2$), 0.83−0.88 (br s, 9H, Si−(CH$_3$)$_3$), 1.25 (br s, 36H, −C(CH$_3$)$_3$), 1.56−1.63 (br s, 4H, Si−CH$_2$CH$_2$), 3.87−4.07 (br s, 4H, Si−CH$_2$CH$_2$CH$_2$), 6.36−6.48, 6.77−6.79, 7.05−7.14 (br m, 16H, phenyl-H), 8.0−8.06 (br s, 4H, perylenediimide-H). ^{29}SiNMR (59.6 MHz, δ, ppm): −22.6 with half-peak width Δ of < 1 ppm for the repeat unit $SiO_{2/2}$.

Results and Discussion

Syntheses and Characterizations of M1 and M2 Precursors. **M1** was synthesized according to literature procedure[19] and purified by flash column chromatography with yield of about 60%. Tetrafunctional **M2** was obtained after hydrolyzing **M1** in dilute THF solution (~5 mg/mL in THF). Also, HCl solution (1 M) used as limiting catalyst and low temperature were strictly controlled to minimize undesired random condensation between the newly formed silanol groups in **M2** (Scheme 1). The structures of **M1** and **M2** were unambiguously verified using FT-IR and ^{1}H NMR (Figures S2 and S3). For the FT-IR spectrum of **M1**, the doublet peaks at 1106 and 1077 cm^{-1} represent the asymmetric Si−O−C stretching bands, and the peaks at the 1178 and 966 cm^{-1} are characteristics of ethoxy group (Figure S2). For **M2**, the wide hydroxyl peak around 3400 cm^{-1} suggests the successful formation of silanol groups after hydrolysis of **M1**. ^{1}H NMR spectra shown in Figure S3 indicated the complete disappearance of protons from Si−OCH_2−CH_3 (e and h) [δ = 3.69−3.75 (q, 8H) and 1.15−1.19 (t, 12H) ppm] when **M1** is hydrolyzed to **M2**. A new resonance attributed to proton of Si−OH [δ 3.01−3.05 (br d, 4H) ppm] was easily identified. The chemical shift changes of Si atom between **M1** and **M2** are also confirmed from ^{29}Si NMR shown in Figure 1.

Synthesis and Characterization of LS. Since **M2** consists of polar silanol groups and nonpolar perylene derivatives, **M2** displays a certain degree of amphiphilicity. We found that **M2** might spontaneously self-assemble into ordered supramolecular structures in several solvents. Considering the planar PDI bridge and H-bonding capability of Si−OH groups, we assumed that **M2** would stack up perpendicular to the PDI molecular plane to form a ladder superstructure (LS) via the synergistic interactions of silanols' square-planar H-bonding[20] and the $\pi-\pi$ stacking of perylenediimide bridges

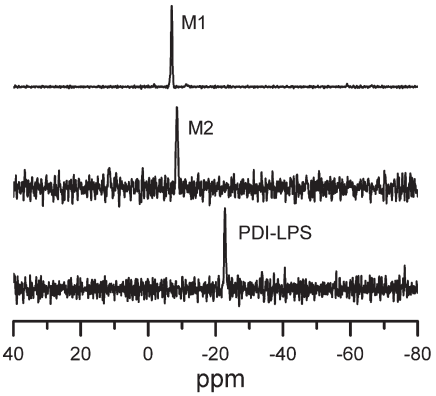


Figure 1. ^{29}Si NMR spectra of **M1**, **M2**, and PDI-LPS in dioxane with half-peak width (Δ) < 1 ppm.

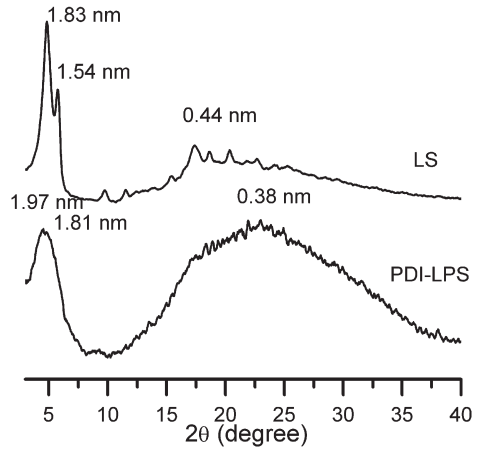


Figure 2. XRD of LS and PDI-LPS.

(Scheme 1), similar to literature reported systems.[18,21] In this way, LS can maximize the H-bonding and $\pi-\pi$ interactions, while minimizing the formation of random branched structures. The regularity of LS was probably the most critical factor to prepare well-defined LPS. In addition, we found that particular experimental conditions, such as temperature, electrodonating ability, and polarity of solvent, can greatly affect the regularity of LS.[21,22] After exploring several reaction systems, we found that dioxane at relatively low temperature can offer LS with good ladder superstructures. Figure 2 shows XRD spectra of freeze-dried LS sample. Note that using freeze-dry method can preserve the pristine ladder structure of LS in solution to a great extent. In particular, the XRD profile of freeze-dried LS sample prepared from dioxane solution shows two primary peaks with d = 1.83 and 1.54 nm. The former represents the width of LS, while the latter corresponds to the thickness of LS. Moreover, there is a diffusing peak ranging from 20° to 30°, within which there were small spikes with d around 0.44 nm presumably arising from the $\pi-\pi$ of PDI groups. The supramolecular nature of LSs can be inferred from their aggregation number, which can be calculated from their number-averaged molecular weight determined using VPO. The corresponding results are summarized in Table 1. As mentioned above, the ladder structure of LS strongly depended on solvent polarity, solvent electrodonating ability, and solution temperature. For example, LS assembled in dioxane at 43 °C had about six repeat units (**M2**). Meanwhile, when the temperature increased to 50 °C, the average repeating number decreased to about one, indicating no LS

Table 1. VPO Results of Ladder Superstructure LS in Different Conditions

T (°C)	solvent/DN[a]	$\overline{M_n}$	$\overline{DP}$[b]
43	dioxane/14.8	7655	6.3
50	dioxane/14.8	1428	1.2
45	THF/20.0	2274	1.9

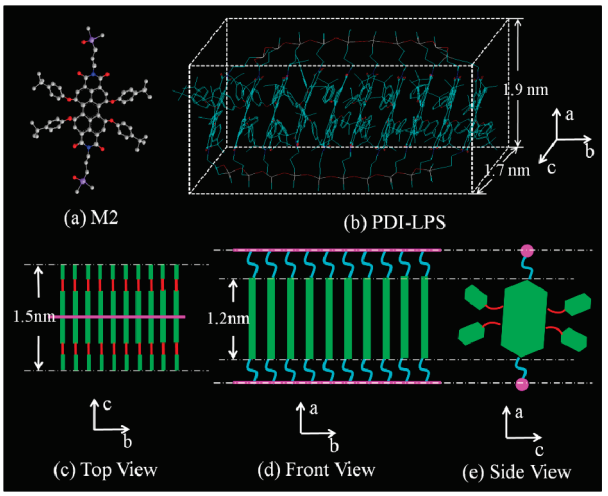
[a] The donor numbers (DN) were given in the literature.[22] [b] Number-averaged degree of polymerization.

formed at this temperature. Solvent also had a similar effect. If we changed the solvent to THF, LS only had repeating number of about two. The effects of temperature and solvent polarity toward ladder structure of LS were also compared by XRD measurements shown in Figure S1. LS prepared in dioxane at 43 °C still kept the ladder structure with characteristic LS width and thickness around 1.83 and 1.54 nm, respectively, consistent with molecular dimension of **M2**. Meanwhile, when the LS was prepared at 50 °C, the resulting samples basically lost its supramolecular ordering. Changing solvent from dioxane to THF had similar effects that **M2** could not form well-ordered ladder structures in such medium.

In addition, the regularity of LS derived from **M2** was also supported by ^{29}Si NMR measurement shown in Figure 1. It was known that the more narrow the NMR resonance peak, the more regular the ladder structure.[23] Figure 1 shows that the half-peak width (Δ) of LS's ^{29}Si NMR spectrum is less than 1 ppm, which indicates all Si atoms almost have the same chemical environment, suggesting a great regularity for LS. Otherwise, the corresponding ^{29}Si NMR will display a broach resonance peak. Combining the results from XRD, VPO, and ^{29}Si NMR, we believed that **M2** predominately self-assembled into ordered ladder superstructure (LS) via presumably synergistic hydrogen-bonding and $\pi-\pi$ stacking interactions in dioxane below 50 °C, instead of randomly conglomerated or branched structures. We then used the LS as precursor template for subsequent polycondensation to make PDI-LPS.

Synthesis and Characterization of PDI-LPS. As Williams pointed out, the acidic environment is favorable to the formation of H-bonding between the silanols, and acidic catalysts usually have stronger condensing ability than basic ones for silanols with electrodonating groups.[24] We thus used concentrated sulfuric acid to polymerize **M2** into the target PDI-LPS. We also found that extension of reaction time helped increasing conversion and molecular weight of LPS. After polycondenstion, we used Me_3SiCl to end-cap the Si−OH end groups to give final product PDI-LPS, which was found soluble in THF, CH_2Cl_2, and toluene, etc. In particular, PDI-LPS had solubility larger than 100 mg/mL in THF, while its low molecular weight counterpart (*N,N*′-bis(3-triethoxysilylpropyl)perylene-3,4:9,10-tetracarboxydiimide) has solubility lower than 1 mg/mL in THF.[19] The M_n of PDI-LPS was about 40 470 Da determined by VPO measurement, which gave the degree of polymerization being about 34. Furthermore, the expected chemical structure of PDI-LPS was verified using FT-IR, ^{1}H NMR, and MALDI-TOF mass spectra available in the Supporting Information. For the FT-IR spectra of PDI-LPS (Figure S2), the characteristic absorptions of the Si−OH group disappeared after polycondensation, and the two strong peaks in the region of 1000−1100 cm^{-1} emerged, which were attributed to the asymmetric Si−O−Si stretching vibration. The ^{29}Si NMR spectrum of PDI-LPS is shown in Figure 1, in which the half-peak width (Δ) was less than 1 ppm, indicating the high ladder regularity of PDI-LPS. In contrast, literature Δ values of oligomeric polyphenylsilsesquioxane were about 4−5 ppm.[25] Figure 2 shows XRD data of PDI-LPS. Compared

Scheme 2. (a) Molecular model of M2; (b) 3D Mode of Molecular Simulated PDI-LPS with 10 Repeat Units (Hyper Chem7.0 Geometry Optimization with RMS Gradient of 0.1 kcal/mol); (c), (d), and (e) Are the Corresponding Molecular Dimensions of PDI-LPS along *a*, *b*, and *c* Axis, Respectively



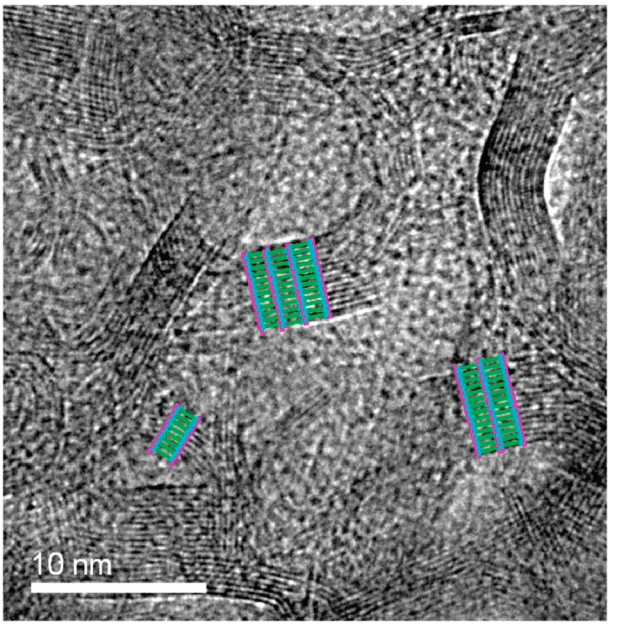


Figure 3. HR-TEM image of PDI-LPS.

to LS, PDI-LPS did not display distinct diffraction of ladder structure width and thickness due possibly to variation of their structure. LS was assembly via oriented $\pi-\pi$ stacking and hydrogen bonding, while PDI-LPS was linked by −O−Si−O− with more freedom. The chain rigid of chemically linked PDI-LPS was actually decreased after polycondensation from hydrogen-bonding-linked LS. As a result, a smeared XRD diffraction pattern was obtained, whereas primary diffraction gives spacing about 1.97 nm, which agrees well with theoretical width of PDI-LPS (Scheme 2). Note that the $\pi-\pi$ stacking of PDI-LPS was apparently less ordered compared to LS from their XRD diffraction. We presume the main reason is also due to decrease of chain rigid converting hydrogen bonded -Si−OH···O(H)-Si- into covalent −Si−O−Si− bond.

HR-TEM Observation of PDI-LPS. From the chemical structure of precursor (Scheme 2a), we can estimate the dimension of **M2** as well as PDI-LPS illustrated in Scheme 2b. The PDI core molecule has length about 1.2 nm along the imide bonds and width being 0.7 nm along PDI bay region. Considering the substitute groups, the spatial dimension of **M2** precursor is 1.2 nm long and 1.5 nm wide. After polymerization, the **M2** precursors were chemically confined within one-dimensional space (Scheme 2b). We thus tried to visualize the ladder structure of PDI-LPS assuming the π-conjugated PDI system might provide sufficient contrast for HR-TEM characterization. The solid PDI-LPS was dispersed in ethanol before casting onto freshly prepared carbon film, which was deposited on mica surface. The sample and carbon film were subsequently transferred to bare TEM grid for characterization. Figure 3 shows a representative HR-TEM image of PDI-LPS sample.

Interestingly, PDI-LPS displayed laminated structures with random orientation. Apparently, rodlike PDI-LPS has three possible orientations when deposited on carbon surface as depicted in Scheme 2. There are two kinds of structures, i.e., the column structure and the layered structure. PDI-LPS contains two types of substituted groups, namely, the aromatic PDI with four steorically hindered *tert*-butoxy groups and polar Si−O−Si double-stranded backbone. The flat aromatic PDI core could choose face-up or edge-on orientation with respect to substrate surface. For the former, PDI-LPS would form columnlike structures standing on carbon surface as illustrated in Scheme 2e, and the Si−O−Si double-stranded backbones are aligned perpendicular to substrate with column width close to ladder thickness (1.7 nm). For the latter, whole PDI-LPS would lie down on substrate, which will give layered structures as illustrated in Scheme 2c and 2d. The periodicity of these layers should be close to $\pi-\pi$ stacking distance. Careful examination of TEM results revealed that the spacing was around 0.3 nm, which was very close to $\pi-\pi$ stacking distance estimated by XRD. Unfortunately, we could not clearly identify the width of PDI-LPS because of the negligible contrast between adjacent samples. Also, additional TEM images at different magnifications are shown in Figure S6.

Photophysical Properties of PDI-LPS. Figure S7 compares the UV−vis spectra of **M1**, **M2**, and PDI-LPS. Apparently, **M1** has nearly identical absorption spectra to **M2**. Both have the characteristic absorption of PDI. The absorption maximum at 570 nm belongs to the electronic S_0-S_1 transition, with a transition dipole moment along the long molecular axis,[26] and the second absorption band in the region of 400−460 nm is attributed to the electronic S_0-S_2 transition, with a transition dipole moment perpendicular to the long molecular axis.[27] The effects of $\pi-\pi$ stacking interactions between **M2**s intensified with increase of concentration. **M2** showed an obvious red shift with increase of sample concentration THF and dioxane, which suggested a dynamic assembly among **M2** in THF and dioxane (Figure S9).[26] In contrast, PDI-LPS had a 12 nm red shift compared to **M2** after polymerization. We believed that such a red shift was presumably induced by delocalization of π-electrons after the aromatic PDIs were confined into one-dimensional ladder space. For PDI-LPS, variation of polymer concentration did not cause noticeable change of UV/vis spectra except the increase of absorption intensity, which indicated that there was no serious aggregation when concentrations were lower than 10^{-4} mg/mL.

Cyclic Voltammetry Study. To test the influence of ladder structure on PDI optoelectronic properties, we found the blends of PDI-LPS and P3HT (1:1) showed enhanced absorption areas spectrum compared to their precursors. Fluorescence measurements showed the blended thin film had strong fluorescence quenching indicating efficient energy transfer from P3HT to PDI-LPS (Figure S8). The HOMO and LUMO

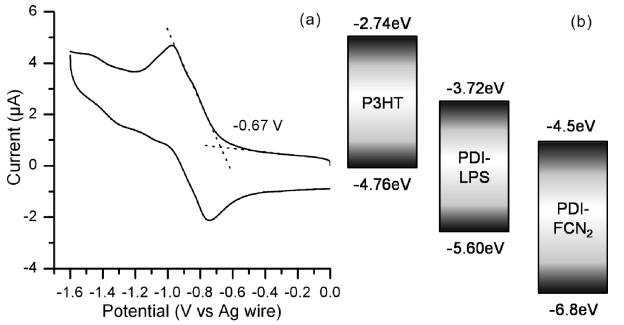


Figure 4. (a) Cyclic voltammetry of PDI-LPS. (b) Energy diagram of ITO/PEDOT:PSS/P3HT:PDI-LPS:PDI-FCN_2.

energy levels of PDI-LPS were determined using cyclic voltammetry (CV) (Figure 4a), and the energy levels were calculated according to the reported method.[28] Figure 4b compares the LUMO and HOMO energy levels of PDI-LPS with represent semiconduct compounds. The LUMO energy level of PDI-LPS was obtained from the onset reduction potentials in Figure 4a: $E_{LUMO} = -e(E_{onset}^{red} + 4.39) = -e(-0.67 + 4.39) = -3.72$ eV. The absorption edge of the film extends to 660 nm, from which the corresponding optical energy gap (E_g^{opt}) is calculated as 1.88 eV. So $E_g^{opt} = -e(E_{HOMO} - E_{LUMO})$ and $E_{HOMO} = -5.60$ eV. As shown in Figure 4b, PDI-LPS has the proper HOMO and LUMO level with P3HT. Compared with the low molar mass PDI derivatives (e.g., PDI-FCN_2[29]), PDI-LPS has higher LUMO level, which could help the solar cell device to own higher open-circuit voltage.

Thermal Properties of PDI-LPS. We also investigated the thermal properties of PDI-LPS (Figure S5). The PDI-LPS began to decompose at 442 °C and lost about 5 wt % at ca. 430 °C. The DSC curve shows that the PDI-LPS does not have any melting peaks, and its glass transition temperature (T_g) locates at ~310 °C, which is much higher than that of the low molar mass PDI derivatives, for example, 135 °C of *N,N′*-bis(cyclohexyl)-(1,7 and 1,6)-dicyanoperylene-3,4,9, 10-bis(dicarboximide) (PDI-CN).[30] We consider the surprisingly higher T_g is due to the excellent regular ladder structure of the PDI-LPS. The double-strained structure could provide this material with excellent thermal property and dimensional stability due to the minimized movements of chain segments.

Conclusion

In summary, we synthesized a novel polymeric electron acceptor based on PDI-bridged ladder polysiloxane (PDI-LPS) via self-assembled ladder superstructure (LS) of the monomer **M2** for the first time. XRD, ^{29}Si NMR, and VPO characterizations supported that supramolecular LS directed the polymerization pathway. Moreover, the target polymer PDI-LPS was confirmed to possess high ladder regularity by an extremely narrow baseline width ($\Delta < 1$ ppm) for $SiO_{2/2}$ unit in ^{29}Si NMR spectra. HR-TEM measurements revealed that the PDI-LPS had layered structures in bulky state. In particular, PDI-LPS exhibited outstanding physical properties such as good solubility, higher thermal stability, a wide absorption region, and proper LUMO energy level in contrast to PDI precursor. We thus think preparation of polymeric n-type semiconductor might be an alternative electron acceptor material for polymer solar cells. Moreover, the methodology used is a universal route to construct ladder electron acceptor materials with other organic semiconductor bridges.

Acknowledgment. The financial support of NSFC [No. 50821062, 50521302, and 50973008] is gratefully acknowledged.

Supporting Information Available: Text giving the experimental information and figures showing XRD of LS, FT-IR spectra, ^{1}H NMR spectra, MALDI-TOF mass spectra, TGA and DSC traces, HR-TEM images, UV/vis, and fluorescence spectra of PDI-LPS. This material is available free of charge via the Internet at http://pubs.acs.org.

References and Notes

(1) Yu, G.; Gao, J.; Hummelen, J. C.; Wudl, F.; Heeger, A. J. *Science* **1995**, *270*, 1789–1791.
(2) Bundgaard, E.; Krebs, F. C. *Sol. Energy Mater. Sol. Cells* **2007**, *91*, 954–985.
(3) Günes, S.; Neugebauer, H.; Sariciftci, N. S. *Chem. Rev.* **2007**, *107*, 1324–1338.
(4) Schmidt-Mende, L.; Fechtenkotter, A.; Mullen, K.; Moons, E.; Friend, R. H.; MacKenzie, J. D. *Science* **2001**, *293*, 1119–1122.
(5) Peumans, P.; Uchida, S.; Forrest, S. R. *Nature* **2003**, *425*, 158.
(6) Liu, J.; Kadnikova, E. N.; Liu, Y.; McGehee, M. D.; Fréchet, J. M. J. *J. Am. Chem. Soc.* **2004**, *126*, 9486–9487.
(7) Li, G.; Shrotriya, V.; Huang, J.; Yao, Y.; Moriarty, T.; Emery, K.; Yang, Y. *Nature Mater.* **2005**, *4*, 864–868.
(8) Kim, Y.; Cook, S.; Choulis, S. A.; Nelson, J.; Durrant, J. R.; Bradley, D. D. C. *Chem. Mater.* **2004**, *16*, 4812–4818.
(9) Veenstra, S. C.; Verhees, W. J. H.; Kroon, J. M.; Koetse, M. M.; Sweelssen, J.; Bastiaansen, J. J. A. M.; Schoo, H. F. M.; Yang, X.; Alexeev, A.; Loos, J.; Schubert, U. S.; Wienk, M. M. *Chem. Mater.* **2004**, *16*, 2503–2508.
(10) Mikroyannidis, J. A.; Stylianakis, M. M.; Sharma, G. D.; Balraju, P.; Roy, M. S. *J. Phys. Chem. C* **2009**, *113*, 7904–7912.
(11) Katz, H. E.; Johnson, A. J. L., J.; Kloc, C.; Siegrist, T.; Li, W.; Lin, Y.-Y.; Dodabalapur, A. *Nature* **2000**, *404*, 478.
(12) Neuteboom, E. E.; Meskers, S. C. J.; van Hal, P. A.; van Duren, J. K. J.; Meijer, E. W.; Janssen, R. A. J.; Dupin, H.; Pourtois, G.; Cornil, J.; Lazzaroni, R.; Brédas, J.-L.; Beljonne, D. *J. Am. Chem. Soc.* **2003**, *125*, 8625–8638.
(13) El-Nahhal, I. M.; El-Ashgar, N. M. *J. Organomet. Chem.* **2007**, *692*, 2861–2886.
(14) Liu, L.; Lu, H.; Wang, H.; Bei, Y.; Feng, S. *Appl. Organomet. Chem.* **2009**, *23*, 429–433.
(15) Brown, J. F.; Vogt, L. H.; Katchman, A.; Eustance, J. W.; Kiser, K. M.; Krantz, K. W. *J. Am. Chem. Soc.* **1960**, *82*, 6194–6195.
(16) Gu, H. W.; Xie, P.; Shen, D.-Y.; Fu, P.-F.; Zhang, J.-M.; Shen, Z.-R.; Tang, Y.-X.; Cui, L.; Kong, B.; Wei, X.-F.; Wu, Q.; Bai, F.-L.; Zhang, R.-B. *Adv. Mater.* **2003**, *15*, 1355–1358.
(17) Zhang, X.; Chen, Z.; Würthner, F. *J. Am. Chem. Soc.* **2007**, *129*, 4886–4887.
(18) Wan, Y.; Yang, L.; Zhang, J.; Zhang, P.; Fu, P.-F.; Zhang, T.; Xie, P.; Zhang, R. *Macromolecules* **2006**, *39*, 541–547.
(19) Schneider, M.; Müllen, K. *Chem. Mater.* **2000**, *12*, 352–362.
(20) Kakudo, M.; Kasai, P. N.; Watase, T. *J. Chem. Phys.* **1953**, *21*, 1894–1895.
(21) Zhang, T.; Deng, K.; Zhang, P.; Xie, P.; Zhang, R. *Chem.—Eur. J.* **2006**, *12*, 3630–3635.
(22) Gutmann, V. *Electrochim. Acta* **1976**, *21*, 661–670.
(23) Zhou, Q. L.; Yan, S. K.; Xie, P.; Zhang, R. B. *Acta Polym. Sin.* **2007**, 918–930.
(24) Williams, E. A.; Cargioli, J. D.; Larochelle, R. W. *J. Organomet. Chem.* **1976**, *108*, 153–158.
(25) Yamamoto, S.; Yasuda, N.; Ueyama, A.; Adachi, H.; Ishikawa, M. *Macromolecules* **2004**, *37*, 2775–2778.
(26) Würthner, F.; Thalacker, C.; Diele, S.; Tschierske, C. *Chem.—Eur. J.* **2001**, *7*, 2245–2253.
(27) Gvishi, R.; Reisfeld, R.; Burshtein, Z. *Chem. Phys. Lett.* **1993**, *213*, 338–344.
(28) Li, Y.; Cao, Y.; Gao, J.; Wang, D.; Yu, G.; Heeger, A. J. *Synth. Met.* **1999**, *99*, 243–248.
(29) Jones, B. A.; Facchetti, A.; Wasielewski, M. R.; Marks, T. J. *J. Am. Chem. Soc.* **2007**, *129*, 15259–15278.
(30) Shin, W. S.; Jeong, H.-H.; Kim, M.-K.; Jin, S.-H.; Kim, M.-R.; Lee, J.-K.; Lee, J. W.; Gal, Y.-S. *J. Mater. Chem.* **2006**, *16*, 384–390.

208 *Macromolecules* **2011**, *44*, 208–214
DOI: 10.1021/ma101803h

Macromolecules
ARTICLE

Detecting Structural Polydispersity in Branched Polybutadienes

Si Wan Li,† Heon E. Park, John M. Dealy,* and Milan Maric

Department of Chemical Engineering, McGill University, Montreal, QC, Canada H3A 2B2

Hyojoon Lee,† Kyuhyun Im,‡ Heungyeal Choi, and Taihyun Chang

Department of Chemistry and Division of Advanced Materials Science, Pohang University of Science and Technology (POSTECH), Pohang 790-784, Korea

M. Shahinur Rahman and Jimmy Mays

Department of Chemistry, University of Tennessee, Knoxville, Tennessee 37996, United States.
†Equal contribution. ‡Current address: Samsung Advanced Institute of Technology, Korea

Received September 27, 2010; Revised Manuscript Received November 9, 2010

ABSTRACT: The structural details of a set of highly entangled H-shaped polybutadienes (PBDs) prepared by anionic polymerization were examined in detail by three reputable laboratories using size exclusion chromatography (SEC) and temperature gradient interaction chromatography (TGIC). While SEC data indicated that samples having the desired structures (i.e., nearly monodisperse H-shaped polymer) had been produced, additional SEC data from other laboratories showed that the samples were structurally more complex than originally thought. TGIC data revealed that while the samples did not contain high molecular weight byproducts, they did contain low molecular weight byproducts. To discern these structural details of the branched PBDs, small amounts of sample were fractionated by TGIC. By combining knowledge of the polymerization process with the TGIC data of fractionated samples, it was possible to work out the detailed compositions of the samples and the branching structures of each component.

Introduction

The polymers described here were synthesized for a study of the effects of long-chain branching and polydispersity on the rheological behavior of entangled polymers, the results of which were to be used for the evaluation of molecular models of viscoelasticity. The desired structural details (arm and crossbar lengths) of these polymers were estimated prior to synthesis so that the polymers would be highly entangled but with terminal behavior accessible using available rheometric techniques. In order to facilitate the evaluation of molecular models as predictors of rheological behavior, a series of molecularly uniform H-shaped polybutadienes (H-PBDs) with a high concentration of 1,4-addition were required, and polydispersity was to be generated by blending. In this way the detailed structures of the samples would be known. H-PBD was chosen because H is the simplest structure containing two branch points, and PBD has a relatively low molecular weight between entanglements (M_e = 2 kg/mol[1]) among polymers that can be synthesized by anionic polymerization. The preference for high 1,4-addition is due to the fact that 1,2-addition results in a vinyl side group (a short branch), and the double bond on the vinyl side group is vulnerable to cross-linking. A novel anionic polymerization method[2] was used to prepare samples having the desired characteristics.

While size exclusion chromatography (SEC) data indicated that this synthesis method had produced the desired materials, later analyses using SEC with different chromatographic detectors and temperature gradient interaction chromatography (TGIC) revealed that while the production of high molecular byproducts had been obviated, the samples were considerably more complex than originally thought. This was discouraging from the point of view of the intended rheological study, but if the detailed composition of the samples could somehow be discerned, they could still be of use. We explain below how this was accomplished. The H-PBD samples are named according to the intended molecular weights of the arms and crossbars; e.g., "HA12B40" denotes a sample with four arms of equal molar mass of 12 kg/mol and a crossbar with a molar mass of 40 kg/mol.

Experimental Section

Synthesis of H-PBDs. A novel strategy for preparing H-PBDs by anionic polymerization was developed by Rahman et al.[2] in order to minimize the formation of high molecular weight byproducts like those reported by Perny et al.[3] It is based on the idea that the coupling of two side arms with trichloromethylsilane prior to any reaction with the crossbar should significantly reduce the production of high molecular weight byproducts.[4] This method requires the use of high-vacuum and ampoulization techniques.[5] Details of the synthesis procedures and dilute solution properties have been described previously.[2] In general, the synthesis involves a difunctional diphenylethylene-based coupling agent 4-(dichloromethylsilyl)diphenylethylene (DCMSDPE), *sec*-BuLi, butadiene, and benzene. As shown in Figure 1, the synthesis consists of five main steps, and this reaction scheme will be used to infer the molecular structures of the resulting polymers in a later section.

Determination of Isomeric Composition. To elucidate microstructures, ^{1}H nuclear magnetic resonance (NMR) was used. As the sensitivity and resolution of NMR spectra increase with magnetic field strength, the characteristic peaks for *cis* and *trans*

*Corresponding author. E-mail: john.dealy@mcgill.ca.

 Published on Web 12/20/2010 © 2010 American Chemical Society

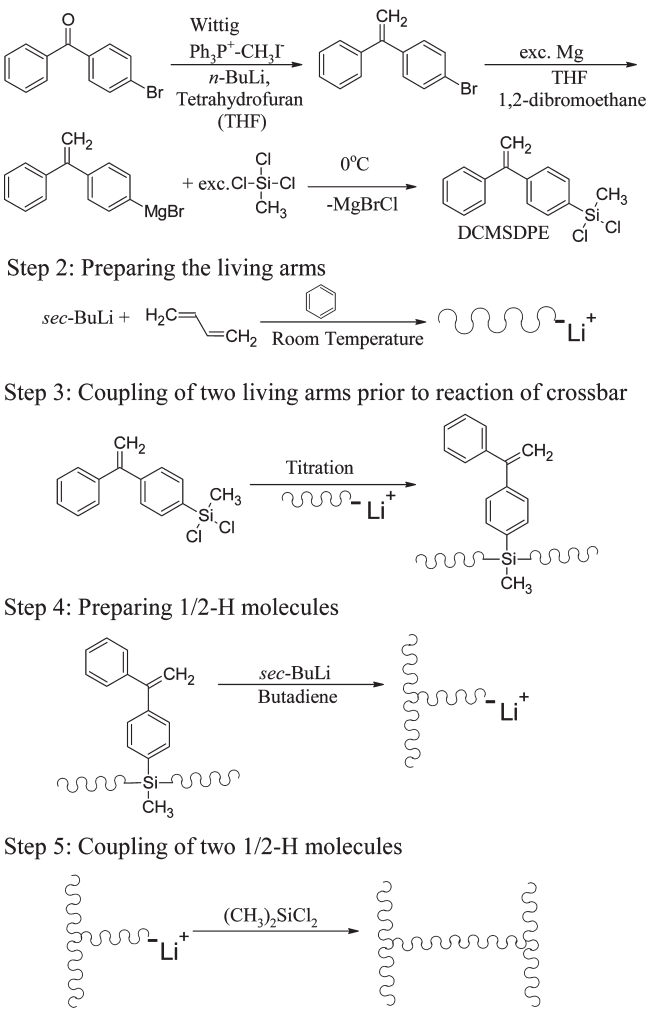


Figure 1. Synthesis steps for the anionic polymerization of H-PBD.

configurations can be resolved by use of 500 MHz field. Our NMR studies were carried out on a 500 MHz Varian unity spectrometer at room temperature. A sample of 10 mg was dissolved in 0.7 mL of deuterated chloroform (Cambridge Isotope Laboratories Inc.) in 5 mm 508 Up NMR tubes. Samples were injected into the probe, shimmed, and scanned 32 times.

Determination of Molecular Weights by SEC. Molecular weights of the H-PBDs were determined in three laboratories under the supervision of qualified scientists. The first characterization (SEC-1) was performed using SEC equipped with two-angle laser light scattering (TALLS) in 30 mW power at a wavelength of 685 nm, a refractive index (RI) detector at a wavelength of 680 nm, and a Viscotek differential viscometer to determine the precursors and final products. The columns were Waters Ultrastyragel HR series, HR-2, HR-4, HR-5E, and HR-6E, with pore sizes 10^3, 10^4, and 10^5 Å. Measurements were done at 40 °C with tetrahydrofuran (THF) as the mobile phase at a flow rate of 1.0 mL/min. An average value of the refractive index increment (dn/dc) 0.130 mL/g was used in determining the molar mass of the intermediate products. The characterization was performed in parallel with the synthesis[2] and thus provided information on the product of each stage of the polymerization (i.e., step 2 and step 4 in Figure 1) in addition to the final product. "Final product" refers to the result of step 5 in Figure 1 after fractionation with toluene/methanol as the solvent/non-solvent pair.[2] The second SEC characterization (SEC-2) was performed on the final product using a SEC system of Waters Alliance 2695 separations module and a Viscotek TDA model 302 consisting of a RI detector at a wavelength of 660 nm, a 4-capillary viscometer, and a 7° light scattering detector (LS) in 3 mW power at a wavelength of 670 nm were used for these samples. Two Polymer Laboratories Polypore columns (300 × 7.5 mm, 5 μm) were used, and the detectors were temperature controlled in the same oven as the Viscotek TDA. Measurements were done at 40 °C with THF as the mobile phase at a flow rate of 1.0 mL/min; dn/dc was allowed to float between 0.133 and 0.138 mL/g. Each sample was injected three times, and the data were mathematically averaged before processing. The third SEC characterization (SEC-3) was performed on the final product, using a Wyatt miniDAWN LS detector in 60 mW power at a wavelength of 658 nm, and a Shodex RI-101 RI detector uses white light as the light source with two PLgel mixed-C columns (300 × 7.5 mm, 5 μm). This characterization was performed at 40 °C with THF as the mobile phase at a flow rate of 0.8 mL/min; dn/dc was 0.128 mL/g.

Determination of Molecular Weights by TGIC. Unlike SEC, TGIC[6,7] is an interaction chromatographic technique in which the separation is driven by enthalpic interactions between the sample and the stationary phase. The interaction strength is controlled by varying the column temperature[7,8] and eluent composition,[9,10] and the molecular weight resolution is little affected by chain architecture. Therefore, TGIC is believed to be more sensitive to the chemical nature of a polymer[7−9] and to have a higher resolution than SEC.[3,11−13] The TGIC separations were carried out using a standard high-performance liquid chromatography (HPLC) system equipped with a C18 bonded silica column (Phenomenex, Kromasil, 300 Å pore, 150 × 4.6 mm, 5 μm particle size); the mobile phase was 1,4-dioxane at a flow rate of 0.5 mL/min, and dn/dc was 0.095 mL/g. The system was equipped on line with a Wyatt miniDAWN LS detector and a Shodex RI-101 RI detector. The column temperature profile is indicated by solid lines in Figure 5 which were adjusted in a way to cover the range of molar mass of each sample.

Results and Discussion

Isomeric Composition. Characteristic peaks determined by ^{1}H NMR for the *cis*/*trans* 1,4 and 1,2 vinyl configurations were identified,[14,15] and the corresponding areas under the peaks were calculated by the operating software. As proposed by Tanaka et al.,[15] the mole fractions of 1,2 and 1,4 units can be calculated by eqs 1 and 2 where the bracket denotes the mole fraction of the respective isomeric unit indicated and $I(\delta)$ is the relative integrated intensity of the signal with chemical shift δ. The ratio of the integrated intensity of the signal of the *trans* type protons to that of the *cis* ones in the 2 ppm (aliphatic) or 5 ppm (olefinic) region indicates the ratio of *trans* to *cis* in the polymer.[14,16] As noted by Santee et al., the aliphatic region is not as distinct as the olefinic region due to spin−spin coupling effects.[14] Thus, the *trans*-to-*cis* ratio was calculated by eq 3 using the olefinic region.

$$\frac{I(1.3)}{I(2.0-2.1)} = \frac{2[1,2]}{[1,2]+4[1,4]} \quad (1)$$

$$[1,2]+[1,4] = 1 \quad (2)$$

$$\frac{I(5.4)}{I(5.4)+I(5.3)} : \frac{I(5.3)}{I(5.4)+I(5.3)} \quad (3)$$

The mole fractions of *cis* 1,4 and *trans* 1,4 are then calculated by multiplying the above ratio by the overall 1,4 content given by eq 2. Results of isomeric content are summarized in Table 1, which shows that all samples had high levels of 1,4-addition (≥94%) as had been desired.

Characterization by SEC. It is well-known that the molar mass averages and molar mass distributions (MMDs) determined by SEC can vary significantly from one laboratory to another, and a comparison of data from 15 sources for a branched polyethylene revealed an interlaboratory variability for M_w of about 18% regardless of the detectors used.[17] Possible causes of these variations in molar mass average and MMD among different laboratories have been examined in detail by Trathnigg.[18] And in our study, the molar mass averages and MMDs determined in three laboratories were quite different from each other. The average molar masses determined by SEC are listed in Table 2. An "arm" is the product of step 2 in Figure 1, "$^1/_2$-H" refers to that of step 4 in Figure 1, and "final product" refers to that of step 5, although this may contain byproducts other than an H molecule, even after fractionation using toluene/methanol as the solvent/nonsolvent pair.[2]

Since the molar mass characterization by SEC-1 was performed in parallel with the synthesis,[2] it is the only one that provides information on precursors at various stages of polymerization. In other words, it contains molar mass information on arms and $^1/_2$-Hs. Complete elution curves at various stages of polymerizations can be found in a previous publication.[2] Generally, the SEC-1 elution profiles of final products, shown in Figure 2, had single peaks and narrow distributions. Moreover, a previous study on the branching parameter *g* for our samples showed very good to fair agreement with literature values on H-shaped polystyrene.[2]

However, the RI elution profiles for the same final products characterized by SEC-2, as shown in Figure 3, had double peaks except for HA12B40. The molecular weights at the two peaks are in a ratio of about 1:2, indicating the presence of $^1/_2$-H molecules, which are equivalent to asymmetric 3-arm stars, implying that most of the samples were actually mixtures of H molecules and asymmetric 3-arm stars ($^1/_2$-H). The weight fraction calculated from the area under the peaks after deconvolution of the RI signal by a Gaussian distribution indicates that the amount of $^1/_2$-H material is significant, ranging from 0 to 47 wt %, as shown in Table 2. We note that the MMD obtained from SEC-2 was the broadest of the distributions from the three laboratories.

The elution profiles obtained by SEC-3 shown in Figure 4 also indicate the presence of low molecular weight byproducts in most of the samples. In most cases, MMDs obtained by SEC-3 were broader than those found by SEC-1, likely due to better separation in SEC-3. For HA30B40 and HA40B40, the molecular weights found by SEC-3 were comparable to those found by SEC-1. However, lower molecular weights were indicated for the other samples using SEC-3

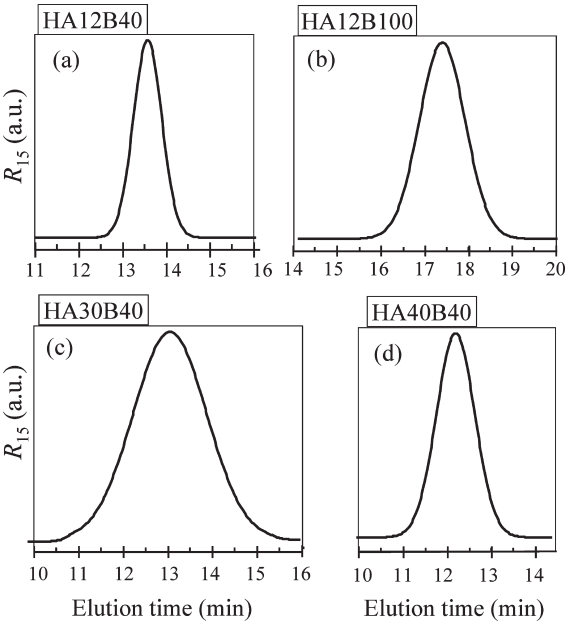


Figure 2. SEC-1 (LS response at 15°) elution profiles on final products; samples were analyzed in THF at 40 °C at a flow rate of 1.0 mL/min.

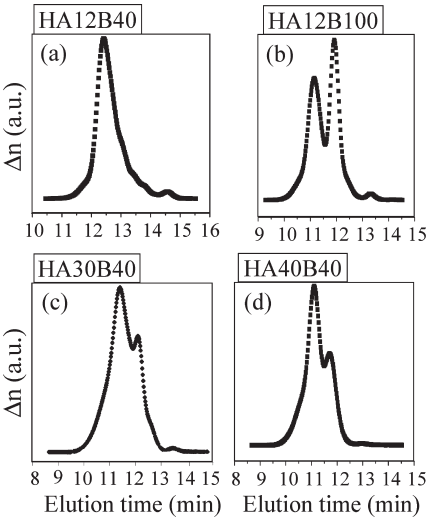


Figure 3. SEC-2 (RI response) elution profiles on final products; samples were analyzed in THF at 40 °C at a flow rate of 1.0 mL/min.

Table 1. Microstructural Characteristic of H-PBDs

	microstructure		
sample code	*cis* 1,4 (%)	*trans* 1,4 (%)	vinyl 1,2 (%)
HA12B40	51	43	6
HA30B40	52	42	6
HA40B40	52	42	6
HA12B100	53	41	6

Table 2. Summary of SEC Characterizations in Three Laboratories (Molar Mass in kg/mol)

	SEC-1						SEC-2			SEC-3	
	arm		$^1/_2$-H		final product		final product			final product	
sample code	M_n	PDI	M_n	PDI	M_n	PDI	M_n	wt %	PDI	M_p[a]	PDI
HA12B40	10.6	1.01	41	1.11	82.3	1.03	70.8	100	1.25	70.6	N.A.[b]
HA30B40	29.6	1.01	80.2	1.05	161	1.06	93.3	8	1.32	164	N.A.
							174	92			
HA40B40	41.6	1.01	106	1.06	212	1.05	109.6	23	1.22	216	N.A.
							218.8	77			
HA12B100	15.3	1.03	82.4	1.07	158	1.04	81.3	47	1.28	114	N.A.
							170	53		196	

[a] Peak molar mass. [b] N.A.: not available.

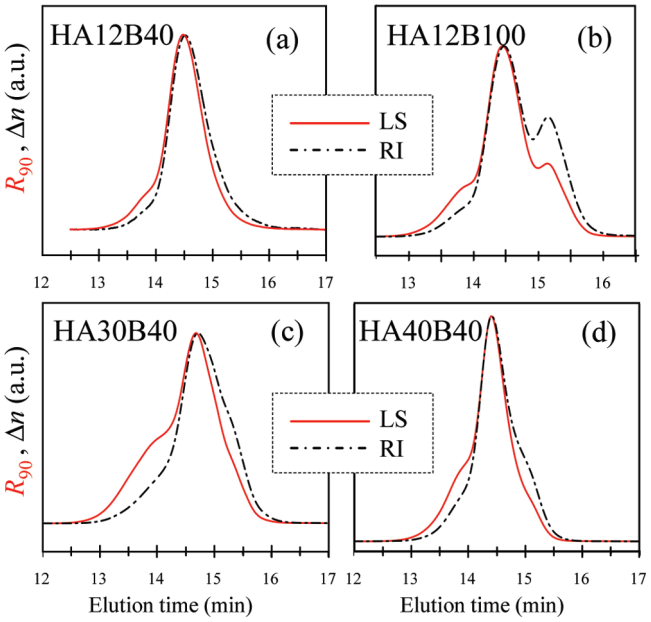


Figure 4. SEC-3 (RI and LS response at 90°) elution profiles on final products; samples were analyzed in THF at 40 °C at a flow rate of 0.8 mL/min.

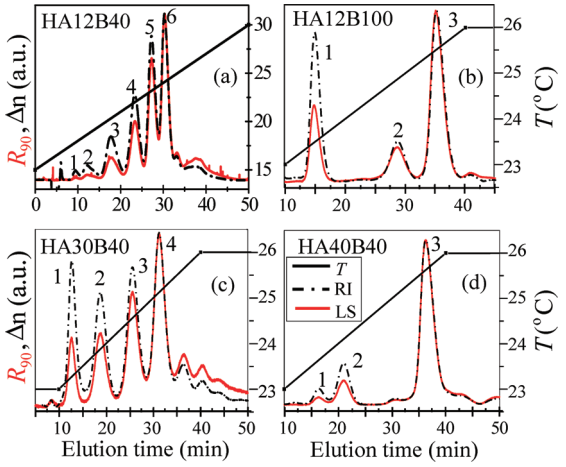


Figure 5. TGIC chromatograms for final products; samples were processed in 1,4-dioxane at a flow rate of 0.5 mL/min. Corresponding peak molar mass is shown in Table 3. Column temperature is also shown in the plot.

Table 3. Peak Molar Mass Measured by TGIC

	peak molar mass M_p (kg/mol)					
sample code	peak 1	peak 2	peak 3	peak 4	peak 5	peak 6
HA12B40	20	28	43	57	70	83
HA30B40	65	117	131	164		
HA40B40	110	121	205			
HA12B100	103	170	198			

compared to SEC-1, despite the fact that both techniques are supposed to yield absolute molecular weights. Although it is well-known that molar mass averages and MMDs vary from one laboratory to another, especially since the light scattered intensity is proportional to the square of dn/dc, using different dn/dc values would cause deviation in molar mass measurement by LS; it should not be confused with our case in which one SEC result shows a single peak while others show double peaks. Thus, we suspected that our samples were structurally more complex than originally thought.

Characterization by TGIC. The SEC profiles shown in Figures 2−4 suggested that some of the samples were binary blends (H and 3-arm stars), but the TGIC chromatograms shown in Figure 5 indicated that all the samples were mixtures of three or more components, even those fractionated with toluene/methanol as the solvent/nonsolvent pair.[2] All samples contained multiple, low molecular weight byproducts as revealed by the molecular weight corresponding to each peak, i.e., M_p shown in Table 3. Although TGIC showed higher resolution than SEC by resolving more peaks, further information is needed to identify the branching structures of these extra components. It is noted that the column temperature profile of HA12B40 is different from the other samples. A lower starting temperature is used on HA12B40 because the sample contains relatively low molecular weight components (e.g., peaks 1, 2, and 3 with M_p < 45 kg/mol). If the starting temperature of HA12B40 is chosen at 23 °C, i.e., same starting temperature as the other samples, these low molecular weight components cannot be resolved. On the other hand, an increasing temperature is needed to elute any high molecular weight components beyond peak 6 of HA12B40.

Inference of Structures. Currently our ability to identify branching structures is quite limited.[19] A commonly used characterizing parameter is the branching contraction parameter $g = \langle R_g^2\rangle_b/\langle R_g^2\rangle_l$, where $\langle R_g^2\rangle$ is the mean-square radius of gyration and the subscripts b and l denote branched and linear polymer of identical molar mass, respectively. This parameter reflects the effect of branching on $\langle R_g^2\rangle$ at a given molar mass. Several quantitative relationships have been proposed to relate g to branching structure.[20,21] Recently, van Ruymbeke et al.[22] developed a method to obtain structural information for systems containing linear and star molecules. The MMD obtained from SEC was split into contributions of various structures using a statistical approach. They found that the calculated structural compositions depended strongly on the MMD used; i.e., the amounts of linear, 3-arm star, and 4-arm star material found by SEC with a RI detector (SEC/RI) were very different from those found by SEC with a multiangle laser light scattering detector (SEC/MALLS). To avoid such discrepancies, they used MMD data from the SEC/RI for low and SEC/MALLS for high molar mass material. However, the switching point from one MMD to the other is arbitrary, and we concluded that for our samples more reliable structural composition information could be obtained by taking advantage of the higher resolution of TGIC.

First, a small amount of material was fractionated using TGIC separation columns, and eluates over given time intervals were collected into separate vials. Average molar masses (M_n and M_w) for each collected fraction of eluates were then determined by SEC-3. We found that the M_n of the last collected fraction $M_{n,\text{highest molecular component}}$ (highest molecular weight fraction in Table 4) of each sample was close to 2 times that of $^1/_2$-H molecules (Table 1) with an average difference of 4% between the two M_n values. Taking into account that the uncertainty of molecular weights measured by SEC/TALLS is typically ±5%,[23] we concluded that the highest molecular weight fraction of each sample consisted of H molecules. The lower molecular weight materials were hypothesized to be the byproducts shown in Figure 6 which was based on the synthesis mechanism shown in Figure 1, and the molecular weights of these components were estimated.

Table 4. Estimated Structures and Compositions of H-PBDs

samples	fraction name	M_n (kg/mol)	PDI	wt %		inferred structure[a]
HA12B40	1′	22	1.01	3	2	linear
	2′	29	1.00	6	3	linear
	3′	43	1.01	15	4 or 6	linear or 3-arm star
	4′	55	1.00	21	8	4-arm star
	5′	69	1.01	25	9	3-arm star
	6′	79	1.01	30		H
HA12B100	1′	103	1.02	33	4 or 6	linear or 3-arm star
	2′	168	1.01	15	9	3-arm star
	3′	187	1.02	52		H
HA30B40	1′	83	1.01	18	4 or 6	linear or 3-arm star
	2′	108	1.01	21	8	4-arm star
	3′	138	1.00	27	9	3-arm star
	4′	167	1.00	34		H
HA40B40	1′	113	1.01	6	4 or 6	linear or 3-arm star
	2′	129	1.01	17	7	3-arm star
	3′	205	1.00	77		H

[a] Number refers to the structure identification number shown in Figure 7.

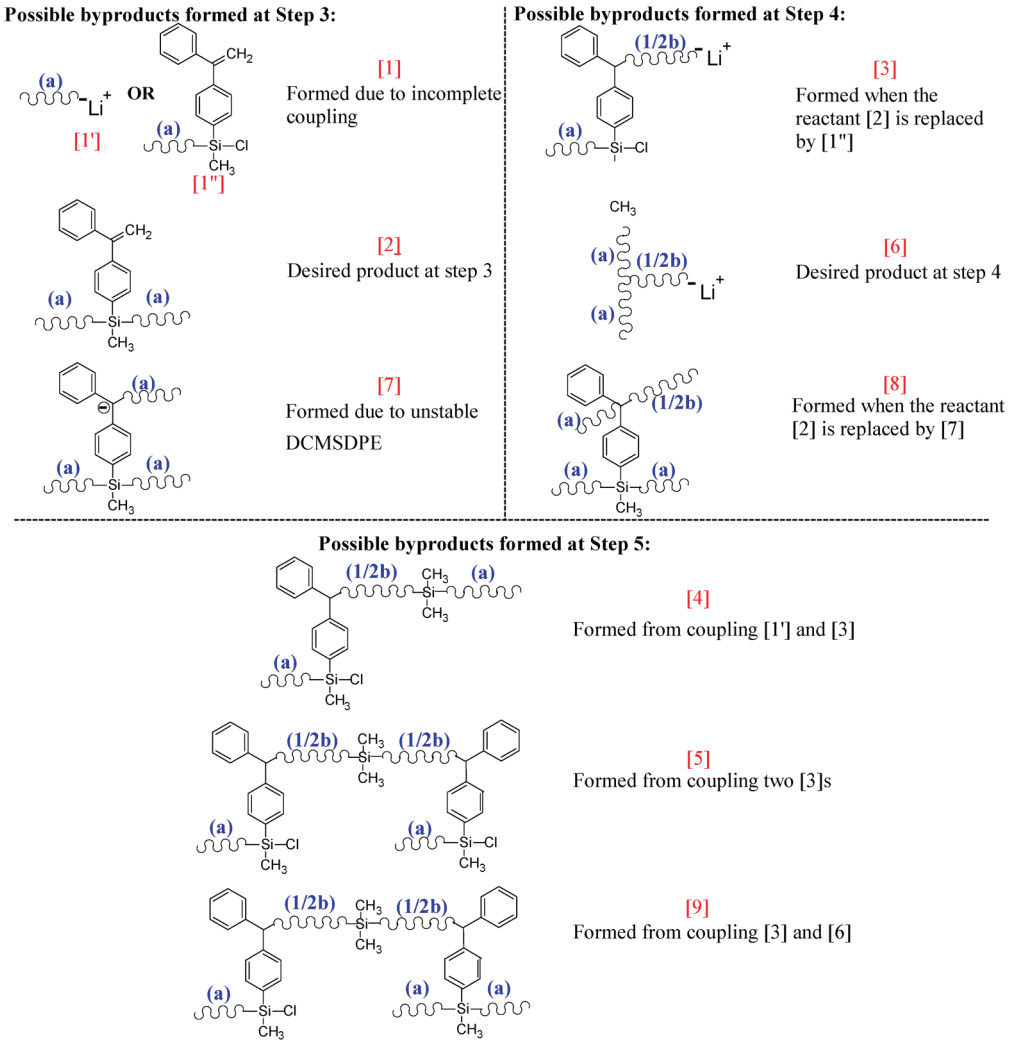


Figure 6. The most possible byproducts formed in the H-PBD synthesis. The number shown in brackets corresponds to the structure identification number shown in Figure 7, while the length of each segment is shown in parentheses with *a* and *b* equal to the arm length shown in Table 2 and the crossbar length calculated by eq 4, respectively.

We estimated $M_{n,crossbar}$ (M_n of the crossbar) by use of eq 4:

$$M_{n,\,\text{crossbar}} = M_{n,\,\text{highest molecular component}} - 4M_{n,\,\text{arm}} \quad (4)$$

where $M_{n,arm}$ is M_n of the arm given in Table 2. Using $M_{n,crossbar}$ and $M_{n,arm}$, we calculated the M_n values of the byproducts most likely to be produced during synthesis according to the composition of arms and crossbars indicated in parentheses in Figure 7. The formation of byproducts other than those shown in Figure 7, with higher molar masses or more complicated structures (e.g., branch-on-branch) is possible but very unlikely due to steric hindrance of the bulky aromatic groups in the DCMSDPE and the poor mobility of a heavy molecule.

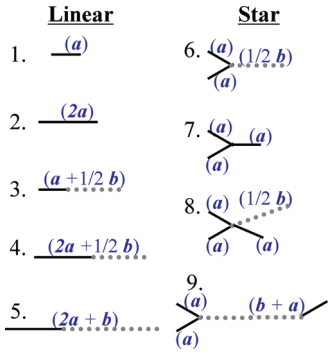


Figure 7. Schematic representations of the most probable structures of low molecular weight byproducts; the length of each segment is shown in parentheses with *a* and *b* equal to the arm length shown in Table 2 and the crossbar length calculated by eq 4, respectively.

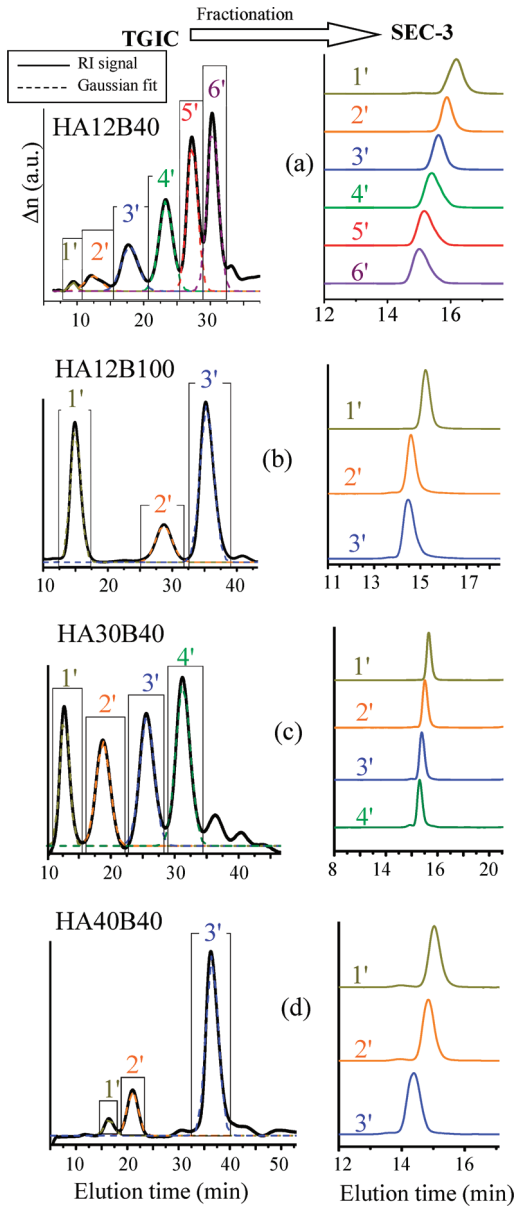


Figure 8. Fractionation of final products by TGIC and the SEC-3 elution profile (RI response) of each collected fraction. The rectangles indicate the time intervals to collect various fractions of the eluate for SEC characterization.

The TGIC data shown in Figure 8 also indicate negligible amounts of higher molecular weights byproducts compared to those shown in Figure 7. We then assigned structures to the remaining fractions by matching their M_n with those of the byproducts shown in Figure 7. Using this method, we found that the measured M_n values of the fractions of eluate shown in Table 4 were very close to the calculated M_n values of the most probable byproducts for all samples, with an average difference of 4%. Finally, to obtain the weight fraction of each structure, the RI signals shown in Figure 8 were deconvoluted using Gaussian fitting, and the results are shown in Table 4.

We use HA12B40 data to illustrate this procedure. The vertical solid lines in the TGIC curve of Figure 8 indicate the time intervals to collect various fractions of the eluate, while the dashed lines are the Gaussian fits of each peak obtained from deconvolution. The measured M_n of fraction 6′ (79 kg/mol) is very close to 2 times that of a $^1/_2$-H molecule (82 kg/mol), implying that fraction 6′ consists of H molecules. Taking $M_{n,arm}$ to be 10.6 kg/mol, as measured on the product of step 2 in Figure 1, allows us to assign fraction 5′ to H molecules with a missing arm (i.e., structure 9). Using eq 4, $M_{n,crossbar}$ was found to be 36.7 kg/mol. With this information, fraction 4′ (M_n = 55 kg/mol) is best described as an asymmetric 4-arm star (i.e., structure 8). The same analysis was applied to the remaining fractions, whereas fractions 1′ and 2′ are best described as linear chains (structures 2 and 3, respectively), and fraction 3′ can be identified as either a linear or an asymmetric 3-arm star (structure 4 or 6).

Conclusions

Size exclusion chromatography (SEC) techniques were unable to resolve the structural compositions of our long chain branched polymers containing various byproducts due to its inherent low resolution. Furthermore, data depending on sample treatment, quality of the separation columns, data acquisition, and processing revealed significant variation in SEC results among three reputable laboratories. Nonetheless, the SEC results implied that samples originally thought to be monodisperse H-shaped polymers were more complex, and this was confirmed by temperature gradient interaction chromatography (TGIC) analysis. We combined knowledge of the synthesis mechanism with TGIC data to infer the detailed structural composition of the samples. The results showed that while the synthesis method had successfully obviated the production of high-molecular-weight byproducts, our polymers were mixtures of the intended H molecules with low-molecular-weight linear, 3-arm star, and 4-arm star byproducts. This made it possible to use these samples for further rheological and molecular modeling studies. At the same time, the results clearly demonstrated the limitation in the SEC-based characterization of branched polymers and the necessity of employing complementary tools such as TGIC for a rigorous characterization.

Acknowledgment. The H-PBDs were produced under the National Science Foundation (NSF) grant-DMR 0604965. The Natural Sciences and Engineering Research Council of Canada (NSERC) provided financial support for the structure study. T.C. acknowledges the support from NRF via NRL (R0A-2007-000-20125-0), SRC (R11-2008-052-03002), and WCU (R31-2008-000-10059-0) programs. S.W.L. gratefully acknowledges the assistance at Drs. Willem deGroot, Ray Brown, and Tianzi Huang at the Dow Chemical Company for the SEC-2 data and Dr. Jacques Roovers for his valuable advice regarding anionic polymerization.

References and Notes

(1) Fetters, L. J.; Lohse, D. J.; Colby, R. H. Chain dimensions and entanglement spacings. In *Physical Properties of Polymers Handbook*; 2nd Ed., Springer: New York, 2006.
(2) Rahman, M. S.; Aggarwal, R.; Larson, R. G.; Dealy, J. M.; Mays, J. *Macromolecules* **2008**, *41*, 8225–8230.
(3) Perny, S.; Allgaier, J.; Cho, D.; Lee, W.; Chang, T. *Macromolecules* **2001**, *34*, 5408–5415.
(4) Roovers, J.; Toporowski, P. M. *Macromolecules* **1981**, *14*, 1174–1178.
(5) Uhrig, D.; Mays, J. W. *J. Polym. Sci., Part A: Polym. Chem.* **2005**, *43*, 6179–6222.
(6) Lee, H. C.; Chang, T. *Polymer* **1996**, *37*, 5747–5749.
(7) Chang, T. *J. Polym. Sci., Part B: Polym. Phys.* **2005**, *43*, 1591–1607.
(8) Chang, T. *Adv. Polym. Sci.* **2003**, *163*, 1–60.
(9) Glöckner, G. *Gradient HPLC of Copolymers and Chromatographic Cross-Fractionation*; Springer Verlag: New York, 1992.
(10) Pasch, H.; Trathnigg, B. *HPLC of Polymers*; Springer Verlag: Berlin, 1998.
(11) Lee, W.; Lee, H. C.; Chang, T.; Kim, S. B. *Macromolecules* **1998**, *31*, 344–348.
(12) Lee, W.; Lee, H.; Cha, J.; Chang, T.; Hanley, K. J.; Lodge, T. P. *Macromolecules* **2000**, *33*, 5111–5115.
(13) Lee, H. C.; Chang, T.; Harville, S.; Mays, J. *Macromolecules* **1998**, *31*, 690–694.
(14) Santee, E. R.; Chang, R.; Morton, M. *J. Polym. Sci., Polym. Lett. Ed.* **1973**, *11*, 449–452.
(15) Tanaka, Y.; Takeuchi, Y. *J. Polym. Sci., Part A-2* **1971**, *9*, 43–57.
(16) Sadeghi, G. M.; Barikani, M.; Morshedian, J.; Taromi, F. A. *Iran. Polym. J.* **2003**, *12*, 515–521.
(17) D'Agnillo, L.; Soares, J. B. P.; Penlidis, A. *J. Polym. Sci., Part B: Polym. Phys.* **2002**, *40*, 902–921.
(18) Trathnigg, B. Size-exclusion chromatography of polymers. In *Encyclopedia of Analytical Chemistry*; John Wiley & Sons Ltd.: Chichester, 2000.
(19) Dealy, J. M.; Larson, R. G. *Structure and Rheology of Molten Polymers: From Structure to Flow Behavior and Back Again*; Hanser-Gardner Publications: Cincinnati, OH, 2006.
(20) Bonchev, D.; Markel, E. J.; Dekmezian, A. H. *Polymer* **2002**, *43*, 203–222.
(21) Zimm, B. H.; Stockmayer, W. H. *J. Chem. Phys.* **1949**, *17*, 1301–1314.
(22) van Ruymbeke, E.; Coppola, S.; Balacca, L.; Righi, S.; Vlassopoulos, D. *J. Rheol.* **2010**, *54*, 507–538.
(23) Terao, K.; Mays, J. W. *Eur. Polym. J.* **2004**, *40*, 1623–1627.

Macromolecules
ARTICLE

Macromolecules **2011**, *44*, 215–220 **215**
DOI: 10.1021/ma102321z

Nitroxide-Mediated Controlled/Living Radical Copolymerization of Methyl Methacrylate with a Low Amount of Styrene in Ionic Liquid.

Ségolène Brusseau,[†,‡] Olivier Boyron,[†] Christopher Schikaneder,[†] Catherine C. Santini,[†] and Bernadette Charleux*[,†]

[†]*Université de Lyon, Univ. Lyon 1, CPE Lyon, CNRS UMR 5265, Laboratoire de Chimie Catalyse Polymères et Procédés (C2P2), Bat 308F, 43 Bd du 11 Novembre 1918, 69616 Villeurbanne, France, and* [‡]*UPMC Univ. Paris 6, CNRS, UMR 7610, Laboratoire de Chimie des Polymères, 4, place Jussieu, 75252 Paris cedex 05, France*

Received October 13, 2010; Revised Manuscript Received December 8, 2010

ABSTRACT: An ionic liquid, 1-butyl-3-methyl imidazolium bis(trifluoromethylsulfonyl)imide ([C_1C_4Im]-NTf_2) was used as the polymerization medium for the SG1-mediated free-radical solution copolymerization of methyl methacrylate with a low percentage of styrene, initiated by the BlocBuilder alkoxyamine at 90 °C. Control over the polymer molar mass and molar mass distribution was good, slightly better than that obtained in bulk or classical organic solvent solutions for the same system. Compared to the results of nitroxide-mediated polymerizations in ionic liquids previously reported in the literature, the quality of control was significantly better. It seems that the ionic liquid did not influence the activation−deactivation mechanism but played a role on the polymerization kinetics only. Indeed, the overall polymerization rate was found to be larger and the final conversion higher, in good agreement with the increase of k_p and the decrease of k_t, which are key features of free-radical polymerization in ionic liquids.

Introduction

The advent of controlled/living free-radical polymerization (CRP)[1,2] based on the reversible deactivation of the propagating radicals has revolutionized the domain of polymer chemistry and allowed the creation of new materials with designed properties. Beyond the laboratory scale synthesis, the implementation of the various CRP techniques at a larger scale will essentially be driven by the choice of an appropriate process, i.e., mainly bulk, solution, or heterogeneous media, which will also depend on the target application. At the industrial scale, free-radical polymerization is seldom performed in organic solvent solution for reasons related to both the process (reaction kinetics, solvent recovery, environmental constraints) and the chemistry (side reactions such as chain transfer to the solvent). In some situations, however, when homogeneous conditions are needed, solution polymerization may be preferred to bulk, for instance for polymers with a high T_g and exhibiting pronounced gel effect as is the case for poly(methyl methacrylate). The change from classic organic solvent to less conventional medium such as ionic liquids (ILs) therefore deserves to be studied carefully. In recent year, ILs have been recognized as good solvents for a range of organic and inorganic materials.[3] They are interesting as potential green solvents in industrial chemical procedures.[4,5] This is mainly due to the fact that ionic liquids are non volatile, exhibit negligible flammability and high thermal and electrochemical stability.[3] Additionally, ionic liquids permit to moderate the exothermicity and pressure increase in polymerization processes.[6] They have been used in various polymerization systems like free-radical polymerization, ring-opening polymerization, and ionic and coordination polymerizations of ethylenic monomers.[7] The ionic liquids were also used in polycondensation and polyaddition and in electrochemical and enzymatic polymerization processes.[7,8] In radical polymerization, they showed an interesting impact on the kinetic aspect of the reaction, with a significant increase in the propagation rate constant k_p (decrease of the activation energy,[9] effect of dipolarity/polarizability and electron pair accepting ability[10,11]) and a decrease of the termination rate constant k_t, leading to a strong increase in the overall polymerization rate.[9,12,13] This impact can be explained by both the polarity and the high viscosity of the medium.[9−11,14,15]

The ILs were used in CRP techniques, mainly ATRP (atom transfer radical polymerization)[16−19] and the analogous copper(I)-mediated CRP,[20−22] reverse ATRP,[23,24] RAFT (reversible addition−fragmentation chain transfer),[25,26] organostilbine-mediated CRP,[27] and NMP (nitroxide-mediated polymerization).[28,29] Among the various CRP techniques, NMP[30] is acknowledged to be simple and efficient as it requires a limited number of reactants, i.e., a simple alkoxyamine initiator, which is activated by temperature, without the need for additional catalyst or radical initiator. It is of interest to study the impact of the use of ILs on the outcome of the reaction. However, the very few results published so far were quite disappointing. For the NMP of styrene (S) and methyl methacrylate (MMA) in l-butyl-3-methylimidazolium hexafluorophosphate ([C_1C_4Im]PF_6), reported by Zhang et al.,[24] both the TEMPO (2,2,6,6-tetramethylpiperidine-*N*-oxyl)/benzoyl peroxide and the 2,2,5-trimethyl-3-(1-phenylethoxy)-4-phenyl-3-azahexane alkoxyamine initiating systems failed in leading to well-defined living polymers. Similarly, Ryan et al.[29] studied the polymerization of methyl acrylate using the 4-oxo-TEMPO (4-oxo-2,2,6,6-tetramethyl-1-piperidinyl-*N*-oxyl)/AIBN (2,2′-azobis(isobutyronitrile)) bimolecular initiator in 1-hexyl-3-methylimidazolium hexafluorophosphate. The system required high temperature, i.e., 140 °C, to reach a reasonable control only. No other examples are actually available in the open literature.

In this work, we decided to study the use of the nitroxide SG1[31] and more particularly of the derived BlocBuilder alkoxyamine (Scheme 1) from Arkema for the copolymerization of MMA and

*Corresponding author. E-mail: bernadette.charleux@lcpp.cpe.fr.

© 2010 American Chemical Society

Published on Web 12/31/2010

styrene in 1-butyl-3-methylimidazolium bis(trifluoromethylsulfonyl)imide ($[C_1C_4Im]NTf_2$) at a temperature of 90 °C. Although the SG1-mediated homopolymerization of MMA cannot lead to controlled/living polymerization,[32,33] the copolymerization with a low percentage of styrene initiated by BlocBuilder allowed well-defined polymers to be synthesized with the SG1-based alkoxyamine at the chain end.[34] The method permits then to target block copolymers with a high crossover efficiency.[35−37] Our aim was to study the impact of the $[C_1C_4Im]NTf_2$ ionic liquid on the polymerization kinetics along with the quality of control.

Experimental Part

1. Materials. Methyl methacrylate (MMA, purest grade, Acros, stabilized with 250 ppm of methylethylhydroquinone) and styrene (S, 99%, Acros stabilized with 10−20 ppm of p-*tert*-butylcatechol) were used without further purification. The *N*-(2-methylpropyl)-*N*-(1-diethylphosphono-2,2-dimethylpropyl)-*O*-(2-carboxyl prop-2-yl) hydroxylamine initiator (the so-called BlocBuilder-MA or BlocBuilder, pure) and the *N*-*tert*-butyl-*N*-(1-diethyl phosphono-2,2-dimethylpropyl) nitroxide (SG1, 85%) were kindly supplied by Arkema. Dimethyl sulfoxide-d_6 (DMSO-d_6, Euriso-top), dimethyl sulfoxide (DMSO, Acros, 99% for analysis), methanol (Laurylab, pure), deionized water (system purelab classic UV, Elga LabWater) were used as received. The 1-butyl-3-methylimidazolium bis(trifluoromethylsulfonyl)-imide, $[C_1C_4Im]NTf_2$ was synthesized according to an already published procedure.[38] The ionic liquid was purified through a basic alumina column, dried under high vacuum (24 h at 10^{-5} mmHg), and kept in a glovebox under argon.

2. Copolymerization of Methyl Methacrylate (MMA) with Styrene (S) in Solution. The copolymerization reactions were carried out at 90 °C (see Table 1). In a typical experiment (experiment **1** in Table 1), a mixture of MMA (2.92 g, 2.47 mol L^{-1}) and S (0.27 g, 2.22×10^{-1} mol L^{-1}, initial molar fraction of S in the comonomer mixture: $f_{0,S} = 0.082$) in $[C_1C_4Im]NTf_2$ (12.05 g) was deoxygenated with a nitrogen stream for 20 min at room temperature. The BlocBuilder initiator (0.115 g, 2.57×10^{-2} mol L^{-1}) was then added and nitrogen bubbling was carried out for 20 more minutes, until the initiator was fully dissolved. The mixture was then transferred into a 25 mL three-neck round-bottom flask, immersed in an oil bath heated at 90 °C. Time zero of the polymerization was taken when the reaction temperature reached 60 °C. Samples for kinetic studies and polymer analysis were withdrawn at regular time intervals and quenched in an iced-water bath. The overall molar conversion was determined by ^{1}H NMR analysis in DMSO d_6 as follows: one H peak of the ionic liquid ($[C_1C_4Im]NTf_2$, $\delta = 9.1$ ppm) was used as an internal reference (peak integral: I_{IL}). The conversion of S (x_S) was calculated on the basis of 2 vinylic H peaks ($\delta = 5.80$ ppm and $\delta = 5.25$ ppm), and the integral I_s for 1 H was the average of the 2 peak integrals. For MMA (conversion = x_{MMA}), the integral I_{MMA} for 1 H was the average of the two $=CH_2$ proton peaks at $\delta = 6.00$ ppm and $\delta = 5.60$ ppm. The overall molar conversion directly accessible via NMR was also calculated from the individual monomer conversions according to the following relationship: $x_{mol} = x_S \times f_{S,0} + x_{MMA} \times f_{MMA,0}$ ($f_{S,0}$ and $f_{MMA,0}$ are the initial molar fractions of S and MMA, respectively, in the reaction mixture). The polymer was subsequently precipitated from the IL using a mixture of methanol and water (75/25 v/v). It was then filtered and dried under vacuum and further analyzed by size exclusion chromatography (SEC) in THF. For the plots representing M_n obtained by SEC analysis versus the overall conversion, the latter was the mass conversion, calculated according to $x_w = x_S \times w_{S,0} + x_{MMA} \times w_{MMA,0}$ ($w_{S,0}$ and $w_{MMA,0}$ are the initial weight fractions of S and MMA, in the reaction medium, respectively).

3. Chain Extension Experiments in Solution. For a typical experiment of chain extension with styrene (experiment **6** in Table 3), the purified macroinitiator (Table 2 experiment **1a**) P(MMA_{79}-*co*-S_9)-SG1 (0.40 g, 3.19×10^{-3} mol L^{-1}) was dissolved at room temperature in 1.16 g of DMSO in the presence of styrene (0.527 g, 3.1 mol L^{-1}). The solution was introduced into a 10 mL round-bottom flask. After degassing for 20 min under nitrogen, the polymerization was carried out at 120 °C for 7.5 h. The final polymerization medium was very viscous indicating high conversion. The flask was then sunk into an ice−water bath to quench the reaction. The copolymer was further analyzed by SEC in THF solution after evaporation of the solvent.

4. Analytical Techniques. ^{1}H NMR spectroscopy for kinetic analysis (i.e., monomer conversion) was performed in 5 mm diameter tubes in DMSO-d_6 at 25 °C in a Bruker Avance 300 (300 MHz) spectrometer. The chemical shift scale was calibrated on the basis of the solvent peak ($\delta = 2.54$ ppm).

The SEC analyses were performed in THF at 40 °C, at a flow rate of 1 mL min^{-1}, using toluene as a flow rate marker. All polymers were analyzed at a concentration of 5 mg·mL^{-1} after filtration through a 0.45 μm pore-size membrane. The separation was carried out on three Polymer Laboratories columns (one column PL-gel 5 μm, 500 Å and two columns PL-Gel 5 μm, MIXED-C). The setup was equipped with a refractive index (RI) detector (Waters 410 differential refractometer at $\lambda = 930$ nm). The average molar masses (number-average molar mass M_n and weight-average molar mass M_w) and the polydispersity index (PDI = M_w/M_n) were derived from the RI signal by a calibration curve based on poly(methyl methacrylate) (PMMA) standards for the copolymers and with a calibration curve based on polystyrene (PS, from Polymer Laboratories) for chain extension experiments. The software used for data collection and calculation was Empower Pro version 5.0 from Waters.

Two samples, **1a** and **1b** in Table 2, were analyzed with a three-angle light scattering (LS) detector from Wyatt technology (MiniDAWN tristar, $\Theta = 35°$, 90° and 135°, with $\lambda = 690$ nm)

Scheme 1. Schematic Representation of the Alkoxyamine Initiator BlocBuilder (a) and the Nitroxide SG1 (b) Used in This Work

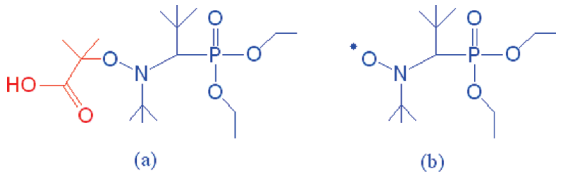


Table 1. Experimental Conditions for the SG1-Mediated Copolymerization of Methyl Methacrylate (MMA) with a Low Amount of Styrene (S) Initiated by the BlocBuilder Alkoxyamine in Various Solvents at 90 °C

expt/ symbol	$[MMA]_0$ (mol L^{-1})	$[S]_0$ (mol L^{-1})	$f_{0,S}$[a]	solvent	$[BlocBuilder]_0$ (mmol L^{-1})	r[b] (%)	target M_n[c] at 100% conv. (g mol^{-1})	overall time (h)
1/◆	2.47	0.22	0.082	$[C_1C_4Im]NTf_2$	25.7	0	10 900	2.0
2/■	2.90	0.29	0.089	dioxane	26.4	0	12 500	3.5
3/▲	2.37	0.25	0.095	$[C_1C_4Im]NTf_2$	26.8	10.3	10 200	2.0
4/●	2.35	0.24	0.090	$[C_1C_4Im]NTf_2$	8.6	0	30 500	3.5
5/×	2.35	0.28	0.088	$[C_1C_4Im]NTf_2$	4.3	0	60 300	4.1

[a] Initial molar fraction of styrene. [b] $r = 100 \times [SG1]_0/[BlocBuilder]_0$ [c] Theoretical number-average molar mass, calculated according to M_n = MM(BlocBuilder) + conversion × initial weight of monomers/initial mol number of BlocBuilder, with conversion = 1 and molar mass of the initiator, MM(BlocBuilder) = 381 g·mol^{-1}.

Table 2. Characteristics of the P(MMA-*co*-S)-SG1 Macroalkoxyamines from Experiment 1 (Table 1) Used for Chain Extension Experiments with Styrene

expt	x^a (%)	$M_n^{theo b}$ (g mol^{-1})	$M_n{}^c$ (g mol^{-1})	$M_w/M_n{}^c$	$F_S{}^d$ (mol %)	average structure
1a	62	6900	9700	1.19	10.3	P(MMA_{79}-*co*-S_9)-SG1
1b	86	9420	12600	1.13	9.6	P(MMA_{102}-*co*-S_{12})-SG1

[a] Overall molar conversion determined by ^{1}H NMR. [b] Theoretical number-average molar mass, calculated according to M_n = MM(BlocBuilder) + conversion × initial weight of monomers/initial mol number of BlocBuilder, with conversion determined by ^{1}H NMR and molar mass of the initiator; MM(BlocBuilder) = 381 g·mol^{-1}. [c] Experimental absolute number-average molar mass determined by SEC in THF solvent, with RI and light scattering detectors. [d] Molar fraction of styrene in the copolymer determined by ^{1}H NMR.

Table 3. Experimental Conditions for the SG1-Mediated Polymerization of Styrene (S) in DMSO at 120°C for 7.5 h Using Two Macroalkoxyamines from Experiment 1 as Macroinitiators

expt	macroinitiator	[macroinitiator]$_0$ (mol L^{-1})	[styrene]$_0$ (mol L^{-1})	target $M_n{}^a$ at 100% convn (g mol^{-1})
6	**1a:** P(MMA_{79}-*co*-S_9)-SG1	3.19×10^{-3}	3.1	135 650
7	**1b:** P(MMA_{102}-*co*-S_{12})-SG1	2.13×10^{-3}	2.6	168 300

[a] Theoretical number-average molar mass, calculated according to M_n = M_n(macroinitiator) + conversion × initial weight of monomers/initial mol number of initiator, with conversion = 1.

coupled with a differential refractive index (RI) detector (Waters 410 Differential Refractometer at λ = 930 nm). The MiniDawn system was calibrated with toluene. The normalization of the detector was performed with a low molar mass, narrowly distributed, polystyrene standard that did not show angular dependence of the light scattering signal. A narrow PS standard was also used to determine the interdetector volume. For each copolymer sample a fixed concentration of 10 mg·mL^{-1} was injected. The signals of the RI and LS detectors were measured simultaneously using the ASTRA version 4.5 software to obtain the absolute M_n and M_w.

Results and Discussion

1. Copolymerization of Methyl Methacrylate with a Low Percentage of Styrene in [C_1C_4Im]NTf_2 at 90 °C. While the SG1-mediated radical homopolymerization of methyl methacrylate cannot lead to a controlled or living system due to the poor stability of the formed alkoxyamine along with the existence of irreversible termination reactions (propagating radical self-termination and β-hydrogen transfer to the nitroxide),[39,40] the copolymerization with a low percentage of styrene was shown to strongly improve the system.[34] All copolymerizations were previously performed either in bulk[34] or in emulsion.[41,42] Under homogeneous conditions in bulk, the reaction medium becomes usually very viscous and a gel effect may take over. The copolymerizations were thus studied in [C_1C_4Im]NTf_2 as an ionic liquid using the same experimental conditions as those developed previously in bulk (see Table 1), i.e., with BlocBluider as an alkoxyamine initiator at a temperature of 90 °C. Two series of experiments were performed. In the first one, the effect of the solvent and of the presence of free SG1 at the beginning of the polymerization was studied (experiments **1**−**3**, Table 1); in the second one, the effect of the initiator concentration was evaluated (experiments **1**, **4** and **5**, Table 1). In all experiments the monomers and the polymers were fully soluble, resulting in a clear solution that increased in viscosity with the polymerization progress. In [C_1C_4Im]NTf_2, polystyrene is not soluble and precipitates while poly(methyl methacrylate) is highly soluble. The obtained results are thus a good indication of the incorporation of styrene in a random copolymer. The polymerization kinetics and the control over molar mass and molar mass distribution were examined.

Parts a and b of Figure 1 show that the experiments **1** and **2**, performed in different solvents, namely [C_1C_4Im]NTf_2 for **1** and 1,4-dioxane for **2**, exhibited different kinetic behavior. In [C_1C_4Im]NTf_2, the copolymerization was significantly faster and reached high conversion within less than 2 h. This can be explained by the already mentioned increase in k_p and the decrease in k_t. The former has a direct effect on the propagation kinetics, while the latter influences the proportion of released SG1 by the persistent radical effect.[43] When k_t decreases, the proportion of self-terminated chains and the concentration of free nitroxide both decrease and consequently, the concentration of propagating radicals is higher.

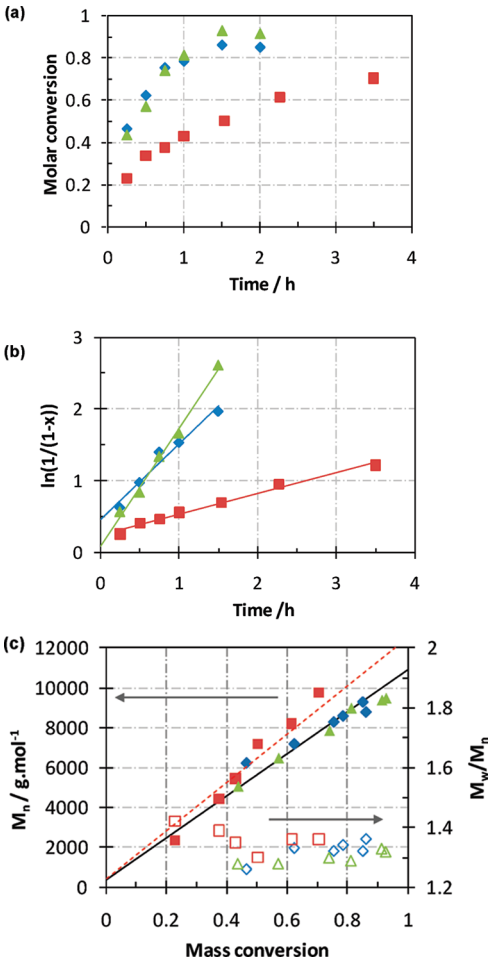


Figure 1. Effect of the solvent and of the presence of free SG1 in the monomer feed for the copolymerizations of methyl methacrylate (MMA) with 9 mol % of styrene at 90 °C determined by direct NMR analysis of the reaction mixture for the experiments **1** (◆, in [C_1C_4Im]NTf_2 without free SG1), **2** (■, in 1,4-dioxane without free SG1) and **3** (▲, in [C_1C_4Im]NTf_2 with 10.3% of free SG1): (a) overall molar conversion vs time, (b) variation of Ln(1/(1 − x)) vs time and (c) number-average molar mass, M_n, and polydispersity index, M_w/M_n (corresponding empty symbols) vs the overall weight conversion (straight black line: theoretical M_n vs conversion for the experiments **1** and **3**. Dotted red line: theoretical M_n vs conversion for the experiment **2**).

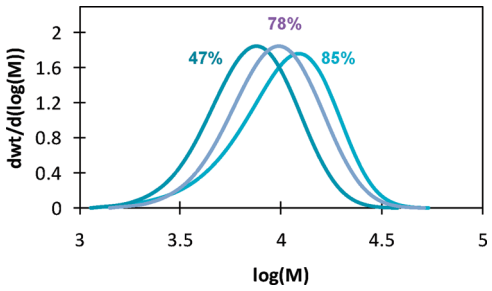


Figure 2. Size exclusion chromatograms as a function of the overall molar conversion for the polymers resulting from the copolymerization of methyl methacrylate with 8.2 mol % of styrene (S) in $[C_1C_4Im]NTf_2$ at 90 °C (experiment **1**).

However, the addition of 10.3 mol % (based on the initiator) of free SG1 at the beginning of the polymerization did not contribute to decrease the polymerization rate significantly (experiment **3**). This means that such a proportion of nitroxide was not sufficiently high in comparison with the amount normally released via the persistent radical effect, indicating that dead chains might exceed 10 mol %. Nevertheless, the control over molar mass and molar mass distribution remained very good as illustrated by Figure 1c. A linear increase of the number-average molar mass, M_n, with monomer conversion was observed in good agreement with the theoretical line, better in $[C_1C_4Im]NTf_2$ than in dioxane. The polydispersity index values were rather low, close to 1.3 and the SEC peaks were narrow, with a clear shift with the increase in conversion (Figure 2). Those results, which indicate a good quality of control, were not different, from those previously obtained in bulk, even slightly better.[34]

When the alkoxyamine concentration was decreased from 25.7 mmol L^{-1} (experiment **1**), to 8.6 mmol L^{-1} (experiment **4**) and finally to 4.3 mmol L^{-1} (experiment **5**), the polymerization rate slightly decreased (Figure 3a and 3b). This result is directly related to the persistent radical effect, which is more pronounced when the alkoxyamine concentration is lower (i.e., the released SG1 over alkoxyamine concentration ratio is higher and hence the propagating radical concentration is lower[44]). The alkoxyamine concentration has also a direct influence on the number-average molar mass evolution with conversion, following the expected trend with a good correlation between the experimental values and the theoretical ones. In all cases the polydispersity indexes reached a value of 1.3. Interestingly, in addition to the good control over the chain growth, those results show that chain transfer to the IL solvent is not an issue in this type of system.

2. Chain Extension in DMSO Solution at 120 °C. To test the living character of a polymer, chain extension is usually an appropriate method. Here, we performed two different experiments of chain extension with styrene in DMSO solution at 120 °C, targeting a final molar mass above 100 000 $g \cdot mol^{-1}$ to favor a clearly visible shift of the SEC peaks. Two different purified P(MMA-*co*-S)-SG1 copolymers from experiment **1** were used as macroinitiators after purification by precipitation as explained in the Experimental Part. The characteristics of those macroinitiators are reported in Table 2. The copolymer compositions were determined by ^1H NMR (molar fraction of styrene, F_S). The proportion of styrene at 62% conversion being larger than the initial value indicates that styrene reacts faster than MMA, which is in good agreement with the reactivity ratios reported for bulk systems.[45]

The results of chain extension can be found in Table 3. As illustrated in Figure 4, the chain extension experiments led

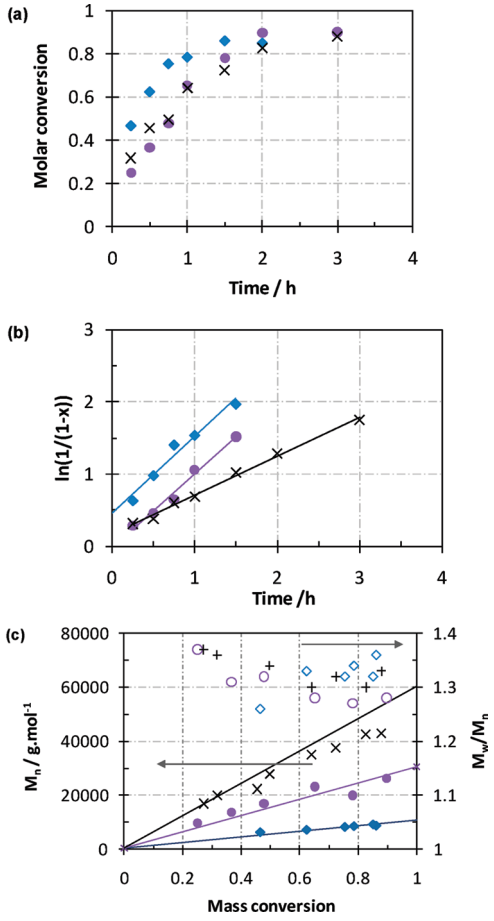


Figure 3. Effect of the BlocBuilder alkoxyamine initiator concentration for the copolymerizations of methyl methacrylate (MMA) with 9 mol % of styrene performed at 90 °C in $[C_1C_4Im]NTf_2$ without free SG1: (a) overall molar conversion vs time for the experiments **1** (◆, $[BlocBuilder]_0 = 25.7$ mmol L^{-1}), **4** (●, $[BlocBuilder]_0 = 8.6$ mmol L^{-1}) and **5** (×, $[BlocBuilder]_0 = 4.3$ mmol L^{-1}); (b) variation of $Ln(1/(1-x))$ vs time and (c) number-average molar mass, M_n, and polydispersity index, M_w/M_n (corresponding empty symbols) vs the overall weight conversion (straight lines: theoretical M_n vs conversion for each experiment).

to a shift of the SEC peak of the macroinitiator. In both cases, however, remaining macroinitiator was detected. The amount was larger for the copolymer $P(MMA_{102}$-*co*-$S_{12})$-*b*-PS (experiment **7**) in Figure 4b than for the copolymer $P(MMA_{79}$-*co*-$S_9)$-*b*-PS (experiment **6**) in Figure 4a. Chain extension was therefore not complete and directly dependent on the monomer conversion reached during the synthesis of the macroalkoxyamine (62% for experiment **6** versus 86% for experiment **7**). Those results support a high chain-end functionalization of the copolymer with an SG1-based alkoxyamine when the proportion of styrene in the copolymerization medium remains high enough. However, upon decrease of the proportion of styrene with the polymerization progress in relation with the reactivity ratios ($r_S = 0.4890$ and $r_{MMA} = 0.4929$),[36,45] the chain livingness is reduced. This trend was corroborated experimentally with the faster relative consumption of styrene with respect to MMA as determined by ^1H NMR: styrene was completely depleted at an overall molar conversion of 85% (Figure 5). As explained above and demonstrated in our previous studies,[34−36] the presence of styrene is mandatory for obtaining living polymers exhibiting a styrene-SG1 terminal unit, which is the key element for sufficient stability of the alkoxyamine end-group.

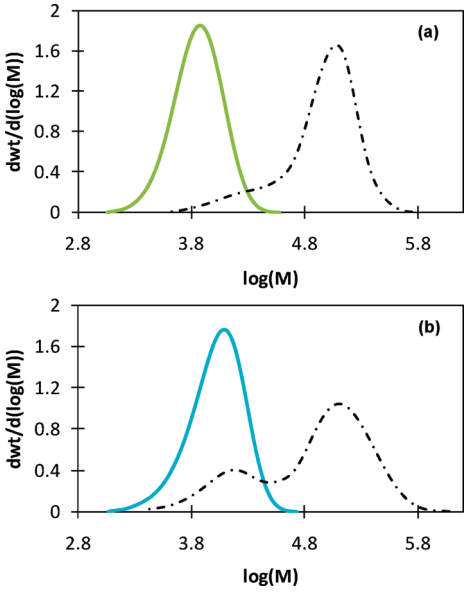


Figure 4. Chain extension of the P(MMA-*co*-S)-SG1 alkoxyamine macroinitiators **1a** and **1b** (Table 2) from experiment **1**, via SG1-mediated polymerization of styrene (S) in DMSO at 120 °C: SEC chromatograms of the macroinitiators (plain lines) and of the copolymers (dotted lines), (a) P(MMA_{79}-*co*-S_9)-*b*-PS from experiment **6** and (b) P(MMA_{102}-*co*-S_{12})-*b*-PS from experiment **7**. The SEC analyses were performed in THF solution with PS calibration.

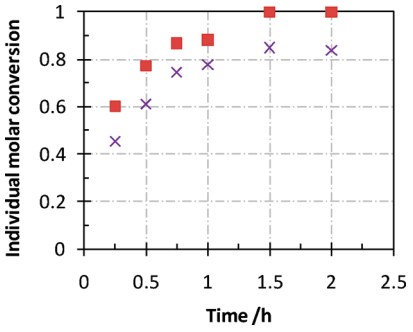


Figure 5. Individual monomer conversions determined by ^{1}H NMR for the copolymerization of methyl methacrylate (×) with 8.2 mol % of styrene (■) and $[BlocBuilder]_0 = 2.57 \times 10^{-2}$ mol L^{-1} in $[C_1C_4Im]NTf_2$ at 90 °C (experiment **1**).

Conclusion

In contrast to other NMP systems published so far in the literature, the SG1-mediated free-radical copolymerization of MMA with S, initiated by the BlocBuilder alkoxyamine in the $[C_1C_4Im]$-NTf_2 ionic liquid at 90 °C was well-controlled. The most important outcome of the reaction was the fast kinetics and high final conversions, in agreement with the IL features generally observed in classical free-radical polymerization. The IL did not seem to influence the activation−deactivation mechanism. In other words, one should not expect an improvement in the alkoxyamine dissociation conditions or in the system livingness, but more importantly consider the advantages provided by the ionic liquids on the polymerization process itself.

Acknowledgment. The authors wish to thank Arkema for the financial support of Ségolène Brusseau's Ph.D. thesis and for kindly providing the nitroxide SG1 and the BlocBuilder-MA alkoxyamine. Christopher Schikaneder acknowledges the grant attributed by the Erasmus program. Laurence Couvreur and Stéphanie Magnet from Arkema are also warmly acknowledged for fruitful discussions.

References and Notes

(1) Matyjaszewski, K.; Davis,T. *Eds.*, *Handbook of Radical Polymerization*: John Wiley & Sons: Hoboken, NJ, 2002.
(2) Braunecker, W. A.; Matyjaszewski, K. *Prog. Polym. Sci.* **2007**, *32*, 93–146.
(3) Wasserscheid, P.; Welton, T. *Ionic liquids in Synthesis*, Wiley-VCH: Weinheim, 2nd ed.; **2008**.
(4) Werner, S.; Haumann, M.; Wasserscheid, P. *Annu. Rev. Chem. Biomol. Eng.; Book Ser.: Annu. Rev. Chem. Biomol. Eng.* **2010**, *1*, 203–230.
(5) Zhu, S.; Chen, R.; Wu, Y.; Chen, Q.; Zhang, X.; Yu, Z. *Chem. Biochem. Eng. Q.* **2009**, *23*, 207–211.
(6) Vijayaraghavan, R.; Surianarayanan, M.; MacFarlane, D. R. *Angew. Chem., Int. Ed.* **2004**, *43*, 5363–5366.
(7) Kubisa, P. *Prog. Polym. Sci.* **2004**, *29*, 3–12.
(8) Erdmenger, T.; Guerrero-Sanchez, C.; Vitz, J.; Hoogenboom, R.; Schubert, U. S. *Chem. Soc. Rev.* **2010**, *39*, 3317–3333.
(9) Harrison, S.; Mackenzie, S. R.; Haddleton, D. M. *Macromolecules* **2003**, *36*, 5072–5075.
(10) Jelicic, A.; Garcia, N.; Lohmannsroben, H. G.; Beuermann., S. *Macromolecules* **2009**, *42*, 8801–8808.
(11) Jelicic, A.; Beuermann, S.; Garcia, N. *Macromolecules* **2009**, *42*, 5062–5072.
(12) Barth, J.; Buback, M.; Schmidt-Naake; Woecht, I. *Polymer* **2009**, *50*, 5708–5712.
(13) Beuermann, S. *Macromol. Rapid Commun.* **2009**, *30*, 1066–1088.
(14) Harrisson, S.; Mackenzie, S. R.; Haddleton, D. M. *Chem. Commun.* **2002**, 2850–2851.
(15) Winterton, N. *J. Mater. Chem.* **2006**, *16*, 4281–4293.
(16) (a) Biedron, T.; Kubisa, P. *Macromol. Rapid Commun.* **2001**, *22*, 1237–1242. (b) Biedron, T.; Kubisa, P. *J. Polym. Sci., Part A: Polym. Chem* **2002**, *40*, 2799–2890.
(17) Tsarevsky, N. V.; Matyjaszewski, K. *J. Polym. Sci., Part A: Polym. Chem.* **2006**, *44*, 5098–5112.
(18) Maria, S.; Biedron, T.; Poli, R.; Kubisa, P. *J. Appl. Sci.* **2007**, *105*, 278–281.
(19) Zhang, H.; Zhang, Y.; Liu, W.; Whang, H. *J. Appl. Polym. Sci.* **2008**, *110*, 244–252.
(20) Carmichael, A. J.; Haddleton, D. M.; Bon, S. A. F.; Seddon, K. R. *Chem. Commun.* **2000**, 1237–1238.
(21) Percec, V.; Grignoras, C. *J. Polym. Sci., Part A: Polym. Chem.* **2005**, *43*, 5609–5619.
(22) Xia, G.; Zhang, H.; Hong, X.; Zhang, G.; Zhou, X.; Xia, B. J. *Appl. Polym. Sci.* **2008**, *108*, 3683–3689.
(23) Ma, H.; Wan, X.; Chen, X.; Zhou, Q.-F. *J. Polym. Sci., Part A: Polym Chem.* **2002**, *41*, 143.
(24) Li, N.; Lu, J.; Xu, Q.; Xia, X.; Wang, L. *J. Appl. Polym. Sci.* **2007**, *103*, 3915–3919.
(25) Perrier, S.; Davis, T. P.; Carnichael, A. J.; Haddleton, D. M. *Eur. Polym. J.* **2003**, *39*, 417–422.
(26) Johnston-Hall, G.; Harjani, J. R.; Scammells, P. J.; Monteiro, M. J. *Macromolecules* **2009**, *42*, 1604–1609.
(27) Cui, G.; Li, J.; Liu, Z.; Dou, J. *Macromol. Chem. Phys.* **2010**, *211*, 1222–1228.
(28) Zhang, H.; Hong, K.; Mays, J. W. *Polym. Bull.* **2004**, *52*, 9–16.
(29) Ryan, J.; Aldabbagh, F.; Zetterlund, P. B.; Yamada, B. *Macromol. Rapid Commun.* **2004**, *25*, 930–934.
(30) Hawker, C. J.; Bosman, A. W.; Harth, E. *Chem. Rev* **2001**, *101*, 3661–3688.
(31) Benoit, D.; Grimaldi, S.; Finet, J.-P. ; Tordo, P.; Fontanille, M. ; Gnanou, Y. *Am. Chem. Soc. Symp Series.* **1998**, *685*, 225−235.
(32) Ananchenko, G.; Souaille, M.; Fischer, H.; Le Mercier, C.; Tordo, P. *J. Polym. Sci., Part A: Polym. Chem.* **2002**, *40*, 3264–3283.
(33) Guillaneuf, Y.; Gigmes, D.; Marque, S. R. A.; Bertin, D.; Tordo, P. *Macromol. Chem. Phys.* **2006**, *207*, 1278–1288.
(34) Charleux, B.; Nicolas, J.; Guerret, O. *Macromolecules* **2005**, *38*, 5485–5492.
(35) Nicolas, J.; Dire, C.; Mueller, L.; Belleney, J.; Charleux, B.; Marque, S. R. A.; Bertin, D.; Magnet, S.; Couvreur, L. *Macromolecules* **2006**, *39*, 8274–8282.
(36) Nicolas, J.; Mueller, L.; Dire, C.; Matyjaszewski, K.; Charleux, B. *Macromolecules* **2009**, *42*, 4470–4478.

(37) Lessard, B.; Maric, M. *J. Polym. Sci., Part A: Polym. Chem* **2009**, *47*, 2574–2588.
(38) Magna, Y.; Chauvin, G.; Niccolai, P.; Basset, J.-M. *Organometallics* **2003**, *22*, 4418–4425.
(39) McHale, R.; Aldabbagh, F.; Zetterlund, P. B. *J. Polym. Sci., Part A: Polym. Chem*. **2007**, *45*, 2194–2203.
(40) Dire, C.; Belleney, J.; Nicolas, J.; Bertin, D.; Magnet, S.; Charleux, B. *J. Polym. Sci., Part A: Polym. Chem* **2008**, *46*, 6333–6345.
(41) Dire, C.; Magnet, S.; Couvreur, L.; Charleux, B. *Macromolecules* **2009**, *42*, 95–103.
(42) Brusseau., S.; Belleney, J.; Magnet, S.; Couvreur, L.; Charleux, B. *Polym. Chem*. **2010**, *1*, 720–729.
(43) Fischer, H. *Chem. Rev*. **2001**, *101*, 3581–3610.
(44) From ref 43, the equation giving the concentration of released free nitroxide due to the persistent radical effect reads: $[SG1] = (3k_tK^2[BB]_0^2t)^{1/3}$ with $[BB]_0$ the initial concentration of alkoxyamine, k_t, the overall rate constant of termination and K, the activation-deactivation equilibrium constant. It comes then that $[SG1]/[BB]_0 = (3k_tK^2[BB]_0^{-1}t)^{1/3}$ is larger at a given time when $[BB]_0$ is lower. As the concentration of propagating radicals reads: $[P^\bullet] = K[BB]_0/[SG1]$, it decreases accordingly, although not in a linear manner.
(45) Coote, M. L.; Johnston, L. P. M.; Davis, M. P. *Macromolecules* **1997**, *30*, 8191–8204.

Macromolecules
ARTICLE

Macromolecules **2011**, *44*, 221–229 **221**
DOI: 10.1021/ma102378w

Toward Well-Controlled ab Initio RAFT Emulsion Polymerization of Styrene Mediated by 2-(((Dodecylsulfanyl)carbonothioyl)sulfanyl)propanoic Acid

Yingwu Luo,*,† Xiaoguang Wang,† Bo-Geng Li,*,† and Shiping Zhu*,‡

†*The State Key Laboratory of Chemical Engineering, Department of Chemical and Biochemical Engineering, Zhejiang University, 38 Zhe Da Road, Hangzhou 310027, PR China, and* ‡*Department of Chemical Engineering, McMaster University, Hamilton, Ontario L8S 4L7, Canada*

Received October 18, 2010; Revised Manuscript Received December 7, 2010

ABSTRACT: Reversible addition−fragmentation chain transfer (RAFT) ab initio emulsion polymerization of styrene mediated by 2-(((dodecylsulfanyl) carbonothioyl) sulfanyl) propanoic acid was investigated with sodium dodecyl sulfate (SDS), poly(acrylic acid)$_{29}$-*b*-polystyrene$_5$ trithiocarbonate macro-RAFT agent (PAA_{29}-PSt_5-RAFT), and poly(acrylic acid)$_{29}$-*b*-polystyrene$_5$ diblock co-oligomer (PAA_{29}-PSt_5) as the surfactant, respectively. Polystyrene latex having controlled molecular weight, relatively low PD and narrow particle size distribution was obtained by postneutralizing PAA_{29}-PSt_5-RAFT and PAA_{29}-PSt_5. This result was in agreement with the superswelling hypothesis that superswollen oligomer-containing particles caused the colloidal instability in the early stage of RAFT emulsion polymerization with SDS as surfactant. The successes of PAA_{29}-PSt_5-RAFT and PAA_{29}-PSt_5 were due to the high interfacial tensions of the styrene/water/surfactant systems that suppressed the superswelling and thus improved the colloidal instability. A majority of the initial RAFT molecules appeared to be converted at a low monomer conversion due to the inhibition period.

Introduction

Controlled/living radical polymerization (CLRP), including nitroxide mediated polymerization (NMP),[1] atom transfer radical polymerization (ATRP),[2,3] and reversible addition−fragmentation chain transfer (RAFT)[4] provides a powerful tool to tailor-make macromolecular architectures. Well-defined block, gradient, brush copolymers of a large variety of monomers have been synthesized under mild conditions.[1−5] CLRP in (mini)-emulsion is of particular interest for the following reasons.[6] The water-based heterogeneous nature of (mini)emulsion facilitates industrial applications of CLRP and the polymerization within nanoparticles leads to the compartmentalization effect of radicals and mediators.[7−14] In RAFT polymerization, the isolation of radicals in different nanoparticles dramatically suppresses bimolecular termination, which offers an opportunity to synthesize high molecular weight polymers at reasonable polymerization rates.[9,15] The RAFT reaction has a significant influence on the average number of radicals per particle following a simple equation: $\bar{n}_{RAFT}^{-1} = \bar{n}_{blank}^{-1} + 2K[\mathrm{RAFT}]_0$, where $\bar{n}_{RAFT}$ and $\bar{n}_{blank}$ are the average numbers of radicals per particle with and without RAFT agent in a (mini)emulsion polymerization system, K is the RAFT equilibrium coefficient, and $[\mathrm{RAFT}]_0$ is the initial RAFT concentration.[8] This equation reveals an intrinsic rate retardation of RAFT polymerization. Use of RAFT agents with low K values increases the polymerization rate but a too low K deteriorates the control over chain growth.

Unfortunately, RAFT ab initio emulsion polymerization often suffered severe colloidal instability, low polymerization rate, broad molecular weight distribution and lack of control over molecular weight.[16,17] Charmot et al.[18] and Monteiro et al.[19−21] reported ab initio emulsion polymerization of styrene mediated by xanthate, a RAFT agent with low chain transfer constant (C_{tr}). Good colloidal stability was obtained but the polydispersity value (PD, PD = M_w/M_n, where M_n and M_w are the number- and weight-average molecular weights) was high due to the relatively low C_{tr}. Claverie et al.[16] reported that when highly reactive RAFT (*S*-thiobenzoylthioglycolic acid) was used, a large amount of flocs (up to 40%) was observed, attributed to the precipitation of unreacted RAFT from monomer droplets that was resulted from transfer limitations of *S*-thiobenzoylthioglycolic acid from the oil phase to the polymer particles. With 1-amino-2-methyl-1-oxopropan-2-yl benzodithioate, the emulsion polymerization of styrene having good colloidal stability was obtained, but PD reached 1.70. Nozari et al.[22,23] studied the effect of RAFT agent hydrophilicity on its transport to particle and found that the RAFT agent concentration inside particle increased with increased hydrophilicity at a slow stirring speed of 50 rpm. The amount of coagulum was less than 9 wt % and M_n and PD decreased with increased water solubility of the RAFT agent. Choe et al.[24,25] carried out an emulsion photopolymerization of methyl methacrylate (MMA) using a surface active RAFT agent (4-thiobenzoyl sulfanylmethyl benzoate) as initiator, chain transfer agent and stabilizer. Good colloidal stability and narrow particle size distribution were realized. The molecular weight increased linearly with monomer conversion. PD was between 1.23 and 1.41. However, the molecular weight of the final product increased significantly at an elevated polymerization temperature. Morbidelli et al.[26] carried out an emulsion polymerization mediated by cumyl dithiobenzoate, using cyclodextrin to facilitate the RAFT agent transport and obtained good colloidal stability, and predicted M_n and low PDs. Luo et al.[27] increased the colloidal stability in MMA emulsion polymerization mediated by 2-cyanprop-2-yl dithiobenzoate by employing high

*Corresponding authors.

© 2010 American Chemical Society

Published on Web 12/30/2010

initiator and surfactant concentrations. At targeted $M_n \leq 40\,000$ g/mol, the latex had negligible coagulum, predicted molecular weight and low PD (< 1.2). However, the PD increased at higher targeted M_n, which was attributed to possible variation of RAFT agent concentration in different particles. Monteiro et al.[28] studied styrene emulsion polymerization mediated by 1-phenylethyl phenyldithioacetate with 10 wt % (based on monomer phase) nonionic surfactant Brij 98. The majority of monomer was found to be initially located in monomer-swollen micelles. Good control was obtained at low targeted M_n (< 9000 g/mol) while lack of control was found at high targeted M_n (> 9000 g/mol), similar to the observation by Luo et al.[27]

Monteiro et al.[17] and Gilbert et al.[29−32] proposed that the often-observed colloidal instabilities were caused by the polymerization within monomer droplets. The oligomeric chains generated in the droplets could not diffuse through water to the particles and thus became coagulum at the end of stage II, when the monomer droplets disappeared. In an effort to suppress the oligomer formation, amphiphilic RAFT agents such as poly(acrylic acid)$_5$-*b*-poly(butyl acrylate)$_{20}$ trithiocarbonate was used as surfactant.[29,33] The colloid stability in styrene emulsion polymerization mediated by fully neutralized poly(sodium acrylate)$_5$-*b*-poly(butyl acrylate)$_{20}$ was excellent. The molecular weight increased linearly with monomer conversion but it was much higher than the theoretical values. Luo et al.[34] used an amphiphilic macro-RAFT agent with much longer acrylic acid segment without neutralization and obtained high rate, predicted M_n, low PD and little coagulum. But the control over molecular weight was lost if acrylic acid was neutralized before the polymerization. Charleux et al.[35,36] used the macro-RAFT agent with poly(ethylene oxide) as amphiphilic segment and found that butyl acrylate polymerized rapidly with good colloidal stability, predicted M_n and low PD. However, the styrene polymerization rate was extremely low. Monteiro et al.[37,38] used poly(*N*-isopropylacrylamide)-*b*-poly(dimethylacrylamide) diblock copolymer as surfactant and oligo-*N*-isopropylacrylamide trithiocarbonate as RAFT agent. At temperature above LCST, poly(*N*-isopropylacrylamide) blocks precipitated out from water and the copolymer chains self-assembled into nanoreactors containing oligo-*N*-isopropylacrylamide trithiocarbonate and swollen with styrene monomer. Very low PD of <1.2 with M_n > 100 000 g/mol and controlled M_n polystyrene chains bearing oligo-*N*-isopropylacrylamide end group were obtained. Similar results were also obtained in the work using poly(*N*-isopropylacrylamide)-*b*-poly(dimethylacrylamide) trithiocarbonate diblock macro-RAFT agent to construct reactive nanoreactors.[39]

The fact that colloidal instability can be avoided by replacing oil-soluble small RAFT agent with amphiphilic macro-RAFT appears to support the hypothesis that coagulum comes from oligomer formed in monomer droplets when small RAFT agents are used.[17,29−32] On the other side, it is well accepted that monomer droplets have about 10 μm in diameter and are far less effective than micelles and polymer particles in capturing radicals from the water phase, due to that the total surface area of monomer droplets (i.e., the product of the number of droplets and the surface area per droplet) is far smaller than that of the micelles.[40,41] It can therefore be questioned if the polymerization in monomer droplets can generate measurable amount of oligomers. As a matter of fact, Luo et al.[27] found that the colloidal stability of MMA emulsion polymerization mediated by 2-cyanprop-2-yl dithiobenzoate was achievable by high initiator and surfactant concentrations. This finding was in agreement with the superswelling hypothesis,[27,42] in which coagulum was assumingly caused by superswelling of some particles formed at the very beginning. The superswelling of particles was recently directly observed by DLS.[37−39]

In this paper, we first theoretically study the influence of interfacial tension on the swelling of particles in the early stage of RAFT ab initio emulsion polymerization of styrene. We then experimentally investigate the emulsion polymerization in the presence of small RAFT agent with SDS, amphiphilic macro-RAFT agent, and deactivated amphiphilic macro-RAFT agent as surfactant. The objectives are 2-fold. On the fundamental side, we aim at elucidating the mechanism involved in coagulum formation. On the practical side, we make effort to develop a route to carry out RAFT ab initio emulsion polymerization using oil-soluble small RAFT agent, which is important for industrial applications.

Effect of Interfacial Tension on Swollen Particle Size

To describe the swelling of latex particles in emulsion polymerization, the Morton equation was adopted[43]

$$RT\left(\ln(1-\phi_2)+\left(1-\frac{1}{j}\right)\phi_2+\phi_2{}^2\chi+\frac{4v_1\gamma}{d_pRT}\right)=0 \quad (1)$$

where γ is interfacial tension between particle and aqueous phase, ϕ_2 is the volume fraction of the polymer in the particle, v_1 is molar volume of monomer in particle, χ is Flory−Huggins interaction parameter of monomer and polymer, R is gas constant, T is polymerization temperature in K, d_p is particle diameter, and j is ratio of the molar volume of oligomer to that of monomer. By definition, we have

$$j = k_1 \mathrm{DP_n} \quad (2)$$

where k_1 is the proportional coefficient close to unity and $\mathrm{DP_n}$ is number-average degree of polymerization. Because of the RAFT agent size contribution, j is higher than unity even at $\mathrm{DP_n} = 1$. In eq 1, the monomer chemical potential in droplets is set zero since the droplet size is larger than 1 μm so that the interfacial tension is insignificant.

Based on the Morton equation, eq 1, Ugelstad et al. pointed out that the swelling capacity of oligomer particles could be dramatically increased with a reduced j value (also termed as "hyperswollen").[44,45] In controlled/living radical emulsion polymerization systems, short chain oligomers, instead of high molecular weight polymers, were generated during the nucleation period. The effect of interfacial tension on the swollen particle size can thus be described and analyzed by eq 1. The RAFT emulsion polymerization of styrene is calculated using the following parameters: $\chi = 0.45$, $v_1 = 1.1845 \times 10^{-4}$ m^3/mol, $M_0 = 104.2$ g/mol, $\rho_2 = 1.044 \times 10^6$ g/m^3, $R = 8.3145$ J/kmol, and $T = 343.15$ K.[46] The calculation is limited to the nucleation stage with an assumed complete coverage of particle surface by surfactant molecules. In such a case, the interfacial tension of styrene/SDS aqueous solution is estimated to be about 2−3 mN/m.[47] The influence of the RAFT agent is negligible here due to its small amount.

We define the dry particle diameter free of unreacted monomer as $d_u = d_p\phi_2{}^{(1/3)}$. Figure 1 shows d_p versus j curves at various d_u and γ. At fixed d_u and j, d_p decreases with increased interfacial tension. At the low γ of 3 mN/m, some particles approach 1 μm and their sizes are far larger than those in conventional emulsion polymerization, i.e., $j \rightarrow \infty$. The emulsion system with such large particles becomes sensitive to shear and is dominated by buoyant force, which leads to colloidal instability. As the γ increases, the swollen particle diameter decreases first and levels off at $\gamma >$ 12 mN/m.

In RAFT emulsion polymerization, the particles born at different times have different d_u and j values. The earliest born particles have the largest d_u. Upon generation of a particle, the original RAFT molecules in the particle quickly convert to oligomer RAFT molecules because of high chain transfer constant.

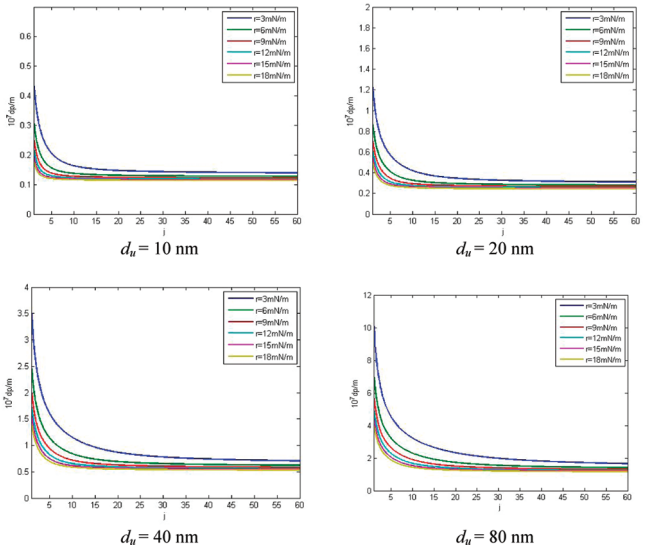


Figure 1. Effect of interfacial tension γ on particle diameter d_p. j is the molar volume ratio of oligomer to that of monomer.

The consumed small RAFT molecules in the particle are quickly replenished by those from the monomer droplets. Little transport between particles of the oligomer RAFT molecules is expected due to their high hydrophobicity. As a result, the early born particles are superswollen. At low γ, the superswollen particles reach 1 μm in diameter and are apt to coagulate by shear and/or buoyancy forces, mixed with the monomer droplets. As suggested by Figure 1, increasing interfacial tension is effective in suppressing the superswelling. If the superswelling leads to the formation of coagulum, increasing interfacial tension becomes an effective approach to increase colloidal stability of RAFT ab initio emulsion polymerization. In the following, RAFT ab initio emulsion polymerization of styrene is experimentally studied to verify this hypothesis.

Experimental Part

Materials. Acrylic acid (AA, >99%) and styrene (St, >99%) were distilled under reduced pressure prior to polymerization. Potassium persulfate (KPS, >99%), 4,4′-azobis(4-cyanopentanoic acid) (V501, >99%), 2,2′-azobis(isobutylronitrile) (AIBN, >99%), 1,4-dioxane (>99%), sodium dodecyl sulfate (SDS, >95%) and sodium hydroxide (NaOH, >96%) were used directly without further purification. The small RAFT agent, 2-(((dodecylsulfanyl) carbonothioyl)sulfanyl)propanoic acid (>95%), was synthesized and purified as described in ref 33.

Synthesis of Poly(acrylic acid)$_{29}$-*b*-polystyrene$_5$ Trithiocarbonate Macro-RAFT Agent. The PAA_{29}-PSt_5-RAFT agent was synthesized by a two-step solution polymerization. First, a solution containing 1.5 g (4.3×10^{-3} mol) of the small RAFT agent, 0.12 g (4.3×10^{-4} mol) of V501, 9.5 g (0.13 mol) of acrylic acid, and 25 g of dioxane were introduced to a flask and the reaction proceeded with stirring at 80 °C for 6 h. The flask was then cooled down to room temperature and another solution containing 4.6 g (4.4×10^{-2} mol) of styrene, 0.12 g (4.3×10^{-4} mol) of V501 and 5 g dioxane was added. The mixture was deoxygenated and reacted for further 12 h at 80 °C. The product was collected by precipitation of the mixture in cyclohexane. The macro-RAFT agent was dried under vacuum at 50 °C. The yield of PAA_{29}-PSt_5-RAFT agent was 80%, estimated by gravimetric analysis and ^{1}H NMR. ^{1}H NMR signals of PAA_{29}-PSt_5-RAFT were assigned as follows (in ppm): 0.84 (3H, $-CH_3$ of $-C_{12}H_{25}$ chain moiety), 1.03 (3H, $-CH_3$ of $-CHCH_3$-(COOH) chain moiety), 1.25 (18H, $-CH_2(CH_2)_9CH_3$ of $-C_{12}$-H_{25} chain), 1.56 ($-C-CH_2-C-$ of PAA−PSt chain), 2.24 ($-CH(COOH)-$ of PAA chain), 7.18 (25H, −Ph−H of PSt chain), 12.6 (30H, −COOH of PAA chain), 3.60 (H of impurities dioxane). The signal at 0.84 ppm (3H, $-CH_3$ of $-C_{12}H_{25}$ chain moiety) was used to estimate the composition. The PAA_{29}-PSt_5-RAFT contained 29 acrylic acid units (12.6 ppm, 30 H, contain one H from the small RAFT agent) and 5 styrene units (7.18 ppm, 25 H). The M_n by ^{1}H NMR was 2958 g/mol.

Synthesis of Poly(acrylic acid)$_{29}$-*b*-polystyrene$_5$ Diblock Co-Oligomer: Cleavage of $-SC(=S)SC_{12}H_{25}$ End Group from Poly-(acrylic acid)$_{29}$-*b*-polystyrene$_5$ Trithiocarbonate Macro-RAFT Agent. PAA_{29}-PSt_5-RAFT agent (5.0 g, 1.69×10^{-3} mol), AIBN (2.8 g, 1.70×10^{-2} mol), and dioxane (30 g) was added to a 100 mL round-bottom flask. The mixture was deoxygenated by purging with nitrogen for 30 min and then heated to 95 °C for 8 h. The polymer was recovered by precipitation into styrene and then cyclohexane, filtered and dried under vacuum for 10 h at 100 °C. The distribution of trithiocarbonate RAFT groups in terms of molecular weight could be detected by GPC UV detector at 311 nm.[48,49] About 92% of the trithiocarbonate RAFT groups had been removed calculated from GPC UV 311 signals.

Ab Initio Emulsion Polymerization of Styrene Mediated by Small RAFT Agent. Taking experiment 1 as an example, 0.10 g (3.60×10^{-4} mol) SDS was dissolved in 37 g of deionized water. Then, 0.12 g of small RAFT agent (3.52×10^{-4} mol) dissolved in styrene (10 g, 20% solid content based on total latex) was mixed with the aqueous solution in a 100 mL flask. During 30 min of deoxygenation by nitrogen purge, the temperature was increased to 70 °C. The initiator potassium persulfate (KPS, 0.020 g, 7.41×10^{-5} mol, in 3 g deionized water) was injected to start the emulsion polymerization. Samples were withdrawn during the process for gravimetric, GPC, and Malvern ZETASIZER analysis.

NMR analysis. The structure of the macro-RAFT agent was determined by ^{1}H NMR using DMSO as solvent on a BRULCER DMX 500 MHz spectrometer.

GPC analysis. Number-average molecular weight (M_n), weight-average molecular weight (M_w) and PD (M_w/M_n) were measured by GPC (Waters 1525 binary HPLC pump, Waters 2414 refractive index detector, Waters 717 autosampler). UV 311 signals were detected by a Waters 2487 dual λ absorbance detector. The samples were dried in a vacuum oven at 120 °C for 2 h and then dissolved in tetrahydrofuran (THF) which contained 2 wt % 1 M hydrochloric acid aqueous solution to mask COOH group interactions with GPC columns.[50] The eluent was THF with a flow rate of 1.0 mL/min and the testing temperature was 30 °C. Considering the different molecular weights, two sets of Waters Styragel columns (HR 5, 4, 3 for the measure range of 4 000 000−500 g/mol and HR 4, 3, 1 for 500 000−100 g/mol. Bead sizes were 5 μm in all columns, pore sizes were 10^5 Å in HR 5, 10^4 Å in HR 4, 10^3 Å in HR 3, and 10^2 Å in HR 1.) were used. The molecular weight and PD data were calculated from a calibration curve based on narrow polystyrene standards from Waters (9 narrow standards in HR 4, 3, 1: 710 000−162 g/mol; 9 narrow standards in HR 5, 4, 3: 3 280 000−580 g/mol).

Particle Size Analysis. The volume-average particle diameter (D_v), number-average particle diameter (D_n) and particle size distribution (D_v/D_n) were measured by Malvern ZETASIZER 3000 HAS at 25 °C. The samples were dried in vacuum at 30 °C for 2 h to remove residual monomer.

Interfacial Tension Measurement. The interfacial tension between PAA_{29}-PSt_5 macro-RAFT aqueous solution and styrene was measured on a video-based contact angle measuring device OCA20 Data-Physics Inc. The measurement was operated at room temperature.

Concentration Measurement. The small RAFT concentration in styrene was measured by Unico 2802 UV/vis spectrophotometer. The measurement was operated at room temperature. The absorption wavelength was 311 nm which was used to detect trithiocarbonate RAFT groups.[48,49] At low conversions, when stirring stopped, the oil phase was separated, which was then withdrawn for measurements.

Table 1. Ab Initio Emulsion Polymerization of Styrene Mediated by Small RAFT Agent Stabilized by SDS, PAA_{29}-PSt_5-RAFT or PAA_{29}-PSt_5 Diblock Co-oligomer

expt[a]	small RAFT ($\times 10^{-4}$ mol)	SDS ($\times 10^{-4}$ mol)	PAA_{29}-PSt_5-RAFT ($\times 10^{-4}$ mol)	PAA_{29}-PSt_5 ($\times 10^{-4}$ mol)	[KPS]:[RAFT][b]	initial pH[c]	time (min)	convn[d] (%)	Coagulum[e] (wt %)
1	3.52	3.60	0	0	1:5	7.0	120	93	3.36
2[f]	3.34	3.59	0	0	1:5	7.1	660	99	3.42
3	3.47	0	3.54	0	1:5	2.9	115	92	0.68
4	3.51	0	3.58	0	1:10	2.9	170	93	0.80
5[g]	3.51	0	3.54	0	1:5	3.0	120	97	0.12
6[h]	0	0	0	3.82	1:5[g]	2.9	60	98	—
7	3.46	0	0	3.88	1:5	3.0	105	90	1.05
8[i]	3.46	0	0	3.86	1:5	2.9	135	98	0.15
9[j]	3.46	0	0	3.88	1:5	5.3	105	97	0.50

[a] All the experiments used KPS as initiator, styrene as monomer. Other reaction ingredients: 40 g of water and 10 g of styrene. The reaction temperature was kept at 70 °C, and the solid content was 20%. Stirring speed was kept at 300 rpm (experiments 1 and 3−8). [b] [KPS] was KPS concentration, and [RAFT] was RAFT concentration which contained both small RAFT and macro-RAFT. [c] The initial pH values of the aqueous phase were measured prior to the polymerization. [d] The monomer conversion was measured by gravimetry. [e] The percent of coagulum was calculated based on the total polymer mass. [f] In experiment 2, the stirring speed was kept at 50 rpm at which the monomer phase was placed on top of the dispersion in the reactor. [g] In experiment 5, NaOH solution ([NaOH]/[macro-RAFT] = 6:1) was injected to the aqueous phase when the conversion reached 17% at 25 min. The final pH value of the aqueous phase was about 5.0 at the end of polymerization. [h] In experiment 6, the amount of KPS was the same as that in experiments 7 and 8. [i] In experiment 8, NaOH solution ([NaOH]/[macro-RAFT] = 6:1) was injected to the aqueous phase when the conversion reached 20% at 45 min. The final pH value of the aqueous phase was about 5.0 at the end of polymerization. [j] In experiment 9, NaOH solution ([NaOH]/[macro-RAFT] = 6:1) was injected to the aqueous phase prior to the polymerization.

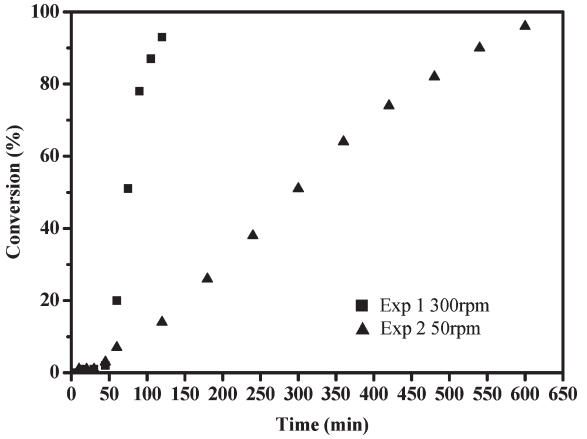


Figure 2. Conversion versus polymerization time plot of RAFT ab initio emulsion polymerization of styrene stabilized by SDS. [KPS]/[RAFT] = 1:5, 20% solid content; T = 70 °C.

pH Value Measurement. The initial pH value of the aqueous phase was measured by LEICI PHS-2C pH-meter with the electrode type of E201−4.

Results

SDS as the Surfactant. As a "standard" surfactant, SDS has been widely used in the conventional emulsion polymerization of styrene. SDS can dramatically reduce styrene/water interfacial tension to 2−3 mN/m for a fully covered interface.[47] However, it has also been well documented that significant amount of coagulum was formed in the RAFT ab initio emulsion polymerization with SDS as surfactant.[16,17]

The RAFT ab initio emulsion polymerization of styrene with SDS as surfactant was carried out. The RAFT agent was 2-(((dodecylsulfanyl)carbonothioyl)sulfanyl)propanoic acid, which was reported to be a good mediator for styrene polymerization.[51] The effect of stirring speed on the polymerization was investigated. Refer to Table 1 for the recipe of experiment 1. The experiment 2 recipe was similar to that of experiment 1 but at the stirring speed of 50 rpm reduced from 300 rpm in experiment 1. Figure 2 shows the kinetic curves. Both runs experienced a significant inhibition period of about 45 min, in agreement with the previous reports.[16,17,19] The inhibition period has been ascribed to exits of the fragmented R radicals from the initial RAFT agent molecules.[18−21,28,32,52−56] The rate of experiment 2 was much slower than experiment 1. Similar observations have been documented in the conventional emulsion polymerization.[41,57−60] It is well accepted that the rate reduction is caused by the rate-determining step of monomer transport from monomer droplets to water. As a matter of fact, at a stirring speed as low as 50 rpm, it is clear to see a monomer layer on the top of emulsion.

Some coagulum was found at the end of both runs, in agreement with the literature.[16,17,22,23] The coagulum amounts were the same about 3.4 wt %. The final molecular weights were much higher than theoretical values as referred to Table 2. In experiment 1, M_n and PD were monitored during the course of the polymerization. Figure 3 shows their results. M_ns increased with conversion, significantly higher than the theoretical values, and PDs were very high. Figure 4 shows GPC curves. A long tail of low molecular weight was clearly seen. The coagulum was composed of oligomers having molecular weight about 800 g/mol, as shown in Table 2, in agreement with the reports on the different systems.[27]

PAA_{29}-PSt_5-RAFT as the Surfactant. In experiments 3 and 4, PAA_{29}-PSt_5-RAFT replaced SDS as the surfactant. The small RAFT agent remained the same amount as in experiments 1 and 2. In experiment 3, the molar ratio of KPS to the total RAFT was set to 1:5, also the same as in experiments 1 and 2. The KPS concentration in water was actually doubled in experiment 3 since the surfactant contained RAFT group at its chain end. In experiment 4, the KPS concentration in water was set to the same as in experiments 1 and 2. Figure 5 shows the kinetic curves of experiments 3 and 4. The inhibition periods were shortened compared to experiments 1 and 2. PAA_{29}-PSt_5-RAFT hindered exits of the R radicals probably due to its viscous interfacial layer. The rate decreased with reduced initiator concentration as expected. The respective coagulum amounts in experiments 3 and 4 were 0.68 and 0.80 wt %, significantly less than in experiments 1 and 2, as listed in Table 2. The colloidal stability of the polymerization system stabilized by PAA_{29}-PSt_5-RAFT was much better than that stabilized by SDS. M_ns were about 20 000 g/mol, still higher than but much closer to the theoretical values (14 700 g/mol). Figure 6 shows that the M_n point at the low conversion of 10% matched its

Table 2. M_ns, PDs, Particle Diameters, and Distributions of ab Initio Emulsion Polymerization of Styrene Mediated by Small RAFT Stabilized by SDS, PAA_{29}-PSt_5-RAFT or PAA_{29}-PSt_5 Diblock Co-Oligomer

	emulsion					coagulum		
expt[a]	$M_{n,theo}$[b] (g/mol)	$M_{n,exp}$ (g/mol)	PD	D_v[c] (nm)	D_v/D_n	percent[d] (% wt)	$M_{n,exp}$ (g/mol)	PD
1	26 800	203 000	2.66	62, 22[e]	bimodal	3.36	785	1.06
2	29 000	148 000	2.41	61, 21[e]	bimodal	3.42	869	1.08
3	14 700	21 200	1.50	82	1.17	0.68	784	1.03
4	14 700	19 300	1.50	85	1.10	0.80	727	1.03
5	15 500	16 700	1.37	76	1.02	0.12	755	1.06
6	—	239 900	2.17	103	1.01	—	—	—
7	26 400	48 900	1.49	83	1.07	1.05	684	1.04
8	28 500	30 500	1.41	76	1.02	0.15	771	1.05
9	29 500	69 900	3.39	45	1.29	0.50	967	1.07

[a] All the experiments used KPS as initiator, styrene as monomer. Other reaction ingredients: 40 g water and 10 g styrene. The reaction temperature was kept at 70 °C and the solid content was 20%. [b] The theoretical M_n values were calculated from $M_{n,theo} = (M_{smallRAFT}$[small RAFT] + $M_{n,macro\text{-}RAFT}$[macro-RAFT])/([small RAFT] + [macro-RAFT]) + $M_{monomer}\,x$ [M]/([small RAFT] + [macro-RAFT]), where [M], [small RAFT] and [macro-RAFT] represent the monomer, small RAFT agent and macro-RAFT agent concentrations, and x is the conversion. [c] D_v is volume-average particle diameter and D_n represents number-average particle diameter measured by Malvern. [d] The percent coagulum was calculated based on the total polymer mass. [e] The particle size distributions in experiments 1 and 2 were bimodal; there were two diameter values corresponding to the two peaks in Malvern data.

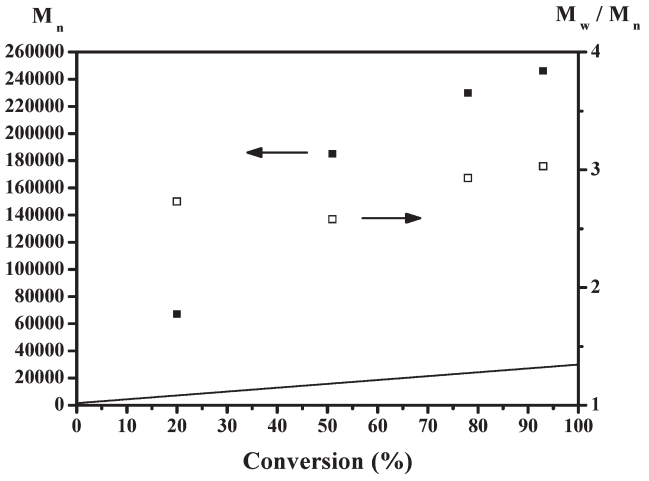


Figure 3. Variation of number-average molecular weight (M_n) and polydispersity (PD) with conversion in RAFT ab initio emulsion polymerization of styrene stabilized by SDS (experiment 1). The line is the theoretical M_n. [KPS]/[RAFT] = 1:5, 20% solid content; T = 70 °C.

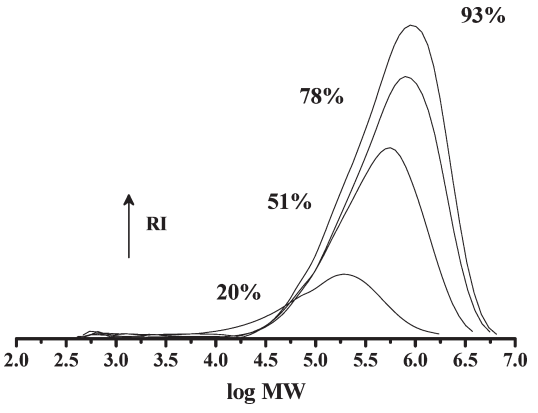


Figure 4. Variation of GPC chromatogram during the RAFT ab initio emulsion polymerization of styrene (experiment 1). [KPS]/[RAFT] = 1:5, 20% solid content; T = 70 °C.

theoretical value. The PDs were 1.50 at 92% conversion. The particle diameters were 82 nm for experiment 3 and 85 nm for experiment 4, and their particle distributions were quite narrow.

In our previous work, it was found that coagulum could also be formed through particle coagulation when the amphiphilic macro-RAFT was used as surfactant. Postaddition

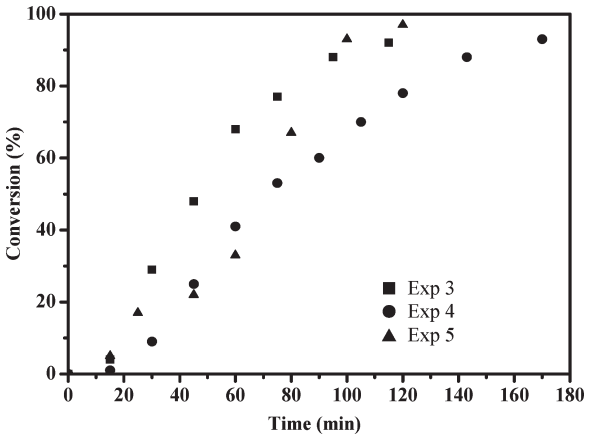


Figure 5. Conversion versus polymerization time plot of RAFT ab initio emulsion polymerization of styrene stabilized by poly(acrylic acid)$_{29}$-*b*-polystyrene$_5$ trithiocarbonate macro-RAFT agent (PAA_{29}-PSt_5-RAFT) (experiments 3−5). The initiator was KPS, solid content was 20%, and the reaction temperature was 70 °C.

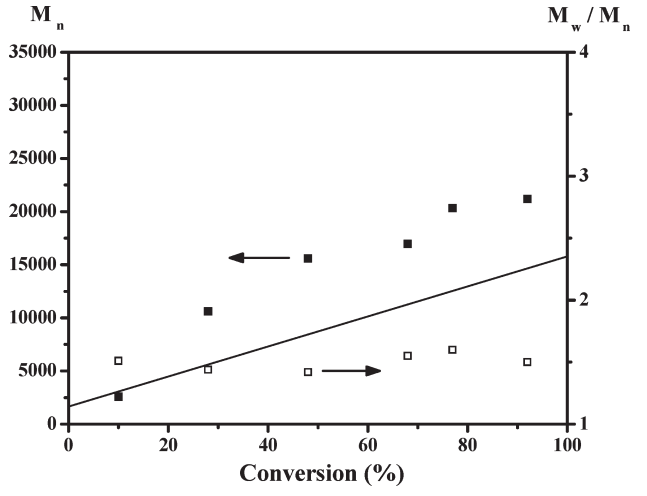


Figure 6. Variation of number-average molecular weight (M_n) and polydispersity (PD) with conversion in RAFT ab initio emulsion polymerization of styrene stabilized by PAA_{29}-PSt_5-RAFT (experiment 3). [KPS]/[RAFT] = 1:5, 20% solid content; T = 70 °C. The line is the theoretical M_n.

of NaOH could avoid the coagulum formation.[34] Therefore, in experiment 5, NaOH solution was injected to the system when the conversion reached 17%. With the addition of

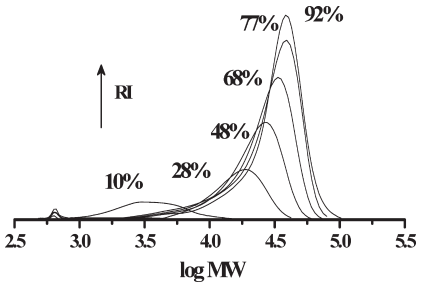


Figure 7. Variation of GPC chromatogram during RAFT ab initio emulsion polymerization of styrene stabilized by PAA_{29}-PSt_5-RAFT (experiment 3). [KPS]/[RAFT] = 1:5, 20% solid content; T = 70 °C.

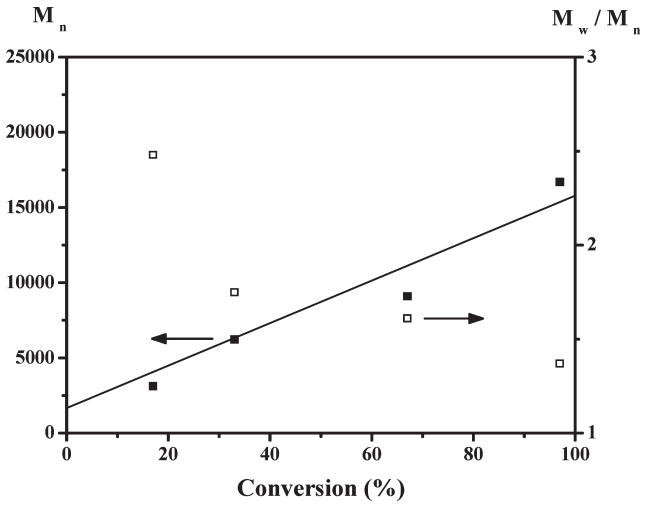


Figure 8. Variation of number-average molecular weight (M_n) and polydispersity (PD) with conversion in RAFT ab initio emulsion polymerization of styrene stabilized by PAA_{29}-PSt_5-RAFT (experiment 5). [KPS]/[RAFT] = 1:5, 20% solid content,; T = 70 °C. NaOH solution was injected to the aqueous phase at 17% conversion and t = 25 min. The line is the theoretical M_n.

NaOH aqueous solution, the pH value increased from 3.0 to 5.0. The polymerization rate slowed down for about 20 min followed by a rapid increase. The increased hydrophilicity of the leaving group of unreacted small RAFT agent might cause radical exit. The coagulum was indeed reduced to a negligible level and the molecular weight was in an excellent agreement with the predication and PD quickly decreased to 1.37 at 97% conversion, as shown in Figure 8.

PAA_{29}-PSt_5 as the Surfactant. The end group of −SC-(=S)$SC_{12}H_{25}$ in PAA_{29}-PSt_5-RAFT was cleaved by RAFT reaction with the primary radical from AIBN. The obtained PAA_{29}-PSt_5 diblock co-oligomers without RAFT end groups were used as surfactant in experiments 6−8. Experiment 6 was the blank experiment without small RAFT agent. As shown in Figure 10, the polymerization proceeded very fast and completed within 60 min. The latex was stable and free of coagulum, suggesting that the PAA_{29}-PSt_5 diblock co-oligomer was a good surfactant. M_n was about 230 000 g/mol and PD was 2.17 in the end of polymerization.

In experiments 7 and 8, the PAA_{29}-PSt_5 diblock co-oligomer was used as surfactant for the RAFT ab initio polymerization. The recipe was summarized in Table 1. In experiment 8, NaOH was postadded. Compared Figure 10 with Figure 5, the polymerization kinetics was found to be very similar to or without the RAFT end group on the surfactant. As a matter of fact, the other aspects such as M_n control, PD, particle size and distribution, coagulum

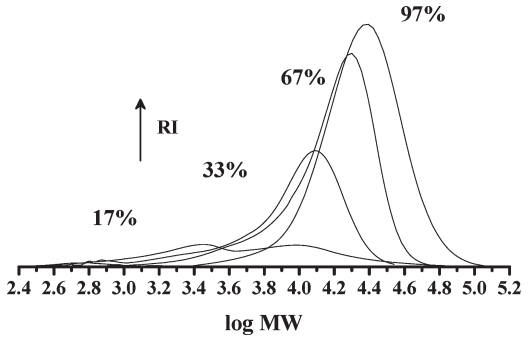


Figure 9. Variation of GPC chromatogram in RAFT ab initio emulsion polymerization of styrene stabilized by PAA_{29}-PSt_5-RAFT (experiment 5). [KPS]/[RAFT] = 1:5, 20% solid content; T = 70 °C. NaOH solution was injected to the aqueous phase at 17% conversion at t = 25 min.

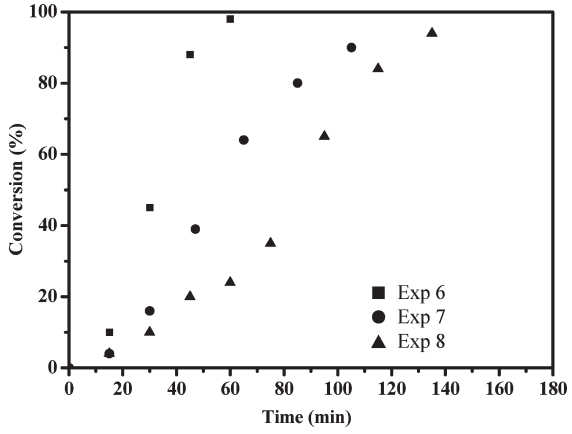


Figure 10. Conversion versus time is RAFT ab initio emulsion polymerization of styrene stabilized by poly(acrylic acid)$_{29}$-*b*-polystyrene$_5$ diblock co-oligomer (PAA_{29}-PSt_5) (experiments 6−8). [KPS]/[RAFT] = 1:5, 20% solid content, T = 70 °C.

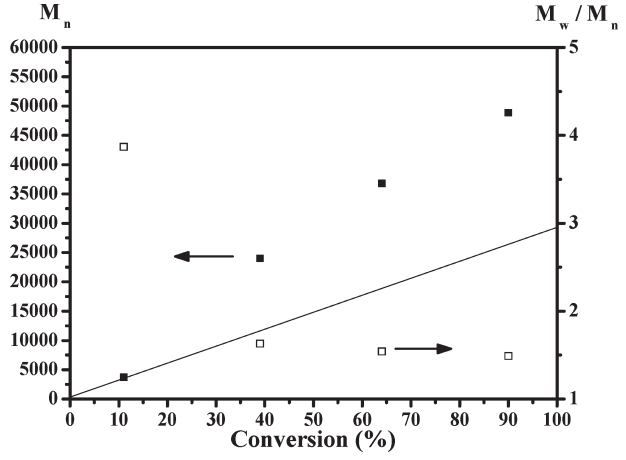


Figure 11. Variation of number-average molecular weight (M_n) and polydispersity (PD) with conversion in RAFT ab initio emulsion polymerization of styrene stabilized by PAA_{29}-PSt_5 (experiment 7). [KPS]/[RAFT] = 1:5, 20% solid content; T = 70 °C. The line is the theoretical M_n.

amount and M_n of the coagulum were all similar, as shown in Table 2 and by comparison between Figures 6−14.

Compared with experiment 8, the aqueous phase was neutralized before the polymerization started in experiment 9. The M_ns deviated significantly from the theoretical values. The particle diameter was small (45 nm) and the size

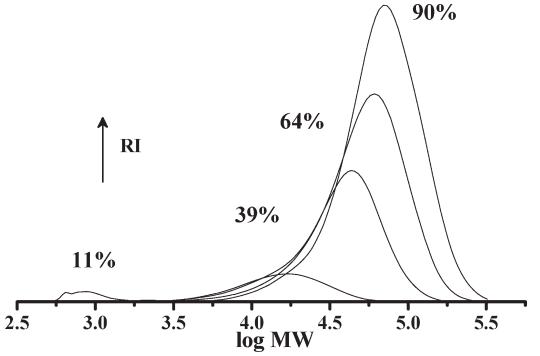


Figure 12. Variation of GPC chromatogram during RAFT ab initio emulsion polymerization of styrene stabilized by PAA_{29}-PSt_5 (experiment 7). [KPS]/[RAFT] = 1:5, 20% solid content; T = 70 °C.

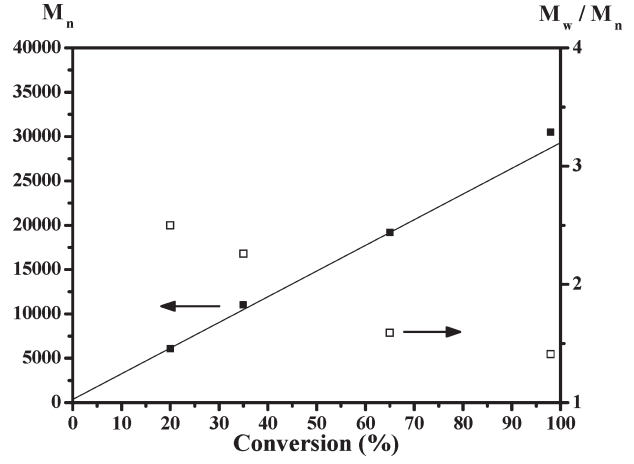


Figure 13. Variation of number-average molecular weight (M_n) and polydispersity (PD) with conversion in RAFT ab initio emulsion polymerization of styrene stabilized by PAA_{29}-PSt_5 (experiment 8). [KPS]/[RAFT] = 1:5, 20% solid content; T = 70 °C. NaOH solution was injected to the aqueous phase at 20% conversion and t = 45 min. The line is the theoretical M_n,.

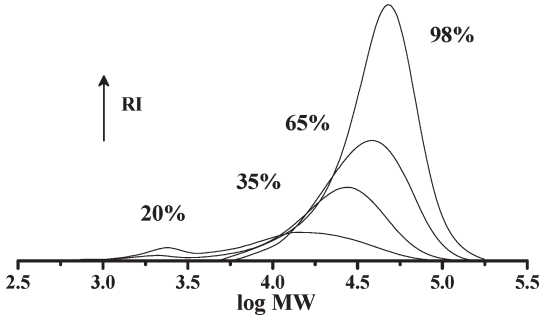


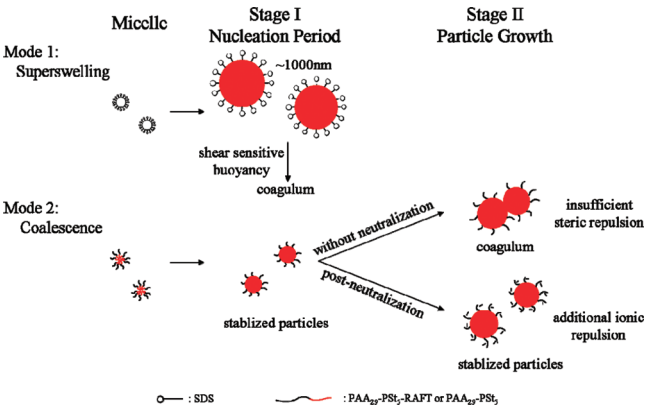
Figure 14. Variation of GPC chromatogram in RAFT ab initio emulsion polymerization of styrene stabilized by PAA_{29}-PSt_5 (experiment 8). [KPS]/[RAFT] = 1:5, 20% solid content; T = 70 °C. NaOH solution was injected to the aqueous phase at 20% conversion and t = 45 min.

distribution was broad, which can be attributed to a continuous nucleation as discussed in the previous literature.[34]

Discussion

Mechanism of Colloidal Instability. As seen in Table 1, the coagulum was composed of oligomers having molecular weights of 700−800 g/mol. Monteiro et al.[17] and Gilbert et al.[29−32] proposed that such oligomers were formed in monomer droplets. Since these oligomers could not transfer

Scheme 1. Mechanism for Colloidal Instability in Small RAFT ab Initio Emulsion Polymerization: Superswelling and Coalescence.[a]



[a] The particle size was not scaled with the actual size.

across water from monomer droplets to polymer particles, coagulum should appear at the end of stage II when monomer molecules in monomer droplets completely transferred to polymer particles. Following this mechanism, primary radicals born in water must be captured by monomer droplets. If so, when the stirring speed was reduced from 300 to 50 rpm, the coagulum amount should become smaller as a result of the significantly reduced surface area of droplets. The latter was evident from the appearance of monomer oil layer and from the decreased polymerization rate as seen in Figure 2. Contrary to the theory, the coagulum amount was actually independent of the stirring speed as listed in Table 2.

Another observation that disagreed with the theory of coagulum formation in monomer droplets was from experiments 5 and 8. In these experiments, the monomer droplets contained oil soluble RAFT agent molecules just as in the case of using SDS as the surfactant. If the coagulum in the SDS runs was formed in the monomer droplets, we should have also collected some coagulum in experiments 5 and 8. However, the coagulum amount was negligible and the polymerization proceeded with controlled molecular weight and relatively low PD. This result suggested that the oligomer coagulum collected in the SDS case was not formed in the monomer droplets. On the other hand, the styrene/water interfacial tension with PAA_{29}-PSt_5-RAFT and PAA_{29}-PSt_5 as surfactant was measured to be 11.4 mN/m. According to the calculation shown in Figure 1, replacing SDS with the oligomeric surfactants suppressed the superswelling and led to the colloidal stability (mode 1 as seen in Scheme 1).

In experiments 3, 4, and 7, the coagulum was still detectable, though the superswelling was equally suppressed according to Figure 1. The coagulum formation in these cases could be ascribed to particle coalescence (mode 2 in Scheme 1) instead of superswelling. The oligomer surfactants in these experiments stabilized the particles mainly by steric hindrance effect. In such cases, very high surfactant coverage was required to prevent particles from coalescence. The coalescence might occur in Stage II, where particle size and thus interfacial area steadily increased but no additional surfactant molecules were available to offer protection to the increased interfacial area. The neutralization of acid groups by NaOH postaddition introduced ionic repulsion and thus prevented the particles from coalescence in experiments 5 and 8. Figure 15 offered some evidence for this coalescence. As shown in Figure 15, the number of "particles" decreased rapidly at the start of polymerization. As it has been pointed out,[34] the estimated number of "particles"

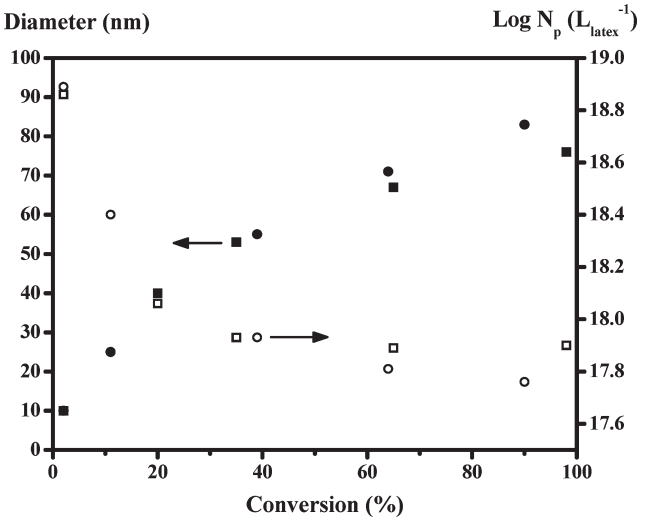


Figure 15. Particle diameter (●, experiment 7; ■, experiment 8) determined by Malvern and number of particles (○, experiment 7; □, experiment 8) vs conversion in experiments 7 and 8. 20% solid content, [KPS]/[RAFT] = 1:5, T = 70 °C. No NaOH was added in experiment 7. NaOH solution was injected to the aqueous phase at 20% conversion and t = 45 min in experiment 8.

from the dynamic light scattering data actually represented the total number of micelles and nucleated particles. With more and more micelles nucleated, the total number decreased. In experiment 8, with postneutralization, the total number leveled off after 35% monomer conversion, indicating the end of nucleation stage. Without NaOH addition, experiment 7 experienced the same nucleation period as experiment 8. The fact that the total number still decreased gradually with monomer conversion after the nucleation period suggested the occurrence of particle coalescence. As a result, the final particles of experiment 7 were larger than those of experiment 8. The particle size in experiment 6 with no RAFT agent addition was significantly larger than that in its counterpart experiment 7, as seen in Table 1. The RAFT agent addition promoted the nucleation of particles and the formation of coagulum, as shown in Table 2.

Because of the coagulum formation, some RAFT agents did not participate efficiently in the chain growth process. The final M_ns were therefore somewhat higher than the theoretical values, depending on the amount of coagulum, as evident in Table 2.

Transportation of Initial RAFT Agent. In ab initio emulsion polymerization of styrene mediated by oil-soluble small RAFT agent, the transport of RAFT agent molecules from monomer droplets to polymer particles at low conversions has been a concern. However, as seen in Figure 6, the M_n data agreed well with the prediction at the conversions as low as 10%, indicating that all the RAFT molecules were transferred to particles at an early stage. We measured the RAFT concentration in the monomer droplets prior to KPS injection and at the end of inhibition period in experiment 3. It was found that only half of the RAFT amount was left in the monomer droplets after the inhibition period at about 2% monomer conversion. As a comparison, 98% RAFT agent amount was in the monomer droplets before the initiation of polymerization.

A period of inhibition is often observed in RAFT (mini)-emulsion polymerization.[18−21,28,32,52−56] The reason is very different from that for RAFT homogeneous polymerization, which has been debated for many years.[61−66] As a matter of fact, the bulk styrene polymerization mediated by the current RAFT agent did not have an inhibition period while its emulsion polymerization did, as seen in Figure 1. The inhibition period has been ascribed to the exit of R radicals to water phase.[18−21,28,32,52−56] During the inhibition period, the initial RAFT molecules in the micelles were converted to oligomeric RAFT agent and the RAFT molecules in the monomer droplets were gradually transferred to the micelles. Meanwhile, the monomer conversion was still very low since the radicals in the micelles could exit to water after the RAFT reaction. As a result, most initial RAFT agent molecules were converted to oligomeric RAFT agent at low monomer conversions during the period of inhibition. It is of great interest to note that the inhibition period of RAFT emulsion polymerization facilitates the effective initiation of polymer chains at low conversions with high nucleation efficiency.

Conclusion

Successful RAFT ab initio emulsion polymerization of styrene mediated by an oil-soluble small RAFT agent was achieved by employing amphiphilic copolymer as surfactant. Polystyrene latex with controlled molecular weight, relatively low PD, narrow particle size distribution was obtained by postneutralization of PAA_{29}-PSt_5-RAFT and PAA_{29}-PSt_5. This result could not be explained by the theory of coagulum formation in monomer droplets proposed for the RAFT ab initio emulsion polymerization with SDS as surfactant. Instead, it agreed well with the superswelling hypothesis. The PAA_{29}-PSt_5 suppressed the superswelling and thus improved the colloidal stability by the high interfacial tension of monomer/water/surfactant system. It was also found that a majority of the initial RAFT molecules were converted to polymer chains at low monomer conversions in the period of inhibition. This work suggests that well-controlled ab initio emulsion polymerization is achievable with small RAFT agent.

Acknowledgment. The authors would like to thank the National Science Foundation of China (NSFC) for research grants No. 20836007 and No. 21076181.

References and Notes

(1) Hawker, C. J.; Bosman, A. W.; Harth, E. *Chem. Rev.* **2001**, *101*, 3661–3688.
(2) Matyjaszewski, K.; Xia, J. *Chem. Rev.* **2001**, *101*, 2921–2990.
(3) Kamigaito, M.; Ando, T.; Sawamoto, M. *Chem. Rev.* **2001**, *101*, 3689–3745.
(4) Chiefari, J.; Chong, Y. K.; Ercole, F.; Krstina, J.; Jeffery, J.; Le, T. P. T.; Mayadunne, R. T. A.; Meijs, G. F.; Moad, C. L.; Moad, G.; Rizzardo, E.; Thang, S. H. *Macromolecules* **1998**, *31*, 5559–5562.
(5) Moad, G.; Rizzardo, E.; Thang, S. H. *Aust. J. Chem.* **2009**, *62*, 1402–1472.
(6) Oh, J. K. *J. Polym. Sci., Part A: Polym. Chem.* **2008**, *46*, 6983–7001.
(7) Butte, A.; Storti, G.; Morbidelli, M. *Macromolecules* **2001**, *34*, 5885–5896.
(8) Luo, Y.; Wang, R.; Yang, L.; Yu, B.; Li, B.; Zhu, S. *Macromolecules* **2006**, *39*, 1328–1337.
(9) Zetterlund, P. B.; Kagawa, Y.; Okubo, M. *Chem. Rev.* **2008**, *108*, 3747–3794.
(10) Zetterlund, P. B.; Okubo, M. *Macromolecules* **2006**, *39*, 8959–8967.
(11) Kagawa, Y.; Zetterlund, P. B.; Minami, H.; Okubo, M. *Macromol. Theory Simul.* **2006**, *15*, 608–613.
(12) Maehata, H.; Buragina, C.; Cunningham, M.; Keoshkerian, B. *Macromolecules* **2007**, *40*, 7126–7131.
(13) Delaittre, G.; Charleux, B. *Macromolecules* **2008**, *41*, 2361–2367.
(14) Simms, R. W.; Cunningham, M. F. *Macromolecules* **2008**, *41*, 5148–5155.
(15) Cunningham, M. F. *Prog. Polym. Sci.* **2008**, *33*, 365–398.
(16) Uzulina, I.; Kanagasabapathy, S.; Claverie, J. *Macromol. Symp.* **2000**, *150*, 33–38.
(17) Monteiro, M. J.; Hodgson, M.; de Brouwer, H. *J. Polym. Sci., Part A: Polym. Chem.* **2000**, *38*, 3864–3874.

(18) Charmot, D.; Corpart, P.; Adam, H.; Zard, S. Z.; Biadatti, T.; Bouhadir, G. *J. Macromol. Symp.* **2000**, *150*, 23–32.
(19) Monteiro, M. J.; Sjoberg, M.; van der Vlist, J.; Gottgens, C. M. *J. Polym. Sci., Part A: Polym. Chem.* **2000**, *38*, 4206–4217.
(20) Monteiro, M. J.; de Barbeyrac, J. *Macromolecules* **2001**, *34*, 4416–4423.
(21) Monteiro, M. J.; Adamy, M. M.; Leeuwen, B. J.; van Herk, A. M.; Destarac, M. *Macromolecules* **2005**, *38*, 1538–1541.
(22) Nozari, S.; Tauer, K.; Ali, A. M. I. *Macromolecules* **2005**, *38*, 10449–10454.
(23) Nozari, S.; Tauer, K. *Polymer* **2005**, *46*, 1033–1043.
(24) Shim, S. E.; Shin, Y.; Jun, J. W.; Lee, K.; Jung, H.; Choe, S. *Macromolecules* **2003**, *36*, 7994–8000.
(25) Shim, S. E.; Shin, Y.; Lee, H.; Choe, S. *Polym. Bull.* **2003**, *51*, 209–216.
(26) Apostolovic, B.; Quattrini, F.; Butte, A.; Storti, G.; Morbidelli, M. *Helv. Chim. Acta* **2006**, *89*, 1641–1659.
(27) Luo, Y.; Cui, X. *J. Polym. Sci., Part A: Polym. Chem.* **2006**, *44*, 2837–2847.
(28) Urbani, C. N.; Nguyen, H. N.; Monteiro, M. J. *Aust. J. Chem.* **2006**, *59*, 728–732.
(29) Ferguson, C. J.; Hughes, R. J.; Pham, B. T. T.; Hawkett, B. S.; Gilbert, R. G.; Serelis, A. K.; Such, C. H. *Macromolecules* **2002**, *35*, 9243–9245.
(30) Save, M.; Guillaneuf, Y.; Gilbert, R. G. *Aust. J. Chem.* **2006**, *59*, 693–711.
(31) Prescott, S. W.; Ballard, M. J.; Rizzardo, E.; Gilbert, R. G. *Macromolecules* **2002**, *35*, 5417–5425.
(32) Prescott, S. W.; Ballard, M. J.; Rizzardo, E.; Gilbert, R. G. *Macromol. Theory Simul.* **2006**, *15*, 70–86.
(33) Ferguson, C. J.; Hughes, R. J.; Nguyen, D.; Pham, B. T. T.; Gilbert, R. G.; Serelis, A. K.; Such, C. H.; Hawkett, B. S. *Macromolecules* **2005**, *38*, 2191–2204.
(34) Wang, X.; Luo, Y.; Li, B.; Zhu, S. *Macromolecules* **2009**, *42*, 6414–6421.
(35) Rieger, J.; Stoffelbach, F.; Bui, C.; Alaimo, D.; Jerome, C.; Charleux, B. *Macromolecules* **2008**, *41*, 4065–4068.
(36) Rieger, J.; Osterwinter, G.; Bui, C.; Stoffelbach, F.; Charleux, B. *Macromolecules* **2009**, *42*, 5518–5525.
(37) Urbani, C. N.; Monteiro, M. J. *Aust. J. Chem.* **2009**, *62*, 1528–1532.
(38) Sebakhy, K. O.; Kessel, S.; Monteiro, M. J. *Macromolecules* **2010**, DOI: 10.1021/ma1019889.
(39) Urbani, C. N.; Monteiro, M. J. *Macromolecules* **2009**, *42*, 3884–3886.
(40) Gilbert, R. G. *Emulsion Polymerization: A Mechanistic Approach*; Academic Press: London, 1995.
(41) Kemmere, M. F.; Meuldijk, J.; Drinkenburg, A. A. H.; German, A. L. *J. Appl. Polym. Sci.* **1999**, *74*, 3225–3241.
(42) Luo, Y.; Tsavalas, J.; Schork, F. J. *Macromolecules* **2001**, *34*, 5501–5507.
(43) Morton, M.; Kaizerman, S.; Altier, M. W. *J. Colloid Sci.* **1954**, *9*, 300–312.
(44) Ugelstad, J. *Makromol. Chem.* **1978**, *179*, 815–817.
(45) Ugelstad, J.; Mork, P. C.; Kaggerud, K. H.; Ellingsen, T.; Berge, A. *Adv. Colloid Interface Sci.* **1980**, *13*, 101–140.
(46) *Polymer Handbook*, 4th ed.; Brandrup, J.; Immergut, E. H.; Grulke, E. A., Eds.; Wiley-Interscience Publication: New York, 1999.
(47) Landfester, K.; Bechthold, N.; Tiarks, F.; Antonietti, M. *Macromolecules* **1999**, *32*, 5222–5228.
(48) Smulders, W. W.; Jones, C. W.; Schork, F. J. *Macromolecules* **2004**, *37*, 9345–9354.
(49) Baussard, J. F.; Habib-Jiwan, J. L.; Laschewsky, A.; Mertoglu, M.; Storsberg, J. *Polymer* **2004**, *45*, 3615–3626.
(50) Barner-Kowollik, C.; Heuts, J. P. A.; Davis, T. P. *J. Polym. Sci., Part A: Polym. Chem.* **2001**, *39*, 656–664.
(51) Konkolewicz, D.; Siauw, M.; Gray-Weale, A.; Hawkett, B. S.; Perrier, S. *J. Phys. Chem. B* **2009**, *113*, 7086–7094.
(52) Peklak, A. D.; Butte, A. *J. Polym. Sci., Part A: Polym. Chem.* **2006**, *44*, 6114–6135.
(53) Luo, Y.; Liu, B.; Wang, Z.; Gao, J.; Li, B. *J. Polym. Sci., Part A: Polym. Chem.* **2007**, *45*, 2304–2315.
(54) Moad, G.; Chiefari, J.; Chong, Y. K.; Krstina, J.; Mayadunne, R. T. A.; Postma, A.; Rizzardo, E.; Thang, S. H. *Polym. Int.* **2000**, *49*, 993–1001.
(55) Pepels, M. P. F.; Holdsworth, C. I.; Pascual, S.; Monteiro, M. J. *Macromolecules* **2010**, *43*, 7565–7576.
(56) Luo, Y.; Yu, B. *Polym. Plast. Technol. Eng.* **2004**, *43*, 1299–1321.
(57) Nomura, M.; Harada, M.; Eguchi, W.; Nagata, S. *J. Appl. Polym. Sci.* **1972**, *16*, 835–847.
(58) Zubitur, M.; Mendoza, J.; de la Cal, J. C.; Asua, J. M. *Macromol. Symp.* **2000**, *150*, 13–22.
(59) Sajjadi, S. *Macromol. Rapid Commun.* **2004**, *25*, 882–887.
(60) Chern, C. S. *Prog. Polym. Sci.* **2006**, *31*, 443–486.
(61) McLeary, J. B.; Calitz, F. M.; McKenzie, J. M.; Tonge, M. P.; Sanderson, R. D.; Klumperman, B. *Macromolecules* **2005**, *38*, 3151–3161.
(62) Perrier, S.; Barner-Kowollik, C.; Quinn, J. F.; Vana, P.; Davis, T. P. *Macromolecules* **2002**, *35*, 8300–8306.
(63) Vana, P.; Davis, T. P.; Barner-Kowollik, C. *Macromol. Theory Simul.* **2002**, *11*, 823–835.
(64) Wang, A. R.; Zhu, S.; Kwak, Y.; Goto, A.; Fukuda, T.; Monteiro, M. J. *J. Polym. Sci., Part A: Polym. Chem.* **2003**, *41*, 2833–2839.
(65) Barner-Kowollik, C.; Buback, M.; Charleux, B.; Coote, M. L.; Drache, M.; Fukuda, T.; Goto, A.; Klumperman, B.; Lowe, A. B.; McLeary, J. B.; Moad, G.; Monteiro, M. J.; Sanderson, R. D.; Tonge, M. P.; Vana, P. *J. Polym. Sci., Part A: Polym. Chem.* **2006**, *44*, 5809–5831.
(66) Barner-Kowollik, C.; Coote, M. L.; Davis, T. P.; Radom, L.; Vana, P. *J. Polym. Sci., Part A: Polym. Chem.* **2003**, *41*, 2828–2832.

230 *Macromolecules* **2011**, *44*, 230–239
DOI: 10.1021/ma102419e

Macromolecules
ARTICLE

Functionalized Nonionic Dextran Backbones by Atom Transfer Radical Polymerization for Efficient Gene Delivery

Z. H. Wang,[†] W. B. Li,[‡] J. Ma,[‡] G. P. Tang,[§] W. T. Yang,[†] and F. J. Xu*,[†]

[†]*State Key Laboratory of Chemical Resource Engineering, Key Laboratory of Carbon Fiber and Functional Polymers, Ministry of Education, College of Materials Science & Engineering, Beijing University of Chemical Technology, Beijing 100029 China,* [‡]*State Key Laboratory of Molecular Oncology, Cancer Institute & Hospital, Chinese Academy of Medical Sciences, Beijing 100021 China, and* [§]*Institute of Chemical Biology and Pharmaceutical Chemistry, Zhejiang University, Hangzhou 310028, China*

Received October 27, 2010; Revised Manuscript Received December 9, 2010

ABSTRACT: It is of crucial importance to modify dextran-based polysaccharides in the design of novel biomedical materials. A simple one-step method, involving the reaction of hydroxyl groups of dextran with α-bromoisobutyric acid in the presence of 1,1′-carbonyldiimidazole, was first developed to produce bromoisobutyryl-terminated dextran as multifunctional initiators for subsequent atom transfer radical polymerization (ATRP). Well-defined comb-shaped copolymers (DPDs) composed of nonionic hydrophilic dextran backbones and cationic poly((2-dimethyl amino)ethyl methacrylate) (or P(DMAEMA)) side chains were subsequently prepared via ATRP for nonviral gene delivery. The P(DMAEMA) side chains of DPDs can be further partially quaternized to produce the quaternary ammonium DPDs (QDPDs). DPD and QDPDs can condense pDNA into complex nanoparticles of 100 to 150 nm in sizes. QDPDs exhibit stronger ability to complex pDNA, due to increased surface cationic charges. DPDs can exhibit much lower cytotoxicity and better gene transfection yield than high-molecular-weight P(DMAEMA) homopolymers and "gold-standard" polyethylenimine (25 kDa) in HEK293 and L929 cell lines. DPDs also exhibit efficient gene delivery ability in different cancer cell lines, especially in MCF7 cells where the DPD-mediated transfection efficiency is almost 3 times higher than that of the popular Lipfectamine 2000 transfection reagent. This study demonstrated that grafting low-molecular-weight polymer chains from natural dextran backbones via ATRP is an effective means to produce novel polysaccharide-based nanobiomaterials.

1. Introduction

Successful gene therapy depends on the design of gene delivery vectors with low cytotoxicity and high transfection efficiency.[1,2] Over the last few decades, cationic polymers have been receiving considerable attention as the major type of nonviral gene delivery nanovectors, because of their low host immunogenicity, high flexibility, and easy preparation.[3,4] Polycations usually contain primary, secondary, tertiary, and/or quaternary amino groups. Under physiological conditions, polycations can spontaneously condense negatively charged DNA into compact nanocomplexes, reduce the electrostatic repulsion between DNA and cell surfaces, protect plasmid DNA from enzymatic degradation by nucleases, and facilitate cellular transfection. A great number of polycations, including polyethylenimine (PEI),[5] poly(tertiary amine methacrylate),[4,6,7] poly(L-lysine),[8] polyamidoamine,[9] and polysaccharide-based cationic carriers,[2,10−12] have emerged as a leading class of transfection reagents. However, most of them suffer from either low gene transfection efficiency or significant toxicity. New cationic polymeric vectors with high gene transfection efficiency and low cytotoxicity will facilitate their applications in gene therapy.

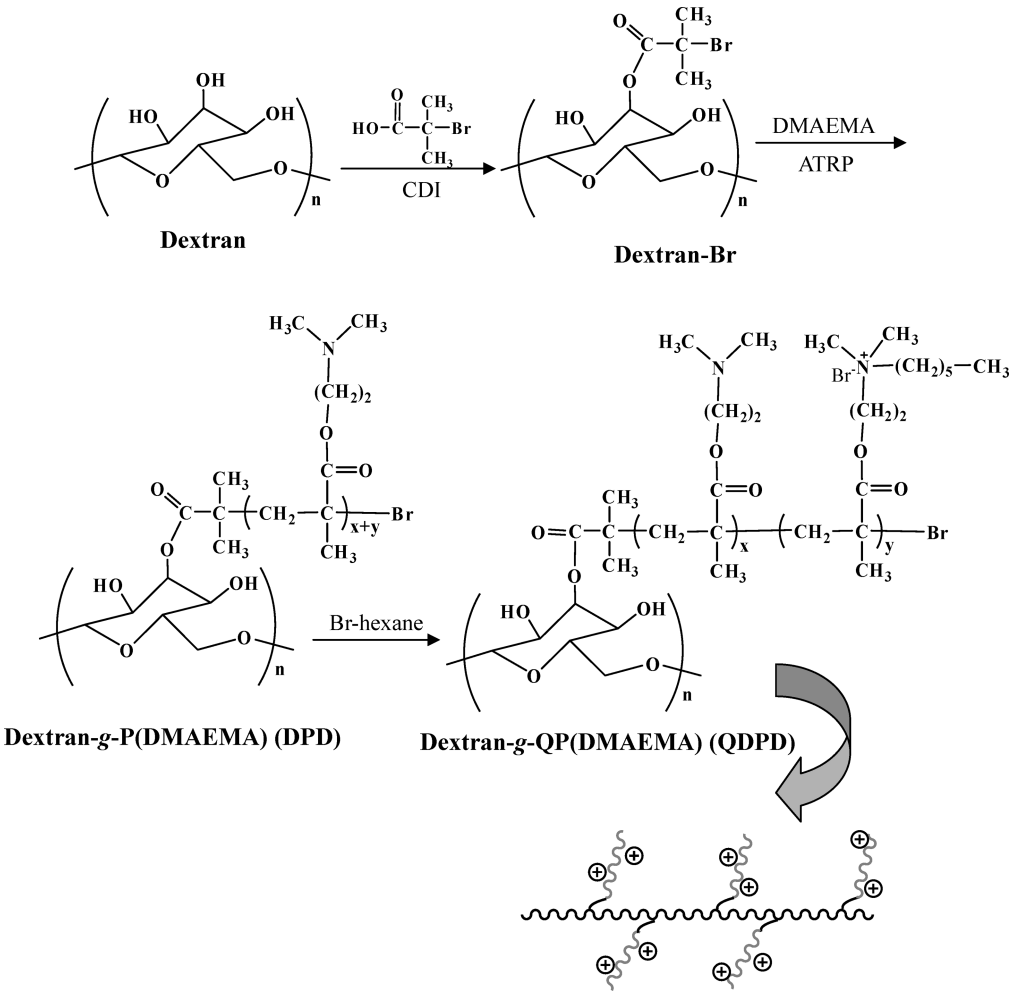
Natural polysaccharides are very suitable candidates for the design of novel biomaterials, because they are renewable, nontoxic, biodegradable and excellent biocompatible materials. Dextran is a highly water-soluble branched polysaccharide composed of glucose units mainly linked by α-1,6-linkages. It is of crucial importance to modify dextran-based polysaccharides in the designing of biomedical materials. A series of dextran-based cationic polymers including diethylaminoethyl−dextran and dextran−spermine were prepared for the efficient delivery of nucleic acids.[2,12−14] Atom transfer radical polymerization (ATRP) is a recently developed 'controlled' radical polymerization method, which has been used to prepare graft copolymers from some polysaccharides.[11,15−18] Recently, we have reported several types of P(DMAEMA)-based polycations via ATRP as efficient gene nanovectors.[6,11,15,16] In particular, comb-shaped copolymers composed of chitosan[15] or hydroxypropyl cellulose[16] backbones and P(DMAEMA) side chains provide a versatile means for designing advanced nonviral gene carriers from nontoxic polysaccharides. Novel comb-shaped gene delivery vectors using dextran as backbones also will be developed if the hydroxyl groups of dextran could be derivatized to serve as effective initiation sites for growing cationic side chains. Dextran can readily dissolve in dimethyl sulfoxide (DMSO). However, the fixation of alkyl halide initiators on dextran via direct esterification of hydroxyl groups is not successful in DMSO, due to the occurrence of Swern secondary reactions.[18] It was reported that such esterification immobilization reaction could be carried out in dimethylformamide (DMF) solvent.[17] Unfortunately, the results were not promising, due to the poor solubility of dextran in DMF.[18] Considering dextran's poor solubility in most traditional solvents, the direct fixation of uniform ATRP initiators on dextran is very difficult, usually involving a mutilstep process including protection/deprotection steps.[8]

In the present study, a simple one-step method was developed to produce bromoisobutyryl-terminated dextran (Dextran−Br)

*To whom correspondence should be addressed. E-mail: xufj@mail.buct.edu.cn.

 Published on Web 12/22/2010 © 2010 American Chemical Society

Scheme 1. Schematic Diagram Illustrating the Preparation Processes of Partially Quaternized P(DMAEMA)-*graft*-dextran Comb Copolymers via Atom Transfer Radical Polymerization (ATRP) from 2-Bromoisobutyryl-Terminated Dextran



as multifunctional ATRP initiators (Scheme 1). Well-defined comb-shaped copolymers (DPDs) composed of nonionic hydrophilic dextran backbones and cationic poly((2-dimethyl amino)-ethyl methacrylate) (or P(DMAEMA)) side chains were subsequently prepared via ATRP for highly efficient nonviral gene delivery. It was reported that the cationic dextran carriers with quaternary ammonium groups can increase the ability to complex plasmid DNA (pDNA).[14,16] The P(DMAEMA) side chains can be further partially quaternized to produce the quaternary ammonium DPDs (QDPDs). DPDs and QDPDs can condense pDNA into complex nanoparticles of 100−150 nm in size. QHPDs exhibit stronger ability to complex pDNA. In comparison with the high-molecular-weight P(DMAEMA) homopolymer and "gold-standard" branched PEI (25 kDa), DPDs exhibit much lower cytotoxicity and better or comparable gene transfection efficiency in HEK293 and L929 cell lines. DPDs also can produce good transfection ability in different cancer cell lines, especially in MCF7 cells where the DPD-mediated transfection efficiency is almost 3 times higher than that of the popular Lipfectamine 2000 transfection reagent. In addition, it was found that DPDs also possess better water solubility and higher transfection efficiency than the hydroxypropyl cellulose-*graft*-P(DMAEAM) comb carriers reported earlier.[16] Thus, the approach grafting low-molecular-weight cationic polymer chains from nonionic hydrophilic dextran backbones can produce a new class of nonviral gene delivery nanovectors with low cytotoxicity and high transfection efficiency for future gene therapy.

2. Experimental Section

2.1. Materials. Dextran from *Leuconostoc* spp. (mol wt 6000 g/mol), branched polyethylenimine (PEI, weight-average molecular weight (M_w) ~25000 Da, 99%), α-bromoisobutyric acid (BIBA, 98%), 1,1′-carbonyldiimidazole (CDI, 97%), 1,4,7,10,10-hexamethyl triethylenetetramine (HMTETA, 99%), copper(I) bromide (CuBr, 99%), and (2-dimethylamino)ethyl methacrylate (DMAEMA, >98%) were obtained from Sigma-Aldrich Chemical Co., St. Louis, MO. DMAEMA was used after removal of the inhibitors in a ready-to-use disposable inhibitor-removal column (Sigma-Aldrich). 3-(4,5-Dimethylthiazol-2yl)-2, 5-diphenyl tetrazolium bromide (MTT, 98%), penicillin G potassium (>98%), and streptomycin sulfate salt (>98%) were purchased from Sigma Chemical Co., St. Louis, MO. HEK293, L929, MCF7, and 973 cell lines were purchased from the American Type Culture Collection (ATCC, Rockville, MD). The control P(DMAEMA) homopolymer with about 180 repeat units of DMAEMA was prepared via ATRP, using the reported ethylene glycol di-2-bromoisobutyrate as the initiator.[11]

2.2. Synthesis of Comb-Shaped Cationic Copolymers via ATRP. The starting bromoisobutyryl-terminated dextran (Dextran−Br) was synthesized via the reaction of hydroxyl groups of dextran with BIBA in the presence of CDI catalyst.[19−21] In separate flasks, BIBA (4.2 g, 26.3 mmol), CDI (2.0 g, 12.3 mmol), and dextran (2.0 g, about 37.0 mmol −OH) were independently dissolved in 10 mL of anhydrous DMSO. The CDI solution was added dropwise at ambient temperature into the flask containing BIBA solution. The reaction was allowed to proceed at room temperature (about 28 °C) for 4 h to produce the acid imidazolide. After the

reaction was complete, the acid imidazolide reaction mixture was added to the dextran solution. The reaction was stirred at 60 °C for 6 h to produce the Dextran−Br macroinitiator. The final reaction mixture was precipitated with 300 mL of diethyl ether. The crude polymer was purified by reprecipitation thrice in 200 mL of diethyl ether/ethanol mixture (20/1, v/v). Finally, the Dextran−Br for the subsequent ATRP was dried under reduced pressure. Yield = 85%. ^{1}H NMR (D_2O, δ/ppm): 3.4−4.0 (*CH*−O and CH_2−O), 4.9 (O−*CH*−O), and 1.92 (C(Br)−CH_3). $M_n = 5.7 \times 10^3$ g/mol and polydispersity index (PDI) = 1.2 from GPC.

The Dextran-*g*-P(DMAEMA) comb-like polymers (DPDs, Scheme 1) were synthesized using a molar feed ratio [DMAEMA (3 mL, 18.7 mmol)]:[CuBr, 0.31 mmol]:[HMTETA, 0.37 mmol] of 60:1:1.2 at room temperature in 8 mL of methanol/water (3/5, v/v) containing Dextran−Br (0.4 g, about 0.31 mmol Br). The reaction was performed in a 25 mL flask equipped with a magnetic stirrer and under the typical conditions for ATRP.[11] DMAEMA, Dextran−Br, and HMTETA were introduced into the flask containing 8 mL of methanol/water (3/5, v/v). After Dextran−Br had dissolved completely, the reaction mixture was degassed by bubbling argon for 30 min. Then, CuBr was added into the mixture under an argon atmosphere. The flask was then sealed with a rubber stopper under an argon atmosphere. The polymerization was allowed to proceed under continuous stirring at room temperature from 5 to 12 h. The reaction was stopped by diluting with tetrahydrofuran (THF). The catalyst complex was removed by passing the blue dilute polymer solution through a short aluminum oxide column. After removal of THF in a rotary evaporator, DPDs were precipitated in 100 mL of *n*-hexane. The crude polymer was purified by reprecipitation twice in hexane to remove the reactant residues, prior to being dried under reduced pressure. About 0.5 g of DPD1 from 5 h ($M_n = 1.49 \times 10^4$ g/mol and PDI = 1.4) and 1.2 g of DPD2 from 12 h ($M_n = 3.02 \times 10^4$ g/mol and PDI = 1.6) were obtained. ^{1}H NMR (D_2O, δ/ppm): 0.89 (C−CH_3), 1.83 (C−CH_2), 2.28 (N−CH_3), 2.67 (N−CH_2), and 4.12 (CH_2−O−C═O).

The Dextran-*g*-QP(DMAEMA) (QDPD) with partially quaternized P(DMAEMA) side chains was prepared at 50 °C for 24 h in 6 mL of THF containing 0.25 g (about 1.23 mmol N) of DPD2 and 0.5 (3.5 mmol) or 1.0 (7.0 mol) mL of 1-bromohexane. The QHPD was precipitated in 50 mL of *n*-hexane and dried under reduced pressure. Yield = 94%. Quaternization extent of P(DMAEMA) side chains determined from XPS: 21% (for DPD2−1 from 0.5 mL) and 35% (for DPD2−1 from 1.0 mL). ^{1}H NMR (D_2O, δ/ppm): 0.89 (C−CH_3), 1.83 (C−CH_2), 2.28 (N−CH_3), 2.67 (N−CH_2) 3.17 (N^+−CH_3), 3.42 (N^+−CH_2) and 4.12 (CH_2−O−C═O).

2.3. Polymer Characterization. The molecular weights of polymers were determined by gel permeation chromatography (GPC), chemical composition by X-ray photoelectron spectroscopy (XPS), and chemical structure by nuclear magnetic resonance (NMR) spectroscopy. GPC measurements were performed on a YL9100 GPC system equipped with a UV/vis detector and Waters Ultrahydrogel 250 (packed with cross-linked hydroxylated polymethacrylate-based gels of 250 Å pore sizes) and Ultrahydrogel Linear (packed with cross-linked hydroxylated polymethacrylate-based gels of different pore sizes) 7.8 × 300 mm columns. The Ultrahydrogel 250 and Ultrahydrogel Linear columns allowed the separation of polymers over the molecular weight ranges of 10^3 to 8×10^4 and 10^3 to 7×10^6, respectively. A pH 3.5 acetic buffer solution was used as the eluent at a low flow rate of 1.0 mL/min at 25 °C. Monodispersed dextran standards were used to obtain a calibration curve. The XPS measurements were performed on a Kratos AXIS HSi spectrometer equipped with a monochromatized AlK_α X-ray source (1486.6 eV photons), using the same procedures as those described earlier.[11] ^{1}H NMR spectra were measured by accumulation of 1000 scans at a relaxation time of 2 s on a Bruker ARX 300 MHz spectrometer, using D_2O as the solvent. Chemical shifts were referred to the solvent peak, δ = 4.70 ppm.

2.4. Characterization of Polymer/pDNA Complexes. The plasmid (encoding *Renilla* luciferase) mainly used in this work was pRL-CMV (Promega Co., Cergy Pontoise, France), which was cloned originally from the marine organism *Renilla reniformis*. The plasmid DNA (pDNA) was amplified in *Escherichia coli* and purified according to the supplier's protocol (Qiagen GmbH, Hilden, Germany). The purity and concentration of the purified DNA were determined by absorption at 260 and 280 nm and by agrose gel electrophoresis.[6] The purified pDNA was resuspended in tris-EDTA (TE) buffer and kept in aliquots of 0.5 mg/mL in concentration. All polymer stock solutions were prepared at a nitrogen concentration of 10 mM in distilled water. Solutions were filtered via sterile membranes (0.2 μm) of average pore size and stored at 4 °C. Comb-like polymers to DNA ratios are expressed as molar ratios of nitrogen (N) in DPD and QDPDs to phosphate (P) in DNA (or as N/P ratios). The average mass weight of 325 per phosphate group of DNA was assumed.[5] All polymer/pDNA complexes were formed by mixing equal volumes of polymer and pDNA solutions to achieve the desired N/P ratio. Each mixture was vortexed and incubated for 30 min at room temperature.

Each cationic polymer was examined for its ability to bind pDNA through agarose gel electrophoresis using the similar procedures as those described earlier.[6] The polymer/pDNA complexes at various N/P ratios were investigated. Gel electrophoresis was carried out in TAE running buffer (40 mM Tris−acetate, 1 mM EDTA) with a voltage of 110 V for 30 min in a Sub-Cell system (Bio-Rad Lab, Hercules, CA). DNA bands were visualized and photographed by a UV transilluminator and BioDco-It imaging system (UVP Inc., Upland, CA). The particle sizes and ζ potentials of the polymer/pDNA complexes were measured using a Zetasizer Nano ZS (Malvern Instruments, Southborough, MA) and procedures similar to those described earlier.[6] The polymer/pDNA complexes were also observed with a field-emission scanning electron microscope equipped with a scanning transmission electron microscopy (STEM) detector (JEOL JSM-6700F) and procedures similar to those described earlier.[6] The complexes were visualized by transmitted electrons (STEM-in-SEM mode) at a low voltage of 15 kV, in comparison to about 200 kV for the conventional TEM. Such low voltage can minimize damage to the polymer/pDNA complex, and allow visualizing of the complex in the TEM mode at high spatial resolution.

2.5. Cell Viability and Transfection Assay. The cytotoxicity of the comb-like polymers was evaluated using the MTT assay in HEK293 and L929 cell lines. They were cultured in Dulbecco's modified eagle medium (DMEM), supplemented with 10% heat-inactivated fetal bovine serum (FBS), 100 units/mL of penicillin, and 100 μg/mL of streptomycin at 37 °C, under 5% CO_2, and 95% relative humidity atmosphere. The cells were seeded in a 96-well microtiter plate at a density of 10^4 cells/well and incubated in 100 μL of DMEM/well for 24 h. The culture media were replaced with fresh culture media containing serial dilutions of polymers, and the cells were incubated for 24 h. Then, 10 μL of sterile-filtered MTT stock solution in PBS (5 mg/mL) was added to each well, reaching a final MTT concentration of 0.5 mg/mL. After 5 h, the unreacted dye was removed by aspiration. The produced formazan crystals were dissolved in DMSO (100 μL/well). The absorbance was measured using a microplate reader (Spectra Plus, Tecan, Zurich, Switzerland) at a wavelength of 570 nm. The cell viability (%) relative to control cells cultured in media without polymers was calculated from $[A]_{test}/[A]_{control} \times 100\%$, where $[A]_{test}$ and $[A]_{control}$ are the absorbance values of the wells (with the polymers) and control wells (without the polymers), respectively. For each sample, the final absorbance was the average of those measured from six wells in parallel.

Transfection assays were performed first using plasmid pRL-CMV as the reporter gene in HEK293 and L929 cell lines in the presence of serum. In brief, the cells were seeded in 24-well plates

at a density of 5×10^4 cells in the 500 μL of medium/well and incubated for 24 h. The comb-shaped polymer/pDNA complexes (20 μL/well containing 1.0 μg of pDNA) at various N/P ratios from 7 to 22 were prepared by adding the polymer into the DNA solutions, followed by vortexing and incubation for 30 min at room temperature. At the time of transfection, the medium in each well was replaced with 300 μL of fresh normal medium (supplemented with 10% FBS). The complexes were added into the transfection medium and incubated with the cells for 4 h under standard incubator conditions. Then, the medium was replaced with 500 μL of the fresh normal medium (supplemented with 10% FBS). The cells were further incubated for an additional 20 h under the same conditions, resulting in a total transfection time of 24 h. The cultured cells were washed with PBS twice, and lysed in 100 μL of the cell culture lysis reagent (Promega Co., Cergy Pontoise, France) using the similar procedures as those described earlier.[6] Luciferase gene expression was quantified using a commercial kit (Promega Co., Cergy Pontoise, France) and a luminometer (Berthold Lumat LB 9507, Berthold Technologies GmbH. KG, Bad Wildbad, Germany). Protein concentration in the cell samples was analyzed using a bicinchoninic acid assay (Biorad Lab, Hercules, CA). Gene expression results were expressed as relative light units (RLUs) per milligram of cell protein lysate (RLU/mg protein).

DPD-mediated transfection was also assessed using the enhanced green fluorescent protein (EGFP) pDNA (BD Biosciences, San Jose, CA) as the reporter gene in human breast cancer MCF7 and human lung adenocarcinoma 973 cell lines, where the commercial Lipfectamine 2000 transfaction reagent was used as the control. The cancer cells were seeded in 24-well plates at a density of 1×10^5 cells in the 500 μL of RPMI 1640 medium(supplemented with 10% FBS)/well and incubated for 24 h before transfection. The transfection procedures are based on those provided by Lipofectamine 2000 protocol. Lipofectamine 2000 (or DPD at a specific N/P ratio)/pDNA complexes (100 μL/well containing 0.8 μg of pDNA) were formed by mixing equal volumes of polymer and pDNA solutions, followed by incubation for 20 min at room temperature. At the time of transfection, the complexes were added into the medium and incubated with the cells for 6 h under standard incubator conditions. Then, the medium was replaced with the fresh normal medium. The cells were further incubated until a total transfection time of 48 h under the same conditions. To visualize the expression of EGFP in the cancer cells, the evaluation of the EGFP expression was performed using a Leica DMIL Fluorescence Microscope. The percentage of the EGFP positive cells was determined using flow cytometry (FCM). FCM analysis was conducted using Epics Elite ESP (Beckman Coulter, USA). EGFP was excited at 488 nm and measured at 525 nm. EXPO 32 ADC software was used to analyze FCM data.

3. Results and Discussion

3.1. Synthesis and Characterization of Comb-Shaped Cationic Polymers Composed of Dextran Backbones and P(DMAEMA) Side Chains. In order to prepare comb-shaped copolymers using dextran as a backbone via ATRP, it is essential to introduce alkyl halide into dextran. In this work, the bromoisobutyryl-terminated dextran (Dextran−Br) multifunctional initiators were prepared via the direct reaction of hydroxyl groups of dextran (mol wt 6000 g/mol) with α-bromoisobutyric acid in the presence of 1,1′-carbonyldiimidazole (CDI) catalyst in DMSO solvent (Scheme 1). The carboxylic acids can be activated by CDI to produce the reactive acid imidazolide, which can be reacted with hydroxyl groups of polysaccharides without purification.[19−21]

The C 1s core-level XPS spectra of the pristine dextran and Dextran−Br are shown in Figure 1, parts a and b, respectively. The C 1s core-level spectrum of dextran can be curve-fitted by three peak components with binding energies (BE's) at about 284.6, 286.2, and 287.6 eV, attributable to the *C*−H/*C*−C, *C*−O, and O−*C*−O species, respectively.[6] The C 1s core-level spectrum of Dextran−Br can be curve-fitted by four peak components with BE's at about 284.6, 286.2, 287.6, and 288.4 eV, attributable to the *C*−H/*C*−C, *C*−O/*C*−Br, O−*C*−O, and *O*═*C*−O species, respectively.[6] The new O−*C*═O peak component is associated with the bromide-capped ester groups of Dextran−Br. The corresponding Br 3d core-level spectrum is shown in Figure 1b′. From the [Br]/[C] ratio of 0.019 (determined from the sensitivity factor-corrected Br 3d and C 1s core-level spectral area ratio), it was calculated that about 8 glucose units of Dextran−Br possess one ATRP initiation site. The chemical structure of Dextran−Br is also characterized by ^{1}H NMR spectroscopy in D_2O (Figure 2a). The broad chemical shifts in the wide region of 3.4−4.0 ppm are mainly associated with the inner methylidyne and methylene protons (***A***, *CH*−O and CH_2−O) on glucose units. The chemical shift associated with the unique methylidyne proton (O−*CH*−O) of glucose units is at about 4.9 ppm. The chemical shift at $\delta = 1.92$ ppm is associated with the methyl protons (***b***, C(Br)-CH_3) of the 2-bromoisobutyryl groups.[6] The area ratio of peak ***b*** and peak ***A*** indicated that very 8.7 glucose units of Dextran−Br possess one initiation site, fairly consistent with that determined by XPS. When ATRP is carried out from a multifunctional backbone with a high local concentration of initiation sites, the radical−radical coupling of the propagating chains will occur and result in a gel. In this work, the prepared Dextran−Br with such moderate initiation sites can avoid potential gelation during ATRP. In addition, the concentration of initiation sites can be controlled by adjusting the BIBA/dextran feed ratio.

Well-defined comb-shaped copolymers (DPDs) of dextran and P(DMAEMA), or Dextran-*g*-P(DMAEMA)s, were subsequently synthesized from Dextran−Br (Scheme 1, Table 1). The DPDs with different lengths of P(DMAEMA) side chains can be synthesized by varying the ATRP time. Table 1 summarizes the GPC results of DPD1 (from 5 h of ATRP) and DPD2 (from 12 h of ATRP). With the increase in reaction time from 5 to 12 h, the M_n of DPD from GPC using linear dextran standards increases from 1.49×10^4 to 3.42×10^4 g/mol, and the total number of DMAEMA repeat units per side chain increases accordingly from 12 to 35, based on the assumption of one initiation site out of every 8 glucose units of Dextran−Br (Table 1). This value is lower than those determined by XPS and 1H NMR (Table 1), probably due to the differences in hydrodynamic volumes between comb-like DPDs and dextran standards. The C 1s core-level spectra of DPDs (Figure 1, parts c and d) can be curve-fitted into five peak components with BE's at about 284.6, 285.5, 286.2, 287.6, and 288.4 eV, attributable to the *C*−H/*C*−C, *C*−N, *C*−O, O−*C*−O, and *O*═*C*−O species, respectively. The *C*−N peak is associated with the P(DMAEMA) side chains. In comparison with the C 1s core-level spectrum (Figure 1b) of Dextran−Br, the increase (and decrease) in intensities of the *C*−N (and *C*−O) species is consistent with the presence of P(DMAEMA). The corresponding N 1s core-level spectra of DPDs are shown in Figure 1, parts c′ and d′. From the [N]/[C] ratios determined by XPS, the number of DMAEMA repeat units per side chain can be calculated (Table 1).

In order to increase the surface cationic charges, the P(DMAEMA) side chains of DPD2 was partially quaternized to produce the Dextran-*g*-QP(DMAEMA)2 (QDPD2) with quaternary ammonium groups. In this work, the QDPD2−1 and QDPD2−2 with different quaternization contents were prepared from DPD2 and 1-bromohexane (Scheme 1 and Table 1). After quaternization, the C 1s core-level spectra of QDPDs (Figure 1, parts e and 1f) can be curve-fitted into five peak components with BE's at about

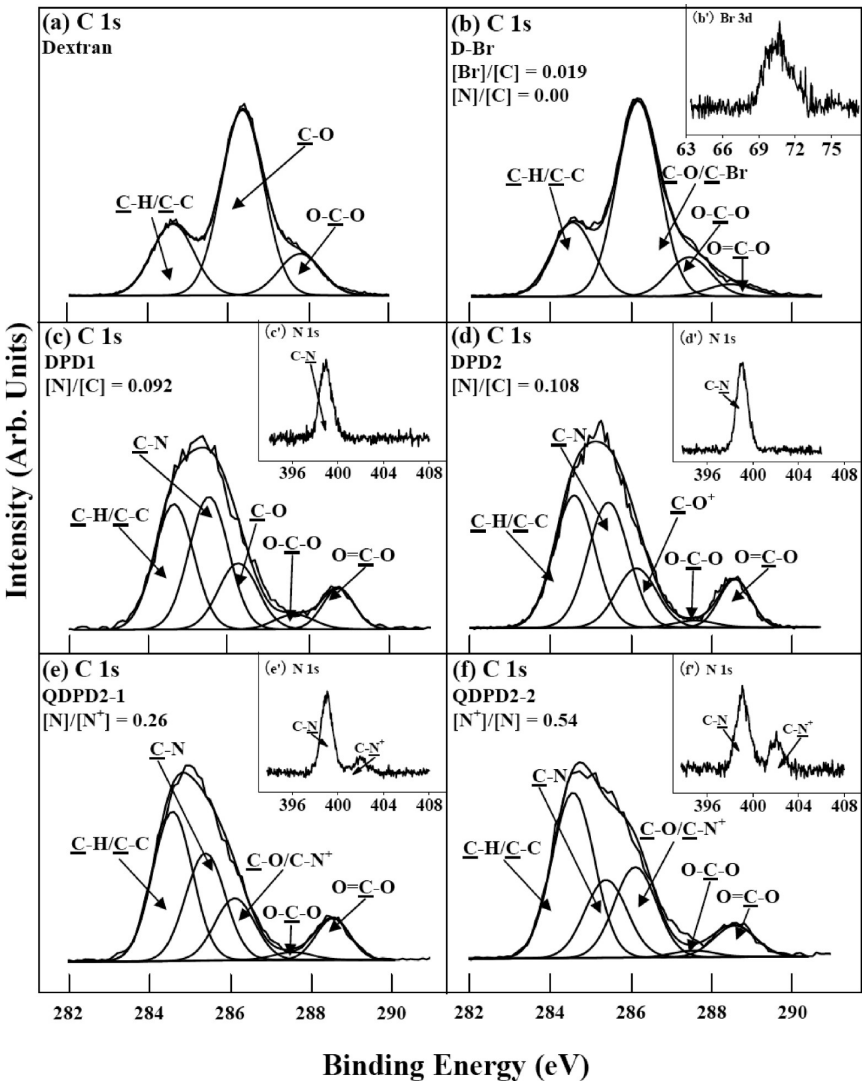


Figure 1. XPS C 1s core-level spectra of (a) Dextran, (b) Dextran−Br, (c) DPD1, (d) DPD2, (e) QDPD2−1, and (f) QDPD2−2, Br 3d core-level spectrum of (b′) Dextran−Br, and N 1s core-level spectra of (c′) DPD1, (d′) DPD2, (e′) QDPD2−1, and (f′) QDPD2−2.

284.6, 285.5, 286.2, 287.6, and 288.4 eV, attributable to the *C*−H/*C*−C, *C*−N, *C*−O/*C*−N^+, O−*C*−O, and *O*═*C*−O species, respectively. In comparison with the C 1s core-level spectrum (Figure 1d) of the starting DPD2, the decrease (and increase) in intensities of the *C*−N (and *C*−O/*C*−N^+) species of QDPDs indicates that the P(DMAEMA) side chains have been successfully quaternized by 1-bromhexane. In comparison with the monopeak component of the N 1s core-level spectrum (Figure 1d′) of DPD2, the N 1s core-level spectra (Figures 1(e′) and 1(f′)) of QDPDs can be curve-fitted into two peak components with BE's at about 399 and 402 eV, attributable to the amino (C−*N*) and positively charged nitrogen (C−N^+) species, respectively. The quaternization extent of P(DMAEMA) side chains can be expressed as the $[N^+]/([N] + [N^+])$ ratio (determined from the corresponding N^+ peak component and total nitrogen spectral area ratio). The average $[N^+]/([N]+[N^+])$ ratios for QDPD2−1 and QDPD2−2 are about 0.21 and 0.35, respectively (Table 1), indicating that about one out of every 4.8 (for QDPD2−1) or 2.9 (for QDPD2−2) DMAEMA repeat units had been quaternized.

Parts b and c of Figure 2 show the respective ^{1}H NMR spectra of DPD2 and QDPDs in D_2O. The typical chemical shifts at about 0.89, 1.83, 2.28, and 2.67 ppm are mainly attributable to the (*c*′) C−CH_3 methyl, (*d*′) C−CH_2 methylene, (*c*) N−CH_3 methyl, and (*d*) N−CH_2 methylene protons of the P(DMAEMA) side chains, respectively. The chemical shift (at δ = 4.12 ppm) associated with the methylene protons adjacent to the oxygen moieties of the ester linkages (*a*′, CH_2−O−C═O) overlapped completely with glucose peaks of dextran. The signal intensities associated with the dextran backbone (*A*) have decreased substantially. From the area ratio of peaks *d*, *d*′, *c* and peaks *A*, *a*′, the number of DMAEMA repeat units per side chain can be estimated (Table 1). After quaternization, the new signals at about 3.17 and 3.42 ppm are attributable to the (*c*‴) N^+−CH_3 methyl and (*d*‴) N^+−CH_2 methylene protons of the quaternized P(DMAEMA) side chains, respectively.[22] The chemical shift at about 1.36 ppm corresponds to the methylene protons of hexane (*d*″, CH_2−C). For QDPD2−1 and QDPD2−2, the signal intensities associated with the quaternized P(DMAEMA) units (*c*‴, *d*″, *d*‴) increased, which is consistent with their corresponding increase in quanternization extent. Because of the serious overlaps in the characteristic shifts of the components, it is very difficult to quantify the P(DMAEMA) and QP(DMAEMA) segments by ^{1}H NMR.

3.2. Polymer/pDNA Complexes. The DNA condensation capability is a prerequisite for polymeric gene vectors. In this

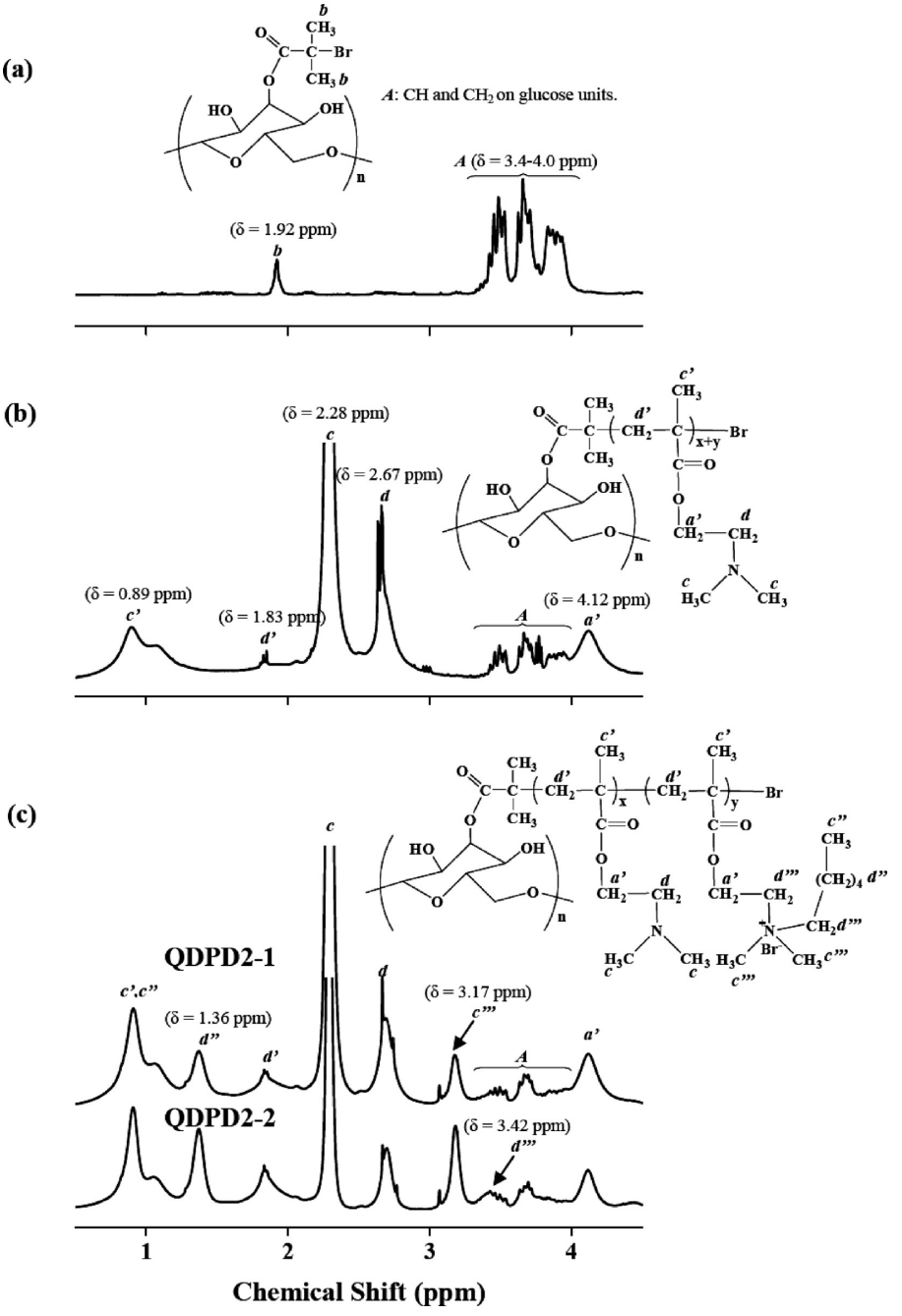


Figure 2. 300 MHz ^{1}H NMR spectra of the (a) Dextran−Br, (b) DPD2, and (c) QDPDs polymers in D_2O.

Table 1. Characterization of the Comb-Shaped Cationic Polymers

sample		reaction time (h)	M_n (g/mol)[c]	polydispersity index (PDI)[c]	[N]/[C][d]	$[N^+]/([N]+[N^+])$[d]	DMAEMA repeat units per side chain
Dextran-*g*-P(DMAEMA)1 or DPD1[a]		5	1.49×10^4	1.4	0.092		13[c] or 17[d] or 20[e]
Dextran-*g*-P(DMAEMA)2 or DPD2[a]		12	3.02×10^4	1.6	0.108		35[c] or 40[d] or 42[e]
Dextran-*g*-QP(DMAEMA)2−1 QDPD2−1[b]	or	24				0.21	
Dextran-*g*-QP(DMAEMA)2−2 QDPD2−2[b]	or	24				0.35	

[a] Synthesized using a molar feed ratio [DMAEMA (3 mL)]:[CuBr]:[HMTETA] of 60:1:1:1.2 at room temperature in 8 mL of methanol/water (3/5, v/v) containing 0.4 g of Dextran−Br ($M_n = 5.7 \times 10^3$ g/mol and PDI = 1.2). About 8 glucose units of Dextran−Br possess one initiation site. [b] Synthesized at 50 °C in 6 mL of THF containing 0.25 g of DPD2 and 0.5 mL (for QDPD2−1) or 1.0 mL (for QDPD2−2) of 1-bromohexane. [c] Determined from GPC results. PDI = weight-average molecular weight/number-average molecular weight, or M_w/M_n. [d] Determined from XPS. [e] Determined from the ^{1}H NMR spectroscopy data.

work, the ability of the comb-shaped cationic copolymers to condense plasmid DNA (pDNA) into particulate structures was confirmed by agarose gel electrophoresis, particle size and ζ potential measurements, as well as STEM imaging. The formation of the copolymer/pDNA complexes was first analyzed by their electrophoretic mobility on an agarose gel

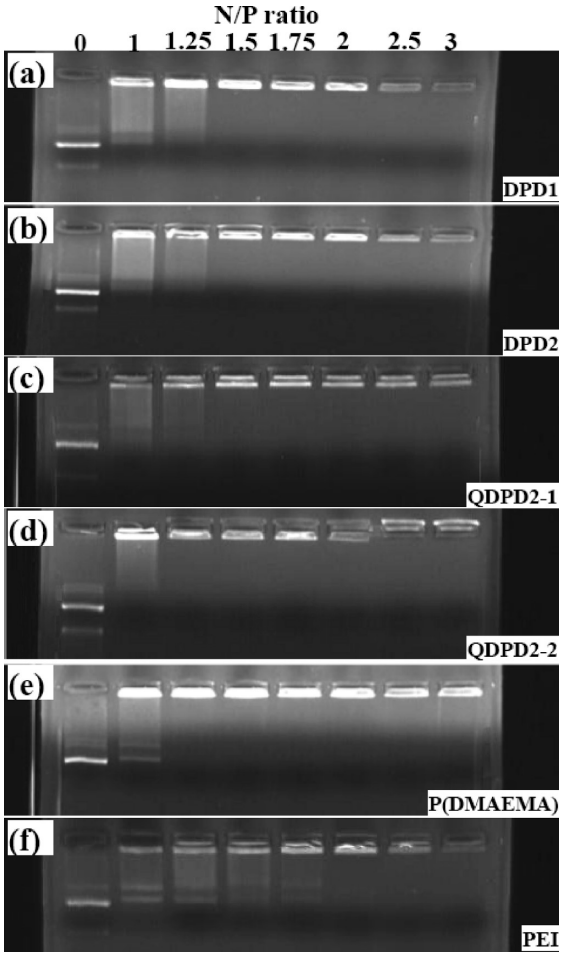


Figure 3. Electrophoretic mobility of plasmid DNA (pDNA) in the complexes of the cationic polymers ((a) DPD1, (b) DPD2, (c) QDPD2−1, (d) QDPD2−2, (e) P(DMAEMA), and (f) PEI at various N/P ratios.

at various N/P ratios. Figure 3 shows the gel retardation results of the cationic comb copolymer (DPD1, DPD2, QDPD2−1, and QDPD2−2)/pDNA complexes with increasing nitrogen (N)/phosphate (P) (or N/P) ratios, in comparison with those of the P(DMAEMA) homepolymer (with about 180 DMAEMA repeat units)/pDNA and branched PEI (25 kDa)/pDNA complexes. All the DPDs and QDPDs can compact pDNA completely within the N/P ratio of 1.5. DPD2, QDPD2−1, and QDPD2−2 show increasing capability to condense pDNA, indicating that the increased cationic charges from quaternization could enhance the condensation capability. The control P(DMAEMA) and PEI could inhibit the migration of pDNA at N/P ratios of 1.25 and 2.0, respectively. QDPD2−2 exhibits similar condensation capability to that of the P(DMAEMA) homopolymer.

The (a) particle size and (b) ζ potential of the cationic polymer (DPD1, DPD2, QDPD2−1, and QDPD2−2)/pDNA complexes are compared to those of the P(DMAEMA)/pDNA and PEI/pDNA complexes at various N/P ratios in Figure 4. Particle size is a crucial factor for determining the rate of cellular uptake of polymer/DNA complexes. All the cationic comb copolymers can efficiently compact pDNA into small particles. Generally, the hydrodynamic sizes of the complexes decrease with increasing N/P ratios. After reaching the N/P ratio of 5, all the comb copolymers, similar to the control P(DMAEMA) and PEI, can condense pDNA into nanoparticles of 100 to 150 nm in diameters. The polymer/pDNA complex within this size range can readily undergo endocytosis.[23] ζ potential, an indicator of

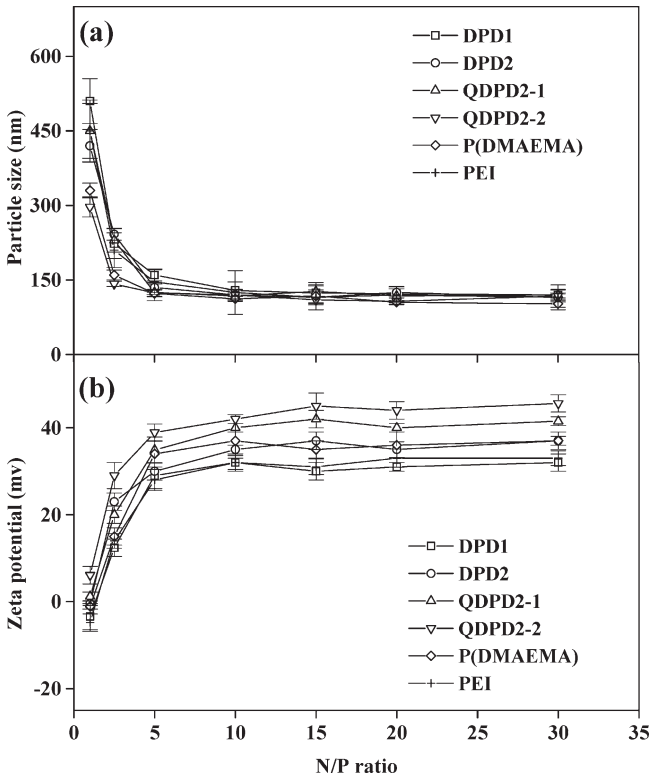


Figure 4. Particle size (a) and ζ potential (b) of the complexes between the cationic polymers (DPD1, DPD2, QDPD2−1, QDPD2−2, P(DMAMEA), and PEI) and pDNA at various N/P ratios.

surface charges on the polymer/pDNA nanoparticles, is another important factor affecting cellular uptake of the complexes. A positively charged surface allows electrostatic interaction with negatively charged cell surfaces and facilitates cellular uptake. For the pDNA complexes of DPD1, DPD2, QDPD2−1, QDPD2−2, P(DMAEMA), and PEI, the net surface charge increases dramatically as the N/P ratio increases from 1 to 5, and stabilizes at N/P ratios of 10 and above (Figure 4b). After reaching the N/P ratio of 10, the ζ potentials of the pDNA complexes of all the cationic polymers are strongly positive. Because of the increasing quaternization of the P(DMAEMA) side chains, the pDNA complexes of DPD2, QDPD2−1, and QDPD2−2 show increasing surface cationic charges, indicating that they will produce increasing affinity for anionic cell surfaces. In addition, the excess cationic polymers probably do not exert any significant effects on the particle size and ζ potential of the complexes (Figure 4).

Figure 5 shows the representative STEM images of the (a) DPD2/pDNA (at a N/P ratio of 1), (b) DPD2/pDNA (at a N/P ratio of 15), and (c) QDPD2−1/pDNA (at a N/P ratio of 15) complexes. The images clearly reveal the morphological difference between the polymer/pDNA complexes at different N/P ratios. For the DPD/pDNA complex at a ratio of 1, loose large aggregates, supercoiled plasmid pDNA, and compact nanoparticles (< 30 nm) are observed at the same time, indicating that pDNA has been partially condensed. In comparison to the partial condensation at low N/P ratio of 1, the same amount of pDNA could be packed tightly and condensed completely into polymer/DNA complexes at a N/P ratio of 15. The compacted complexes of pDNA with DPD2 and QDPD2−1 display a characteristic globular morphology and exist in the form of spherical nanoparticles (< 150 nm in size).

3.3. Cell Viability Assay. Cytotoxicity is one of the most important factors to be considered in selecting polymeric gene carriers. Figure 6 shows the *in vitro* MTT assay results

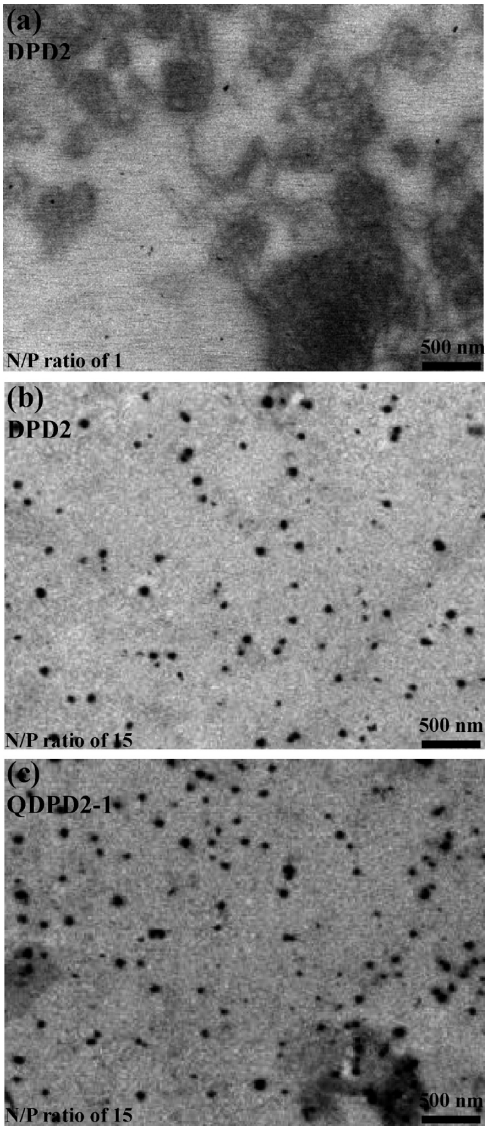


Figure 5. STEM images of the (a) DPD2/pDNA (at a ratio of 1), (b) DPD2/pDNA (at a ratio of 15), and (c) QDPD2−1/pDNA (at a ratio of 15) complexes.

of cytotoxicity of DPD1, QDPD2, QDPD2−1, QDPD2−2, P(DMAEMA), and PEI in (a) HEK293 and (b) L929 cells. All of the cationic polymers exhibit a dose-dependent cytotoxicity effect. Nevertheless, DPD exhibit lower toxicity than P(DMAEMA) and PEI (the controls). The slopes of the dose-dependent cytotoxicity curves for P(DMAEMA) and PEI are much steeper than that for DPDs. A high concentration of amino groups is always considered an important factor leading to high cytotoxicity. The introduction of the biocompatible dextran backbones not only results in a lower relative concentration of amino groups, but has also imparted biocompatible characteristics to the cationic carriers. As discussed above, the quaternization of the P(DMAEMA) side chains could enhance the surface cationic charges and DNA-condensing ability, but QDPD2−1 and QDPD2−2 exhibit increasing toxicity, indicating the introduced quaternary ammonium groups can increase the cytotoxicity.[14] The above results are also supported by the calculated median inhibitory concentration (IC_{50}).[23] The IC_{50} values of P(DMAEMA) and PEI are less than 35 μg/mL, in comparison with those of DPD1 (102 μg/mL) and DPD2 (91 μg/mL). After quaternization, the IC_{50} values of QDPD2−1 and QDPD2−2 are 63 and

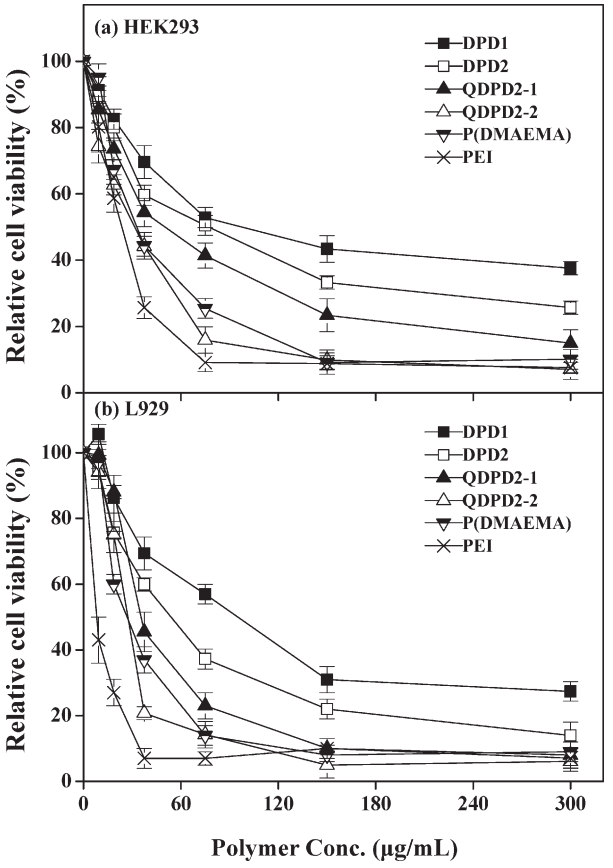


Figure 6. Cell viability assay in (a) HEK293 and (b) L929 cells with various concentrations of DPD1, DPD2, QDPD2−1, QDPD2−2, P(DMAEMA), and PEI. Cell viability was determined by the MTT assay and expressed as a percentage of the control cell culture. Error bars represent the standard deviation of six measurements.

32 μg/mL, respectively. A similar trend was also observed in L929 cells.

3.4. *In vitro* Gene Transfection Assay Using Luciferase Expression. The *in vitro* gene transfection efficiency of the cationic polymers/pDNA complexes was first assessed using luciferase as a gene reporter. Figure 7 shows the gene transfection efficiency of DPD1, DPD2, QDPD2−1, and QDPD2−2 in comparison with those of P(DMAEMA) and PEI at N/P ratios from 7 to 22 in 10% serum culture of (a) HEK293 and (b) L929 cells. In the present work, the optimal N/P ratios in the HEK293 (or L929) cell lines for DPD1, DPD2, QDPD2−1, QDPD2−2, P(DMAEMA), and PEI are 16 (or 16), 16 (or 13), 10 (or 10), 7 (or 10), 16 (or 10), and 10 (or 16), respectively. DPD2, QDPD2−1, and QDPD2−2 exhibit decreasing optimal N/P ratio at both cases, consistent with their increasing DNA condensation capability arising from introduced quaternary ammonium groups (Figures 3 and 4). In both cell lines, the transfection efficiency generally first increases at lower N/P ratios and then decreases with the increase in N/P ratios. At lower N/P ratios, pDNA cannot be condensed efficiently by the polymers, and the resultant loose polymer/pDNA complex cannot enter the cell easily. At higher N/P ratios, the transfection formulation contain also free polymer, besides the compact and positively charged polymer/pDNA complexes. Because of the presence of an increasing amount of free cationic polymers with the increase in N/P ratios, the increasing cytotoxicity may result in a reduction in the transfection efficiency.

As shown in Figure 7, the transfection efficiency mediated by DPD1 is lower than that mediated by DPD2 at various N/P ratios. This observation indicates that the transfection efficiency

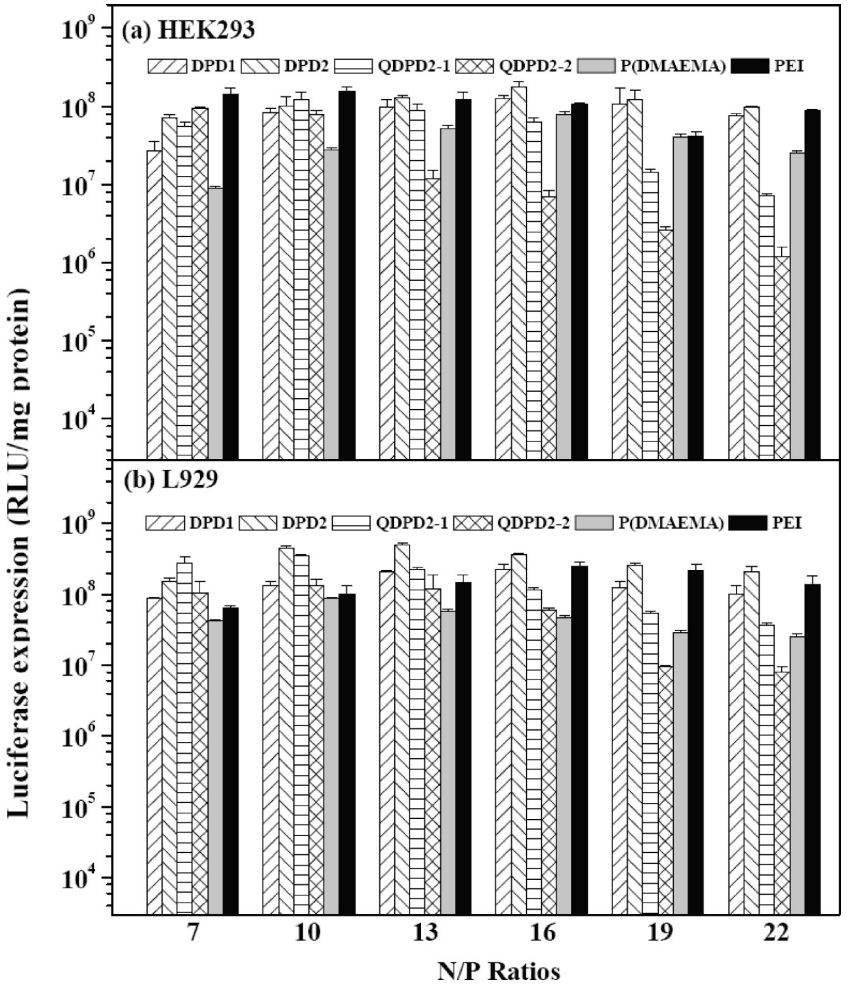


Figure 7. *In vitro* luciferase expression of the cationic polymers (DPD1, DPD2, QDPD2−1, QDPD2−2, P(DMAEMA), and PEI)/pDNA complexes at various N/P ratios in (a) HEK293 and (b) L929 cells. Error bars represent the standard deviation of three measurements.

for DPDs is dependent on the side lengths of P(DMAEMA). The long P(DMAEMA) side chains can increase the binding ability and complex stability, probably leading to a much higher transfection efficiency. The transfection efficiency mediated by DPDs is higher than that mediated by the control P(DMAEMA) homopolymer. The averaged number of DMAEMA repeat units per side chain of DPDs (Table 1) is much lower than that (about 180) of the P(DMAEMA) homopolymer, indicating that the high-molecular-weight comb copolymers composed of biocompatible dextran backbones and low-molecular-weight P(DMAEMA) side chains can enhance gene transfection efficiency. One possible reason is that such unique architectures could enhance the interaction of the cationic P(DMAEMA) with pDNA or cellular membranes. It should be noted that the transfection efficiency mediated by DPD2 is comparable to (in HEK293 cell lines, Figure 7a) or better than (in L929 cell lines, Figure 7b) that of "gold-standard" PEI (25 kDa) at most N/P ratios. In our work reported earlier, the hydroxypropyl cellulose-*graft*-P(DMAEAM) comb carriers also can exhibit good transfection efficiency comparbale to that of "gold-standard" PEI (25 kDa) in HEK 293 cell lines.[16] However, the comparative anlaylsis revealed that the transfection efficiency mediated by the hydroxypropyl cellulose-*graft*-P(DMAEAM) comb carriers (denoted as HPDs) is substantially lower than that of the control PEI (25 kDa) in L929 cell lines, indicating that dextran is a better natural biopolymer backbone for the design of the novel comb-shaped gene vectors. In comparison with HPDs, DPDs possess highly water-soluble polysaccharide backbones, which may benefit the transfection efficiency.

Because of increased surface cationic charges, QDPD2−1 and QDPD2−2 were expected to strongly complex pDNA and result in higher transfection yields than DPD2. However, their corresponding transfection efficiency decreased substantially, with the increasing cationic charges (Figure 7). This observation indicates that quaternary ammonium groups caused the loss of the transfection activity, probably due to the increased cytotoxicity[14] (see above) and weakened buffering capacity of polymer/DNA complexes. This observation was also consistent with the quaternized hydroxypropyl cellulose-*graft*-P(DMAEAM) comb carriers.[16] After cellular entry, the polymer/plasmid complexes are transported into the lysome. The cationic polymers should retain substantial buffering capacity over a wide range of pHs, not only to protect the DNA from degradation inside the lysosome, but is thought to also lead to lysosomal swelling and rupture via protonization. The latter process in turn provides an escape mechanism for DNA particles into the cytoplasm.[24,25] Quaternization of DMAEMA units may weak the buffering capacity of P(DMAEMA) inside the lysosome, which prevented the subsequent release of pDNA and caused some loss of the transfection activity.

3.5. *In Vitro* DPD-Mediated EGFP Expression. The good transfection efficiency of DPD2 in above HEK293 and L929 cells urged us to further investigate the DPD2-mediated transfection ability in cancer cells. In order to directly visualize the

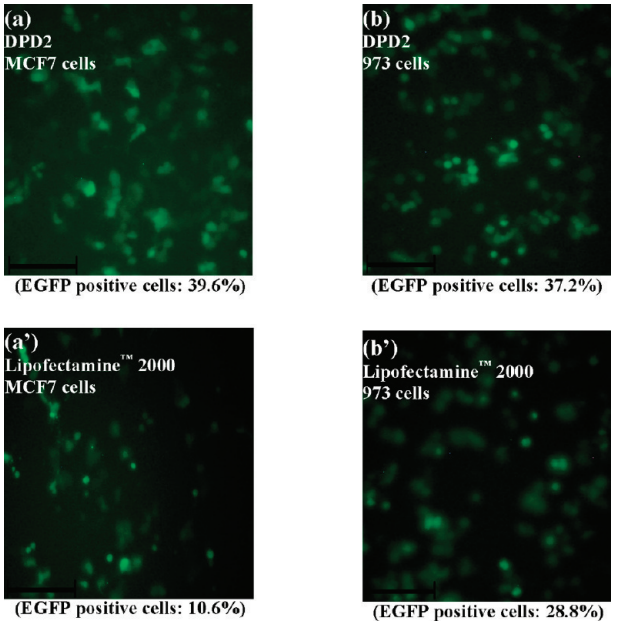


Figure 8. Representative photos of DPD2-mediated (N/P ratio = 13, a, b) and Lipfectamine 2000-mediated (a′, b′) EGFP expression *in vitro* in (a, a′) breast cancer MCF7 and (b, b′) lung adenocarcinoma 973 cells, where the percentage of the EGFP positive cells was determined using flow cytometry. Figure scale bar = 100 μm.

transfected cells, the enhanced green fluorescent protein (EGFP) expression analysis was used to evaluate the transfection efficiency in cancer cells. Using the transfection procedures of Lipofectamine 2000 protocol, the breast cancer MCF7 and lung adenocarcinoma 973 cells were transfected *in vitro* with DPD2/pEGFP (at a N/P ratio of 13) and Lipfectamine 2000/pEGFP complexes. Figure 8 shows the representative photos of DPD2-mediated and Lipfectamine 2000-mediated EGFP expression, which were taken at 48 h after transfection. The transfection efficiency, as reflected by the percentage of the EGFP positive cells, was qualitatively determined using flow cytometry. The percentages of DPD2-mediated (or Lipfectamine 2000-mediated) EGFP positive cells were around 39.6% (or 10.6%) in MCF7 cells and 37.2% (or 28.8%) in 973 cells, respectively. Especially, it should be noted that the transfection ability of DPD2 in MCF7 cells is almost 3 times higher than that of the expensive popular Lipfectamine 2000 transfection reagent. The above results indicated that DPD2 can possess good potentials as the efficient gene delivery agent for cancer gene therapy.

4. Conclusions

ATRP has been successfully used to prepare well-defined comb-shaped copolymers (DPDs) consisting of biocompatible dextran backbones and P(DMAEMA) side chains for nonviral gene delivery. The P(DMAEMA) side chains can be further partially quaternized to produce the QDPDs with quaternary ammonium groups. DPDs and QDPDs as gene carriers can effectively bind pDNA to form nanoparticle complexes of 100 to 150 nm in sizes. DPDs exhibit much lower cytotoxicity and better gene transfection efficiency than P(DMAEMA) and PEI (25 kDa) in HEK293 and L929 cell lines. The partial quaternization of QDPDs can increase condensation ability to pDNA, but will cause some loss of the transfection activity. In addition, DPD2 also possesses good transfection ability in cancer cell lines, especially in MCF7 cells where the DPD2-mediated transfection capacity is almost 3 times higher than that of the popular Lipfectamine 2000 transfection reagent. With the versatility of ATRP, properly grafting a-low-molecular-weight side chains from a natural backbone is an effective means for designing novel polysaccharide-based nanobiomaterials.

Acknowledgment. This work was supported by National Natural Science Foundation of China (grant no. 21074007), Research Fund for the Doctoral Program of Higher Education of China (project no. 20090010120007), Program for New Century Excellent Talents in University (NCET-10-0203), and Fundamental Research Funds for the Central Universities (ZZ0904).

References and Notes

(1) De Smedt, S. C.; Demeester, J.; Hennink, W. E. *Pharm. Res.* **2000**, *17*, 113–126.
(2) Yudovin-Farber, I.; Domb, A. J. *Mater. Sci. Eng., C* **2007**, *27*, 595–598.
(3) Dai, F.; Sun, P.; Liu, Y.; Liu, W. G. *Biomaterials* **2010**, *31*, 559–569.
(4) Jiang, X.; Lok, M. C.; Hennink, W. E. *Bioconjug. Chem.* **2007**, *18*, 2077–2084.
(5) Bisht, H. S.; Manickam, D. S.; You, Y.; Oupicky, D. *Biomacromolecules* **2006**, *7*, 1169–1178.
(6) Xu, F. J.; Li, H. Z.; Li, J.; Zhang, Z. X.; Kang, E. T.; Neoh, K. G. *Biomaterials* **2008**, *29*, 3023–3033.
(7) Agarwal, A.; Unfer, R.; Mallapragada, S. K. *J. Controlled Release* **2005**, *103*, 245–258.
(8) Dimitrova, M.; Arntz, Y.; Lavalle, P.; Meyer, F.; Wolf, M.; Schuster, C.; Haïkel, Y.; Voegel, J. C.; Ogier, J. *Adv. Funct. Mater.* **2007**, *17*, 233–245.
(9) Kukowska-Latallo, J. F.; Bielinska, A. U.; Johnson, J.; Spindler, R.; Tomalia, D. A.; Baker, J. R., Jr *Proc. Natl. Acad. Sci. U.S.A.* **1996**, *93*, 4897–4902.
(10) Thanou, M.; Florea, B. I.; Geldof, M.; Junginger, H. E.; Borchard, G. *Biomaterials* **2002**, *23*, 153–159.
(11) Gonzalez, H.; Hwang, S. J.; Davis, M. E. *Bioconjugate Chem.* **1999**, *10*, 1068–1074.
(12) Azzam, T.; Eliyahu, H.; Shapira, L.; Linial, M.; Barenholz, Y.; Domb, A. J. *J. Med. Chem.* **2002**, *45*, 1817–1824.
(13) Azzam, T.; Raskin, A.; Makovitzki, A.; Henry, B.; Vierling, P.; Lineal, M.; Domb, A. J. *Macromolecules* **2002**, *35*, 9947–9953.
(14) Yudovin-Farber, I.; Yanay, C.; Azzam, T.; Linial, M.; Domb, A. J. *Bioconjug. Chem.* **2005**, *16*, 1196–1203.
(15) Ping, Y.; Liu, C. D.; Tang, G. P.; Li, J. S.; Li, J.; Yang, W. T.; Xu, F. J. *Adv. Funct. Mater.* **2010**, *20*, 3106–3116.
(16) Xu, F. J.; Ping, Y.; Ma, J.; Tang, G. P.; Yang, W. T.; Li, J.; Kang, E. T.; Neoh, K. G. *Bioconjugate Chem.* **2009**, *20*, 1449–1458.
(17) Bontempo, D.; Leonardis, P. D.; Mannina, L.; Capitani, D.; Crescenzi, V. *Biomacromolecules* **2006**, *7*, 2154–2161.
(18) Dupayage, L.; Save, M.; Dellacherie, E.; Nouvel, C.; Six, J. L. *J. Polym. Sci., Part A: Polym. Chem.* **2008**, *46*, 7606–7620.
(19) Liebert, T.; Heinze, T. *Biomacromolecules* **2005**, *6*, 333–340.
(20) Hornig, S.; Liebert, T.; Heinze, T. *Polym. Bull.* **2007**, *59*, 65–71.
(21) Rannard, S. P.; Rogers, S. H.; Hunter, R. *Chem. Commun.* **2007**, 362–364.
(22) Ma, Y.; Tang, Y.; Billingham, N. C.; Armes, S. P.; Lewis, A. L.; Lloyd, A. W.; Salvage, J. P. *Macromolecules* **2003**, *36*, 3475–3484.
(23) Wetering, P. V. D.; Moret, E. E.; Nieuwenbroek, N. M. E.; Steenbergen, M. J. V.; Hennink, W. E. *Bioconjug. Chem.* **1999**, *10*, 589–597.
(24) Tang, M. X.; Szoka, F. C. *Gene Ther.* **1997**, *4*, 823–832.
(25) Ferrari, S.; Moro, E.; Pettenazzo, A.; Behr, J. P.; Zacchello, F.; Scarpa, M. *Gene Ther.* **1997**, *4*, 1100–1106.

240 *Macromolecules* **2011**, *44*, 240–247
DOI: 10.1021/ma102313q

Macromolecules
ARTICLE

Synthesis of Cyclic (Co)polymers by Atom Transfer Radical Cross-Coupling and Ring Expansion by Nitroxide-Mediated Polymerization

Renaud Nicolaÿ and Krzysztof Matyjaszewski*

Center for Macromolecular Engineering, Department of Chemistry, Carnegie Mellon University, 4400 Fifth Avenue, Pittsburgh, Pennsylvania 15213, United States

Received October 8, 2010; Revised Manuscript Received November 25, 2010

ABSTRACT: A novel approach to prepare cyclic polymers via a combination of atom transfer radical polymerization (ATRP) and atom transfer radical cross-coupling (ATRC) is presented. A functional ATRP initiator possessing an alkoxyamine group was synthesized and used to prepare well-defined linear telechelic α-nitroxy,ω-bromo homo- and block copolymers via ATRP and subsequent thermal deprotection of the α-terminal nitroxide function. Cyclization reactions were achieved by intramolecular ATRC under high dilution. Ring expansion of a cyclic polystyrene alkoxyamine prepared by ATRC was conducted via nitroxide-mediated polymerization (NMP) of styrene and yielded a mixture of linear and cyclic polycondensates. This result is discussed in detail and explained by the persistent radical effect (PRE), thermal initiation, and the occurrence of radical crossover reactions during chain extension via NMP.

Introduction

Cyclic polymers are fascinating materials for physicists and theoreticians.[1,2] The absence of chain-ends imposes a topological restriction that results in a variety of physical properties that significantly distinguish macrocycles from their linear counterparts. For example, it has been shown that cyclic polymers have smaller hydrodynamic volumes and are less viscous than their linear analogues.[1,2] In addition, rheological studies of cyclic polymers, which cannot reptate in the conventional sense, due to a lack of chain-ends, could help improving the current understanding of the fundamentals of polymer chain dynamics.[3−5]

However, the synthesis of well-defined cyclic polymers is still a challenge in polymer science.[1,2] Cyclic polymers can be obtained in several different ways. Macrocycles can be directly recovered, as a more or less important fraction, in polymer systems exposed to ring−chain equilibria, or they can be synthesized using either ring expansion or ring closure of linear chains by end-to-end coupling.

Only few reports describe the formation of large rings by direct insertion of a monomer into a reactive cyclic precursor.[2] Although very attractive, this approach requires use of polymerization processes in which chain transfer and exchange reactions between active species are absent. One of the most striking examples of macrocycles synthesis by monomer insertion is the ring expansion of a cyclic carbene ruthenium complex by ring-opening metathesis polymerization (ROMP).[6−8]

The simplest and most appropriate methods for the synthesis of cyclic polymers, with controlled size and narrow molecular weight distribution (MWD), are based on the end-to-end chain coupling of α,ω-hetero-difunctional linear chains in highly dilute reaction conditions.[2] This approach offers several significant advantages over other approaches as it may be used both for polymers having in-chain reactive functions and for systems with no labile linkages in their backbone, such as saturated carbon−carbon bonds polymers. Since the macrocycle is directly obtained from the linear parent by ring closing, and the size of linking unit is negligible, this approach provides linear and cyclic structures with same molar mass. Moreover, the use of living polymerization techniques for the preparation of the linear precursors allows control of the molecular weight with narrow MWD. This is of special importance for direct comparison of the properties of materials consisting of linear or cyclic chains.

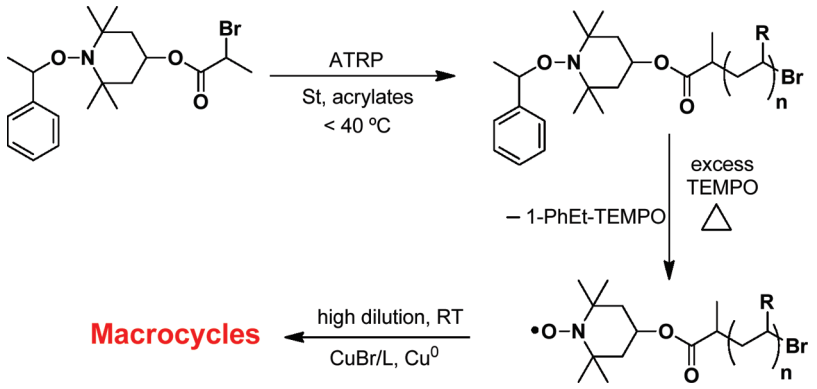
Such an approach has been applied to controlled radical polymerization (CRP).[9] A strategy to prepare macrocycles via the combination of atom transfer radical polymerization (ATRP)[10−13] and click chemistry[14−16] was recently reported.[17] Linear PSt precursors were prepared by ATRP of St, using propargyl 2-bromoisobutyrate, as an initiator, followed by nucleophilic substitution of the terminal bromine atom by an azido group.[18] The cyclization reaction was conducted under high dilution conditions, with Cu^{I}/L complexes as catalyst. The functionalization and the cyclization were essentially quantitative, eliminating the need for purification. This approach was subsequently extended to the synthesis of cyclic poly(*N*-isopropylacrylamide)[19] (PNIPAM) and cyclic poly(methyl acrylate)-*b*-polystyrene (PMA-*b*-PSt) block copolymers.[20] However, in the latter case, the alkyne moiety of the ATRP initiator had to be protected with a trimethylsilyl group, which added an additional deprotection step to the synthesis. Recently, reversible addition−fragmentation chain transfer (RAFT) polymerization[21,22] and nitroxide-mediated radical polymerization (NMP)[23,24] were also combined with Huisgen 1,3-dipolar cycloaddition reaction to prepare cyclic PNIPAM[25] and PSt.[26−28]

Click reactions are perfectly suited for the preparation of cyclic polymers, due to the near-quantitative yields and high selectivity, even in the presence of other functional groups. However, the synthesis of cyclic polymers via a combination of CRP and azide−alkyne click coupling always requires one or two post-polymerization functionalization steps in order to introduce the reactive chain-end groups. Therefore, the search for a synthetic route that would lead to well-defined cyclic polymers in high

*Corresponding author: Tel +1-412-268-3209; e-mail km3b@andrew.cmu.edu.

 Published on Web 12/23/2010 © 2010 American Chemical Society

Scheme 1. Synthesis of Cyclic Polymers via a Combination of ATRP and ATRC



yields, without postpolymerization functionalization, or with a single, simple, deprotection step before the cyclization, is still ongoing.

In the present work, we introduce a novel approach to prepare cyclic polymers via a combination of ATRP and atom transfer radical cross-coupling (ATRC)[29,30] (Scheme 1). Linear telechelic α-nitroxy-ω-bromo precursors were prepared via ATRP at relatively low temperature, using an initiator bearing an alkoxyamine group, followed by thermal deprotection of the nitroxide function. Cyclization reactions were subsequently achieved by intramolecular ATRC, under high dilution conditions. Well-defined cyclic PMA, PSt, and cyclic PMA-*b*-PSt block copolymer were prepared using this approach.

Experimental Section

Materials. Methyl acrylate (MA, 99%) and styrene (St, 99%) were purchased from Aldrich and purified by passing through a column filled with basic alumina to remove inhibitors or antioxidants. Dichloromethane was distilled from calcium hydride. 4-Hydroxy-TEMPO was received from NOVA Molecular Technologies Inc. Tris(2-pyridylmethyl)amine (TPMA) was purchased from ATRP Solutions. All other reagents, including (1-bromoethyl)benzene, 2-bromopropionyl bromide, Cu^0 powder (75 μm), CuBr, $CuBr_2$, *N,N,N′,N″,N″*-pentamethyldiethylenetriamine (PMDETA), pyridine, and 2,2,6,6-tetramethylpiperidine 1-oxyl (TEMPO), and solvents were purchased from Aldrich with the highest purity available and used as received without further purification.

Analyses. NMR spectra were recorded on a Bruker instrument operating at 300 MHz. Monomer conversions were determined by ^{1}H NMR. MW and MWD were determined by size exclusion chromatography (SEC). The SEC analysis was conducted with a Waters 515 pump and Waters 410 differential refractometer using Polymer Standards Services (PSS) columns (Styrogel 10^5, 10^3, and 10^2 Å) in THF as eluent at 35 °C and at a flow rate of 1 mL/min. The apparent MW ($M_{n,SEC}$ and $M_{w,SEC}$) and M_w/M_n values were determined with a calibration based on polystyrene (PSt) standards. Mass spectral data were acquired using a PerSeptive Voyager STR MS matrix-assisted laser desorption ionization (MALDI) time-of-flight (TOF) mass spectrometer using the reflection positive ion mode. Dithranol was used as the matrix, and silver trifluoroacetate as the cation source. The relaxation delay was set to 450 ns, with an acceleration voltage of 20 kV.

Synthesis of the 1-Phenylethylhydroxy-TEMPO Alkoxyamine (1-(1-Phenylethoxy)-2,2,6,6-tetramethylpiperidin-4-ol), 3. A Schlenk flask was charged with hydroxy-TEMPO (7.89 g, 45.8 mmol), copper powder (11.6 g, 183 mmol), copper bromide (52.5 mg, 0.366 mmol), and 50 mL of anisole. The solution was degassed by bubbling with nitrogen for 30 min, and then PMDETA (76.6 μL, 0.366 mmol) was added. After 5 min, (1-bromoethyl)benzene (5 mL, 36.6 mmol) was added, and the solution was then heated to 40 °C for 18 h. The solution was filtered and concentrated under vacuum. The crude product was purified by column chromatography eluting with hexane/ethyl acetate (95/5 gradually increasing to 5/5) to afford 8.15 g (yield = 80.2%) of a white solid. ^{1}H NMR ($CDCl_3$) δ: 7.38−7.00 (m, 5H), 4.80 (q, 1H, J = 5.54 Hz), 4.05−3.88 (m, 1H), 1.87 (td, 1H, J_d = 10.2 Hz, J_t = 3.2 Hz), 1.74 (td, 1H, J_d = 10.3 Hz, J_t = 3.2 Hz), 1.58−1.39 (m, 2H), 1.52 (d, 3H, J = 5.63 Hz), 1.36 (s, 3H), 1.25 (s, 3H), 1.11 (s, 3H), 0.71 (s, 3H). ^{13}C NMR ($CDCl_3$) δ: 145.60, 128.19, 127.08, 126.80, 83.44, 63.47, 60.35, 60.14, 49.07, 48.97, 34.60, 34.28, 23.49, 21.40.

Synthesis of the 2-Bromopropionate Alkoxyamine, 4. 1-Phenylethylhydroxy-TEMPO alkoxyamine (**3**) (3 g, 10.8 mmol) and pyridine (1.26 mL, 15.5 mmol) were dissolved in dry dichloromethane (17.5 mL). The reaction mixture was cooled in an ice−water bath, and a solution of 2-bromopropionyl bromide (1.42 mL, 13.5 mmol) in dry dichloromethane (7.5 mL) was slowly added while stirring. The mixture was stirred in the cooling bath for 1 h and then at room temperature for 16 h. The excess 2-bromo-2-methylpropionyl bromide was neutralized with 0.2 mL of water, and the reaction mixture was then poured into a solution of hydrochloric acid (100 mL, 0.3 M). The organic layer was washed with a solution of sodium hydroxide (100 mL, 0.3 M), dried over magnesium sulfate, and concentrated under vacuum. The product was purified by flash column chromatography on basic alumina using THF as solvent to afford 4.460 g (quantitative yield) of yellow oil. ^{1}H NMR ($CDCl_3$) δ: 7.37−7.17 (m, 5H), 5.11−4.96 (m, 1H), 4.78 (q, 1H, J = 5.58 Hz), 4.31 (q, 1H, J = 5.74 Hz), 1.97−1.83 (m, 2H), 1.80 (d, 3H, J = 5.78 Hz), 1.70−1.54 (m, 2H), 1.49 (d, 3H, J = 5.48 Hz), 1.35 (s, 3H), 1.27 (s, 3H), 1.13 (s, 3H), 0.68 (s, 3H). ^{13}C NMR ($CDCl_3$) δ: 169.97, 145.41; 128.23, 127.18, 126.84, 83.55, 68.86, 60.08, 44.38, 44.15, 40.58, 34.50, 34.19, 23.37, 21.70, 21.24.

General Procedure for the ATRP of MA and St with the 2-Bromopropionate Alkoxyamine 4 or a PMA Macroinitiator. In a typical experiment, CuBr (71.7 mg, 0.5 mmol) and $CuBr_2$ (11.2 mg, 0.05 mmol) were charged to a flask. The flask was deoxygenated by purging with N_2 for 30 min. Deoxygenated acetone (3.25 mL) and PMDETA (115 μL, 0.55 mmol) were added. After 5 min, deoxygenated methyl acrylate (6.5 mL, 72 mmol) and 2-bromopropionate alkoxyamine, **4** (412 mg, 1 mmol), were added. An initial sample was taken, and then the flask was placed in an oil bath thermostated at 40 °C for 20.5 h. The polymerization was stopped via exposure to air and dilution in THF (M_n = 2620, M_w/M_n = 1.09, conversion = 38.0%).

General Procedure for the Synthesis of α-Nitroxy-ω-Bromo PMA, PSt, and PMA-*b*-PSt. In a typical experiment, TEMPO (6.25 g, 40 mmol), α-aminooxy-ω-bromo PMA (1.05 g, 0.4 mmol, M_n = 2620, M_w/M_n = 1.09), and anisole (15 mL) were charged to a 25 mL Schlenk flask and bubbled with nitrogen for 30 min. The flask was then placed in an oil bath thermostated at 120 °C for 3 h. The polymer was purified by precipitation into isopropanol cooled with dry ice (M_n = 2540; M_w/M_n = 1.06).

Scheme 2. Synthesis of the 2-Bromopropionate Alkoxyamine Initiator, 4

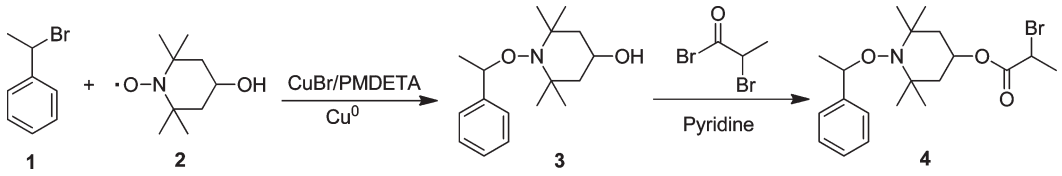


Table 1. ATRP of MA and St with the 2-Bromopropionate Alkoxyamine 4 and Synthesis of α-Nitroxy-ω-bromo and Cyclic (Co)polymers

entry	M/I/CuBr/$CuBr_2$/L	conv (%)	$M_{n,th}$	$M_{n,SEC}$; M_w/M_n	$M_{n,SEC}$; M_w/M_n after deprotection	$M_{n,SEC}$; M_w/M_n after cyclization
1[a]	72/1/0.5/0.05/0.55	38	2790	2620; 1.09	2540; 1.06	1850; 1.07
2[b]	131/1/0.75/0.25/1	18.8	2990	3200; 1.10	3030; 1.09	2580; 1.24
3[c]	262/1/0.75/0.25/1	4.8	3930	3670; 1.07	3530; 1.07	2900; 1.12

[a] M/I/L = MA/**4**/PMDETA, MA/acetone = 2/1 v/v, 40 °C, 20.5 h. [b] M/I/L = St/**4**/TPMA, St/anisole = 2/1 v/v, 40 °C, 220 min. [c] M/I/L = St/PMA (from entry 1)/TPMA, St/anisole/acetone = 2/2/1 v/v/v, 40 °C, 360 min.

General Procedure for the Synthesis of Cyclic PMA, PSt, and PMA-*b*-PSt. In a typical experiment, CuBr (28.7 mg, 0.2 mmol), TPMA (58.1 mg, 0.2 mmol), and Cu^0 (31.8 mg, 0.5 mmol) were charged to a flask. The flask was deoxygenated by purging with N_2 for 30 min, and then deoxygenated acetone (30 mL) was introduced. The contents of the flask were stirred for 15 min, and then a solution of α-nitroxy-ω-bromo PMA (2,540, 50.8 mg, 0.02 mmol) in 20 mL of deoxygenated acetone was introduced over a period of 30 h. The solution was subsequently stirred for 5 h at RT. The solution was passed through a neutral alumina column to remove the copper catalyst and concentrated under vacuum, and the resulting polymer was analyzed by SEC without any additional treatment (M_n = 1850; M_w/M_n = 1.07).

General Procedure for the Ring Expansion of Cyclic PSt by NMP of St. In a typical experiment, cyclic PSt (22 mg, 0.01 mmol, M_n = 2200, M_w/M_n = 1.24) and deoxygenated St (0.6 mL, 5.24 mmol) were charged in a deoxygenated flask. The flask was placed in an oil bath thermostated at 125 °C for 10 h. The polymerization was stopped via immersion in an ice bath.

Results and Discussion

Synthesis of the 2-Bromopropionate Alkoxyamine Initiator, 4. An ATRP initiator carrying alkoxyamine and bromoester groups was prepared in two steps (Scheme 2). The first step was the synthesis of the 1-phenylethylhydroxy-TEMPO alkoxyamine (1-(1-phenyl-ethoxy)-2,2,6,6-tetramethylpiperidin-4-ol), **3**, in 80.2% yield, by an ATRC reaction between (2-bromoethyl)benzene, **1**, and 4-hydroxy-TEMPO, **2**. The 2-bromopropionate alkoxyamine, **4**, was obtained, in quantitative yield by condensation of **3** with 2-bromopropionyl bromide.

Synthesis of Cyclic PMA. The conditions for the ATRP of MA with the 2-bromopropionate alkoxyamine **4** were chosen to limit, as much as possible, termination events between propagating radicals, since any such reactions would affect the chain-end functionality of polymer chains. Therefore, 10% of Cu^{II}/L deactivator was initially introduced to limit the concentration of propagating radicals by shifting the ATRP equilibrium toward the dormant species and reducing the concentration of radicals in the system. In addition, to suppress the homolytic cleavage of the terminal alkoxyamine bond, a low reaction temperature (40 °C) was used, and the polymerization was stopped at relatively low conversion (38%) (Table 1).

The ATRP of MA, initiated by the 2-bromopropionate alkoxyamine **4**, was conducted in 33% acetone solution (v/v) at 40 °C with a ratio $[MA]_0/[\mathbf{4}]_0/[CuBr]_0/[CuBr_2]_0/[PMDETA]_0$ = 72/1/0.5/0.05/0.55 (Table 1). After 20.5 h, a well-defined PMA, with M_n = 2620 ($M_{n,th}$ = 2790) and M_w/M_n = 1.09, was obtained (Figure 1).

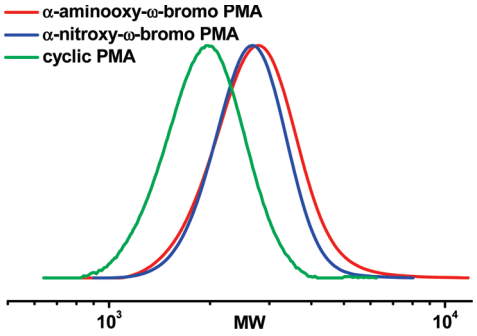


Figure 1. SEC traces of the α-aminooxy-ω-bromo PMA, the α-nitroxy-ω-bromo PMA obtained after deprotection of the alkoxyamine function, and the final cyclic PMA.

Deprotection of the nitroxide function was achieved by heating the α-aminooxy-ω-bromo PMA in anisole ([PMA] = 26.7 mmol/L), at 120 °C for 3 h, in the presence of 100 equiv of TEMPO. The deprotected PMA (M_n = 2540 and M_w/M_n = 1.06) was recovered by precipitation into cold (dry ice) isopropanol (Figure 1). The fact that deprotection of the nitroxide function had occurred was confirmed by MALDI-TOF analysis. A loss of mass 107.7 g/mol, corresponding to the terminal phenylethyl group plus a proton, was observed going from the α-aminooxy-ω-bromo PMA population to the α-nitroxy-ω-bromo PMA population (Figure 2). The isotopic pattern of the bromine atom could not be observed in the spectra, indicating that the bromine chain-end of the polymers was cleaved during the ionization process.

The telechelic PMA was subsequently cyclized by ATRC at RT under nitrogen atmosphere and high dilution conditions. A 20 mL deoxygenated solution of α-nitroxy-ω-bromo PMA (n = 0.02 mmol, M_n = 2540, M_w/M_n = 1.06) in acetone was introduced over a period of 30 h (0.67 mL/h) into a 30 mL deoxygenated solution of acetone containing 0.2 mmol of CuBr/TPMA complex and 0.5 mmol of Cu^0. After completion of the addition of the α-nitroxy-ω-bromo PMA solution, the resulting reaction mixture was stirred for an additional 5 h at RT. The SEC analysis of the polymer after reaction showed a decrease of the apparent molecular weight (M_n = 1850; M_w/M_n = 1.07) (Figure 1).

The ratio of the apparent molecular weights of the macrocyclic PMA and of its α-nitroxy-ω-bromo linear precursor is 0.73, in excellent agreement with the literature.[31,32] This result confirms the cyclic nature of the polymer obtained by intramolecular ATRC of the α-nitroxy-ω-bromo PMA, under high dilution conditions. Furthermore, the SEC trace

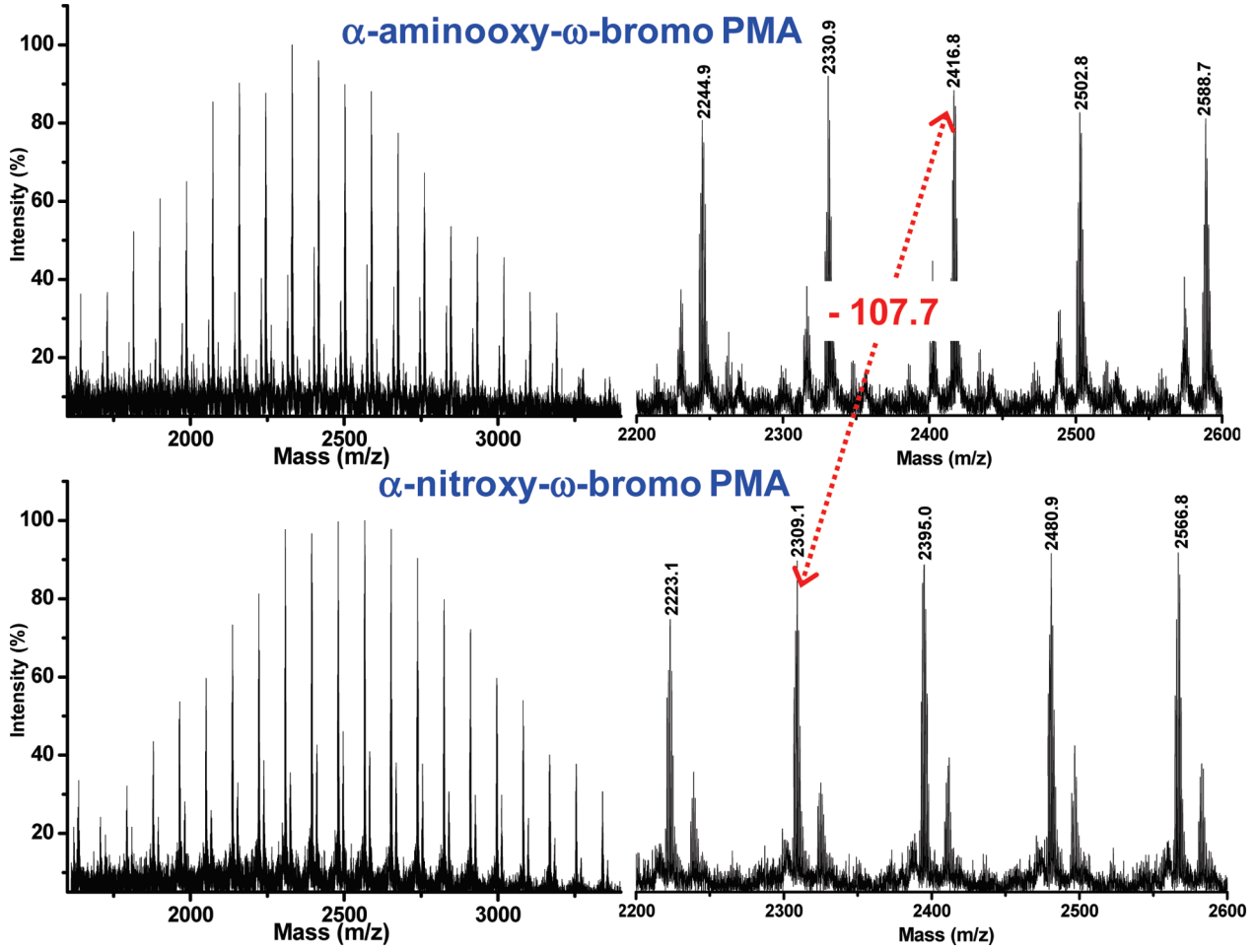


Figure 2. MALDI-TOF spectra of the α-aminooxy-*ω*-bromo PMA (top) and of the α-nitroxy,*ω*-bromo PMA (bottom) obtained after deprotection of the alkoxyamine.

of the final polymer does not show any tailing toward high molecular weight, indicating an essentially quantitative yield of the cyclic polymer via intramolecular process.

Synthesis of Cyclic PSt. The conditions for the ATRP of St were also selected to limit, as much as possible, termination events between propagating radicals (Table 1).

The ATRP of St, initiated by the 2-bromopropionate alkoxyamine **4**, yielded a well-defined PSt, with $M_n = 3200$ ($M_{nth} = 2990$) and $M_w/M_n = 1.10$ (Table 1 and Figure 3).

Deprotection of the nitroxide function was achieved by heating the α-aminooxy-*ω*-bromopolystyrene in anisole at 120 °C for 3 h, in the presence of 100 equiv of TEMPO. The deprotected PSt ($M_n = 3030$ and $M_w/M_n = 1.09$) was purified by three successive precipitations into cold (dry ice) isopropanol (Table 1).

The telechelic PSt was subsequently cyclized by ATRC at RT under nitrogen atmosphere and high dilution conditions. The SEC analyses of the polymers after reaction demonstrate a decrease of the apparent molecular weight, with $M_n = 2580$ ($M_w/M_n = 1.24$) (Table 1). The SEC trace of the final PSt shows the presence of higher molecular weight polymer, indicating that some intermolecular coupling occurred during the cyclization (estimated to be ~5% by deconvolution of the SEC trace) (Figure 3). The occurrence of intermolecular coupling under these conditions could indicate that the linear precursor was not perfectly functionalized. Chain-end functionality defects could result from the partial homolytic cleavage of the terminal C−Br bond during the deprotection of the α-aminooxy-*ω*-bromopolystyrene at 120 °C.

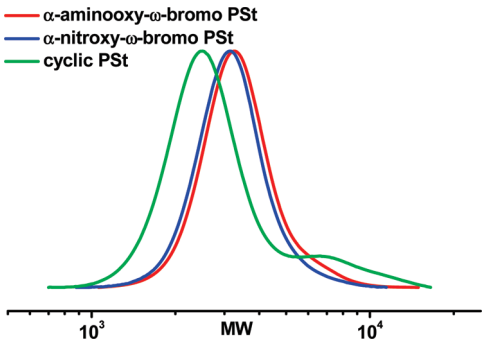


Figure 3. SEC traces of the α-aminooxy-*ω*-bromo PSt, the α-nitroxy-*ω*-bromo PSt obtained after deprotection of the alkoxyamine function, and the final cyclic PSt.

However, the ratio of the apparent molecular weights of the final PSt and of the α-nitroxy-*ω*-bromo linear precursor is 0.85, demonstrating that most of the final polymer chains were the product of intramolecular cyclization.[31,32]

Synthesis of Cyclic PMA-*b*-PSt. Diblock copolymers demonstrate a unique ability to self-assemble into complex nanoscale morphologies in bulk (e.g., lamellae, hexagonally packed cylinders, bicontinuous gyroids, and body-centered-cubic arrays of spheres) or in solution (e.g., micelle, vesicle, tube).[2,33−36] Cyclic block copolymers could self-assemble in new morphologies in solution or in bulk due to their unique topology.[2,36]

Cyclic PMA-*b*-PSt block copolymers were prepared in order to exemplify the wide range of cyclic polymers accessible via this new approach. A linear α-aminooxy-ω-bromo PMA (entry 1, Table 1), prepared with the 2-bromopropionate alkoxyamine **4**, was chain extended by ATRP of St to yield a well-defined PMA-*b*-PSt, with M_n = 3930 ($M_{n,th}$ = 3670) and M_w/M_n = 1.07 (entry 3, Table 1). The SEC chromatogram of the linear PMA-*b*-PSt block copolymer did not present any shoulder toward low molecular weight, indicating high initiation efficiency for the block extension from the PMA macroinitiator (MI) (Figure 4). Deprotection and cyclization of the resulting α-nitroxy-ω-bromo PMA-*b*-PSt copolymer were conducted under the same conditions as described for the homopolymers. The apparent MW of the cyclic block copolymer (M_n = 2900; M_w/M_n = 1.12) was significantly lower (M_n = 3530; M_w/M_n = 1.07) than that of its linear α-nitroxy-ω-bromo PMA-*b*-PSt precursor, confirming the efficient cyclization (Figure 4 and entry 3, Table 1). The SEC trace of the final PMA-*b*-PSt copolymer shows the presence of higher MW copolymer, indicating that a small fraction of the copolymer underwent intermolecular coupling during the cyclization reaction (estimated to be less than 2% by deconvolution of the SEC trace) (Figure 4).

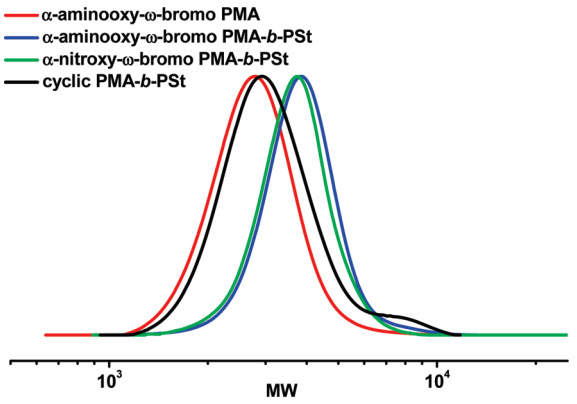


Figure 4. SEC traces of the α-aminooxy-ω-bromo PMA, the α-aminooxy-ω-bromo PMA-*b*-PSt, the α-nitroxy-ω-bromo PMA-*b*-PSt obtained after deprotection of the alkoxyamine function, and the final cyclic PMA-*b*-PSt.

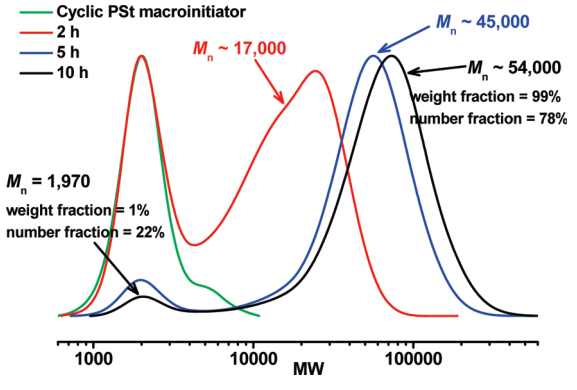


Figure 5. Evolution of SEC traces during the NMP of St with a cyclic PSt MI. Conditions: St/MI = 525, bulk, 125 °C, 10 h.

Ring Expansion of Cyclic PSt. The direct synthesis of well-defined cyclic polymers from cyclic initiators is an attractive route to cyclic polymers as it eliminates the need to prepare linear precursors. However, this approach requires cyclic initiators and polymerization processes in which chain transfer and exchange reactions between active species are absent. There have been only three reports in the literature regarding the synthesis of macrocycles by ring expansion of cyclic alkoxyamines.[28,37,38] These reports indicated difficulty associated with the preparation of well-defined macrocycles by NMP from cyclic alkoxyamines. Therefore, we were interested in conducting further studies on this process using macrocyclic alkoxyamines prepared by ATRC.

A macrocyclic polystyrene alkoxyamine (M_n = 2200; M_w/M_n = 1.24) was used as macroinitiator for the NMP of St. The polymerization was conducted in bulk over 10 h at 125 °C with an initial ratio [St]/[MI] = 525 (Figure 5 and Table 2). SEC analyses of the reaction medium during the NMP of St from the macrocyclic polystyrene alkoxyamine revealed the existence of two populations (Figure 5). A high MW population corresponding to a mixture of cyclic and linear polystyrene chains, with approximately three to four alkoxyamine functions per chain on average (Table 2). The high MW population peak shifts toward higher MW as the reaction progressed (Figure 5 and Table 2). In contrast, the peak corresponding to a low MW population does not shift as the reaction progressed and its relative intensity decreases with time (Figure 5 and Table 2). The low MW population corresponds to monocyclic PSt and to dead chains. Deconvolution of the final SEC curve (Figure 5, 10 h) indicates that the low and high MW populations represent approximately 22% and 78% of the total number of chains, respectively. This corresponds to a weight fraction of 1% for the low MW population and 99% for the high MW population.

These results are in good agreement with previous literature reports and confirm the challenges for ring expansion of cyclic (macro)alkoxyamines.[28,37,38]

Three phenomena, namely the PRE,[39,40] radical crossover reactions,[24,41] and styrene thermal self-initiation,[42,43] are responsible for the fact that ring expansion of (macro)cyclic alkoxyamine did not yield well-defined (mono)macrocycles but a mixture of cyclic and linear polyadducts. While styrene thermal self-initiation is specific to styrene, the PRE and radical crossover reaction are inherent to any NMP systems.

The persistent radical effect in NMP describes the variation of concentrations of growing (transient) and persistent (nitroxyl) radicals involved in this polymerization process.[39,40,44] At the early stages, a (small) fraction of the growing radicals R$^\bullet$ formed by dissociation of the unimolecular cyclic macroinitiator undergo radical−radical coupling. This leads, in the present case, to terminated PSt ($^\bullet$Y—RR—Y$^\bullet$ species) and loss of two growing radicals, R$^\bullet$ (Scheme 3). However, by its nature, the persistent radical, Y$^\bullet$, does not undergo coupling,

Table 2. Ring Expansion of Cyclic PSt by NMP of St[a]

time (h)	conv (%)	ln([M]$_0$/[M]$_t$)	$M_{n,th}$[b]	$M_{n,th\ cyclic}$[c]	$M_{n,SEC(low\ MW\ population)}$	$M_{n,SEC(high\ MW\ population)}$	$M_{n,SEC(high\ MW\ population)}/M_{n,th}$	$M_{n,SEC(high\ MW\ population)}/M_{n,th\ cyclic}$
0	0	0	2 200	1 650				
2	6.5	0.0673	5 750	4 310	1950	17 000	2.96	3.94
5	20.9	0.234	13 600	10 200	1920	45 000	3.30	4.41
10	31.5	0.378	19 400	14 500	1970	54 300	2.80	3.73

[a] [St]$_0$/[MI]$_0$ = 525, bulk, 125 °C, 10 h. [b] $M_{n,th}$ = [St]$_0$/[MI]$_0$ × 104.15 × conv + 2200; no correction made regarding the cyclic nature of the polymers. [c] $M_{n,th\ cyclic}$ corresponds to the theoretical apparent M_n that would be observed by SEC assuming a cyclic topology: $M_{n,th\ cyclic} = M_{n,th} \times 0.75$.

and its overall concentration should continuously increase. This increase of [Y•] is self-controlling since a higher concentration leads to more efficient formation of the dormant alkoxyamines R−Y and a decrease in the amount of radical−radical coupling (Scheme 3). Therefore, the persistent radical effect, which is a key feature to the nature of control in a NMP, breaks the stoichiometric balance between growing and persistent radicals (needed for preservation of cyclic structures).

The equilibrium concentration of propagating radicals can be easily calculated from the rate of polymerization (eq 1). This concentration was found to be equal to 4.55×10^{-9} mol/L, using a propagation rate constant of 2310 L mol^{-1} s^{-1} (pre-exponential factor of $10^{7.63}$ L mol s^{-1} and activation energy of 32.5 kJ mol^{-1})[45,46] for styrene at 125 °C.

$$R_p = \frac{-d[M]}{dt} = k_p[R^\bullet][M] \Rightarrow \ln\left(\frac{[M]_0}{[M]}\right) = k_p[R^\bullet]t \Rightarrow [R^\bullet] = \frac{\ln\left(\frac{[M]_0}{[M]}\right)}{k_p t} = 4.55 \times 10^{-9}\ \text{mol/L} \quad (1)$$

Knowing the concentration of propagating radicals at the equilibrium, one can estimate the concentration of chains that underwent termination after the equilibrium was reached (eq 2).

$$R_t = \frac{-d[R^\bullet]}{dt} = \frac{d[P]}{dt} = 2k_t[R^\bullet]^2 \Rightarrow [P] = 2k_t[R^\bullet]^2 t = 5.96 \times 10^{-4}\ \text{mol/L} \quad (2)$$

Taking a rate constant of termination of $\sim 4 \times 10^8$ L mol^{-1} s^{-1} for styrene at 125 °C,[47] the estimated concentration of dead chains after 10 h should be 5.96×10^{-4} mol/L, i.e., ~3.6% of the initial MI concentration. This would indicate that only a small fraction of chains were lost through irreversible termination after the equilibrium was reached.

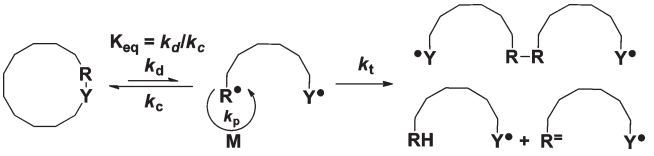
However, such a calculation does not take into account the fact that styrene undergoes spontaneous thermal polymerization at high temperatures.[42,43] It has been shown, for the bulk polymerization of styrene at 125 °C in the presence of the PSt-TEMPO adduct, that the rate of polymerization is independent of the adduct concentration and is equal to the rate of thermal polymerization.[46,48−50] The proposed kinetic scheme assumes a stationary state with respect to both [R•] and [Y•], with a concentration of R• determined by the equality of the rate of thermal initiation and that of R•−R• biradical termination.[46,49−51] Under the conditions used in our study for the ring expansion of cyclic PSt, i.e., 10 h in bulk at 125 °C, the concentration of radicals generated during the course of the reaction could be as much as 5 mM, that is, ~30% of the initial concentration of cyclic PSt.[52]

The unbalanced stoichiometry between growing and persistent radicals, resulting from the PRE (Scheme 4a), and the generation of new chains by thermal initiation (Scheme 4b) both shift the topology of polymer chains from purely cyclic to a mixture of linear and cyclic polymers (Scheme 4).

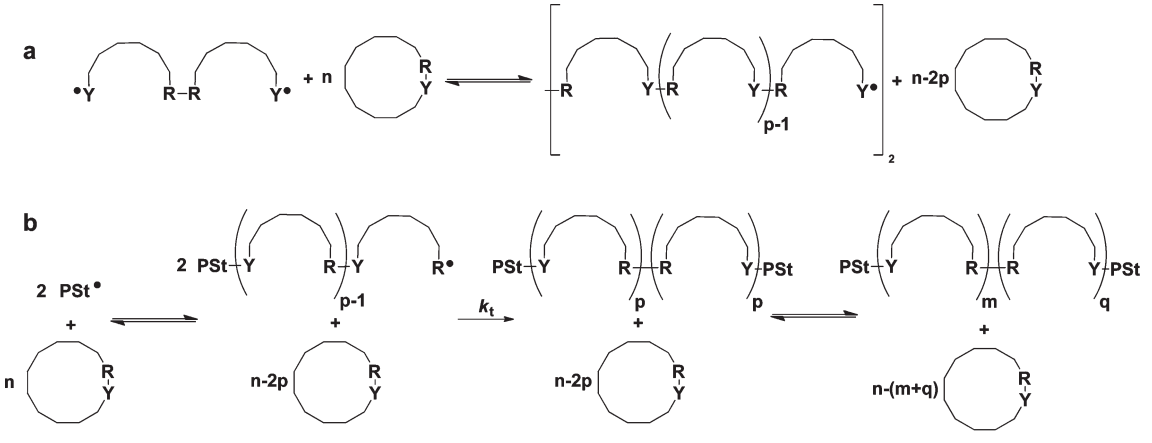
This topological change also reflects radical crossover reactions[41] taking place during NMP. Radical crossover corresponds to the recombination of a growing radical R^1 with a persistent radical Y^2 generated from the homolytic cleavage of two distinct alkoxyamines R^1−Y^1 and R^2−Y^2. For example, it has been reported that the NMP of St at 125 °C, using a 1:1 mixture of unfunctionalized alkoxyamine, **5**, and dihydroxy alkoxyamine, **6**, yielded a mixture of polystyrene macromolecules where all four possible products (**7**, **8**, **9**, and **10**) were present in an approximately statistical ratio (Scheme 5).[41] It was concluded from these results that persistent nitroxide radicals are free to diffuse out of the reaction cage during NMP and that statistical exchange of the chain ends should occur even at an early stage of the polymerization.

Crossover reactions between growing and persistent radicals are incompatible with the formation of well-defined macrocycles. These exchange reactions will lead to the formation of different populations that could still present a cyclic topology but will contain different number of alkoxyamine functions per chain (Scheme 6). Such reshuffling reactions will occur even if the stoichiometric balance between growing and persistent radicals is preserved. In addition, in the presence of persistent radicals and/or thermal

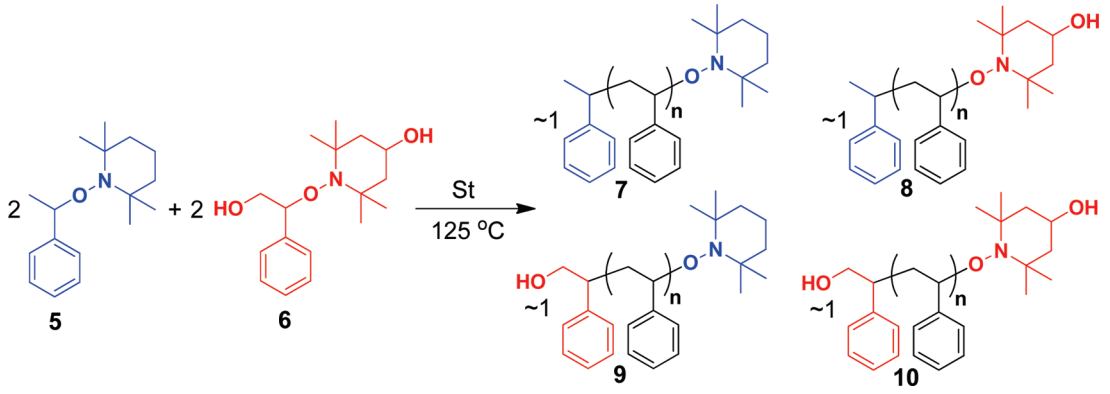
Scheme 3. General Scheme for NMP from Cyclic Alkoxyamines



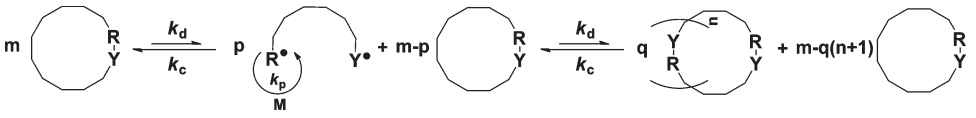
Scheme 4. Equilibrium between Linear and Cyclic Polymer Chains during NMP with Cyclic Alkoxyamines



Scheme 5. Radical Crossover during NMP of St from a 1:1 Mixture of Unfunctionalized and Dihydroxy Alkoxyamines[41]



Scheme 6. Population Redistribution via Radical Crossover during NMP with Cyclic Alkoxyamines



initiation, crossover reactions will convert part of the cyclic polymers into linear polyadducts (Scheme 4).

Conclusion

A novel approach to prepare cyclic polymers via a combination of ATRP and ATRC was developed. A functional ATRP initiator carrying an alkoxyamine group was synthesized in two steps with an overall yield of 80%. This initiator was successfully employed to prepared well-defined linear telechelic α-nitroxy,ω-bromo homo- and block copolymers via ATRP of MA or St and subsequent thermal deprotection of the terminal nitroxide function. Cyclization reactions were achieved by intramolecular ATRC, under high dilution conditions. Well-defined, low MW cyclic PMA, PSt as well as cyclic PMA-*b*-PSt block copolymers were prepared using this approach. This approach requires a minimal number of high yield steps to prepare well-defined macrocycles by radical means. The ring expansion of a cyclic polystyrene alkoxyamine prepared by ATRC was conducted via NMP of St and resulted in the formation of a mixture of products, comprising cyclic and linear polymers with an average of three to four alkoxyamine functions per chain. The presence of linear polymer chains reflects the nonstoichiometric balance between growing and persistent radicals, caused by the PRE, as well as the generation of new chains by thermal initiation. Radical crossover amplifies these phenomena and also leads to the formation of cyclic polycondensates during NMP. Therefore, ring expansion of cyclic (macro)alkoxyamines by NMP does not appear to be a suitable approach, by nature, for the preparation of well-defined macrocycles.

Acknowledgment. The authors thank Professor JPA Heuts for valuable discussions. The authors thank the NSF (CHE-07-15494 and DMR-0549353) and the members of the CRP Consortium at Carnegie Mellon University for their financial support. R. Nicolaÿ thanks Dr. and Mrs. McWilliams (Astrid and Bruce McWilliams Fellowship) for their financial support.

References and Notes

(1) Semlyen, J. A., Ed.; *Cyclic Polymers*, 2nd ed.; Kluwer Academic Publishers: Dordrecht, 2000; p 790.
(2) Deffieux, A.; Borsali, R. Controlled synthesis and properties of cyclic polymers. In *Macromolecular Enginering*; Matyjaszewski, K., Gnanou, Y., Leibler, L., Eds.; Weinheim: Germany, 2007; Vol. *2*, pp 875−908.
(3) De Gennes, P. G. *J. Chem. Phys.* **1971**, *55*, 572–579.
(4) Sperling, L. H. In *Introduction to Physical Polymer Science*, 2nd ed.; Wiley: New York, 1992; pp 104−105.
(5) McLeish, T. C. B. *Adv. Phys.* **2002**, *51*, 1379–1527.
(6) Bielawski, C. W.; Benitez, D.; Grubbs, R. H. *Science* **2002**, *297*, 2041–2044.
(7) Bielawski, C. W.; Benitez, D.; Grubbs, R. H. *J. Am. Chem. Soc.* **2003**, *125*, 8424–8425.
(8) Boydston, A. J.; Holcombe, T. W.; Unruh, D. A.; Frechet, J. M. J.; Grubbs, R. H. *J. Am. Chem. Soc.* **2009**, *131*, 5388–5389.
(9) Braunecker, W. A.; Matyjaszewski, K. *Prog. Polym. Sci.* **2007**, *32*, 93–146.
(10) Wang, J.-S.; Matyjaszewski, K. *J. Am. Chem. Soc.* **1995**, *117*, 5614–5615.
(11) di Lena, F.; Matyjaszewski, K. *Prog. Polym. Sci.* **2010**, *35*, 959–1021.
(12) Matyjaszewski, K.; Xia, J. *Chem. Rev.* **2001**, *101*, 2921–2990.
(13) Matyjaszewski, K.; Tsarevsky, N. V. *Nature Chem.* **2009**, *1*, 276–288.
(14) Kolb, H. C.; Finn, M. G.; Sharpless, K. B. *Angew. Chem., Int. Ed.* **2001**, *40*, 2004–2021.
(15) Tsarevsky, N. V.; Sumerlin, B. S.; Matyjaszewski, K. *Macromolecules* **2005**, *38*, 3558–3561.
(16) Binder, W. H.; Sachsenhofer, R. *Macromol. Rapid Commun.* **2007**, *28*, 15–54.
(17) Laurent, B. A.; Grayson, S. M. *J. Am. Chem. Soc.* **2006**, *128*, 4238–4239.
(18) Coessens, V.; Matyjaszewski, K. *J. Macromol. Sci., Pure Appl. Chem.* **1999**, *A36*, 667–679.
(19) Xu, J.; Ye, J.; Liu, S. *Macromolecules* **2007**, *40*, 9103–9110.
(20) Eugene, D. M.; Grayson, S. M. *Macromolecules* **2008**, *41*, 5082–5084.
(21) Chiefari, J.; Chong, Y. K.; Ercole, F.; Krstina, J.; Jeffery, J.; Le, T. P. T.; Mayadunne, R. T. A.; Meijs, G. F.; Moad, C. L.; Moad, G.; Rizzardo, E.; Thang, S. H. *Macromolecules* **1998**, *31*, 5559–5562.
(22) Moad, G.; Rizzardo, E.; Thang, S. H. *Aust. J. Chem.* **2006**, *59*, 669–692.
(23) Georges, M. K.; Veregin, R. P. N.; Kazmaier, P. M.; Hamer, G. K. *Macromolecules* **1993**, *26*, 2987–2988.
(24) Hawker, C. J.; Bosman, A. W.; Harth, E. *Chem. Rev.* **2001**, *101*, 3661–3688.
(25) Qiu, X.-P.; Tanaka, F.; Winnik, F. M. *Macromolecules* **2007**, *40*, 7069–7071.
(26) Goldmann, A. S.; Quemener, D.; Millard, P.-E.; Davis, T. P.; Stenzel, M. H.; Barner-Kowollik, C.; Mueller, A. H. E. *Polymer* **2008**, *49*, 2274–2281.
(27) O'Bryan, G.; Ningnuek, N.; Braslau, R. *Polymer* **2008**, *49*, 5241–5248.

(28) Narumi, A.; Zeidler, S.; Barqawi, H.; Enders, C.; Binder, W. H. *J. Polym. Sci., Part A: Polym. Chem.* **2010**, *48*, 3402–3416.
(29) Matyjaszewski, K.; Woodworth, B. E.; Zhang, X.; Gaynor, S. G.; Metzner, Z. *Macromolecules* **1998**, *31*, 5955–5957.
(30) Nicolay, R.; Marx, L.; Hemery, P.; Matyjaszewski, K. *Macromolecules* **2007**, *40*, 9217–9223.
(31) Keul, H.; Höcker, H. Cycloalkanes and Related Oligomers and Polymers. In *Large Ring Molecules*; Semlyen, J. A., Ed.; Wiley: New York, 1996; p 397.
(32) Lepoittevin, B.; Perrot, X.; Masure, M.; Hemery, P. *Macromolecules* **2001**, *34*, 425–429.
(33) Bates, F. S. *Science* **1991**, *251*, 898–905.
(34) Lodge, T. P. *Macromol. Chem. Phys.* **2003**, *204*, 265–273.
(35) Lecommandoux, S.; Borsali, R. *Polym. Int.* **2006**, *55*, 1161–1168.
(36) Schappacher, M.; Deffieux, A. *Science* **2008**, *319*, 1512–1515.
(37) Lepoittevin, B. *Synthèse et caractérisation d'architectures à base de polystyrène cyclique préparé par polymérisations contrôlées*; Pierre et Marie Curie University (Paris 6): Paris, 2000.
(38) Ruehl, J.; Ningnuek, N.; Thongpaisanwong, T.; Braslau, R. *J. Polym. Sci., Part A: Polym. Chem.* **2008**, *46*, 8049–8069.
(39) Fischer, H. *Macromolecules* **1997**, *30*, 5666–5672.
(40) Fischer, H. *Chem. Rev.* **2001**, *101*, 3581–3610.
(41) Hawker, C. J.; Barclay, G. G.; Dao, J. *J. Am. Chem. Soc.* **1996**, *118*, 11467–11471.
(42) Hui, A. W.; Hamielec, A. E. *J. Appl. Polym. Sci.* **1972**, *16*, 749–769.
(43) Mardare, D.; Matyjaszewski, K. *Polym. Prepr.* (*Am. Chem. Soc., Div. Polym. Chem.*) **1994**, *35*, 778–779.
(44) Tang, W.; Fukuda, T.; Matyjaszewski, K. *Macromolecules* **2006**, *39*, 4332–4337.
(45) Manders, B. G.; Chambard, G.; Kingma, W. J.; Klumperman, B.; van Herk, A. M.; German, A. L. *J. Polym. Sci., Part A: Polym. Chem.* **1996**, *34*, 2473–2479.
(46) Fukuda, T.; Terauchi, T. *Chem. Lett.* **1996**, 293–294.
(47) Buback, M.; Busch, M.; Kowollik, C. *Macromol. Theory Simul.* **2000**, *9*, 442–452.
(48) Greszta, D.; Matyjaszewski, K. *Macromolecules* **1996**, *29*, 5239–5240.
(49) Fukuda, T.; Terauchi, T.; Goto, A.; Ohno, K.; Tsujii, Y.; Miyamoto, T.; Kobatake, S.; Yamada, B. *Macromolecules* **1996**, *29*, 6393–6398.
(50) Greszta, D.; Matyjaszewski, K. *Macromolecules* **1996**, *29*, 7661–7670.
(51) Goto, A.; Fukuda, T. *Prog. Polym. Sci.* **2004**, *29*, 329–385.
(52) Tobolsky, A. V.; Baysal, B. *J. Polym. Sci.* **1953**, *11*, 471–486.

248 *Macromolecules* **2011**, *44*, 248–255
DOI: 10.1021/ma102010s

Macromolecules
ARTICLE

Synthesis and Characterization of Poly(9,9-dialkylfluorenevinylene benzobisoxazoles): New Solution-Processable Electron-Accepting Conjugated Polymers.

Jeremy J. Intemann,[†] Jared F. Mike,[†] Min Cai,[‡] Sayantan Bose,[†] Teng Xiao,[‡] Timothy C. Mauldin,[†] Robert A. Roggers,[†] Joseph Shinar,[‡] Ruth Shinar,[§] and Malika Jeffries-EL*,[†]

[†]*Department of Chemistry, Iowa State University, Ames Iowa 50011, United States,* [‡]*Ames Laboratory-USDOE and Department of Physics and Astronomy, Iowa State University, Ames, Iowa 50011, United States, and* [§]*Microelectronics Research Center and Department of Electrical and Computer Engineering, Iowa State University Ames, Iowa 50011, United States*

Received August 31, 2010; Revised Manuscript Received November 30, 2010

ABSTRACT: We present the synthesis of four new solution-processable, fluorescent poly(arylenevinylene)s containing benzobisoxazole and fluorene moieties. Two different moieties (*cis*- and *trans*-benzobisoxazole) and two different alkyl substituents (octyl and 3,7-dimethyloctyl) were used to study the impact of the structure on the electronic, optical, and thermal properties of these polymers. The polymers were characterized using UV−visible and fluorescence spectroscopy, cyclic voltammetry, thermal gravimetric analysis (TGA), and differential scanning calorimetry (DSC). All of the polymers possess moderate molecular weights, good solubility in aprotic organic solvents, high fluorescence quantum efficiencies in dilute solutions, and high electron affinities. Cyclic voltammetry revealed quasi-reversible reduction for these polymers. Solution-processed light-emitting diodes using dilute blends of the polymer in a poly(*N*-vinyl carbazole) matrix gave blue emission with luminous efficiencies of up to 1 Cd/A at ∼470 nm which is very promising for deep blue-emitting polymer LEDs.

Introduction

During the past three decades, conjugated polymers and the opportunities they provide for the development of organic-based electronic devices have stimulated the scientific community.[1] The benefits of conjugated polymers include low-cost processing via solution-based techniques such as spin-coating or inkjet printing and the ability to optimize the electronic, optical, and physical properties for various applications through chemical synthesis. Among the various classes of conjugated polymers, poly(9,9-dialkylfluorene)s (PDAF)s and substituted poly(phenylenevinylene)s (PPV)s are the most widely studied. PDAFs are popular due to their blue emission; high solid-state fluorescence efficiency; excellent chemical, thermal, and photo stability; good solubility; and ease of synthesis.[2] However, like most emissive conjugated polymers, PDAFs have low electron affinities and larger hole mobilities than electron mobilities; this difference in mobilities causes an imbalance in charge injection and transport. Collectively, these problems result in a decrease of external quantum efficiency (EQE) and ultimately diminish the performance of single-layer organic light emitting diodes (OLED)s.[3]

To improve device performance, low-work function cathodes such as calcium (Ca) have been utilized to improve electron injection, and multilayer devices have been fabricated using a separate electron-transport (n-type) material with an emissive p-type polymer.[4] Another approach for increasing EQE is to synthesize emissive copolymers containing both hole-transporting and electron-transporting moieties. This design strategy is expected to produce polymers with improved electron affinity and balanced charge transport, which would facilitate the fabrication of efficient single-layer OLEDs. In this regard, the synthesis of poly(arylenevinylene)s containing heterocyclic groups in the polymer backbone is a promising approach, since heteroatoms such as oxygen, nitrogen, and sulfur have higher electronegativities than carbon. Therefore, the incorporation of heterocycles can increase the electron affinity of π-conjugated polymers.[5]

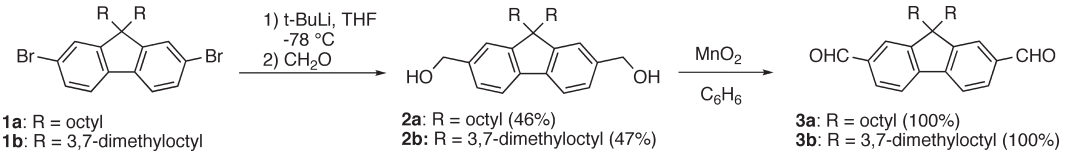
Polybenzobisazoles such as poly(*p*-phenylene benzobisthiazole), and poly(*p*-phenylene benzobisoxazole) are known to have high electron affinities,[5a] efficient electron transport,[4a,6] photoluminescence[5d,7] and thermal stability.[8] Although these properties make polybenzobisazoles promising materials, their development has been limited by two factors: (1) their poor solubility, requiring processing from harsh acidic solutions; (2) their harsh reaction conditions, limiting the types of substituents that can be incorporated onto the polymer backbone.[9] To facilitate the synthesis of such polymers, we have developed new monomers based on 2,6-functionalized benzobisazoles.[10] These monomers can be used to prepare a number of new benzobisazole containing polymers, such as poly(arylenevinylene-*co*-benzobisoxazole)s, bearing solubilizing side-chains using mild conditions.[11] This is beneficial since it is known that extending the conjugation of the polybenzobisazole backbone by adding double bonds increases the electron affinity of the resulting polymers.[6a]

Previously, we synthesized poly(phenylenevinylene-*co*-benzobisoxazole)s which exhibited reversible reduction processes and were the first examples of benzobisoxazoles that were soluble in nonacidic organic solvents. Herein we describe the synthesis, characterization and electroluminescent properties of four poly(fluorene vinylene-*co*-benzobisoxazole)s, namely: poly[(9,9-dioctylfluorene-2,7-vinylene)-*alt*-benzo[1,2-*d*;5,4-*d*′]bisoxazole-2,6-diyl] (**P43a**), poly[(9,9-bis(3,7-dimethyloctyl)fluorene-2,7-vinylene)-*alt*-benzo[1,2-*d*;5,4-*d*′]bisoxazole-2,6-diyl] (**P43b**), poly[(9,9-dioctylfluorene-2,7-vinylene)-*alt*-benzo[1,2-*d*;4,5-*d*′]bisoxazole-2,6-diyl]

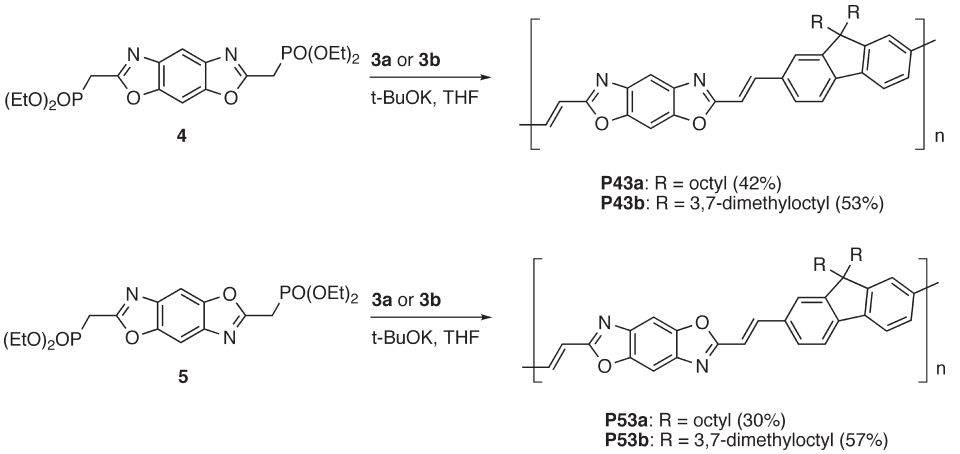
*Corresponding author. E-mail: malikaj@iastate.edu..

 Published on Web 12/17/2010 © 2010 American Chemical Society

Scheme 1. Synthesis of 9,9-Dialkylfluorene Monomers



Scheme 2. Synthesis of Poly(fluorene vinylene-*co*-benzobisoxazole)s



(**P53a**), and poly[(9,9-bis(3,7-dimethyloctyl)fluorene-2,7-vinylene)-*alt*-benzo[1,2-*d*;4,5-*d*′]bisoxazole-2,6-diyl] (**P53b**). The combination of the electron-transporting benzobisoxazole and 9,9-dialkylfluorene moieties into one polymer backbone results in new emissive, high electron-affinity polymers. Guest−host PLED devices fabricated from **P43a** and **P53a** in a poly(*N*-vinyl carbazole) matrix exhibited stable blue light emission with luminous efficiencies of up to 1 Cd/A at ∼470 nm. These early results rival the performance of other known deep blue-emitting polymers, demonstrating the promise of these polymers for the development of blue PLEDs.[5e,o,7d,12]

Results and Discussion

Monomer Synthesis. The 2,7-dibromo-9,9-dialkylfluorenes **1a**[13] and **1b**[14] and the isomeric benzobisoxazole monomers **4** and **5** were synthesized according to the literature procedures.[10a,11] These benzobisoxazole monomers differ in the arrangement of the oxygen atoms around the central benzene ring, which is known to give rise to different optical and electronic properties.[15] Whereas the fluorene monomers bore either linear octyl or branched 3,7-dimethyloctyl side chains, and were carefully purified via column chromatography to remove any monoalkylated side products.[16] The synthetic routes for the fluorene monomers are outlined in Scheme 1. The direct synthesis of 9,9-dialkylfluorene-2,7-dicarboxaldehydes **3a** and **3b** from the corresponding 2,7-dibromo-9,9-dialkylfluorenes **1a** and **1b** resulted in mixtures of the mono and dicarboxaldehydes that were difficult to separate via column chromatography. For this reason we developed a two-step sequence to carry out the synthesis of the dicarboxaldehydes where the 2,7-dibromo-9,9-dialkylfluorenes **1a** and **1b** were reacted with *tert*-butyllithium and then paraformaldehyde to yield the 9,9-dialkylfluorenes-2,7-dimethanols **2a** and **2b**, which were readily separated from the monosubstituted side products. While the yield for this step is moderate, it is more efficient than the other reported methods for the synthesis of 9,9-dialkylfluorenes-2,7-dimethanols.[13,17] Oxidation of **2a** and **2b** afforded the corresponding 9,9-dialkylfluorene-2,7-dicarboxaldehydes **3a** and **3b**, quantitatively.

Table 1. Physical Properties of Poly(fluorene vinylene-*co*-benzobisoxazole)s

polymer	M_n[a]	M_w[a]	PDI	T_d (°C)[b]	T_g (°C)[c]
P43a	6900	11 100	1.59	342	177
P43b	8300	18 100	2.18	332	170
P53a	9700	20 200	2.08	332	182
P53b	13 900	46 500	3.35	303	186

[a] Determined by GPC in THF using polystyrene standards. [b] 5% weight loss temperature by TGA under N_2. [c] Data from second scan reported, heating rate 15 °C/min under N_2.

Polymer Synthesis. The general synthetic route for the new benzobisoxazole copolymers is shown in Scheme 2. These polymers were synthesized using the Horner−Wadsworth−Emmons (HWE) polycondensation reaction between the 9,9-dialkylfluorene-2,7-dicarboxaldehydes **3a** and **3b** and the benzobisoxazole monomers **4** and **5** in anhydrous THF, and used a slight excess of potassium *tert*-butoxide. These reaction conditions were selected because the HWE reaction is known to produce polymers with all *trans*-double bonds. This method also prevents cross-linking, incomplete double bond formation, and other undesirable structural defects. Using these conditions, all four polymers were obtained with satisfactory yields (30−57%), after removing low molecular weight material via Soxhlet extraction. All of the polymers are soluble in common organic solvents, such as m-cresol, chloroform, *o*-dichlorobenzene, and THF. The ^{1}H NMR spectra for polymers **P43a**, **P43b**, **P53a**, and **P53b** were in agreement with the proposed polymer structures (see Supporting Information). All spectra showed signals in the range of 0.782−1.73 ppm, which can be assigned to the aliphatic protons on the side chains. The vinylic protons are doublets at approximately 7.3 and 8.0 ppm, while the aromatic protons are indistinguishable and exist together between 7.74 and 7.83 ppm.

Polymer Characterization. We estimated the relative molecular weights of polymers **P43a**, **P43b**, **P53a**, and **P53b** by gel permeation chromatography (GPC). The results are summarized in Table 1. **P43b** and **P53b**, bearing branched side chains, were obtained with higher yields, molecular weights,

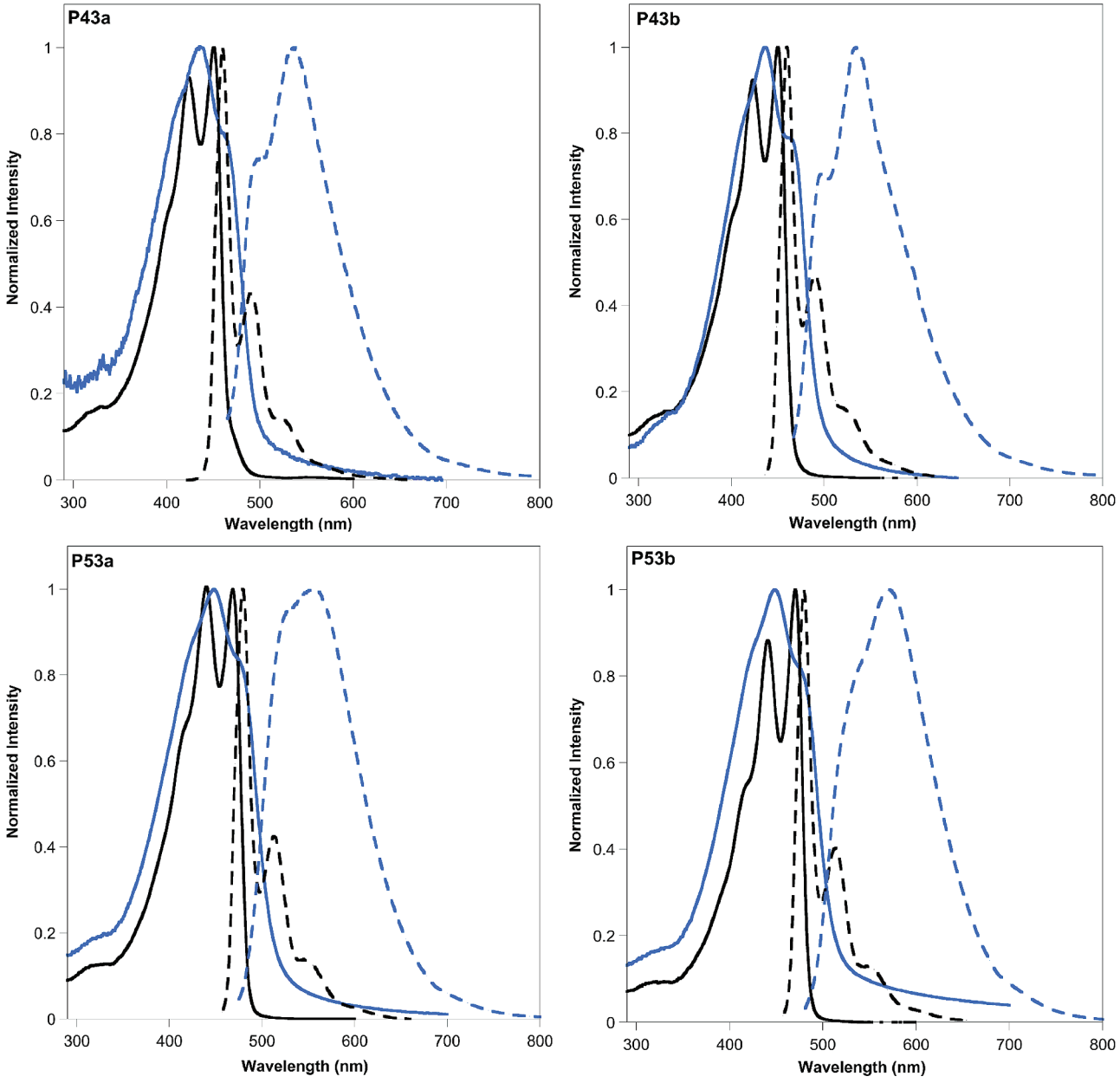


Figure 1. UV−vis (solid lines) and fluorescence (dashed lines) spectra **P43a**, **P43b**, **P53a**, and **P53b** in solution THF (black) and as thin films (blue).

and PDI's than **P43a** and **P53a**, which bear linear side chains. This is due to the increased solubility of **P43b** and **P53b** in THF as a result of the branched alkyl chain. Conversely, the limited solubility of **P43a** and **P53a** in THF resulted in precipitation of these polymers at lower molecular weight and also reduced the amount of soluble material recovered. We evaluated the thermal properties of the polymers using thermogravimetric analysis and differential scanning calorimetry. The TGA thermogram of the polymers is shown in Figure S12 (see Supporting Information). The incorporation of flexible side chains to improve the solubility of a conjugated polymer is only beneficial if the chains do not significantly diminish the thermal stability of the polymer. We found all of the polymers to be thermally stable with 5% weight loss onsets occurring in the range of 303−342 °C (Table 1). Typical second-heating differential scanning calorimetry (DSC) scans of all polymers showed weak glass transitions (T_g) for each polymer (Table 1). These values ranged from 170−186 °C and were similar to those obtained for poly-(9,9-dioctylfluorene)-2,7-vinylene, and were higher than other known poly(fluorenevinylene) copolymers.[5e,l,18] The presence of alkyl chains had a significant effect on the glass transition, as unsubstituted polybenzobisoxazoles did not show any observable transitions before their decomposition temperature. Varying the side chain length had little impact in the thermal properties of the polymers. In all cases, the glass transition temperatures were sufficiently high to withstand the joule heating associated with the operation of organic electronic devices.[19]

Optical Properties. The photophysical characteristics of the polymers were evaluated by UV−vis absorption and fluorescence spectroscopy both as dilute solutions in THF and thin films. The normalized absorbance and emission spectra for all of the polymers are shown in Figure 1, and the data is summarized in Table 2. Regardless of the length of the side chains, the benzobisoxazole group determined the polymer's optical properties in solution. The UV spectra of the polymers have two absorbance bands at approximately 424 and 450 nm for **P43a**, and **P43b**, whereas the peaks are red-shifted to approximately 440 and 470 nm for **P53a**, and **P53b**.

Table 2. Electronic and Optical Properties of PFVBBOs

polymer	media	λ^{abs}_{max} (nm)	λ^{em}_{max} (nm)	E_g^{opt} (eV)[a]	EA (eV)[b]	IP (eV)[c]	Φ_{re}	τ (ps)[f]
P43a	THF	451	460				0.64[d]	550 ± 5
	film	435	538	2.49	2.87	5.36	0.01[e]	83 ± 3
P43b	THF	450	460				0.63[d]	440 ± 5
	film	437	534	2.49	2.87	5.36	0.01[e]	170 ± 10
P53a	THF	469	479				0.68[d]	510 ± 5
	film	450	555	2.40	2.89	5.29	0.01[e]	120 ± 5
P53b	THF	470	480				0.71[d]	430 ± 5
	film	450	572	2.40	2.89	5.29	0.01[e]	260 ± 10

[a] Estimated from the optical absorption edge. [b] EA = −4.8 − (E^{red}_{onset} − 0.44 V) (eV). [c] IP = EA + E_g^{opt} (eV). Electrochemical properties were measured using a three-electrode cell (electrolyte: 0.1 mol/L (TBA)PF_6 in acetonitrile) with an Ag/Ag^+ reference electrode, a platinum auxiliary electrode, and a platinum button electrode as the working electrode. Reported values are referenced to Fc. Polymer films were made by drop coating a tetrahydrofuran solution of the polymers on to the working electrode. All cyclic voltammetry experiments were recorded at a scan rate of 50 mV/s. [d] Solution fluorescence quantum yield relative to Coumarin 6 in ethanol (Φ_f = 0.78, λ_{ex} = 490 nm). [e] Solid-state quantum yield relative to perylene 10 wt % in PMMA (Φ_f = 0.87, λ_{ex} = 520 nm). [f] Fluorescence lifetimes were obtained using a triexponential decay fit (see Supporting Information).[20] The average lifetimes are given.

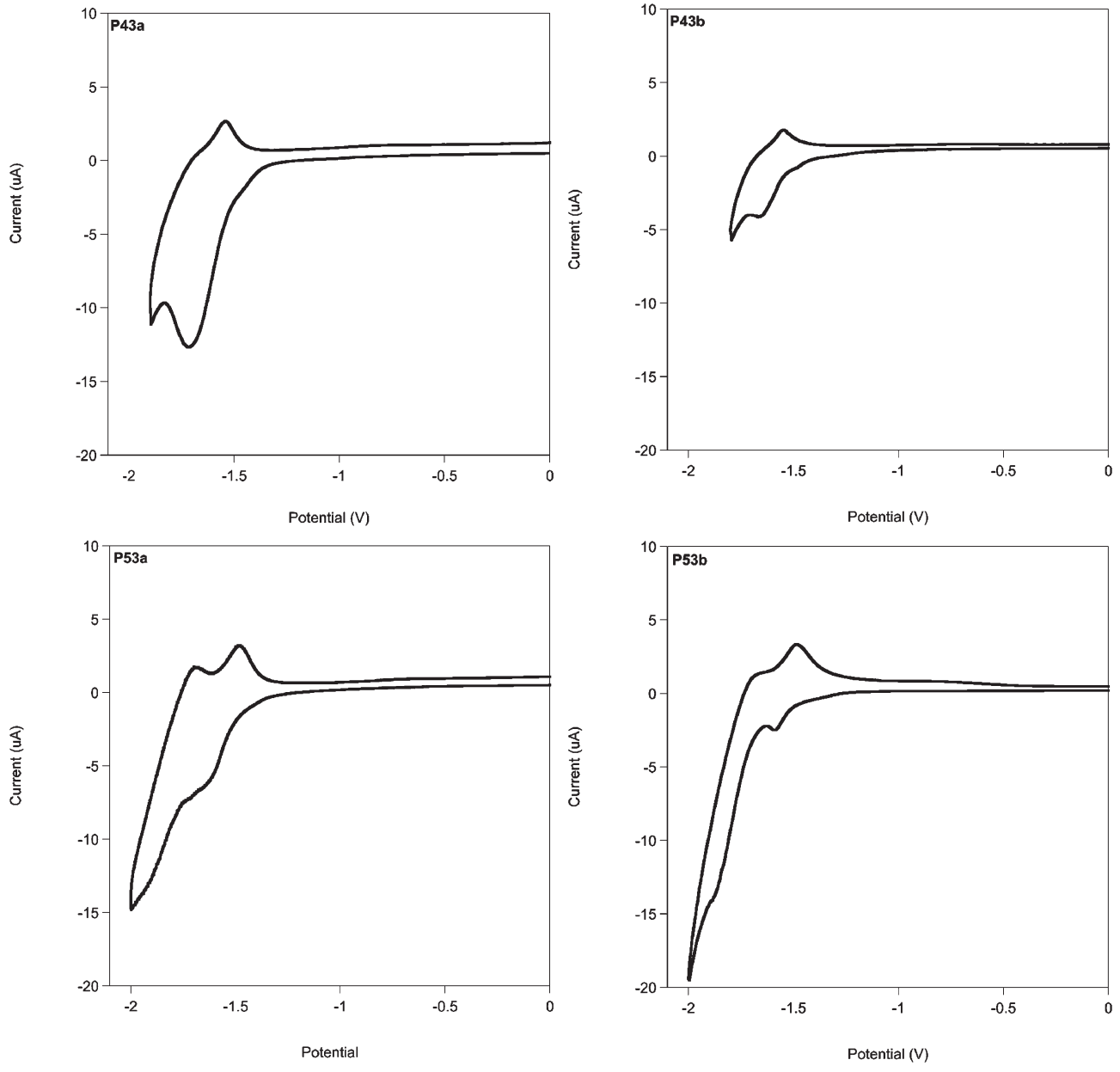


Figure 2. CV curves of **P43a**, **P43b**, **P53a**, and **P53b**.

The thin film absorbance spectra for all of the polymers were broader than their solution spectra, and the vibronic coupling diminished giving rise to a maximum absorption at a shorter wavelength. The onsets of absorption for the polymers ranged from 497 to 516 nm, resulting in optical band gaps of 2.40−2.49 eV. **P53a**, and **P53b** had smaller band gap indicating a higher degree of electron delocalization within these polymers in comparison to **P43a** and **P43b**. Furthermore, as thin

films, the absorbance spectra for the **P43a** and **P53a**, which bear linear side chains is almost identical to the absorbance spectra for the **P43b** and **P53b**, with branched side chains. This is an indication that the side chains do not affect the solid-state packing for these polymers. This assumption is supported by X-ray analysis, which shows that thin films of all polymers are amorphous.

In solution, all of the polymers are efficient fluorophores with fluorescence quantum yields of 0.64−0.71. The solution fluorescence spectra of the *cis*-PFVBBO polymers have $\lambda^{em}{}_{max}$ at 460 nm for **P43a** and **P43b** each with a shoulder at 491 nm, whereas the *trans*-PFVBBO polymers have $\lambda^{em}{}_{max}$ at 480 nm for **P53a** and **P53b** each with a shoulder at 514 nm. As neat films, **P43a** and **P43b** exhibit green emission while the emission of **P53a** and **P53b** is red-shifted resulting in yellow-green emission. The emission spectra of the polymer thin films were considerably red-shifted, relative to corresponding solution spectra and the fluorescence quantum yield is drastically diminished in the solid state with quantum yields of 0.01. This phenomenon is most likely caused by aggregation and excimer formation, and was generally independent of side chain structure. We performed fluorescence lifetime measurements for all of the polymers in both THF solution and thin films (cast from THF). In all cases the fluorescence decay curves were analyzed as the sum of three exponential decay curves; the average values are summarized in Table 2, and the details shown in Figures S13 and S14 (Supporting Information).

The $\lambda^{abs}{}_{max}$ and $\lambda^{em}{}_{max}$ in solution of the poly(fluorene vinylene-*co*-benzobisoxazole)s are blue-shifted relative to those reported previously for the related poly(arylene vinylene-*co*-benzobisoxazole)s; poly(phenylenevinylene-*co*-benzobisoxazole)s ($\lambda^{abs}{}_{max}$ 405−450 nm and $\lambda^{em}{}_{max}$ 495−518 nm)[11] and poly(thiophene vinylene-*co*-benzobisoxazole) ($\lambda^{abs}{}_{max}$ 480−507 nm and $\lambda^{em}{}_{max}$ 635−653 nm).[21] The $\lambda^{abs}{}_{max}$ in solution of **P53a** and **P53b** is red-shifted relative to that of the homopolymer poly(fluorene vinylene) (414 - 458 nm) an blue-shifter relative to the $\lambda^{abs}{}_{max}$ **P43a** and **P43b**. The $\lambda^{em}{}_{max}$ of the homopolymers (453−496 nm) is within the same range as all of the poly(fluorene vinylene-*co*-benzobisoxazole)s.[13]

Electrochemical Properties. To evaluate the redox properties of the polymers, cyclic voltammetry measurements of polymer thin films were performed. The results are summarized in Table 2, and cyclic voltammograms for the polymer redox processes are presented in Figure 2. All polymers had quasi- reversible reduction waves with onsets at −1.93 V, versus Fc/Fc^+ for both **P43a** and **P43b** and onsets at −1.91 V versus Fc/Fc^+ for both **P53a** and **P53b**. Using 4.8 eV as the SCE energy level relative to vacuum,[22] we estimated electron affinities (EA)s values of 2.87 eV for **P43a** and **P43b** and 2.89 eV for **P53a** and **P53b**. We only observed polymer degradation during oxidation cycle and no oxidation peak was seen. Since we could not directly determine the ionization potential (IP) from the electrochemical spectra, we calculated the IP using the previously measured optical band gaps, EA values and the relation IP = EA + E_g (eV).[23] Thus, we obtained IP values of 5.36 eV for **P43a** and **P43b** and 5.29 eV, for **P53a** and **P53b**. The optical band gaps for these poly(fluorene vinylene-*co*-benzobisoxazole)s are larger than those reported previously for the related polymers poly(phenylenevinylene-*co*-benzobisoxazole)s (2.2 - 2.4 eV)[5 L] and poly(thiophene vinylene-*co*-benzobisoxazole)s (2.04 - 2.17 eV),[21] as a result of the incorporation of the fluorene moiety. However, the EAs for these new polymers are higher than those obtained previously for poly(arylene vinylene-*co*-fluorene)s with electron withdrawing moieties in the backbone (2.83−3.17 eV).[18] This indicates that the electron-deficient benzobisoxazole moiety is beneficial for increasing the EA of conjugated polymers.

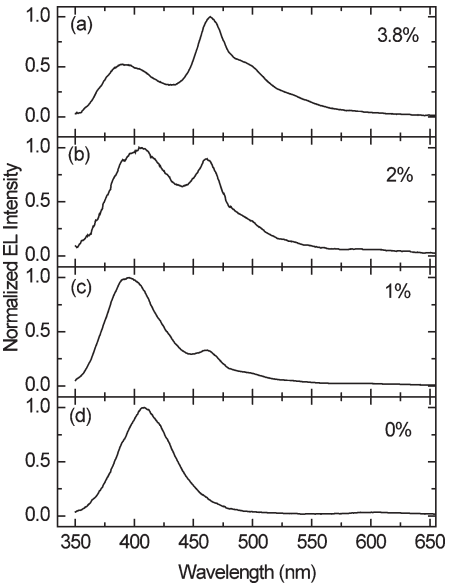


Figure 3. Normalized EL spectra of devices ITO/PEDOT:PSS(60 nm)/**P43a**:PVK (55 nm)/CsF(1 nm)/Al(120 nm)(type I) with different concentrations (in wt %) of **P43a**. The OLEDs were driven at 113 mA/cm^2.

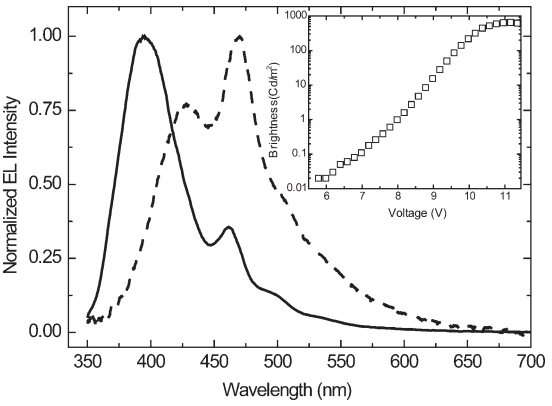


Figure 4. Comparison of the EL spectra of type I (solid line) and type II (dashed line) devices driven at 28 mA/cm^2. The inset shows the brightness as a function of bias voltage for the type II device with the BPhen layer. The **P43a** concentration was 1 wt %.

Electroluminescent Devices. The fluorescence quantum yields of the poly(arylenevinylene) copolymers in solution are 0.64 and 0.68 for **P43a** and **P53a**, respectively. In the solid state, however, they are only ∼0.01 (see Table 2). Because of this apparently strong concentration quenching in the films, the materials cannot be used as a neat emitting layer in OLEDs.[24] These materials, however, show good solubility in organic solvents and high electron affinity, which makes them promising candidates for use in guest−host PLEDs. We therefore tested them as low levels dopants in PVK-based PLEDs.

Figure 3 shows the normalized EL spectra of OLEDs with the structure: ITO/PEDOT:PSS(60 nm)/PVK:**P43a**(55 nm)/CsF(1 nm)/Al(120 nm)(type I). In these devices the **P43a** was blended with PVK at different weight ratios. As seen, the intensity of the **P43a** emission at 460 nm increases relative to that of the PVK (peaks at ∼410 nm) with increasing **P43a** level, and at ∼4 wt % the **P43a** emission surpasses that of the PVK, becoming the dominant emission peak. This behavior indicates energy transfer from the PVK to **P43a** or direct

Table 3. Device Characteristics of OLEDs Based on Poly(arylenevinylene) Copolymers

	device[a]									
polymer	type	wt % in PVK	V_{on}[b] [V]	drive voltage [V]	current density [J, mA/cm^2]	brightness [Cd/m^2]	efficiency [Cd/A, (%EQE)[c]]	λ_{max}^{EL} [nm] P43a, PVK	r_{max}	CIE 1931 [x, y]
P43a	I	0.0	6.2	8.8	116	45	0.06 (0.18)	409	0	(0.18, 0.06)
		1.0	6.4	8.2	253	350	0.19 (0.43)	460, 395	0.35	(0.17, 0.09)
		2.0	6.0	7.8	504	240	0.07 (0.10)	462, 404	0.90	(0.17, 0.11)
		3.8	8.0	12.8	493	177	0.06 (0.05)	464, 395	1.85	(0.16, 0.17)
	II	0.0	5.8	11.2	306	250	0.31 (0.30)	437	0	(0.17, 0.10)
		1.0	8.0	11.0	208	686	0.93 (0.69)	472, 428	1.32	(0.18, 0.18)
		2.0	8.0	12.8	394	548	0.56 (0.50)	464, 429	1.92	(0.17, 0.14)
P53a	II	1.0	8.6	12.8	672	528	0.25 (0.34)	489, 422	0.26	(0.17, 0.10)
		2.0	7.8	11.8	670	427	0.17 (0.22)	489, 422	0.28	(0.18, 0.11)
		3.8	9.4	13.4	514	343	0.10 (0.10)	482, 431	0.83	(0.18, 0.14)

[a] Device type I: ITO/PEDOT:PSS/PVK: poly(arylenevinylene) copolymers/CsF/Al; device type II: ITO/PEDOT:PSS/PVK: poly(arylenevinylene) copolymers/BPhen/LiF/Al. [b] Turn-on voltage (at which EL is visible to the eyes). [c] EQE = external quantum efficiency.

carrier injection to the **P43a** guest. Further increasing the **P43a** concentration in the blend did not enhance the emission from **P43a**, and it decreased the overall performance of the devices, likely due to quenching of the **P43a** emission. The device with 1 wt % **P43a** showed the highest brightness (350 Cd/m^2) and the highest luminous efficiency (0.19 Cd/A).

To further improve the performance of the **P43a**:PVK-based diodes, we fabricated devices of the structure ITO/PEDOT:PSS(60 nm)/ **P43a**:PVK (55 nm)/BPhen(40 nm)/LiF(1 nm)/Al(120 nm)(type II). That is, a BPhen electron transporting/hole blocking layer was added by thermal vacuum evaporation of BPhen powder.[25] The normalized EL spectrum of the 1 wt % type II device is shown in Figure 4 together with that of the type I device for comparison. In the type II device, the **P43a** emission at 460 nm is the main emission peak. This situation indicates that the BPhen enhances exciton formation on **P43a**. The LUMO levels of PVK, **P43a**, and BPhen are −2.2, −2.9, and −3.0 eV, respectively. Hence, the electrons injected through the BPhen layer are transported preferentially to the **P43a** molecules in comparison to the PVK molecules, leading to exciton formation on the previous. Thus, the addition of the BPhen layer further enhances the device performance. A highest brightness of 686 Cd/m^2 and a maximal luminous efficiency of 0.93 Cd/A were obtained for 1 wt % type II devices, which is 4 times more efficient than the 1 wt % type I devices (see Table 3). We note that a luminous efficiency of ∼1 Cd/A at ∼470 nm is very promising for solution-processed deep blue-emitting polymer LEDs.

Type II diodes based on **P53a**:PVK at different weight ratios were also tested. The device with 1 wt % showed the highest brightness (528 Cd/m^2) and the highest luminous efficiency (0.25 Cd/A); these values, however, are lower than those of the **P43a**:PVK-based devices. This situation may be due to the higher molecular weight and PDI of the **P53a** (see Table 1). It is suspected that the higher molecular weight increases aggregation of **P53a** in the **P53a**:PVK layer, which decreases the overall device performance due to increased **P53a**-induced concentration quenching of the emission. These initial results indicate that the poly(arylenevinylene)s copolymers can be used as dopants in other polymers used in PLEDs to control, following optimization, the emission wavelength and improve the overall device performance. Optimization of such PLEDs is ongoing.

Conclusions

In conclusion, four new benzobisoxazole containing polymers have been synthesized with good molecular weights and yields via the Horner−Wadsworth−Emmons coupling reaction. The optical and electronic properties of the polymers are determined by the type of benzobisoxazole monomer used and not impacted by the size of the side chain. The flexible side chains on the fluorene ring led to good solubility, while maintaining good thermal stability, whereas the incorporation of the electron-accepting benzobisoxazole moiety into the polymer chain led to high electron affinity. Preliminary electroluminescence studies showed that these polymers exhibit promising brightness in guest−host OLEDs. Collectively, these results suggest that poly(9,9-dialkylfluorene vinylene) benzobisoxazoles have great potential for use in organic semiconducting applications. The facile synthetic approach will enable the development of new derivatives of poly(arylenevinylene-*co*-benzobisoxazole)s with improved properties.

Experimental Methods

Materials and General Experimental Details. Tetrahydrofuran was dried using an Innovative Technologies solvent purification system. The following compounds were prepared according to literature procedures: 2,7-dibromo-9,9-dioctyl-9*H*-fluorene (**1a**),[26] 2,7-dibromo-9,9-bis(3,7-dimethyloctyl)fluorene (**1b**),[14] 2,6-dimethylbenzo[1,2-*d*;5,4-*d*′]bisoxazolediethylphosphonate ester (**4**),[11] and 2,6-dimethylbenzo[1,2-*d*;4,5-*d*′]bisoxazolediethylphosphonate ester (**5**).[11] The synthesis of compounds **2a**, **2b**, **3a** and **3b** is described in the Supporting Information. Poly(3,4-ethylenedioxy thiophene): poly(4-styrenesulfonate) (PEDOT:PSS) was purchased from H. C. Starck and used as the hole injection layer (HIL). Poly(*N*-vinyl carbazole) (PVK) and 4,7-diphenyl-1,10-phenanthroline (BPhen) were purchased from Sigma-Aldrich. All other materials were purchased from commercial sources and used without further purification.

General Polymerization Procedure. A dry round-bottom flask was placed under argon atmosphere and then charged with 1 mmol of fluorene monomer **3a** or **3b**, 1 mmol of benzobisoxazole monomer **4** or **5**, and 15 mL of dry THF. The mixture was stirred at room temperature while adding 2.5 mL of 1 M solution of potassium tert-butoxide in THF dropwise over 20 min. The mixture to was left to stir at room temperature for 2 days and then added another 15 mL of dry THF to the reaction flask. The reaction was then allowed to stir for another 3 days before quenching it by pouring the mixture into 100 mL of methanol. The precipitated polymer was filtered into a cellulose extraction thimble and then washed in a Soxhlet extractor with methanol, followed by hexane and last THF. The THF extract was poured into a crystallizing dish and the polymer recovered upon evaporation of the solvent

Poly[(9,9-dioctylfluorene-2,7-vinylene)-*alt*-benzo[1,2-*d*;5,4-*d*′]-bisoxazole-2,6-diyl] (P43a). The polymer was obtained as an orange solid (0.25 g, 42% yield). ^{1}H NMR (THF-d_8), δ: 0.80 (br m, $-CH_2-$), 0.89 (br m, $-CH_3$), 1.11 (br m, $-CH_2-$), 1.29 (m, $-CH_2-$), 2.20 (br m, homobenzylic $-CH_2-$), 7.28 (d, vinylic $=CH-$), 7.65−7.98 (br m, Ar−H and vinylic $=CH-$), 10.52 (terminal aldehyde peak), 10.69 (terminal P(=O)(OH)$_2$. GPC: M_n = 6941, M_w = 11 067, PDI = 1.59.

Poly[(9,9-bis(3,7-dimethyloctyl)fluorene-2,7-vinylene)-*alt*-benzo-[1,2-*d*;5,4-*d*′]bisoxazole-2,6-diyl] (P43b). The polymer was obtained as an orange solid (0.35 g, 53% yield). ^{1}H NMR (THF-d_8), δ: 0.79 (br m, −CH2− and −CH_3), 1.14 (br m, −CH_2−), 2.18 (br m, homobenzylic −CH_2−), 7.27 (d, vinylic =CH−), 7.62−7.98 (br m, Ar−H and vinylic =CH−), 10.70 (terminal P(=O)$(OH)_2$ peak). GPC: M_n = 10 348, M_w = 22 515, PDI = 2.18.

Poly[(9,9-dioctylfluorene-2,7-vinylene)-*alt*-benzo[1,2-*d*;4,5-*d*′]-bisoxazole-2,6-diyl] (P53a). The polymer was obtained as a red-orange solid (0.18 g, 30% yield). ^{1}H NMR (THF-d_8), δ: 0.80 (br m, −CH_2− and −CH_3), 1.11 (br m, −CH_2−), 2.20 (br m, homobenzylic −CH_2−), 7.28 (d, vinylic =CH−), 7.64−7.98 (br m, Ar−H and vinylic =CH−), 10.51 (terminal aldehyde peak), 10.68 (terminal P(=O)$(OH)_2$ peak). GPC: M_n = 9739, M_w = 20 242, PDI = 2.08.

Poly[(9,9-bis(3,7-dimethyloctyl)fluorene-2,7-vinylene)-*alt*-benzo-[1,2-*d*;4,5-*d*′]bisoxazole-2,6-diyl] (P53b). The polymer was obtained as a red-orange solid (0.37 g, 57% yield). ^{1}H NMR (THF-d_8), δ: 0.79 (br m, −CH_2− and −CH_3), 1.10 (br m, −CH_2−), 2.20 (br s, benzylic −CH_2−), 7.28 (d, vinylic =CH−), 7.68−8.00 (br m, Ar−H and vinylic =CH−), 10.51 (terminal aldehyde peak), 10.69 (terminal P(=O)$(OH)_2$ peak). GPC: M_n = 13 879, M_w = 46 534, PDI = 3.35.

Fabrication and Characterization of OLEDs. OLEDs were fabricated on nominally 20 Ω/square, 140 nm-thick ITO-coated glass substrates (Colorado Concept Coatings). The substrates were first cleaned with a detergent and organic solvents; they were then treated in a UV/ozone oven to increase the work function of the ITO and hence facilitate hole injection, as described elsewhere.[27] A 60 nm PEDOT:PSS layer was spin-coated on the ITO and then baked in air at 250 °C for 30 min. Blends of PVK and poly(arylenevinylene) copolymers in chlorobenzene solutions were spin-coated on top of the PEDOT:PSS layer in an Ar-filled glovebox. The combined concentration of the PVK and **P43a** was kept constant at 9 mg/mL; the **P43a** concentration varied in the range 0.09 to 0.36 mg/mL. The solution was spin coated at 1000 rpm for 60 s. Under these conditions the light-emitting layer was ∼55 nm thick. The fabricated structure was then annealed at 60 °C for 30 min. Following this annealing step, the samples were transferred into a thermal evaporator within the glovebox and the BPhen, LiF or CsF, and Al layers were deposited sequentially by thermal evaporation at a base pressure of $\sim 2 \times 10^{-6}$ Torr. The OLEDs were characterized by monitoring their electroluminescence (EL) spectra, brightness as a function of the applied voltage, and luminous efficiency.

Acknowledgment. We thank the 3M Foundation, the National Science Foundation (DMR-0846607), and Iowa State University for financial support of this work. Partial support for this work was provided by the Director for Energy Research, Office of Basic Energy Sciences, USDOE. Ames Laboratory is operated by Iowa State University for the US Department of Energy (USDOE) under Contract No. DE-AC 02-07CH11358. The authors also thank Dr. Kamel Harrata and the Mass Spectroscopy Laboratory of Iowa State University for analysis of our compounds, Dr. Jacob Petrich for use of equipment for fluorescence lifetime measurements and Ms. Trisha Andrew (MIT) for PL spectra and PL quantum yield measurements.

Supporting Information Available: Synthetic methods for intermediates **2a**, **2b**, **3a**, and **3b** and ^{1}H NMR spectra, X-ray data, fluorescence lifetimes, DSC traces, and TGA thermographs of **P43a**, **P43b**, **P53a** and **P53b**. This material is available free of charge via the Internet at http://pubs.acs.org.

References and Notes

(1) (a) Forrest, S. R. *Nature* **2004**, *428*, 911. (b) Kelley, T. W.; Baude, P. F.; Gerlach, C.; Ender, D. E.; Muyres, D.; Haase, M. A.; Vogel, D. E.; Theiss, S. D. *Chem. Mater.* **2004**, *16*, 4413.

(2) Leclerc, M. *J. Polym. Sci. A* **2001**, *39*, 2867.

(3) (a) Kraft, A.; Grimsdale, A. C.; Holmes, A. B. *Angew. Chem., Int. Ed. Engl.* **1998**, *37*, 403. (b) Friend, R. H.; Gymer, R. W.; Holmes, A. B.; Burroughes, J. H.; Marks, R. N.; Taliani, C.; Bradley, D. D. C.; Dos Santos, D. A.; Bredas, J. L.; Logdlund, M.; Salaneck, W. R. *Nature* **1999**, *397*, 121. (c) Greenham, N. C.; Moratti, S. C.; Bradley, D. D. C.; Friend, R. H.; Holmes, A. B. *Nature* **1993**, *365*, 628.

(4) (a) Jenekhe, S. A.; de Paor, L. R.; Chen, X. L.; Tarkka, R. M. *Chem. Mater.* **1996**, *8*, 2401. (b) Kulkarni, A. P.; Tonzola, C. J.; Babel, A.; Jenekhe, S. A. *Chem. Mater.* **2004**, *16*, 4556. (c) Tonzola, C. J.; Alam, M. M.; Bean, B. A.; Jenekhe, S. A. *Macromolecules* **2004**, *37*, 3554.

(5) (a) Ahmed, E.; Kim, F. S.; Xin, H.; Jenekhe, S. A. *Macromolecules* **2009**, *42*, 8615. (b) Grimsdale, A. C.; Leok Chan, K.; Martin, R. E.; Jokisz, P. G.; Holmes, A. B. *Chem. Rev.* **2009**, *109*, 897. (c) Osaheni, J. A.; Jenekhe, S. A. *Chem. Mater.* **1992**, *4*, 1282. (d) Osaheni, J. A.; Jenekhe, S. A. *Macromolecules* **1993**, *26*, 4726. (e) Mikroyannidis, J. A.; Gibbons, K. M.; Kulkarni, A. P.; Jenekhe, S. A. *Macromolecules* **2008**, *41*, 663. (f) Mikroyannidis, J. A.; Spiliopoulos, I. K.; Kasimis, T. S.; Kulkarni, A. P.; Jenekhe, S. A. *Macromolecules* **2003**, *36*, 9295. (g) Lee, Y.-Z.; Chen, X.; Chen, S.-A.; Wei, P.-K.; Fann, W.-S. *J. Am. Chem. Soc.* **2001**, *123*, 2296. (h) Barberis, V. P.; Mikroyannidis, J. A. *J. Polym. Sci. A.* **2006**, *44*, 3556. (i) Yang, W.; Huang, J.; Liu, C.; Niu, Y.; Hou, Q.; Yang, R.; Cao, Y. *Polymer* **2004**, *45*, 865. (j) Fu, D.-K.; Xu, B.; Swager, T. M. *Tetrahedron* **1997**, *53*, 15487. (k) Kim, J. L.; Kim, J. K.; Hong, S. I. *Polym. Bull.* **1999**, *42*, 511. (l) Mikroyannidis, J. A.; Fakis, M.; Spiliopoulos, I. K. *J. Polym. Sci. A.* **2009**, *47*, 3370. (m) Lee, B. H.; Jaung, J. Y.; Cho, J.-w.; Yoon, K. J. *Polym. Bull.* **2003**, *50*, 9. (n) Karastatiris, P.; Mikroyannidis, J. A.; Spiliopoulos, I. K.; Kulkarni, A. P.; Jenekhe, S. A. *Macromolecules* **2004**, *37*, 7867. (o) Kulkarni, A. P.; Zhu, Y.; Jenekhe, S. A. *Macromolecules* **2005**, *38*, 1553.

(6) (a) Alam, M. M.; Jenekhe, S. A. *Chem. Mater.* **2002**, *14*, 4775. (b) Babel, A.; Jenekhe, S. A. *Adv. Mater.* **2002**, *14*, 371. (c) Babel, A.; Jenekhe, S. A. *J. Phys. Chem. B.* **2002**, *106*, 6129.

(7) (a) Chen, Y.; Wang, S.; Zhuang, Q.; Li, X.; Wu, P.; Han, Z. *Macromolecules* **2005**, *38*, 9873. (b) Feng, D.; Wang, S.; Zhuang, Q.; Wu, P.; Han, Z. *Polymer* **2004**, *45*, 8871. (c) Jenekhe, S. A.; Osaheni, J. A. *Chem. Mater.* **1994**, *6*, 1906. (d) Osaheni, J. A.; Jenekhe, S. A. *Macromolecules* **1994**, *27*, 739. (e) Osaheni, J. A.; Jenekhe, S. A. *Chem. Mater.* **1995**, *7*, 672. (f) Osaheni, J. A.; Jenekhe, S. A.; Burns, A.; Du, G.; Joo, J.; Wang, Z.; Epstein, A. J.; Wang, C. S. *Macromolecules* **1992**, *25*, 5828. (g) Zhang, X.; Jenekhe, S. A. *Macromolecules* **2000**, *33*, 2069.

(8) (a) Wolfe, J. F. Polybenzothiazoles and Polybenzoxazoles. In *Encyclopedia of Polymer Science and Engineering*; John Wiley and Sons: New York, 1988; Vol. *11*, pp 601;(b) Wolfe, J. F.; Arnold, F. E. *Macromolecules* **1981**, *14*, 909. (c) Wolfe, J. F.; Loo, B. H.; Arnold, F. E. *Macromolecules* **1981**, *14*, 915.

(9) (a) Guo, P.; Wang, S.; Wu, P.; Han, Z. *Polymer* **2004**, *45*, 1885. (b) Kricheldorf, H. R.; Domschke, A. *Polymer* **1994**, *35*, 198. (c) Liu, X.; Xu, X.; Zhuang, Q.; Han, Z. *Polym. Bull.* **2008**, *60*, 765. (d) Wang, S.; Lei, H.; Guo, P.; Wu, P.; Han, Z. *Eur. Polym. J.* **2004**, *40*, 1163.

(10) (a) Mike, J. F.; Makowski, A. J.; Jeffries-EL, M. *Org. Lett.* **2008**, *10*, 4915. (b) Mike, J. F.; Inteman, J. J.; Ellern, A.; Jeffries-El, M. *J. Org. Chem.* **2010**, *75*, 495.

(11) Mike, J. F.; Makowski, A. J.; Mauldin, T. C.; Jeffries-El, M. *J. Polym. Sci. A* **2010**, *48*, 1456.

(12) (a) Hancock, J. M.; Gifford, A. P.; Tonzola, C. J.; Jenekhe, S. A. *J. Phys. Chem. C* **2007**, *111*, 6875. (b) Huang, F.; Zhang, Y.; Liu, M.; Cheng, Y. J.; Jen, A. Y. *Adv. Fun. Mater.* **2007**, *17*, 3808.

(13) Anuragudom, P.; Newaz, S. S.; Phanichphant, S.; Lee, T. R. *Macromolecules* **2006**, *39*, 3494.

(14) Kannan, R.; He, G. S.; Lin, T.-C.; Prasad, P. N.; Vaia, R. A.; Tan, L.-S. *Chem. Mater.* **2004**, *16*, 185.

(15) (a) Bhaumik, D.; Welsh, W. J.; Jaffe, H. H.; Mark, J. E. *Macromolecules* **1981**, *14*, 951. (b) Bhaumik, D.; Jaffe, H. H.; Mark, J. E. *Macromolecules* **1981**, *14*, 1125. (c) Welsh, W. J.; Bhaumik, D.; Mark, J. E. *Macromolecules* **1981**, *14*, 947. (d) Bhaumik, D.; Mark, J. E. *J. Polym. Sci., Polym. Phys. Ed.* **1983**, *21*, 1111. (e) Welsh, W. J.; Mark, J. E. *J. Mater. Sci.* **1983**, *18*, 1119.

(16) (a) Craig, M. R.; Kok, M. M. d.; Hofstraat, J. W.; Schenning, A. P. H. J.; Meijer, E. W. *J. Mater. Chem.* **2003**, *13*, 2861. (b) Cho, S. Y.; Grimsdale, A. C.; Jones, D. J.; Watkins, S. E.; Holmes, A. B. *J. Am. Chem. Soc.* **2007**, *129*, 11910.

(17) Liu, B.; Yu, W. L.; Pei, J.; Liu, S. Y.; Lai, Y. H.; Huang, W. *Macromolecules* **2001**, *34*, 7932.

(18) Grisorio, R.; Piliego, C.; Cosma, P.; Fini, P.; Mastrorilli, P.; Gigli, G.; Suranna, G. P.; Nobile, C. F. *J. Polym. Sci. A*. **2009**, *47*, 2093.
(19) Tonzola, C. J.; Alam, M. M.; Jenekhe, S. A. *Macromolecules* **2005**, *38*, 9539.
(20) (a) Bose, S.; Adhikary, R.; Mukherjee, P.; Song, X.; Petrich, J. W. *J. Phys. Chem. B* **2009**, *113*, 11061. (b) Chowdhury, P. K.; Halder, M.; Sanders, L.; Calhoun, T.; Anderson, J. L.; Armstrong, D. W.; Song, X.; Petrich, J. W. *J. Phys. Chem. B* **2004**, *108*, 10245.
(21) Mike, J. F.; Nalwa, K.; Makowski, A. J.; Putnam, D.; Tomlinson, A. L.; Chaudhary, S.; Jeffries-El, M. *Phys. Chem. Chem. Phys.* **2011**, DOI: 10.1039/C0CP00353K.
(22) Agrawal, A. K.; Jenekhe, S. A. *Chem. Mater*. **1996**, *8*, 579.
(23) Janietz, S.; Bradley, D. D. C.; Grell, M.; Giebeler, C.; Inbasekaran, M.; Woo, E. P. *Appl. Phys. Lett*. **1998**, *73*, 2453.
(24) (a) Gontia, I.; Frolov, S. V.; Liess, M.; Ehrenfreund, E.; Vardeny, Z. V.; Tada, K.; Kajii, H.; Hidayat, R.; Fujii, A.; Yoshino, K.; Teraguchi, M.; Masuda, T. *Phys. Rev. Lett*. **1999**, *82*, 4058. (b) Hidayat, R.; Tatsuhara, S.; Kim, D. W.; Ozaki, M.; Yoshino, K.; Teraguchi, M.; Masuda, T. *Phys. Rev. B* **2000**, *61*, 10167.
(25) Wu, J.-S.; Lu, H.-H.; Hung, W.-C.; Lin, G.-H.; Chen, S.-A. *Appl. Phys. Lett*. **2010**, *97*, 023304.
(26) Ranger, M.; Rondeau, D.; Leclerc, M. *Macromolecules* **1997**, *30*, 7686.
(27) Zhou, Z.; Shinar, R.; Allison, A. J.; Shinar, J. *Adv. Fun. Mater*. **2007**, *17*, 3530.

256 *Macromolecules* **2011**, *44*, 256–262
DOI: 10.1021/ma102183f

Macromolecules
ARTICLE

Synthesis of Novel Semiconducting Polymers Consisting of *p*-Phenylene, *p*-Phenylenevinylene, and Styrylamine Structures: Copolymerization and Dehydrogenation of 1,3-Cyclohexadiene and 4-Diphenylaminostyrene

Itaru Natori,* Shizue Natori, Kosuke Tsuchiya, and Kenji Ogino

Chemical and Material Systems, Graduate School of Bio-Applications and Systems Engineering, Tokyo University of Agriculture and Technology, 2-24-16 Naka-chou, Koganei-city, Tokyo 184-8588, Japan

Received September 20, 2010; Revised Manuscript Received November 24, 2010

ABSTRACT: Well-defined semiconducting copolymers consisting of *p*-phenylene (PP), *p*-phenylenevinylene (PV), and styrylamine (SA) ternary molecular structures (PP/PV/SA copolymer) were synthesized by living anionic polymerization for the random copolymerization of 1,3-cyclohexadiene (1,3-CHD) and 4-diphenylaminostyrene (4-DAS) and the complete dehydrogenation of the 1,3-CHD/4-DAS copolymer. To obtain PP/PV/SA copolymer, the 1,3-CHD/4-DAS random copolymer, consisting of the 1,4-cyclohexadiene (1,4-CHD) and cyclohexadiene (CHD)-diphenylaminostyrene (DAS) structures as a prerequisite prepolymer, was prepared by the random copolymerization of 1,3-CHD and 4-DAS with *tert*-butyllithium in cyclohexane. The completely dehydrogenated 1,3-CHD/4-DAS random copolymer was achieved without decomposition of the polymer chain when 2,3,5,6-tetrachloro-1,4-(*p*-)-benzoquinone was used as a dehydrogenation reagent. Gel permeation chromatography, ^{1}H nuclear magnetic resonance, UV/vis, and photoluminescence analyses confirmed that the completely dehydrogenated 1,3-CHD/4-DAS random copolymer consisting of the 1,4-CHD and CHD−DAS structures was PP/PV/SA copolymer.

Introduction

Semiconducting polymers have attracted much attention due to their applications in advanced technologies such as organic light emitting diodes (OLEDs),[1] photovoltaic devices,[2] and field effect transistors.[3] In OLEDs with semiconducting polymers, three different functionalities are required for the active layer(s): hole-transport (HT), electron-transport (ET), and light-emission (LE). Therefore, various combinations of HT semiconducting polymers, ET small molecules, and LE small molecules (or HT and LE semiconducting polymers and ET small molecules) have been studied after fundamental examination of each pristine semiconducting polymer.

From the standpoint of polymer synthesis, the incorporation of plural functionalities into one polymer chain is a very interesting research subject. It is well-known that the functionality of molecules is controlled by the chemical structure of molecules. That is, HT, ET, and LE functionalities are achieved by HT, ET, and LE structure molecules. For example, the incorporation of both HT and ET structures into one polymer chain was performed to prepare bipolar semiconducting copolymers.[4−12] Semiconducting copolymers consisting of both HT and LE structures (or both ET and LE structures) in the polymer chain have also been synthesized.[13−15] The most promising polymer chain structure in this field seems to be the incorporation of HT, ET, and LE structures into one polymer chain. Deng et al. reported the incorporation of triphenylamine (a HT structure), oxiadiazole (a ET structure), and phosphor (a LE structure) into one polymer chain through living radical polymerization.[16] However, the synthesis of well-defined semiconducting copolymers (i.e., semiconducting copolymer having well-controlled and defined polymer chain structure) consisting of HT, ET, and LE ternary molecular structures is considerably difficult, even using living radical polymerization. Therefore, a new effective method to prepare well-defined semiconducting copolymers is required. Therefore, a lot of studies to obtain such semiconducting polymers by (living) anionic polymerization have been attempted. For example, polyphenylene (PPH) and its derivatives,[17−25] poly(9-vinylanthracene) (PVAN),[26−31] poly(*N*-vinylcarbazole) (PNVC),[32] and poly(4-diphenylaminostylene) (PDAS)[33,34] have been synthesized since 1950s. However, the formation of a well-controlled and defined polymer chain structure for semiconducting polymers was very difficult.

Recently, we have attempted the synthesis of well-defined semiconducting polymers through (living) anionic polymerization, and various semiconducting polymers with well-defined polymer chain structures [e.g., poly(*p*-phenylene) (PPP) and PDAS] have been successfully synthesized.[35−50] From these results, (living) anionic polymerization has proven to have great potential for the preparation of well-defined semiconducting copolymers consisting of HT, ET, and LE ternary molecular structures, and we have noted that *p*-phenylene (PP; a ET structure[38]), *p*-phenylenevinylene (PV; a HT structure[51]), and styrylamine (SA; a LE structure[52]) ternary molecular structures could be derived by the complete dehydrogenation of 1,3-cyclohexadiene (1,3-CHD)/4-diphenylaminostyrene (4-DAS) copolymers (Scheme 1).

In this paper, we report the synthesis of well-defined semiconducting copolymers consisting of PP, PV, and SA ternary molecular structures (PP/PV/SA copolymer) through (living) anionic polymerization. The copolymerization of 1,3-CHD and 4-DAS by anionic polymerization and the dehydrogenation of 1,3-CHD/4-DAS copolymers are also described in detail.

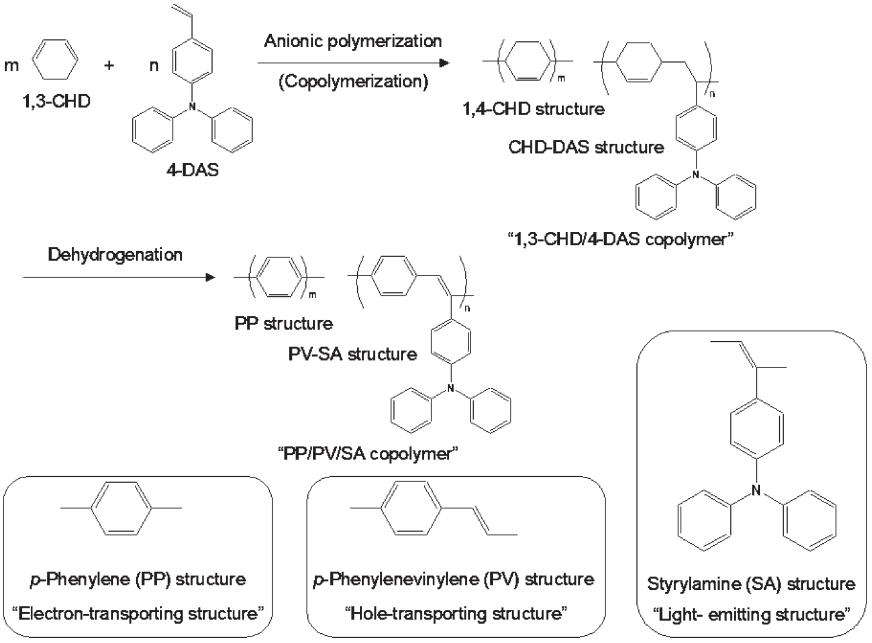
Experimental Section

Materials. Cyclohexane (≥99.5%), toluene (≥99.8%), and 1,3-CHD (97%) were refluxed over calcium hydride (CaH_2,

*Corresponding author. E-mail: itaru_natori@yahoo.co.jp.

 Published on Web 12/28/2010 © 2010 American Chemical Society

Scheme 1. Synthesis of Semiconducting Copolymer Consisting of *p*-Phenylene, *p*-Phenylenevinylene, and Styrylamine Ternary Molecular Structures



95%) and then distilled under dry argon. 4-DAS was prepared via a previously reported standard Wittig reaction.[41] 2,3-Dichloro-5,6-dicyano-1,4-benzoquinone (DDQ) and 2,3,5,6-tetrachloro-1,4-(*p*-)-benzoquinone (TCQ) were dried under reduced pressure. Other reagents were used as received unless otherwise stated. All reagents were purchased from Aldrich.

Polymerization. 4-DAS (0.50, 1.00, 2.50, 5.00, or 3.75 mmol) was placed into a well-dried 50 mL Schlenk tube and dried under reduced pressure. The Schlenk tube was alternately evacuated and filled with dry argon several times, and 10.0 mL of cyclohexane (or toluene) was added at room temperature (*ca.* 25 °C) using a syringe. 1,3-CHD (7.75, 8.75, or 11.25 mmol) was then supplied to this solution with a syringe and the solution was magnetically stirred under dry argon at room temperature for 10 min. *tert*-Butyllithium (*t*-BuLi; 1.70 mol/L in *n*-pentane) was then injected to this solution with a syringe and the reaction mixture was magnetically stirred under dry argon at room temperature. After the polymerization, dry methanol (MeOH) was added to the reaction mixture in an equimolar amount to the lithium (Li) atoms present in the reaction mixture, in order to terminate the reaction. The polymerization mixture was then poured into a large volume of ethanol to precipitate the polymer, which was then separated by filtration. The product was dried under reduced pressure at room temperature for 24 h, resulting in a white powdery polymer.

Dehydrogenation. 1,3-CHD/4-DAS copolymer (0.20 g) was placed into a 100 mL three-necked round-bottom flask equipped with a reflux condenser and dried under reduced pressure. The round-bottom flask was alternately evacuated and filled with dry argon several times. Dry and degassed 1,2,4-trichlorobenzene (TCBz, 20 mL) was then added with a syringe and the mixture was stirred until the polymer was fully dissolved. TCQ (10 mmol) was added under dry argon and the reaction mixture was magnetically stirred under dry argon at 150 °C for 24 h. After dehydrogenation, the reaction mixture was poured into a large volume of MeOH to precipitate the reaction product, which was then separated by filtration. The product was washed with an excess amount of MeOH and dried under reduced pressure at room temperature for 24 h, resulting in a brown powdery product in almost quantitative yield.

Measurements. The number-average molecular weight (M_n), weight-average molecular weight (M_w), and polydispersity index (PDI, M_w/M_n) were determined using gel permeation chromatography (GPC) equipment with a differential refractive index (RI) detector (Shimadzu RID-6A), a UV detector (Shimadzu SPD-6A), and a Shimadzu Shim-pack GPC-80 M column (length: 300 mm; diameter: 8 mm; effective molecular weight range of 100−4 000 000) at 40 °C. Tetrahydrofuran (THF) was used as the eluent, and the flow rate was 1.0 mL/min. A molecular weight calibration curve was obtained using polystyrene (PSt) standards. ^{1}H nuclear magnetic resonance (NMR) spectra of the polymers were measured in deuterated chloroform ($CDCl_3$) at 500 MHz using a Jeol ECA 500 spectrometer. UV/vis spectroscopic measurements were performed in THF using a Shimadzu UV-3101 PC with quartz cells. Photoluminescence (PL) spectra of the polymers were measured in THF using a Shimadzu RF-5300 PC with quartz cells.

Results and Discussion

Copolymerization of 1,3-CHD and 4-DAS. As shown in Scheme 1, to obtain PP/PV/SA copolymer, the synthesis of a prepolymer consisting of the 1,4-cyclohexadiene (1,4-CHD) and cyclohexadiene (CHD)-diphenylaminostyrene (DAS) structures was prerequisite. The 1,4-CHD structure can be obtained by the anionic polymerization of 1,3-CHD in cyclohexane with *t*-BuLi as an initiator.[44] Furthermore, *t*-BuLi acts as an initiator for the anionic polymerization of 4-DAS.[41] Therefore, in order to examine the formation of the 1,4-CHD and CHD−DAS structures in the polymer chain, copolymerization of various molar ratios of 1,3-CHD and 4-DAS was performed in cyclohexane with *t*-BuLi at room temperature for 4 h (Scheme 2), and the results obtained are summarized in Table 1.

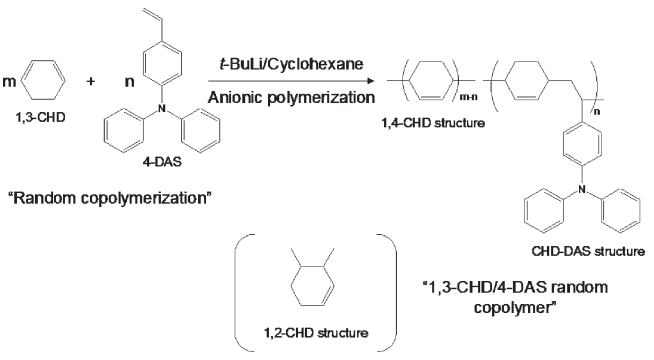
The copolymerization of 1,3-CHD and 4-DAS with *t*-BuLi in cyclohexane was considerably affected by the molar ratio of $[4\text{-DAS}]_0/[1,3\text{-CHD}]_0$. The polymerization system was homogeneous when the molar ratio of $[4\text{-DAS}]_0/[1,3\text{-CHD}]_0$ was lower than 0.32 (Table 1, nos. **1**−**3**). The orange anion was observed during the polymerization, and the yield of copolymer was increased with the increase of the molar ratio of $[4\text{-DAS}]_0/[1,3\text{-CHD}]_0$ (Table 1, nos. **1**−**3**). Thus, the addition of 4-DAS into the polymerization system appeared to accelerate the reaction rate in the copolymerization of 1,3-CHD and 4-DAS. However, the solubility of

Table 1. Copolymerization of 1,3-CHD and 4-DAS[a]

polymer no.	$[1,3\text{-CHD}]_0/[4\text{-DAS}]_0/[\text{Li}]_0$	yield (wt %)	M_n (g/mol)	PDI	CHD/DAS/*t* Bu (mol)[b]
1	15.5/1.00/1.00	76	1500	1.17	14.4/1.00/1.00
2	15.5/2.00/1.00	80	1970	1.18	14.7/2.10/1.00
3	15.5/5.00/1.00	94	2810	1.22	15.3/5.31/1.00
4[c]	15.5/10.0/1.00	86	3570	1.30	18.2/11.3/1.00
5[d]	15.5/10.0/1.00	98	3800	1.25	15.3/9.98/1.00

[a] Copolymerization of 1,3-CHD and 4-DAS with *t*-BuLi was carried out in cyclohexane (10.0 mL) under dry argon at room temperature for 4 h. Cycloliexane/*t*-BuLi = 10.0 mL/0.50 mmol. [b] Polymer chain structure. Estimated by ^{1}H NMR. [c] The reaction system was heterogeneous. [d] Toluene was used as polymerization solvent instead of cyclohexane.

Scheme 2. Random Copolymerization of 1,3-Cyclohexadiene and 4-Diphenylaminostyrene with *tert*-Butyllithium in Cyclohexane



polymer lithium (polymer−Li) decreased with the increase of the molar ratio of $[4\text{-DAS}]_0/[1,3\text{-CHD}]_0$, due to the low solubility of the DAS structure in cyclohexane.[41] When the molar ratio $[4\text{-DAS}]_0/[1,3\text{-CHD}]_0$ was 0.65 (Table 1, no. **4**), the color of the reaction system changed from orange to light orange and became an opaque solution. After some time, the reaction system gradually became heterogeneous and a light orange colored powder appeared. As a result, the yield of copolymer decreased, while the PDI range of the copolymer became broad (Table 1, no. **4**). The solubility of polymer-Li was improved when the copolymerization was carried out in toluene (Table 1, no. **5**), although the polymer chain contained a small amount of the 1,2-cyclohexadiene (1,2-CHD) structure (Scheme 2).[53]

Figure 1 shows typical ^{1}H NMR spectra for 1,3-CHD/4-DAS copolymers synthesized by anionic copolymerization with *t*-BuLi in cyclohexane [(a) polymer **1**, (b) polymer **2**, (c) polymer **3**]. The peaks from 6.8 to 7.3 ppm (Ha) are assigned to aromatic protons on the triphenylamino groups in the DAS structure and those around 5.7 ppm (Hc) are assigned to olefinic protons in the 1,4-CHD structure. The peaks from 1.2 to 2.6 ppm (Hb and Hd) are assigned to methine and methylene protons, respectively, in the 1,4-CHD and DAS structures. The peaks around 0.9 ppm are assigned to methyl protons in the butyl residues on the 1,4-CHD (*t*-Bu-CHD) and DAS (*t*-Bu-DAS) structures from *t*-BuLi.[44] Therefore, it was confirmed that each 1,3-CHD/4-DAS copolymer had the 1,4-CHD and DAS structures.

As shown in Figure 1, the peak from *t*-Bu-CHD was decreased with the increase of the molar ratio of $[4\text{-DAS}]_0/[1,3\text{-CHD}]_0$. When the molar ratio of $[4\text{-DAS}]_0/[1,3\text{-CHD}]_0$ was 0.32 (Figure 1c), the peaks due to *t*-Bu-CHD almost disappeared. Therefore, in the anionic polymerization for the copolymerization of 1,3-CHD and 4-DAS with *t*-BuLi in cyclohexane, the initiation reaction of 4-DAS is thought to be considerably faster than that of 1,3-CHD.

With respect to the polymer chain structure of 1,3-CHD/4-DAS copolymer, the molar ratio of 1,4-CHD structure/DAS structure/ *t*-Bu residue [CHD/DAS/*t*-Bu (mol)] in the polymer chain was calculated from ^{1}H NMR spectra of

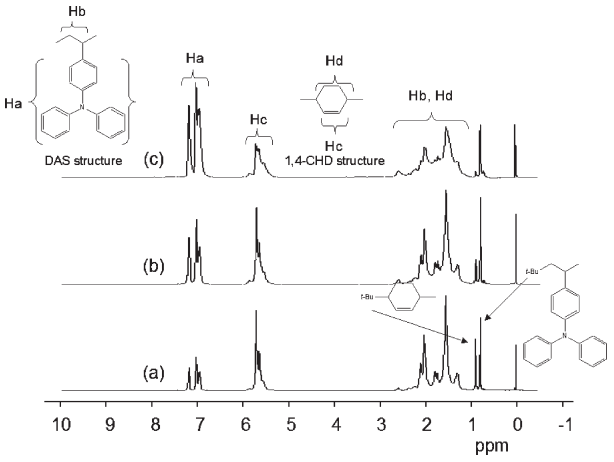


Figure 1. ^{1}H NMR spectra of 1,3-cyclohexadiene/4-diphenylaminostyrene random copolymers (a, M_n = 1500, PDI 1.17, polymer **1**; b, M_n = 1970, PDI 1.18, polymer **2**; c, M_n = 2810, PDI 1.22, polymer **3**), measured in a 3.0 wt % solution of $CDCl_3$ at 50 °C.

1,3-CHD/4-DAS copolymers, as shown in Table 1. Therefore, the conversion (%) from 1,3-CHD to the 1,4-CHD structure (or from 4-DAS to the DAS structure) can be calculated from the yield of 1,3-CHD/4-DAS copolymer and CHD/DAS/*t*-Bu (mol) as follows:

$$\text{Conversion (\%) of 1,3-CHD (or 4-DAS)} = [x/\text{1,3-CHD (or 4-DAS) (g)}] \times 100;$$

$$x = yz, z = 80a\ (\text{or}271b)/80a + 271b + (57+1)c$$

where x, y, z, a, b, c, 80, 271, 57, and 1 were the yield (g) of the 1,4-CHD (or DAS) structure, yield (g) of 1,3-CHD/4-DAS copolymer, wt % of the 1,4-CHD (or DAS) structure, molar ratio of the 1,4-CHD structure, molar ratio of the DAS structure, molar ratio of the *t*-Bu residue, molecular weight of the 1,4-CHD structure, molecular weight of the DAS structure, molecular weight of the *t*-Bu residue, and the molecular weight of terminal hydrogen atoms formed through the termination reaction by MeOH, respectively.

From the results of Table 1, the conversions of 1,3-CHD for polymers **1**−**3** were 72, 75, and 88%, and that of 4-DAS was 76, 83, and 95%, respectively. That is, when the molar ratio of $[4\text{-DAS}]_0/[1,3\text{-CHD}]_0$ was lower than 0.32, the conversion of 1,3-CHD was close to that of 4-DAS. Therefore, the copolymerization of 1,3-CHD and 4-DAS with *t*-BuLi in cyclohexane appears to be random copolymerization, and it is thought to afford the 1,3-CHD/4-DAS random copolymer with 1,4-CHD and CHD−DAS structures in the polymer chain (Scheme 2).

Characteristics of Copolymerization. In order to examine the characteristics of the copolymerization of 1,3-CHD and 4-DAS in detail, the polymerization of a mixture of 1,3-CHD and 4-DAS was carried out in cyclohexane

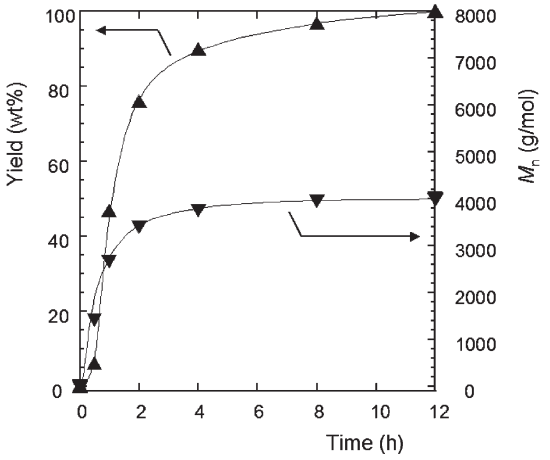


Figure 2. Time−yield and time−M_n curves for the copolymerization of 1,3-cyclohexadiene and 4-diphenylaminostyrene with *tert*-butyllithium in cyclohexane. Polymerization was performed under dry argon at room temperature (*ca.* 25 °C). $[1,3\text{-cyclohexadiene}]_0/[4\text{-diphenylaminostyrene}]_0/[tert\text{-butyllithium}]_0 = 22.5/7.50/1.00$. 1,3-cyclohexadiene/4-diphenylaminostyrene/cyclohexane = 11.25 mmol/3.75 mmol/10.0 mL.

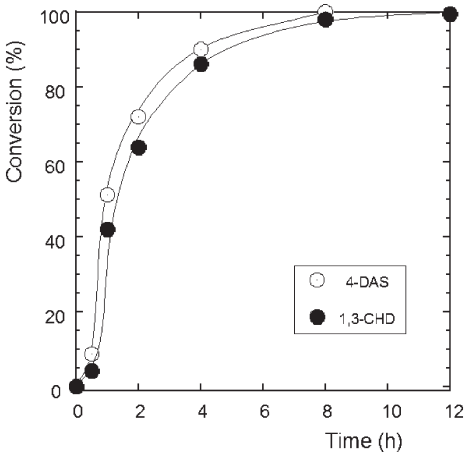


Figure 3. Time−conversion curves for the copolymerization of 1,3-cyclohexadiene and 4-diphenylaminostyrene with *t*-butyllithium in cyclohexane. Polymerization was performed under dry argon at room temperature (*ca.* 25 °C). $[1,3\text{-cyclohexadiene}]_0/[4\text{-diphenylaminostyrene}]_0/[t\text{-butyllithium}]_0 = 22.5/7.50/1.00$. 1,3-cyclohexadiene/4-diphenylaminostyrene/cyclohexane = 11.25 mmol/3.75 mmol/10.0 mL.

at room temperature for 12 h using *t*-BuLi as an initiator ($[1,3\text{-CHD}]_0/[4\text{-DAS}]_0/[\text{Li}]_0 = 22.5/7.50/1.00$).

Figure 2 shows typical time−yield and time−M_n curves for the copolymerization of 1,3-CHD and 4-DAS with *t*-BuLi in cyclohexane. The yield (wt %) of copolymer was increased with the passage of time. After 12 h, an almost quantitative yield of copolymer was obtained. The M_n of the copolymer gradually approached 4000 (g/mol), which was close to the value calculated from the molar ratio of $[1,3\text{-CHD}]_0/[4\text{-DAS}]_0/[\text{Li}]_0 = 22.5/7.50/1.00$ ($22.5 \times 80 + 7.5 \times 271 + 57 + 1 = 3891$).

Figure 3 shows typical time−conversion curves of 1,3-CHD and 4-DAS during the copolymerization. The conversion of 4-DAS was close to that of 1,3-CHD, although the molar ratio of $[1,3\text{-CHD}]_0/[4\text{-DAS}]_0$ was 0.33 ($[1,3\text{-CHD}]_0/[\text{DAS}]_0/[\text{Li}]_0 = 22.5/7.50/1.00$). The conversions of 4-DAS and 1,3-CHD were 100% after 8 h and 98% after 12 h, respectively. It should be noted that the GPC peak is unimodal (Figure 4), which indicates that the product is not a

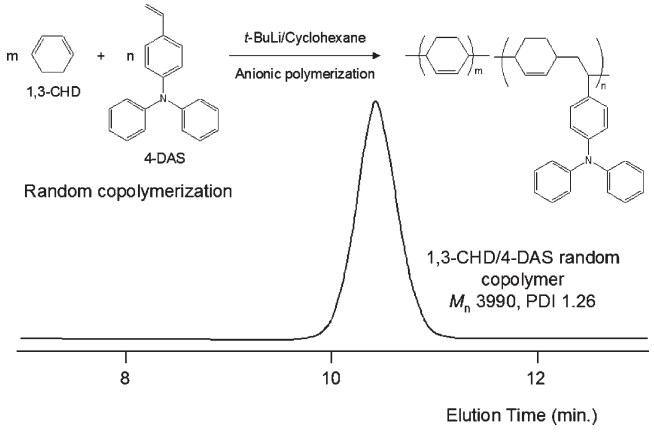


Figure 4. GPC trace of 1,3-cyclohexadiene/4-diphenylaminostyrene random copolymer (M_n = 3990, PDI 26) in THF at 40 °C (sample/THF = 5.0 mg/5.0 mL).

mixture of homopolymers. This polymerization behavior suggests that the copolymerization of 1,3-CHD and 4-DAS with *t*-BuLi in cyclohexane is a random copolymerization. Therefore, the copolymer obtained from 1,3-CHD and 4-DAS (Figure 4, M_n 3990, PDI 1.26) is thought to have a structure close to a random copolymer having 1,4-CHD and CHD−DAS structures.

Subsequently, three 1,3-CHD/4-DAS random copolymers having different molecular weight and same polymer chain structure were synthesized using the obtained information. The copolymerization of 1,3-CHD and 4-DAS with *t*-BuLi was carried out in cyclohexane at room temperature for 24 h ($[1,3\text{-CHD}]_0/[4\text{-DAS}]_0/[\text{Li}]_0 = 15.0/5.00/1.00$, 30.0/10.0/1,00, and 60.0/20.0/1.00, $[4\text{-DAS}]_0/[1,3\text{-CHD}]_0 = 0.33$) and the results obtained are presented in Table 2.

After copolymerization, each copolymer was obtained in almost quantitative yield. The M_n of the copolymer was increased with the increase in the molar ratio of $[1,3\text{-CHD} + 4\text{-DAS}]_0/[\text{Li}]_0$. These copolymers are 1,3-CHD/4-DAS random copolymers having the 1,4-CHD and CHD−DAS structures in the polymer chain (Scheme 2).

Dehydrogenation of PDAS. In order to obtain PP/PV/SA copolymer, the complete dehydrogenation of 1,3-CHD/4-DAS copolymer is required (Scheme 1). We have previously reported the dehydrogenation reaction of the 1,4-CHD structure in detail through the dehydrogenation of poly(1,3-CHD) (PCHD) (Scheme 3a).[36,39,46] On the other hand, the dehydrogenation of PDAS has not been reported (Scheme 3b); therefore, the dehydrogenation reaction of the CHD−DAS structure to form the PV-SA structure has been unclear until now.

Wangwijit et al. observed the abstraction of the benzylic hydrogen atom in triphenylamine derivatives/benzaldehyde copolymer using DDQ as an oxidation reagent.[54] François et al. reported that the abstraction of α- and β-hydrogen atoms of the styrene (St) structure in 1,3-CHD/St copolymer occurred with TCQ.[23] Furthermore, DDQ and TCQ act as good dehydrogenation reagents for the 1,4-CHD structure in PCHD to form the PP structure.[36,39] Therefore, it was expected that DDQ and TCQ have potential for the dehydrogenation of 1,3-CHD/4-DAS copolymer.

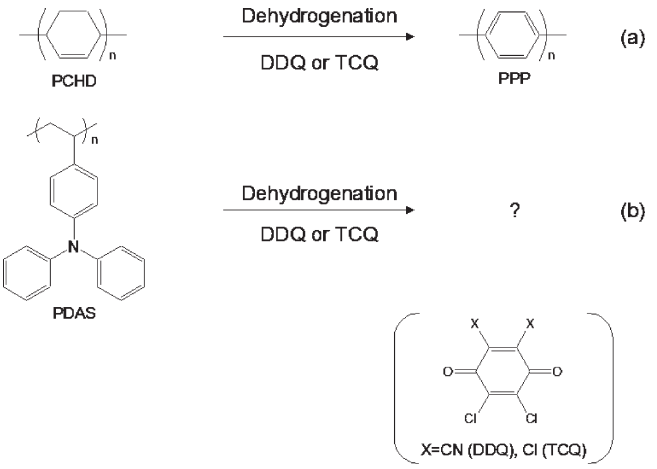
Prior to the dehydrogenation of 1,3-CHD/4-DAS copolymer, the dehydrogenation of PDAS with DDQ (or TCQ) (Scheme 4) was performed to obtain basic information on the dehydrogenation of the DAS structure.[55] The dehydrogenation of PDAS with DDQ was carried out in 1,2-dichlorobenzene (DCBz, 20.0 mL) under dry argon at 90 °C for 96 h

Table 2. Synthesis of 1,3-CHD/4-DAS Copolymer[a]

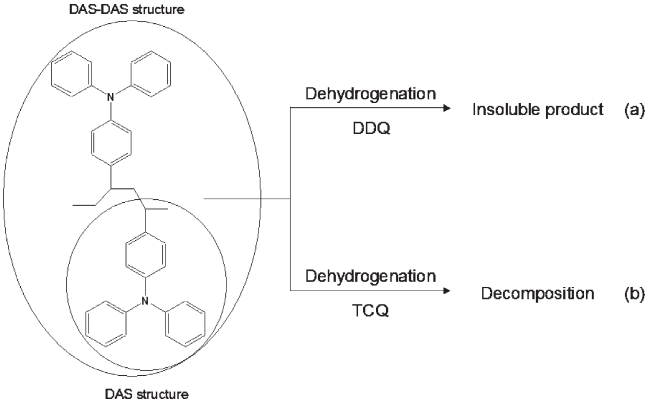
polymer no.	$[1,3\text{-CHD}]_0/[4\text{-DAS}]_0/[\text{Li}]_0$	yield (wt %)	M_n (g/mol)	PDI	CHD/DAS/*t*-Bu (mol)[b]
6	15.0/5.00/1.00	100	2790	1.22	15.2/5.20/1.00
7	30.0/10.0/1.00	97	5710	1.23	30.7/10.1/1.00
8	60.0/20.0/1.00	94	11 300	1.25	61.7/20.7/1.00

[a] Copolymerization of 1,3-CHD and 4-DAS with *t*-BuLi was carried out in cyclohexane (10.0 mL) under dry argon at room temperature for 24 h. Cyclohexane/*t*-BuLi = 10.0 mL/0.50, 0.25, or 0.125 mmol. [b] Polymer chain structure. Estimated by ^{1}H NMR.

Scheme 3. Dehydrogenation of Poly(1,3-cyclohexadiene) and Poly(4-diphenylaminostyrene)



Scheme 4. Dehydrogenation Reaction of Poly(4-diphenylaminostyrene) with 2,3-Dichloro-5,6-dicyano-1,4-benzoquinone [or 2,3,5,6-Tetrachloro-1,4-(*p*-)-benzoquinone]



(polymer/DDQ = 0.20 g/10.0 mmol, a typical complete dehydrogenation reaction condition of DDQ for the 1,4-CHD structure). Meanwhile, the dehydrogenation of PDAS with TCQ was carried out in TCBz (20.0 mL) under dry argon at 150 °C for 24 h (polymer/TCQ = 0.20 g/10.0 mmol, a typical complete dehydrogenation reaction condition of TCQ for the 1,4-CHD structure). The results obtained are summarized in Table 3.

When DDQ was used as dehydrogenation reagent (Table 3, no. **9**), the obtained black product was insoluble in organic solvents such as THF, cyclohexane, toluene, and MeOH. The yield was 155 wt %, which suggested this insoluble product was a DDQ adduct of PDAS. Therefore, DDQ was thought to be an unfavorable dehydrogenation reagent for the DAS structure (Scheme 4a). On the other hand, when TCQ was used as a dehydrogenation reagent (Table 3, no. **10**), the polymer chain of PDAS was almost completely decomposed. Therefore, it was expected that the abstraction of α- and *β*-hydrogen atoms in the DAS structures of PDAS was accompanied by decomposition of the C−C bonds between the DAS structures in the polymer chain (Scheme 4b). The results suggest that TCQ has potential as a dehydrogenation reagent for the complete dehydrogenation of the CHD−DAS structure to obtain a PV−SA structure (Scheme 1).

Effect of Polymer Chain Structure on the Dehydrogenation of 1,3-CHD/4-DAS Random Copolymer with TCQ. In order to obtain a PP/PV/SA copolymer, the dehydrogenation of 1,3-CHD/4-DAS copolymer with TCQ (or DDQ) was performed. When the dehydrogenation of 1,3-CHD/4-DAS copolymer with DDQ was carried out in DCBz under dry argon at 90 °C for 96 h, the reaction product was insoluble, similar to the case for PDAS (Table 4, no. 13, Scheme 5a). However, when the dehydrogenation of 1,3-CHD/4-DAS copolymer with TCQ was performed in TCBz under dry argon at 150 °C (or 130 °C) for 24 h, a soluble product was obtained in almost quantitative yield. The results obtained are summarized in Table 4.

The M_n of dehydrogenated copolymer was close to that of each original copolymer (Table 4, nos. **11**, **12**, **14**, **16**, and **17**), except for polymer no. **15** in Table 4. This means that decomposition of the polymer chain does not occur in the dehydrogenation of 1,3-CHD/4-DAS copolymer with TCQ when the molar ratio of $[4\text{-DAS}]_0/[1,3\text{-CHD}]_0$ is lower than 0.33 (Table 4, nos. **11**, **12**, **14**, **16**, and **17**), in contrast to the dehydrogenation of PDAS with TCQ (Table 3, no. **10**). Meanwhile, when the molar ratio of $[4\text{-DAS}]_0/[1,3\text{-CHD}]_0$ is 0.65 (Table 4, no. **15**), a small portion of the polymer chain with the DAS−DAS structure is thought to be decomposed. That is, the sequence of DAS structures (i.e., DAS-DSA structure, Scheme 4) does not appear to be present in the polymer chain when the molar ratio of $[4\text{-DAS}]_0/[1,3\text{-CHD}]_0$ is lower than 0.33.

Therefore, 1,3-CHD/4-DAS copolymer obtained by the copolymerization of 1,3-CHD and 4-DAS (molar ratio of $[4\text{-DAS}]_0/[1,3\text{-CHD}]_0$ lower than 0.33) with *t*-BuLi in cyclohexane (Tables 1, nos. **1**−**3** and Table 2, nos. **6**−**8**) is thought to be a random copolymer consisting of 1,4-CHD and CHD−DAS structures (Scheme 2). The CHD−DAS structure seems to be stable during dehydrogenation with TCQ, and the PV-SA structure is successfully obtained without decomposition of the C−C bond in the CHD−DAS structure (Scheme 5b).

Figure 5 shows typical ^{1}H NMR spectra of the dehydrogenated 1,3-CHD/4-DAS copolymers [(a) polymer **11**, (b) polymer **12**, (c) polymer **14**]. Compared with the ^{1}H NMR spectra of 1,3-CHD/4-DAS copolymers (Figure 1), the signals from olefinic protons [around 5.7 ppm (Hc)] are absent, which indicates complete dehydrogenation of the 1,4-CHD structure. In addition, the signals from methine and methylene protons in the 1,4-CHD and DAS structures [1.2 to 2.6 ppm (Hb and Hd)] are also entirely absent, which confirms the complete dehydrogenation of the 1,4-CHD and DAS structures. New peaks at around 7.6 ppm (Hf) are assigned to aromatic protons in the PP structure. New broad peaks at around 6.8 ppm (He) are assigned to olefinic protons in the SA structure. The peaks at around 0.9 ppm are assigned to methyl protons in the butyl residues on both the

Table 3. Dehydrogenation of Poly(4-diphenylaminostyrene)

		before dehydrogenation		after dehydrogenation		
polymer no.	quinone	M_n (g/mol)	PDI	M_n(g/mol)	PDI	yield (wt %)
9[a]	DDQ	2730	1.12	insoluble	—	155
10[b]	TCQ	2780	1.10	—	—	trace

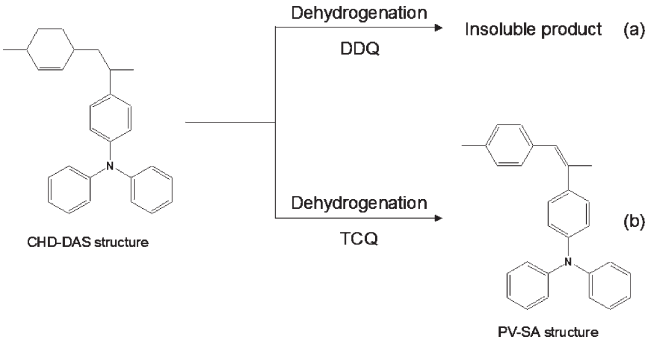
[a] Dehydrogenation of PDAS with DDQ was carried out in 1,2-dichlorobenzene (20.0 mL) under dry argon at 90 °C for 96 h (polymer/DDQ = 0.20 g/10.0 mmol). [b] Dehydrogenation of PDAS with TCQ was carried out in 1,2,4-trichlorobenzene (20.0 mL)under dry argon at 150 °C for 24 h (polymer/TCQ = 0.20 g/10.0 mmol).

Table 4. Dehydrogenation of 1,3-CHD/4-DAS Copolymer with 2,3,5,6-Tetrachloro-1,4(*p*)-benzoquinone[a]

		before dehydrogenation		after deliydrogenation	
polymer no.	prepolymer	M_n (g/mol)	PDI	M_n (g/mol)	PDI
13	polymer **1**	1500	1.17	1900	1.24
15	polymer **2**	1970	1.18	2360	1.28
13[b]	polymer **3**	2810	1.22	insoluble	—
14	polymer **3**	2810	1.22	2780	1.29
15	polymer **4**	3570	1.30	2400	1.43
16	polymer **7**	5710	1.23	5650	1.29
17	polymer **8**	11 300	1.25	10 950	1.30

[a] Dehydrogenation of 1,3-CHD/4-DAS copolymer with TCQ was carried out in 1,2,4-trichlorobenzene under dry argon at 150 °C (nos. **11**, **12**, **14**, and **15**) or 130 °C (nos. **16** and **17**) for 24 h. Each dehydrogenated polymer was obtained in almost quantitative yield. [b] Dehydrogenation of l,3-CHD/4-DAS copolymer with DDQ was carried out in 1,2-dichlorobenzene under dry argon at 90 °C for 96 h.

Scheme 5. Dehydrogenation of 1,3-Cyclohexadiene/4-Diphenylaminostyrene Random Copolymer



PP and SA structures. Therefore, complete dehydrogenation seems to be successfully achieved not only for the 1,4-CHD structure, but also for the DAS structure (Schemes 5b). As a result, PP/PV/SA copolymer is thought to be obtained through the complete dehydrogenation of the 1,3-CHD/4-DAS random copolymer with TCQ.

UV/vis and PL spectra of the completely dehydrogenated 1,3-CHD/4-DAS copolymer (Table 4, no. 14) are shown in Figure 6. The UV/vis spectrum (Figure 6a) shows absorption bands in the region from 260 to 440 nm, and the maximum point ($\lambda^{ab}{}_{max}$) of absorption was at approximately 310 nm. PL spectra of the completely dehydrogenated 1,3-CHD/4-DAS copolymer (Table 4, no. **14**), PPP (M_n 1640, PDI 1.26),[56] and PDAS (M_n 2730, PDI 1.12)[55] are shown in Figure 6b−d. Two emission peaks around 400 and 470 nm are observed in the PL spectrum of the completely dehydrogenated 1,3-CHD/4-DAS copolymer (Figure 6b). The emission peak around 400 nm is overlaps with the emission peak of PPP (Figure 6c). Therefore, the completely dehydrogenated 1,3-CHD/4-DAS copolymer is thought to have the PP structure in the polymer chain. However, no emission peak at around 380 nm is observed, although this emission peak is caused by PDAS (Figure 6d). Therefore, the completely dehydrogenated 1,3-CHD/4-DAS copolymer has no DAS

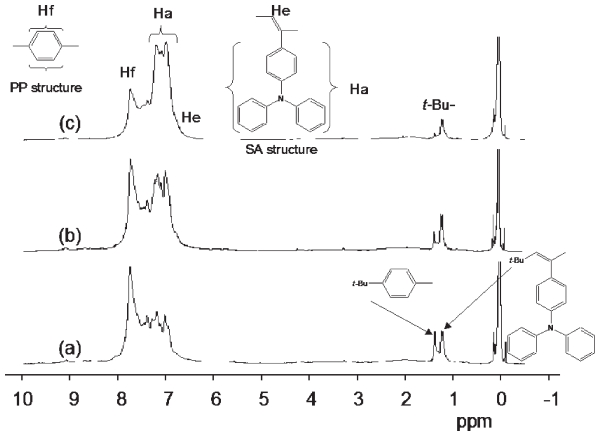


Figure 5. ^{1}H NMR spectra of dehydrogenated 1,3-cyclohexadiene/4-diphenylaminostyrene random copolymers (a, M_n = 1900, PDI 24, polymer **11**; b, M_n = 2360, PDI 1.28, polymer **12**; c, M_n = 2780, PDI 1.29, polymer **14**), measured in a 3.0 wt % solution of $CDCl_3$ at 50 °C.

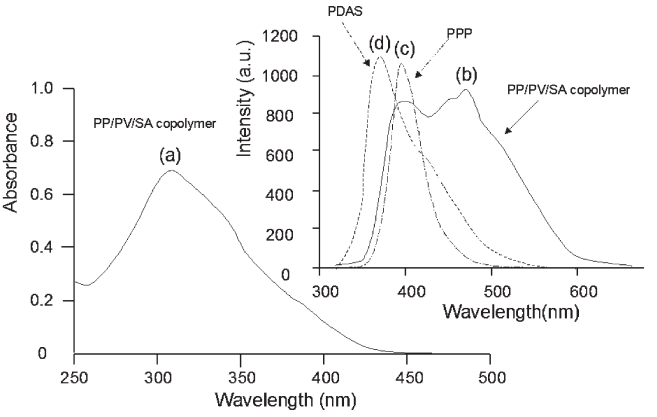


Figure 6. (a) UV/vis spectrum of completely dehydrogenated 1,3-cyclohexadiene/4-diphenylaminostyrene random copolymer (polymer **14**). (b-d) PL spectra of completely dehydrogenated 1,3-cyclohexadiene/4-diphenylaminostyrene random copolymers (b, polymer **14**), poly(*p*-phenylene) (c, M_n 1640, PDI 1.26)), and poly(4-diphenylaminostyrene) (d, M_n 2730, PDI 1.12), measured in tetrahydrofuran. Polymer/solvent = 0.10 mg/10.0 mL. PL excitation wavelengths were 310 nm for completely dehydrogenated 1,3-cyclohexadiene/4-diphenylaminostyrene random copolymer and poly(4-diphenylaminostyrene) and 330 nm for poly(*p*-phenylene).

structure in the polymer chain. A new emission peak at around 470 nm is observed for the completely dehydrogenated 1,3-CHD/DAS copolymer, and this is thought to be due to the SA structure.[52] From the results obtained, it was concluded that the completely dehydrogenated 1,3-CHD/4-DAS random copolymer is PP/PV/SA copolymer (Scheme 1).

Conclusion

The synthesis of well-defined semiconducting copolymers consisting of PP, PV, and SA ternary molecular structures (PP/

PV/SA copolymer) was attempted through the anionic copolymerization of 1,3-CHD and 4-DAS and the complete dehydrogenation of 1,3-CHD/4-DAS copolymer. To obtain PP/PV/SA copolymer, the 1,3-CHD/4-DAS random copolymer, consisting of the 1,4-CHD and CHD−DAS structures as a prerequisite prepolymer, was prepared by the random copolymerization of 1,3-CHD and 4-DAS with *tert*-butyllithium in cyclohexane. When the molar ratio of $[4\text{-DAS}]_0/[1,3\text{-CHD}]_0$ was lower than 0.33, the obtained 1,3-CHD/4-DAS copolymer consisted of the 1,4-CHD and CHD−DAS structures. When the molar ratio of $[4\text{-DAS}]_0/[1,3\text{-CHD}]_0$ was 0.65, the obtained 1,3-CHD/4-DAS copolymer contained the DAS−DAS structure in the polymer chain. Dehydrogenation of the 1,3-CHD/4-DAS copolymer with DDQ afforded an insoluble reaction product. The DAS−DAS structure was decomposed during dehydrogenation with TCQ. However, the CHD−DAS structure was stable during dehydrogenation with TCQ. Decomposition of the polymer chain did not occur during dehydrogenation of the 1,3-CHD/4-DAS random copolymer consisting of 1,4-CHD and CHD−DAS structures, and the completely dehydrogenated 1,3-CHD/4-DAS random copolymer was obtained in almost quantitative yield. GPC, ^{1}H NMR, UV/vis, and PL analyses confirmed that the completely dehydrogenated 1,3-CHD/4-DAS random copolymer was PP/PV/SA copolymer.

References and Notes

(1) Burroughes, J. H.; Bradley, D. D. C.; Brown, A. R.; Marks, R. N.; Mackey, K.; Friend, R. H.; Bum, R. L.; Holmes, A. B. *Nature* **1990**, *347*, 539–541.
(2) Yu, G.; Gao, J.; Hummelen, J. C.; Wudl, F.; Heeger, A. J. *Science* **1995**, *270*, 1789–1791.
(3) Koezuka, H.; Tsumura, A. *Synth. Met*. **1989**, *28*, 753–760.
(4) Peng, H.; Bao, Z. N.; Galvin, M. E. *Chem. Mater*. **1998**, *10*, 2086–2090.
(5) Liu, Y.; Ma, H.; Jen, A. K-Y. *Chem. Commun*. **1998**, 2747–2748.
(6) Zhan, X.; Liu, Y.; Zhu, D.; Jiang, X.; Jen, A. K-Y. *Chem. Macromol. Chem. Phys*. **2001**, *202*, 2341–2345.
(7) Liu, Z.; Zhang, Y.; Hu, Y.; Su, G.; Ma, D.; Wang, L.; Jing, X.; Wang, F. *J. Polym. Sci., Part A: Polym. Chem*. **2002**, *40*, 1122–1126.
(8) Ma, B.; Kim, J. K.; Deng, L.; Poulsen, D. A.; Thompson, M. E.; Fréchet, J. M. J. *Macromolecules* **2007**, *40*, 8156–8161.
(9) Washizu, T.; Pei, Y.; Ha, J.; Vacha, M.; Tani, K.; Ogino, K.; Sato, H. *J. Polym. Sci., Part A: Polym. Chem*. **2007**, *45*, 3083–3089.
(10) Wang, P.; Chai, C.; Yang, Q.; Wang, F.; Shen, Z.; Guo, H.; Chen, X.; Fan, X.; Zou, D.; Zhou, Q. *J. Polym. Sci., Part A: Polym. Chem*. **2008**, *46*, 5452–5460.
(11) Tao, Y.; Ma, B.; Segalman, R. A. *Macromolecules* **2008**, *41*, 7152–7159.
(12) Lee, T. H.; Lai, K. M.; Leung, L. M. *Polymer* **2009**, *50*, 4602–4611.
(13) Kim, D. U.; Tsutsui, T.; Saito, S. *Chem. Lett*. **1995**, 587–588.
(14) Kim, D. U.; Tsutsui, T.; Saito, S. *Polymer* **1995**, *36*, 2481–2483.
(15) Lu, J.; Hlil, A. R.; Sun, Y.; Hay, A. S.; Maindorn, T.; Dodelet, J.-P.; D'Iorio, M. *Chem. Mater*. **1999**, *11*, 2501–2507.
(16) Deng, L.; Furuta, P. T.; Garon, S.; Li, J.; Kavulak, D.; Thompson, M. E.; Fréchet, J. M. J. *Chem. Mater*. **2006**, *18*, 386–395.
(17) Marvel, C. S.; Hartzell, G. E. *J. Am. Chem. Soc*. **1959**, *81*, 448–452.
(18) Frey, D. A.; Hasegawa, M.; Marvel, C. S. *J. Polym. Sci., Part A: Polym. Chem*. **1963**, *1*, 2057–2065.
(19) Lefebver, G.; Dawans, F. *J. Polym. Sci., Part A: Polym. Chem*. **1964**, *2*, 3277–3295.
(20) Cassidy, P. E.; Marvel, C. S. *J. Polym. Sci., Part A: Polym. Chem*. **1965**, *3*, 1533–1565.
(21) Zhong, X. F.; François, B. *Makromol. Chem. Rapid. Commun*. **1988**, *9*, 411–416.
(22) Zhong, X. F.; François, B. W. *Makromol. Chem*. **1991**, *192*, 2277–2291.
(23) François, B.; Izzillo, S.; Iratçabal, P. *Synth. Met*. **1999**, *102*, 1211–1212.
(24) Williamson, D. T.; Buchanan, T. D.; Long, T. E. *Polym. Prepr*. **2002**, *43*, 1201–1202.
(25) Mignard, E.; Hiorns, R. C.; François, B. *Macromolecules* **2002**, *35*, 6132–6141.
(26) Rembaum, A.; Henly, A.; Waits, H. *Prepr. Pap*. (*Am. Chem. Soc., Div. Polym. Chem*.) **1963**, *4*, 109–120.
(27) Eisenberg, A.; Rembaum, A. *J. Polym. Sci., Part B: Polym. Lett*. **1964**, *2*, 157–162.
(28) Michel, R. H.; Baker, W. P. *J. Polym. Sci., Part B: Polym. Lett*. **1964**, *2*, 163–168.
(29) Stolka, M.; Yanus, J. F.; Pearson, J. M. *Macromolecules* **1976**, *9*, 715–719.
(30) Yanus, J. F.; Stolka, M.; Pearson, J. M. *Macromolecules* **1976**, *9*, 719–723.
(31) Natori, I.; Natori, S. *Polym. Adv. Technol*. **2010**, *21*, 784–788.
(32) Natori, I. *Macromolecules* **2006**, *39*, 6017–6024.
(33) Feast, W. J.; Peace, R. J.; Sage, I. C.; Wood, E. L. *Polym. Bull*. **1999**, *42*, 167–174.
(34) Tew, G. N.; Pralle, M. U.; Stupp, S. I. *Angew. Chem., Int. Ed*. **2000**, *39*, 517–521.
(35) Natori, I.; Sato, H. *J. Polym. Sci., Part A, Polym. Chem*. **2006**, *44*, 837–845.
(36) Natori, I.; Natori, S.; Sato, H. *Macromolecules* **2006**, *39*, 3168–3174.
(37) Natori, I.; Sato, H. *J. Polym. Sci., Part A, Polym. Chem*. **2006**, *44*, 3526–3537.
(38) Natori, I.; Natori, S.; Sato, H. *Polymer* **2006**, *47*, 7123–7130.
(39) Natori, I.; Sato, H. *Polym. Int*. **2007**, *56*, 810–815.
(40) Natori, I.; Natori, S. *J. Polym. Sci., Part A, Polym. Chem*. **2008**, *46*, 3282–3293.
(41) Natori, I.; Natori, S.; Usui, H.; Sato, H. *Macromolecules* **2008**, *41*, 3852–3858.
(42) Natori, I.; Natori, S.; Sasaki, S.; Sekikawa, H.; Sato, H. *Polym. Adv. Technol*. **2008**, *19*, 1635–1642.
(43) Natori, I.; Natori, S.; Sasaki, S.; Sekikawa, H.; Sato, H. *Polym. Adv. Technol*. **2008**, *19*, 1868–1875.
(44) Natori, I.; Natori, S.; Sekikawa, H.; Sato, H. *J. Polym. Sci., Part A: Polym. Chem*. **2008**, *46*, 5223–5231.
(45) Natori, I.; Natori, S.; Sekikawa, H.; Sato, H. *React. Funct. Polym*. **2008**, *68*, 1266–1271.
(46) Natori, I.; Natori, S.; Ogino, K. *Macromolecules* **2009**, *42*, 1964–1969.
(47) Natori, I.; Natori, S.; Sekikawa, H.; Ogino, K. *React. Funct. Polym*. **2009**, *69*, 613–618.
(48) Natori, I.; Natori, S.; Sekikawa, H.; Ogino, K. *J. Polym. Sci., Part A: Polym. Chem*. **2009**, *48*, 342–350.
(49) Natori, I.; Natori, S.; Sekikawa, H.; Takahashi, T.; Ogino, K.; Tsuchiya, K.; Sato, H. *Polymer* **2010**, *51*, 1501–1506.
(50) Natori, I.; Natori, S.; Sekikawa, H.; Takahashi, T.; Sato, H. *J. Appl. Polym. Sci*. **2010**, *118*, 69–73.
(51) Blom, P. W. M.; de Jong, M. J. M.; Vleggaar, J. J. M. *Appl. Phys. Lett*. **1996**, *68*, 3308–3310.
(52) Hosokawa, C.; Kawasaki, N.; Sakamoto, S.; Kusumoto, T. *Appl. Phys. Lett*. **1992**, *61*, 2503–2505.
(53) Natori, I.; Natori, S. *J. Polym. Sci., Part A: Polym. Chem*. **2008**, *46*, 6604–6611.
(54) Wangwijit, T.; Sato, H.; Tantayanon, S. *Polym. Adv. Technol*. **2002**, *13*, 25–32.
(55) Each PDAS was obtained by the living anionic polymerization of 4-DAS with the benzyllithium/*N*,*N*,*N*′,*N*′-tetramethylethylenediamine (1.00/1.25) system in toluene ($[4\text{-DAS}]_0/[\text{Li}]_0 = 12.0$) according to the procedure previously reported.[41]
(56) PPP (M_n 1640, PDI 1.26) obtained in the previous paper (ref 44) was used.

Macromolecules
ARTICLE

Macromolecules **2011**, *44*, 263–268 **263**
DOI: 10.1021/ma1022346

Emulsifier-Free, Organotellurium-Mediated Living Radical Emulsion Polymerization of Styrene: Effect of Stirring Rate

Hirotaka Moribe, Yukiya Kitayama, Toyoko Suzuki, and Masayoshi Okubo*

Department of Chemical Science and Engineering, Graduate School of Engineering, Kobe University, Kobe 657-8501, Japan

Received September 28, 2010; Revised Manuscript Received November 30, 2010

ABSTRACT: The effect of stirring rate on control/livingness and particle formation in emulsifier-free organotellurium-mediated living radical emulsion polymerization (emulsion TERP) of styrene at 60 °C was investigated at two stirring rates (220 and 1000 rpm), in which styrene phase floated as a layer on an aqueous phase at 220 rpm or dispersed as droplets at 1000 rpm. A water-soluble TERP agent, poly(methacrylic acid) (PMAA)−methyltellanyl ($PMAA_{30}$-TeMe) (degree of polymerization of PMAA, 30), and a water-soluble thermal initiator, 4,4′-azobis(4-cyanovaleric acid), at high pH were used. The polymerization rate was not affected by the stirring rate, but the control/livingness was significantly improved when the stirring rate was increased from 220 to 1000 rpm. This difference would be caused by a larger amount of consumed $PMAA_{30}$-TeMe in the aqueous phase and higher monomer concentration inside polymerizing particles as polymerization loci at 1000 rpm than at 220 rpm. The stirring rate also affected the particle size distribution: both nanometer-sized and submicrometer-sized particles were prepared at 220 rpm, and mainly nanometer-sized particles were prepared at 1000 rpm. From these results, it is concluded that the stirring rate is an important parameter in emulsion TERP to obtain good control/livingness and control particle formation.

Introduction

Controlled/living radical polymerization (CLRP) has dramatically developed as a powerful tool for the preparation of well-defined polymer having a narrow molecular weight distribution (MWD) and complex macromolecular architecture in the past 15 years.[1−4] Several methods were developed as CLRP techniques, for example, nitroxide-mediated living radical polymerization (NMP),[5−8] atom transfer radical polymerization (ATRP),[9−14] and reversible addition−fragmentation chain transfer (RAFT) polymerization.[15−17]

Recently, Yamago and co-workers developed a novel CLRP technique: organotellurium-mediated living radical polymerization (TERP). TERP has a sufficiently high chain transfer constant (C_{ex}), which is important for the control/livingness, and does not form intermediate radicals, resulting in the less selectivity of macroinitiator for the preparation of block copolymer. Until now, TERP has been developed mainly in homogeneous systems such as bulk and solution polymerizations since 2002.[18−26]

In recent years, the applications of CLRP techniques to aqueous heterogeneous systems, such as miniemulsion polymerization, microemulsion polymerization, and emulsion polymerization, have been taken notice because of the nontoxic environmentally friendly media.[4,27] Because control agent used for CLRP was so far normally hydrophobic, most of the researches were mainly studied in miniemulsion polymerization, which proceeds ideally in monomer droplets.[28−32]

Emulsion polymerization is industrially useful; however, it had been difficult to apply CLRP to the system from a viewpoint of controlled/livingness because the hydrophobic control agent does not smoothly transfer from monomer droplets into micelles as polymerization loci via an aqueous phase, although a part of hydrophobic control agent was also partitioned in the monomer-swollen micelles.[33−35] For example, in the case of RAFT polymerization in emulsion system, the unreacted RAFT agent remained even after polymerization.[34] In order to solve this problem, Hawkett and co-workers proposed a novel efficient method, which is an emulsifier-free RAFT emulsion polymerization utilizing the self-assembly mechanism.[36,37] Since then, some successful researches of applying NMP[38−44] and RAFT[45−51] in emulsion polymerization systems have been reported.

Hawkett and co-workers employed monomer feed method throughout the polymerization where there was no monomer droplet in the system to prevent the adsorption of RAFT agent having surface activity at monomer/water interface.[37] The adsorption would hinder RAFT agent from entering polymerization loci smoothly, resulting in bad control of molecular weight distribution. However, it needs a long polymerization time to carry out emulsion polymerization without monomer droplet because monomer must be slowly added to the system.

In a previous work, employing the self-assembly approach, we succeeded to apply TERP of *n*-butyl acrylate (BA) to a batch emulsifier-free emulsion polymerization system (emulsion TERP) using a highly hydrophilic TERP agent, which is poly(methacrylic acid) (PMAA)−methyltellanyl ($PMAA_{30}$-TeMe) (degree of polymerization of PMAA: 30) to suppress the adsorption of control agent at monomer/water interface.[52] It was confirmed that stirring rate significantly affected the polymerization rate (R_p), MWD of the obtained polymers, and particle size distribution. Such phenomena due to the stirring rate have not been revealed yet.

Styrene is commonly used as a monomer in a typical model system of emulsion polymerization and poly(styrene) (PS) particles with a higher glass temperature (T_g) than room temperature, which is very convenient to estimate accurately the particle size with a transmission electron microscope (TEM), whereas poly(BA) (PBA) particles with much lower T_g than room temperature flatten out on a TEM grid. It was already confirmed that

*Corresponding author. Tel/Fax: +81-78-803-6161.

© 2010 American Chemical Society

Published on Web 12/31/2010

emulsion TERP of styrene at 220 rpm proceeded, maintaining livingness.[53]

In this article, emulsion TERP of styrene will be carried out at two different stirring rates of 220 and 1000 rpm to clarify the effects of stirring rate in the emulsion TERP on R_p, control/livingness, and particle size distribution, in comparison with the previous results obtained in the emulsion TERP of BA.[52]

Experimental Part

Materials. Styrene (Nacalai Tesque, Japan) was purified by distillation under reduced pressure in a nitrogen atmosphere. Deionized water used in all experiments was obtained using an Elix UV (Millipore Japan) purification system and had a resistivity of 18.2 MΩ cm^{-1}. 4,4′-Azobis(4-cyanovaleric acid) (V-501, Wako Pure Chemicals, Japan) was purified by recrystallization in water. $PMAA_{30}$-TeMe (ratio of weight-average molecular weight (M_w) to number-average molecular weight (M_n) (M_w/M_n) ~ 1.1) was supplied from Otsuka Chemical Co., Ltd., Osaka, Japan, and trimethylsilyldiazomethane (TMSD, Nacalai Tesque) was used as received.

Emulsion TERP of Styrene. A typical procedure is described below. Water and styrene were separately deoxygenized by nitrogen bubbling. First, V-501 (10.5 mg, 37.8 μmol) and NaOH aqueous solution (45 g, 1.68×10^{-3} M, equivalent to carboxyl groups of V-501) were added into a round-bottom Schlenk flask, which was sealed off with a silicon rubber septum and then degassed using several N_2/vacuum cycles. $PMAA_{30}$-TeMe (295 μL, 0.127 M aqueous solution neutralized by NaOH (pH = 13), 37.8 μmol) was injected into the system using a syringe. After styrene (1.57 g, 15 mmol) had been injected, and the mixture was degassed again using several vacuum/N_2 cycles, the flask was then placed in a water bath at 60 °C (taken to be the start of the polymerization, $t = 0$). The polymerization was allowed to proceed for a given time at two different stirring rates with a magnetic stirrer.

Characterization. Conversion was measured by gravimetry. M_n and MWD were measured by gel permeation chromatography (GPC) using two styrene/divinylbenzene gel columns (TOSOH Corp., TSKgel GMH_{HR}-H, 7.8 mm i.d × 30 cm) using THF as an eluent at 40 °C at a flow rate of 1.0 mL/min employing refractive index (RI) (TOSOH RI-8020/21) and ultraviolet (UV) detectors (TOYO SODA UV-8II). The columns were calibrated with six standard PS samples (1.05×10^3−5.48×10^6, M_w/M_n = 1.01−1.15). Before GPC measurement, $PMAA_{30}$-TeMe and $PMAA_{30}$-*b*-PS-TeMe were modified by methylation of the carboxyl group using TMSD as follows. After acidification of the carboxyl group, each polymer was recovered by drying the polymer emulsion. The polymer was dissolved in a mixture of dimethylformamide and methanol at room temperature. A yellow solution of TMSD was added at room temperature into the polymer solution, and the reaction was allowed to continue overnight. After excess TMSD was destroyed by acetic acid, poly(methyl methacrylate) $(PMMA)_{30}$-TeMe and $PMMA_{30}$-*b*-PS-TeMe solutions were diluted with a large amount of THF and used for GPC measurement. Theoretical molecular weight ($M_{n,th}$) was calculated by the following equation:

$$M_{n,\mathrm{th}} = \mathrm{MW}_{\mathrm{PMAA_{30}\text{-}TeMe}} + \frac{[\mathrm{M}]_0 \mathrm{MW}_\mathrm{M} \alpha}{[\mathrm{PMAA\text{-}TeMe}]_0} \quad (1)$$

where α is the conversion of monomer, $MW_{PMAA30\text{-}TeMe}$ and MW_M are the molecular weights of $PMAA_{30}$-TeMe and styrene, respectively, and $[PMAA_{30}\text{-}TeMe]_0$ and $[M]_0$ are the initial concentrations of $PMAA_{30}$-TeMe and monomer, respectively.

The consumption of the $PMAA_{30}$-TeMe was estimated by transforming from the MWDs to the number distributions ($w(\log M)/M^2$) vs M. The weight distributions ($w(\log M)/M$) vs M were normalized with respect to each conversion before the transformation. The number of chains could be calculated as the integral of the number distributions; therefore, the number of remaining $PMAA_{30}$-TeMe was obtained.

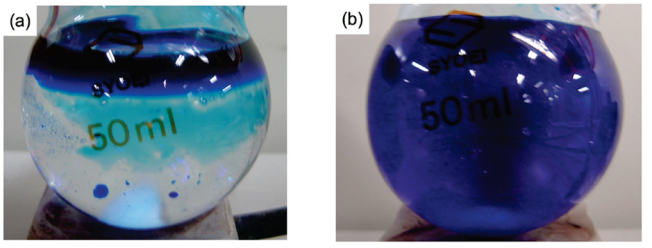


Figure 1. Photographs indicating mixing states at (a) 220 and (b) 1000 rpm before emulsion TERP. Styrene phase was dyed with Oil Blue.

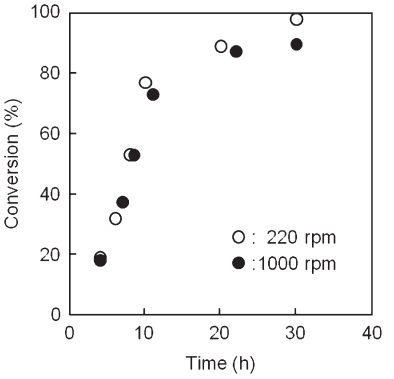


Figure 2. Conversion vs time plots for emulsion TERP using $PMAA_{30}$-TeMe and V-501 at 60 °C with stirring at 220 rpm (open circles) and 1000 rpm (closed circles). Styrene/$PMAA_{30}$-TeMe/V-501 (molar ratio) = 400/1/1.

Monomer concentration in polymer particles ($[M]_p$) was estimated using gas chromatography (GC, GC-18A, Shimadzu Co.) according to a previous article.[54]

Particle size distribution and number-average particle diameter (d_n) were measured using a TEM (JEOL JEM-1230) and dynamic light scattering (DLS, FPAR-1000 RK, fiber-optics particle analyzer, Photal Otsuka Electronics, Osaka, Japan). Before the TEM observation, each emulsion was diluted to ~50 ppm, and then a drop was placed on a carbon-coated copper grid and dried at room temperature in a desiccator. In the DLS measurement, 1−2 droplets of emulsion samples withdrawn from reactor were diluted with ~8 mL of distilled water before measurement in the dilution mode at the light scattering angle of 90° at 25 °C using the Contin analysis routine.

Results

Polymerization Rate. In this article, emulsion TERP of styrene was carried out at 60 °C at two different stirring rates of 220 and 1000 rpm. Figure 1 shows photographs indicating mixing states at 220 (a) and 1000 rpm (b) before starting polymerization, where monomer phases were dyed with Oil Blue for clear observation of the dispersion states. Actual polymerizations were conducted without dyeing. The stirring rate greatly affected the dispersed state of styrene. At 220 rpm, most of styrene floated as an upper layer; on the other hand, at 1000 rpm a large number of styrene droplets were dispersed in the aqueous medium.

Figure 2 shows conversion vs time plots for emulsion TERP of styrene at 60 °C with stirring at 220 and 1000 rpm. Both polymerizations smoothly proceeded without an induction period with a similar rate, and the polymerizations were almost completed in 30 h. In emulsion TERP of BA in

the previous work, R_p at 1000 rpm was faster than at 220 rpm.[52]

Control/Livingness. Parts a and b of Figure 3 show MWDs (RI detector) of PS at various conversions of the emulsion TERP at 220 and 1000 rpm, respectively. In both systems, MWDs shifted to higher molecular weight with increasing conversion, indicating that both polymerizations maintained living nature. The MWD of PS obtained was narrower at 1000 rpm than at 220 rpm. These behaviors were similar to those in emulsion TERP of BA at the two stirring rates.[52] At 220 rpm, a peak due to $PMAA_{30}$-TeMe was observed at a low molecular weight (log M = 3.5) until high conversion. On the other hand, at 1000 rpm, $PMAA_{30}$-TeMe was consumed faster than at 220 rpm. This consumption of $PMAA_{30}$-TeMe behavior will be discussed later.

Parts a and b of Figure 4 show M_n (open circles) and M_w/M_n (closed circles) of PS at different conversions of the emulsion TERP at 220 and 1000 rpm, respectively. M_n and M_w/M_n values were estimated from the peak due to obtained polymer in the MWDs shown in Figure 3 after being divided into the peaks due to $PMAA_{30}$-TeMe and the obtained polymer. Since, at 1000 rpm, the two peaks in the MWDs at low conversions (18 and 37%) could not be divided because of overlapping peaks with each other, the M_w/M_n values of these polymers look slightly high compared to the other polymers. At 1000 rpm, M_n increased linearly throughout the polymerization, while at 220 rpm, M_n increased linearly up to 80% conversion but decreased at the final stage of the polymerization. The decreasing M_n was caused by newly formed polymers having low M_n.[53,55] Experimental M_n at 1000 rpm was very close to theoretical M_n ($M_{n,th}$) compared to that at 220 rpm. The M_w/M_n values at 1000 rpm were sufficiently low (~1.3) relative to those at 220 rpm except for the first stage.

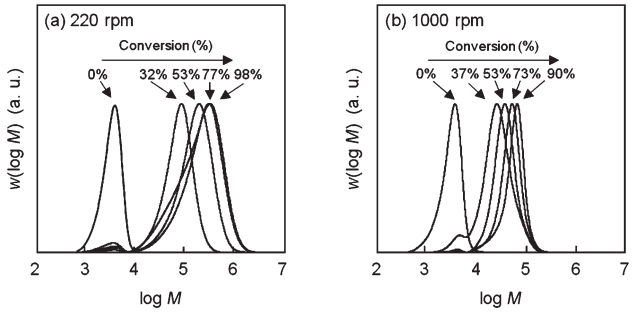


Figure 3. MWDs (RI detector) of $PMMA_{30}$-*b*-PS-TeMe (after methylation) at different conversions (as indicated in %) of emulsion TERP using $PMAA_{30}$-TeMe and V-501 at 60 °C with stirring at 220 (a) and 1000 rpm (b). Styrene/$PMAA_{30}$-TeMe/V-501 (molar ratio) = 400/1/1.

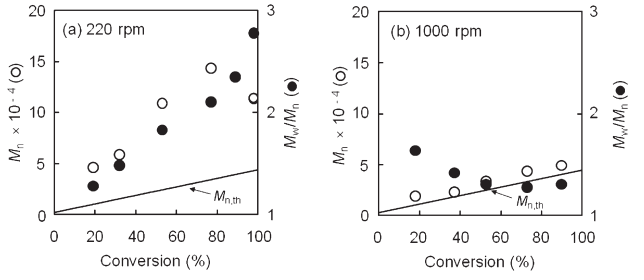


Figure 4. M_n (open circles) and M_w/M_n (closed circles) of $PMMA_{30}$-*b*-PS-TeMe (after methylation) at different conversions of emulsion TERP using $PMAA_{30}$-TeMe and V-501 at 60 °C with stirring at 220 (a) and 1000 rpm (b). Styrene/$PMAA_{30}$-TeMe/V-501 (molar ratio) = 400/1/1. Full line is $M_{n,th}$.

Particle Size Distribution. Figure 5 shows particle size distributions (weight distribution) measured by DLS of PS emulsions prepared by the emulsion TERP at 60 °C with stirring at 220 rpm (a: 98% conversion) and 1000 rpm (b: 90% conversion). The size distribution of PS particles obtained at 220 rpm was bimodal distribution consisting of nanometer- and submicrometer-size (d_n = 40 and 150 nm), and the volume ratio of nanometer-sized particles to submicrometer-sized ones was approximately unit, while that obtained at 1000 rpm was a monomodal distribution consisting of nanometer size (d_n = 50 nm). TEM photographs of the PS particles are shown in Figure 6. Similarly to the DLS measurements (Figure 5), nanometer- and submicrometer-sized particles were observed at 220 rpm, and most of the particles were nanometer-sized at 1000 rpm. Both final particle size distributions in the different stirring systems in the emulsion TERP of styrene were similar to those in the emulsion TERP of BA.[52]

Discussion

In general emulsion polymerization, high $[M]_p$ increases R_p. In emulsion TERP of styrene, $[M]_p$ values were always significantly higher at 1000 rpm than at 220 rpm except for the final stage of the polymerization (Figure 7). Because total monomer/water interfacial area was much larger at 1000 rpm than at 220 rpm, the monomer should smoothly transfer to polymerizing particles across the aqueous phase. Although it was presumed that higher $[M]_p$ at 1000 rpm induces faster R_p than at 220 rpm, which was actually observed in the emulsion TERP of BA,[52] the R_p values in both systems of styrene were similar. This phenomenon might be caused by the lower $[M]_p$ at 220 rpm. In our unpublished work, T_g values of styrene−methacrylic acid copolymer (P(S-MAA),

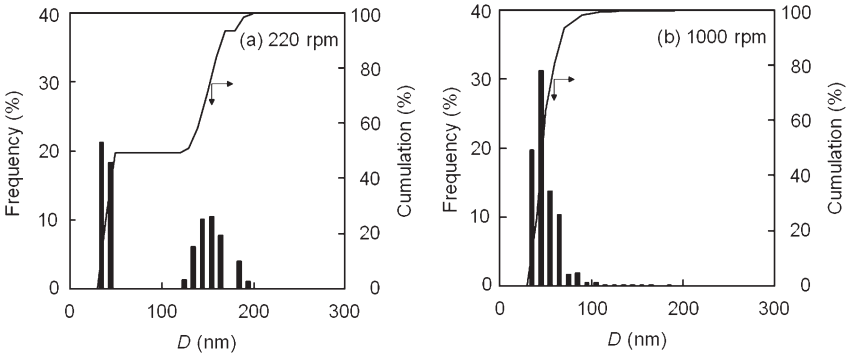


Figure 5. Particle size distributions (weight distribution) (measured by DLS) of PS emulsion prepared by emulsion TERP of styrene using $PMAA_{30}$-TeMe and V-501 at 60 °C with stirring at 220 rpm (a: 98% conversion) and 1000 rpm (b: 90% conversion). Styrene/$PMAA_{30}$-TeMe/V-501 (molar ratio) = 400/1/1.

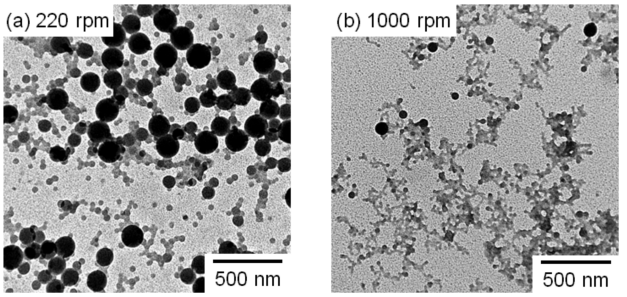


Figure 6. TEM photographs of PS particles prepared by emulsion TERP using $PMAA_{30}$-TeMe and V-501 at 60 °C with stirring at 220 rpm (a: 98% conversion) and 1000 rpm (b: 90% conversion). Styrene/$PMAA_{30}$-TeMe/V-501 (molar ratio) = 400/1/1.

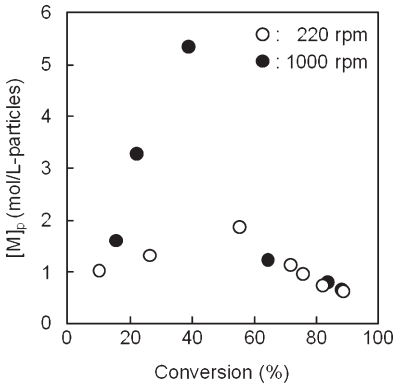


Figure 7. Monomer concentrations in the PS particles ($[M]_p$) at different conversions of emulsion TERP using $PMAA_{30}$-TeMe and V-501 at 60 °C with stirring at 220 rpm (open circles) and 1000 rpm (closed circles). Styrene/$PMAA_{30}$-TeMe/V-501 (molar ratio) = 400/1/1.

10 mol % MAA) particles containing various amounts of styrene (that is, at various $[M]_p$) were measured with a power compensation-type highly sensitive differential scanning calorimeter. Because $T_{g,P(S\text{-}MAA)}$ at 1.4 mol/(L particles) of $[M]_P$ was ~60 °C, the viscosity of polymerizing particles in the emulsion TERP of styrene at 60 °C with stirring at 220 rpm where $[M]_p$ was 1−2 mol/(L particles) in the conversion range of 10−70% would be extremely high, resulting in slow diffusion of polymer chains and decrease of rate constant of termination reaction (k_t) between two polymer radicals.[56] The decrease of k_t increases average number of radicals per particle. On the other hand, the rate constant of propagation reaction (k_p) between radical and monomer should barely change below T_g even under high viscosity.[57] As a result, R_p at 220 rpm became faster than that presumed as above. In the emulsion TERP of BA, because $T_{g,PBA}$ is much lower than polymerization temperature: 60 °C ($T_{g,PBA}$ = −54 °C, $T_{g,PS}$ = 100 °C),[58] viscosity in polymerizing particles would not be so high even if it proceeds at low $[M]_p$ at 220 rpm that k_t does not change much. Consequently, the effect of stirring rate on R_p in emulsion TERP depends on T_g of polymerizing particles.

TERP proceeds via two control mechanisms, which are thermal dissociation (TD) and degenerative chain transfer (DT), in which the main control mechanism is DT at 60 °C.[20] Two factors could be considered about the reason for the improving control/livingness by increasing stirring rate from 220 to 1000 rpm (Figure 4), in which the total monomer/water interfacial area markedly increased. One would be lower viscosity inside polymerizing particles due to higher $[M]_p$ at 1000 rpm than 220 rpm (Figure 7). Although the chain transfer reaction in the TERP is also a reaction between radical and dormant species having a certain level of molecular weight, high diffusion of the reactants (radical and dormant species) at 1000 rpm should allow chain transfer reaction to

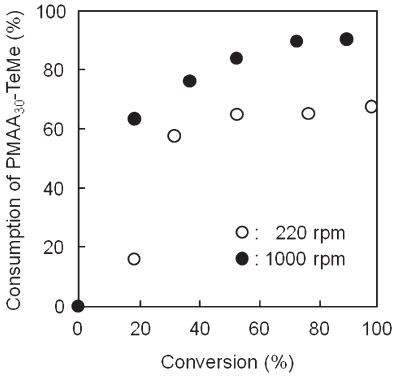


Figure 8. Consumptions of $PMAA_{30}$-TeMe at different conversions of emulsion TERP using $PMAA_{30}$-TeMe and V-501 at 60 °C with stirring at 220 rpm (open circles) and 1000 rpm (closed circles). Styrene/$PMAA_{30}$-TeMe/V-501 (molar ratio) = 400/1/1.

proceed smoothly, resulting in good control/livingness. However, because the viscosity inside polymerizing particles was higher due to lower $[M]_p$ at 220 rpm than 1000 rpm, slow diffusion of the reactants results in decrease of the chain transfer rate constant (k_{tr}) similarly to the decrease of k_t as mentioned above. It seems that higher $[M]_p$ leads to a greater number of monomer units added per activation−deactivation step and became less control over the MWD at 1000 rpm. $[M]_p$ at 1000 rpm (ca. 5.3 mol/(L particles)) was ~3 times as high as that at 220 rpm (ca. 1.9 mol/(L particles)), which leads that the R_p at 1000 rpm was 3 times larger than that at 220 rpm. On the other hand, chain transfer reaction would be diffusion controlled similarly to termination reaction because both chain transfer reaction and termination reaction were polymer−polymer reactions. The diffusion controlled k_t in bulk system was investigated by Zetterlund and coworkers.[56] In the paper, the k_t decreased 100 times from conversion 45% ([M]: 5.5 mol/L) to 80% ([M]: 2.0 mol/L). Therefore, R_{tr} would be significantly (ca. 100 times) larger at 1000 rpm than at 220 rpm. Thus, lower M_w/M_n value at 1000 rpm is based on higher R_{tr}. On the other hand, the k_p barely changes even under high viscosity as described above. As a result, control/livingness became bad at 220 rpm.

The other factor to obtain the high control/livingness at 1000 rpm is the high consumption of the control agent, which is important for maintaining a narrow MWD. Figure 8 shows the consumption of $PMAA_{30}$-TeMe at different conversions of the emulsion TERP at 220 and 1000 rpm. At 220 rpm, more than 30% $PMAA_{30}$-TeMe still remained even at 98% conversion. On the other hand, at 1000 rpm, 90% $PMAA_{30}$-TeMe was consumed until 90% conversion, indicating that larger amount of $PMAA_{30}$-TeMe could participate in the polymerization. In a DT system, higher concentration of control agent in polymerization loci would lead to narrower MWD,[59] which accorded with the result that MWD was sufficiently controlled at 1000 rpm compared to 220 rpm (Figure 3).

In Figure 4a,b, $M_{n,th}$ was calculated using eq 1 assuming that $PMAA_{30}$-TeMe is completely consumed at the beginning of the polymerization. Because the large differences between $M_{n,th}$ and M_n at 220 rpm might be caused by the gradual consumption of $PMAA_{30}$-TeMe, theoretical M_n, which is estimated by defining $M^*_{n,th}$, was calculated using eq 2.

$$M^*_{n,\,th} = MW_{PMAA_{30}\text{-}TeMe} + \frac{[M]_0 MW_M \alpha}{[PMAA\text{-}TeMe]_0 \beta} \qquad (2)$$

where β is the fraction of consumed $PMAA_{30}$-TeMe. However, contrary to our expectation, the difference between $M^*_{n,th}$ and M_n only became a little lower and still persisted. In a previous

Table 1. Number-Average Particle Sizes (d_n), $M_{n,th}$, M_n, and M_w/M_n of Centrifugally Separated Fraction of PS Particles, Which Were Prepared by Emulsion TERP Using $PMAA_{30}$-TeMe and V-501 at 60 °C with Stirring at 220 rpm (Conversion 98%) and 1000 rpm (Conversion 90%)

stirring rate (rpm)	size	weight fraction (%)	d_n (nm)	$M_{n,th}$	M_n	M_w/M_n
220	submicrometer	51	130	4.4×10^4	1.4×10^5	2.9
	nanometer	49	34	4.4×10^4	9.0×10^4	2.7
1000	submicrometer	1	110	4.1×10^4	6.9×10^4	1.5
	nanometer	99	31	4.1×10^4	4.5×10^4	1.3

article, it is already revealed that nanometer- and submicrometer-sized particles were generated from self-assembly and homogeneous nucleations, respectively.[55] On the basis of the particle size distributions (Figures 5a and 6a), it would be an alternative explanation that the large difference between $M_{n,th}$ and M_n at 220 rpm is attributed to the presence of the two particle nucleation mechanisms. Thus, polymerizing particles generated from the homogeneous nucleation, polymerization was barely controlled by TERP because of low concentration of TeMe derivatives in the polymerizing particles, resulting in polymer having much higher molecular weight than $M_{n,th}$, although it was well controlled in polymerizing particles generated from the self-assembly nucleation because of high concentration of TeMe derivatives. This explanation was supported by results (Table 1) that M_n of polymer obtained from submicrometer-sized particles after separation by centrifugation was higher than that obtained from nanometer-sized particles at both stirring rates.

The interfacial tensions of a styrene/water interface and styrene/$PMAA_{30}$-TeMe aqueous solution interface measured using the pendant drop method were 35.1 and 21.4 mN/m, respectively. These results indicate that a certain amount of $PMAA_{30}$-TeMe had been adsorbed at the interface between styrene and water until the monomer phase disappeared. It seems to be extremely low in the adsorption state to react with initiator (and oligomer) radicals formed in the aqueous phase, which should delay the consumption of $PMAA_{30}$-TeMe. The total monomer/water interfacial area was much larger at 1000 rpm than at 220 rpm. Accordingly, it presumed that the percentage of $PMAA_{30}$-TeMe adsorbed at the monomer/water interface must be much larger at 1000 rpm, resulting in worse living control. However, the obtained result was quite contrary as shown in Figure 5. Considering the result, there must be other factors induced by the different stirring rates affecting the consumption of $PMAA_{30}$-TeMe.

As indicated in Figure 7, $[M]_p$ values were higher at 1000 rpm than at 220 rpm; in other words, transfer of monomer to polymerizing particles at 1000 rpm was faster than at 220 rpm. As a result, the monomer phases disappeared at a lower conversion (40%) at 1000 rpm than at 220 rpm (70%). Therefore, $PMAA_{30}$-TeMe that had been adsorbed at the monomer/water interface moved into the aqueous phase at lower conversion at 1000 rpm than at 220 rpm, resulting in the rapid consumption of $PMAA_{30}$-TeMe and better living control at 1000 rpm.

At 1000 rpm, the consumption of $PMAA_{30}$-TeMe was also faster than at 220 rpm in the early stage of the polymerization around 20% conversion (Figure 8). This might be induced by difference of monomer concentration in aqueous phase in the early stage of the polymerization at the different stirring conditions. The difference of monomer concentration would affect particle nucleation in an early stage of the emulsion TERP. This will be discussed in detail in the near future.

Conclusions

Emulsion TERP of styrene was successfully carried out in the two different stirring systems (220 and 1000 rpm) using $PMAA_{30}$-TeMe and V-501 at 60 °C. In both stirring systems, R_p values were of the same degree, which was different from the result in emulsion TERP of BA. The difference based on the kind of monomer seems to depend on T_g of polymerizing particles. MWD was sufficiently controlled at 1000 rpm compared to that at 220 rpm, where the disappearance of monomer phase was earlier at 1000 rpm than at 220 rpm. After the disappearance of monomer phase, $PMAA_{30}$-TeMe that had been adsorbed at monomer/water interface should work as control agent. The stirring rate seriously affected the particle size distribution and MWD similarly to the emulsion TERP of BA. The final particle size distribution at 220 rpm was bimodal with nanometer- and submicrometer-sized, whereas that at 1000 rpm was monomodal with nanometer-sized. From these results, it is concluded that the stirring rate is an important factor to control MWD and particle size distribution in emulsion TERP. In the following work, the differences of the MWD and particle size distribution due to the stirring rate will be discussed in terms of the particle nucleation, focusing on the early stage of the polymerization.

Acknowledgment. The authors are grateful to Otsuka Chemical Co., Ltd., for supplying organotellurium compounds. This work was partially supported by Grant-in-Aid for Scientific Research (A) (Grant 21245050) from the Japan Society for the Promotion of Science (JSPS) and by Research Fellowship of JSPS for Young Scientists (given to Y.K.).

References and Notes

(1) Matyjaszewski, K. *Controlled/Living Radical Polymerization: Progress in ATRP, NMP, and RAFT*; American Chemical Society: Washington, DC, 2000.
(2) Matyjaszewski, K. *Advances in Controlled/Living Radical Polymerization*; American Chemical Society: Washington, DC, 2003.
(3) Braunecker, W.; Matyjaszewski, K. *Prog. Polym. Sci.* **2007**, *32*, 93–146.
(4) Zetterlund, P. B.; Kagawa, K.; Okubo, M. *Chem. Rev.* **2008**, *108*, 3747–3794.
(5) Georges, M. K.; Veregin, R. P. N.; Kazmaier, P. M.; Hamer, G. K. *Macromolecules* **1993**, *26*, 2987–2988.
(6) Hawker, C. J.; Bosman, A. W.; Harth, E. *Chem. Rev.* **2001**, *101*, 3661–3688.
(7) Nakamura, T.; Zetterlund, P. B.; Okubo, M. *Macromol. Rapid Commun.* **2006**, *27*, 2014–2018.
(8) Zetterlund, P. B.; Okubo, M. *Macromolecules* **2006**, *39*, 8959–8967.
(9) Kato, M.; Kamigaito, M.; Sawamoto, M.; Higashimura, T. *Macromolecules* **1995**, *28*, 1721–1723.
(10) Wang, J.; Matyjaszewski, K. *J. Am. Chem. Soc.* **1995**, *117*, 5614–5615.
(11) Kamigaito, K.; Ando, T.; Sawamoto, M. *Chem. Rev.* **2001**, *101*, 3689–3745.
(12) Matyjaszewski, K.; Xia, J. *Chem. Rev.* **2001**, *101*, 2921–2990.
(13) Kagawa, Y.; Zetterlund, P. B.; Minami, H.; Okubo, M. *Macromol. Theory Simul.* **2006**, *15*, 608.
(14) Kagawa, Y.; Zetterlund, P. B.; Minami, H.; Okubo, M. *Macromolecules* **2007**, *40*, 3062–3069.
(15) Chiefari, J.; Chong, Y. K.; Ercole, F.; Krstina, J.; Jeffery, J.; Le, T. P. T.; Mayadunne, R. T. A.; Meijs, G. F.; Moad, C. L.; Moad, G.; Rizzardo, E.; Thang, S. H. *Macromolecules* **1998**, *31*, 5559–5562.
(16) Moad, G.; Chong, Y. K.; Postma, A.; Rizzardo, E.; Thang, S. H. *Polymer* **2005**, *46*, 8458–8468.
(17) Moad, G.; Rizzardo, E.; Thang, S. H. *Aust. J. Chem.* **2006**, *59*, 669–692.
(18) Yamago, S.; Iida, K.; Yoshida, J. *J. Am. Chem. Soc.* **2002**, *124*, 2874–2875.
(19) Yamago, S.; Iida, K.; Yoshida, J. *J. Am. Chem. Soc.* **2002**, *124*, 13666–13667.
(20) Goto, A.; Kwak, Y.; Fukuda, T.; Yamago, S.; Iida, K.; Nakajima, M.; Yoshida, J. *J. Am. Chem. Soc.* **2003**, *125*, 8720–8721.

(21) Yamago, S.; Iida, K.; Nakajima, M.; Yoshida, J. *Macromolecules* **2003**, *36*, 3793–3796.
(22) Yamago, S.; Ray, B.; Iida, K.; Yoshida, J.; Tada, T.; Yoshizawa, K.; Kwak, Y.; Goto, A.; Fukuda, T. *J. Am. Chem. Soc.* **2004**, *126*, 13908–13909.
(23) Yamago, S. *J. Polym. Sci., Part A: Polym. Chem.* **2006**, *44*, 1–12.
(24) Kwak, Y.; Goto, A.; Fukuda, T.; Kobayashi, Y.; Yamago, S. *Macromolecules* **2006**, *39*, 4671–4679.
(25) Kwak, Y.; Tezuka, M.; Goto, A.; Fukuda, T.; Yamago, S. *Macromolecules* **2007**, *40*, 1881–1885.
(26) Yamago, S. *Chem. Rev.* **2009**, *109*, 5051–5068.
(27) Cunningham, M. F. *Prog. Polym. Sci.* **2008**, *33*, 365–398.
(28) Sugihara, Y.; Kagawa, Y.; Yamago, S.; Okubo, M. *Macromolecules* **2007**, *40*, 9208–9211.
(29) Pan, G.; Sudol, E. D.; Dimonie, V. L.; El-Aasser, M. S. *Macromolecules* **2001**, *34*, 481–488.
(30) Qiu, J.; Charleux, B.; Matyjaszewski, K. *Prog. Polym. Sci.* **2001**, *26*, 2083.
(31) Cunningham, M. F. *Prog. Polym. Sci.* **2002**, *27*, 1039–1067.
(32) Zetterlund, P. B.; Alam, M. N.; Minami, H.; Okubo, M. *Macromol. Rapid Commun.* **2005**, *26*, 955–960.
(33) Monteiro, M. J.; de-Barbeyrac, J. *Macromolecules* **2001**, *34*, 4416–4423.
(34) Prescott, S. W.; Ballard, M. J.; Rizzardo, E.; Gilbert, R. G. *Macromolecules* **2002**, *35*, 5417–5425.
(35) Prescott, S. W.; Ballard, M. J.; Rizzardo, E.; Gilbert, R. G. *Aust. J. Chem.* **2002**, *55*, 415–424.
(36) Ferguson, C. J.; Hughes, R. J.; Pham, B. T. T.; Hawkett, B. S.; Gilbert, R. G.; Serelis, A. K.; Such, C. H. *Macromolecules* **2002**, *35*, 9243–9245.
(37) Ferguson, C. J.; Hughes, R. J.; Nguyen, D.; Pham, B. T. T.; Gilbert, R. G.; Serelis, A. K.; Such, C. H.; Hawkett, B. S. *Macromolecules* **2005**, *38*, 2191–2204.
(38) Nicolas, J.; Charleux, B.; Guerret, O.; Magnet, S. *Angew. Chem., Int. Ed.* **2004**, *43*, 6186–6189.
(39) Delaittre, G.; Nicolas, J.; Lefay, C.; Save, M.; Charleux, B. *Chem. Commun.* **2005**, *5*, 614–616.
(40) Nicolas, J.; Charleux, B.; Guerret, O.; Magnet, S. *Macromolecules* **2005**, *38*, 9963–9973.
(41) Delaittre, G.; Nicolas, J.; Lefay, C.; Save, M.; Charleux, B. *Soft Matter* **2006**, *2*, 223–231.
(42) Nicolas, J.; Charleux, B.; Magnet, S. *J. Polym. Sci., Part A: Polym. Chem.* **2006**, *44*, 4142–4153.
(43) Maehata, H.; Liu, X.; Cunningham, M. F.; Keoshkerian, B. *Macromol. Rapid Commun.* **2008**, *29*, 479–484.
(44) Dire, C.; Magnet, F.; Couvreur, L.; Charleux, B. *Macromolecules* **2009**, *42*, 95–103.
(45) Stoffelbach, F.; Tibiletti, L.; Rieger, J.; Charleux, B. *Macromolecules* **2008**, *41*, 7850–7856.
(46) Ferguson, C. J.; Hughes, R. J.; Pham, B. T. T.; Hawkett, B. S.; Gilbert, R. G.; Serelis, A. K.; Such, C. H. *Macromolecules* **2002**, *35*, 9243–9245.
(47) Sprong, E.; Leswin, J. S. K.; Lamb, D. J.; Ferguson, C. J.; Hawkett, B. S.; Pham, B. T. T.; Nguyen, D.; Such, C. H.; Serelis, A. K.; Gilbert, R. G. *Macromol. Symp.* **2006**, *231*, 84–93.
(48) Hartmann, J.; Urbani, C.; Whittaker, M. R.; Monteiro, M. J. *Macromolecules* **2006**, *39*, 904–907.
(49) Manguian, M.; Save, M.; Charleux, B. *Macromol. Rapid Commun.* **2006**, *27*, 399–404.
(50) Ganeva, D. E.; Sprong, E.; Bruyn, H. d.; Warr, G. G.; Such, C. H.; Hawkett, B. S. *Macromolecules* **2007**, *40*, 6181–6189.
(51) dos Santos, A. M.; Pohn, J.; Lansalot, M.; D'Agosto, F. *Macromol. Rapid Commun.* **2007**, *28*, 1325–1332.
(52) Okubo, M.; Sugihara, Y.; Kitayama, Y.; Kagawa, Y.; Minami, H. *Macromolecules* **2009**, *42*, 1979–1984.
(53) Kitayama, Y.; Chaiyasat, A.; Okubo, M. *Macromol. Symp.* **2010**, *288*, 25–32.
(54) Okubo, M.; Kobayashi, H.; Matoba, T.; Oshima, Y. *Langmuir* **2006**, *22*, 8727–8731.
(55) Kitayama, Y.; Chaiyasat, A.; Minami, H.; Okubo, M. *Macromolecules* **2010**, *43*, 7465–7471.
(56) Zetterlund, P. B.; Yamazoe, H.; Yamada, B.; Hill, D. J. T.; Pomery, P. J. *Macromolecules* **2001**, *34*, 7686–7691.
(57) Yamazoe, H.; Zetterlund, P. B.; Yamada, B.; Hill, D. J. T.; Pomery, P. J. *Macromol. Chem. Phys.* **2001**, *202*, 824.
(58) Brandrup, J.; Immergut, E. H.; Grulke, E. A. *Polymer Handbook*; John Wiley & Sons: New York, 1999; Section VI, pp 193−277.
(59) Wang, A. R.; Zhu, S. *J. Polym. Sci., Part A: Polym. Chem.* **2003**, *41*, 1553–1566.

Macromolecules
ARTICLE

Macromolecules **2011**, *44*, 269–277 **269**
DOI: 10.1021/ma101878w

Thieno[3,4-*c*]pyrrole-4,6-dione-Based Donor−Acceptor Conjugated Polymers for Solar Cells

Xugang Guo,[†] Hao Xin,[‡] Felix Sunjoo Kim,[‡] Arawwawala D. T. Liyanage,[†] Samson A. Jenekhe,*[,‡] and Mark D. Watson*[,†]

[†]*Department of Chemistry, University of Kentucky, Lexington, Kentucky 40506-0055, United States, and* [‡]*Department of Chemical Engineering and Department of Chemistry, University of Washington, Seattle, Washington 98195-1750, United States*

Received August 16, 2010; Revised Manuscript Received November 29, 2010

ABSTRACT: Three new donor−acceptor conjugated polymers incorporating thieno[3,4-*c*]pyrrole-4,6-dione (TPD) acceptor and dialkoxybithiophene or cyclopentadithiophene units as donor have been synthesized and explored in bulk heterojunction (BHJ) solar cells and organic field-effect transistors (OFETs). The TPD-containing polymers had optical band gaps of 1.50−1.70 eV and HOMO levels of −4.85 to −5.26 eV. The highly electron-rich character of dialkoxybithiophene in **P1** and **P2** destabilizes their HOMOs which significantly affects the photovoltaic efficiency. However, polymer **P3** containing cyclopentadithiophene donor units results in a deeper HOMO level of −5.26 eV. The field-effect mobility of holes varied from 2×10^{-4} cm^2/(V s) in **P2** to $\sim 1 \times 10^{-2}$ cm^2/(V s) in **P3**-based transistors. BHJ solar cells using polymer **P1** or **P2** as the electron donor and (6,6)-phenyl-C_{71}-butyric acid ester ($PC_{71}BM$) as the electron acceptor exhibit low open circuit voltages (V_{oc} = 0.40−0.60 V) and power conversion efficiencies below 1.5%. However, BHJ solar cells based on the TPD−cyclopentadithiophene copolymer (**P3**) achieved a high V_{oc} of ∼0.8 V and power conversation efficiency greater than 3%. These results demonstrate the tuning of the open circuit voltage and thus the photovoltaic efficiency of BHJ solar cells based on copolymers containing thieno[3,4-*c*]pyrrole-4,6-dione acceptor.

Introduction

Organic polymer-based solar cells have great potential as alternative clean energy sources due to the low cost of device fabrication using solution-based processing technology and their mechanical flexibility which is compatible with foldable or rollable substrates.[1−4] The performance of polymer solar cells has been significantly improved in the past decade through optimization of device structure,[1] interfacial layer engineering,[5−7] processing condition,[8−11] and synthesis of new high-performance polymer semiconductors.[12−17] To date, the bulk heterojunction (BHJ) device architecture using polymer semiconductors as electron donors and high-electron-affinity fullerene derivatives such as [6,6]-phenyl-C_{61}-butyric acid methyl ester ($PC_{61}BM$) or [6,6]-phenyl-C_{71}-butyric acid methyl ester ($PC_{71}BM$) as electron acceptors has proven to be the most successful concept in polymer solar cells (PSCs).[1,18,19] Power conversion efficiencies of greater than 7% have recently been achieved by using new donor−acceptor copolymer semiconductors and optimizing device processing conditions.[14,20,21]

Although the power conversion efficiency (PCE) of polymer solar cells has been significantly improved in the past decade,[20] their performance is still much lower than their inorganic counterparts, such as silicon, GaAs, CdTe, and CIGS,[22] which prevents the practical applications in large scale. Design and synthesis of new polymer semiconductors with appropriate band gap and frontier molecular orbitals (FMOs) is one of the key approaches to improving the PCE of polymer solar cells.[12,13,15] The target materials should have appropriate band gaps with high absorption coefficient to efficiently harvest solar irradiation and also have appropriate energy levels of the lowest unoccupied molecular orbitals (LUMOs) for efficient exciton dissociation at the donor/acceptor interface and deep highest occupied molecular orbitals (HOMOs) for achieving high open circuit voltage (V_{oc}) and device stability.[16,23−25] The relatively high HOMO energy of P3HT significantly limits the V_{oc} and thus PCE of the most studied P3HT/PCBM solar cells.[26] Furthermore, the donor polymers and acceptor fullerenes should segregate to a bicontinuous network with domain widths within twice the exciton diffusion length to facilitate the dissociation of excitons at donor/acceptor interfaces and to provide efficient pathways for the dissociated charges to reach their respective electrodes. However, it is challenging to tailor all these features in one single polymer component. The development of PBT7[27] demonstrates how to synergistically integrate the desired properties to increase device performance. PBT7 has a band gap of 1.60 eV which enables efficient harvesting of solar irradiation around the region with the highest photon flux of the solar spectrum (∼700 nm) and a low HOMO level of −5.15 eV which facilitates a high V_{oc} (0.75 eV). BHJ solar cells based on PTB7/$PC_{71}BM$ exhibit a PCE up to 7.4% after optimizing the film morphology to form a nanoscale interpenetrating network.[27]

The donor−acceptor (D−A) strategy has been demonstrated to be efficient in not only band-gap engineering but also tuning of the energy levels of the frontier molecular orbitals (FMOs).[28,29] Among different acceptor units, imide-functionalized arenes are an interesting class of building blocks and are gaining more attention due to their solubilizing ability and electronic structures. Recently, they have been successfully used as acceptor units in the construction of high-performance D−A polymer semiconductors[30] for applications in organic field-effect transistors

*Corresponding authors. E-mail: jenekhe@u.washington.edu (S.A.J.); mdwatson@uky.edu (M.D.W.).

© 2010 American Chemical Society
Published on Web 12/23/2010

(OFETs) and polymer solar cells. Alternating D−A copolymers using naphthalene diimide (NDI)[31] and perylene diimide (PDI)[32] as electron acceptor units have demonstrated high electron mobilities[33−35] and high-mobility ambipolar charge transport,[36] and all-polymer solar cells using PDI-based polymers as acceptor layer showed a promising efficiency of up to 1.5% PCE.[37] Furthermore, D−A copolymers constructed from bithiophene imide[38] and phthalimide[39] have also demonstrated good hole mobilities in OFETs. We have previously demonstrated that phthalimide-based D−A copolymer PhBT12 is promising as donor component for applications in BHJ solar cells.[40] We concurrently[41] began studies using thieno[3,4-*c*]pyrrole-4,6-dione (TPD),[42,43] an obvious next step, as the acceptor unit in D−A polymer semiconductors (Figure 1). TPD's geometry and electronic structure make it an intriguing acceptor unit. On the basis of comparison of aromatic resonance energy of benzene (1.56 eV) and thiophene (1.26 eV), polymers based on TPD should in principle have decreased bond-length alternation.[17,29] Furthermore, TPD's geometry should present decreased steric repulsion to neighboring backbone units, and potentially attractive sulfur−oxygen interactions could assist backbone planarization.[44−46] TPD-based D−A copolymers should, therefore, have smaller band gaps than the corresponding phthalimide-based copolymers and potentially closer intermolecular $\pi-\pi$ interactions for efficient charge transport.

In this paper, we report the synthesis and characterization of three new D−A copolymer semiconductors based on TPD and their initial applications in BHJ solar cells and organic field-effect transistors (OFETs). Partially due to their donor−acceptor repeating structure, the new polymers show lower band gaps in comparison to that of the most studied P3HT,[26] which can lead to better absorption of solar irradiation. OFETs fabricated from **P3** achieved a hole mobility (μ_h) of 8.9×10^{-3} cm^2/(V s) and current modulation (I_{on}/I_{off}) of 10^5. Photovoltaic properties of the new polymers were investigated by fabricating BHJ devices using these polymers as donor and $PC_{71}BM$ as acceptor. An average power conversion efficiency of 3.06% was achieved for **P3** with a high V_{oc} of ~0.8 V. Because of promising charge transport properties of pure **P3** film and the relatively high V_{oc} of **P3**/$PC_{71}BM$ cells, we believe the device performance of polymer **P3** analogues can be further improved by optimizing the side chains of **P3** as well as device fabrication conditions. While we were preparing this report other groups have recently obtained highly efficient solar cells (4.2−6.8% PCE)[47−50] from a D−A copolymer with TPD as acceptor and benzodithiophene as donor. The current study adds to this body of work by revealing the effects of combining other donors and substituents with the highly promising TPD acceptor.



Figure 1. Chemical structures of phthalimide (left) and thieno[3,4-*c*]-pyrrole-4,6-dione (right).

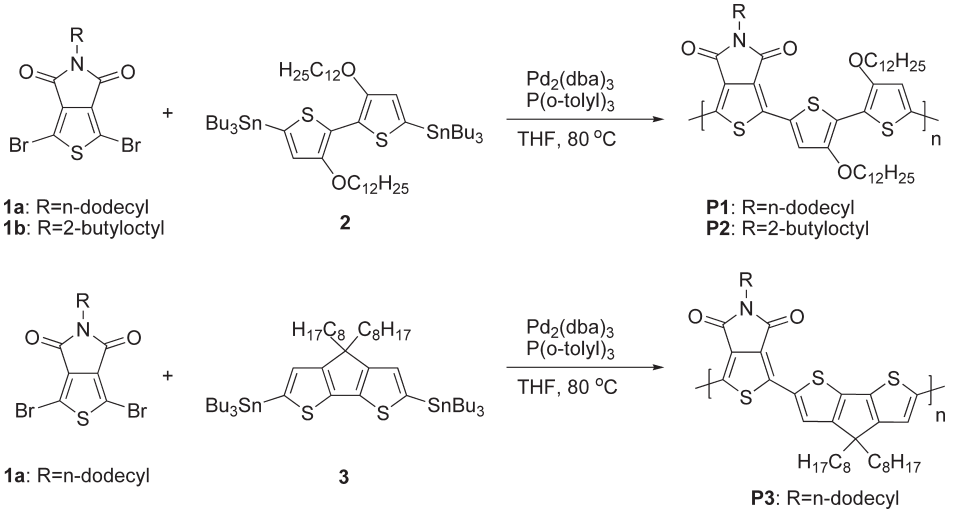
Results and Discussion

The new polymers were first characterized by NMR, GPC, DSC, electronic absorption spectroscopy, and differential pulse voltammetry (DPV). OFET devices were then fabricated to investigate the charge transport properties of the polymer thin films. XRD and AFM investigations followed to characterize and analyze the morphology of thin films. Finally, photovoltaic devices were fabricated and tested using polymer/$PC_{71}BM$ blend films by varying the polymer/$PC_{71}BM$ BHJ blend composition, and the morphology of polymer/$PC_{71}BM$ blend films was investigated by AFM to partially explain the observed solar cell performance.

Material Synthesis. All monomers (Supporting Information) were prepared by following published procedures,[31,43,51,52] and polymerizations were effected via Stille coupling. After polymerization, the materials were purified via sequential Soxhlet extractions to remove oligomers and low molecular weight polymers. Polymer molecular weight is an important factor that can affect the device performance of OFETs[53] and solar cells.[54] The electron-deficient TPD monomers are ideal coupling partner with electron-rich distannylated thiophene monomers, leading to high number-average molecular weights from 32 kDa for **P1** to 55 kDa for **P2** and to 64 kDa for **P3**, and the high isolated yields indicate excellent conversion.

Resolved ^{1}H NMR spectra of polymers **P1**−**P3** (Supporting Information, Figures S1−S3) could be obtained only at elevated temperature (130 °C) due to aggregation. However, no ^{13}C signals arising from polymer backbones could be observed even after 12 h collection at 130 °C. Compared to our previously reported phthalimide analogue PhBT12 having identical side chains and a molecular weight of 207.5 kDa,[39] **P1** has about 1 order of magnitude lower molecular weight, which could be due to its relatively low solubility, resulting in

Scheme 1. Synthesis of New TPD-Based Copolymers



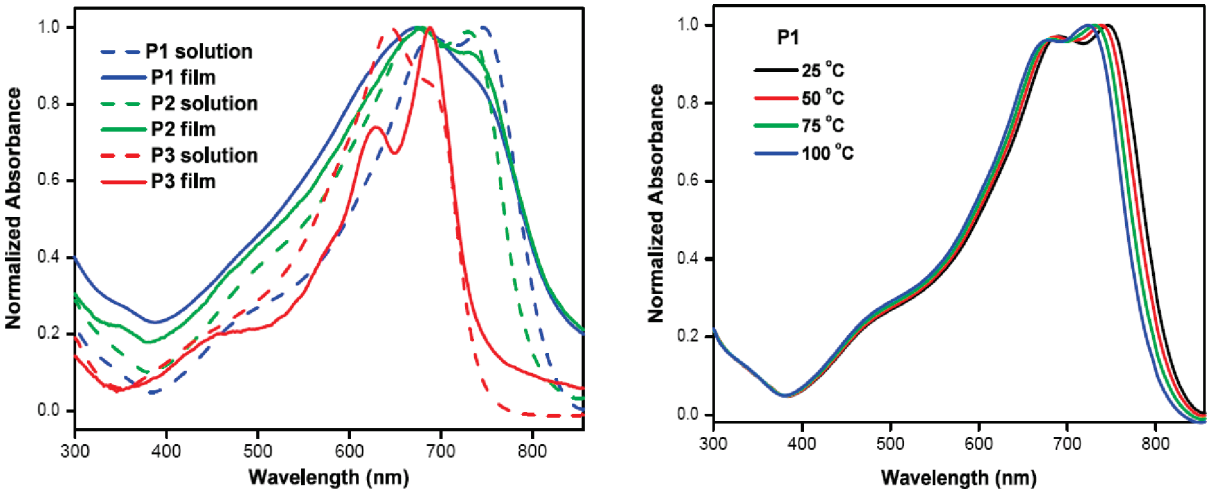


Figure 2. Absorption spectra of **P1**, **P2**, and **P3** in chlorobenzene solution at room temperature (1×10^{-5} M) and as thin films (cast from 5 mg/mL chlorobenzene solution) (left) and thermochromism of **P1** solution (1×10^{-5} M in chlorobenzene) as a function of solution temperature (right).

Table 1. Molecular Weight as Well as Optical and Electrochemical Properties of TPD Copolymers

polymer	M_n (kDa)	PDI	T_m/T_c[a] (°C)	λ_{max}^{abs} film[b] (nm)	E_g^{opt}[c] (eV)	HOMO[d] (eV)	LUMO[e] (eV)
P1	32	2.8		676	1.50	−4.85	−3.35
P2	55	2.0		680	1.50	−5.05	−3.53
P3	64	4.7	328/305	688	1.67	−5.26	−3.59

[a] Peak melting/crystallization point, differential scanning calorimetry (10 °C/min). [b] Thin film absorption spectra from film cast from 5 mg/mL chlorobenzene solution. [c] Optical energy gap estimated from the absorption edge of as-cast thin film. [d] Determined by differential pulse voltammetry, versus Fc/Fc^+. [e] Estimated from LUMO = HOMO + E_g^{opt}.

termination of polymerization at an earlier stage. The lower molecular weight and the poor processability of **P1** can be the factors which affect the film morphology and limit the carrier mobility in OFET devices.[53] Replacing the *n*-dodecyl TPD substituent in **P1** with 2-butyloctyl in **P2** imparts better solubility and processability. Despite the fused-ring structure of cyclopentadithiophene (CDT), copolymer **P3** shows decent solubility which can be ascribed to the out-of-plane orientation of the alkyl chains on the CDT unit. Polymers **P2** and **P3** can be dissolved at higher concentrations at lower temperature than **P1** in chlorinated solvents.

Optical Properties. Absorption spectra were recorded from chlorobenzene solution (1×10^{-5} M) and thin films (Figure 2), and the related data are collected in Table 1. The absorption maxima are 675, 680, and 688 nm for as-cast films of **P1**, **P2**, and **P3**, respectively. The thin films of these polymers exhibit both an absorption maximum and a shoulder, which are similar to the vibronic structures seen in regioregular polythiophene spectra.[55] From solution to thin film, no significant differences were observed in the absorption spectra for all three polymers, which indicate some degree of rigid chain conformation and/or aggregation[56,57] in solution at room temperature. In molecularly dissolved solutions, absorption spectra are usually broad and featureless, reflecting random thermal population of rotational states. Thermochromism of **P1** solutions (Figure 2; for **P2** and **P3**, see Figures S5 and S6) is manifested by blue shifts in the absorption profile with increasing temperature. From room temperature to 100 °C, the absorption maximum of **P1** solution was blue-shifted by 25 nm from 748 to 723 nm. This could correspond to increased torsional activity or changes in aggregation number.

The optical band gaps of polymer films calculated from absorption edges are 1.50, 1.50, and 1.67 eV for **P1**, **P2**, and **P3**, respectively, which are much smaller than the optical band gap of P3HT (~1.90 eV),[58] due to their donor−acceptor makeup.[59] As predicted, the band gap of **P1** is smaller than that of the analogous phthalimide polymer PhBT12 (1.64 eV) with the same donor unit.[39] The 0.17 eV narrower band gap of **P1** and **P2** compared to that of **P3** is ascribed to the stronger electron-donating capability of dialkoxybithiophene units relative to cyclopentadithiophene units. Although potentially enhancing absorption of solar energy due to decreased band gap, these stronger donors destabilize HOMO energy levels which can limit V_{oc} in PSCs (vide infra).

Electrochemical Properties. The electrochemical redox properties of the polymers were investigated by differential pulse voltammetry (DPV).[60] DPV provides better sensitivity and sharper onsets than cyclic voltammetry (CV) by minimizing the contributions from the charging background currents when investigating π-conjugated systems.[7] The polymer thin films were drop-cast onto a platinum button electrode from 1 mg/mL chlorobenzene solution and characterized using a platinum wire as the counter electrode and a silver wire as the reference electrode. The estimated potentials were calibrated using the onset of the Fc/Fc^+ redox couple (referenced as −4.8 eV), and the calculated HOMO and LUMO levels are collected in Table 1 (see Figures S7−S9 for the corresponding differential pulse voltammograms). The high-lying HOMO of **P1** (−4.85 eV) is due to the electron-rich character of the dialkoxybithiophene units. Interestingly, although polymers **P1** and **P2** have the same backbone structure and the same optical band gap, the onset of oxidation for **P2** is 0.2 V more positive. This effect might be attributed to changes in solid-state ordering, e.g., backbone torsion or π-contacts. A similar change of HOMO levels was also observed in other TPD-based polymer semiconductors, when *n*-octyl chains were replaced with branched 3,7-dimethyloctyl chains.[49] The calculated HOMO energy is −5.26 eV for **P3**, which is about 0.2 eV deeper than that of **P2** and 0.4 eV deeper than **P1**. The low-lying HOMO of **P3** is due to the synergetic interaction between the weak

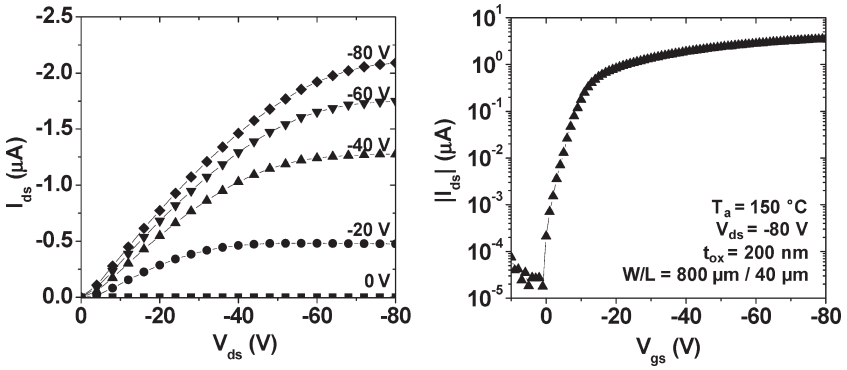


Figure 3. Output and transfer characteristic of **P3**-based field-effect transistors after annealing the films at 150 °C.

Table 2. Electrical Parameters of OFETs Based on P1−P3[a]

polymer	T_a (°C)[b]	mobility (cm^2/(V s))	I_{on}/I_{off}	V_t (V)
P1	110	5.6×10^{-4}	10^2	5.8
	150	7.2×10^{-4}	10^2	4.7
	200	8.3×10^{-4}	10^2	3.7
P2	110	2.1×10^{-4}	10^3	−3.9
	150	2.0×10^{-4}	10^3	−3.3
	200	1.3×10^{-4}	10^3	−5.4
P3	110	8.4×10^{-3}	10^5	−6.1
	150	8.9×10^{-3}	10^5	−0.3
	200	7.8×10^{-3}	10^5	−5.8

[a] Average of six devices measured under inert conditions. [b] Annealing temperature, 10 min.

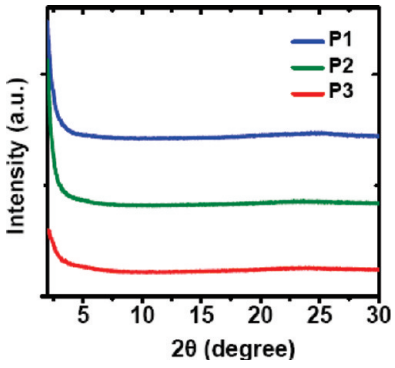


Figure 4. X-ray diffraction (XRD) scans of TPD-based polymer **P1**−**P3** films on glass substrates after annealing at 150 °C.

electron donor (cyclopentadithiophene unit) and the strong electron acceptor (TPD unit). The estimated differences in the HOMO energies of three polymers have important implications for OFET and PSC performance. The lower-lying HOMO of **P3** should diminish p-doping by atmospheric dopants, leading to lower OFET off-currents and increase open circuit voltage (V_{oc}) in solar cells.

Field-Effect Transistors. Thin films of **P1**−**P3** with a thickness of 30−50 nm were deposited onto octyltrichlorosilane (OTS8)-modified silicon/silicon dioxide substrates to evaluate charge transport properties of these polymers.[36,39] All devices were fabricated by employing the bottom-gate bottom-contact configuration, and all the polymers showed typical hole-transport properties (Figure S10). Unlike **P1** and **P2**, a superlinear increase was seen in the output curves of **P3** (Figure S10). This is likely caused by contact resistance between gold electrodes (work function ~5.1 eV) and the deeper HOMO level of **P3** (−5.26 eV). Among the new polymers, **P3** showed the highest average hole mobility of 8.9×10^{-3} cm^2/(V s) with an I_{on}/I_{off} ratio greater than 10^5 (Figure 3). **P1** and **P2** exhibited hole mobilities of 7.2×10^{-4} and 2.0×10^{-4} cm^2/(V s), respectively (Table 2 and Figure S11), which are an order of magnitude lower than that of **P3**. Thermal annealing at temperatures between 110 and 200 °C did not have a significant effect on the OFET characteristics of the polymers (Table 2 and Figure S11). The independence of the carrier mobility on annealing temperature is also expected as we were unable to detect any thermal transitions by DSC within the range of the study (110−200 °C) (Figure S4). More or less subtle changes were noted in room-temperature thin-film UV/vis absorption spectra after annealing at 180 °C for 30 min (Figure S12). The low-energy shoulders in the spectra for **P1** and **P2** become more pronounced after annealing, while for **P3**, fine structure actually decreases.

Film microstructures and surface morphology were investigated by X-ray diffraction (XRD) and atomic force microscopy (AFM). It is interesting to compare the X-ray diffraction patterns of films of **P1** and our previously reported phthalimide-based analogue PhBT12.[39] The film of PhBT12 shows intermediate and wide-angle diffraction maxima, indicating lamellar ordering and close π-stacking distance of 3.6 Å, while the diffractogram from **P1** is essentially featureless. In fact, all the TPD-based polymers (thin films on glass) reported here do not give rise to any observable Bragg reflections (Figure 4) when using a $\theta-2\theta$ geometry. Furthermore, the AFM images (Figure 5) of polymer films on the transistor surfaces are featureless with rms roughness lower than 1 nm; no terrace-like structures or nanofibrillar morphology was detected, which are frequently seen in highly ordered polymer semiconductors.[39,61,62] Though it will require further studies (e.g., grazing-incidence X-ray diffraction, GIXD) to confirm, the replacement of benzene in phthalimide-based PhBT12 with thiophene in **P1** may actually severely curtail long-range solid-state order, contrary to our predictions. This could account for the more than 2 orders of magnitude lower mobility of **P1** than that of PhBT12. Although XRD and AFM suggest amorphous microstructures for polymer **P3**, a moderate field-effect mobility was achieved for this material. The amorphous character of the polymer can be beneficial for the reproducibility of device performance during the device fabrication.[63]

Photovoltaic Devices. Photovoltaic properties of **P1**, **P2**, and **P3** were evaluated after fabricating bulk heterojunction solar cells using fullerene derivative $PC_{71}BM$ as acceptor. Two sets of solar cells with polymer/$PC_{71}BM$ composition of 1:1 and 1:2 (wt:wt) were fabricated. The films have a thickness of 80−90 nm, and all the solar cells have an active area of 9 mm^2. The device size used in this study is much larger than our previously reported PhBT12 solar cells (4 mm^2)[40] to minimize overestimation of the photovoltaic performance and for more consistent comparison among different

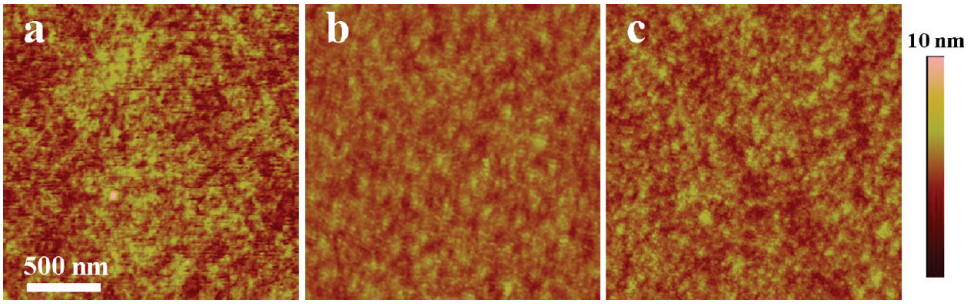


Figure 5. Topographic AFM images of thin films of **P1** (a), **P2** (b), and **P3** (c) after annealing at 200 °C. Root-mean-square roughness (R_q) values are 0.87, 0.48, and 0.67 nm for **P1**, **P2**, and **P3**, respectively.

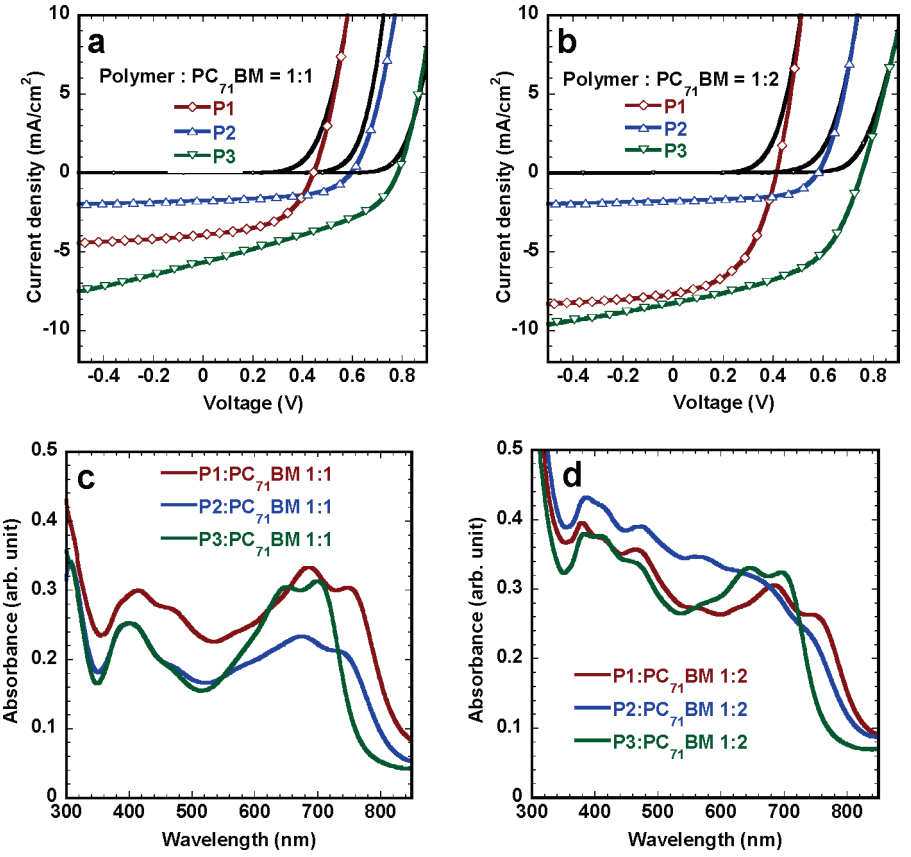


Figure 6. $J-V$ curves (a, b) and absorption spectra (c, d) of **P1**, **P2**, and **P3**/$PC_{71}BM$ solar cells with a weight ratio of 1:1 (a, c) and 1:2 (b, d). The absorption spectra were measured directly from the devices using ITO/PEDOT:PSS substrate as a reference.

laboratories. The current density−voltage ($J-V$) characteristics of the solar cells measured under dark and 100 mW/cm^2 AM1.5 simulated sunlight and the absorption spectra of the blend films measured from the solar cells are shown in Figure 6. The photovoltaic parameters of the solar cells are summarized in Table 3.

The short-circuit current density (J_{sc}), the open-circuit voltage (V_{oc}), and the fill factor (FF) observed in 1:1 **P1**:$PC_{71}BM$ solar cells are 3.56 mA/cm^2, 0.45 V, and 0.49, respectively, resulting in an average power conversion efficiency (PCE) of 0.78%. When the composition of **P1**:$PC_{71}BM$ increased to 1:2, the PCE was improved to 1.44% with the J_{sc} greatly increased to 7.39 mA/cm^2 and the V_{oc} and *FF* slightly decreased to 0.41 V and 0.48, respectively. It is obvious that the more than doubled J_{sc} accounts for the efficiency improvement in the 1:2 solar cells. Comparison of the absorption profiles of the pure polymer and the blends suggests that the enhanced current density in the 1:2 blends could in part be due to increased light absorption at wavelengths below 620 nm, but nanoscale morphology changes may play a more important role. The higher loading of fullerene in the 1:2 solar cells may lead to formation of mixed polymer/fullerene phases together with more continuous fullerene pathways for electron transport.[64] Solar cells based

Table 3. Summary of the Photovoltaic Properties of P1, P2, and P3 Bulk Heterojunction Solar Cells[a]

polymer	polymer:$PC_{71}BM$	J_{sc} (mA/cm^2)	V_{oc} (V)	FF	PCE (%)[b]
P1	1:1	3.56	0.45	0.49	0.78 (0.90)
	1:2	7.39	0.41	0.48	1.44 (1.54)
P2	1:1	1.59	0.59	0.54	0.57 (0.64)
	1:2	1.49	0.58	0.58	0.50 (0.61)
P3	1:1	5.76	0.79	0.39	1.76 (1.78)
	1:2	8.12	0.76	0.50	3.06 (3.15)

[a] Average of four solar cells. [b] In parentheses is the peak PCE.

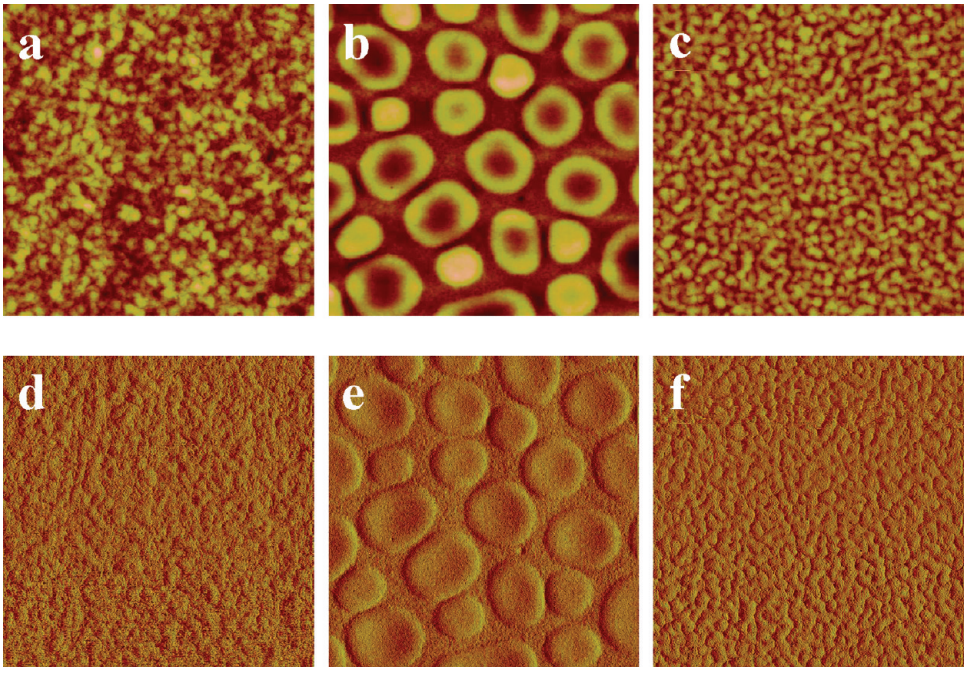


Figure 7. Tapping mode AFM topography (a, b, c) and phase (d, e, f) images of **P1**/$PC_{71}BM$ (a, d), **P2**/$PC_{71}BM$ (b, e), and **P3**/$PC_{71}BM$ (c, f) blend films. The dimension is 5×5 μm for all the images, the height is 30 nm for topography images, and the scale is 30 deg for the phase images. The images were generated from the solar cell devices, and the composition of polymer:$PC_{71}BM$ is 1:2 for all films.

on polymer **P2** show poor photovoltaic performance with a power conversion efficiency of only 0.57% and 0.50% for 1:1 and 1:2 **P2**:$PC_{71}BM$ composition. We note that different from **P1** (and **P3**) all the solar cell parameters in **P2** devices are almost independent of the blend composition. The best photovoltaic performance was achieved in **P3** solar cells. The average PCE achieved in the 1:1 **P3**:$PC_{71}BM$ solar cells was 1.76% with the J_{sc}, V_{oc}, and FF of 5.76 mA/cm^2, 0.79 V, and 0.39, respectively. When the ratio of **P3**:$PC_{71}BM$ changed to 1:2, the average PCE was improved to 3.06%. The peak efficiency achieved in **P3**:$PC_{71}BM$ (1:2) solar cells was 3.15% with J_{sc}, V_{oc}, and FF of 8.29 mA/cm^2, 0.76 V, and 0.50, respectively. Different from **P1** solar cells, in which increasing fullerene loading only led to improved J_{sc}, both J_{sc} and FF were greatly enhanced in 1:2 **P3**:$PC_{71}BM$ solar cells relative to 1:1 **P3**:$PC_{71}BM$ solar cells (Table 3), indicating more balanced charge transport in the 1:2 composition.

The observed very different photovoltaic properties of **P1**, **P2**, and **P3**, as seen in Figure 6 and Table 3, come from the variation in J_{sc}; the highest J_{sc} was achieved in **P3** solar cells and the lowest in **P2** solar cells. It is obvious that the difference in the J_{sc} cannot be merely explained by the different absorption intensity as all the blend films have very similar absorption spectra and intensity (Figure 6d). The hole mobility of the polymers is one of the reasons for the variation in J_{sc}; the highest photocurrent density was observed in highest hole mobility **P3**-based solar cells. However, the hole mobility itself cannot explain the very low J_{sc} of **P2** solar cells since the hole mobilities of **P2** and **P1** are of the same order of magnitude. As already well-known, morphology plays a great role in the efficiency of bulk heterojunction polymer solar cells.[3,11] To better understand the origin of the photovoltaic performance difference in the polymer solar cells, AFM images were collected (Figure 7). Separated toroid-shaped domains with micrometer sizes can be clearly seen in the **P2**:$PC_{71}BM$ (1:2) film, indicating reduced interfacial area for exciton dissociation and a lack of effective percolation for charge transport in the blend film.[65] This means only charges dissociated near the electrodes can be collected, which explains the very low and composition-independent photocurrent density. In contrast, nanoscale phase separation is observed in both **P1**:$PC_{71}BM$ and **P3**:$PC_{71}BM$ blend films, resulting in higher photocurrent density from better exciton dissociation and more efficient charge transport. Compared to **P1**:$PC_{71}BM$, **P3**:$PC_{71}BM$ film shows a clearer and more interconnected biphasic nanostructure, accounting for the higher photocurrent density in this film.

Interestingly, from polymer **P1**, to **P2**, and to **P3**, the V_{oc} of the solar cells increases from 0.45 to 0.59 V and to 0.79 V (1:1 polymer/$PC_{71}BM$ solar cells). The replacement of linear side chains in **P1** by the branched side chains in **P2** results in $\sim$0.2 V increase of V_{oc}, and this enhancement is in good agreement with the electrochemically estimated HOMO levels (Table 1). Furthermore, replacement of strongly donating dialkoxybithiophene units in **P1** with cyclopentadithiophene units in **P3** leads to $\sim$0.4 V increase in V_{oc}, also in perfect agreement with electrochemical estimation of HOMO energy levels. The stronger electron releasing capability of dialkoxybithiophene units destabilizes the HOMOs in polymers **P1** and **P2**. The variation of the photovoltaic properties of these new polymers indicates that strong acceptor and weak donor could be ideal partners[16,66] for constructing high-performance donor−acceptor polymers with appropriate band gap and frontier molecular orbitals for application in BHJ solar cells.[67]

Conclusions

In summary, we have incorporated the electron-deficient unit, TPD, into three new donor−acceptor copolymer semiconductors for applications in BHJ solar cells and field-effect transistors. These donor−acceptor copolymers provide intermediate band gaps (1.5−1.7 eV) with variable HOMO energy levels (−4.9 to −5.3 eV) suitable for tuning the photovoltaic properties of BHJ solar cells. In marked contrast to phthalimide-based polymer PhBT12, thin films of all the TPD-based polymers reported here do not defract X-rays in a typical $\theta-2\theta$ instrument or exhibit

features in AFM images characteristic of long-range order. Among these polymers, **P3** shows the best OFET performance with a moderate hole mobility of 0.009 $cm^2/(V\,s)$ and I_{on}/I_{off} ratio of 10^5. The best solar cells using **P3** as donor and $PC_{71}BM$ as acceptor exhibit efficient device performance with a V_{oc} of 0.76 V and a PCE greater than 3%. However, the performance of **P1**- and **P2**-based solar cells was mainly hindered by the high HOMO level, poor charge transport properties, and suboptimal film morphology. Therefore, the PCEs of the solar cells fabricated from **P1** and **P2** were lower than 1.5%. Because of the appropriate band gap, low-lying HOMO energy, and high hole mobility of **P3**, we believe that the power conversion efficiency of **P3**-based BHJ devices can be further improved by optimizing the film morphology and device fabrication condition as well as by variation in polymer side chains.

Experimental Section

Materials and Methods. All reagents were purchased from commercial sources and used without further purification unless otherwise stated. Monomer 5,5′-bis(tributylstannyl)-3,3′-bis-(dodecyloxy)-2,2′-bithiophene (**2**) was prepared according to published procedures.[31] Anhydrous dichloromethane was distilled from calcium hydride; anhydrous diethyl ether, THF, and toluene were distilled from Na/K alloy. All manipulations and reactions were carried out under inert atmosphere using standard Schlenk line techniques. UV−vis spectra of pure polymer solutions and films were recorded on a Cary model 1 UV−vis spectrophotometer with accurate temperature control. UV−vis absorption spectra of polymer/$PC_{71}BM$ blend films were recorded on a Perkin-Elmer model Lambda 900 UV/vis/near-IR spectrophotometer. Differential scanning calorimetry (DSC) was performed by using TA model DSC 2920. ^1H and ^{13}C NMR spectra were recorded on a Varian INOVA 400 MHz spectrometer (purchased under the CRIF Program of the National Science Foundation, grant CHE-9974810); chemical shifts were referenced to residual protio-solvent signals. Relative molecular weight determinations were made using a Waters 600E HPLC system, driven by Waters Empower software and equipped with two linear mixed-bed GPC columns (American Polymer Standards Corp., AM Gel Linear/15) in series. Eluting polymers were detected with both refractive index and photodiode array detectors. The system was calibrated with 11 narrow PDI polystyrene samples in the range $580-2 \times 10^6$ Da with THF as eluent at a flow rate of 1 mL/min. Differential pulse voltammetry (DPV) was performed on BAS 100 B/W electrochemical analyzer (Bioanalytical Systems, Inc., Lafayette, IN). 0.1 M tetra-*n*-butylammonium hexafluorophosphate in acetonitrile was used as supporting electrolyte. A platinum disk working electrode, a platinum wire counter electrode, and silver wire reference electrode were employed, and Fc/Fc^+ was used to calibrate all measurements. The scan rate was 20 mV/s, and polymer films were produced by drop-casting from 1 mg/mL chlorobenzene solutions. The supporting electrolyte solution was thoroughly purged with N_2 before all CV measurements. Film thickness was measured on an Alpha-Step 500 profilometer (KLA-Tencor, San Jose, CA). AFM images were obtained from OFET and solar cell devices using a Veeco Dimension 3100 in tapping mode with force modulation etched silicon probe (FESP) tips. Polymer thin films for X-ray diffraction (XRD) were prepared by drop-casting of solutions on glass microscope slides. XRD data were obtained using a Bruker-AXS D8 Focus diffractometer with Cu Kα beam (40 kV, 40 mA) in $\theta-2\theta$ scans.

General Procedure for Polymerizations. To an air-free flask containing two monomers (0.2 mmol for each) were added a mixture of $Pd_2(dba)_3$ and tri(*o*-tolyl)phosphine (1:8 molar ratio between $Pd_2(dba)_3$ and P(*o*-tolyl)$_3$; Pd loading: 0.03 equiv). The flask was subjected to three pump/purge cycles with argon followed by addition of THF (4 mL) via syringe. The sealed reaction mixture was stirred at 80 °C for 24 h. After cooling to room temperature, the reaction mixture was dripped into 100 mL of vigorously stirred methanol (containing 5 mL of 12 N HCl). The precipitated solid was stirred for 4 h and collected by centrifugation and decantation. The solid polymers were redissolved and reprecipitated into methanol. After filtration and drying under reduced pressure, the polymers were subjected to sequential Soxhlet extraction using methanol, acetone, hexane, and chloroform as solvents. The final chloroform solution was then concentrated to ~20 mL and precipitated into 100 mL of methanol; the solid was collected by centrifugation and dried under reduced pressure to give a deeply colored solid.

P1. This polymer was obtained as blue solid (164 mg, 96% yield). M_n: 32.3 kDa; PDI: 2.77. ^1H NMR (400 MHz, $C_2D_2Cl_4$, 130 °C): δ 8.09 (brs, 2H), 4.37 (br, 4H), 3.73 (br, 2H), 2.08 (br, 4H), 1.36 (m, 56H), 0.97 (m, 9H).

P2. This polymer was obtained as blue solid (140 mg, 82% yield). M_n: 55.3 kDa; PDI: 1.97. ^1H NMR (400 MHz, $C_2D_2Cl_4$, 130 °C): δ 8.09 (brs, 2H), 4.39 (br, 4H), 3.77 (br, 2H), 2.09 (br, 4H), 1.89 (br, 1H), 1.74 (br, 4H), 1.43 (m, 48H), 0.95 (m, 12H).

P3. This polymer was obtained as deep blue solid (124 mg, 86% yield). M_n: 64.0 kDa; PDI: 4.70. ^1H NMR (400 MHz, $C_2D_2Cl_4$, 130 °C): δ 7.97 (brs, 2H), 3.78 (br, 2H), 2.08 (br, 4H), 1.82 (br, 2H), 1.36 (m, 42H), 0.93 (m, 9H).

Fabrication and Characterization of Organic Field-Effect Transistors (OFETs). OFETs were fabricated on silicon substrates coated with a thermal silicon dioxide top layer (200 nm). Gold source-drain electrodes with an adhesive layer of chromium were patterned by using photolithography and thermal evaporation. Channel widths and lengths were 800 and 40 μm, respectively. The SiO_2 surface was cleaned by sequential ultrasonication in acetone and isopropanol and then hydrophobically modified with a monolayer of octyltrichlorosilane (OTS8). Polymer thin films (30−50 nm) were deposited by spin-coating of polymer solutions (6−8 mg/mL) in 1,2-dichlorobenzene (ODCB) onto substrates. Films were then annealed at 110−200 °C for 10 min. Transistors were tested by using an HP4145B semiconductor parameter analyzer. Transistors were fabricated and tested in a nitrogen filled glovebox.

Solar Cell Fabrication and Characterization. 10 mg/mL polymer solutions were prepared by dissolving 15 mg sample in 1.5 mL of ODCB on an 80 °C hot plate with stirring and the hot solution was filtered through a 0.45 μm GHP filter and stored in a glovebox for use. A $PC_{71}BM$ solution (60 mg/mL) was prepared by dissolving 120 mg of $PC_{71}BM$ (Nano C, Co., Westwood, MA) in 2 mL of ODCB at room temperature with stirring in a glovebox for 2 h. The solution was stored in the glovebox until use after passing through a 0.45 μm PTFE filter. The blend solution of polymer:$PC_{71}BM$ with a composition of 1:1 or 1:2 (wt:wt) ratio was prepared by mixing 1.2 or 0.6 mL of the 10 mg/mL polymer solution and 0.20 mL of 60 mg/mL $PC_{71}BM$ solution and stirring for 10 min at room temperature.

Solar cells were fabricated by first spin-coating a PEDOT:PSS buffer layer on top of ITO-coated glass substrates (10 Ω/□, Shanghai B. Tree Tech. Consult Co., Ltd., Shanghai, China) at 4500 rpm for 40 s and annealed at 150 °C for 10 min under vacuum. The substrates were transferred to the glovebox (where the polymer:$PC_{71}BM$ solution was prepared) for the deposition of the active layer. The active layer was spin-coated on top of PEDOT:PSS layer at 800 rpm for 20 s. **P1**/$PC_{71}BM$ and **P2**/$PC_{71}BM$ films were first slowly dried in covered Petri dishes for 100 min (aging) followed by 10 min thermal annealing on a hot plate. **P3**/$PC_{71}BM$ films were dried by direct thermal annealing at 180 °C for 10 min without aging. The substrates were then taken out of the glovebox and loaded in a thermal evaporator for the deposition of the cathode. The cathode, consisting of 1.0 nm LiF and 100 nm aluminum layers, was sequentially deposited through a shadow mask on top of the active layers after the chamber vacuum reached 8×10^{-7} Torr. Each substrate contained 5 pixels with each pixel having an active area of 3×3 mm^2. Current−voltage characteristics were measured using an HP4155A

semiconductor parameter analyzer (Yokogawa Hewlett-Packard, Tokyo). The light intensity of AM 1.5 sunlight from a filtered Xe lamp was calibrated by a Si photodiode calibrated at the National Renewable Energy Laboratory (NREL). All the characterization steps were carried out under ambient laboratory air.

Acknowledgment. Work at the University of Kentucky was supported by the NSF (CHE-0616759). Work (Excitonic Solar Cells) at the University of Washington was supported by the US Department of Energy, Office of Basic Energy Sciences, Division of Materials Sciences, under Award DE-FG02-07ER46467. The charge transport measurements were supported by the NSF (DMR-0805259 and DMR-0120967). Part of this work was conducted at the University of Washington NanoTech User Facility, a member of the NSF National Nanotechnology Infrastructure Network (NNIN).

Supporting Information Available: Details of monomer synthesis/characterization; ^{1}H NMR spectra, DSC curves, and DPV curves of **P1**−**P3**; thermochromism of **P2** and **P3** in chlorobenzene; output plots and transfer plots of devices fabricated with **P1**−**P3**; charge carrier mobilities of **P1**−**P3** as a function of annealing temperatures. This material is available free of charge via the Internet http://pubs.acs.org.

References and Notes

(1) Coakley, K. M.; McGehee, M. D. *Chem. Mater.* **2004**, *16*, 4533.
(2) Günes, S.; Neugebauer, H.; Sariciftci, N. S. *Chem. Rev.* **2007**, *107*, 1324.
(3) Thompson, B. C.; Fréchet, J. M. J. *Angew. Chem., Int. Ed.* **2008**, *47*, 58.
(4) Dennler, G.; Scharber, M. C.; Brabec, C. J. *Adv. Mater.* **2009**, *21*, 1323.
(5) Irwin, M. D.; Buchholz, B.; Hains, A. W.; Chang, R. P. H.; Marks, T. J. *Proc. Natl. Acad. Sci. U.S.A.* **2008**, *105*, 2783.
(6) Park, S. H.; Roy, A.; Beaupre, S.; Cho, S.; Coates, N.; Moon, J. S.; Moses, D.; Leclerc, M.; Lee, K.; Heeger, A. J. *Nat. Photonics* **2009**, *3*, 297.
(7) Beaujuge, P. M.; Subbiah, J.; Choudhury, K. R.; Ellinger, S.; McCarley, T. D.; So, F.; Reynolds, J. R. *Chem. Mater.* **2010**, *22*, 2093.
(8) Xin, H.; Kim, F. S.; Jenekhe, S. A. *J. Am. Chem. Soc.* **2008**, *130*, 5424.
(9) Peet, J.; Kim, J. Y.; Coates, N. E.; Ma, W.; Moses, D.; Heeger, A. J.; Bazan, G. C. *Nat. Mater.* **2007**, *6*, 497.
(10) Lee, J. K.; Ma, W.; Brabec, C. J.; Yuen, J.; Moon, J. S.; Kim, J. Y.; Lee, K.; Bazan, G. C.; Heeger, A. J. *J. Am. Chem. Soc.* **2008**, *130*, 3619.
(11) Peet, J.; Heeger, A. J.; Bazan, G. C. *Acc. Chem. Res.* **2009**, *42*, 1700.
(12) Liang, Y.; Wu, Y.; Feng, D.; Tsai, S.-T.; Son, H.-J.; Li, G.; Yu, L. *J. Am. Chem. Soc.* **2009**, *131*, 56.
(13) Liang, Y.; Feng, D.; Wu, Y.; Tsai, S.-T.; Li, G.; Ray, C.; Yu, L. *J. Am. Chem. Soc.* **2009**, *131*, 7792.
(14) Chen, H.; Hou, J.; Zhang, S.; Liang, Y.; Yang, G.; Yang, Y.; Yu, L.; Wu, Y.; Li, G. *Nat. Photonics* **2009**, *3*, 649.
(15) Hou, J.; Chen, H.-Y.; Zhang, S.; Chen, R.; Yang, Y.; Wu, Y.; Li, G. *J. Am. Chem. Soc.* **2009**, *131*, 15586.
(16) Zheng, Q.; Jung, B. J.; Sun, J.; Katz, H. E. *J. Am. Chem. Soc.* **2010**, *132*, 5394.
(17) Cheng, Y. J.; Yang, S. H.; Hsu, C. S. *Chem. Rev.* **2009**, *109*, 5868.
(18) Yu, G.; Gao, J.; Hummelen, J. C.; Wudl, F.; Heeger, A. J. *Science* **1995**, *270*, 1789.
(19) Halls, J. J. M.; Walsh, C. A.; Greenham, N. C.; Marseglia, E. A.; Friend, R. H.; Moratti, S. C.; Holmes, A. B. *Nature* **1995**, *376*, 498.
(20) Liang, Y.; Yu, L. *Acc. Chem. Res.* **2010**, *43*, 1227.
(21) Li, C.; Liu, M.; Pschirer, N. G.; Baumgarten, M.; Müllen, K. *Chem. Rev.* **2010**, *110*, 6817.
(22) Green, M. A.; Emery, K.; Hishikawa, Y.; Warta, W. *Prog. Photovoltaics* **2010**, *18*, 144.
(23) Ohkita, H.; Cook, S.; Astuti, Y.; Duffy, W.; Tierney, S.; Zhang, W.; Heeney, M.; McCulloch, I.; Nelson, J.; Bradley, D. D. C.; Durrant, J. R. *J. Am. Chem. Soc.* **2008**, *130*, 3030.
(24) Wu, P.-T.; Bull, T.; Kim, F. S.; Luscombe, C. K.; Jenekhe, S. A. *Macromolecules* **2009**, *42*, 671.
(25) Ahmed, E.; Kim, F. S.; Xin, H.; Jenekhe, S. A. *Macromolecules* **2009**, *42*, 8615.
(26) Li, G.; Shrotriya, V.; Huang, J.; Yao, Y.; Moriarty, T.; Emery, K.; Yang, Y. *Nat. Mater.* **2005**, *4*, 864.
(27) Liang, Y.; Xu, Z.; Xia, J.; Tsai, S. T.; Wu, Y.; Li, G.; Ray, C.; Yu, L. *Adv. Mater.* **2010**, *22*, E135.
(28) Jenekhe, S. A.; Lu, L.; Alam, M. M. *Macromolecules* **2001**, *34*, 7315.
(29) Roncali, J. *Chem. Rev.* **1997**, *97*, 173.
(30) Sakai, N.; Mareda, J.; Vauthey, E.; Matile, S. *Chem. Commun.* **2010**, *46*, 4225.
(31) Guo, X.; Watson, M. D. *Org. Lett.* **2008**, *10*, 5333.
(32) Zhan, X.; Tan, Z.; Domercq, B.; An, Z.; Zhang, X.; Barlow, S.; Li, Y.; Zhu, D.; Kippelen, B.; Marder, S. R. *J. Am. Chem. Soc.* **2007**, *129*, 7246.
(33) Chen, Z.; Zheng, Y.; Yan, H.; Facchetti, A. *J. Am. Chem. Soc.* **2009**, *131*, 8.
(34) Yan, H.; Chen, Z.; Zheng, Y.; Newman, C.; Quinn, J. R.; Dotz, F.; Kastler, M.; Facchetti, A. *Nature* **2009**, *457*, 679.
(35) Durban, M. M.; Kazarinoff, P. D.; Luscombe, C. K. *Macromolecules* **2010**, *43*, 6348.
(36) Kim, F. S.; Guo, X.; Watson, M. D.; Jenekhe, S. A. *Adv. Mater.* **2010**, *22*, 478.
(37) Tan, Z.; Zhou, E.; Zhan, X.; Wang, X.; Li, Y.; Barlow, S.; Marder, S R. *Appl. Phys. Lett.* **2008**, *93*, 073309.
(38) Letizia, J. A.; Salata, M. R.; Tribout, C. M.; Facchetti, A.; Ratner, M. A.; Marks, T. J. *J. Am. Chem. Soc.* **2008**, *130*, 9679.
(39) Guo, X.; Kim, F. S.; Jenekhe, S. A.; Watson, M. D. *J. Am. Chem. Soc.* **2009**, *131*, 7206.
(40) Xin, H.; Guo, X.; Kim, F. S.; Ren, G.; Watson, M. D.; Jenekhe, S. A. *J. Mater. Chem.* **2009**, *19*, 5303.
(41) Guo, X. Ph.D. Thesis, University of Kentucky, 2009.
(42) Zhang, Q. T.; Tour, J. M. *J. Am. Chem. Soc.* **1997**, *119*, 5065.
(43) Nielsen, C. B.; Bjornholm, T. *Org. Lett.* **2004**, *6*, 3381.
(44) Irvin, J. A.; Schwendeman, I.; Lee, Y.; Abboud, K. A.; Reynolds, J. R. *J. Polym. Sci., Part A: Polym. Chem.* **2001**, *39*, 2164.
(45) Pomerantz, M.; Amarasekara, A. S. *Synth. Met.* **2003**, *135*, 257.
(46) Pomerantz, M. *Tetrahedron Lett.* **2003**, *44*, 1563.
(47) Zou, Y.; Najari, A.; Berrouard, P.; Beaupré, S.; Badrou, R. A.; Tao, Y.; Leclerc, M. *J. Am. Chem. Soc.* **2010**, *132*, 5330.
(48) Zhang, Y.; Hau, S. K.; Yip, H.-L.; Sun, Y.; Acton, O.; Jen, A. K. Y. *Chem. Mater.* **2010**, *22*, 2696.
(49) Piliego, C.; Holcombe, T. W.; Douglas, J. D.; Woo, C. H.; Beaujuge, P. M.; Fréchet, J. M. J. *J. Am. Chem. Soc.* **2010**, *132*, 7579.
(50) Zhang, G.; Fu, Y.; Zhang, Q.; Xie, Z. *Chem. Commun.* **2010**, *46*, 4997.
(51) Brzezinski, J. Z.; Reynolds, J. R. *Synthesis* **2002**, 1053.
(52) Pal, B.; Yen, W. C.; Yang, J. S.; Chao, C. Y.; Hung, Y. C.; Lin, S. T.; Chuang, C. H.; Chen, C. W.; Su, W. F. *Macromolecules* **2008**, *41*, 6664.
(53) Kline, R. J.; McGehee, M. D.; Kadnikova, E. N.; Liu, J.; Fréchet, J. M. J.; Toney, M. F. *Macromolecules* **2005**, *38*, 3312.
(54) Ma, W.; Kim, J. Y.; Lee, K.; Heeger, A. J. *Macromol. Rapid Commun.* **2007**, *28*, 1776.
(55) McCullough, R. D.; Williams, S. P. *J. Am. Chem. Soc.* **1993**, *115*, 11608.
(56) Kim, J.; Swager, T. M. *Nature* **2001**, *411*, 1030.
(57) Zhao, X.; Pinto, M. R.; Hardison, L. M.; Mwaura, J.; Muller, J.; Jiang, H.; Witker, D.; Kleiman, V. D.; Reynolds, J. R.; Schanze, K. S. *Macromolecules* **2006**, *39*, 6355.
(58) Wu, P.-T.; Xin, H.; Kim, F. S.; Ren, G.; Jenekhe, S. A. *Macromolecules* **2009**, *42*, 8817.
(59) Zhu, Y.; Champion, R. D.; Jenekhe, S. A. *Macromolecules* **2006**, *39*, 8712.
(60) Wong, W. W. H.; Ma, C.; Pisula, W.; Yan, C.; Feng, X.; Jones, D. J.; Müllen, K.; Janssen, R. A. J.; Bauerle, P.; Holmes, A. B. *Chem. Mater.* **2010**, *22*, 457.
(61) McCulloch, I.; Heeney, M.; Bailey, C.; Genevicius, K.; MacDonald, I.; Shkunov, M.; Sparrowe, D.; Tierney, S.; Wagner, R.; Zhang, W. M.; Chabinyc, M. L.; Kline, R. J.; Mcgehee, M. D.; Toney, M. F. *Nat. Mater.* **2006**, *5*, 328.
(62) Kim, D. H.; Lee, B.-L.; Moon, H.; Kang, H. M.; Jeong, E. J.; Park, J.-I.; Han, K.-M.; Lee, S.; Yoo, B. W.; Koo, B. W.; Kim, J. Y.; Lee,

W. H.; Cho, K.; Becerril, H. A.; Bao, Z. *J. Am. Chem. Soc.* **2009**, *131*, 6124.
(63) Choi, T.-L.; Han, K.-M.; Park, J.-I.; Kim, D. H.; Park, J.-M.; Lee, S. *Macromolecules* **2010**, *43*, 6045.
(64) Mayer, A. C.; Toney, M. F.; Scully, S. R.; Rivnay, J.; Brabec, C. J.; Scharber, M.; Koppe, M.; Heeney, M.; McCulloch, I.; McGehee, M. D. *Adv. Funct. Mater.* **2009**, *19*, 1173.
(65) Bull, T. A.; Pingree, L. S. C.; Jenekhe, S. A.; Ginger, D. S.; Luscombe, C. K. *ACS Nano* **2009**, *3*, 627.
(66) Blouin, N.; Michaud, A.; Gendron, D.; Wakim, S.; Blair, E.; Neagu-Plesu, R.; Belletete, M.; Durocher, G.; Tao, Y.; Leclerc, M. *J. Am. Chem. Soc.* **2008**, *130*, 732.
(67) Scharber, M. C.; Wuhlbacher, D.; Koppe, M.; Denk, P.; Waldauf, C.; Heeger, A. J.; Brabec, C. L. *Adv. Mater.* **2006**, *18*, 789.

278 *Macromolecules* **2011**, *44*, 278–285
DOI: 10.1021/ma102005s

Macromolecules
ARTICLE

UV-enhanced Ordering in Azobenzene-Containing Polystyrene-*block*-Poly(*n*-Butyl Methacrylate) Copolymer Blends

Wei Chen,[†] Jia-Yu Wang,[‡] Xinyu Wei,[†] Ji Xu,[†] Anna C. Balazs,[§] Krzysztof Matyjaszewski,[⊥] and Thomas P. Russell*,[†]

[†]*Department of Polymer Science and Engineering, University of Massachusetts Amherst, Amherst, Massachusetts 01003, United States,* [‡]*Department of Chemistry, The University of Chicago, Chicago, Illinois 60637, United States,* [§]*Department of Chemical Engineering, University of Pittsburgh, Pittsburgh, Pennsylvania 15260, United States, and* [⊥]*Department of Chemistry, Carnegie Mellon University, Pittsburgh, Pennsylvania 15213, United States*

Received August 30, 2010; Revised Manuscript Received December 9, 2010

ABSTRACT: Reversible photocontrol on the ordering of block copolymers through the disorder-to-order transition (DOT) is important to promote long-range laterally ordered nanostructures over a macroscopic scale by "photo-combing", similar to the classic zone refining used to produce highly pure, large single crystals. In this report, we have synthesized two deuterated polystyrene-*b*-poly(*n*-butyl methacrylate-*r*-2-(4-(phenylazo)benzoate)ethyl methacrylate) (PS-d_8-*b*-P(nBMA-*r*-AzoEMA)) block copolymers containing photoisomerizable azobenzene functionalities. These two block copolymers and their binary mixtures exhibit an entropy-driven lower DOT (LDOT). Upon UV irradiation, the photoisomerization of azobenzene led to a gain in entropy, originating from conformational changes and density variations. Such an increase in entropic contributions significantly enhanced the ordering, thereby driving the phase-mixed copolymer blends toward a fully ordered state, as evidenced by small-angle neutron scattering (SANS) and specular neutron reflectivity (NR). This process could also be reversed by exposure to visible light via photoinduced *cis*−*trans* isomerization of azobenzene.

Introduction

Currently, one of the challenges in materials science is establishing a simple way to generate an ultradense array of addressable nanoscopic elements on a macroscopic scale.[1] The addressability of nanomaterials is essential for many applications, ranging from high-density magnetic storage to high-density, ultrahigh resolution displays to photovoltaics. Among the strategies available, the self-assembly of block copolymers (BCPs) is emerging as a promising route to generate templates and scaffolds for the fabrication of highly ordered nanomaterials, offering a potential solution to this challenge.[1−7] BCPs are two or more chemically different polymer chains joined their ends with a covalent bond.[8] These copolymers have the ability to mix or microphase-separate into ordered arrays of microdomains, tens of nanometers in size. Recently, considerable advances have been made to enhance the ordering of BCP microdomains in thin films.[2,3,7] However, it remains a challenge to achieve perfect order over a macroscopic length scale, since the self-assembled BCPs usually contain various defects, like grain boundaries, edge dislocations, and disclinations. Hashimoto and co-workers[9−15] have demonstrated that arrays of highly ordered BCP microdomains could be achieved by a zone heating method, similar to the classic zone refinement[16] used to produce highly pure, large single crystals. In this process, a moving temperature gradient was imposed on the BCPs during the ordering process from the disordered state to epitaxially "crystallize" the BCP microdomains in a moving front, creating macroscopically ordered and oriented nanostructures—a single-grain lamellar structure[9,10] and a columnar grain texture having a special orientation of hexagonally packed cylindrical microdomain structure.[11−15] Consequently, when the ordering process through the disorder-to-order transition (DOT) is controlled by applied external fields, BCP microdomains can be directed to self-assemble into arrays having long-range lateral order, like the growth of large single crystals.

Most recently, Balazs and co-workers[17,18] theoretically proposed that "photo-combing" could lead to the formation of defect-free structures in polymer blends. This process is initiated by shining a spatially uniform "background" light on a photosensitive polymer blend, which thereby undergoes a reversible chemical reaction and a phase separation. Following that, a well-collimated, higher intensity light that locally increases the rate of reaction is introduced to raster over the sample. In effect, the secondary light acts as a "comb" that sweeps out all of the defects with each successive pass over the sample and creates highly regular structures. In this system, light, instead of heat, induces the phase transition through reversible photoreactions. Similarly, if a BCP is reversibly brought through an ordering transition from a disordered state to ordered state by light, long-range ordering of BCP microdomains can be produced over a macroscopic scale by photorastering BCP samples with a series of light bands and combing out defects via a process comparable to the classic zone refinement.

To apply photocombing, it is necessary to achieve control over the DOT in BCP films by reversible photoreactions. Generally, most BCPs undergo a disordering transition upon heating. This order-to-disorder transition (ODT) is driven by the reduction in enthalpic interactions between the components.[8] For certain BCP systems, however, increasing temperature from the disordered state can lead to microphase separation. Such an ordering transition was termed as the lower disorder-to-order transition

*To whom correspondence should be addressed. E-mail: russell@mail.pse.umass.edu.

 Published on Web 12/31/2010 © 2010 American Chemical Society

Scheme 1. Synthetic Pathway of PS-d_8-*b*-P(*n*BMA-*r*-AzoEMA) copolymers

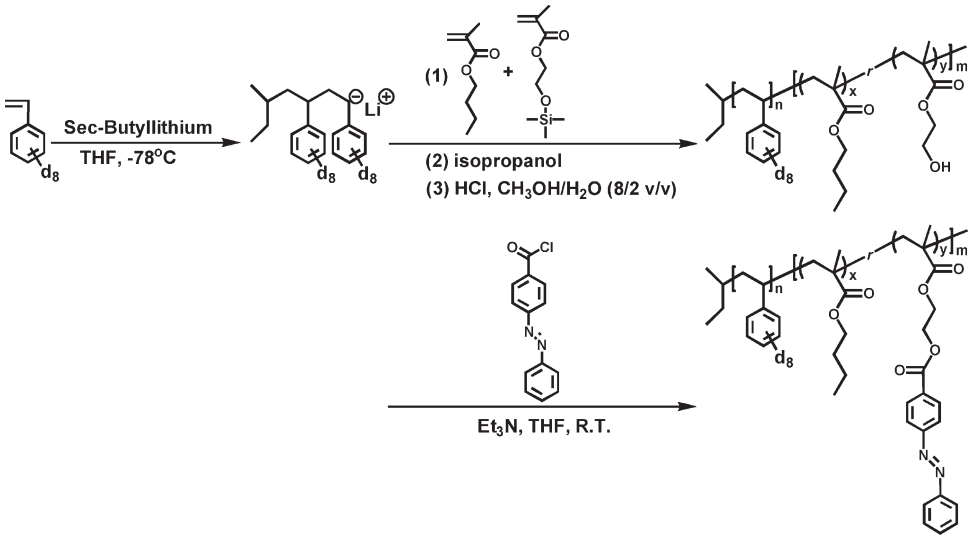


Table 1. Characteristics of Two PS-d_8-*b*-P(*n*BMA-*r*-AzoEMA) Copolymers[a]

	M_n	M_w	PDI	PS-d_8:PAzoEMA:PnBMA (wt %)	morphology
Azo83K	83 000	87 000	1.05	53.1:21.9:25.0	lamellae
Azo24K	24 000	25 000	1.04	58.3:16.7:25.0	disorder

[a] Note: The weight fraction of PS-d_8 was determined by GPC and the ratio of PAzoEMA and P*n*BMA was measured by ^{1}H NMR.

(LDOT), which was first discovered in polystyrene-*block*-poly(*n*-butyl methacrylate) (PS-*b*-P*n*BMA) BCP.[19−31] For weakly interacted PS-*b*-P*n*BMA BCPs, the molecular packing differences between two blocks lead to disparities in the free volume of each component, which are reflected in their densities and thermal expansion coefficients.[32−40] The LDOT originates from an increase in entropy and, hence, is sensitive to density changes. Among photoaddressable chromophores, azobenzene is particularly useful for our purpose to reversibly photocontrol the ordering process of PS-*b*-P*n*BMA BCPs, given that the photoisomerization of azobenzene is a form of light-induced molecular motion, leading to a local density variation.[41−46] Azobenzene usually exists in a stable *trans* state. After absorption of UV light, the molecule isomerizes into a metastable *cis* state. The *cis* isomer can be switched back to the *trans* by visible light or heat. When azobenzene is integrated into a PS-*b*-P*n*BMA BCP that is phase-mixed, but close to the LDOT, these light-induced motions will lead to a significant increase in entropy, as a result of conformational changes and density variations, which may bring about a photoinduced ordering transition from a homogeneous mixture to an ordered state with microdomains of each block. Even though the photoisomerization might cause an enthalpic contribution, regarding the entropy-driven nature of the LDOT, the influence of enthalpic contribution is very small, and thus can be ignored, when the block copolymer system locates close to the boundary of the LDOT.

Here, azobenzene functionalities were randomly incorporated into P*n*BMA blocks, forming deuterated polystyrene-*block*-poly(*n*-butyl methacrylate-*random*-2-(4-(phenylazo)benzoate)ethyl methacrylate) (PS-d_8-*b*-P(*n*BMA-*r*-AzoEMA)) BCPs. Their phase behavior and photoresponses were investigated by small-angle neutron scattering (SANS). An enhanced ordering arising from UV-induced *trans*-*cis* isomerization of azobenzene was observed in the films of phase-mixed PS-d_8-*b*-P(nBMA-*r*-AzoEMA)) copolymer blends that were close to the LDOT. This process could also be reversed by exposure to visible light via photoinduced *cis*-*trans* isomerization of azobenzene, as evidenced by specular neutron reflectivity (NR). It is evident that reversible photocontrol on the LDOT is achievable for PS-d_8-*b*-P(nBMA-*r*-AzoEMA)) BCPs through the photoisomerization of azobenzene.

Experimental Section

Synthesis of PS-d_8-*b*-P(*n*BMA-*r*-AzoEMA) BCP. PS-d_8-*b*-P(*n*BMA-*r*-AzoEMA) BCPs composed of a PS-d_8 block and one random copolymer block with *n*BMA and azobenzene-functionalized HEMA repeat units were obtained via two-step synthesis (Scheme 1). At first, the copolymers were synthesized by sequential anionic polymerization with *sec*-butyl lithium as the initiator. After deprotection to the hydroxyl group, the azobenzene side group was attached through an esterification reaction (see the Supporting Information for details). Molecular weights (MWs) and polydispersity indices (PDIs) of PS-d_8-*b*-P(*n*BMA-*r*-AzoEMA) BCPs were characterized by gel permeation chromatography (GPC) and their compositions were determined by ^{1}H nuclear magnetic resonance (NMR) spectroscopy. Table 1 shows the characteristics of two PS-d_8-*b*-P(*n*BMA-*r*-AzoEMA) BCPs with M_n = 83 000 (designated as Azo83K) and M_n = 24 000 (designated as Azo24K), respectively.

Preparation of Binary Copolymer Mixtures. Various compositions of binary mixtures consisting of Azo83K and Azo24K copolymers were prepared by dissolving a predetermined amount of the mixtures in THF (10 wt % in THF) and slowly evaporating the solvent over 3 days at room temperature. To remove the residual solvent, the mixtures were dried under vacuum at 60 °C for 24 h. After the complete removal of the solvent, the samples were further annealed at 130 °C for 48 h.

Characterization. NMR spectra were recorded in $CDCl_3$ on Brüker Avance 400 (^{1}H) spectrometer with a Brüker BBO5 probe. MWs and PDIs were estimated by GPC using a Knauer K-501 Pump with a K-2301 refractive index (RI) detector and K-2600 UV detector, and a column bank consisting of two Polymer Laboratories PLGel Mixed D columns, and one PLGel 50 Å column (15 × 300 mm) in THF as eluent at a flow rate of 1.0 mL/min against linear polystyrene standards. Fourier transform infrared (FT-IR) absorption spectra of the copolymer films were collected on a BioRad ExCalibur spectrometer with a resolution

of 1 cm^{-1} over a wavenumber range from 4000 to 400 cm^{-1}. Spectra were obtained by using copolymer films cast on high resistance silicon wafers with a bare wafer providing the background spectrum. UV−vis absorption spectra were recorded on a PerkinElmer LAMBDA 850 UV−vis spectrophotometer. Small-angle X-ray scattering (SAXS) experiments were performed at the Materials Research Science and Engineering Center (MRSEC) at the University of Massachusetts Amherst. A SAXS instrument, consisting of a three-pinhole collimation system, had an Osmic MaxFlux X-ray (Cu k_α, 1.542 Å) source generated by a copper anode. SAXS measurements were performed at room temperature under vacuum with an exposure time of 2 h. All SAXS data presented here are raw data without the corrections for background and empty cell scattering. Film thickness was measured with a Rudolph Research AutoEL-II ellipsometer using a helium−neon laser (λ = 632.8 nm) at a 70° incidence angle and a Filmetrics F20−UV thin film measurement system (Filmetrics Inc.) with a regulated deuterium and tungsten−halogen high power UV−vis fiber light source (HAMAMATSU Inc.) over a wavelength range from 200 to 1100 nm with the incident light normal to the sample surface. The data were fit using a single layer model to obtain the film thickness. X-ray photoelectron spectra (XPS) were recorded on a Physical Electronics Quantum 2000 spectrometer with Al Kα excitation at a spot size of 100 μm at 25 W. Spectra were obtained at 15° takeoff angle with respect to the plane of the sample surface. To access the component information on PS-d_8-*b*-P(*n*BMA-*r*-AzoEMA) BCPs at the substrate by XPS, a special procedure was applied to our samples. The BCPs were spin-coated on a Si substrate with a SiO_2 layer of ~250 nm. After thermal annealing, the BCP films were floated onto the surface of a 5% HF aqueous solution by etching the SiO_2 layer and, then, flipped over and transferred onto another Si substrate. The XPS measurement was performed on the flipped film, so that the composition close to the substrate could be determined.

Temperature-dependent SANS measurements were performed from 140 to 200 °C with an interval of 10 °C at the NG7 30 m SANS instrument at the National Institute of Standards and Technology in Gaithersburg, MD (see ref 47 for details of instrument design and operation). Neutrons of wavelength λ = 6 Å with full width half-maximum $\Delta\lambda/\lambda$ = 0.11 were used. Three configurations were used: one with the detector offset by 20 cm and a sample−detector distance of 1 m, the second with a sample−detector distance of 4 m, and the third with a sample−detector distance of 13 m, to give a scattering vector (q) range of 0.0036−0.5669 $Å^{-1}$. The scattering intensity was corrected for instrument dark current, empty cell scattering, the sensitivity of individual detector pixels, and beam transmission to obtain the absolute neutron intensity by use of the available data reduction macros based on the Igor Pro data analysis package through the direct beam flux method.[48] Data were analyzed using the smeared random phase approximation (RPA) model for binary mixtures of di-BCPs.[49−54] Compressibility[33,34] and BLFH fluctuation[55−58] corrections are also considered. The incoherent scattering was set as one of the fitting parameters and was corrected for the fitting results (see the Supporting Information for details).

Bulk samples for the SANS measurements were prepared by compression-molding Azo83K and Azo24K copolymers and their blends into 1.5 cm diameter disks with ~0.8 mm thickness at 130 °C. The disks were then annealed at 130 °C under vacuum for 72 h. Samples for analysis were placed into demountable titanium cells fitted with quartz windows. The entire assembly was mounted on a remote-controlled multisampling block with a heating setup designed for the neutron spectrometer. Prior to each measurement, the samples were allowed 30 min to achieve thermal equilibrium. The temperature was monitored and controlled by a thermocouple located in close proximity to the samples. The temperature control was within ±1 °C at each temperature.

To investigate the effects of UV irradiation, a Newport's Oriel light source equipped with a high power mercury arc lamp (500 W), a digital light intensity controller, and two 365 and 436 nm wavelength filters was used for UV and visible light irradiation. Since azobenzene strongly absorbs UV light with a wavelength of 365 nm, the maximum penetration depth is ~3 μm.[41] For bulk samples, UV-induced *trans*−*cis* isomerization can occur only in a thin layer on the surface. Therefore, toluene solutions of the blends of Azo83K and Azo24K copolymers were spin-coated onto silicon wafers, forming films with a thickness of ~1.2 μm. After annealing at 180 °C under vacuum for 48 h, these films were cut into two pieces with the same shape and size. One was kept in the dark; the other was exposed to UV light with a wavelength of 365 nm and an intensity of 35 mW/cm^2 for 1 h at 180 °C in an inert gas environment. After UV treatments, the thin film was quenched to low temperature using liquid nitrogen. SANS measurements were performed on them at room temperature and the incident neutron beam was perpendicular to the films. To confirm the UV effect and reversibility, specular NR was also measured on three different films that were spin-coated from a toluene solution of the copolymer blend with an Azo83K weight fraction of 60% onto silicon wafers under the same conditions, forming a film with a thickness of ~850 nm. One was kept in the dark; the second was exposed to UV light with a wavelength of 365 nm and an intensity of 35 mW/cm^2 for 1 h at 180 °C under an inert gas protection; the third was irradiated first by UV light under the same conditions as above and then by visible light with a wavelength of 436 nm for one more hour. NR measurements were performed on the NG7 neutron reflection spectrometer with a wavelength λ of 4.76 Å and a $\Delta\lambda/\lambda$ of 0.04 ($\Delta q/q$ is variable with slits from 0.02 to 0.15) at the NIST Center for Neutron Research at the National Institute of Standards and Technology in Gaithersburg, MD. The programs from the REFPAK suite were used for data reduction.[59] The fitting procedure used in this study is very similar to that applied to polystyrene-*block*-poly(*n*-alkyl methacrylate) di-BCPs that have been described in detail elsewhere.[60−63]

Results and Discussion

Phase Behavior. Neutron scattering is a unique technique for studying the phase behavior of PS-d_8-*b*-P(*n*BMA-*r*-AzoEMA) BCPs, because of the low electron density contrast for X-ray (ρ_{PnBMA} = 0.3419 $Å^{-3}$ and ρ_{PS} = 0.3412 $Å^{-3}$ for Cu Kα) and the analogous molecular structures of two blocks for electron microscope measurements (hard to stain one block to enhance the contrast). Two sets of SANS experiments were conducted on Azo83K and Azo24K BCPs and their blends. To investigate the UV-induced ordering transition from a disordered state, a BCP close to its phase transition boundary is preferred as the photoinduced LDOT is more easily achieved. SANS was first measured at room temperature on Azo83K and Azo24K BCPs and their blends as a function of weight fraction of Azo83K BCP to find the boundary composition, where the DOT would occur. And then, the temperature-dependent SANS was employed on the copolymer blends, which are in a disordered state but very close to the boundary of DOT, to verify whether they still have a LDOT behavior, because the phase behavior of PS-*b*-P*n*BMA BCPs may be significantly changed after the incorporation of azobenzene functionality. Both experiments generated azimuthally symmetric two-dimensional SANS patterns, which were reduced to one-dimensional absolute scattering intensity profiles as a function of wave vector $q = 4\pi(\sin\theta)/\lambda$, where λ is the neutron wavelength and 2θ is the scattering angle.

Figure 1 showed SANS profiles for pure Azo83K and Azo24K BCPs and their binary mixtures at room temperature. No obvious macrophase separation was observed at all compositions of the BCP blends, in agreement with the previous observations of the BCP blends with a ratio of molecular

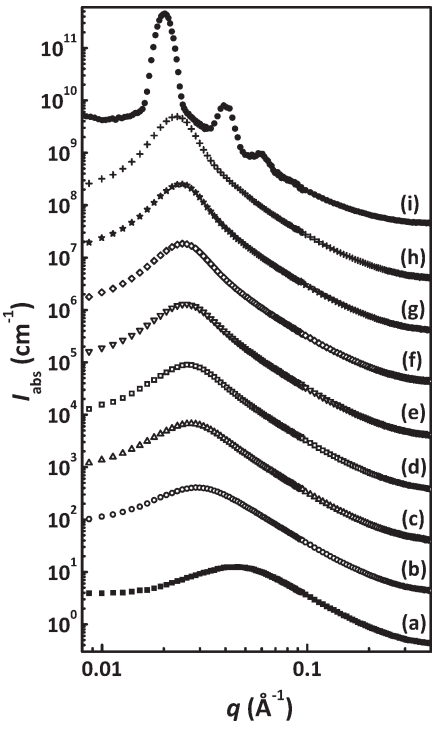


Figure 1. SANS profiles of Azo24K and Azo83K BCPs and their copolymer blends at room temperature: (a) pure Azo24K, (b) 30Azo83K−70Azo24K, (c) 40Azo83K−60Azo24K, (d) 45Azo83K−55Azo24K, (e) 50Azo83K−50Azo24K, (f) 55Azo83K−45Azo24K, (g) 60Azo83K−40Azo24K, (h) 70Azo83K−30Azo24K, and (i) pure Azo83K. Note: the profiles have been shifted vertically by a factor of 10 for clarity.

weights less than 5.[64,65] For the pure Azo24K BCP (Figure 1a), a single, broad scattering peak was observed at $q^* = 0.04609$ Å^{-1}, arising from the correlation-hole scattering of a block copolymer in a disordered state, whereas for the pure Azo83K BCP (Figure 1i), a sharp primary peak at $q^* = 0.02017$ Å^{-1}, as well as three higher-order reflections at $2q^*$, $3q^*$, and $4q^*$ was seen, indicating that this BCP phase-separated into a lamellar morphology. In the scattering profiles of their binary mixtures, the weak correlation-hole scattering peaks sharpened and shifted to lower q^* values as the fraction of Azo83K BCP increased. For the 80Azo83K−20Azo24K and 90Azo83K−10Azo24K BCP blends (where the number in front of Azo83K or Azo24K represents the weight percent of the corresponding BCP in the binary copolymer blends), the second-order reflection appeared in their SAXS profiles (not shown here). It is evident that the BCP blends gradually transited from a disordered to an ordered state, depending on the overall molecular weight of the mixture, which is given by $M_n = x_{azo83K} M_{n,azo83K} + x_{azo24K} M_{n,azo24K}$, where x_{azo83K} and x_{azo24K} are the mole fraction of each component.

The composition dependence of the DOT could be observed more clearly in Figure 2. The wave vector, q^*, at the first-order scattering maximum decreased monotonically as a function of the weight fraction of the Azo83K BCP in the copolymer blends,[64] but the slopes remarkably changed at an Azo83K weight fraction of ~0.33. Meanwhile, a discontinuous increase of the corresponding maximum absolute intensity, I_{max}, occurred at an Azo83K weight fraction of ~0.68. Thus, a fluctuation-dominated (partially ordered) region between a disordered and an ordered region was defined by the two boundary compositions, at which I_{max} and q^* exhibited two discontinuities at the transition, respectively. According to these two boundaries, it is easy to find that 50Azo83K−50Azo24K,

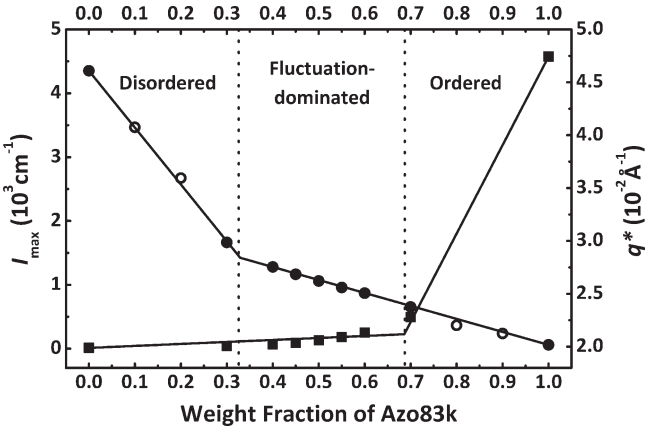


Figure 2. Absolute intensity at the first-order scattering maximum (I_{max}) (■) and the corresponding wave vector (q^*) (●) as a function of weight fraction of Azo83K BCP for Azo24K and Azo83K BCPs copolymer blends at room temperature. Note: q^* values represented by open circles (○) were obtained by SAXS experiments at room temperature.

55Azo83K−45Azo24K, and 60Azo83K−40Azo24K BCP blends were in a phase-mixed state, but very close to the DOT.

To investigate the phase behavior, temperature-dependent SANS was performed on the above three BCP blends at 7 different temperatures in 10 °C increments from 140 to 200 °C. The correlation-hole scattering for these three copolymers persisted, giving evidence that they were phase-mixed over the entire experimental temperature range (S-Figure 4−S-Figure 6 in the Supporting Information). The SANS profiles could be described using the effective interaction parameter χ_{eff} by fitting $I(q)$ to RPA model for binary mixtures of di-BCPs on the basis of a modified scattering function $S(q)$. Here, the coherent absolute intensity, $I_{abs}(q)$ is given by

$$I_{abs}(q) = K(a-b)^2 S(q) \quad (1)$$

with

$$S(q) = \left[\frac{G(q)}{W(q)} - 2\chi_{eff}\right]^{-1} \quad (2)$$

where q is the magnitude of the scattering vector, K is a proportional constant, a and b are the coherent neutron scattering length densities, χ_{eff} is the effective interaction parameter, $G(q)$ is the sum of Fourier transforms of the different density−density correlation functions and $W(q)$ is the determinant of these same terms (see the Supporting Information for more details). Thus, $\chi_{eff}N$ can be extracted from the calculated SANS profiles. As temperature increased, $\chi_{eff}N$ for three copolymer blends increased, and then reached a maximum around 180 °C followed by a slight decrease (Figure 3), similar to the observations in their parent PS-*b*-P*n*BMA BCPs.[23,24] Moreover, increasing temperature resulted in a sharpening of the scattering peak and an increase of the scattering maximum, I_{max}, (S-Figure 7 in the Supporting Information), confirming that the copolymers blends were approaching the ordering transition (LDOT) as temperature increased. Consequently, the three PS-d_8-*b*-P(*n*BMA-*r*-AzoEMA) copolymer blends had a LDOT behavior similar to their parent PS-*b*-P*n*BMA di-BCPs.

UV-Enhanced Ordering. Figure 4 revealed the influence of UV-induced *trans*−*cis* isomerization of azobenzene on the above BCP blends, 50Azo83K−50Azo24K, 55Azo83K−45Azo24K, and 60Azo83K−40Azo24K. After irradiation with

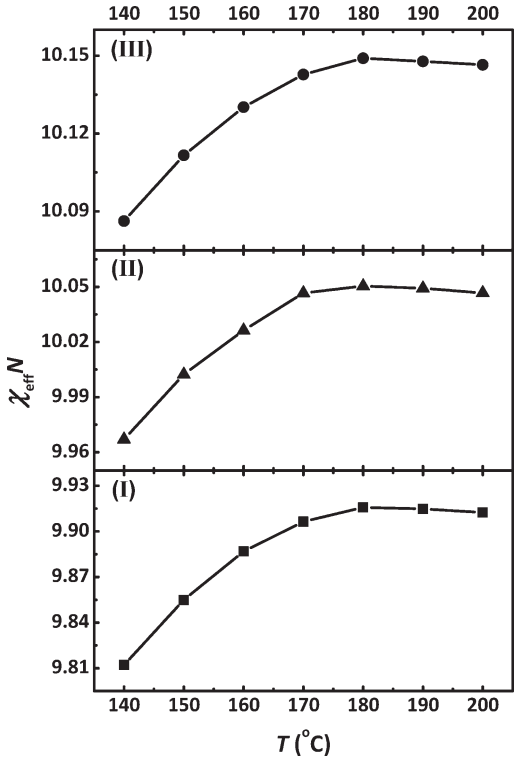


Figure 3. Temperature dependence of $\chi_{eff}N$ extracted from SANS data for the copolymer blends of (I) 50Azo83K−50Azo24K, (II) 55Azo83K−45Azo24K, and (III) 60Azo83K−40Azo24K by a smeared RPA fitting for binary mixtures of di-BCPs.

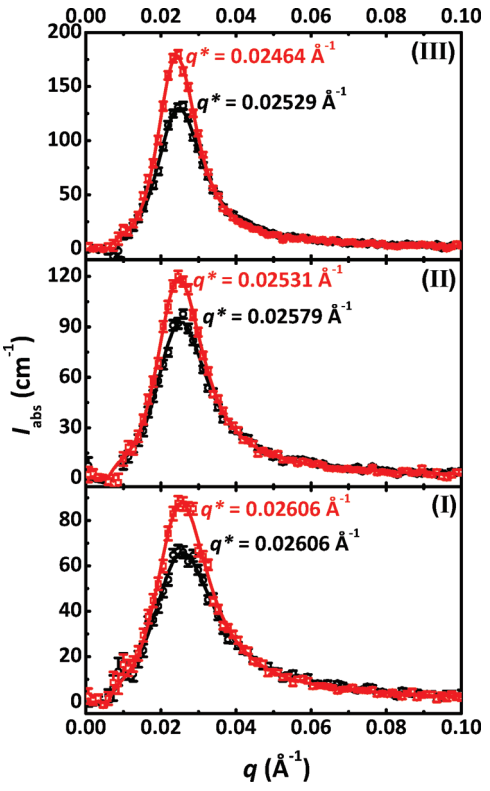


Figure 4. SANS profiles (open symbols) and the corresponding smeared RPA fits (solid lines) for the film of (I) 50Azo83K−50Azo24K, (II) 55Azo83K−45Azo24K, and (III) 60Azo83K−40Azo24K copolymer blends before (black) and after (red) exposure to UV light with a wavelength of 365 nm and an intensity of 35 mW/cm^2 for 1 h at 180 °C in an inert gas environment. Note: all the films were preannealed at 180 °C under vacuum for 48 h.

365 nm UV-light, the absolute intensity of correlation-hole scattering, I_{max}, for all three copolymer blends increased. For the 50Azo83K−50Azo24K blend, the peak remained at the same $q^* = 0.02606$ Å^{-1} before and after UV irradiation (Figure 4I), whereas for 55Azo83K−45Azo24K and 60Azo83K−40Azo24K blends much closer to transition boundary between fluctuation-dominated (partially ordered) and fully ordered regions than 50Azo83K−50Azo24K blend, the peaks shifted from $q^* = 0.02579$ Å^{-1} and 0.02529 Å^{-1} to lower $q^* = 0.02531$ Å^{-1} and 0.02464 Å^{-1}, respectively (Figure 4, parts II and III). Both the increase in I_{max} and the shift in q^* gave evidence that the ordering of three copolymer blends was significantly enhanced by UV irradiation and the blends were driven toward a fully ordered state. Such a UV-enhanced ordering originated from the increase in entropic contribution. Upon UV exposure, *trans*−*cis* isomerization of azobenzene in P(*n*BMA-*r*-AzoEMA) blocks enriched the conformations of copolymer chains and caused density variations, leading to a gain in entropy. The increased entropy could be directly reflected by the increase in $\chi_{eff}N$, which was extracted through the RPA analysis of SANS profiles of the above BCP blends in films. After UV irradiation, $\chi_{eff}N$ for the three copolymer blends increased from 9.53, 9.79, and 9.93 to 9.86, 9.96, and 10.12, respectively.

Considering that the photoisomerization of azobenzene is reversible and the *trans*- and *cis*- isomers can be switched with UV and visible light, UV-enhanced ordering and its reversibility were monitored in the film of 60Azo83K−40Azo24K blend by specular NR. Profile a in Figure 5I (open symbols) is its reflectivity without UV exposure. For the specular reflection, the scattering vector, $q = k_f - k_i$, is only in the z-direction which is normal to the interface. Since $q_x = q_y = 0$, it is given by $q_z = (4\pi/\lambda)[\sin \alpha_i]$, where α_i is the incident angle. The most pronounced feature of this profile is a broad Bragg reflection occurring near $q_z^* = 0.0285$ Å^{-1} (as illustrated by the black dotted line), indicative of phase coherence and a partial ordering in the film. The refraction-corrected expression for the Bragg law is

$$\left(\frac{2\pi}{L}\right)^2 = {q_{Bragg}}^2 = {q_z^*}^2 - {q_c}^2 \qquad (3)$$

where q_c is the critical wave vector of total reflection. This yields a period of $L = 243.5$ Å, identical to the above SANS data. As shown in Figure 5I, the typical best-fit to the reflectivity profile (a) (solid line) was calculated from the scattering length density profile (a) shown in Figure 5II. As described previously,[60−63] the fitting was obtained using the expression in eq 4 proposed by Fredrickson[66] for the polymer concentration profile,

$$\phi_{PS}(z) = \max\left[\phi_A e^{-z/\xi_1}\cos\left(\frac{2\pi z}{L}\right), \phi_S e^{-E-z/\xi_2}\cos\left(\frac{2\pi(E-z)}{L}\right)\right] + \bar{\phi}_{PS} \qquad (4)$$

where $\phi_{PS}(z)$ is the volume fraction of PS segments a distance z from the free surface in a film with a total thickness E. L is the average period of copolymer blend; ξ_1 and ξ_2 are the decay lengths from the air−polymer and polymer−substrate interfaces and representative of the distance over which there is order (concentration gradients) in the film; and $\bar{\phi}_{PS}$ is the average concentration of PS in the film of copolymer blend. ϕ_A and ϕ_S are excess PS concentration at the polymer−air

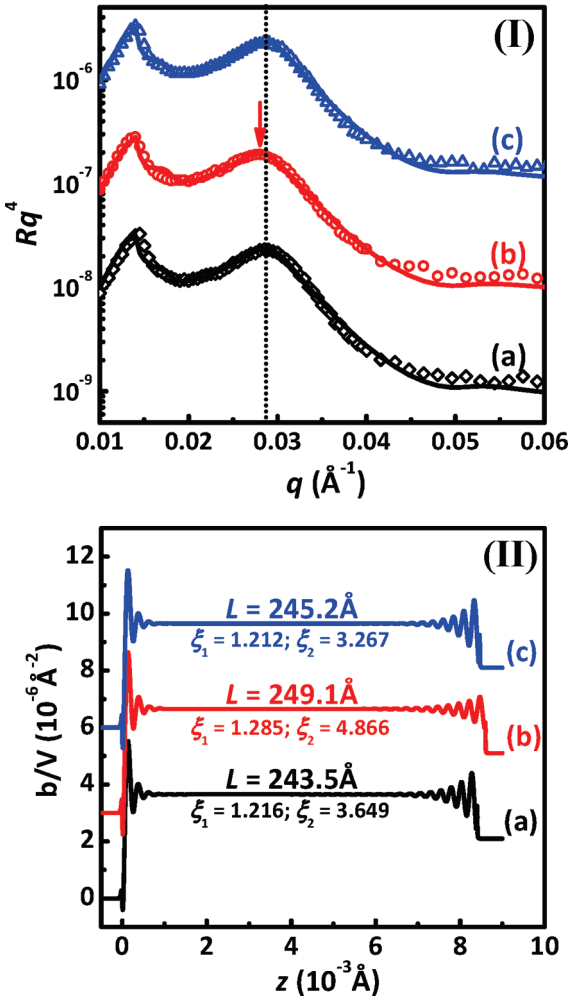


Figure 5. (I) Specular NR profiles (open symbols) for three films of 60Azo83K−40Azo24K copolymer blend and the corresponding best fits (solid lines) by using the functional form of the concentration profiles exponentially damped cosine variation from both air/copolymer and substrate/copolymer interfaces. Film (a) was kept in the dark (black); film (b) was exposed to UV-light with a wavelength of 365 nm and an intensity of 35 mW/cm^2 for 1 h at 180 °C under an inert gas protection (red); film (c) was irradiated at 180 °C in an inert gas environment by UV light with a wavelength of 365 nm and an intensity of 35 mW/cm^2 for 1 h followed by visible light with a wavelength of 436 nm for one more hour (blue). (II) The calculated SLD b/V profiles as a function of depth z, where $z = 0$ is the air/copolymer interface, were obtained from the best fits shown above. Note: the profiles have been shifted vertically for clarity.

interface and polymer−substrate interface, respectively. Because of the lower surface energy and the preferential interactions with the substrate,[62] P(*n*BMA-*r*-AzoEMA) block is preferentially located at both the polymer−air interface and polymer−substrate interface, as confirmed by XPS. These results are also consistent with previous reports that polymethacrylates preferentially interact with Si substrates.[60−63] The calculated scattering length density profile of 60Azo83K−40Azo24K blend without UV exposure (profile a in Figure 5II) is characterized by oscillations in the concentration that are rapidly damped as one moves away from the interfaces to a point where the oscillations are fully damped to the average composition of copolymer blend, since the decay lengths, $\xi_1 = 1.216$ Å and $\xi_2 = 3.649$ Å, are much smaller than the film thickness. After irradiation with 365 nm UV light, the Bragg reflection (profile (b) in Figure 5I) shifted to a lower q_z* (as illustrated by the red arrow) and the period, L, increased to 249.1 Å, confirming the SANS results that UV-induced *trans*−*cis* isomerization of azobenzene enhanced the ordering in the film of PS-d_8-*b*-P(*n*BMA-*r*-AzoEMA) BCP blends. The enhanced ordering is also evident in the decay lengths, ξ_1 and ξ_2, which increased to 1.285 and 4.866 Å, respectively, because the closer the ordering transition is, the greater the decay length is. The UV-enhanced ordering could be reversed by exposure to visible light with a wavelength of 430 nm via the photo-induced *cis*-*trans* isomerization of azobenzene. As can be clearly seen from profile c in Figure 5I, the Bragg reflection shifted back to the original position and the period, L, relaxed back to 245.2 Å. In addition, the decay lengths, ξ_1 and ξ_2, were reduced to 1.212 and 3.267 Å, respectively, similar to their initial values without UV irradiation. It is obvious that UV-enhanced ordering in the film of PS-d_8-*b*-P(*n*BMA-*r*-AzoEMA) BCP blends is reversible through photocontrolling the *trans*−*cis*−*trans* isomerization cycle of azobenzene.

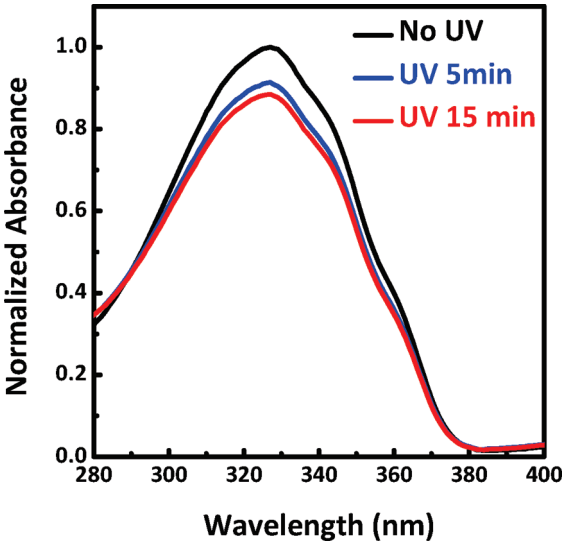


Figure 6. UV−vis absorption spectra of a PS-d_8-*b*-P(nBMA-*r*-AzoEMA) BCP film on a clean, UV-transmitted quartz slide without UV irradiation (black line) and after exposure to UV light with a wavelength of 365 nm and an intensity of 2 mW/cm^2 for 5 min (blue line) and 15 min (red lie) at room temperature. Note: the film was annealed at 180 °C under vacuum for 48 h before the measurement of UV−vis spectra.

Although these ordering changes arising from azobenzene photoisomerization are well observed in BCP thin films, a stronger driving force to perform photocombing is still required. As shown in Figure 6, UV−vis spectroscopy was used to monitor the azobenzene photoisomerization in BCP thin films. The absorbance of *trans*-isomers gradually decreased under an irradiation of UV light with an intensity of ∼2 mW/cm^2, indicating the photoisomerization of azobenzene from the *trans*- to the *cis*-state in the thin film of PS-d_8-*b*-P(*n*BMA-*r*-AzoEMA) BCP.[45] After UV exposure for 5 and 15 min, ∼9% and ∼13% of *trans*-isomers were isomerized into *cis*-isomers, respectively. While a higher intensity (35 mW/cm^2) could increase the percentage of *cis*-isomers, the yield of azobenzene photoisomerization in block copolymer thin films, in comparison with those previously reported azobenzene-containing polymers,[41−46] would be still low due to the thermo-induced reversed *cis*−*trans* isomerization. As a consequence, only a weak driving force for UV-induced LDOT could be generated, which determined that the changes in both SANS and NR were not significant.

Conclusions

We have successfully synthesized azobenzene-containing PS-d_8-*b*-P(*n*BMA-*r*-AzoEMA) BCPs (Azo24K and Azo83K) through sequential anionic polymerization and postfunctionalization. Their binary copolymer blends exhibited a gradual transition from a disordered state to a lamellar phase as the weight fraction of Azo83K BCP increased. Temperature-dependent SANS further illustrated that they had a LDOT behavior, similar to their parent PS-*b*-P*n*BMA BCPs. By manipulating the photoisomerization of azobenzene with UV or visible lights, the reversible control on an ordering process was obtained in the film of PS-d_8-*b*-P(*n*BMA-*r*-AzoEMA) BCP blends which was phase-mixed but close to the transition boundary. Conclusively, it is very promising to fabricate long-range ordered nanomaterials over a large distance by photocombing BCP microdomains without touching samples via a reversibly photocontrollable ordering process as proposed in the Introduction.

Acknowledgment. This research was supported by the Department of Energy, Office of Basic Energy Science (DE-FG02-02ER45998) and the National Science Foundation-supported Material Research Science and Engineering Center (MRSEC) at the University of Massachusetts, Amherst (DMR-0213695). We thank Jack Hirsch for the assistance with XPS measurements. We also thank Dr. B. Hammouda and Dr. S. K. Satija for the helpful discussions and Dr. Y. Liu and Dr. B. Akgun for the assistance with SANS and NR measurements. This work utilized facilities supported in part by the National Science Foundation under Agreement No. DMR-0454672. We acknowledge the support of the National Institute of Standards and Technology, U.S. Department of Commerce, in providing the neutron research facilities used in this work.

Supporting Information Available: Discussion of materials and synthetic details, GPC traces and ^{1}H NMR spectra, FT-IR spectrum, temperature-dependent SANS profiles, temperature dependence of the maximum absolute intensity (I_{max}), UV−vis absorption spectra, RPA model for SANS analysis, Igor codes for SANS fitting, and FORTRAN codes for NR fitting. This material is available free of charge via the Internet at http://pubs.acs.org.

References and Notes

(1) Rogers, J. A.; Lee, H. H., *Unconventional Nanopatterning Techniques and Applications*; John Wiley & Sons, Inc: Hoboken, NJ, 2009.
(2) Ross, C. A.; Cheng, J. Y. *MRS Bull.* **2008**, *33*, 838–845.
(3) Hawker, C. J.; Russell, T. P. *MRS Bull.* **2005**, *30*, 952–966.
(4) Li, M.; Coenjarts, C. A.; Ober, C. K. *Adv. Polym. Sci.* **2005**, *190*, 183–226.
(5) Segalman, R. A. *Mater. Sci. Eng.* **2005**, *R48*, 191–226.
(6) Park, C.; Yoon, J.; Thomas, E. L. *Polymer* **2003**, *44*, 6725–6760.
(7) Bang, J.; Jeong, U.; Ryu, D. Y.; Russell, T. P.; Hawker, C. J. *Adv. Mater.* **2009**, *21*, 4769–4792.
(8) Hamley, I. W., *The Physics of Block Copolymers*; Oxford University Press: New York, 1998.
(9) Hashimoto, T.; Bodycomb, J.; Funaki, Y.; Kimishima, K. *Macromolecules* **1999**, *32*, 952–954.
(10) Bodycomb, J.; Funaki, Y.; Kimishima, K.; Hashimoto, T. *Macromolecules* **1999**, *32*, 2075–2077.
(11) Mita, K.; Tanaka, H.; Saijo, K.; Takenaka, M.; Hashimoto, T. *Macromolecules* **2007**, *40*, 5923–5933.
(12) Mita, K.; Tanaka, H.; Saijo, K.; Takenaka, M.; Hashimoto, T. *Polymer* **2008**, *49*, 5146–5157.
(13) Mita, K.; Takenaka, M.; Hasegawa, H.; Hashimoto, T. *Macromolecules* **2008**, *41*, 8789–8799.
(14) Mita, K.; Tanaka, H.; Saijo, K.; Takenaka, M.; Hashimoto, T. *Macromolecules* **2008**, *41*, 6780–6786.
(15) Mita, K.; Tanaka, H.; Saijo, K.; Takenaka, M.; Hashimoto, T. *Macromolecules* **2008**, *41*, 6787–6792.
(16) Anthony, R. W., *Solid State Chemistry and its Application*; John Wiley & Sons: New York, 1984.
(17) Travasso, R. D. M.; Kuksenok, O.; Balazs, A. C. *Langmuir* **2005**, *21*, 10912–10915.
(18) Travasso, R. D. M.; Kuksenok, O.; Balazs, A. C. *Langmuir* **2006**, *22*, 2620–2628.
(19) Russell, T. P.; Karis, T. E.; Gallot, Y.; Mayes, A. M. *Nature* **1994**, *368*, 729–731.
(20) Hammouda, B.; Bauer, B. J.; Russell, T. P. *Macromolecules* **1994**, *27*, 2357–2359.
(21) Karis, T. E.; Russell, T. P.; Gallot, Y.; Mayes, A. M. *Macromolecules* **1995**, *28*, 1129–1134.
(22) Ryu, D. Y.; Jeong, U.; Lee, D. H.; Kim, J.; Youn, H. S.; Kim, J. K. *Macromolecules* **2003**, *36*, 2894–2902.
(23) Ryu, D. Y.; Shin, C.; Cho, J.; Lee, D. H.; Kim, J. K.; Lavery, K. A.; Russell, T. P. *Macromolecules* **2007**, *40*, 7644–7655.
(24) Ruzette, A. V. G.; Banerjee, P.; Mayes, A. M.; Pollard, M.; Russell, T. P.; Jerome, R.; Slawecki, T.; Hjelm, R.; Thiyagarajan, P. *Macromolecules* **1998**, *31*, 8509–8516.
(25) Weidisch, R.; Stamm, M.; Schubert, D. W.; Arnold, M.; Budde, H.; Horing, S. *Macromolecules* **1999**, *32*, 3405–3411.
(26) Ryu, D. Y.; Jeong, U.; Kim, J. K.; Russell, T. P. *Nat. Mater.* **2002**, *1*, 114–117.
(27) Kim, E. Y.; Lee, D. J.; Kim, J. K.; Cho, J. *Macromolecules* **2006**, *39*, 8747–8757.
(28) Ruzette, A. V. G.; Mayes, A. M.; Pollard, M.; Russell, T. P.; Hammouda, B. *Macromolecules* **2003**, *36*, 3351–3356.
(29) Ryu, D. Y.; Lee, D. H.; Jeong, U.; Yun, S.-H.; Park, S.; Kwon, K.; Sohn, B.-H.; Chang, T.; Kim, J. K.; Russell, T. P. *Macromolecules* **2004**, *37*, 3717–3724.
(30) Ryu, D. Y.; Park, M. S.; Chae, S. H.; Jang, J.; Kim, J. K.; Russell, T. P. *Macromolecules* **2002**, *35*, 8676–8680.
(31) Pollard, M.; Russell, T. P.; Ruzette, A. V.; Mayes, A. M.; Gallot, Y. *Macromolecules* **1998**, *31*, 6493–6498.
(32) Dudowicz, J.; Freed, K. F. *Macromolecules* **2000**, *33*, 5292–5299.
(33) Tang, H.; Freed, K. F. *Macromolecules* **1991**, *24*, 958–966.
(34) Yeung, C.; Desai, R. C.; Shi, A.-C.; Noolandi, J. *Phys. Rev. Lett.* **1994**, *72*, 1834–1837.
(35) Ruzette, A. V. G.; Banerjee, P.; Mayes, A. M.; Russell, T. P. *J. Chem. Phys.* **2001**, *114*, 8205–8209.
(36) Dudowicz, J.; Freed, K. F. *Macromolecules* **1993**, *26*, 213–220.
(37) Hino, T.; Prausnitz, J. M. *Macromolecules* **1998**, *31*, 2636–2648.
(38) Cho, J. *Macromolecules* **2000**, *33*, 2228–2241.
(39) Cho, J. *Macromolecules* **2001**, *34*, 1001–1012.
(40) Cho, J. *Macromolecules* **2004**, *37*, 10101–10108.
(41) Sekkat, Z.; Knoll, W., *Photoreactive organic thin films*; Academic Press: San Diego, CA, 2002.
(42) Natansohn, A.; Rochon, P. *Chem. Rev.* **2002**, *102*, 4139–4176.
(43) Tanchak, O. M.; Barrett, C. J. *Macromolecules* **2005**, *38*, 10566–10570.
(44) Yager, K. G.; Tanchak, O. M.; Godbout, C.; Fritzsche, H.; Barrett, C. J. *Macromolecules* **2006**, *39*, 9311–9319.
(45) Huang, C.-F.; Chen, W.; Russell, T. P.; Balazs, A. C.; Chang, F.-C.; Matyjaszewski, K. *Macromol. Chem. Phys.* **2009**, *210*, 1484–1492.
(46) Fukuoka, M.; Nakanishi, H.; Norisuye, T.; Tran-Cong-Miyata, Q. *J. Phys. Chem. B* **2009**, *113*, 14950–14956.
(47) Glinka, C. J.; Barker, J. G.; Hammouda, B.; Krueger, S.; Moyer, J. J.; Orts, W. J. *J. Appl. Crystallogr.* **1998**, *31*, 430–445.
(48) Kline, S. R. *J. Appl. Crystallogr.* **2006**, *39*, 895–900.
(49) Leibler, L. *Macromolecules* **1980**, *13*, 1602–1617.
(50) Bates, F. S.; Hartney, M. A. *Macromolecules* **1985**, *18*, 2478–2486.
(51) Benoit, H.; Hadziioannou, G. *Macromolecules* **1988**, *21*, 1449–1464.
(52) Hashimoto, T.; Koizumi, S.; Hasegawa, H. *Macromolecules* **1994**, *27*, 1562–1570.
(53) Bidkar, U. R.; Sanchez, I. C. *Macromolecules* **1995**, *28*, 3963–3972.
(54) Sakurai, S.; Nomura, S. *Polymer* **1997**, *38*, 4103–4112.
(55) Fredrickson, G. H.; Helfand, E. *J. Chem. Phys.* **1987**, *87*, 697–705.
(56) Bates, F. S.; Rosedale, J. H.; Fredrickson, G. H.; Glinka, C. J. *Phys. Rev. Lett.* **1988**, *61*, 2229–2232.

(57) Bates, F., S.; Rosedale, J. H.; Fredrickson, G. H. *J. Chem. Phys.* **1990**, *92*, 6255–6270.
(58) Barrat, J.-L.; Fredrickson, G. H. *J. Chem. Phys.* **1991**, *95*, 1281–1289.
(59) Kienzle, P. A.; O'Donovan, K. V.; Ankner, J. F.; Berk, N. F.; Majkrzak, C. F. **2000**−**2006**.
(60) Anastasiadis, S. H.; Russell, T. P.; Satija, S. K.; Majkrzak, C. F. *Phys. Rev. Lett.* **1989**, *62*, 1852–1855.
(61) Menelle, A.; Russell, T. P.; Anastasiadis, S. H.; Satija, S. K.; Majkrzak, C. F. *Phys. Rev. Lett.* **1992**, *68*, 67–70.
(62) Mansky, P.; Tsui, O. K. C.; Russell, T. P.; Gallot, Y. *Macromolecules* **1999**, *32*, 4832–4837.
(63) Vogt, B. D.; RamachandraRao, V. S.; Gupta, R. R.; Lavery, K. A.; Francis, T. J.; Russell, T. P.; Watkins, J. J. *Macromolecules* **2003**, *36*, 4029–4036.
(64) Hashimoto, T.; Yamasaki, K.; Koizumi, S.; Hasegawa, H. *Macromolecules* **1993**, *26*, 2895–2904.
(65) Matsen, M. W. *J. Chem. Phys.* **1995**, *103*, 3268–3271.
(66) Fredrickson, G. H. *Macromolecules* **1987**, *20*, 2535–2542.

286 *Macromolecules* **2011**, *44*, 286–298
DOI: 10.1021/ma102048v

Macromolecules
ARTICLE

Stereoregular Diblock Copolymers of Syndiotactic Polystyrene Derivatives and Polylactide: Syntheses and Self-Assembled Nanostructures

Ting-Jui Hsiao, Jing-Yu Lee, Yung-Cheng Mao, Yu-Chin Chen, and Jing-Cherng Tsai*

Department of Chemical Engineering, National Chung Cheng University, Chia-Yi 62142, Taiwan

Shih-Chieh Lin and Rong-Ming Ho*

Department of Chemical Engineering, National Tsing Hua University, Hsinchu 30013, Taiwan

Received September 3, 2010; Revised Manuscript Received December 10, 2010

ABSTRACT: Structurally well-defined stereoregular diblock copolymers, syndiotactic poly(4-methylstyrene)-*b*-poly(L-lactide) (sPMS-*b*-PLLA), were prepared by the controlled ring-opening polymerization of an aluminum alkoxide end-capped sPMS macroinitiator with L-lactide. The aluminum alkoxide end-capped sPMS macroinitiator was generated via the reaction between hydroxyl-capped sPMS and triethylaluminum. The hydroxyl-capped sPMS was prepared from the hydroboration of ethenyl-capped sPMS. The ethenyl-capped sPMS was generated by the desilylation of dimethylphenylvinylsilane-capped sPMS prepared via a unique vinylsilane-inducing selective chain transfer reaction during the syndiospecific polymerization of 4-methylstyrene conducted in the presence of dimethylphenylvinylsilane using Cp*Ti-$(OMe)_3$/MAO as catalyst. The proposed synthetic method can be used for the preparation of a broad variety of end-functionalized syndiotactic polystyrene derivatives (syndiotactic polystyrenes) end-capped with various end groups and facilitates the synthesis of syndiotactic polystyrenes-based stereoregular BCPs. The method offers effective control over the stereoregularity of polystyrenes and facilitates linking between blocks to provide stereoregular BCPs, which are capable of generating well-ordered nanostructures resulting from the self-assembly of stereoregular BCPs, as evidenced by small-angle X-ray scattering (SAXS) and transmission electron microscopy (TEM).

Introduction

Block copolymers (BCPs) are characterized by their distinct chemical structures, where two or more polymer blocks are jointed by covalent bonds.[1] Because of this unique chemical architecture, structurally well-defined BCPs are able to self-organize into ordered nanostructures. BCPs have thus been the subject of numerous theoretical and experimental studies in recent decades.[2] To provide structurally well-defined BCPs for the formation of well-ordered nanostructures from self-assembly, significant advancements in polymer chemistry through living or controlled-living polymerizations have been made that permit the synthesis of BCPs with precise control of their molecular chain length and molecular weight distribution.[3] Unfortunately, the most widely used methods for the preparation of BCPs fail to provide effective stereoregularity control for α-olefin polymerizations. Therefore, the synthesis of structurally well-defined polyolefin-based stereoregular BCPs, which can be self-organized into well-ordered nanostructures, remains challenging.

Several crystalline polymers are known to have main chain stereoregularity, which is one of the key factors in the formation of crystalline lattices via molecular self-assembly.[4] The incorporation of a stereoregular block into BCPs provides an additional self-assembly pathway for tuning the molecular level self-organization processes and increases the morphological richness[5] due to the presence of stereointeractions between stereoregular entities.[6] To date, few studies have been conducted on the self-assembly of polyolefin-based stereoregular BCPs. This is mainly due to the difficulty of synthesizing structurally well-defined polyolefin-based stereoregular BCPs as their synthesis requires not only a perfect linking method between various blocks but also stereospecific control during the preparation of the stereoregular blocks from polymerizations of α-olefin monomers.

Simultaneous stereoregularity control and block length control during α-olefin polymerization have been investigated using two stereospecific living polymerization systems: (i) using stereospecific living coordination catalysts to mediate the sequential living polymerization of various α-olefins,[7] and (ii) conducting the stereospecific living polymerization of α-olefins in the presence of stereospecific controlled-living radical polymerization catalysts.[8] For route i, the variety of obtainable block copolymers is extremely limited because their preparation requires the addition polymerization of structurally similar olefin monomers to a single active species. This limitation drastically hampers the utilization of this synthetic route for obtaining stereoregular BCPs for self-assembly studies because stereoregular BCPs constituted with structurally similar blocks may not offer sufficient segregation strength between blocks to induce microphase separation. In contrast, route ii lacks effective stereoregularity control; thus, BCPs prepared via this synthetic route typically have insufficient stereoregularity.

Another approach for the preparation of polyolefin-based stereoregular BCPs is conducting a selective chain transfer reaction during stereospecific polymerization of α-olefins for the generation of an end-functionalized stereoregular prepolymer

*To whom correspondence should be addressed. (J.-C.T.) Telephone: 886-5-2720411 ext 33460. Fax: 886-5-2721206. E-mail: chmjct@ccu.edu.tw. (R.-M. Ho) Telephone: 886-3-5738349. Fax: 886-3-5715408. E-mail: rmho@mx.nthu.edu.tw.

 Published on Web 12/23/2010 © 2010 American Chemical Society

Table 1. Preparations of End-Functionalized Syndiotactic Polystyrene, Syndiotactic Poly(*p*-methylstyrene) and Syndiotactic Poly(*p*-fluorostyrene) via the Vinylsilane Inducing Selective Chain Transfer Reaction[a]

run	styrene (mmol)	*p*-MS (mmol)	*p*-FS (mmol)	DMPVS (mmol)	yield (g)	M_n[b] (kDa)	PDI	T_m[c] (°C)	tacticity[d]
1	14	-		-	1.41	335	2.6	267	
2	-	-		14	-	-	-	-	-
3	14	-		3.5	1.01	19.6	2.2	262	
4	14	-		4.7	0.85	15.3	1.9	262.5	
5	14	-		7	0.58	9.8	1.6	261	91
6	14	-		14	0.33	4.2	1.4	256	90
7	-	14		3.5	1.27	23.2	2.1	-	
8	-	14		4.7	1.08	17.3	1.8	-	
9	-	14		7	0.71	11.1	1.7	-	
10		14		9.3	0.63	8.3	1.5		91
11	-	14		14	0.51	4.7	1.4	-	90
12			14	3.5	0.42	14.1	1.7		
13			14	4.7	0.31	9.8	1.5	308	
14			14	7	0.26	7.5	1.4		
15			14	14	0.19	3.6	1.3	287	88

[a] Polymerization conditions: 50 mL of toluene, [catalyst] = 6×10^{-6} mol, MAO = 6×10^{-4} mol, reaction temperature 30 °C and reaction time = 3 h. [b] M_n (number-average molecular weight) in g/mol and PDI (polydispersity, M_w/M_n) were determined by high-temperature GPC (solvent 1,2,4-trichlorobenzene; temperature 135 °C) [c] T_m (melting temperature) was determined by DSC. [d] Tacticity (syndiotacticity in *rrrrr*) was determined via ^{13}C NMR.

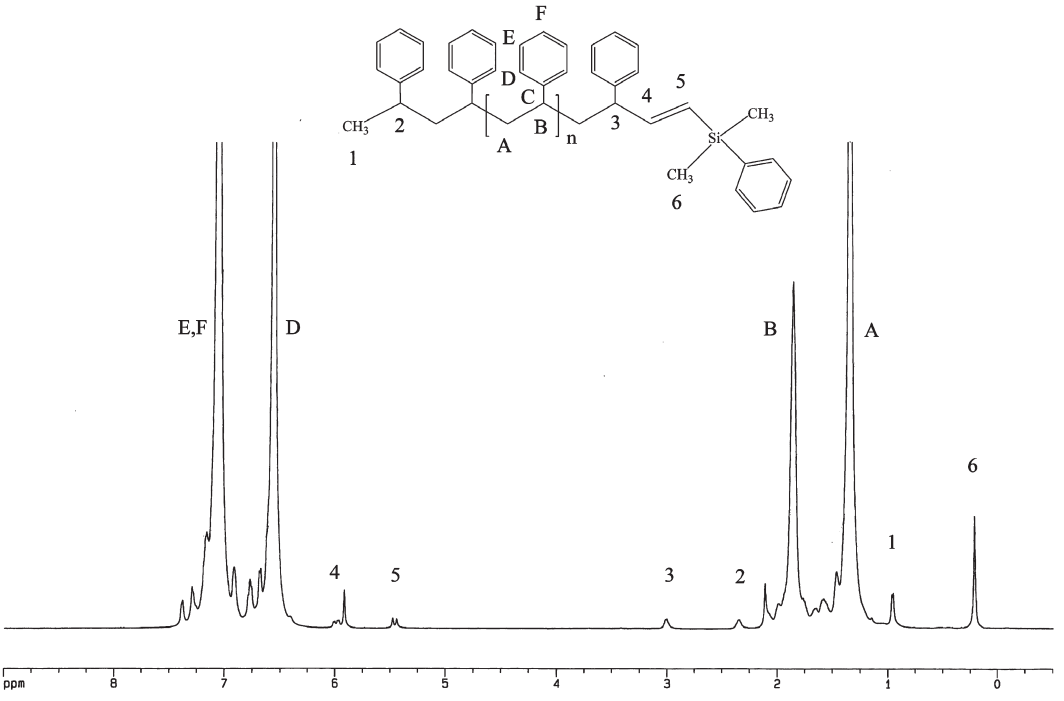


Figure 1. ^1H NMR (500 MHz) spectrum of $C_6H_5-Si(CH_3)_2-CH=CH$-capped sPS (M_n = 4200 g/mol, M_w/M_n = 1.8; entry 6 of Table 1) (solvent $C_2D_2Cl_4$; temperature 90 °C).

in the first step, and then using the stereoregular prepolymer in postpolymerization reaction for block formation in the second step.[9] The two-step process allows for a broad variety of polymer architectures linked onto the stereoregular block, but it has the problem of poor linking efficiency in the block formation step. In order to improve the linking efficiency, it is highly desirable that the block connecting reaction start from a structurally well-defined stereoregular end-functionalized prepolymer containing a reactive terminal group, which serves as a linkage for connecting blocks. Although functional group end-capped stereoregular prepolymers can be generated using several synthetic approaches by inducing a selective chain transfer reaction during the stereospecific polymerization of α-olefins, end-functionalized stereoregular polymers prepared by the selective chain transfer route may not have a highly reactive terminal functional group to ensure high linking efficiency.

Recently, these obstacles have been circumvented by conducting the stereospecific polymerization of α-olefins using triethylaluminum (TEA) as the selective chain transfer agent to obtain end-functionalized stereoregular polyolefins end-capped with a hydroxyl terminal group. The resulting hydroxyl-capped polyolefins can serve as macroinitiators, which undergo subsequent living block copolymerization reactions for connecting to other polymer blocks with nearly perfect linking efficiency.[9a,10] Although selective chain transfer to TEA offers the optimal solution for the preparation of various polyolefin-based stereoregular BCPs for self-assembly studies, syndiotactic polystyrene derivatives (syndiotactic polystyrenes) containing stereoregular BCPs cannot be prepared using this synthetic route because chain transfer to TEA (or other trialkylaluminums) is not the dominant chain transfer pathway during the syndiospecific polymerization of styrene derivatives.[11] In other words, the synthesis of structurally

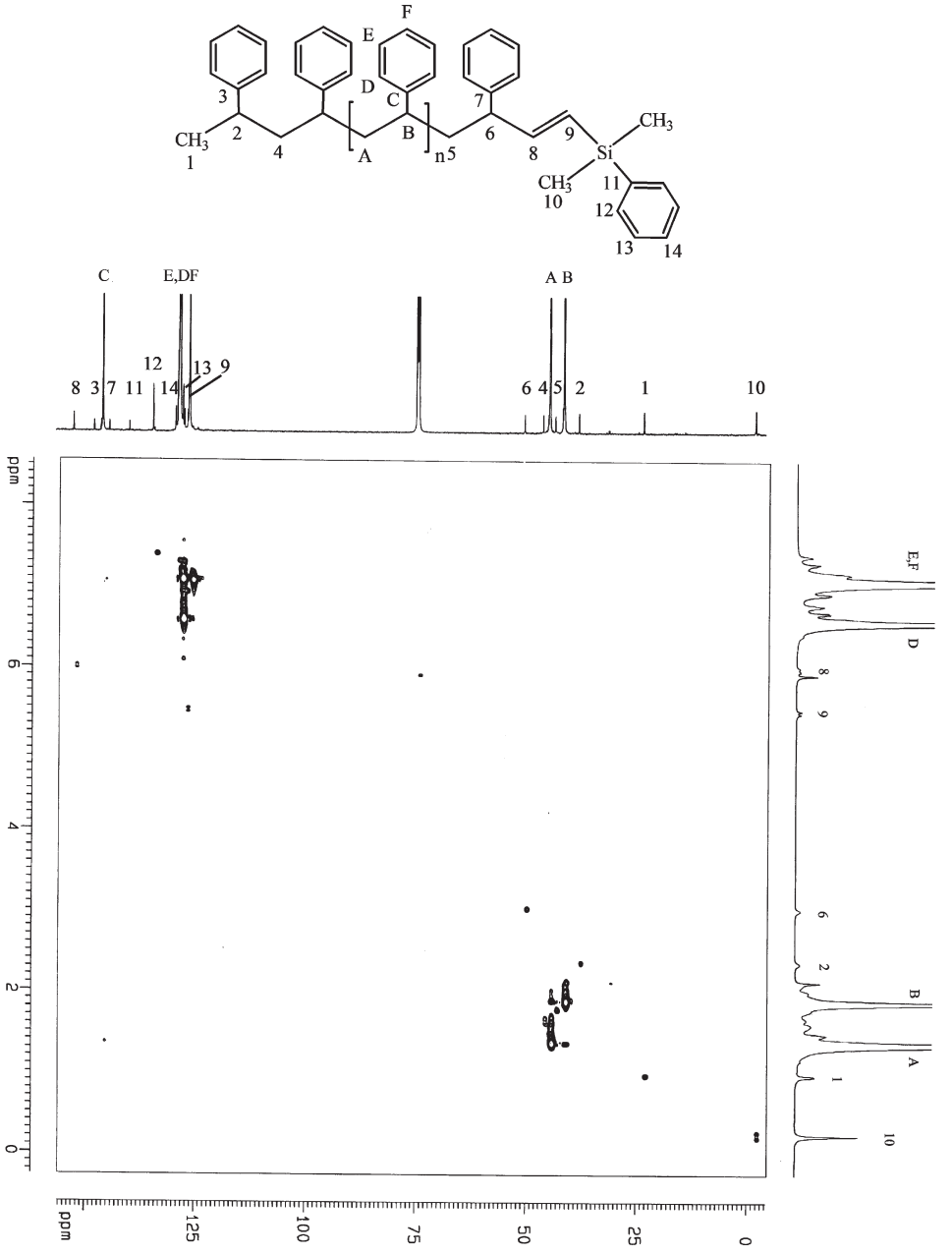
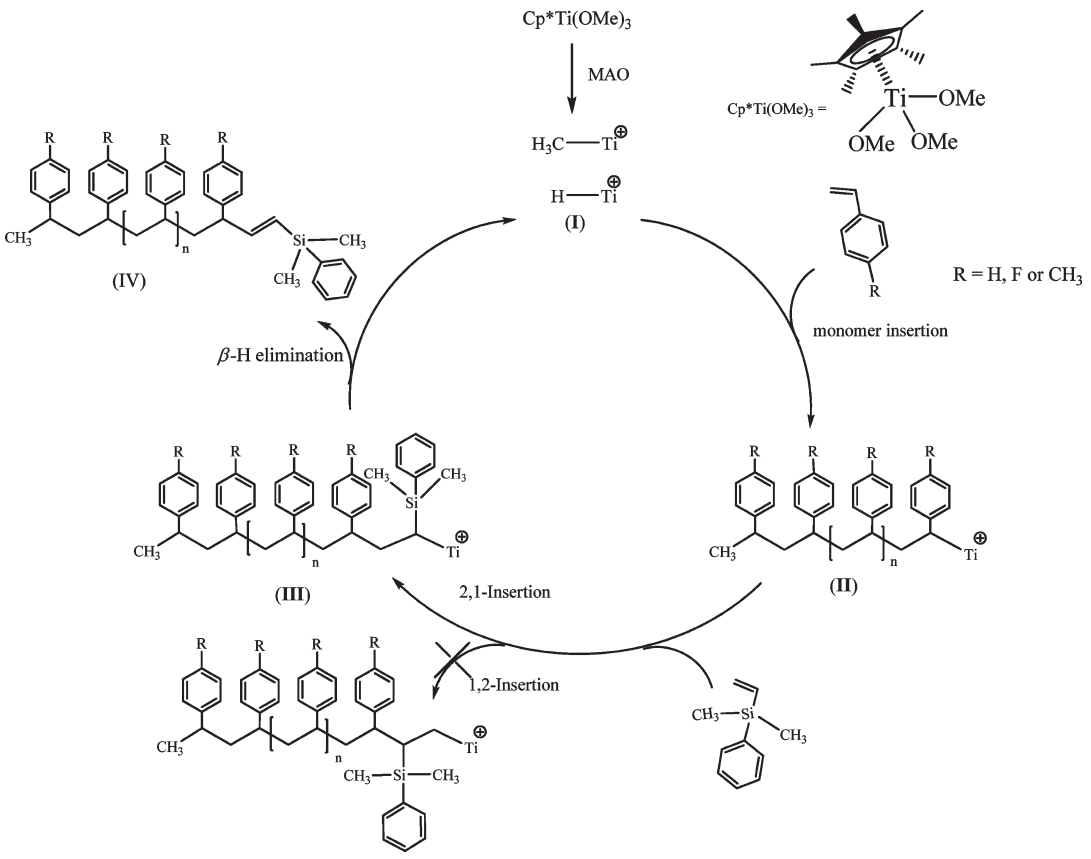


Figure 2. $^{1}H-^{13}C$ HMQC spectrum of $C_6H_5-Si(CH_3)_2-CH{=}CH$-capped sPS ($M_n$ = 4200 g/mol, M_w/M_n = 1.8; run 6 of Table 1) (solvent $C_2D_2Cl_4$; temperature 90 °C).

well-defined syndiotactic polystyrenes-based stereoregular BCPs, which can be used in self-assembly studies, remains difficult.[12]

In this paper, we demonstrate the preparation of structurally well-defined syndiotactic polystyrenes-based stereoregular BCPs via a two-step process, namely, the end-functionalization of syndiotactic polystyrenes in the first step followed by the post-polymerization of end-functionalized syndiotactic polystyrenes for the construction of block copolymers in the second step. The end-functionalized syndiotactic polystyrenes were prepared via a unique selective chain transfer reaction that uses metallocene catalyst to mediate the syndiospecific polymerization of styrene derivatives in the presence of vinylsilanes to provide the vinylsilane end-capped syndiotactic polystyrenes. The resulting vinylsilane end groups undergo subsequent functional group transformation to provide hydroxyl-capped syndiotactic polystyrenes. Subsequently, treating the hydroxyl-capped syndiotactic polystyrenes with triethylaluminum provides aluminum alkoxide-capped syndiotactic polystyrenes, which can act as a macroinitiator to undergo the controlled ring-opening polymerization reaction for the synthesis of polyesters, such as polylactides, to provide syndiotactic polystyrenes-*b*-polylactide with high yields. Our selection of polylactide as the second block for connecting onto the syndiotactic polystyrenes block stems from the fact that polylactide can be removed by hydrolysis. Thus, nanostructures from the self-assembly of polylactide-containing BCPs, in particular, nanostructured thin films, are ideal templates for the formation of nanostructured hybrids and nanocomposites. Of note, a series of polylactide-containing BCPs having amorphous atactic PS as the second block were synthesized and used to construct nanoporous polystyrene (PS) template from the self-assembly of the BCPs after hydrolysis[13,14] of polylactide blocks so as to provide the templates as nanoreactors for conducting nanoscale reactions in different applications.[14−16] The utilization of the stereoregular polystyrenes containing BCPs in templating can be extremely useful because the presence of the crystallizable

Scheme 1



stereoregular polystyrene block offers elevated physical properties (e.g., high heat resistance) for use as advanced templates in practical applications.

Experimental Section

General Procedure. All reactions and manipulations were conducted under a nitrogen atmosphere using the standard Schlenk line or drybox techniques. Solvents and common reagents were commercially obtained and used either as received or purified by distillation with sodium/benzophenone. Styrene (purity >98%), 4-methylstyrene (purity >98%), 4-fluorostyrene (purity >99%), and dimethylphenylvinylsilane (DMPVS; purity >97%) were purchased from ACROS and purified by distillation from CaH_2. The L-lactide (98%), purchased from Aldrich, was purified by recrystallization in toluene and dried under vacuum before use. Pentamethylcyclopentadienyltitaniumtrimethoxide [$Cp^*Ti(OMe)_3$] was purchased from Strem Chemicals and used as received. Trifuoroacetic acid (CF_3COOH, purity >99%), triethylaluminum (TEA, 1 M in hexane), and borane-tetrahydrofurane complex (1.5 M solution in THF) were purchased from Aldrich and used as received. Methylaluminoxane (MAO, 14% in toluene), purchased from Albemarle, was dried under vacuum to remove residual trimethylaluminum (TMA).[17] The resulting TMA-free MAO was diluted in toluene to the desired concentration before use.

Synthesis of $C_6H_5-Si(CH_3)_2-CH=CH$-Capped Syndiotactic Polystyrene Derivatives. Representative experiment (for entry 6 of Table 1): A 250 mL Schlenk tube, equipped with a magnetic stirrer, was allowed to dry at 80 °C under vacuum. After being refilled with nitrogen, the reactor was maintained at 30 °C and then charged sequentially with 14 mmol of styrene, 14 mmol of DMPVS, 0.6 mmol of MAO, and 50 mL of toluene. After the resulting solution was stirred at 30 °C for 5 min, the reactor was charged with $Cp^*Ti(OMe)_3$ (6.0 μmol) to initiate the polymerization. Polymerization was conducted at 30 °C for 3 h, after which the resulting polymerization solution was quenched with .20 mL of acidic methanol (1 N HCl solution in methanol), which led to the deposition of the styrene polymer as a white precipitate. After isolation by filtration, the resulting polymer was purified by removing the atactic polystyrene through boiling MEK extraction in a Soxhlet extractor. The resulting insoluble fraction of the polymer was dried under vacuum to provide 0.33 g of $C_6H_5-Si(CH_3)_2-CH=CH$-capped sPS as an off-white powder. M_n = 4200 g/mol, M_w/M_n = 1.4 by GPC (in 1,2,4-trichlorobenzene at 135 °C). Syndiotacticity (*rrrrr*) = 90% by ^{13}C NMR (in 1,1,2,2-tetrachloroethane-d_2 at 90 °C).[18]

Synthesis of Ethenyl-Capped sPMS ($CH_2=CH$-Capped sPMS). A CH_2Cl_2 solution containing 0.6 g of $C_6H_5-Si(CH_3)_2-CH=CH$-capped sPMS (M_n = 8300 g/mol, M_w/M_n = 1.5, syndiotacticity (*rrrrr*) = 91%; entry 10 of Table 1) was charged with 3.1 mmol of CF_3COOH. The desilylation reaction was allowed to proceed at 90 °C for 12 h. The solution was charged with excess methanol, which led to the deposition of the methylstyrene-based polymer as a white precipitate. The resulting polymer was collected by filtration and dried under vacuum to provide 0.51 g of ethenyl-capped sPMS. M_n = 8200 g/mol, M_w/M_n = 1.5 by GPC (in 1,2,4-trichlorobenzene at 135 °C).

Synthesis of Hydroxyl-Capped sPMS (OH-Capped sPMS). A THF solution containing 0.50 g of ethenyl-capped sPMS (M_n = 8200 g/mol, M_w/M_n = 1.5) and 1.46 mmol of borane–tetrahydrofurane complex was stirred at 50 °C for 12 h. After being cooled to room temperature, the solution was charged sequentially with 2.9 mL of NaOH (1 M in water) and 1.5 mL of H_2O_2 (30% aqueous solution), and then stirred at room temperature for 6 h. The solution was then charged with excess methanol, which led to the deposition of styrene polymer as a white precipitate. The resulting polymer was collected by filtration and dried under vacuum to provide

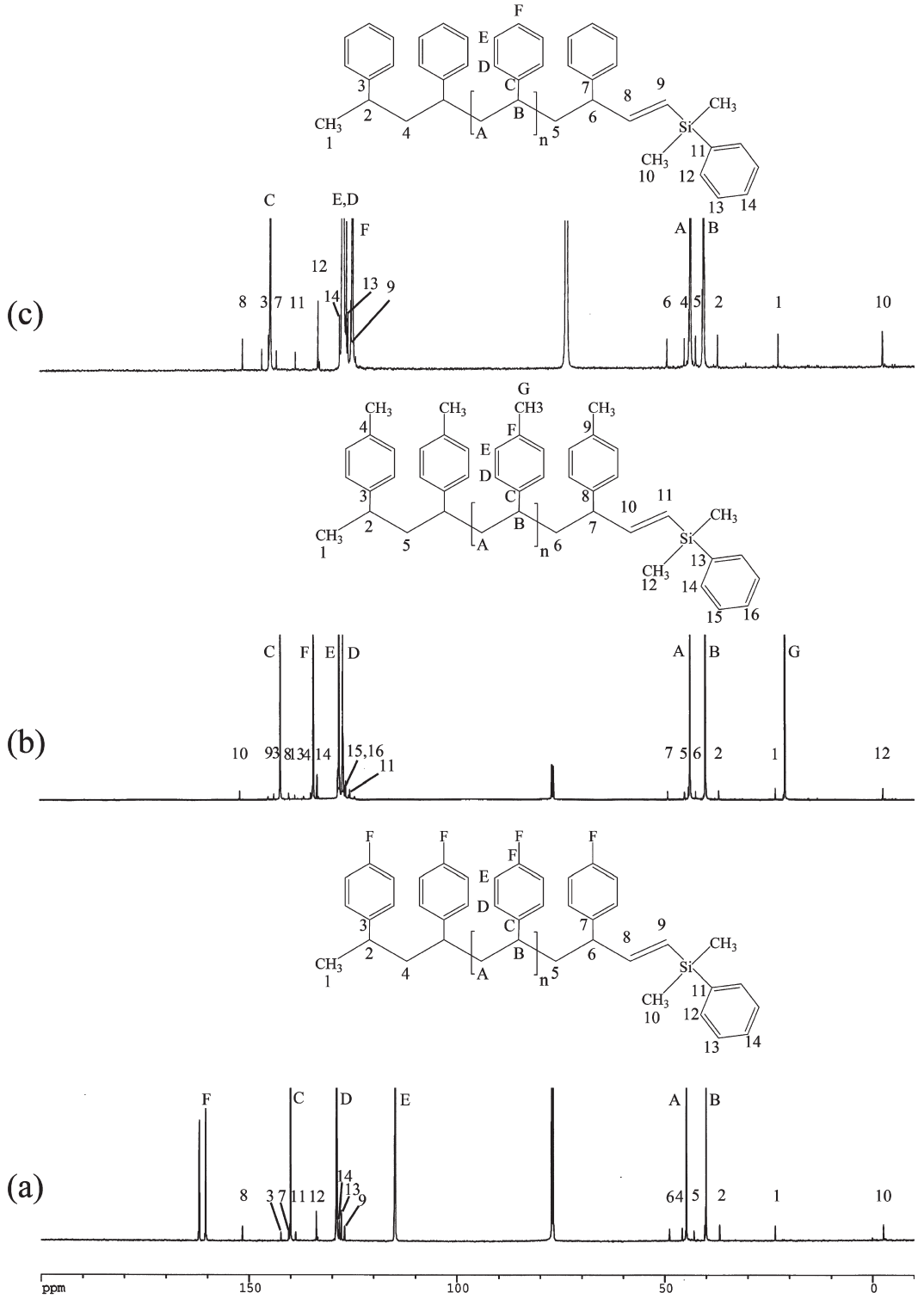


Figure 3. ^{13}C (125 MHz) NMR spectra of (a) $C_6H_5-Si(CH_3)_2-CH=CH$-capped sPFS (M_n = 3600 g/mol, M_w/M_n = 1.6; run 15 of Table 1) (solvent $CDCl_3$; temperature 60 °C). (b) $C_6H_5-Si(CH_3)_2-CH=CH$-capped sPMS (M_n = 4700 g/mol, M_w/M_n = 1.7; run 11 of Table 1) (solvent $CDCl_3$; temperature 60 °C). (c) $C_6H_5-Si(CH_3)_2-CH=CH$-capped sPS (M_n = 4200 g/mol, M_w/M_n = 1.8; run 6 of Table 1) (solvent $C_2D_2Cl_4$; temperature 90 °C).

0.45 g of hydroxyl-capped sPMS. M_n = 8300 g/mol, M_w/M_n = 1.45 by GPC (in 1,2,4-trichlorobenzene at 135 °C).

Synthesis of sPMS-*block*-PLLA. In a drybox, a 100 mL Schlenk flask, equipped with a magnetic stirrer, was sequentially charged with 0.20 g of the OH-capped sPMS (M_n = 8300 g/mol, M_w/M_n = 1.45), 30 mL of toluene, and then TEA (0.025 mmol). The resulting solution was stirred at room temperature for 12 h for macroinitiator formation. Then, L-lactide (0.32 g, 2.2 mmol) was added to the flask. The Schlenk flask was then removed from the drybox. It was then immersed in a 90 °C oil bath to undergo the controlled ring-opening polymerization reaction at 90 °C for 24 h. The polymerization reaction was then terminated with acidic methanol, which led to the deposition of the reaction product as an off-white precipitate. The resulting precipitate was isolated by filtration and allowed to undergo Soxhlet extraction with boiling cyclohexane to remove residual sPMS.

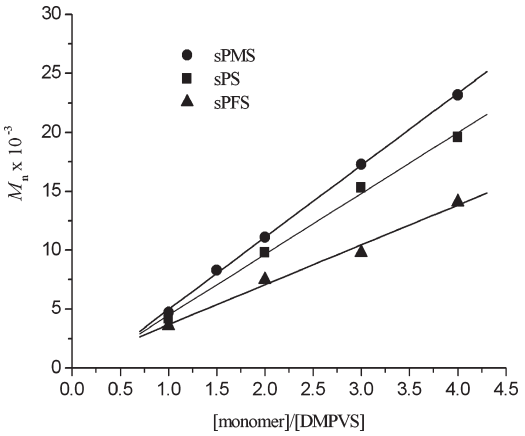


Figure 4. Plot of number average molecular weight (M_n) of $C_6H_5-Si-(CH_3)_2-CH=CH$-capped sPMS, sPS, and sPFS vs the mole ratio of [monomer]/[DMPVS] (run 3—15 of Table 1).

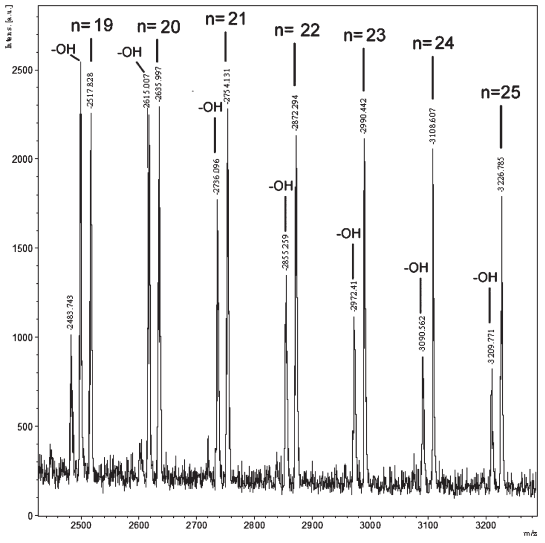
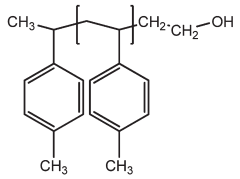
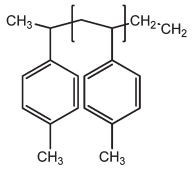


Figure 5. MALDI−TOF mass spectrum obtained with 2,5-dihydroxybenzoic acid (DHB)/dithranol/silver nitrate matrix for the $HO-CH_2-CH_2$-capped sPMS (M_n = 4700 g/mol, M_w/M_n = 1.4).

The resulting sPMS-*b*-PLLA was dried under vacuum for 24 h to provide 0.41 g of sPMS-*b*-PLLA [M_n = 14800, M_w/M_n = 1.22, determined by GPC (in 1,2,4-trichlorobenzene at 135 °C); the conversion of L-lactide was 65.6% based on isolation yield].

Polymer Analysis. The molecular weight and MWD (M_w/M_n) were determined by gel permeation chromatography (Waters 150-CALAC/GPC) with a refractive index (RI) detector and a set of U-Styragel HT columns of 10^6, 10^5, 10^4, and 10^3 pore sizes in series. The measurements were taken at 135 °C using tetrahydrofuran as the solvent. Polystyrene samples with narrow MWDs were used as the standards for calibration. The standards were in the range of absolute molecular weight, which is from 980 to 2,110,000, and the *R* square of the ideal calibrated line was limited to up to 0.999. All ^1H and ^{13}C NMR spectra were recorded on a Bruker AV-500 NMR spectrometer. The sPS-based polymer samples were dissolved in 1,1,2,2-tetrachloroethane-d_2. The spectra were recorded at a temperature of 90 °C. MALDI−TOF MASS spectra were recorded on a Bruker Autoflex III spectrometer equipped with a 337 nm nitrogen laser. Samples for MALDI−TOF MASS were prepared by mixing10 μL of polymer solution (10 mg mL^{-1} in THF), 10 μL of cationizing agent (silver nitrate) (2 mg mL^{-1} in THF) and 50 μL of matrices. The matrices were prepared by mixing 10 mg of 1,8-dihydroxy-9(10*H*)-anthracenone (dithranol) and 15 mg of 2,5-dihydroxybenzoic acid (DHB) in 1 mL of THF. The ions were accelerated to 20 kV and measured in the reflection mode of spectrometer.

Table 2. Structural Assignments for Fragment Peaks in MALDI−TOF Mass Spectra of Hydroxyl-Capped sPMS

entry	structure	Mass(*m/z*) of Ag^+ complex
a		n(118.18) +272.05
b		n(118.18)+254.05

Preparation of Bulk Samples. Bulk samples of sPMS-PLLA block copolymers were prepared by solution casting from a nonselective solvent, dichloromethane (CH_2Cl_2), at a concentration of 10 wt % sPMS-PLLA at room temperature. After the polymer completely dissolved, the solution was filtrated through a filter with 0.45 μm pathways to remove impurities. The solution was then transferred to a vial and sealed well by aluminum foil with punch holes for the slow evaporation of the solvent. After drying, the bulk samples were further dried in a vacuum oven to remove residual solvent.

Characterization of Nanostructures. Differential scanning calorimetry (DSC) experiments were performed in a Perkin-Elmer DSC 7 to measure the thermal behavior of the sPMS-*b*-PLLA. The DSC thermograms were recorded during the second heating cycle from 0 to 250 °C with a heating rate of 10 °C/min after fast cooling by 150 °C/min from the melt sate of samples at 250 °C. Bright-field transmission electron microscopy (TEM) images were obtained using the mass thickness contrast with a JEOL JEM-2100 LaB_6 transmission electron microscope at an accelerating voltage of 200 kV. The bulk samples were sectioned at room temperature by a Leica ultramicrotome. Then, the microsections were collected on copper grids. Staining was accomplished by exposing the sample grids to the vapor of an aqueous RuO_4 solution for 3 h. RuO_4 reacts with the aromatic groups in the sPMS blocks, rendering these domains dark in TEM images via mass thickness contrast. Small-angle X-ray scattering (SAXS) experiments were conducted at the synchrotron X-ray beamline 23A1 at the National Synchrotron Radiation Research Center (NSRRC) in Hsinchu, Taiwan.

Results and Discussion

End-Functionalization of Syndiotactic Polystyrenes by Vinylsilane-Inducing Selective Chain Transfer Reactions. Alkenylsilanes, which contain a pendent silyl group separated from the polymerizable double bond, have been reported to provide in chain functionalization of polyolefins.[19] By contrast, studies on polymerization of vinylsilanes (with the silicon functional group direct attaching to vinyl group) have been extremely limited.[20] In our efforts to achieve in-chain functionalization of syndiotactic polystyrene (sPS) by the incorporation of vinylsilane (e.g., dimethylphenylvinylsilane, DMPVS) units into the sPS main chain via the syndiospecific polymerization of styrene conducted in the presence of DMPVS using $Cp^*Ti(OMe)_3$/MAO as the catalyst, we

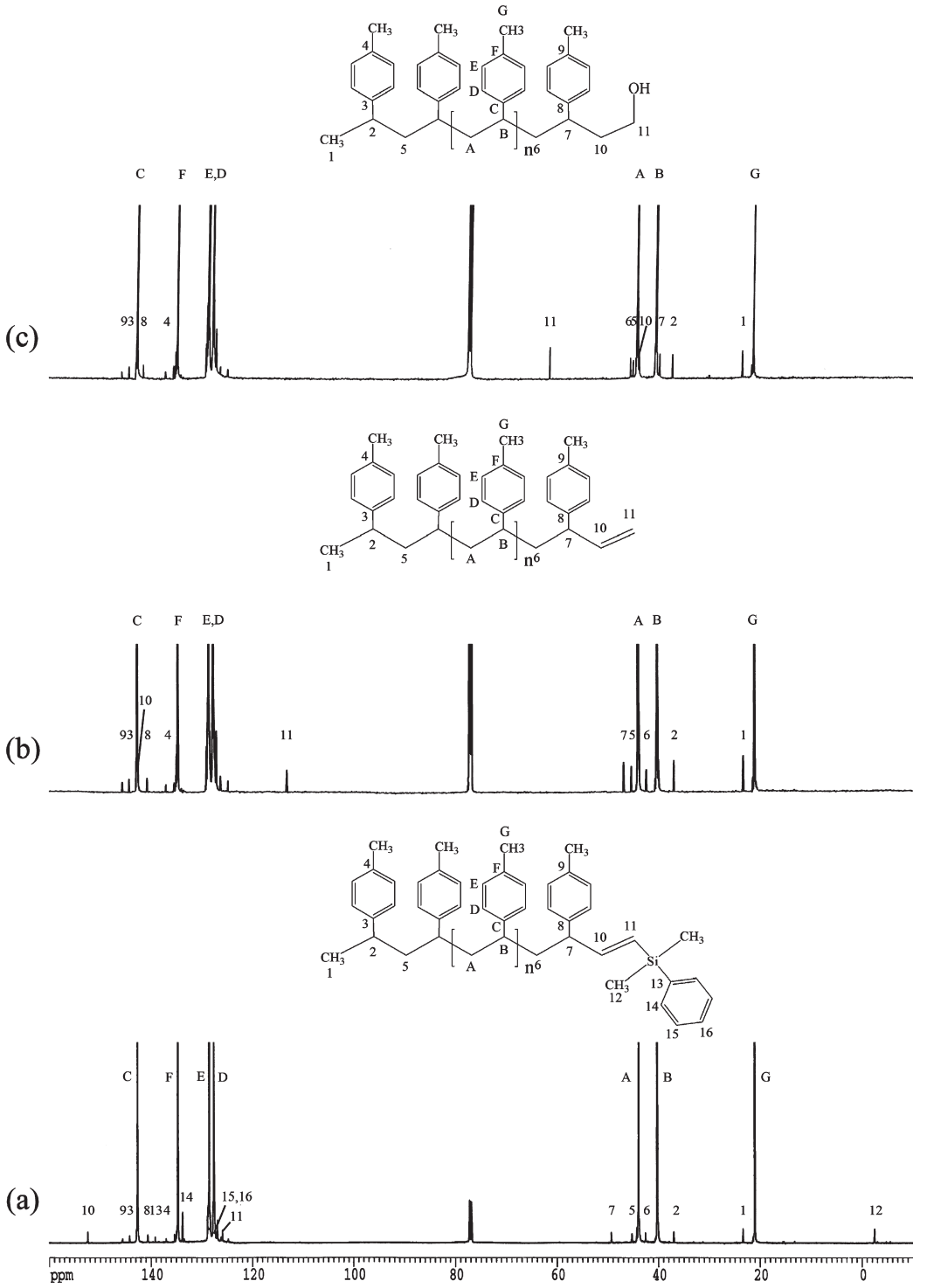


Figure 6. ^{13}C (125 MHz) NMR spectra of (a) $C_6H_5-Si(CH_3)_2-CH=CH$-capped sPMS, (b) ethenyl-capped sPMS, and (c) hydroxyl-capped sPMS (M_n = 4700 g/mol, M_w/M_n = 1.4; run 11 of Table 1) (solvent $CDCl_3$; temperature 60 °C).

found that the addition of DMPVS into the styrene polymerization solution led to a drastic reduction of polymer yields (entries 1−6 of Table 1). We also noted that an increase in the concentration of DMPVS led to a decrease in both the polymer molecular weight and polymer yields (entries 3−6 of Table 1). The reduction in the polymer yield by increasing the concentration of DMPVS is mainly due to the increase in the DMPVS concentration significantly reduces the catalyst activity for monomer conversion as revealed by the comparison between entries 3−6, 7−11, and 12−15 of Table 1. Efforts to synthesize the homopolymer of dimethylphenylvinylsilane by the polymerization of DMPVS, however, did not provide isolable products, as revealed by entry 2 of Table 1. Detailed structural analyses using ^1H (Figure 1) and 2-D ($^1H-^{13}C$ HMQC) NMR spectra (Figure 2) reveal that polymers prepared under these conditions have long syndiotactic polystyrene sequences, which constitute the polymer backbone. Detailed chain-end structural analyses using ^{13}C (DEPT-135) and 2-D ($^1H-^{13}C$ HMBC) NMR spectra (see Supporting Information) reveal that the resulting polymer has saturated [$-CH(C_6H_5)-CH_3$] and unsaturated [$-CH=CH-Si(CH_3)_2-C_6H_5$] terminal groups. The

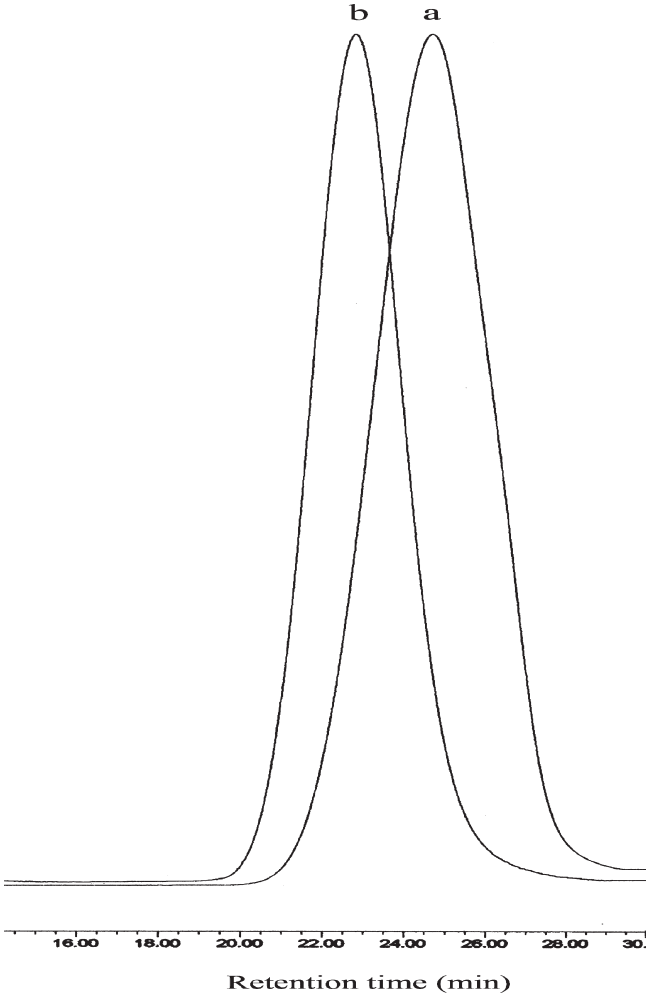


Figure 7. GPC curves comparison between (a) OH-capped sPMS (M_n = 8300 g/mol, PDI = 1.45) and (b) sPMS-*block*-PLLA (M_n = 14800 g/mol, PDI = 1.22).

formation of the [−CH(C_6H_5)−CH_3] end group can be explained by the 2,1-insertion of the first styrene unit by titanium hydride species (structure **I** of Scheme 1), which can be typically generated via the β-hydride elimination chain transfer reaction, which is the dominant chain transfer reaction in metallocene-catalyst-mediated syndiospecific styrene polymerization.[21] In contrast, the [−CH=CH-Si-(CH_3)$_2$−C_6H_5] terminal group was generated after the 2,1-insertion of a DMPVS end unit by the active catalyst, which undergoes a subsequent β-hydride elimination transfer that places the unsaturated dimethylphenylsilyl functional group at the very last carbon of the sPS main chain. There are no other vinylic resonances associated with the formation of the unsaturated [−CH=CH−C_6H_5] end group, which can be generated via β-hydride elimination chain transfer from a 2,1-inserted styrene end unit. In addition, we are unable to detect the formation of the [−CH(C_6H_5)−CH_2−CH_3] terminal group (formed in the chain initiation step via 2,1-insertion of a styrene unit by Ti−Me species) associated with the presence of other chain transfer pathways (i.e., chain transfer to methylaluminum of MAO).[22] Evidently, at the high level of DMPVS employed, the incorporation of DMPVS overwhelms all the others chain transfer mechanism that offers a unique chain transfer pathway for the selective generation of end-functionalized sPS end-capped with a uniform [−CH=CH-Si(CH_3)$_2$−C_6H_5] terminal group. Of note, the incorporation of the DMPVS unit by the unusual 2,1-insertion pattern is the key step that favors the formation of the DMPVS end group through the selective chain transfer pathway because this insertion pattern situates the bulky DMPVS end group at a steric jamming position (β-position) from the active center (see structure **III** of Scheme 1). This unfavorable steric interaction not only stalls the chain propagation for styrene insertion but also suppresses other possible chain transfer mechanisms, producing end-functionalized sPS (IV) with the identical [−CH=CH−Si(CH_3)$_2$−C_6H_5] terminal group and providing the titanium hydride species (**I**), which reenters the chain propagation processes. The proposed mechanism for selective generations of end-functionalized polymers (**IV**) is illustrated in Scheme 1.

The preparation of the end-functionalized sPS via the unique selective chain transfer route is not limited to the use of DMPVS; other vinylsilanes (e.g., trimethylvinylsilane and triphenylvinylsilane) have demonstrated a similar capability for inducing selective chain transfer reactions for the preparation of end-functionalized sPS end-capped with various vinylsilane terminal groups (see Supporting Information). Furthermore, the production of end-functionalized sPS via vinylsilane-inducing selective chain transfer is not limited to the polymerization of styrene monomer; styrene derivatives, including methylstyrene, chlorostyrnene, and fluorostyrene, can be used for the preparation of vinylsilane end-capped syndiotactic polystyrenes via this unique chain transfer route. For example, DMPVS-capped syndiotactic poly-4-methylstyrene (sPMS; entries 7−11 of Table 1) and syndiotactic poly-4-fluorostyrene (sPFS; entries 12−15 of Table 1) are accessible by employing DMPVS to mediate the selective chain transfer reaction in the presence of the respective styrene derivatives. Figure 3 shows a comparison of ^{13}C NMR spectra between DMPVS-capped sPS (Figure 3a), DMPVS-capped sPMS (Figure 3b), and DMPVS-capped sPFS (Figure 3c).

Figure 4 shows a plot of the polymer molecular weight (M_n) vs [styrenes]/[DMPVS] for polymers obtained via the syndiospecific polymerization of styrene derivatives, including styrene, 4-methylstyrene, and 4-fluorostyrene, respectively, in the presence of Cp*Ti(OMe)$_3$/MAO. The nearly linear relationship between M_n and [styrenes]/[DMPVS] indicates that the slow DMPVS insertion reaction (with rate constant k_{tr}) followed by the relatively fast β-hydride elimination constitutes the chain transfer processes, which compete with the chain propagating reaction (with rate constant k_p). The degree of polymerization (X_n) follows the relationship $X_n = k_p$[styrenes]/k_{tr}[DMPVS]. From Figure 4, the best-fit estimates for the relative chain transfer constants are k_{tr}/k_p = 1/49.69 for C_6H_5−Si(CH_3)$_2$−CH=CH-capped sPS, k_{tr}/k_p = 1/51.84 for C_6H_5−Si(CH_3)$_2$−CH=CH-capped sPMS, and k_{tr}/k_p = 1/27.67 for C_6H_5−Si-(CH_3)$_2$−CH=CH-capped sPFS. Of note, the relatively small chain transfer constant in the preparation of C_6H_5−Si-(CH_3)$_2$−CH=CH-capped sPMS and the relatively large chain transfer constant in the preparation of C_6H_5−Si-(CH_3)$_2$−CH=CH-capped sPFS can be explained by the fact that an electron deficient cationic active center (Ti) was involved in mediating the syndiospecific polymerization of monomers of styrene derivatives. Therefore, C_6H_5−Si-(CH_3)$_2$−CH=CH-capped sPFS has a greater chain transfer constant (k_{tr}/k_p) due to the slower chain propagation rate (k_p) in the polymerization of the strong electron withdrawing fluoride containing 4-fluorostyrene monomer; in contrast, the C_6H_5−Si(CH_3)$_2$−CH=CH-capped sPMS has a slower chain transfer constant due to the presence of the

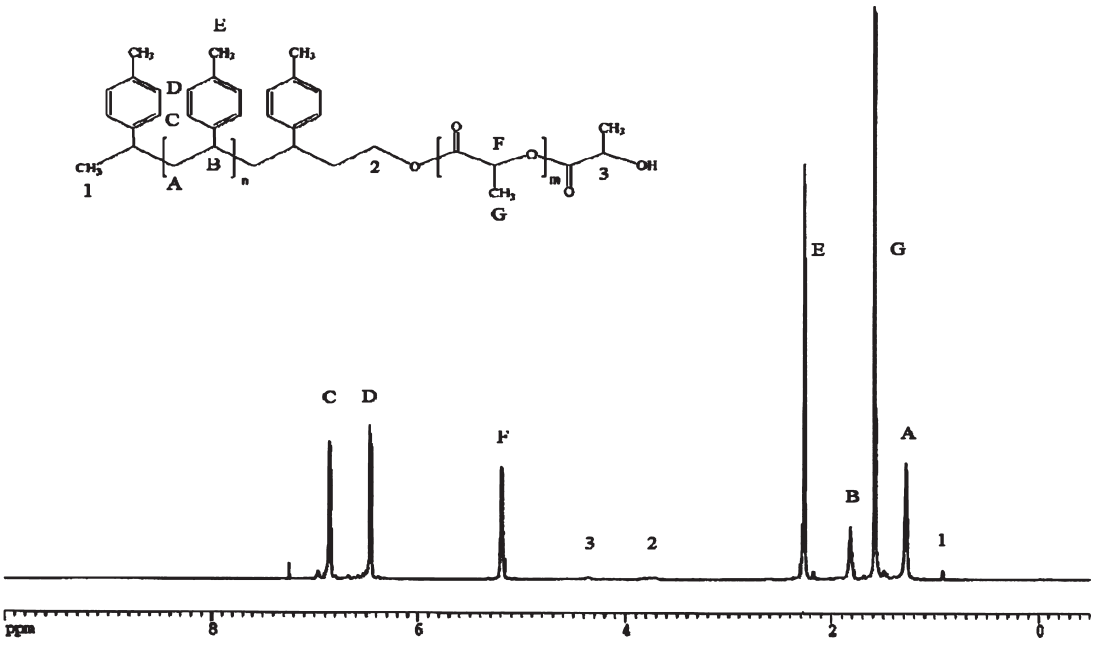


Figure 8. ^{1}H NMR (700 MHz) spectrum of the sPMS-*block*-PLLA (M_n = 14800 g/mol, PDI = 1.22) prepared from OH-capped sPMS (M_n = 8300 g/mol, PDI = 1.45) (solvent, $CDCl_3$; temperature, 60 °C).

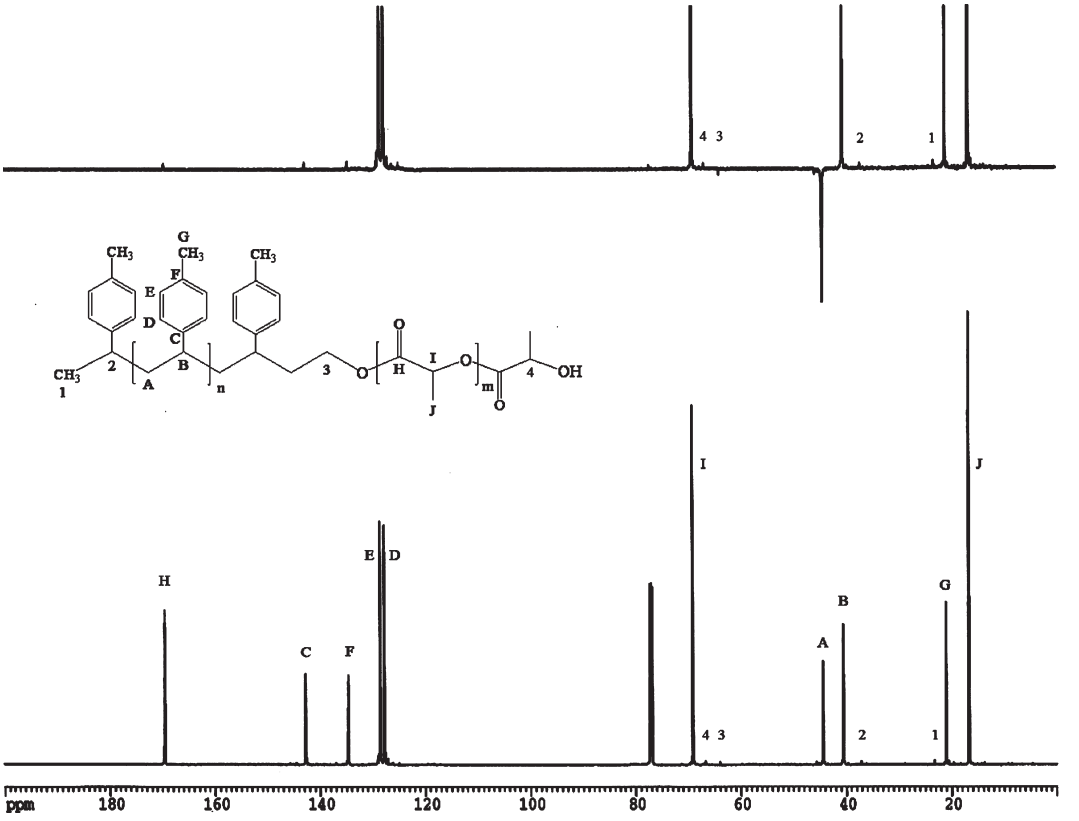
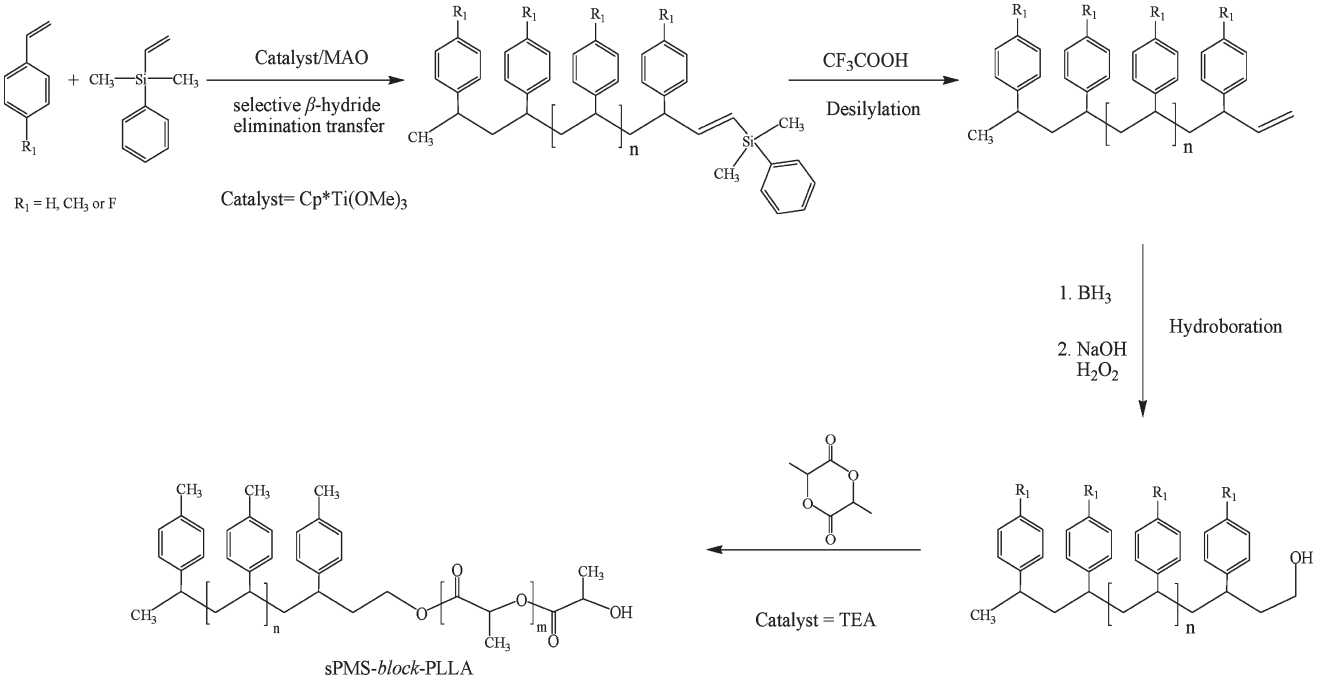


Figure 9. ^{13}C (DEPT-135) NMR (125 MHz) spectrum of the sPMS-*block*-PLLA (M_n = 14800 g/mol, PDI = 1.22) prepared from OH-capped sPMS (M_n = 8300 g/mol, PDI = 1.45). (solvent $CDCl_3$; temperature 60 °C).

electron-donating methyl group on the aryl group, which accelerates the chain propagation rate (k_p).

The vinylsilane end groups generated by the vinylsilane-induced selective chain transfer reaction can be readily converted into various functional groups, and the resulting end-functionalized stereoregular polymers can serve as stereoregular prepolymers for the preparation of syndiotactic polystyrene derivatives containing stereoregular BCPs using the terminal functional group as a linkage for connecting to other polymer blocks. As structurally well-defined syndiotactic polystyrenes containing stereoregular BCPs are extremely difficult to obtain using existing methods, the proposed synthetic route offers the opportunity for self-assembly studies of these unique stereoregular BCPs.

Scheme 2



Preparation of Syndiotactic Polystyrenes-Based Stereoregular BCPs. For the preparation of syndiotactic polystyrenes containing stereoregular BCPs, the terminal DMPVS group of the $C_6H_5-Si(CH_3)_2-CH=CH$-capped syndiotactic polystyrenes were allowed to undergo a desilylation reaction through treatment with trifluoroacetic acid to provide ethenyl group end-capped syndiotactic polystyrenes with high yields.[23] Subsequently, the ethenyl end group of the $CH_2=CH$-capped syndiotactic polystyrenes can be converted into a hydroxyl group by a subsequent hydroboration reaction.[24] The resulting hydroxyl-capped syndiotactic polystyrenes can be treated with alkylaluminum for conversion into aluminum alkoxide-capped syndiotactic polystyrenes which can act as macroinitiators for mediating the controlled ring-opening polymerization of cyclic esters for the production of syndiotactic polystyrenes-*b*-polyesters as structurally well-defined stereoregular BCPs.[9a,10] Of note, the synthesis of the hydroxyl-capped stereoregular polystyrenes is the key step for the successful preparation of the syndiotactic polystyrenes containing stereoregular BCPs since the construction stereoregular BCPs depends on the purity of the macroinitiator, which needs to be generated form a highly pure hydroxyl-capped end-functionalized prepolymer. In order to ensure that the hydroxyl-capped syndiotactic polystyrenes prepared by the unique selective chain transfer reaction has a high functional group incorporation ratio to be used as the end-functionalized prepolymer, the hydroxyl-capped prepolymer was further analyzed by MALDI−TOF mass spectroscopy. Figure 5 shows the MALDI−TOF mass spectrum of a lower molecular weight sample of hydroxyl-capped sPMS (M_n = 4600 g/mol, M_w/M_n = 1.5) prepared from run 11 of Table 1. The results of MALDI−TOF mass analyses indicate the presence of two series of m/z(s), which correspond to the $HO-CH_2-CH_2$-capped sPMS (structure a in Table 2) and CH_2-CH_2-capped sPMS (structure b in Table 2), respectively. Of note, Structure b corresponds to the m/z fragment, which was generated by losing of the hydroxyl end group of the $HO-CH_2-CH_2$-capped sPMS (structure a). Since both structures a and b were deriving from hydroxyl-capped sPMS, these results clearly indicate that end-functionalized polymer prepared by the unique selective chain transfer route has a nearly quantitative end functional group incorporation ratio and is suitable to be used as the end-functionalized prepolymer for the construction of structurally well-defined stereoregular BCPs.

Accordingly, the $C_6H_5-Si(CH_3)_2-CH=CH$-capped sPMS sample (M_n = 8400, M_w/M_n = 1.5, syndiotacticity-(rrrrr) = 91%, entry 10 of Table 1) was allowed to undergo the desilylation reaction by being treated with trifluoroacetic acid to provide $CH_2=CH$-capped sPMS (M_n = 8400, M_w/M_n = 1.5; see Figure 6b). The resulting $CH_2=CH$-capped sPMS was then allowed to undergo the hydroboration reaction for the production of hydroxyl-capped sPMS (M_n = 8300, M_w/M_n = 1.5; see Figure 6c). The resulting OH-capped sPMS was then treated with an equal molar of TEA that led to the *in situ* formation of aluminum alkoxid-capped sPMS macroinitiator. Subsequently, conducting the controlled ring-opening polymerization of the sPMS macroinitiator with L-lactide at 90 °C provides sPMS-*b*-PLLA with a good L-lactide conversion ratio and a high BCP yield. Figure 7 compares the GPC elusion curves of OH-capped sPMS (M_n = 8300, M_w/M_n = 1.5) with those of sPMS-*b*-PLLA (M_n = 14800, M_w/M_n = 1.22, f^v_{PLLA}=0.39, named sPMS83-PLLA65). Figure 8 and Figure 9 show the ^1H NMR and ^{13}C and ^{13}C (DEPT 135) NMR spectra (with insets showing the expanded region and chemical shift assignments of the sPMS-*b*-PLLA, respectively). The effectiveness of this synthetic strategy for the synthesis of structurally well-defined syndiotactic polystyrenes-based BCPs was further demonstrated by the successful preparation of a second sPMS-*b*-PLLA sample (M_n = 15800, M_w/M_n = 1.20, f^v_{PLLA} = 0.43, named sPMS83-PLLA75), which was also synthesized from the identical OH-capped sPMS (M_n = 8300, M_w/M_n = 1.5), which was prepared from entry 10 of Table 1. The detailed synthetic routes for the preparation of these structurally well-defined sPMS-*b*-PLLA samples are illustrated in Scheme 2. It should be noted that the reported synthetic route is not limited for the preparation of block copolymers of sPMS because other stereoregular BCPs, which contain the sPS and the sPFS blocks, respectively,

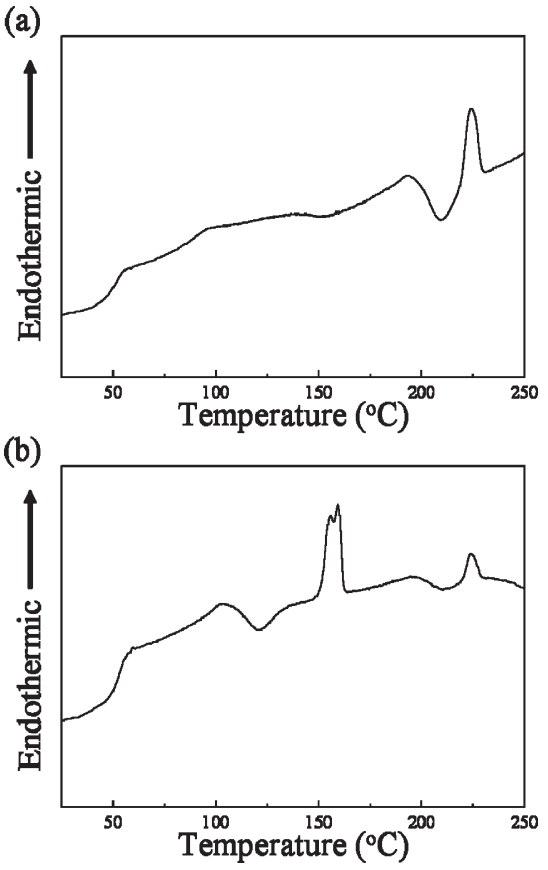


Figure 10. DSC thermograms of sPMS-PLLA block copolymers with PLLA volume fraction of (a) 0.39 and (b) 0.43, respectively. The heating rate is 10 °C/min.

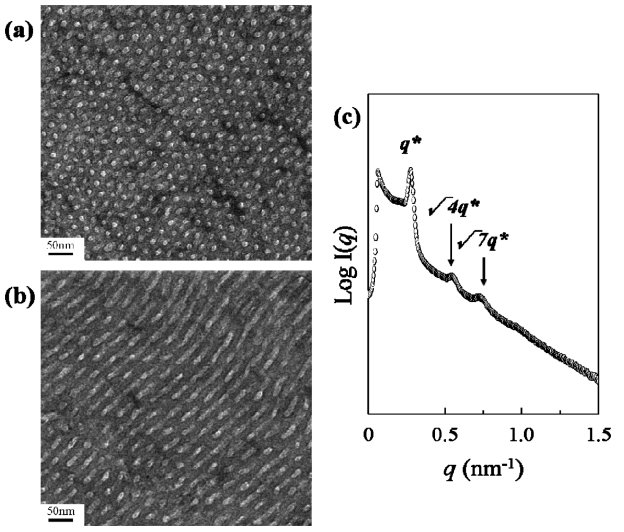


Figure 11. TEM micrographs of sPMS-PLLA (f^{v}_{PLLA} = 0.39) block copolymer with hexagonal-packed cylinder nanostructure: (a) viewing parallel and (b) normal to cylindrical axes. The microdomains of sPMS appear dark due to staining of RuO_4 while the PLLA microdomains display bright. (c) Corresponding one-dimensional SAXS profile.

have been prepared by the similar route illustrated in scheme 2 (^{13}C NMR spectra of these stereoregular BCPs can be found in the Supporting Information).

Self-Assembled Nanostructures of Stereoregular BCPs. Owing to crystallizable sPMS and PLLA blocks, the thermal behavior of the sPMS-*b*-PLLA was first examined using

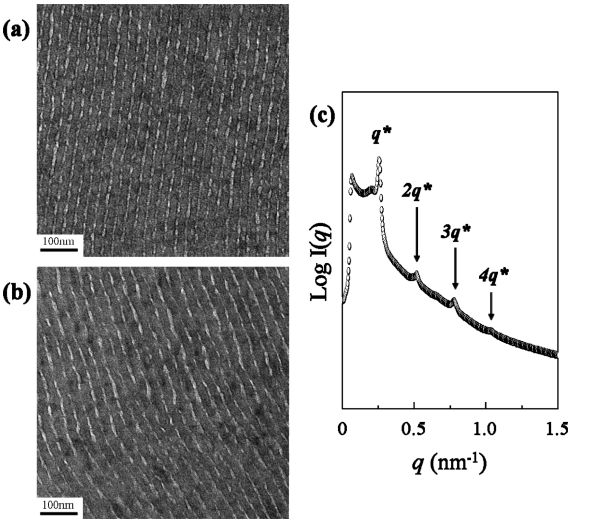


Figure 12. TEM micrographs of sPMS-PLLA (f^{v}_{PLLA} = 0.43) block copolymer with lamellae nanostructure: (a) viewing perpendicular to lamellar normal and (b) viewing perpendicular to lamellar normal at different rotation. The microdomains of sPMS appear dark due to staining of RuO_4 while the PLLA microdomains display bright. (c) Corresponding one-dimensional SAXS profile.

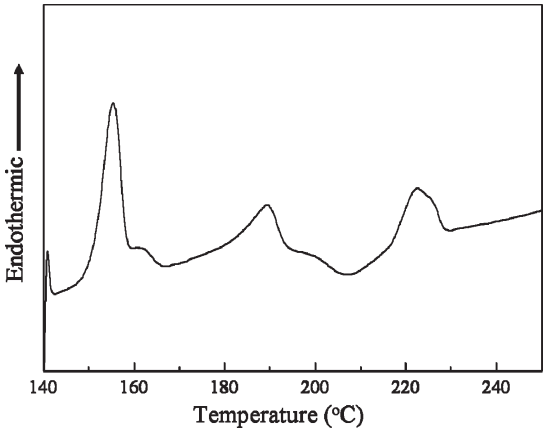


Figure 13. DSC heating curves of sPMS-b-PLLA (f^{v}_{PLLA} = 0.43) block copolymer with isothermal crystallization at 140 °C for 3 h after rapidly cooling process (150 °C/min) from microphase-separated melt to 0 °C. The heating rate is 10 °C/min.

DSC. From DSC profiles of the second heating process (Figure 10), the sPMS-*b*-PLLA with various volume fractions of PLLA exhibit different thermal properties. For sPMS83-PLLA65 with a small volume fraction of PLLA (i.e., f^{v}_{PLLA} = 0.39), the glass transition temperatures (T_g) of PLLA and sPMS blocks are determined as 50 and 91 °C, respectively (Figure 10a). In the high temperature region, more complex thermal behavior reflects the polymorphic crystallization behavior of the sPMS block.[25−27] The first endothermic peak appears at 194 °C, corresponding to the melting temperature of the sPMS crystalline form IV.[28,29] An accompanying exothermic peak at 209 °C indicates the formation of the crystalline form III. The sPMS blocks melt from crystalline form III at 224 °C.[29] The absence of a PLLA crystallization temperature and melting point is attributed to the confinement effect for PLLA chains restricted in the glassy sPMS matrix.[30] For comparison, sPMS83-PLLA75 with a high volume fraction of PLLA (i.e., f^{v}_{PLLA} = 0.43) gives glass transition temperatures of PLLA and sPMS blocks at 50 and 100 °C, respectively (Figure 10b).

In contrast to the amorphous PLLA in sPMS83-PLLA65, an exothermic peak at 121 °C for the PLLA crystallization temperature (T_c) and an endothermic peak at 159 °C for the PLLA melting point (T_m) can be observed, further confirming the confined effect on the crystallization of PLLA in sPMS83-PLLA65. Similar to sPMS83-PLLA65, the high stereoregularity of the sPMS block in sPMS83-PLLA75 gives rise to complicated thermal behavior.

To achieve the formation of well-ordered nanostructures from the self-assembly of sPMS-*b*-PLLA block copolymers in the bulk state, the bulk samples of sPMS-*b*-PLLA were first heated to the maximum annealing temperature, T_{max} = 250 °C, for 3 min to eliminate the sPMS and PLLA crystalline residues produced during sample preparation. The thermally treated bulk samples were obtained after quenching at a rate of 150 °C/min from the melt state. For sPMS83-PLLA65, hexagonally packed cylindrical nanostuctures were observed in TEM images (Figure 11, parts a and b). Due to RuO_4 staining of the sPMS blocks, white cylinders (indicating unstained PLLA microdomains) are dispersed in the dark sPMS matrix. The self-assembled morphology was further identified by SAXS experiments. Corresponding one-dimensional SAXS profile (Figure 11c) shows well-ordered reflections with peak positions at the q ratios of 1:$\sqrt{4}$:$\sqrt{7}$, indicating a well-ordered cylindrical phase with hexagonal packing. Using the primary peak, the d-spacing of the (100) plane was determined as 22.8 nm and the interspacing of each cylinder was then calculated as 26.3 nm, in line with the TEM observations. These results suggest that T_{max} is below the order−disorder transition temperature (T_{ODT}) and the self-assembled nanostructure driven from the incompatibility of the sPMS and PLLA blocks can be successfully developed. In contrast, Figure 12, parts a and b, shows the lamellar nanostructure of sPMS83-PLLA75 resulting from the self-assembly in the melt state. For SAXS experiments, the self-assembled morphology of the sPMS-b-PLLA is identified as a lamellar phase according to the reflection peaks at the q ratios of 1:2:3:4 (Figure 12c). The d-spacing of the (100) plane was determined as 24.4 nm from the primary peak of the reflections, which is consistent with the TEM observations. To further demonstrate the idea of these semicrystalline materials that could be useful as high-temperature templates for nanopatterning, the crystalline sPMS from the microphase-separated state can be obtained by taking advantage of cool crystallization. The crystallinity of sPMS can be generated by slowly heating the rapidly cooled sample from ambient condition to preset temperature for isothermal crystallization. The occurrence of PLLA crystallization might carry out first during heating so as to create crystalline PLLA microdomains. Subsequently, sPMS crystallization can be conducted isothermally below the melting temperature of PLLA (~160 °C). As a result, the microphase-spearated nanostructures should not be largely affected by the crystallization event of sPMS block due to the preformed PLLA crystallinity. Figure 13 shows DSC heating curves of sPMS-b-PLLA (f^v_{PLLA} = 0.43) block copolymer with isothermal crystallization at 140 °C for 3 h after rapidly cooling process (150 °C/min) from microphase-separated melt to 0 °C. In comparison with Figure 10b which shows the melting peak of sPMS crystalline form IV at 194 °C is insignificant after rapid cooling process, the sPMS block exhibits an obvious melting peak at the same temperature after the isothermal crystallization at 140 °C for 3 h, indicating an obvious increase in the crystallinity of sPMS crystalline form IV. In higher temperature region, the exothermic peak at 209 °C is attributed to the crystallization of sPMS crystalline form III, and the melting peak of the sPMS crystallites appears at 224 °C. Consequently, by taking advantage of high melting temperature and slow crystallization of sPMS combining with the degradable PLLA block, the formation of microphase-separated nanostructures from sPMS-b-PLLA is a convenient method for creating a well-ordered heat-resistant sPMS nanoporous template via the hydrolysis of PLLA[31] so as to enhance the functionalities and applications of BCPs in nanotechnology.

Conclusions

We demonstrated a unique synthetic method that can be used to prepare stereoregular BCPs of syndiotactic polystyrenes via the postpolymerization of vinylsilane end-capped syndiotactic polystyrenes, which were prepared via a unique vinylsilane-inducing selective chain transfer reaction. The vinylsilane end group of the end-functionalized syndiotactic polystyrenes can be converted into ethenyl end-group and then converted into the hydroxyl end group by subsequent organic transformation reactions. The resulting hydroxyl-capped syndiotactic polystyrenes can be treated with triethylaluminum for the *in situ* formation of an aluminum alkoxide-capped stereoregular macroinitiator that can be used for the construction of stereoregular BCPs of syndiotactic polystyrenes via the controlled living polymerization of cyclic esters. Accordingly, structurally well-defined sPMS-*b*-PLLA, which is difficult to prepare using existing methods, can be synthesized with high yield using the methods developed in this study. Moreover, the well-ordered nanostructures from the self-assembly of sPMS-PLLA BCPs in the bulk state can be identified as evidenced by TEM micrographs and SAXS profiles. These results demonstrate that our synthetic route can provide an effective control on stereoregularity during the α-olefin polymerization and improve linking efficiency between the constituent blocks so as to give well-ordered nanostructures via self-assembly. By taking the advantage of tacticity control through stereospecific polymerization and molecular weight control through controlled-living radical polymerization, stereoregular BCPs with semicrystalline character can be synthesized as the advanced functional materials for application in nanotechnology.

Acknowledgment. The authors would like to thank the National Science Council of Taiwan for financial support for this research under Contracts NSC-98-2216E-194-003 and NSC-98-2216E-110-009.

Supporting Information Available: Figures showing NMR spectra of end-functionalized syndiotactic polystyrenes and syndiotactic polystyrenes-based stereoregular diblock copolymers. This material is available free of charge via the Internet at http://pubs.acs.org.

References and Notes

(1) (a) Lazzari, M.; Liu, G.; Lecommandoux, S. *Block Copolymers in Nanoscience*; Wiley-VCH Verlag GmbH & Co. KGaA: Weinheim, Germany, 2006.(b) Abetz, V.; Hadjichristidis, H.; Iatrou, H.; Pitsikalis, M.; Simon, P. F. W. *Adv. Polym. Sci.* **2005**, *189*, 1–124. (c) Hadjichristidis, N.; Pispas, S.; Floudas, G. *Block Copolymers: Synthetic Strategies, Physical Properties and Applications*; John Wiley and Sons: New York, 2003. (d) Alexandridis, P.; Lindman, B. *Amphiphilic Block Copolymers: Self-Assembly and Applications*; Elsevier: Amsterdam, 2000. (e) Calleja, F. J. B.; Roslaniec, J. *Block Copolymers*; Marcel Dekker: New York, 2000.

(2) (a) Bates, F. S.; Fredrickson, G. H. *Annu. Rev. Phys. Chem.* **1990**, *41*, 525–557. (b) Bates, F. S.; Fredrickson, G. H. *Phys. Today* **1999**, *52*, 32–38.

(3) (a) Hatada, K.; Kitayama, T.; Ute, K.; Nishiura, T. *Macromol. Rapid Commun.* **2004**, *25*, 1447–1477. (b) Scherman, O. A.; Rutenberg, I. M.; Grubbs, R. H. *J. Am. Chem. Soc.* **2003**, *125*, 8515–8522.

(4) (a) Defaux, M.; Vidal, L.; Möller, M.; Gearba, R. I.; Dimasi, E.; Ivanov, D. A. *Macromolecules* **2009**, *42*, 3500–3509. (b) Pisula, W.; Zorn, M.; Chang, J. Y.; Müllen, K.; Zentel, R. *Macromol. Rapid Commun.* **2009**, *30*, 1179–1202. (c) Naga, N.; Yabe, T.; Sawaguchi, A.; Sone, M.; Noguchi, K.; Murase, S. *Macromolecules* **2008**, *41*, 7448–7452.

(5) (a) Klok, H. A.; Langenwalter, J. F.; Lecommandoux, S. *Macromolecules* **2000**, *33*, 7819–7826. (b) Chen, J. T.; Thomas, E. L.; Ober, C. K.; Hwang, S. S. *Macromolecules* **1995**, *28*, 1688–1697. (c) Schneider, A.; Zanna, J. J.; Yamada, M.; Finkelmann, H.; Thomann, R. *Macromolecules* **2000**, *33*, 649–651. (d) Cui, L.; Miao, J. J.; Zhu, L.; Sics, I.; Hsiao, B. S. *Macromolecules* **2005**, *38*, 3386–3394.

(6) (a) Green, M. M.; Peterson, N. C.; Sato, T.; Teramoto, A.; Cook, R.; Lifson, S. *Science* **1995**, *268*, 1860–1866. (b) Palmans, A. R. A.; Meijer, E. W. *Angew. Chem., Int. Ed. Engl.* **2007**, *46*, 8948–8968. (c) Ho, R.-M.; Chung, T.-M.; Tsai, J.-C.; Kuo, J.-C.; Hsiao, B. S.; Sics, I. *Macromol. Rapid Commum.* **2005**, *26*, 107–111. (d) Chung, T.-M.; Ho, R.-M.; Kuo, J.-C.; Tsai, J.-C.; Hsiao, B. S.; Sics, I. *Macromolecules* **2006**, *39*, 2739–2742. (e) Ho, R.-M.; Chiang, Y.-W.; Tsai, C.-C.; Lin, C.-C.; Ko, B.-T.; Huang, B.-H. *J. Am. Chem. Soc.* **2004**, *126*, 2704–2705.

(7) (a) Kawabe, M.; Murata, M. *J. Polym. Sci., Part A: Polym. Chem.* **2001**, *39*, 3692–3706. (b) Ban, H. T.; Tsunogae, Y.; Shiono, T. *J. Polym. Sci., Part A: Polym. Chem.* **2005**, *43*, 1188–1195. (c) Ban, H. T.; Kase, T.; Kawabe, M.; Miyazawa, A.; Ishihara, T.; Hagihara, H.; Tsunogae, Y.; Murata, M.; Shiono, T. *Macromolecules* **2006**, *39*, 171–176. (d) Kawabe, M.; Murata, M. *Macromol. Chem. Phys.* **2001**, *202*, 1799–1805. (e) Kawabe, M.; Murata, M. *Macromol. Chem. Phys.* **2002**, *203*, 24–30. (f) Kaita, S.; Hou, Z.; Wakatsuki, Y. *Macromolecules* **2001**, *34*, 1539–1541. (g) Zhang, H.; Nomura, K. *Macromolecules* **2006**, *39*, 5266–5274. (h) Hatada, K.; Kitayama, T.; Ute, K.; Nishiura, T. *Macromol. Rapid Commun.* **2004**, *25*, 1447–1477. (i) Tian, J.; Hustad, P. D.; Coates, G. W. *J. Am. Chem. Soc.* **2001**, *123*, 5134–5135. (j) Ruokolainen, J.; Mezzenga, R.; Fredrickson, G. H.; Kramer, E. J.; Hustad, P. D.; Coates, G. W. *Macromolecules* **2005**, *38*, 851–860. (k) Cazzaniga, L.; Cohen, R. E. *Macromolecules* **1991**, *24*, 5817–5822.

(8) (a) Satoh, K.; Kamigaito, M. *Chem. Rev.* **2009**, *109*, 5120–5156. (b) Satoh, K.; Kamigaito, M. *Macromolecules* **2008**, *41*, 269–276. (c) Miura, Y.; Shibata, T.; Satoh, K.; Kamigaito, M.; Okamoto, Y. *J. Am. Chem. Soc.* **2006**, *128*, 16026–16027. (d) Okamoto, Y.; Habaue, S.; Isobe, Y.; Nakamo, T. *Macromol. Symp.* **2002**, *183*, 83–88. (e) Ray, B.; Isobe, Y.; Matsumoto, K.; Habaue, S.; Kamigaito, M.; Okamoto, Y.; Sawamoto, M. *Macromolecules* **2004**, *37*, 1702–1710.

(9) (a) Tzeng, F.-Y.; Lin, M.-C.; Wu, J.-Y.; Kuo, J.-C.; Tsai, J.-C.; Hsiao, M.-S.; Chen, H.-L.; Cheng, Stephen Z. D. *Macromolecules* **2009**, *42*, 3073–3085. (b) Kuo, J.-C.; Tsai, J.-C.; Chung, T.-M.; Ho, R.-M. *Macromolecules* **2006**, *39*, 7520–7526. (c) Lin, W.-F.; Tsai, J.-C. *J. Polym. Sci., Part A: Polym. Chem.* **2008**, *46*, 2167–2176. (d) Lin, W.-F.; Hsiao, T.-J.; Tsai, J.-C.; Chung, T.-M.; Ho, R.-M. *J. Polym. Sci., Part A: Polym. Chem.* **2008**, *46*, 4843–4856. (e) Kuo, J.-C.; Lin, W.-F.; Yu, C.-H.; Tsai, J.-C.; Wang, T.-C.; Chung, T.-M.; Ho, R.-M. *Macromolecules* **2008**, *41*, 7967–7977. (f) Dong, J. Y.; Wang, Z. M.; Hong, H.; Chung, T. C. *Macromolecules* **2002**, *35*, 9352–9359. (g) Chung, T. C. *Prog. Polym. Sci.* **2002**, *27*, 39–85. (h) Mogstad, A.-L.; Waymouth, R. M. *Macromolecules* **1994**, *27*, 2313–2315.

(10) (a) Boudouris, B. W.; Frisbie, C. D.; Hillmyer, M. A. *Macromolecules* **2010**, *43*, 3566–3569. (b) Wang, Y.; Hillmyer, M. A. *Macromolecules* **2000**, *33*, 7395–7403. (c) Schmidt, S. C.; Hillmyer, M. A. *Macromolecules* **1999**, *32*, 4794–4801.

(11) (a) Vasilenko, I. V.; Kostjuk, S. V.; Kaputsky, F. N.; Nedorezova, P. M.; Aladyshev, A. M. *Macromol. Chem. Phys.* **2008**, *209*, 1255–1265. (b) Schellenberg, J. *Prog. Polym. Sci.* **2009**, *34*, 688–718. (c) Zambelli, A.; Longo, P.; Grassi, A. *Macromolecules* **1989**, *22*, 2186–2189.

(12) Syndiotactic polystyrenes-based BCPs containing blocks of various polystyrene derivatives have been prepared by sequential living polymerization of different monomers of styrene derivatives (see ref 7, parts a−e).

(13) Ho, R. M.; Tseng, W. H.; Fan, H. W.; Chiang, Y. W.; Lin, C. C.; Ko, B. T.; Huang, B. H. *Polymer* **2005**, *46*, 9362–9377.

(14) Zalusky, A. S.; Olayo-Valles, R.; Taylor, C. J.; Hillmyer, M. A. *J. Am. Chem. Soc.* **2001**, *123*, 1519–1520.

(15) Ko, B. T.; Lin, C. C. *J. Am. Chem. Soc.* **2001**, *123*, 7973–7977.

(16) Hsueh, H.-Y.; Chen, H.-Y.; She, M.-S.; Chen, C.-K.; Ho, R.-M.; Gwo, S.; Hasegawa, H.; Thomas, E. L. *Nano Lett.* **2010**, ASAP.

(17) Hasan, T.; Ioku, A.; Nishii, K.; Shiono, T.; Ikeda, T. *Macromolecules* **2001**, *34*, 3142–3145.

(18) Feil, F.; Harder, S. *Macromolecules* **2003**, *36*, 3446–3448.

(19) (a) Amin, S. B.; Marks, T. J. *J. Am. Chem. Soc.* **2006**, *128*, 4506–4507. (b) Amin, S. B.; Marks, T. J. *J. Am. Chem. Soc.* **2007**, *129*, 2938–2953. (c) Amin, S. B.; Marks, T. J. *Angew. Chem., Int. Ed.* **2008**, *47*, 2006–2025.

(20) (a) Itoh, M.; Iwata, K.; Kobayashi, M.; Takeuchi, R.; Kabeya, T. *Macromolecules* **1998**, *31*, 5609–5615. (b) Ganicz, T.; Stanczyk, W. A.; Gladkova, N. K.; Sledzinska, I. *Macromolecules* **2000**, *33*, 289–293.

(21) (a) Kawabe, M.; Murata, M. *Macromol. Chem. Phys.* **2001**, *202*, 2440–2446. (b) Zambelli, A.; Longo, P.; Pellecchia, C.; Grassi, A. *Macromolecules* **1987**, *20*, 2035–2037. (c) Duncalf, D. J.; Wade, H. J.; Waterson, C.; Derrick, P. J.; Haddleton, D. M.; McCamley, A. *Macromolecules* **1996**, *29*, 6399–6403.

(22) (a) Schellenberg, J.; Tomotsu, N. *Prog. Polym. Sci.* **2002**, *27*, 1925–1982. (b) Schellenberg, J. *Macromol. Mater. Eng.* **2005**, *290*, 833–842. (c) Tomotsu, N.; Ishihara, N.; Newman, T. H.; Malanga, M. T. *J. Mol. Catal. A: Chem.* **1998**, *128*, 167–190.

(23) Xi, Z.; Song, Z.; Liu, G.; Liu, X.; Takahashi, T. *J. Org. Chem.* **2006**, *71*, 3154–3158.

(24) Takeuchi, D.; Inoue, A.; Ishimaru, F.; Osakada, K. *J. Polym. Sci., Part A: Polym. Chem.* **2009**, *47*, 959–972.

(25) Iuliano, M.; Guerra, G.; Petraccone, V.; Corradini, P.; Pellecchia, C. *New Polym. Mater.* **1992**, *3*, 133–144.

(26) (a) De Rosa, C.; Petraccone, V.; Guerra, G.; Manfredi, C. *Polymer* **1996**, *37*, 5247–5253. (b) Ruiz de Ballesteros, O.; Auriemma, F.; De Rosa, C.; Floridi, G.; Petraccone, V. *Polymer* **1998**, *39*, 3523–3528.

(27) (a) De Rosa, C.; Petraccone, V.; Dal Poggetto, F.; Guerra, G.; Pirozzi, B.; Di Lorenzo, M. L.; Corradini, P. *Macromolecules* **1995**, *28*, 5507–5511. (b) Petraccone, V.; La Camera, D.; Pirozzi, B.; Rizzo, P.; De Rosa, C. *Macromolecules* **1998**, *31*, 5830–5836. (c) Petraccone, V.; La Camera, D.; Caporaso, L.; De Rosa, C. *Macromolecules* **2000**, *33*, 2610–2615. (d) Petraccone, V.; Esposito, G.; Tarallo, O.; Caporaso, L. *Macromolecules* **2005**, *38*, 5668–5674. (e) Esposito, G.; Tarallo, O.; Petraccone, V. *Macromolecules* **2006**, *39*, 5037–5042.

(28) Li, H.; Abraham, S.; Yan, W.; Ha, C.-S.; Kim, I. *Macromol. Rapid Commun.* **2007**, *28*, 1534–1539.

(29) Guerra, G.; Corradini, P.; De Rosa, C.; Iuliano, M.; Oliva, L.; Petraccone, V. U.S. Patent 5,468,823, 1995.

(30) (a) Chiang, Y.-W.; Ho, R.-M.; Ko, B.-T.; Lin, C.-C. *Angew. Chem., Int. Ed.* **2005**, *44*, 7969–7972. (b) Chiang, Y.-W.; Ho, R.-M.; Thomas, E. L.; Burger, C.; Hsiao, B. S. *Adv. Funct. Mater.* **2009**, *19*, 448–459.

(31) (a) Tseng, W.-H.; Chen, C.-K.; Chiang, Y.-W.; Ho, R.-M.; Akasaka, S.; Hasegawa, H. *J. Am. Chem. Soc.* **2009**, *131*, 1356–1357. (b) Ho, R.-M.; Chiang, Y.-W.; Chen, C.-K.; Wang, H.-W.; Hasegawa, H.; Akasaka, S.; Thomas, E. L.; Burger, C.; Hsiao, B. S. *J. Am. Chem. Soc.* **2009**, *131*, 18533–18542.

Macromolecules
ARTICLE

Macromolecules **2011**, *44*, 299–312 **299**
DOI: 10.1021/ma102386j

Facile Access to Polymeric Vesicular Nanostructures: Remarkable ω-End group Effects in Cholesterol and Pyrene Functional (Co)Polymers

Jiangtao Xu, Lei Tao, Cyrille Boyer, Andrew B. Lowe,* and Thomas P. Davis*

Centre for Advanced Macromolecular Design (CAMD), School of Chemical Engineering, University of New South Wales, Kensington, 2052, Sydney, Australia

Received October 20, 2010; Revised Manuscript Received December 8, 2010

ABSTRACT: Hydrophilic homopolymers of *N*,*N*-dimethylacrylamide (DMA) and *N*-(2-hydroxypropyl) methacrylamide (HPMA), as well as select examples of statistical copolymers with *N*-acryloxysuccinimide (NAS) were prepared with well-defined molecular characteristics employing a series of new RAFT chain transfer agents containing 1−4 hydrophobic functional groups in the R fragment based on pyrene, cholesterol, or octadecane, resulting in hydrophilic homopolymers containing between only 6−23 wt % hydrophobic end groups. PolyDMA (PDMA) and polyHPMA (PHPMA) homopolymers, of varying molar masses, with either bis pyrenyl or cholesteryl end groups self-assembled in aqueous media forming spherical vesicles with sizes in the range of several hundred nm up to ca. one micrometer. Lower molar mass PDMA−NAS copolymers with two cholesteryl end-groups at the ω-termini assemble to give clear tubular vesicles, whereas such copolymers of a higher molar mass preferentially form spherical polymersomes. The presence of two spatially close rigid rings at the ω-terminus is shown to be crucial in vesicle formation since a PDMA homopolymer with two octadecyl ω-end-groups self-assembles to yield polymeric micelles with an average hydrodynamic diameter of ~20 nm as determined by dynamic light scattering. The presence of a C16 alkyl spacer in the R fragment in a novel dithioester CTA with two pyrenyl functional groups and its use in the polymerization of a PDMA homopolymer yields spherical polymersomes in water, in a similar manner to those formed using a CTA without a spacer, except there is no direct FE-SEM evidence of open-mouth species perhaps indicating that the added flexibility associated with the spacer groups helps facilitate full vesicle closure. The synthesis of a biodegradable bis-pyrenyl dithioester, containing disulfide bridges, facilitates the preparation of PDMA-based polymersomes capable of dithiothreitol-induced pyrene release as evidenced by fluorescence emission spectroscopy. The same biodegradable polymersomes are also shown to be able to sequester the hydrophilic model drug Rhodamine B whose controlled release is demonstrated to be dependent on the presence, or absence, of dithiothreitol as determined by UV−vis spectroscopy.

Introduction

Amphiphilic molecules, such as phospholipids, are well-known to undergo self-directed assembly in an aqueous environment forming lipid bilayers (commonly referred to as liposomes or lipid vesicles) and form the major component in cell membranes.[1−3] The primary driving force for self-organization in such systems is the hydrophobic effect[4] whereby minimization of unfavorable solute−solvent interactions between the alkyl chains and water is accomplished by the 'clustering' of the hydrophobic alkyl chains forming micelles, vesicles and other ordered mesophases. However, secondary forces such as H-bonding[5] or π-π interactions[6−8] can aid in the self-assembly and structuring process.[9] Polymeric vesicles (polymersomes)[10−14] can also be formed from synthetic amphiphilic block copolymers, with impressive chemical structure variation and "smart" properties possible,[15−26] but possess some distinct beneficial features when compared to liposomes including enhanced robustness and stability.[12] The formation of self-assembled structures from block copolymers is dependent on at least three key features as noted by Discher and Eisenberg,[10] namely the average molar mass, the mass or volume fraction, f, of each block, and the effective interaction energy between monomers in the blocks. Importantly, it has been consistently shown that the formation of polymersomes requires a phospholipid-like ratio of hydrophilic-to-hydrophobic species with $f_{\text{hydrophilic}} \approx 35 \pm 10\%$.

Herein, we report a novel and facile approach to prepare spherical and tubular polymeric-based vesicles, including an example of a biodegradable species, formed from the self-directed assembly of hydrophilic (co)polymers containing ***only*** hydrophobic ω-cholesteryl or pyrenyl end-groups preared via RAFT[27−31] radical polymerization employing a series of new dithioester-based chain transfer agents (CTAs). The presence of two spatially close rigid rings is demonstrated to be a crucial structural requirement for polymersome formation and is demonstrated to occur even in hydrophilic homopolymers with hydrophobic contents as low as 6 wt %.

Experimental Section

Materials and Reagents. 4,4′-Azobis(4-cyanovaleric acid) (ACVA, Fluka, 98%), diethanolamine (Aldrich, 99%), 2-mercaptothiazoline (Aldrich, 98%), *N*,*N*′-dicyclohexylcarbodiimide (DCC, Aldrich, 99%), 4-(dimethylamino)pyridine (DMAP, Aldrich, 99%), cholesterol (Aldrich, 95%), 1-pyrenebutyric acid (PyBA, Aldrich, 97%), 1-pyrenebutanol (Aldrich, 99%), 3,3′-dithiodipropionic acid (Aldrich, 99%), DL-dithiothreitol (DTT, Fluka, 99%), Rhodamine B (Aldrich, 99%), *N*-hydroxysuccinimide (NHS, Aldrich, 98%), acryloyl chloride (Aldrich, 97%), succinic anhydride (Lancaster, 99%), hexylamine (Aldrich, 99%), 1,16-hexadecanediol (Aldrich, 99%), and *N*-(2-hydroxypropyl) methacrylamide (HPMA,

*Authors to whom correspondence should be addressed. E-mail: (T.P.D.) t.davis@unsw.edu.au; (A.B.L.) a.lowe@unsw.edu.au.

© 2010 American Chemical Society

Published on Web 12/23/2010

Polysciences Inc., 97%) were used as received. *N,N*-dimethylacrylamide (DMA, Aldrich, 99%) was passed through a basic aluminum oxide column to remove inhibitor prior to use. 4-(Dimethylamino)-pyridinium-4-toluene sulfonate (DPTS) was prepared according to the procedure described in the literature.[32] *N*-Acryloxysuccinimide (NAS) was synthesized according to the literature procedure by the direct esterification of NHS and acryloyl chloride in the presence of triethylamine.[33] All other chemicals were used as received.

Synthesis of *N,N′*-Bis(2-(cholesteryl butyric-1-carbonyloxo)-ethyl)cyanopentanoic Amide Dithiobenzoate, CTA4. The RAFT CTAs **CTA4** and **CTA5** (Scheme S1 in Supporting Information), were prepared from the precursor dithioesters 4,4′-((((4-cyano-4-((phenylcarbonothioyl)thio)pentanoyl)azanediyl)bis(ethane-2,1-diyl))bis(oxy))bis(4-oxobutanoic acid) (**CTA3**) and 5-(bis(2-hydroxyethyl)amino)-2-cyano-5-oxopentan-2-yl benzodithioate (**CTA2**) respectively which were themselves prepared according to previously published procedures.[34,35]

Precursor **CTA3** (0.40 g, 0.706 mmol) and DCC (0.32 g, 1.55 mmol) were dissolved in dichloromethane (DCM, 6.0 mL). Cholesterol (1.08 g, 2.87 mmol) and DPTS (0.024 g, 0.078 mmol) dissolved in DCM (6.0 mL) were added slowly. The reaction mixture was warmed to 40 °C and stirred overnight. After removal of the undissolved solid, the solution was concentrated and purified by column chromatography on silica gel, eluting with *n*-hexane/ethyl acetate (1/1) (R_f = 0.8) to give the RAFT agent **CTA4** as a pink solid powder (0.52 g, 56.6% yield). ^{1}H NMR (300 MHz, $CDCl_3$): δ (ppm) 7.92 (d, 2H, phenyl group), 7.56 (t, 1H, phenyl group), 7.39 (t, 2H, phenyl group), 5.36 (d, 2H, protons on double bond of cholesterol), 4.59 (m, 2H, $CH_2COOC\mathbf{H}(CH_2)(CH_2)$), 4.26 (m, 4H, $CON(CH_2C\mathbf{H}_2OCO)_2$), 3.68 (t, 2H), 3.62 (t, 2H, $CON(C\mathbf{H}_2CH_2OCO)_2$), 2.76 (t, 2H, $(CN)C(CH_3)CH_2C\mathbf{H}_2CON$), 2.60 (m, 8H, $CH2OCOC\mathbf{H}_2C\mathbf{H}_2$-COOCH), 2.47−2.39 (m, 2H, $(CN)C(CH_3)C\mathbf{H}_2CH_2CON$), 2.30 (d, 4H, $CH_2COOCH(C\mathbf{H}_2)(CH_2)$), 1.97, 1.83, 1.56, 1.49, 1.32, 1.12, 0.92, 0.88, 0.87, 0.85, 0.67. ESI MS: 1327.10 (MNa^+).

Synthesis of *N,N′*-Bis(2-(1-pyrenebutyrate)ethyl)cyanopentanoic Amide Dithiobenzoate, CTA5. Precursor **CTA2** (0.401 g, 1.07 mmol) and DCC (0.606 g, 2.94 mmol) were dissolved in tetrahydrofuran (THF, 6 mL). 1-Pyrenebutyric acid (0.77 g, 2.68 mmol) and DPTS (0.046 g, 0.146 mmol), dissolved in THF (6 mL), were added slowly. The reaction mixture was stirred overnight at room temperature. After removal of the undissolved solid the solution was concentrated and purified by column chromatography on silica gel, eluting with *n*-hexane/ethyl acetate (2/1) (R_f = 0.5) to give the RAFT agent **CTA5** as a pink solid powder (0.70 g, 72.4% yield). ^{1}H NMR (300 MHz, $CDCl_3$): δ (ppm) 8.29−7.90, (m, 18H, pyrenyl group), 7.81 (d, 2H, phenyl group), 7.48 (t, 1H, phenyl group), 7.30 (t, 2H, phenyl group), 4.21, 4.11 (m, 4H, $N(CH_2C\mathbf{H}_2OCO)_2$), 3.53 (m, 4H, $N(C\mathbf{H}_2CH_2OCO)_2$), 3.34 (m, 4H,$CH_2CH_2C\mathbf{H}_2$−pyrene), 2.67 (t, 2H, $(CN)C(CH_3)CH_2$-$C\mathbf{H}_2CON$), 2.43 (t, 4H, $CH2OCOC\mathbf{H}_2CH_2CH_2$−pyrene), 2.40−2.31 (m, 2H, $(CN)C(CH_3)C\mathbf{H}_2CH_2CON$), 2.14 (m, 4H, $CH_2C\mathbf{H}_2$-CH_2−pyrene), 1.78 (s, 3H, $(C\mathbf{H}_3)C(CN)S$). ^{13}C NMR (75 MHz, $CDCl_3$): 222.4 (Ph**C**=S), 173.4 (**C**=O), 144.4, 135.3, 132.9, 131.3, 130.75, 129.9, 128.7, 128.5, 127.4, 127.3, 126.7, 126.6, 125.8, 125.0, 124.9, 124.8, 123.1, 118.6, 63.0, 45.9, 38.9, 33.9, 33.5, 32.6, 31.7, 26.5, 24.1. UV−vis absorption: 267, 278, 314, 328, 344 nm. ESI MS: 930.23 (MNa^+).

Synthesis of O,O′-(((4-Cyano-4-((phenylcarbonothioyl)thio)-pentanoyl)azanediyl)bis(ethane-2,1-diyl)) bis(((4-(pyren-1-yl)-butanoyl)oxy)hexadecyl) Disuccinate, CTA6. CTA6 was prepared via a two step procedure as follows (see Scheme S2 in Supporting Information).

Initially, 16-hydroxyhexadecyl(4-pyren-1-yl) butanoate was prepared via the reaction of PyBA with 1,16-hexadecanediol: 1,16-hexadecanediol (0.91 g, 3.56 mmol) and DCC (0.53 g, 2.58 mmol) were dissolved in THF (8.0 mL). In a separate flask, PyBA (0.62 g, 2.15 mmol) and DMAP (0.013 g, 0.11 mmol) were dissolved in THF (8.0 mL) and added to the above solution. The reaction mixture was left to stir overnight at room temperature. After removal of the undissolved solid, the solution was concentrated and the product, 16-hydroxyhexadecyl(4-pyren-1-yl) butanoate, purified by column chromatography on silica gel, eluting with DCM (R_f = 0.3) to give the target compound (0.41 g, 36.1% yield). ^{1}H NMR (300 MHz, $CDCl_3$): δ (ppm) 8.32−7.80, (m, 9H, pyrenyl group), 4.10, (t, 2H, $CH_2C\mathbf{H}_2OCO$), 3.62 (q, 2H, $HOC\mathbf{H}_2(CH_2)_{14}CH_2OCO$), 3.39 (t, 2H,$CH_2CH_2$-$C\mathbf{H}_2$−pyrene), 2.46 (t, 2H, $CH_2OCOC\mathbf{H}_2CH_2CH_2$−pyrene), 2.22 (m, 2H, $CH_2C\mathbf{H}_2CH_2$−pyrene), 1.58 (m, 4H), 1.24 (m, 24H). ESI MS: 551.12 (MNa^+).

Subsequently, 16-hydroxyhexadecyl(4-pyren-1-yl)butanoate (0.36 g, 0.68 mmol) and DCC (0.13 g, 0.62 mmol) were dissolved in DCM (3.0 mL). In a separate flask, **CTA3** (0.16 g, 0.29 mmol) and DPTS (0.01 g, 0.039 mmol) were dissolved in DCM (3.0 mL) and were added to the above solution. The reaction mixture was stirred overnight at room temperature. After removal of the undissolved solid, the solution was concentrated and the target product purified by column chromatography on silica gel, eluting with *n*-hexane/ethyl acetate (2/1) (R_f = 0.25) to give the RAFT agent **CTA6** as a pink solid (0.34 g, 74.1% yield). ^{1}H NMR (300 MHz, $CDCl_3$): δ (ppm) 8.29−7.90, (m, 18H, pyrenyl group), 7.81 (d, 2H, phenyl group), 7.48 (t, 1H, phenyl group), 7.30 (t, 2H, phenyl group), 4.25 (q, 4H), 4.11 (m, 8H), 3.59 (m, 4H), 3.38 (m, 4H), 2.72 (t, 2H), 2.60 (m, 9H), 2.45 (t, 5H), 2.22 (m, 4H), 1.96 (s, 3H), 1.58 (m, 8H), 1.24 (m, 48H). ESI MS: 1612.3 (MNa^+).

Synthesis of 2-(4-Cyano-4-((phenylcarbonothioyl)thio)pentanamido)ethyl 4-(Pyren-1-yl) Butanoate, CTA7. For the general scheme see Scheme S3 in the Supporting Information.

2-Cyano-5-((2-hydroxyethyl)amino)-5-oxopentan-2-yl benzodithioate, was prepared from the reaction of 2-cyano-5-oxo-5-(2-thioxothiazolidin-3-yl)pentan-2-yl benzodithioate with 2-aminoethanol as follows: Aminoethanol (0.092 g, 1.51 mmol) dissolved in THF (2 mL) was added slowly to 2-cyano-5-oxo-5-(2-thioxothiazolidin-3-yl)pentan-2-yl benzodithioate (0.57 g, 1.52 mmol) also dissolved in THF (2 mL). The reaction mixture was stirred overnight. The mixture was concentrated and purified by column chromatography on silica gel, eluting with gradient DCM/methanol (40/0−40/1) to give the target compound as a pink oil (0.42 g, 86.8% yield). ^{1}H NMR (300 MHz, $CDCl_3$): δ (ppm) 7.92 (d, 2H, phenyl group), 7.56 (t, 1H, phenyl group), 7.40 (t, 2H, phenyl group), 5.81 (t, 1H,$CH_2CO\mathbf{NH}CH_2$), 3.49 (m, 4H, $NHC\mathbf{H}_2CH_2OH$), 1.97 (s, 3H, $(C\mathbf{H}_3)C(CN)S$). ^{13}C NMR (75 MHz, $CDCl_3$): δ (ppm) 222.3 (Ph**C**=S), 172.51 (**C**=O), 144.1, 132.8, 128.4, 126.3, 118.6 (**C**N), 65.3 ($NHCH_2\mathbf{C}H_2OH$), 61.8, 45.8, 34.1, 27.5, 24.1. FT-IR: 3315−3100 (O−H and N−H), 1679 (C=O), 1568 (N−H), 1512 (N−C), 1160 (PhC=S). ESI MS: 344.90 (MNa^+).

2-Cyano-5-((2-hydroxyethyl)amino)-5-oxopentan-2-yl benzodithioate (0.2 g, 0.62 mmol) and DCC (0.18 g, 0.85 mmol) were dissolved in THF (3 mL). PyBA (0.22 g, 0.78 mmol) and DMAP (0.005 g, 0.04 mmol), dissolved in THF (3 mL), were added into the above solution. The reaction mixture was stirred overnight at room temperature. After removal of the undissolved solid, the solution was concentrated and purified by column chromatography on silica gel, eluting with *n*-hexane/ethyl acetate (2/1) (R_f = 0.4) to give the RAFT agent **CTA7** as a pink powder (0.31 g, 84.3% yield). ^{1}H NMR (300 MHz, $CDCl_3$): δ (ppm) 8.32−7.80, (m, 9H, pyrenyl group), 7.96 (d, 2H, phenyl group), 7.53 (t, 1H, phenyl group), 7.36 (t, 2H, phenyl group), 5.81 ((t, 1H,$CH_2CO\mathbf{NH}CH_2$), 4.17, (t, 2H, $NHCH_2C\mathbf{H}_2OCO$), 3.53 (m, 2H, $NHC\mathbf{H}_2CH_2OCO$), 3.34 (t, 2H,$CH_2CH_2C\mathbf{H}_2$−pyrene), 2.67 (t, 2H, $(CN)C(CH_3)CH_2C\mathbf{H}_2CON$), 2.41 (t, 2H, $CH2OCOC\mathbf{H}_2CH_2CH_2$−pyrene), 2.40−2.31 (m, 2H, $(CN)C(CH_3)$-$C\mathbf{H}_2CH_2CON$), 2.21 (m, 2H, $CH_2C\mathbf{H}_2CH_2$−pyrene), 1.86 (s, 3H, $(C\mathbf{H}_3)C(CN)S$). ^{13}C NMR (75 MHz, $CDCl_3$): 222.4 (Ph**C**=S), 173.4 (**C**=O), 144.4, 135.3, 132.9, 131.3, 130.75, 129.9, 128.7, 128.5, 127.4, 127.3, 126.7, 126.6, 125.8, 125.0, 124.9, 124.8, 123.1, 118.6, 63.0, 45.9, 38.9, 33.9, 33.5, 32.6, 31.7, 26.5, 24.1. UV−vis absorption: 267, 278, 314, 328, 344 nm. ESI MS: 615.33 (MNa^+).

Synthesis of *O,O′*-(((4-Cyano-4-((phenylcarbonothioyl)thio)-pentanoyl)azanediyl)bis(ethane-2,1-diyl)) Dioctadecyl Disuccinate, CTA8. For the general scheme, see Scheme S3 in the Supporting Information.

Precursor **CTA3** (0.2 g, 0.35 mmol) and DCC (0.16 g, 0.76 mmol) were dissolved in DCM (3 mL). 1-Octadecanol (0.23 g, 0.85 mmol) and DPTS (0.01 g, 0.039 mmol) dissolved in DCM (3 mL) were added into the above solution, and the reaction mixture stirred overnight at 40 °C. After removal of the undissolved solid, the filtrate was concentrated and purified by column chromatography on silica gel, eluting with *n*-hexane/ethyl acetate (2/1) (R_f = 0.4) to give the RAFT agent **CTA8** as a pink oil (0.26 g, 68.8% yield). ^{1}H NMR (300 MHz, $CDCl_3$): δ (ppm) 7.91 (d, 2H, phenyl group), 7.56 (t, 1H, phenyl group), 7.39 (t, 2H, phenyl group), 4.20 (m, 4H, N(CH_2-*C*$\mathbf{H}_2$OCO)$_2$), 4.08 (m, 4H, COO*C*$\mathbf{H}_2$(CH_2)$_{16}$), 3.68, 3.62 (doble t, 4H, N(*C*$\mathbf{H}_2$$CH_2$OCO)$_2$), 2.78 (m, 2H, (CN)C-($CH_3$)$CH_2$-*C*$\mathbf{H}_2$CON), 2.61 (m, 9H, (CN)C(CH_3)-*C*$\mathbf{H}_2$$CH_2$CON, OCO*C*$\mathbf{H}_2$-*C*$\mathbf{H}_2COOCH_2$), 2.47 (m, 1H, CN)C($CH_3$)-*C*$\mathbf{H}_2$$CH_2$-CON), 1.97 (s, 3H, (*C*$\mathbf{H}_3$)C(CN)S), 1.25 (m, 64H, COOCH_2-(*C*$\mathbf{H}_2$)$_{16}$$CH_3$), 0.88 (m, 6H, COO$CH_2$($CH_2$)$_{16}$-*C*$\mathbf{H}_3$). ESI MS: 1094.32 ($MNa^+$).

Synthesis of Four-Functional Pyrene Dendritic Wedge Dithibenzoate (CTA9). The target CTA was prepared via a multistep procedure as described below.

Precursors ((4-cyano-4-((phenylcarbonothioyl)thio)pentanoyl)-azanediyl)bis(ethane-2,1-diyl) bis(4-oxo-4-(2-thioxothiazolidin-3-yl)butanoate) (**1**) and ((4-cyano-4-((phenylcarbonothioyl)thio)-pentanoyl)-azanediyl)bis(ethane-2,1-diyl) bis(4-(bis(2-hydroxyethyl)-amino)-4-oxobutanoate) (**2**) were synthesized by similar procedures as previously reported (Scheme S4 in Supporting Information).[34,35] Precursor **1**: ^{1}H NMR (300 MHz, $CDCl_3$): δ (ppm) 7.89 (d, 2H, phenyl group), 7.56 (t, 1H, phenyl group), 7.39 (t, 2H, phenyl group), 4.57 (t, 4H, N*C*$\mathbf{H}_2$$CH_2$S), 4.28 (q, 4H, NCH_2-*C*$\mathbf{H}_2$OCO), 3.70−3.65 (m, 4H, N*C*$\mathbf{H}_2$$CH_2$OCO), 3.52 (m, 4H, OCOCH*C*$\mathbf{H}_2$CON), 3.28 (t, 4H, NCH_2-*C*$\mathbf{H}_2$S), 2.78−2.40 (m, 12H), 1.95 (s, 3H, (*C*$\mathbf{H}_3$)C(CN)S). ^{13}C NMR (75 MHz, $CDCl_3$): δ (ppm) 222.5 (Ph*C*═S), 201.6 (N*C*═S), 172.3 (*C*═O), 144.5, 132.9, 128.5, 126.6, 118.6 (*C*N), 62.4, 61.8, 55.9, 53.3, 51.9, 47.3, 46.0, 45.4, 34.2, 28.8, 24.3. IR:1696 (C═O), 1166 (PhC═S), 1046 cm^{-1} (NC═S). ESI MS: 791.3 (MNa^+). Precursor **2**: ^{1}H NMR (300 MHz, $CDCl_3$): δ (ppm) 7.89 (d, 2H, phenyl group), 7.56 (t, 1H, phenyl group), 7.39 (t, 2H, phenyl group), 4.28 (q, 4H, NCH_2-*C*$\mathbf{H}_2$OCO), 3.78 (m, 8H, NCH_2-*C*$\mathbf{H}_2$OH), 3.70−3.61 (m, 4H, N*C*$\mathbf{H}_2$$CH_2$OCO), 3.50 (m, 8H, N*C*$\mathbf{H}_2$$CH_2$OH), 2.78−2.40 (m, 12H), 1.95 (s, 3H, (*C*$\mathbf{H}_3$)C(CN)S). ^{13}C NMR (75 MHz, $CDCl_3$): δ (ppm) 222.5 (Ph*C*═S), 201.6 (N*C*═S), 172.3 (*C*═O), 144.5, 132.9, 128.5, 126.6, 118.6 (*C*N), 62.4, 61.8, 60.1, 53.4, 52.1, 47.5, 46.1, 45.7, 34.1, 28.9, 24.1. IR: 1696 (C═O), 1166 (PhC═S). ESI MS: 763.51 (MNa^+).

Precursor **2** (0.07 g, 0.094 mmol) and DCC (0.196 g, 0.95 mmol) were dissolved in THF (2.0 mL). 1-Pyrenebutyric acid (0.27 g, 0.95 mmol) and DMAP (0.006 g, 0.05 mmol) were dissolved in THF (3.0 mL) and the solution added slowly to the solution of **2** and DCC. The reaction mixture was stirred for 2 days at room temperature. After removal of the undissolved solid, the solution was concentrated and the product purified by column chromatography on silica gel, eluting with gradient DCM/MeOH (40/0−40/1) to give the RAFT agent **CTA9** as a pink powder (0.15 g, 75.6% yield). ^{1}H NMR (300 MHz, $CDCl_3$): δ (ppm) 8.29−7.90, (m, 36H, pyrenyl group), 7.81 (d, 2H, phenyl group), 7.48 (t, 1H, phenyl group), 7.30 (t, 2H, phenyl group), 4.18 (m, 12H), 3.52 (m, 12H), 3.31 (m, 8H, CH_2CH_2-*C*$\mathbf{H}_2$−pyrene), 2.80−2.30 (m, 20H), 2.15 (m, 8H, CH_2-*C*$\mathbf{H}_2$$CH_2$−pyrene), 1.88 (s, 3H, (*C*$\mathbf{H}_3$)C(CN)S). UV−vis absorption: 267, 278, 314, 328, 344 nm. ESI MS: 1845.2 (MNa^+).

Synthesis of ((4-Cyano-4-((phenylcarbonothioyl)thio)pentanoyl)azanediyl)bis(ethane-2,1-diyl) Bis(3-((3-oxo-3-(4-(pyren-1-yl)butoxy)propyl)disulfanyl)propanoate) (CTA10). The target compound was prepared as follows (see Scheme S5 in the Supporting Information):

3,3′-Dithiodipropionic acid (1.15 g, 5.47 mmol) and DCC (0.56 g, 2.73 mmol) were dissolved in THF (5.0 mL). 1-Pyrenebutanol (0.50 g, 1.82 mmol) and DMAP (0.017 g, 0.14 mmol), dissolved in THF (5.0 mL), was mixed with the above solution, and the reaction solution stirred for 20 h at room temperature. After removal of the undissolved solid, the solution was concentrated and the product purified by column chromatography on silica gel, eluting with gradient solvent DCM/methanol (40/0−40/1) to give 3-((3-oxo-3-(4-(pyren-1-yl)butoxy)propyl)disulfanyl)-propanoic acid (0.75 g, 81.3% yield). ^{1}H NMR (300 MHz, DMSO-d_6): δ (ppm) 8.34−7.85, (m, 9H, pyrenyl group), 4.10, (t, 2H, SSCH_2-*C*$\mathbf{H}_2$COO), 3.34 (t, 2H, CH_2CH_2-*C*$\mathbf{H}_2$-pyrene), 2.89−2.80 (m, 4H, HOOCCH_2-*C*$\mathbf{H}_2$SS*C*$\mathbf{H}_2$$CH_2$COO), 2.67 (t, 2H, HOOCC$H_2$-$CH_2SSCH_2$-*C*$\mathbf{H}_2$COO), 2.59 (t, 2H, HOOC*C*$\mathbf{H}_2$$CH_2SSCH_2$-$CH_2$COO), 1.90−1.67 (m, 4H, CH_2-*C*$\mathbf{H}_2$-*C*$\mathbf{H}_2$$CH_2$−pyrene).

The above compound (0.69 g, 1.45 mmol) and DCC (0.336 g, 1.63 mmol) were dissolved in THF (5.0 mL). **CTA2** (0.202 g, 0.55 mmol) and DMAP (0.01 g, 0.081 mmol) dissolved in THF (3.0 mL) were then added into the above solution. The reaction mixture was stirred for 24 h at room temperature. After removal of the undissolved solid, the filtration was concentrated and purified by column chromatography on silica gel, eluting with gradient solvent *n*-hexane/ethyl acetate (2/1−2/4) to give the RAFT agent **CTA10** as a pink powder (0.44 g, 63.6% yield). ^{1}H NMR (300 MHz, $CDCl_3$): δ (ppm) 8.30−7.88, (m, 18H, pyrenyl group), 7.84 (d, 2H, phenyl group), 7.50 (t, 1H, phenyl group), 7.33 (t, 2H, phenyl group), 4.16 (q, 8H), 3.55 (m, 4H), 3.34 (m, 4H), 2.84 (m, 8H), 2.70 (m, 12H), 2.45 and 2.42 (m, 2H), 1.96 (s, 3H), 1.90 (m, 4H), 1.77 (m, 4H). ESI MS: 1285.48 (MNa^+).

Polymer Synthesis. Detailed below are the general procedures for (co)polymer synthesis. See Figure S1 in Supporting Information for general structures.

*Preparation of Bis-ω-pyrenyl End-Functional Homopolymers of N,N-Dimethylacrylamide, **PDMA-diPy**.* **CTA5** (36 mg, 0.040 mmol), DMA (0.39 g, 3.97 mmol), and the initiator ACVA (2.2 mg, 0.0079 mmol) were dissolved in 1,4-dioxane (2.0 mL). The solution was subsequently purged with nitrogen for 30 min. The flask was then immersed in a preheated oil bath set to 70 °C and polymerization allowed to proceed for 6 h. The polymerization was halted by quenching with liquid nitrogen. An aliquot was withdrawn from the reaction solution to determine conversion by ^{1}H NMR spectroscopy (∼64%). The polymer was purified by dialysis against methanol for 24 h with 2−3 changes of solvent (membrane MWCO: 3500), isolated by removal of MeOH in vacuo and subjected to GPC and NMR measurements for molecular weight. The molecular weight determination measured by ^{1}H NMR was calculated by comparing the integration of the peak of the pyrene proton at 8.26 ppm or $-CH_2-$ close to ester bonds at 4.12 ppm to that of repeat unit of polymer at 2.20−3.10 ppm. This polymer was designated **PDMA-diPy 6K**: $M_{n,GPC}$ = 7800 Da, $M_{n,NMR}$ = 5900 Da, PDI = 1.08 (The number of DMA repeating unit n_{DMA} is 50). A second PDMA homopolymer with higher molecular weight was synthesized by a similar procedure, and denoted **PDMA-diPy 13K**: $M_{n,GPC}$ = 17200 Da, $M_{n,NMR}$ = 13500 Da, PDI = 1.11 (The number of DMA repeating unit n_{DMA} is 128).

*Synthesis of Bis-ω-cholesteroyl End-Functional Homopolymers of N,N-Dimethylacrylamide, **PDMA-diChol**.* **CTA4** (42.0 mg, 0.032 mmol), DMA (0.32 g, 3.22 mmol), and initiator ACVA (1.8 mg, 0.0064 mmol) were dissolved in 1,4-dioxane (2.0 mL). The mixture was then purged with nitrogen for 30 min. The flask was then immersed in a preheated oil bath set to 70 °C and polymerization allowed to proceed for 4 h. The polymerization was halted by quenching with liquid nitrogen. An aliquot was withdrawn from the reaction solution to determine conversion by ^{1}H NMR spectroscopy (∼55%). The polymer was purified by dialysis against methanol for 24 h with 2−3 changes of solvent (membrane MWCO: 3500), isolated by removal of MeOH in vacuo and subjected to GPC and NMR analysis for molecular weight determination. The molecular weight measured by ^{1}H NMR was

calculated by comparing the integration of the peak of the cholesterol proton at 5.40 ppm or $-CH_2-$ close to ester bonds at 4.12 ppm to that of repeat unit of polymer at 2.20−3.10 ppm. This polymer was designated as **PDMA-diChol 5K**: $M_{n,GPC}$ = 5920 Da, $M_{n,NMR}$ = 5060 Da, and PDI = 1.07 (n_{DMA} = 38). A second polymer with higher molecular weight was also prepared by a similar procedure and designated **PDMA-diChol 11K**: $M_{n,GPC}$ = 13100 Da, $M_{n,NMR}$ = 10500 Da, and PDI = 1.08 (n_{DMA} = 93).

*Synthesis of Bis-ω-cholesteroyl End-Functional Homopolymers of 2-Hydroxypropyl Methacrylamide, **PHPMA-diChol**.* **CTA4** (40 mg, 0.031 mmol), HPMA (0.31 g, 2.09 mmol), and initiator ACVA (2.2 mg, 0.0077 mmol) were dissolved in *N*,*N*-dimethylacetamide (DMAc, 3.0 mL). The mixture was purged with nitrogen for 30 min. The polymerization was carried out at 70 °C for 4 h and quenched by liquid nitrogen. An aliquot mixture was withdrawn to measure conversion by ^{1}H NMR (∼67%). The polymer was purified by dialysis against methanol for 24 h with 2−3 changes of solvent (membrane MWCO: 3500), isolated by removal of MeOH in vacuo and subjected to GPC and NMR analysis for molecular weight determination. The molecular weight measured by ^{1}H NMR was calculated by comparing the integration of the peak of the cholesterol proton at 5.48 ppm to that of repeat unit of polymer at 3.62 ppm. The polymer was designated **PHPMA-diChol 6K**: $M_{n,GPC}$ = 9800 Da, $M_{n,NMR}$ = 6220 Da, and PDI = 1.12 (n_{HPMA} = 34). A second polymer with higher molecular weight was synthesized by similar procedure, and denoted **PHPMA-diChol 14K**: $M_{n,GPC}$ = 23400 Da, $M_{n,NMR}$ = 13900 Da, and PDI = 1.19 (n_{HPMA} = 88).

*Synthesis of Bis-ω-pyrenyl End-Functional Copolymers, **PDN-diPy**.* **CTA5** (40.4 mg, 0.045 mmol), DMA (0.535 g, 5.40 mmol), NAS (0.18 g, 1.08 mmol), and azo initiator ACVA (2.5 mg, 0.0090 mmol) were dissolved in 1,4-dioxane (4.0 mL), and the mixture was purged with nitrogen for 30 min. The solution was immersed in a preheated oil bath at 60 °C and polymerization allowed to proceed for 4 h prior to being quenched with liquid nitrogen. The polymer was purified by dialysis against methanol for 24 h with 2−3 changes of solvent (membrane MWCO: 3500), isolated by removal of MeOH in vacuo and subjected to analysis by GPC and NMR. To determine the number of NAS repeat units the random copolymer (5.7 mg) was dissolved in $CDCl_3$ (1.2 mL) followed by addition of hexylamine (1.5 mg). After 2 h, the solution was examined by ^{1}H NMR spectroscopy to determine the number of NAS repeating units by comparing the integration of the peak of the amide proton at 7.1−6.0 ppm to that of two standard pyrene protons at 8.26 ppm. The number of DMA repeating units can be calculated by comparing the integration of signal at 3.25−2.2 ppm due to all protons in DMA and NAS units except the $-CH_2-$ on the backbone and that of two pyrene protons at 8.26 ppm. This polymer was designated as **PDN-diPy 5K**: $M_{n,GPC}$ = 7060 Da, $M_{n,NMR}$ = 5130 Da, and PDI = 1.16 (n_{DMA} = 29, n_{NAS} = 8). Two additional statistical copolymers with higher molecular weight were synthesized by a similar procedure and are denoted **PDN-diPy 18K**: $M_{n,GPC}$ = 21750 Da, $M_{n,NMR}$ = 17570 Da, and PDI = 1.09 (n_{DMA} = 115, n_{NAS} = 31). **PDN-diPy 36K**: $M_{n,GPC}$ = 41640 Da, $M_{n,NMR}$ = 36500 Da, and PDI = 1.14 (n_{DMA} = 240, n_{NAS} = 69).

*Synthesis of Bis-ω-cholesteryl End-Functional Copolymers, **PDN-diChol**.* **CTA4** (40.1 mg, 0.031 mmol), DMA (0.304 g, 3.07 mmol), NAS (0.104 g, 0.61 mmol), and initiator ACVA (1.7 mg, 0.0061 mmol) were dissolved in 1,4-dioxane (2.0 mL), and the mixture was purged with nitrogen for 30 min. The solution was immersed in a preheated oil bath at 60 °C and polymerization allowed to proceed for 5 h prior to being quenched with liquid nitrogen The polymer was purified by dialysis against methanol for 24 h with 2−3 changes of solvent (membrane MWCO: 2000), isolated by removal of MeOH in vacuo, and then subjected to GPC and NMR measurement. The number of DMA and NAS repeating units were measured and calculated by similar procedure as described for **PDN-diPy**, using the standard peak signal associated with the two double bond protons in cholesterol at 5.37 ppm. This polymer was designated as **PDN-diChol 7K**: $M_{n,GPC}$ = 6980 Da, $M_{n,NMR}$ = 6090 Da, and PDI = 1.11 (n_{DMA} = 33, n_{NAS} = 9). Two additional copolymers polymers with higher molecular weight were synthesized by a similar procedure and designated as **PDN-diChol 13K**: $M_{n,GPC}$ = 16800 Da, $M_{n,NMR}$ = 12900 Da, and PDI = 1.09 (n_{DMA} = 82, n_{NAS} = 21). **PDN-diChol 36K**: $M_{n,GPC}$ = 43100 Da, $M_{n,NMR}$ = 35200 Da, and PDI = 1.15 (n_{DMA} = 240, n_{NAS} = 62).

*Synthesis of Bis-ω-octadecyl End-Functional Homopolymer, **PDMA-diODE**.* **CTA8** (32 mg, 0.028 mmol), DMA (0.35 g, 3.56 mmol), and initiator ACVA (1.7 mg, 0.0059 mmol) were dissolved in 1,4-dioxane (4.0 mL) and the mixture was purged with nitrogen for 30 min. The solution was immersed in a preheated oil bath at 70 °C and polymerization allowed to proceed for 3.5 h prior to being quenched with liquid nitrogen The polymer was purified by dialysis against methanol for 24 h with 2−3 changes of solvent (membrane MWCO: 3500), isolated by removal of MeOH in vacuo, and subjected to analysis by GPC and NMR. This polymer was denoted as **PDMA-diODE 7K**: $M_{n,GPC}$ = 9580 Da, $M_{n,NMR}$ = 6620 Da, and PDI = 1.06 (n_{DMA} = 56).

*Synthesis of Monopyrenyl End-Functional DMA Homopolymer, **PDMA-monoPy**.* **CTA7** (39.0 mg, 0.066 mmol), DMA (0.78 g, 7.89 mmol), and initiator ACVA (3.7 mg, 0.0132 mmol) were dissolved in 1,4-dioxane (5.0 mL), and the mixture was purged with nitrogen for 30 min. The polymerization was carried out at 70 °C for 5 h prior to quenching with liquid nitrogen. The polymer was purified by dialysis against methanol for 24 h with 2−3 changes of solvent (membrane MWCO: 3500), isolated by removal of MeOH in vacuo, and subjected to GPC and NMR analysis. This polymer is denoted as **PDMA-monoPy 7K**: $M_{n,GPC}$ = 11200 Da, $M_{n,NMR}$ = 7030 Da, and PDI = 1.06 (n_{DMA} = 67).

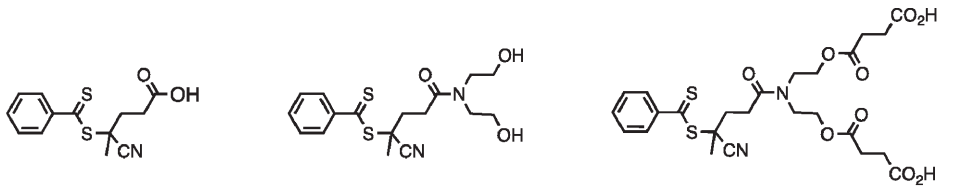
*Preparation of Bis-ω-pyrenyl End-Functional DMA Homopolymer with a C16 Spacer, **PDMA-diC$_{16}$Py**.* **CTA6** (50.0 mg, 0.031 mmol), DMA (0.63 g, 6.29 mmol), and initiator ACVA (1.8 mg, 0.0062 mmol) were dissolved in 1,4-dioxane (4.0 mL), and the mixture was purged with nitrogen for 30 min. The polymerization was carried out at 70 °C for 3 h and quenched by liquid nitrogen. The polymer was purified by dialysis against methanol for 24 h with 2−3 changes of solvent (membrane MWCO: 3500), isolated by removal of MeOH in vacuo, and analyzed by GPC and NMR. This polymer is designated as **PDMA-diC$_{16}$Py 10K**: $M_{n,GPC}$ = 13500 Da, $M_{n,NMR}$ = 9800 Da, and PDI = 1.12 (n_{DMA} = 83).

*Preparation of a Tetra-ω-pyrenyl End-Functional DMA Homopolymer, **PDMA-tetraPy**.* **CTA9** (40.0 mg, 0.022 mmol), DMA (0.35 g, 3.51 mmol), and initiator ACVA (1.2 mg, 0.0044 mmol) were dissolved in 1,4-dioxane (3.0 mL), and the mixture was purged with nitrogen for 30 min. The flask was immersed in a preheated oil bath at 70 °C and polymerization allowed to proceed for 6 h prior to being quenched by liquid nitrogen. The polymer was purified by dialysis against methanol for 24 h with 2−3 changes of solvent (membrane MWCO: 3500), isolated by removal of MeOH in vacuo, and analyzed by GPC and NMR. This polymer is denoted as **PDMA-tetraPy 13K**: $M_{n,GPC}$ = 12800 Da, $M_{n,NMR}$ = 13550 Da, and PDI = 1.15 (n_{DMA} = 116).

*Preparation of a Bis-ω-pyrenyl DMA Homopolymer Bearing Disulfide Linkages, **PDMA-diSSPy**.* **CTA10** (40.0 mg, 0.032 mmol), DMA (0.63 g, 6.32 mmol), and initiator ACVA (1.8 mg, 0.0063 mmol) were dissolved in 1,4-dioxane (2.0 mL), and the mixture was purged with nitrogen for 30 min. The flask was immersed in a preheated oil bath at 70 °C and polymerization allowed to proceed for 3 h prior to being quenched by liquid nitrogen. The polymer was purified by dialysis against methanol for 24 h with 2−3 changes of solvent (membrane MWCO: 3500), isolated by removal of MeOH in vacuo, and subjected to GPC and NMR analysis. This polymer is denoted as **PDMA-diSSPy 13K**: $M_{n,GPC}$ = 13700 Da, $M_{n,NMR}$ = 12800 Da, and PDI = 1.12 (n_{DMA} = 117).

Preparation and Characterization of Polymeric Self-Assemblies

Preparation and Morphological Characterization of Polymeric Aggregates. The end-functionalized polymers were first dissolved



4-cyanopentanoic acid dithiobenzoate (CPDB, **CTA1**)

5-(bis(2-hydroxyethyl)amino)-2-cyano-5-oxopentan-2-yl benzodithioate (**CTA2**)

4,4'-((((4-cyano-4-((phenylcarbonothioyl)thio)pentanoyl)azanediyl)bis(ethane-2,1-diyl))bis(oxy))bis(4-oxobutanoic acid) (**CTA3**)

Figure 1. Chemical structures of diacid and dialcohol functional precursor RAFT chain transfer agents employed in the preparation of cholesterol and pyrene-functional dithioesters.

in 1,4-dioxane (1 mL) at a concentration of 20 mg/mL. Samples were then filtered through a PTFE filter (pore size 0.45 μm). Subsequently, Milli-Q deionized water (3.0 mL) was added dropwise to the dioxane solution using a syringe pump at a rate of 1 mL/hour with gentle stirring. The solution was then dialyzed against water for 2 days to remove dioxane using Spectra/Por (Spectrum Laboratories Inc.) regenerated cellulose membrane with a molecular weight cutoff of 3500 Da. Morphological analyses of the polymer micellar suspensions were performed by FE-SEM.

Preparation of Samples for Field Emission Scanning Electron Microscopy. The obtained freshly prepared 5.0 mg/mL end-functionalized polymersome solution (1.0 mL) was freeze-dried to obtain a light solid powder. The powder was adhered on conductive double-sided carbon adhesive tape that was fixed on a metal stand. After coating with chromium, the sample was visualized using a Hitach S4500 field emission scanning electron microscope operating at an acceleration voltage of 15 kV.

Degradation of Polymeric Vesicles. The freshly prepared **PDMA-diSSPy** polymersome solution (1.0 mL, 5 mg/mL) was diluted to 2.0 mL (2.5 mg/mL) with Milli-Q deionized water. Dithiothreitol (DTT) (0.2 mg) was added into the above solution. The mole ratio of polymer and DTT was ~1 to 6. The fluorescence emission of the mixed solution was measured at predetermined time intervals. The degrees of degradation (%) were calculated by the following equation: Degradation percentage (%) = $(I_{480}(0)/I_{379}(0) - I_{480}(t)/I_{379}(t))/(I_{480}(0)/I_{379}(0)) \times 100$. $I_{480}(0)$, $I_{379}(0)$ were the starting emission intensities at 480 and 379 nm wavelength. $I_{480}(t)$, $I_{379}(t)$ were the emission intensities at 480 and 379 nm wavelength at the specific time intervals.

Model Drug Loading and Controlled Release. *Rhodamine B Loading into Polymer Vesicles*. The end-functional polymer **PDMA-diSSPy 13K** was first dissolved in 1,4-dioxane (1.0 mL at a concentration of 20.0 mg/mL). The sample was then filtered through a PTFE filter (pore size 0.45 μm). Milli-Q deionized water (1.0 mL) containing the hydrophilic model drug Rhodamine B (5.0 mg) was then added dropwise using syringe pump at a rate of 1.0 mL/hour with gentle stirring. Subsequently, an additional 2.0 mL of DI water was added dropwise into the vesicle/Rhodamine solution. After standing overnight, the final solution was dialyzed against water for 24 h to remove dioxane and any free Rhodamine B using dialysis membrane with a molecular weight cutoff of 3500 Da. Using the Beer−Lambert equation with the predetermined extinction coefficient of Rhodamine B (ε = 840 000 M^{-1} cm^{-1} in water) and the absorbance at 554 nm in the UV−vis spectrum, the amount of loaded Rhodamine B was measured, ultimately leading to a loading content into the polymersomes of 1.7% (0.017 mg Rhodamine B/mg polymer), and loading efficiency of 6.6%.

Controlled Release of Rhodamine B. Rhodamine B-containing vesicle solution (2.0 mL) was loaded into a dialysis membrane (MWCO 3500) and transferred to 300 mL of a DTT solution (0.2 mg/mL). An aliquot of the solution (25 μL) in the dialysis membrane was withdrawn, at varying time intervals, and diluted to 500 μL with deionized water for measurement in the UV−vis spectrophotometer. A control experiment was carried out without DTT in the dialysis solution.

Instrumentation. Gel permeation chromatography (GPC) was performed using *N*,*N*-dimethylacetamide (DMAc) (0.03% w/v LiBr, 0.05% BHT stabilizer) as the continuous phase at 50 °C and a flow rate of 1 mL min^{-1}. A Shimadzu modular system was employed comprising a DGU-12A solvent degasser, an LC-10AT pump, a CTO-10A column oven, and a RID-10A refractive index detector. The system was equipped with a Polymer Laboratories 5.0 mm bead-size guard column (50 × 7.8 mm^2) followed by four 300 × 7.8 mm^2 linear PL columns (10^5, 10^4, 10^3, and 500). Calibration was achieved using low polydispersity polystyrene standards ranging from 500 to 10^6 g mol^{-1}.

Nuclear magnetic resonance (NMR) spectroscopy was carried out on a Bruker DPX 300 spectrometer operating at 300.17 MHz for ^{1}H and 75.48 MHz for ^{13}C using $CDCl_3$ as solvents and tetramethylsilane (TMS) as a reference. Data were reported as follows: chemical shift (δ) measured in ppm downfield from TMS; multiplicity; proton count. Multiplicities were reported as singlet (s), broad single (bs), doublet (d), triplet (t), and multiplet (m).

Electrospray ionization mass spectra (ESI MS) were obtained using a Finnigan LCQ Deca mass spectrometer (Thermo Finnigan, San Jose, CA) equipped with an atmospheric pressure ionization source operating in the nebulizer-assisted electrospray mode. Positive ion spectra were obtained by direct infusion at a solvent flow rate of 3.0 μL min^{-1} and a spray voltage of 5 kV, with nitrogen as sheath gas. Xcalibur ver. 1.3 (Finnigan Co.) was used for spectral processing. UV−vis spectra were recorded on a Varian Cary 300scan spectroscope using wavelengths from 200 to 700 nm.

FT-IR spectra were obtained using a Bruker Spectrum BX FT-IR system using diffuse reflectance sampling accessories.

Dynamic light scattering (DLS) measurements were performed on a Malvern Instruments Zetasizer NanoZS equipped with a 4 mV He−Ne laser operationg at λ = 633 nm, an avalanche photodiode detector with high quantum efficiency, and an ALV/LSE-5003 multiple τ digital correlator electronics system with a measurement angle of 173°.

Fluorescence emission spectra were measured on a Perkin-Elmer LS-50B luminance spectrometer at an excitation wavelength of 347 nm. Pyrene preferred to stack under specific conditions to form an excimer giving 440−560 nm emission, whereas the monomer gave 370−430 nm emission. Fluorescence emission photos were taken under a 365 nm excitation UV lamp (SPECTROLINE MODEL CM-10) using an Olympus digital camera (Mju Tough 8010).

Results and Discussion

RAFT radical polymerization offers a convenient route to preparing end-functional polymers via a number of approaches[36] including the incorporation of specific desired functionality in either the Z or R groups of a given RAFT chain transfer agent

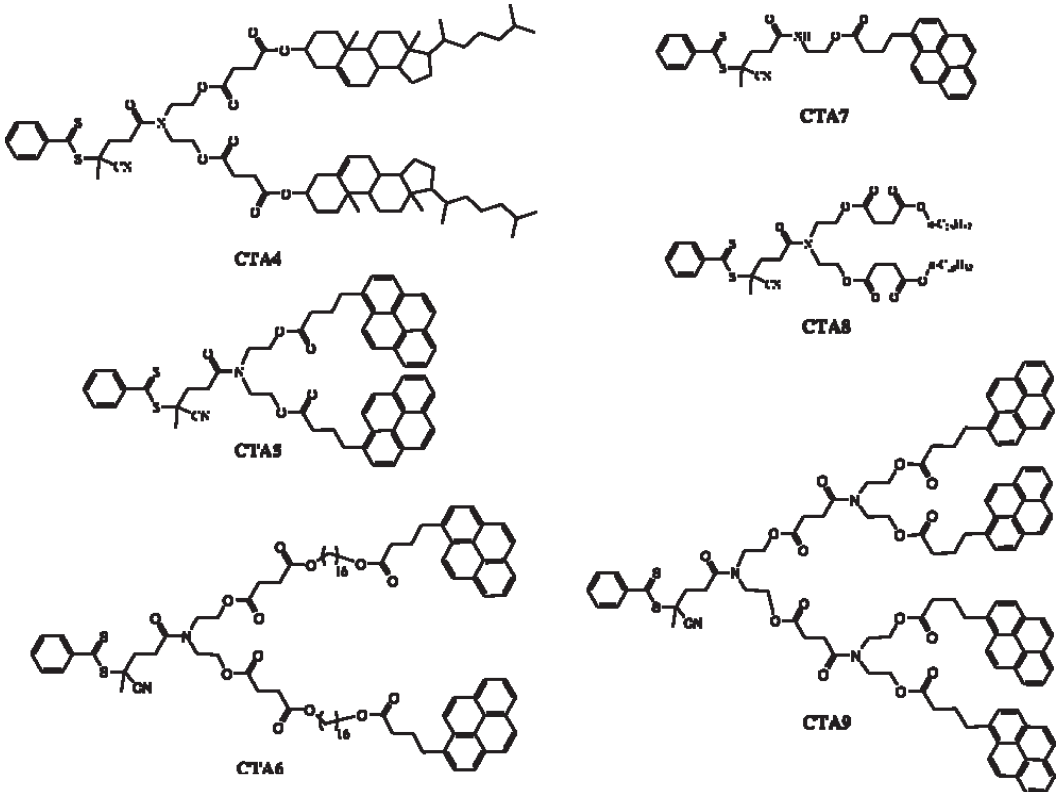


Figure 2. Chemical structure of mono-, bis-, and tetra-functional RAFT CTAs containing pyrenyl, cholesteryl, and octadecyl functionality in the R group used for (co)polymer synthesis.

(CTA), with modification of the R group being a more versatile approach. For example, 4-cyanopentanoic acid dithiobenzoate (**CTA1**, Figure 1), with the terminal acid functionality in the R-group, and readily obtained derivatives thereof, is an attractive substrate suitable for the introduction of a wide range of desired structural motifs. Employing this CTA as the parent substrate a range of dithioester-based RAFT CTAs, **CTA4−9**, were prepared incorporating between 1 and 4 desired functional species as part of the R-group, Figure 2. **CTA1−3** were prepared according to previously published procedures and served as the reactive precursors to the desired CTAs.[34,35]

The target CTAs, **CTA4−9** Figure 2, were prepared in high yield and purity as described in the Experimental Section. Each of these CTAs can serve as a convenient mediating agent for the introduction of cholsteryl, pyrenyl or octadecyl functional groups at the ω-chain end of RAFT-synthesized (co)polymers. The presence of 1−4 rigid ring structures at the ω-termini was hypothesized to result in novel aqueous solution properties. Indeed, the presence of functionality at chain termini, including at the α, ω, or α and ω chain ends is well-known to influence (co)polymer properties in solution and can affect, for example, LCST and aggregation behavior.[37−44]

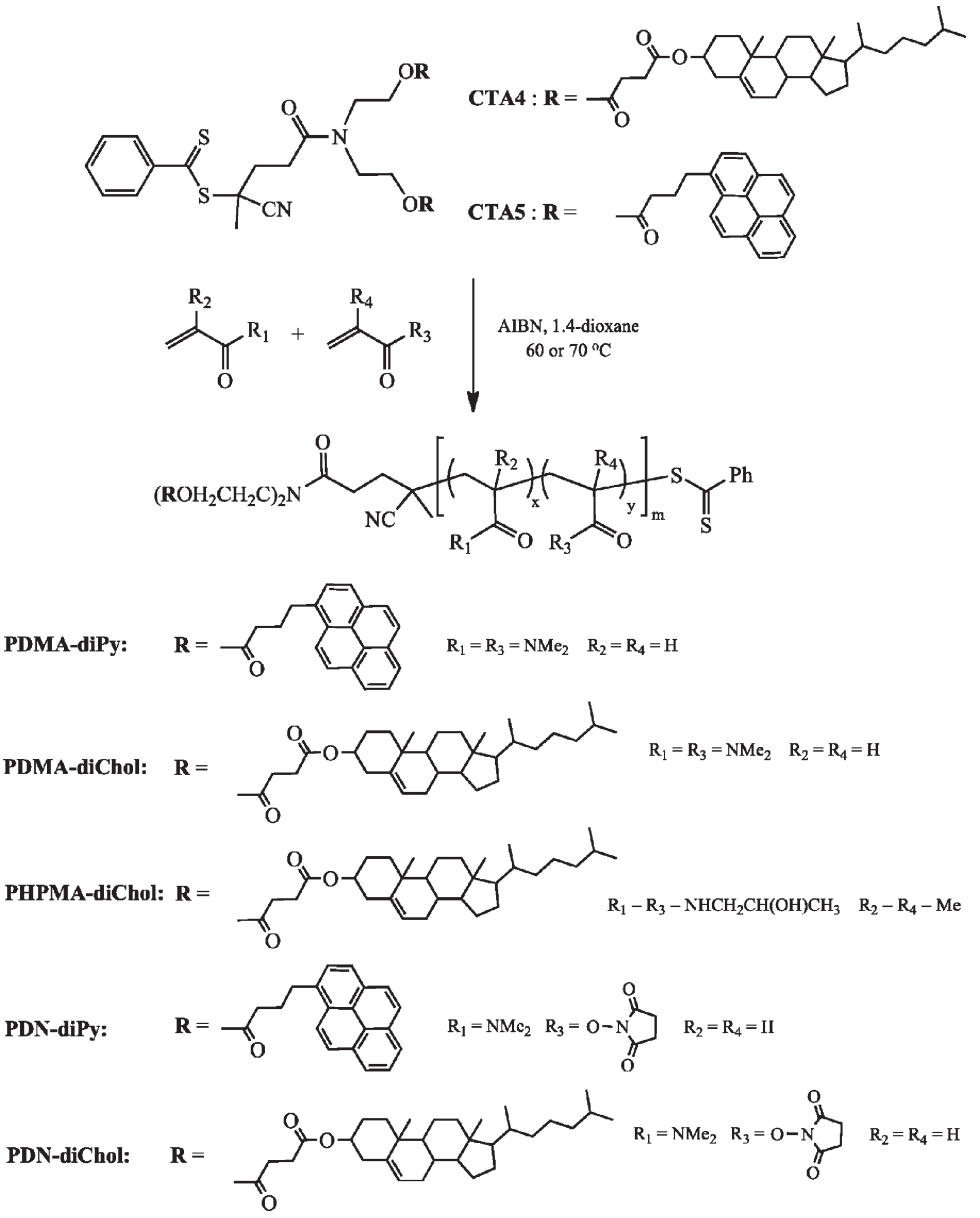
With the novel multifunctional CTAs in-hand a range of copolymers based on *N*,*N*-dimethylacrylamide (DMA) and 2-(hydroxy)propyl methacrylamide (HPMA) were prepared initially employing the bis-cholesteryl and pyrenyl RAFT agents **CTA4** and **CTA5** as outlined in Scheme 1.

The compositions, experimentally determined average molar masses, polydispersity indices (PDIs) and hydrophobic/hydrophilic ratios of the (co)polymers prepared and evaluated in this study are listed in Table 1.

Several points are worth noting. First, and consistent with previous reports on the application of RAFT radical polymerization, (co)polymers with variable molar masses and low PDIs are readily obtained with, for example, all measured PDIs being $\leq$1.19 and more typically $<$ 1.10.[37,45−50] In addition to the bis-ω-cholesteryl/pyrenyl functional PDMA and PHPMA homopolymers, examples of statistical copolymers of DMA with *N*-acryloxysuccinimide (NAS) bearing both pyrene and cholesterol end groups were also prepared. NAS is a commonly employed reactive monomer that readily facilitates post polymerization modification including, but not limited to, bioconjugation[51,52] and cross-linking.[53] Finally, it is highlighted that these (co)polymers have hydrophobic/hydrophilic ratios that are significantly lower than those typically associated with vesicle-forming materials, vide infra. With a range of amphiphilic (co)polymers of varying molar mass and chain end functionality in-hand the self-assembly of these novel materials in aqueous media was examined. Aggregation of these end-functional (co)polymers was induced as shown in Scheme 2. Self-assembly was promoted via the dropwise addition of water to 1,4-dioxane solutions (a nonselective solvent) of the amphiphilic (co)polymers followed by dialysis against water to remove 1,4-dioxane giving a final (co)polymer concentration of 5 g/L. Subsequently, the (co)polymer solutions were lyophilized prior to chromium coating and imaging via field-emission scanning electron microscopy (FE-SEM). Consider first **PDMA-diPy 6K**, **PDMA-dichol 5K**, and **PHPMA-dichol 6K** with hydrophobic/hydrophilic ratios of 13/87, 23/76, and 19/81 respectively, Figure 3. The FE-SEM images clearly show that these amphiphilic ***homopolymers*** undergo self-directed assembly forming essentially spherical particles with diameters in the range of $\sim$150 nm -1 μm. The presence of holes and fractured sections in a number of the particles (highlighted with arrows) clearly demonstrates the hollow nature of the particles and their vesicular structure.

Similar "open-mouth" vesicles were recently reported by Changez et al.[16] in their studies of the self-assembly of the amphiphilic homopolymer poly(2-(4-vinylphenyl)pyridine) and have also been documented for rod−coil and rod−rod block copolymers where the stiffness of the rod-block was assumed to

Scheme 1. Outline for the Preparation of DMA and HPMA-Based (Co)Polymers with RAFT Agents CTA4 and CTA5[a]



[a] **PDMA-diPy**: poly(*N*,*N*-dimethylacrylamide) with bis-ω-pyrenyl groups; **PDMA-diChol**: poly(*N*,*N*-dimethylacrylamide) with bis-ω- cholesteryl groups; **PHPMA-diChol**: poly(*N*-(2-hydroxypropyl) methacrylamide) with bis-ω-cholesteryl groups; **PDN-diPy**: poly(*N*,*N*-dimethylacrylamide-*co*-*N*-acryloxysuccinimide) with bis-ω-pyrenyl groups; **PDN-diChol**: poly(*N*,*N*-dimethylacrylamide-*co*-*N*-acryloxysuccinimide) with bis-ω-cholesteryl groups.

be responsible for the inability of the membranes to fully close/seal. We postulate that the presence of two rigid cholesterol or pyrene rings at the ω-chain termini may be having a similar effect in these systems in terms of directing vesicle formation. Increasing the molar mass of the homopolymers still results in the formation of open-mouth vesicular structures even with a hydrophobic/hydrophilic ratio close to 6/94. For example, Figure 4 shows the FE-SEM images obtained from **PDMA-diPy 13K**, **PDMA-diChol 11K**, and **PHPMA-diChol 14K**. Interestingly, the supramolecular vesicular assemblies have a size that is comparable to those formed from the lower molar mass homopolymers, perhaps indicating there is little molar mass dependence on vesicle formation. To reiterate, and taking **PHPMA-diChol 14K** as a representative example, this particular amphiphilic homopolymer has a hydrophobic/hydrophilic ratio of only 8/92 again highlighting the dramatic effect of the presence of two rigid ring structures at one chain terminus on the self-assembly behavior in aqueous media.

The assembly of the **PDN-diPy** statistical copolymers also resulted in the formation of polymersomes, Figure 5. It should be noted that the NAS comonomer possesses hydrophobic character and as such is likely a contributing factor in directing self-assembly. Indeed, these **PDN-diPy** copolymers contain a significantly higher overall hydrophobic content than the amphiphilic homopolymers, and it is well documented that the hydrophobic component in amphiphilic species is primarily responsible for driving self-assembly.

In the case of **PDN-diPy 5K** (Figure 5, parts A and B) open-mouth vesicles with sizes in the range 200 nm $-2\,\mu$m are observed. Somewhat smaller assemblies are observed in the case of the higher molar mass species **PDN-diPy 18K** and **PDN-diPy 36K**, Figure 5, parts C and D.

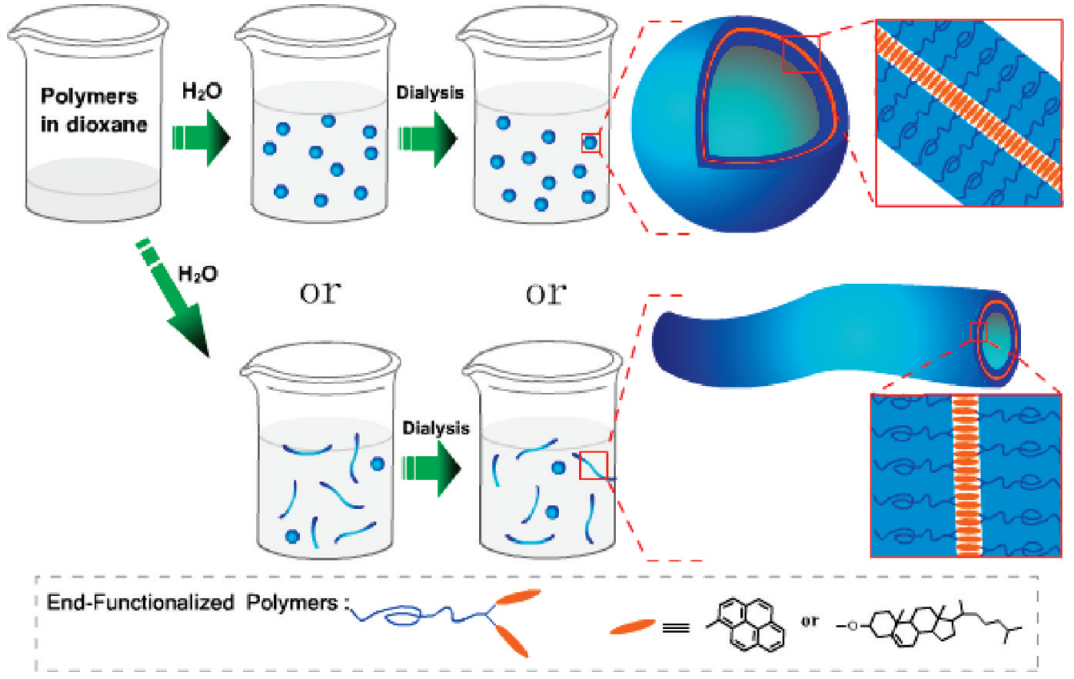
Interestingly, in the case of **PDN-diChol 7K** the coexistence of spherical and tublar vesicles with diameters of $\sim$150$-$200 nm and lengths of approximately 3$-$10 μm were observed, Figure 6 A-C.

Table 1. Chemical Structures, Number Average Molar Masses, Polydispersity Indices, and Hydrophobic/Hydrophilic Ratios of End-Functionalized Polymers Employed in This Study

				molecular weight			
	designation	used CTA	(co)polymer composition[a]	SEC[b]	NMR[c]	PDI	hydrophobic/hydrophilic ratio (wt %)[d]
PDMA-diPy	**PDMA-diPy 6K**	**CTA5**	**$PDMA_{50}$-diPy**	7800	5900	1.08	13/87
	PDMA-diPy 13K		**$PDMA_{128}$-diPy**	17 200	13 500	1.11	6/94
PDMA-diChol	**PDMA-diChol 5K**	**CTA4**	**$PDMA_{38}$-diChol**	5920	5060	1.07	23/76
	PDMA-diChol 11K		**$PDMA_{93}$-diChol**	13 100	10 500	1.08	11/89
PHPMA-diChol	**PHPMA-diChol 6K**	**CTA4**	**$PHPMA_{34}$-diChol**	9800	6220	1.12	19/81
	PHPMA-diChol 14K		**$PHPMA_{88}$-diChol**	23 400	13 900	1.19	8/92
PDN-diPy	**PDN-diPy 5K**	**CTA5**	**poly(DMA_{29}-*co*-NAS_8)-diPy**	7060	5130	1.16	(15^e + 26^f)/59
	PDN-diPy 18K		**poly(DMA_{115}-*co*-NAS_{31})-diPy**	21 750	17 570	1.09	(5 + 29)/66
	PDN-diPy 36K		**poly(DMA_{240}-*co*-NAS_{69})-diPy**	41 640	36 500	1.14	(4 + 28)/68
PDN-diChol	**PDN-diChol 7K**	**CTA4**	**poly(DMA_{33}-*co*-NAS_9)-diChol**	6980	6090	1.11	(19 + 25)/56
	PDN-diChol 13K		**poly(DMA_{82}-*co*-NAS_{21})-diChol**	16 800	12 900	1.09	(9 + 25)/64
	PDN-diChol 35K		**poly(DMA_{240}-*co*-NAS_{62})-diChol**	43 100	35 200	1.15	(4 + 29)/67
PDMA-diODE	**PDMA-diODE 7K**	**CTA8**	**$PDMA_{56}$-diODE**	9580	6620	1.06	14/86
PDMA-monoPy	**PDMA-monoPy 7K**	**CTA7**	**$PDMA_{67}$-monoPy**	11 200	7030	1.06	6/94
PDMA-diC_{16}Py	**PDMA-diC_{16}Py 10K**	**CTA6**	**$PDMA_{83}$-diC_{16}Py**	13 500	9800	1.12	15/85
PDMA-tetraPy	**PDMA-tetraPy 13K**	**CTA9**	**$PDMA_{116}$-tetraPy**	12 800	13 550	1.15	12/88
PDMA-diSSPy	**PDMA-diSSPy 13K**	**CTA10**	**$PDMA_{117}$-diSSPy**	13 700	12 800	1.12	9/91

[a] The numbers in subscript denote the average degree of polymerization. [b] Measured by size exclusion chromatography (SEC) in dimethylacetamide (DMAc), calibrated with linear, narrow molecular weight distribution polystyrene standards. Values reported are M_n. [c] Calculated by a comparison of integral(s) associated with end groups and that of polymer chain. [d] Calculated by a comparison of the molecular weights of hydrophobic end-functionalities (diPy (754), diChol (1151), diODE (918), monoPy (440), diC_{16}Py (1435), tetraPy (1669), diSSPy (1110)) to that of hydrophilic PDMA polymers. [e] Hydrophobic end-group contribution. [f] Hydrophobic NAS monomer contribution.

Scheme 2. General Procedure for the Preparation of Polymeric Self-Assembled Structures



The tubular vesicles possess open-mouths, as highlighted in Figure 6C and have a membrane thickness of 30 ± 5 nm which is entirely consistent with the proposed bilayer structure.

In the case of the higher molar mass species, **PDN-diChol 13K** and **PDN-diChol 35K**, the copolymers self-assemble yielding particles with a spherical vesicular morphology, Figure 6, parts D and E.

This dramatic influence of the two rigid fused-ring structures at the ω-terminus, whether it be cholesteryl or pyrenyl groups, is evident when the self-assembly behavior of a PDMA homopolymer of similar molar mass and hydrophobic/hydrophilic balance as **PDMA-diPy 6K**, but bearing two octadecyl groups at the ω-termini (prepared using **CTA8** Figure 2, **PDMA-diODE 7K**, Table 1) is examined. Dynamic light scattering (DLS) analysis in water indicates the presence of a single population of aggregates with an average hydrodynamic diameter (D_h) of ~20 nm, Figure 7, which is consistent with the formation of spherical micelles. Essentially identical results were obtained by Bathfield et al.[54] in their studies with a poly(*N*-acryloylmorpholine) of comparable molar mass (9200 g/mol) end-functionalized with a twin-tailed phospholipid moiety yielded self-assembled micelles in aqueous media with a measured D_h of 18 nm as determined by DLS.

Clearly, the presence of two rigid, spatially close, fused-ring structures is a crucial architectural feature of these (co)polymers in directing vesicle formation. Indeed, the presence of cholesterol groups in polymers, for example, is known to induce to formation of a variety of interesting assembled states including hydrogels, nanogels, as well as other unusual self-assembled structures

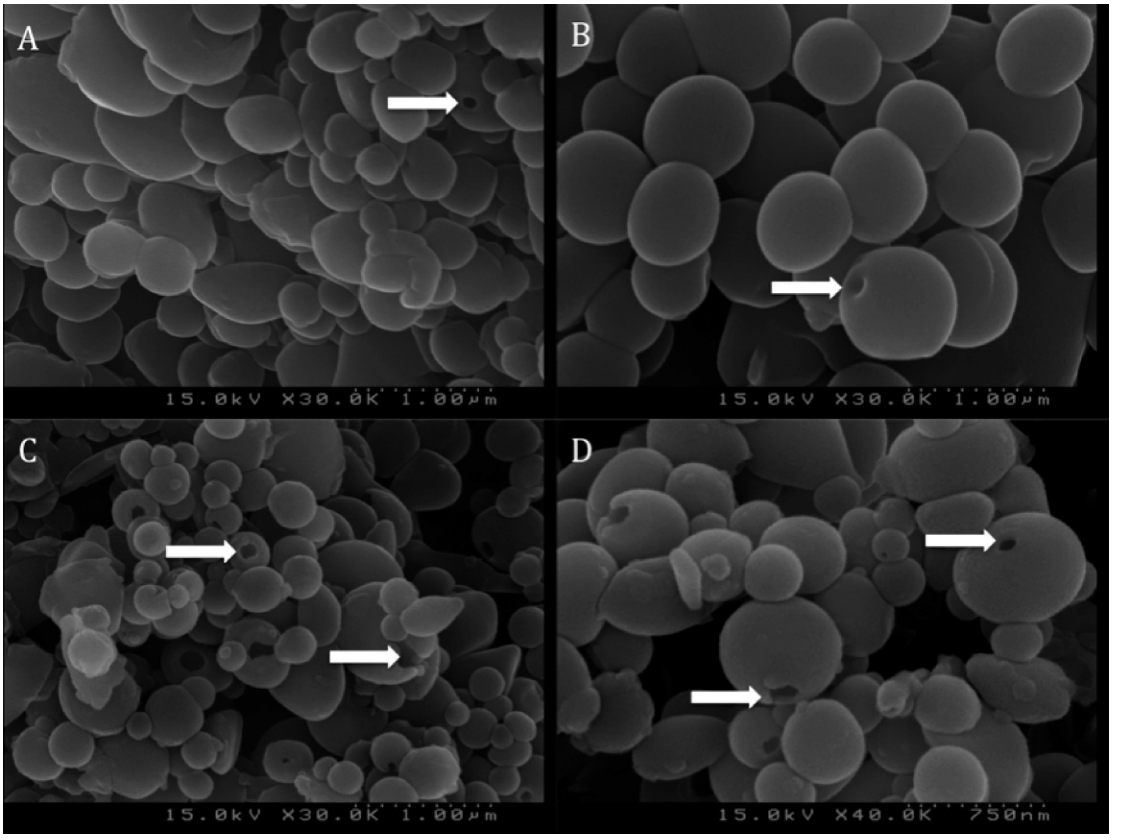


Figure 3. FE-SEM images of (A) **PDMA-diPy 6K**; (B) **PDMA-diChol 5K**; (C and D) **PHPMA-diChol 6K** demonstrating the spherical vesicular morphology.

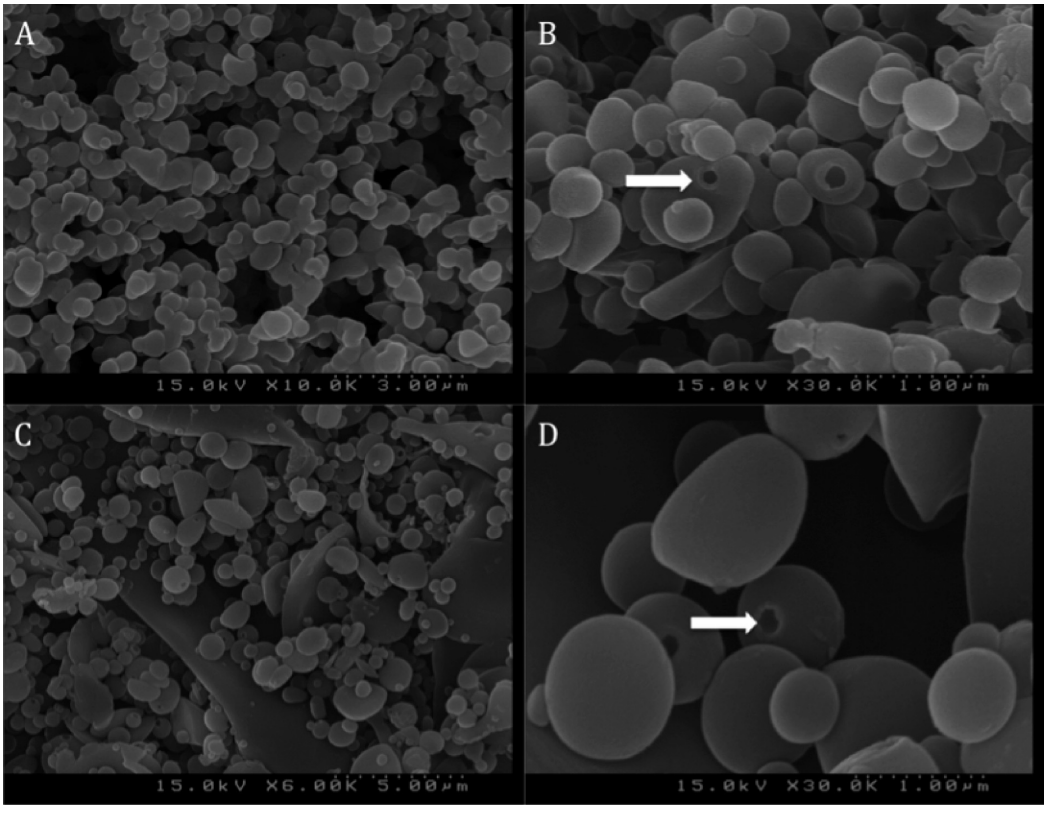


Figure 4. FE-SEM images of (A) **PDMA-diPy 13K**; (B) **PDMA-diChol 11K**; (C and D) **PHPMA-diChol 14K**.

via a combination of proposed side-by-side or layer-by-layer packing.[38−40] This difference in self-assembly behavior between (co)polymers bearing either rigid fused-rings or flexible alkyl chains prompted us to examine the self-assembly of two

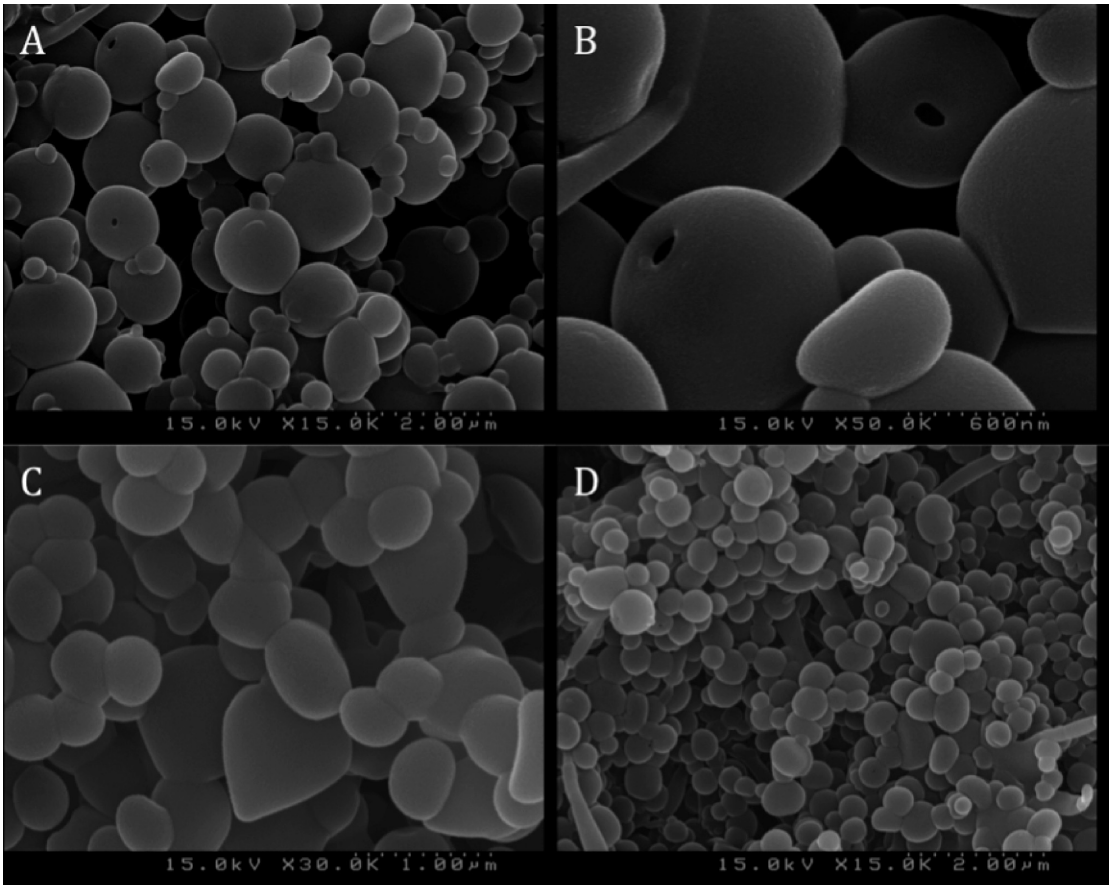


Figure 5. FE-SEM images of (A and B) **PDN-diPy 5K**, (C) **PDN-diPy 18K**, and (D) **PDN-diPy 36K**.

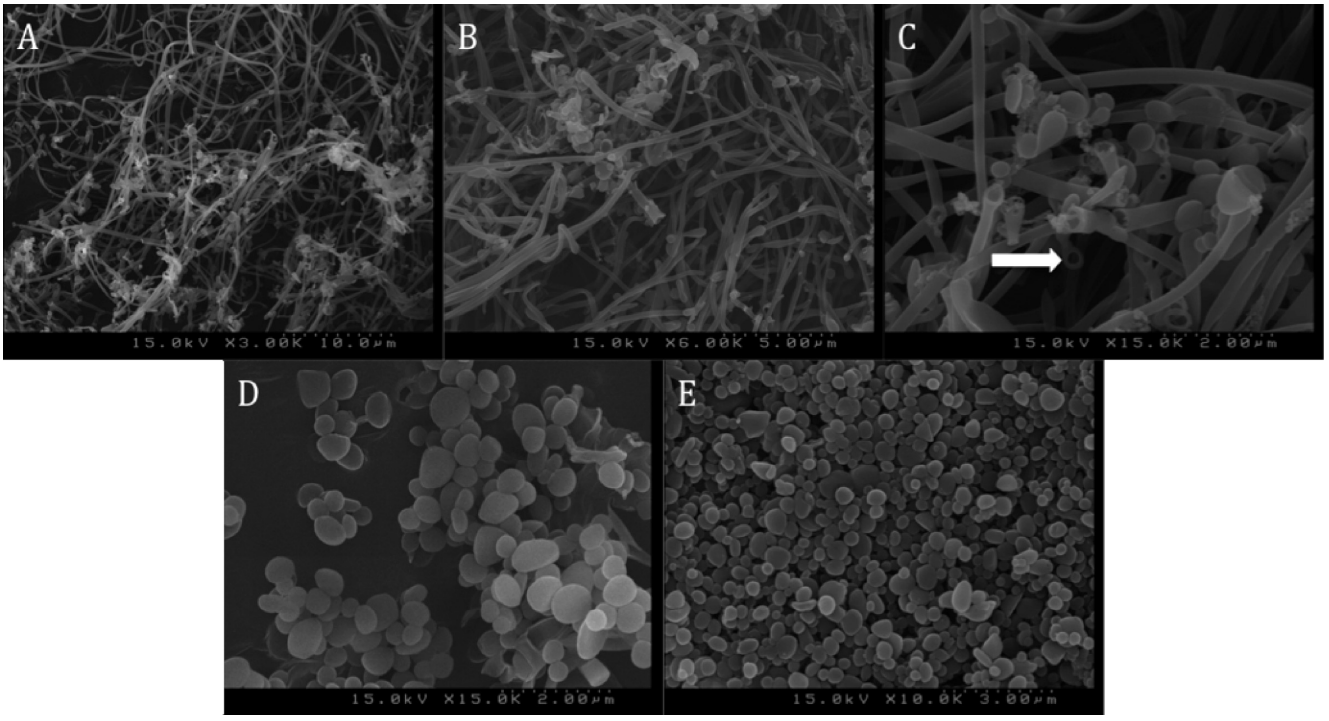


Figure 6. FE-SEM images of (A−C) **PDN-diChol 7K** highlighting tubular vesicle formation and (D) **PDN-diChol 13K** and (E) **PDN-diChol 35K** showing spherical polymersomes.

homopolymers prepared using **CTA6** and **CTA9**. **CTA6** is structurally similar to **CTA5** except a 16-carbon spacer has been introduced forcing the two pyrenyl end-groups farther apart, and was employed to prepare a PDMA homopolymer (designated **PDMA-diC$_{16}$Py 10K**) with a target M_n of 10K, Table 1. Self-assembly and susequent FE-SEM characterization, Figure 8A,

indicated the presence of two distinct morphologies, namely spheres and tubes, with the former representing the major component. Interestingly, there is no evidence of open-mouth vesicles perhaps indicating that the added flexibility associted with the 16-carbon spacer helps facilitate the closure of the vesicular species. **CTA9** bears four spatially close pyrene groups in the R fragment of the dithioester CTA and was also employed in the preparation of a PDMA homopolymer, Table 1 (**PDMA-tetraPy 13K**).

Figure 8B shows the FE-SEM of the resulting aggregated species derived from **PDMA-tetraPy 13K**. Clearly self-assembly of this particular species yields neither spherical or tubular aggregates but rather results in the formation of an apparent tubular network-like structure. While we have no direct evidence we postulate, however, that this network-like assembly is of a bilayer nature.

The existence of interactions, and specifically $\pi-\pi$ stacking, between the hydrophobic end-groups in the case of the pyrene-modified polymers can be confirmed by fluorescence. Figure 9 shows the fluorescence emission spectra (A) and images (B) for **PDMA-diPy 13K** in water and dioxane, **PDMA-monoPy 7K** in water and dioxane, and pyrenebutyric acid (PyBA). Consider first **PDMA-diPy 13K**. The emission spectra in both water, a selective solvent, and dioxane, a nonselective solvent (a and b Figure 9A) clearly show the presence of a red-shifted emission band between 430 and 580 nm and is attributed to the stacked pyrene excimer emission. The difference in the intensities of the excimer peak between **PDMA-diPy 13K** in water and dioxane, of approximately 10.0 nm, is likely a reflection of the different molecular environments of the pyrene molecules. In water, **PDMA-diPy 13K** presumably assembles to give a bilayer structure in which the pyrene molecules are stacked, whereas in dioxane the polymer is molecularly dissolved to give the dimer structure, as shown schematically in Figure 9C. In contrast, **PDMA-monoPy** (in both water and dioxane), and the small molecule PyBA all exhibit emission spectra consistent with free pyrene (Figure 9A, parts c, d, and e). The differences in these proposed interactions can also be visualized under a UV lamp at 365 nm, Figure 9B. In those systems where $\pi-\pi$ interactions exist excitation results in a green emission that is slightly blue-shifted going from a → b which is again attributed to the different solvation/molecular states associated with the different species, whereas the monopyrene species give a purple emission, Figure 9B, parts c and d.

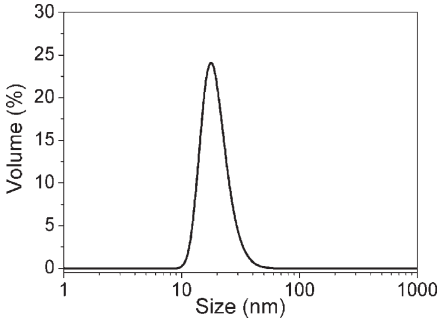


Figure 7. Volume-average size distribution of aggregates formed from **PDMA-diODE 7K** in water obtained via dynamic light scattering analysis.

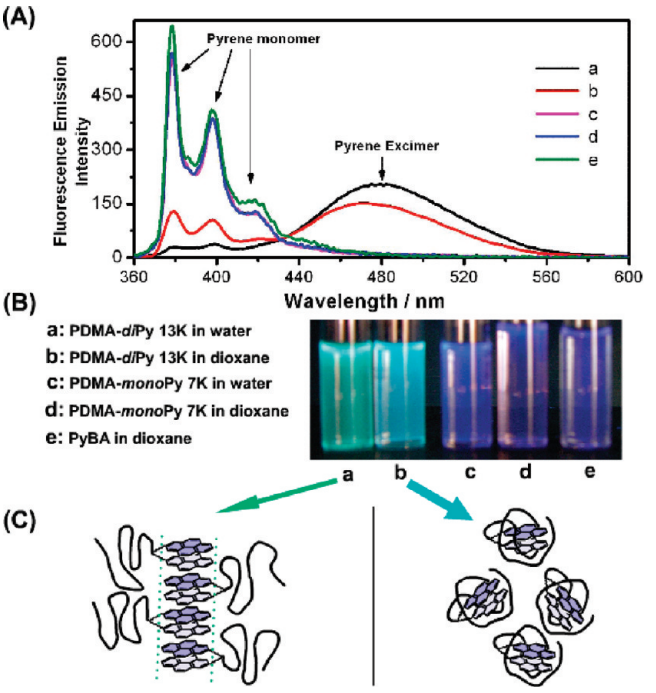


Figure 9. Fluorescence emission spectra (A), fluorescence emission images (B) of **PDMA-monoPy 7K**, **PDMA-diPy 13K**, and pyrenebutyric acid (PyBA) in 1,4-dioxane and water, and proposed stacking mechanism (C). Sample concentration: 0.15 mM (pyrene molar concentration), λ_{ex} = 347 nm (A) and λ_{ex} = 365 nm (B).

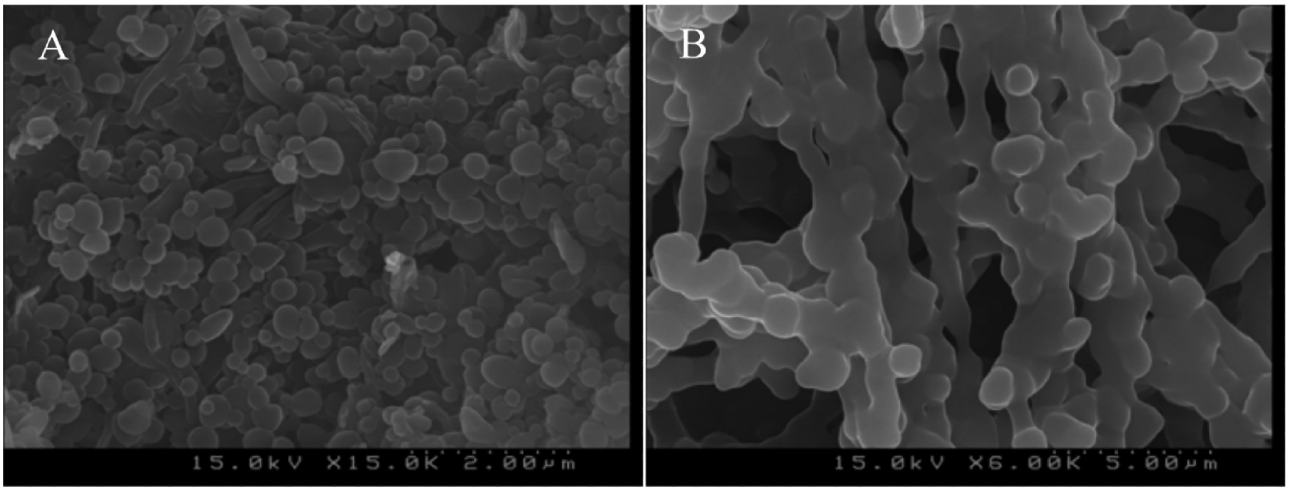
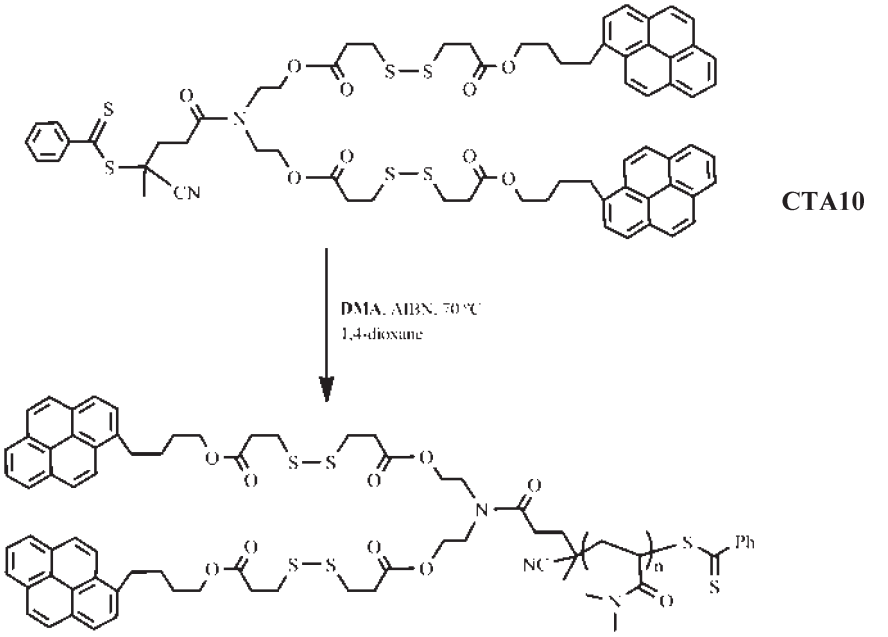


Figure 8. FE-SEM images of (A) vesicles derived from **PDMA-diC$_{16}$Py 10K**, and (B) a tubular network-like structure obtained from **PDMA-tetraPy 13K**.

Scheme 3. Polymerization of *N*,*N*-Dimethylacrylamide Mediated by ((4-Cyano-4-((phenylcarbonothioyl)thio)pentanoyl)azanediyl)bis(ethane-2,1-diyl) bis(3-((3-oxo-3-(4-(pyren-1-yl)butoxy)propyl)disulfanyl)propanoate) (CTA10)



While it is perhaps not surprising that such $\pi-\pi$ interactions are present in the twin-tailed pyrene species (CTA and polymers) given the spatially confined nature of their structures it is likely that such intermolecular interactions serve as an additional stabilizing force in the polymersomes and may also serve as a secondary influence in directing the self-assembly process.

Polymersomes have the potential to find application in areas as diverse as (bio)catalysis, diagnostics, imaging, and drug delivery. To demonstrate the potential of the materials described herein to serve as carriers for hydrophilic and/or hydrophobic molecules, a new biodegradable bis-ω-pyrene CTA (**CTA10**) containing a disulfide linkage in the R group fragment was first synthesized and employed in the homopolymerization of DMA, Scheme 3, Table 1, designated **PDMA-diSSPy 13K**. Consistent with the structually similar **PDMA-diPy 13K** (without a disulfide link) **PDMA-diSSPy 13K** self-assembles in aqueous media to give spherical vesicles, Figure 10.

The bilayer structure of these polymersomes with the disulfide-bearing pyrene moieties forming the hydrophobic domain presents a novel approach for controlled release of a hydrophobic moiety.[55] The ability of polymersomes to encapsulate hydrophobic species is well documented and, ideally, applications of such loaded species in drug delivery, for example, requires the controlled release of the payload in response to an external stimulus. One potential problem with the encapsulation-release approach is that it can be difficult to achieve high "drug" loadings. If we consider the pyrene functionality as a model "drug", then the approach for vesicle formation described herein offers a route to highly drug-loaded polymersomes simply by incorporation of the desired hydrophobic payload as a part of the parent polymer end-group. The potential of these biodegradable polymersomes to effectively release pyrene is clear when the fluoresence emission of the pyrene excimer at ~480 nm is monitored in the presence of dithiothreitol (DTT), Figure 11.

Treatment of the polymersomes derived from **PDMA-diSSPy 13K** with DTT results in a gradual decrease in the intensity of the excimer emission band, Figure 11A. This observation is consistent with DTT cleaving the disulfide bonds and releasing pyrene molecules ultimately leading to disintegration of the polymersomes. The time-release profile for the pyrene molecules is shown

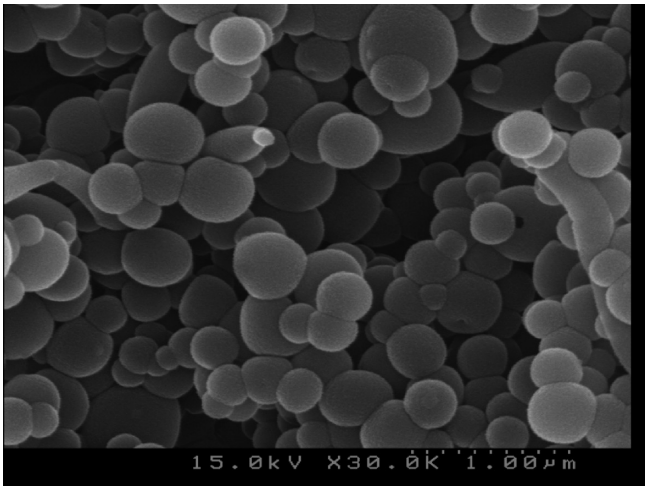


Figure 10. FE-SEM image of vesicles obtained from **PDMA-diSSPy 13K**.

in Figure 11B indicating essentially complete disappearance of the stacked pyrene configuration within approximately 3 h. One advantage of polymersomes compared to polymeric micelles is the potential for the former to not only encapsulate hydrophobic species but also hydrophilic molecules in the interior of the polymersome. Rhodamine B was employed as a model hydrophilic drug and was encapsulated into the **PDMA-diSSPy 13K** polymersome at a loading of 1.7% and its release subsequently monitored by UV−vis spectroscopy in the presence and absence of DTT, Figure 12.

In the absence of DTT, Figure 12A/C, we note that the release of Rhodamine B is relatively slow with only ~20% of free Rodamine B being detected after 240 min. In contrast, in the presence of DTT, Figure 12B/C, the release of Rhodamine B is signficantly enhanced with ~70% of the initial payload being released in the same period, further highlighting the potential benefit of incorporating a biodegradable linkage in the hydrophobic domain as a release trigger for both hydrophilic and hydrophobic molecules.

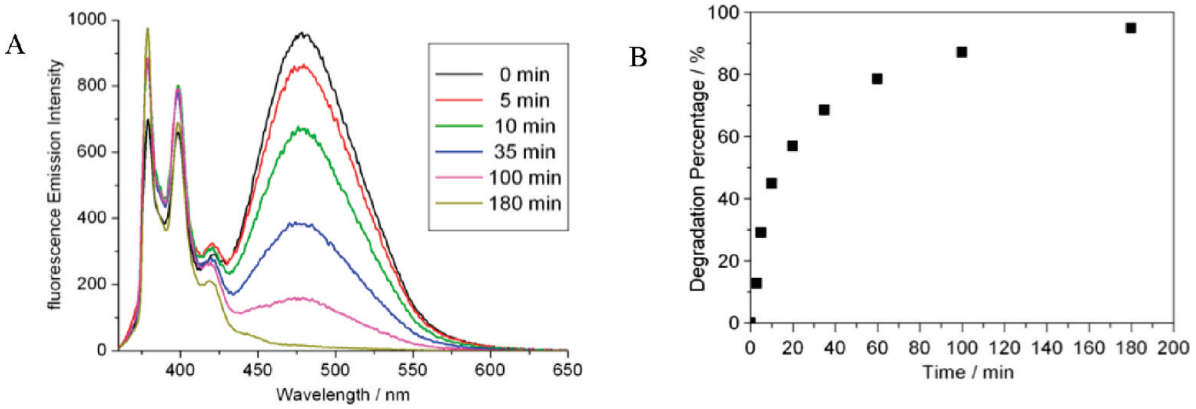


Figure 11. Fluoresence emission spectra of polymersomes derived from **PDMA-diSSPy 13K**, in the presence of DDT, as a function of time (A) and time-release profile calculated based on the decrease in the fluoresence emission band of the pyrene dimer excimer (B).

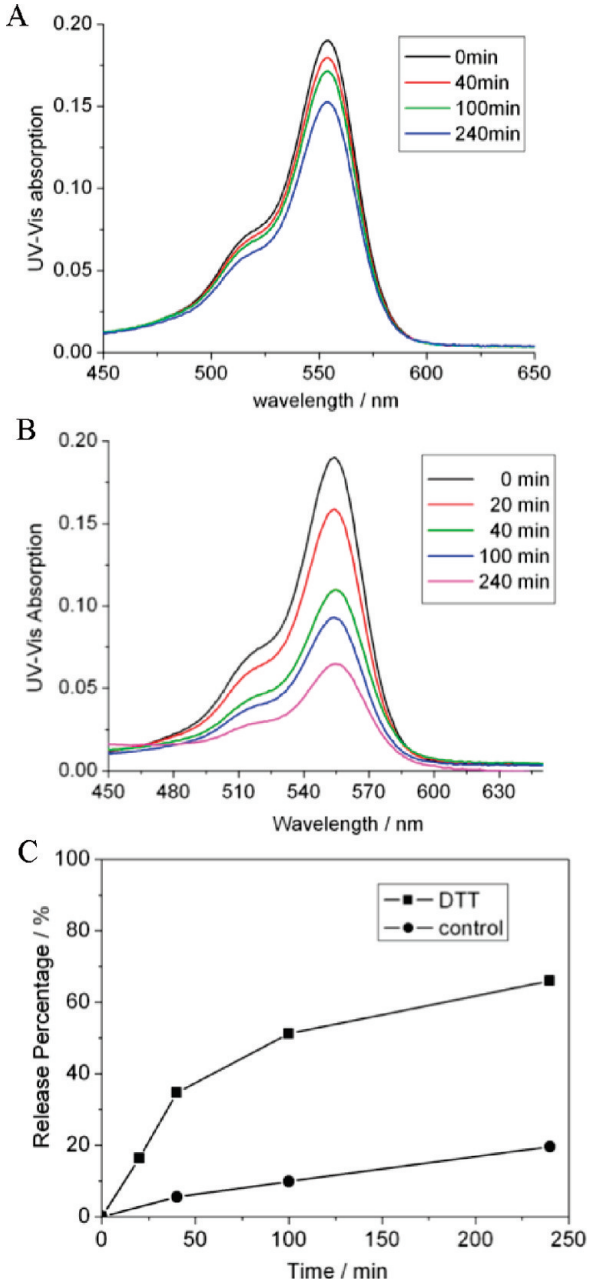


Figure 12. UV−vis absorption spectra of Rhodamine B loaded in **PDMA-diSSPy 13K** polymersomes in the absence (A) and presence (B) of DTT and the resulting controlled release profiles (C).

Conclusion

A novel and facile approach enabling the fabrication of spherical and tubular polymersomes via the self-assembly of hydrophilic homo- and copolymers of poly(*N*,*N*-dimethylacrylamide) (PDMA) and poly(*N*-(2-hydroxypropyl) methacrylamide) (PHPMA) in water bearing two hydrophobic pyrene or cholesterol groups at the ω-terminus is described. In distinct contrast to classical vesical forming amphiphilic (co)polymers polymersome formation was observed in systems with a remarkably low molar hydrophobic content (typically 6−23 wt %) of either pyrene or cholesterol end-groups. The presence of two such rigid rings was shown to be an architectural requirement for vesicle formation with a PDMA homopolymer bearing two flexible octadecyl chains at the ω-terminus forming spherical micelles. Introduction of a C16 spacer in a bis-ω-pyrenyl treminal PDMA homopolymer still results in the formation of shperical vesicles although it appears that the added flexible spacer helps facilitate full closure of the polymersomes. Increasing chain end functionality to the synthesis of a PDMA homopolymer with four pyrenyl units yields a network-like tubular structure that, we postulate, is of a bilayer nature. Incorporation of disulfide bridges into a novel bis-pyrenyl dithioester CTA facilitates the preparation of polymersomes with a biodegradable component the effectiveness of which was demonstrated in fluoresence emission experiments. The ability of these novel polymersomes to sequester and release a hydrophilic model drug, Rhodamine B, was demonstrated by UV−vis spectrophotometry. These novel polymersomes offer a potential novel route to new self-assembled polymeric structures with biodegradable functionality with applications in drug loading and controlled release.

Acknowledgment. T.P.D. acknowledges the ARC for a Federation Fellowship. A.B.L. thanks UNSW for strategic funds.

Supporting Information Available: General schemes for the synthesis of **CTAs4−10**, idealized structures for all (co)polymers derived from the novel CTAs, gel permeation chromatograms for the **PDN-diChol** and **PDN-diPy** statistical copolymers, and representative ^{1}H NMR spectra of CTAs and the corresponding polymers. This material is available free of charge via the Internet at http://pubs.acs.org.

References and Notes

(1) Lipowsky, R. *Nature* **1991**, *349*, 475.
(2) Reynwar, B. J.; Illya, G.; Harmandaris, V. A.; Muller, M. M.; Kremer, K.; Deserno, M. *Nature* **2007**, *447*, 461.
(3) Lasic, D. D. *Nature* **1996**, *380*, 561.
(4) Tanford, C. *Science* **1978**, *200*, 1012.

(5) Yan, D.; Zhou, Y.; Hou, J. *Science* **2004**, *303*, 65.
(6) Grohn, F.; Klein, K.; Brand, S. *Chem.—Eur. J.* **2008**, *14*, 6866.
(7) Grohn, F.; Klein, K.; Koynov, K. *Macromol. Rapid Commun.* **2010**, *31*, 75.
(8) Ruthard, C.; Maskos, M.; Kolb, U.; Grohn, F. *Macromolecules* **2009**, *42*, 830.
(9) Antonietti, M.; Förster, S. *Adv. Mater.* **2003**, *15*, 1323.
(10) Discher, D. E.; Eisenberg, A. *Science* **2002**, *297*, 967.
(11) Kita-Tokarczyk, K.; Grumelard, J.; Haefele, T.; Meier, W. *Polymer* **2005**, *46*, 3540.
(12) Hamley, I. W. *Soft Matter* **2005**, *1*, 36.
(13) Discher, B. M.; Won, Y.-Y.; Ege, D. S.; Lee, J. C. M.; Bates, F. S.; Discher, D. E.; Hammer, D. A. *Science* **1999**, *284*, 1143.
(14) Shen, H.; Eisenberg, A. *Angew. Chem., Int. Ed.* **2000**, *39*, 3310.
(15) (a) Bu, W.; Uchida, S.; Mizuno, N. *Angew. Chem., Int. Ed.* **2009**, *48*, 8281. (b) Bermúdez, H.; Aranda-Espinoza, H.; Hammer, D. A.; Disher, D. E. *Europhys. Lett.* **2003**, *64*, 550. (c) Photos, P. J.; Bermúdez, H.; Aranda-Espinoza, H.; Shillcock, J.; Disher, D. E. *Soft Matter* **2007**, *3*, 364.
(16) Changez, M.; Kang, N.-G.; Lee, C. H.; Lee, J.-S. *Small* **2010**, *6*, 63.
(17) Du, J.; Armes, S. P. *J. Am. Chem. Soc.* **2005**, *127*, 12800.
(18) Du, J.; Tang, Y.; Lewis, A. L.; Armes, S. P. *J. Am. Chem. Soc.* **2005**, *127*, 17982.
(19) Yu, S.; Azzam, T.; Rouiller, I.; Eisenberg, A. *J. Am. Chem. Soc.* **2009**, *131*, 10557.
(20) Schatz, C.; Louguet, S.; Le Meins, J.-F.; Lecommandoux, S. *Angew. Chem., Int. Ed.* **2009**, *48*, 2572.
(21) Pasparakis, G.; Alexander, C. *Angew. Chem., Int. Ed.* **2008**, *47*, 4847.
(22) Vriezema, D. M.; Garcia, P. M. L.; Oltra, N. S.; Hatzakis, N., S.; Kuiper, S. M.; Nolte, R. J. M.; Rowan, A. E.; van Hest, J. C. M. *Angew. Chem., Int. Ed.* **2007**, *46*, 7378.
(23) Morishima, Y. *Angew. Chem., Int. Ed.* **2007**, *46*, 1370.
(24) Pradeep, C. P.; Misdrahi, M. F.; Li, F.-Y.; Zhang, J.; Xu, L.; Long, D.-L.; Liu, T.; Cronin, L. *Angew. Chem., Int. Ed.* **2009**, *48*, 8309.
(25) Li, Y.; Lokitz, B. S.; McCormick, C. L. *Angew. Chem., Int. Ed.* **2006**, *45*, 5792.
(26) Cornelissen, J. J. L. M.; Fischer, M.; Sommerdijk, N. A. J. M.; Nolte, R. J. M. *Science* **1998**, *280*, 1427.
(27) Moad, G.; Rizzardo, E.; Thang, S. H. *Aust. J. Chem.* **2005**, *58*, 379.
(28) Boyer, C.; Bulmus, V.; Davis, T. P.; Ladmiral, V.; Liu, J.; Perrier, S. *Chem. Rev.* **2009**, *109*, 5402.
(29) Moad, G.; Rizzardo, E.; Thang, S. H. *Aust. J. Chem.* **2009**, *62*, 1402.
(30) Moad, G.; Rizzardo, E.; Thang, S. H. *Aust. J. Chem.* **2006**, *59*, 669.
(31) Lowe, A. B.; McCormick, C. L. *Prog. Polym. Sci.* **2007**, *32*, 283.
(32) Moore, J. S. *Macromolecules* **1990**, *23*, 65.
(33) Pollak, A.; Blumenfeld, H.; Wax, M.; Baughn, R. L.; Whitesides, G. M. *J. Am. Chem. Soc.* **1980**, *102*, 6324.
(34) Xu, J.; Tao, L.; Boyer, C.; Lowe, A. B.; Davis, T. P. *Macromolecules* **2010**, *43*, 20.
(35) Xu, J.; Tao, L.; Liu, J.; Bulmus, V.; Davis, T. P. *Macromolecules* **2009**, *42*, 6893.
(36) Willcock, H.; O'Reilly, R. *Polym. Chem.* **2010**, *1*, 149.
(37) Yu, B.; Chan, J. W.; Hoyle, C. E.; Lowe, A. B. *J. Polym. Sci., Part A: Polym. Chem.* **2009**, *47*, 3544.
(38) Yao, N.; Jamieson, A. M. *Polymer* **2000**, *41*, 2925.
(39) Liu, X.-M.; Yang, Y.-Y.; Leong, K. W. *J. Colloid Interface Sci.* **2003**, *266*, 295.
(40) Akiyoshi, K.; Kang, E.-C.; Kurumada, S.; Sunamoto, J. *Macromolecules* **2000**, *33*, 3244.
(41) Xia, Y.; Burke, N. A. D.; Stöver, H. D. H. *Macromolecules* **2006**, *39*, 2275.
(42) Xia, Y.; Yin, X.; Burke, N. A. D.; Stöver, H. D. H. *Macromolecules* **2005**, *38*, 5937.
(43) Kujawa, P.; Segui, F.; Shaban, S.; Diab, C.; Okada, Y.; Tanaka, F.; Winnik, F. M. *Macromolecules* **2006**, *39*, 341.
(44) Wu, C.; Li, W.; Zhu, X. X. *Macromolecules* **2004**, *37*, 4989.
(45) Lowe, A. B.; Torres, M.; Wang, R. *J. Polym. Sci., Part A: Polym. Chem.* **2007**, *45*, 5864.
(46) Lowe, A. B.; Wang, R. *Polymer* **2007**, *48*, 2221.
(47) Tao, L.; Xu, J.; Gell, D.; Davis, T. P. *Macromolecules* **2010**, *43*, 3721.
(48) Li, H.; Yu, B.; Matsushima, H.; Hoyle, C. E.; Lowe, A. B. *Macromolecules* **2009**, *42*, 6537.
(49) Hussain, H.; Tan, B. H.; Mya, K. Y.; Liu, Y.; He, C. B.; Davis, T. P. *J. Polym. Sci., Part A: Polym. Chem.* **2010**, *48*, 152.
(50) Jia, Z.; Liu, J.; Davis, T. P.; Bulmus, V. *Polymer* **2009**, *50*, 5928.
(51) Erout, M.-N.; Troesch, A.; Pichot, C.; Cros, P. *Bioconjugate Chem.* **1996**, *7*, 568.
(52) Zhou, S.; Zhang, C.; Wang, D.; Zhao, M. *Analyst* **2008**, *133*, 903.
(53) Li, Y.; Lokitz, B. S.; McCormick, C. L. *Macromolecules* **2006**, *39*, 81.
(54) Bathfield, M.; Daviot, D.; D'Agosto, F.; Spitz, R.; Ladavière, C.; Charreyre, M.-T.; Delair, T. *Macromolecules* **2008**, *41*, 8346.
(55) Ahmed, F.; Pakunlu, R.; Srinivas, G.; Brannan, A.; Bates, F.; Klein, M. L.; Minko, T.; Discher, D. E. *Mol. Pharmaceutics* **2005**, *3*, 340.

Macromolecules
ARTICLE

Macromolecules **2011**, *44*, 313–319 **313**
DOI: 10.1021/ma102072p

Effect of the Sequence Length Distribution on the Lamellar Crystal Thickness and Thickness Distribution of Polyethylene: Perfectly Equisequential ADMET Polyethylene vs Ethylene/α-Olefin Copolymer.

Satoru Hosoda,* Yoshinobu Nozue, Yasutoyo Kawashima, Kouei Suita, Shuichiro Seno, and Tatsuhiro Nagamatsu

Petrochemicals Research Lab. Sumitomo Chemical Co., Ltd., Kitasode 2-1, Sodegaura, Chiba, Japan 299-0295

Kenneth B. Wagener,* Bora Inci, Fabio Zuluaga,† Giovanni Rojas, and James K. Leonard

The George and Josephine Butler Polymer Research Lab., University of Florida, Gainesville, Florida 32611-7200, United States. † Present address; Department of Chemistry, University of Valle, AA 25360, Cali, Colombia.

Received September 8, 2010; Revised Manuscript Received December 2, 2010

ABSTRACT: The morphology of ADMET-synthesized polyethylene with *n*-butyl branches precisely spaced on every 39th carbon (EH39) was studied in comparison with an ethylene/1-hexene addition copolymer possessing the same branching probability, the goal being to elucidate the effect of the intramolecular sequence length heterogeneity on the lamella crystal thickness and its distribution. EH39 was found to have an orthorhombic crystalline polymorphism, which is normal for commercialized polyethylenes and different from that of the other ADMET polyethylenes with shorter CH_2 spacing (C15, C21). EH39 exhibits a narrow lamella thickness distribution; the average thickness ($l_{c,av.}$) corresponds exactly to the space length between two consecutive branches, suggesting the complete exclusion of *n*-butyl branches from the crystal stem. The average thickness, $l_{c,av.}$ mentioned above is also coincident with that obtained from WAXS and SAXS. On the other hand, the 1-hexene copolymer forms much thicker lamellae and a broader thickness distribution than ADMET polyethylene. Here, the average thickness $l_{c,av.}$ determined by TEM observation of the copolymer is 1.5 times larger than that calculated from the most probable ethylene sequence length obtained from ^{13}C NMR, or for a theoretical ethylene sequence length distribution, indicating that the lamellae are composed predominantly of the sparsely branched longer ethylene sequences that are statistically included. The intramolecular sequence distribution is considered significant to determine the lamella thickness and thickness distribution for short chain-branched polyethylenes with a narrow intermolecular chemical composition distribution.

1. Introduction

Many studies have been carried out using ethylene/α-olefin copolymers and hydrogenated polybutadiene to investigate the effects of the molecular structure and morphological parameters on the mechanical properties of linear low density polyethylene (LLDPE).[1−7] We have been investigating the relationship between the lamella thickness distribution and the mechanical properties of LLDPE, and we have observed that a narrower lamella thickness distribution results in higher impact strength.[8] Consequently, controlling the lamella thickness distribution is considered important from the viewpoint of product design for high performance LLDPE. Previous work[8−10] has shown that the lamella thickness distribution of LLDPE is determined by three structural factors: the intermolecular comonomer composition distribution (CCD), the intramolecular comonomer distribution, and the identity of the comonomer. The intermolecular comonomer composition distribution is especially important in the case of LLDPE prepared with a Ziegler−Natta catalyst, which causes a wide intermolecular CCD due to the heterogeneous active sites on the catalyst surface. The intramolecular comonomer distribution also becomes important in a metallocene-catalyzed LLDPE, because the CCD is generally narrow. Short chain branching species are considered important because the crystallinity and lamella thickness distribution are affected by the degree of branch inclusion in the crystalline phase. It would be useful to evaluate the effect of each factor separately, but this is generally unfeasible, especially for the last two factors, because all types of α-olefin copolymers have more or less an intramolecular heterogeneity; i.e., the comonomer sequence length distribution varies with the catalyst used.[11]

In this regard, polyethylene made without any intermolecular or intramolecular heterogeneity is of great interest from the viewpoint of crystalline structure homogeneity. Various kinds of polyethylenes with precisely placed short chain branches (completely *equisequential* structure) have been synthesized by the metathesis polycondensation: acyclic diene methathesis (ADMET) chemistry.[12] Several techniques have been used for the determination of the solid structure of these perfectly sequential ethylene/α-olefin model copolymers. Leiser et al[13] investigated the packing behavior of the precisely methyl branched ADMET polyolefin with 14 or 20 carbon spacers and found that a triclinic crystal is formed which incorporates the methyl branch into the crystal. Alamo et al[14] reported a unique halogen-included crystalline

*Corresponding authors: (S.H.) Present address: Corporate Planning and Coordination Office, Sumitomo Chemical Co. Ltd., Shinkawa 2-27-1, Chuo-ku, Tokyo, Japan. E-mail: hosodas@sc.sumitomo-chem.co.jp. (K.B.W.) E-mail address: wagener@chem.ufl.edu.

© 2010 American Chemical Society

Published on Web 12/29/2010

Table 1. Characteristic Data of ADMET Polyethylene and Ethylene/1-Hexene Copolymer

sample	M_w[a] × 10^3	M_w/M_n[a]	T_m^p[b] (°C)	T_m^f[c] (°C)	ΔH_m (J/g)	branch type	branch 1/1000C[d]
ADMET EH39	67	1.4	75.3	81.6	101.0	*n*-butyl	25.6
C_2'/1-C_6' copolymer mEH	70	2.0	98.9	105.1	96.5	*n*-butyl	25.3

[a] Determined by GPC. [b] DSC peak melting temperature. [c] DSC final melting temperature. [d] Branching degree per 1000 backbone carbons.

structure for a series of halogenated ADMET polyolefins. The dynamic chain motions of precisely branched polyethylene with deuterated methyl pendant groups were investigated using a solid state NMR by Wei et al.[15] The effect of branching species identity on the wide-angle X-ray diffraction peak position and DSC melting peak temperature was examined for a series of ADMET polyethylenes by Rojas et al.[16] We have recently reported the homogeneous lamella thickness distribution[17] and a unique crystallization behavior[18] in ADMET polyethylene having ethyl or *n*-hexyl branches precisely spaced on every 21st carbon. In this paper, the lamella morphology of polyethylene with *n*-butyl branches precisely placed on every 39th carbon was investigated. This material, which is closer to the real hexene-1 type LLDPE in terms of branching degree, was compared to ethylene/1-hexene addition copolymers with the same degree of *n*-butyl branches to elucidate the effect of the sequence length distribution on the lamella crystalline structure independent of the other factors described above.

2. Experimental Section

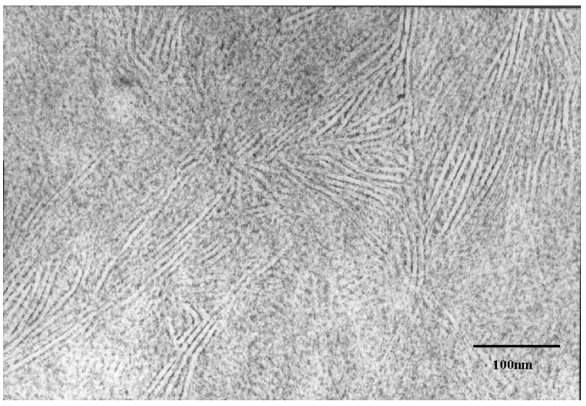
2.1. Materials. ADMET polyethylene EH39 with *n*-butyl branches on each and every 39th carbon was prepared by the polymerization of the appropriate acyclic-diene monomer, as described elsewhere.[19] The copolymer of ethylene and 1-hexene (mEH) was obtained by polymerization using a bis(cyclopentadienyl)-zirconium dichloride/MAO catalyst system in toluene at 50 °C for 10 min. The product polymer was purified by reprecipitation into 1 N HCl/MeOH solution.

2.2. Characterization. The characteristics of samples are listed in Table 1. Molecular weight and polydispersity of the samples were measured via size exclusion chromatography using trichlorobenzene mobile phase at 140 °C. The ^{13}C NMR spectra were measured at 150 MHz using a Bruker AVANCE 600 at 130 °C in a 1,2-dichlorobenzene/1,2-dichlorobenzene-d_4 (75/25) mixed solvent. The triad sequence ratio and other structural parameters of the ethylene/α-olefin copolymer were obtained according to the method of Randall and Hsieh.[20−22] Thermal analyses were performed using an indium-calibrated DSC6200 (Seiko Instrument Inc.). Samples were kept at 110 °C for 5 min and then cooled to 0 at 60 °C/min. The melting thermograms were recorded from 0 to 110 °C at 10 °C/min. WAXS and SAXS were performed on a Nanoviewer X-ray system equipped with RA-Micro7 (Rigaku Co. Ltd.) using Cu Kα radiation. The precise camera length was calibrated with 111 reflection of silicon powder. Samples were cooled from 110 °C to room temperature at 60 °C/min. The sample temperature was controlled by a LINKAM hot stage (THMS600) during X-ray measurements. X-ray crystallinity was determined by subtracting the amorphous halo, according to the method of Agawall et al.[23] The long period was evaluated from the circularly averaged Lorentz-corrected SAXS profile.

2.3. Morphology Observations. The specimen for TEM was prepared in a temperature controlled LINKAM hot stage (THMS600) from the melt (105 °C for EH39 and 120 °C for mEH) at a cooling rate of 60 °C/min, which was the same as that for DSC and X-ray measurements. After cooling, sample specimens were stained at room temperature with RuO_4 aqueous vapor and sectioned with an ultramicrotome in a liquid nitrogen vapor atmosphere. TEM observations were conducted with a HITACHI H-8000 transmission electron micrograph using an accelerating voltage of 200 kV. The lamella thickness distribution was obtained by measuring both the length and the thickness of more than 100 lamellae. The thickness was counted for every 4 Å and the area occupied by lamellae was obtained for each thickness division. A frequency histogram was expressed as an area-based occupation fraction.



(a)

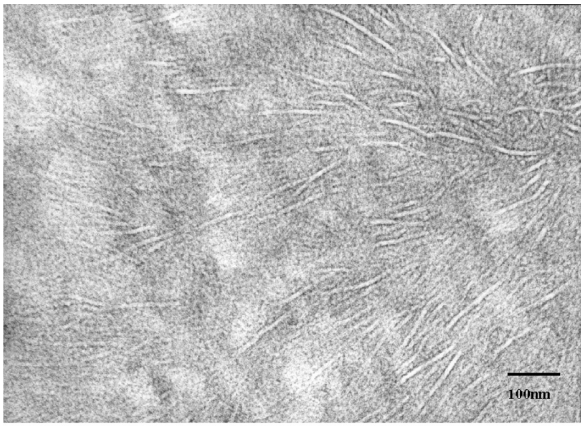


(b)

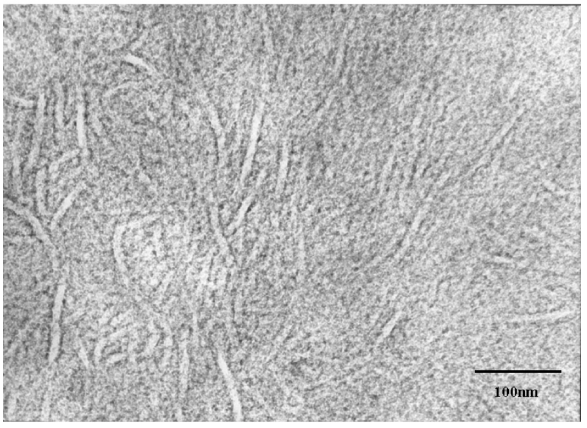
Figure 1. TEM images of ADMET EH39.

3. Results

3.1. Morphology Observations. Figures 1 and 2 show the lamella crystal morphologies (TEM images) for ADMET polyethylene EH39 and the random addition copolymer mEH, respectively. Lamellar stacks with an axialitic organization were observed over the entire image for EH39. Long and straight lamellae were dominant, and straight lamellae propagated to lengths of about a few thousand Angstroms. Spherulitic and wavy lamellae, which are common to general LLDPE, were not found in this ADMET sample. On the other hand, the copolymer mEH, which was prepared with a metallocene homogeneous catalyst and has the same degree of *n*-butyl branches as EH39, exhibited shorter and wavy thicker lamellae compared with EH39. Lamellae suggestive of a spherulitic growth can be observed (Figure 2(a); the upper-right-hand area may be near the center of a spherulite). These wavy lamellae are common to metallocene-catalyzed ethylene/α-olefin copolymers.[24]



(a)



(b)

Figure 2. TEM images of ethylene/1-hexene copolymer, mEH.

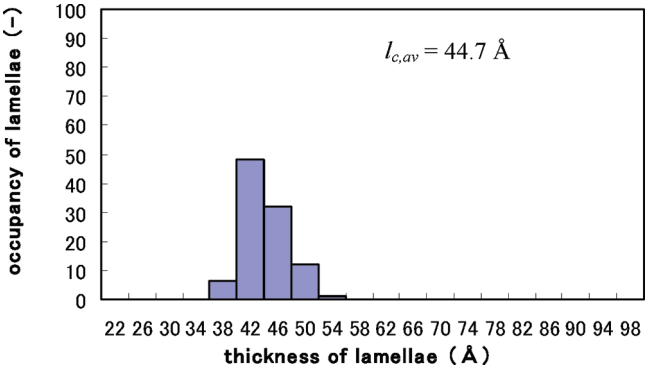


Figure 3. Lamella thickness distribution of ADMET polyethylene EH39 obtained from TEM images.

Lamella thickness distributions of EH39 and mEH are shown in Figures 3 and 4. ADMET EH39 shows a narrow distribution; all lamellae have thicknesses between 38 and 54 Ångstroms (the average lamella thickness, $l_{c,av.}$ = 44.7 Å, standard deviation, SD = 3.37 Å). This narrow lamella thickness distribution was also observed for other ADMET polyethylenes with *n*-hexyl and ethyl branches on every 21st carbon.[17] However, the copolymer mEH of the same branching degree as EH39 exhibits a wider lamella thickness distribution, with thicknesses between 46 and 94 Å ($l_{c,av.}$ = 72.6 Å, SD = 7.79 Å).

3.2. Characterization via WAXS and SAXS Measurements. The WAXS pattern of EH39 shown in Figure 5 (a), indicates

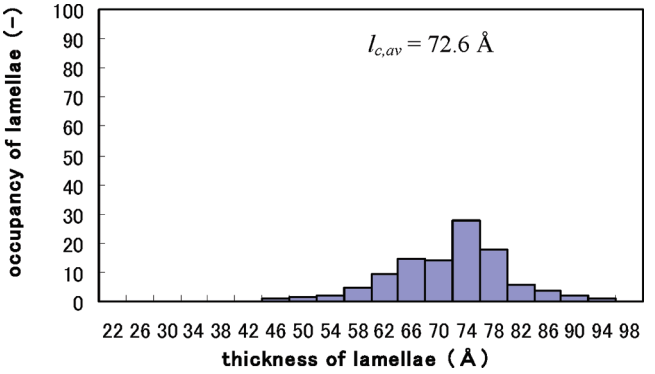


Figure 4. Lamella thickness distribution of ethylene/1-hexene copolymer mEH obtained from TEM images.

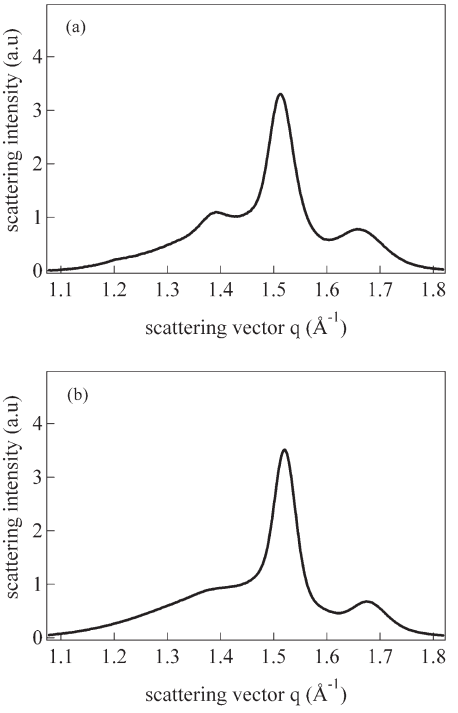


Figure 5. X-ray diffraction pattern of (a) ADMET EH39 and (b) ethylene/1-hexene copolymer mEH.

a typical orthorhombic scattering pattern as a whole; 110 and 200 reflections at q = 1.514 and 1.656 Å^{-1}, respectively, and an amorphous halo at q = 1.360 Å^{-1}, where $q = 4\pi/\lambda(\sin\theta)$ and θ is scattering angle. It is interesting that *n*-butyl branched polyethylene with a precise 38 carbon spacing gives an orthorhombic type crystal, the normal crystalline form of commercial polyethylenes, even though other precision-branched ADMET polyethylenes with shorter branch intervals (C15, C21) have monoclinic, triclinic, or hexagonal structures.[12,13,17,18,25] Therefore, it becomes obvious that a spacing of more than 20 carbons is necessary to form an orthorhombic crystal lattice. This observation seems to have similarity with observations for *n*-alkanes in terms of crystalline structure vs carbon number relationships; i.e., even numbered alkanes of $n \geq 38$ form orthorhombic crystal, while those of n less than 36 form triclinic or monoclinic (triclinic, $12 \leq n \leq 26$; monoclinic, $28 \leq n \leq 36$).[26,27]

As mentioned in a previous paper,[19] the amorphous diffraction of EH39 is sharper than that of commercial polyethylene, suggesting that the other crystalline form may overlap on the amorphous halo. Deconvolution of the

pattern by subtracting normal orthorhombic reflections gives a new small peak at $q = 1.353$ Å^{-1}. The intensity of this new peak and other diffraction peaks seems to be dependent on the cooling rate during sample preparation. The temperature-dependent polymorphism of ADMET EH39 is now being investigated. The copolymer mEH exhibited typical orthorhombic crystal reflections with the (110) plane at $q = 1.517$ Å^{-1} and the (200) plane at $q = 1.677$ Å^{-1} over the broad amorphous halo (Figure 5 (b)). The lattice dimensions calculated from reflection peaks are; $a = 7.540$ Å and $b = 4.961$ Å for EH39, and $a = 7.477$ Å and $b = 4.960$ Å for mEH. The slightly larger value of the lattice size of EH39 is attributed to the effect of a disordered interface area, where *n*-butyl branches are densely placed as a result of the exclusion of branches from the crystalline core.

As shown in Figure 6, SAXS data for ADMET EH39 show a sharp single scattering peak at long period of 60 Å, suggesting the presence of a narrow distribution of a higher structural ordering (fwhm $= 0.024$ Å^{-1}). The copolymer mEH exhibits a scattering peak at a lower scattering vector, corresponding to the long period of 117 Å at the peak position (fwhm $= 0.054$ Å^{-1}).

3.3. Thermal Behavior by DSC Measurements. Polymer EH39 exhibited a very sharp endothermic curve (Figure 7(a)) similar to that of the other *n*-butyl branched ADMET polyethylenes with 20 carbon spacings.[28] The sharp melting curve, which is less than 20 °C in width, indicates the high homogeneity of the crystalline structure. This is quite reasonable, considering the TEM and SAXS results described above. The addition copolymer mEH, on the other hand, gave a broad melting curve that ranged from 50 to 105 °C. Even though the two compounds have the same branch frequency, their peak melting temperatures were clearly different, with the T_m of the copolymer much higher at 98.9 °C. These results show the same trend as those for *n*-butyl branched ADMET polyethylene with a precise sequence (EH21; 48 branches/1000 backbone carbons. Comparisons were made with regular ADMET copolymers (sharp $T_m = 14$ °C) and ADMET copolymer with an irregular sequence by the copolycondensation between *n*-butyl branched diene monomer and nonbranched diene monomer (EH-43.5; 43.5 branches/1000 backbone carbons. Broad melting from −50 to +70 °C was observed for the irregular copolymer.[28] This suggests that introduction of the sequence length distribution by ADMET polycondensation method also gives a broad endothermogram indicative of a broad lamella thickness distribution, similar to that for the addition copolymerization of ethylene with 1-hexene.

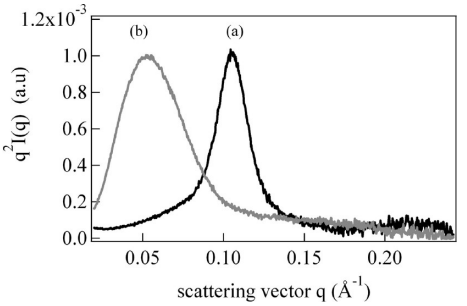


Figure 6. Small angle X-ray scattering pattern of (a) ADMET EH39 and (b) ethylene/1-hexene copolymer mEH.

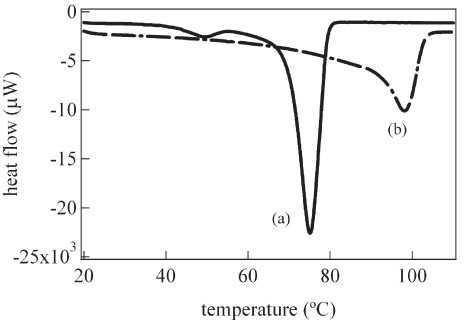


Figure 7. DSC endothermic curve of (a) ADMET polyethylene EH39 and (b) ethylene/1-hexene copolymer mEH.

4. Discussion

4.1. Average Lamella Thickness and Branch Participation in the Crystal.

4.1.1. ADMET Polyethylenes. The average lamella thicknesses obtained from TEM observation and that calculated from the long period (from SAXS peak position) as well as the volume crystallinity from WAXS, for ADMET EH39 and the ethylene/1-hexene copolymer mEH are shown in Table 2. It is interesting that lamella thicknesses obtained from those different experimental methods are quite comparable to each other for both samples. The last column in Table 2 is the CH_2 sequence length calculated by assuming that the CH_2-CH_2 bonds are in all *trans* zigzag conformation in the crystal. Consequently, it can be said that the lamella stem of EH39 is composed of a single CH_2 sequence between the consecutive *n*-butyl branches, and thus it provides presumptive evidence of complete exclusion of the *n*-butyl branch from the lamella stem. As shown in the previous paper,[17] the lamella thickness of ADMET polyethylene with *n*-hexyl branches on every 21st carbon was 25−26 Å. This value is clearly thinner than that of EH39 and corresponds to a single CH_2 sequence length between *n*-hexyl branches. As for the ethyl branch, it was concluded from the same type of data for ADMET polyethylene with precise 20 carbon spacers[17] that one ethyl branch per one crystalline stem can be included in the crystal judging from the lamella thickness of double the sequence length. Furthermore, Rojas et al.[16] measured the melting temperatures of a series of 20 carbon-spaced ADMET samples with various branches from methyl to adamantyl, and showed that they were approximately constant for the samples with branches longer than *n*-propyl, indicating that branches longer than *n*-propyl are excluded from the crystalline stem. The exclusion of bulkier branches from the crystalline phase would be thermodynamically favorable. On the other hand, one possible cause for methyl and ethyl branch inclusion in ADMET polyethylene is the thermodynamic favorability of

Table 2. Lamella Thickness of ADMET-PE and Ethylene/1-Hexene Copolymer

sample	SAXS L,[a] Å	[WAXS X_c,[b] %]	[l_c,[c] ($= LX_c$) Å]	TEM l_c,[d] Å	CH_2 sequence length l_c, Å
ADMET EH39	60	67	40	44.7	49.5[e]
C_2'/1-C_6' copolymer mEH	117	51	60	72.6	46.4[f]

[a] Long period from SAXS peak position. [b] Crystallinity (vol %) calculated from WAXS. [c] {long period} × {X_c} [d] Area based average lamella thickness by TEM for the melt crystallized sample. [e] Assumes that CH_2s are placed in a *trans* zigzag conformation in the crystal. *c*-axis length; 2.54 Å. [f] Calculated from the average ethylene sequence length; n_E (Table 3) measured by ^{13}C NMR. $n_E \times 2.54$ Å.

the thick crystalline phase involving these small branches compared to the thinner crystal that would result if the branches were excluded.

Consequently, for ADMET precisely equisequential polyethylenes, the lamella thickness is determined by the CH_2 sequence length between two consecutive branches in the case of branches longer than *n*-propyl. On the other hand, lamellae of double the CH_2 sequence length are formed by the inclusion of the branch in the crystal for ethyl-branched ADMET polyethylene.

4.1.2. Ethylene/α-Olefin Addition Copolymers. For the average lamella thickness of ethylene/α-olefin addition copolymers, it is clear that the comonomer content largely affects the thickness; the higher the content, the thinner the lamellae. This is because the average crystallizable ethylene sequence length decreases with increasing branching degree. However, it is not yet clear which length in the ethylene sequence distribution corresponds to the average lamella crystal thickness. The average ethylene sequence length can be obtained by ^{13}C NMR triad sequence analysis. As shown in the last column of Table 2, the average ethylene sequence length for the copolymer mEH obtained by ^{13}C NMR is considerably smaller than the average crystal thickness from TEM images and X-ray scattering. This indicates that the average crystal thickness of ethylene/1-hexene copolymer is not governed by the average ethylene sequence length, and that sequences longer than the average must play an important role in determining the average lamella thickness.

As for the effect of branching species of ethylene/α-olefin copolymers on the average crystal thickness, the tendency of branch inclusion in the crystal is considered significant because the branch inclusion produces thicker lamellae. Nitric acid etching followed by ^{13}C NMR spectrum measurement is a convenient and direct method to quantify the concentration of comonomer included in the crystalline phase for ethylene or propylene/olefin copolymers.[29−33] Our previous studies on melt-quenched ethylene/α-olefin copolymers showed that a bulkier comonomer has less tendency to be included in the crystalline phase compared to the smaller comonomer.[32] Consequently, the tendency of branch inclusion in the crystal was found to be reflected in the average lamella thickness of α-olefin copolymers.[10]

4.2. Sequence Length Distribution and Lamella Thickness Distribution. Unlike EH39, which has a uniform CH_2 sequence length between branches for every molecule, ethylene/1-hexene addition copolymer mEH possesses a statistical distribution of sequence lengths. Statistical data of triad sequence distribution, average sequence length and the product of reactivity ratio, r_1r_2, of the copolymer mEH, were calculated from the ^{13}C NMR spectrum according to the method of Hsieh and Randall,[20−22] and some of these data are listed in Table 3. Judging from the value of r_1r_2, this copolymer has an alternating tendency, and it is not a random copolymer statistically. Equilibrium crystal length distribution for copolymers with perpetuation probability (p) can be obtained by Flory's theory,[34] where w_n is the normalized weight fraction of the sequence of n ethylene units, according to the equation.

$$w_n = n(1-p)^2p^{n-1} \quad (1)$$

The probability p of statistical copolymer ($r_1r_2 \neq 1$) is related to r_1r_2 and the ethylene mol fraction (X_E) by eq 2 proposed by Allegra et al.[35]

$$p = 1 - \frac{1-[1-4(1-r_1r_2)X_E(1-X_E)]^{1/2}}{2(1-r_1r_2)X_E} \quad (2)$$

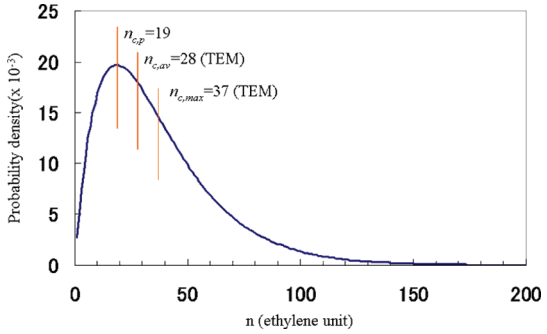


Figure 8. Ethylene sequence length distribution of ethylene/1-hexene copolymer mEH.

Table 3. Sequence Analysis of Ethylene/1-Hexene Copolymer mEH by ^{13}C NMR Spectrum

monomer content	ethylene (mol fraction)	0.95
	1-hexene (mol fraction)	0.05
average sequence length	ethylene monomer unit; n_E	18.27
reactivity ratio	r_1r_2	0.18

Table 4. Ethylene Sequence Unit Number for Ethylene/1-Hexene Copolymer Calculated by Various Methods

	n_E(NMR)[a]	n_c(TEM)[b]	n_c(DSC)[c]	n_E(calcd)[d]	n_c(TEM)/ n_E(NMR)
mEH	18.3	28.6	31.4	19	1.56

[a] Average ethylene unit by NMR (n_E in Table 3). [b] Average ethylene unit by TEM (l_c in Table 2 divided by c-axis length 2.54 Å). [c] Calculated from eqs 3 and 4 using DSC final melting temperature. [d] Ethylene unit at the peak probability density in the theoretical ethylene sequence distribution (Figure 8).

The calculated ethylene sequence length distribution for the copolymer mEH is shown in Figure 8. As shown in the figure, the average lamella thickness ($l_{c,av.}$) obtained from TEM observation does not coincide with the most probable sequence length at 18−19 ethylene units, corresponding to the average sequence length n_E of 18.3 calculated from ^{13}C NMR spectrum. The average and most probable lamella ($l_{c,av.}$ = 71 Å; average ethylene units, $n_{c,av.}$ = 28.1) is composed of 1.5 times the number of longer ethylene sequences compared to the most probable crystallizable sequence n_E (Table 4). And the observed maximum lamellae (~94 Å; n_c = 37) are formed from even longer ethylene sequences.

Although the crystallizable ethylene sequences theoretically vary over a very wide range, the actual crystallization in the longer and shorter sequence length region is hindered by the kinetic factors of secondary nucleation barriers and mass transport of especially long ethylene sequences, as indicated by Crist et al.[36] The shortest sequences may not form stable crystals and remain in the amorphous phase.

Next, the relationship between the observed lamella thickness and DSC endothermic curve has been verified. The equilibrium melting point of the copolymer (T_m^c), where the comonomer unit is excluded from the crystal, is described by Flory's equation, where T_m^0 is the melting point of the perfect crystal (418.7 K for polyethylene),[37] R is the gas constant, p is the ethylene perpetuation probability after revision by eq 2, and ΔH_u is the heat of fusion for a repeat unit (8.284 kJ/mol).[38]

$$\frac{1}{T_m^c} = \frac{1}{T_m^0} - \frac{R}{\Delta H_u} \ln p \quad (3)$$

The final melting temperature of the copolymer is correlated with the crystal sequence unit, n_c, by a modified Gibbs

equation,[39,40] where σ_e is the surface energy (90 mJ/m^2 for polyethylene[38]), and a_0 is the cross-sectional area of a chain (1.10×10^5 m^2/mol).[41]

$$T_m^f = T_m^c\left(1 - \frac{2\sigma_e a_0}{\Delta H_u n_c}\right) \quad (4)$$

The DSC final melting temperature (T_m^f) of the copolymer mEH (378.3K) is correlated with n_c of 31.4 using eqs 3 and 4, in close agreement with the average lamella thickness obtained from TEM observation (n_c = 28.1), and is far from the most probable ethylene sequence unit (n_c = 18−19). It is interesting that the observed lamella thickness by TEM observation is equivalent to that calculated from DSC final melting temperature, even though a few reports have shown that the DSC melting temperature does not correspond to the most probable ethylene unit and is dependent on the sequence randomness.[9,11,40,42−44]

ADMET polyethylenes exhibit narrower lamella thickness distributions and thinner average lamella thicknesses than ethylene/α-olefin addition copolymers of the same branching probability. This is likely due to the difference in the crystallization mechanism, which in turn is determined by the difference in the sequence structures of these two kinds of branched polyethylenes. ADMET polyethylene without any sequence length distribution is composed of CH_2 sequences of the same potential to crystallize. In other words, there is no sequence that crystallizes faster or slower than others, and thus the crystallization is considered rather suppressed. From our study on the crystallization behavior of ADMET polyethylene with ethyl or *n*-hexyl branches precisely spaced on every 21st carbon by WAXS and SAXS,[18] cooperative chain alignment would be the first step preceding the crystallization, and this type of crystallization through a cooperative chain alignment may be key to the formation of a uniform lamella thickness for ADMET polyethylene.

On the other hand, since the copolymers of ethylene and α-olefins prepared by addition polymerization have a statistical sequence distribution, there are ethylene sequences that are longer and shorter than the average. Longer sequences can crystallize more rapidly than the average length sequences to make thicker lamellae, and the crystallization of shorter sequences follows thereafter. This stepwise crystallization eventually causes a wide lamella thickness distribution for ethylene/α-olefin copolymers, as Mirabella[43,44] indicated from in situ AFM observations and DSC analysis. As for 1-butene copolymers, in addition to the effect of the sequence length distribution, inclusion of the ethyl branch in the crystal makes lamella thickness distribution broad and centered at larger thicknesses.[17]

5. Conclusion

In order to elucidate the effect of the intramolecular sequence heterogeneity on lamella crystal thickness and its distribution, ADMET-synthesized polyethylene with *n*-butyl branches precisely spaced on every 39th carbon (EH39) and an ethylene/1-hexene addition copolymer with the same branching probability were studied by TEM, WAXS, SAXS, DSC, and ^{13}C NMR. The ADMET polyethylene EH39, which has no sequence length distribution, showed a narrow lamella thickness distribution like the other ADMET samples with *n*-hexyl (EO21) or ethyl branch (EB21) on every 21st carbon which we reported previously. EH39 was found to have an orthorhombic crystalline form which is normal for commercialized polyethylenes and different from that of the other ADMET polyethylenes with shorter CH_2 spacing. The average lamella thickness ($l_{c,av.}$) of EH39 corresponds very closely to the space length between two consecutive branches, suggesting complete exclusion of *n*-butyl branches from the crystalline stem, just as in *n*-hexyl branched ADMET EO21 reported in our previous study. The $l_{c,av.}$ obtained from TEM images agrees well with that calculated from WAXS and SAXS. On the other hand, the 1-hexene addition copolymer forms 1.5 times thicker lamellae than the thickness predicted from the most probable ethylene sequence length obtained from ^{13}C NMR spectra and a theoretical sequence length distribution. This indicates that crystallization is dominated by the sparsely branched longer ethylene sequences that are statistically produced as a result of addition copolymerization.

For short chain-branched polyethylenes with a narrow intermolecular composition distribution, such as metallocene catalyzed LLDPE, intramolecular sequence length distribution and the identity of the branching species play key roles in determining the lamella thickness and thickness distribution.

Acknowledgment. The authors are grateful for Mr. S. Utsumi and Mr. S. Muramatsu for their enthusiastic experimental support. Support by the National Science Foundation in preparation of the polymers is gratefully acknowledged. Catalysis studies needed to produce the polymers of appropriate size were supported by the Army Research Office.

References and Notes

(1) Popli, R.; Mandelkern, L. *J. Polym. Sci., Polym. Phys. Ed* **1987**, *25*, 441.
(2) Kennedy, M.; Peacock, A.; Mandelkern, L. *Macromolecules* **1994**, *27*, 5297.
(3) Kennedy, M.; Peacock, A.; Failla, M.; Lucas, J.; Mandelkern, L. *Macromolecules* **1995**, *28*, 1407.
(4) Graham, J.; Alamo, R.; Mandelkern, L. *J. Polym. Sci., Polym. Phys. Ed.* **1997**, *35*, 213.
(5) Peacock, A.; Mandelkern, L.; Alamo, R.; Fatou, J. *J. Mater. Sci.* **1998**, *33*, 2255.
(6) Nitta, K.; Tanaka, A. *Polymer* **2001**, *42*, 1219.
(7) Nitta, K.; Takayanagi, M. *J. Macromol. Sci., Part B* **2003**, *B42*, 107.
(8) Hosoda, S.; Uemura, A. *Polym. J.* **1992**, *24*, 939.
(9) Hosoda, S. *Polym. J.* **1988**, *20*, 383.
(10) Hosoda, S.; Kojima, K.; Furuta, M. *Makromol. Chem.* **1986**, *187*, 1501.
(11) Hung, J.; Cole, A.; Waymouth, R. *Macromolecules* **2003**, *36*, 2454.
(12) Qiu, W.; Sworen, J.; Pyda, M.; Nowak-Pyda, E.; Habenschuss, A.; Wagener, K.; Wunderlich, B. *Macromolecules* **2006**, *39*, 204.
(13) Lieser, G.; Wegner, G.; Smith, J.; Wagener, K. *Colloid Polym. Sci.* **2004**, *282*, 773.
(14) Alamo, R.; Jeon, K.; Smith, R.; Boz, E.; Wagener, K.; Bockstaller, M. *Macromolecules* **2008**, *41*, 7141.
(15) Wei, Y.; Graf, R.; Sworen, J.; Cheng, C.; Bowers, C.; Wagener, K.; Spiess, H. W. *Angew. Chem., Int. Ed.* **2009**, *48*, 4617.
(16) Rojas, G.; Inci, B.; Wei, Y.; Wagener, K. *J. Am. Chem. Soc.* **2009**, *131*, 17376.
(17) Hosoda, S.; Nozue, Y.; Kawashima, Y.; Utsumi, S.; Nagamatsu, T.; Wagener, K.; Berda, E.; Rojas, G.; Baughman, T.; Leonard, J. *Macromol. Symp.* **2009**, *282*, 50.
(18) Nozue, Y.; Kawashima, Y.; Seno, S.; Nagamatsu, T.; Hosoda, S.; Berda, E.; Rojas, G.; Baughman, T.; Wagener, K. Manuscript in submission.
(19) Zuluaga, F.; Inci, B.; Nozue, Y.; Hosoda, S.; Wagener, K. *Macromolecules* **2009**, *42*, 4953.
(20) Randall, J. *J. Polym. Sci., Polym. Phys. Ed.* **1973**, *11*, 275.
(21) Hsieh, E.; Randall, J. *Macromolecules* **1982**, *15*, 353.
(22) Hsieh, E.; Randall, J. *Macromolecules* **1982**, *15*, 1402.
(23) Aggarwal, S.; Tilley, G. *J. Polym. Sci.* **1955**, *18*, 17.
(24) Hosoda, S.; Uemura, A.; ,, Shigematsu, Y.; Yamamoto, I.; Kojima, K. *Catalyst Design for Tailor-made Polyolefins*; Soga, K., Terano, M., Eds.; Kodansha: Tokyo, 1994, p365.
(25) Sworen, J.; Smith, J.; Wagener, K.; Baugh, L.; Rucker, S. *J. Am. Chem. Soc.* **2003**, *125*, 2228.
(26) Dorset, D. *Crystallography of the Polymethylene Chain*; Oxford University Press Inc.: New York, 2005; Chapter 3

(27) Craig, S.; Hastie, G.; Roberts, K.; Sherwood, J. *J. Mater. Sci.* **1994**, *4*, 977.
(28) Rojas, G.; Wagener, K. *Macromolecules* **2009**, *42*, 1934.
(29) Palmer, R.; Cobbold, A. *Makromol. Chem.* **1964**, *74*, 174.
(30) Maeda, Y.; Kanetsuna, H. *Polymer J.* **1981**, *13*, 357.
(31) Cagiao, M.; Rueda, D.; Caleja, F. B. *Polym. Bull.* **1980**, *3*, 305.
(32) Hosoda, S.; Nomura, H.; Gotoh, Y.; Kihara, H. *Polymer* **1990**, *31*, 1999.
(33) Hosoda, S.; Hori, H.; Yada, K.; Nakahara, S.; Tsuji, M. *Polymer* **2002**, *43*, 7451.
(34) Flory, P. J. *Trans Faraday Soc.* **1955**, *51*, 848.
(35) Allegra, G.; Marchessault, R.; Bloembergen, S. *J. Polym. Sci., Polym. Phys. Ed.* **1992**, *30*, 809.
(36) Crist, B.; Howard, P. *Macromolecules* **1999**, *32*, 3057.
(37) Mandelkern, L.; Alamo, R. In *Physical Properties of Polymers Handbook*; Mark, J., Ed.; American Institute of Physics: Woodbury, NY, 1996; Chapter 11
(38) Hoffman, J.; Miller, R. *Polymer* **1997**, *38*, 3151.
(39) Sanchez, I.; Eby, R. *Macromolecules* **1975**, *8*, 639.
(40) Crist, B.; Mirabella, F. *J. Polym. Sci., Polym. Phys.* **1999**, *37*, 3131.
(41) Clark, E. In *Physical Properties of Polymers Handbook*; Mark, J., Ed; American Institute of Physics: Woodbury, NY, 1996; Chapter 30
(42) Mirabella, F.; Crist, B. *J. Polym. Sci., Polym. Phys. Ed.* **2004**, *42*, 3416.
(43) Mirabella, F. *J. Polym. Sci., Polym. Phys. Ed.* **2006**, *44*, 2369.
(44) Mirabella, F. *J. Appl. Polym. Sci.* **2008**, *108*, 987.

320 *Macromolecules* **2011**, *44*, 320–324
DOI: 10.1021/ma102348g

Macromolecules
ARTICLE

Hybrid Solvents Incubated $\pi-\pi$ Stacking in Quenched Conjugated Polymer Resolved by Multiscale Computation

Cheng K. Lee,[†] Chi C. Hua,*[,†] and Show A. Chen[‡]

[†]*Department of Chemical Engineering, National Chung Cheng University, Chia-Yi 621, Taiwan, R.O.C., and* [‡]*Department of Chemical Engineering, National Tsing Hua University, Hsin-Chu 30013, Taiwan, R.O.C.*

Received October 14, 2010; Revised Manuscript Received December 9, 2010

ABSTRACT: Multiscale computations were utilized to resolve the detailed solvent−polymer interactions in binary (aliphatic/aromatic) solvent media of a standard amphiphilic conjugated polymer, poly(2-methoxy-5-(2′-ethylhexyloxy)-1,4-phenylenevinylene) (MEH-PPV), revealing an unequivocal pathway specific solvents or hybrid solvents impact the nanomorphology in the eventual quenching state. The significant finding is that, through sophisticatedly compromised, local-phase solvent particle distribution encompassing the polymer chain, certain solvent compositions (i.e., chloroform/chlorobenzene = 2:1 and chloroform/toluene = 1:1 in number density) were noted to bolster exceptional, highly extended chain conformations in solution, which in turn greatly facilitate the incubation of ordered $\pi-\pi$ stacking upon solvent evacuation via a relatively regular chain folding along the pivotal tetrahedral defects. Overall, the simulation helps clarify a long-standing ambiguity as to the molecular effects of specific solvents and, in particular, unveils previously unnoticed physics underlying the promising features of hybrid solvents in casting polymer thin films, as evidenced by recent experiments.

Introduction

Conducting conjugated polymers have nowadays become a popular molecular material for fabricating solution-processable polymer light-emitting diodes (PLED)[1−3] and plastic solar cells.[4−6] Among the most appealing features of exploiting long-chain organic semiconductors is the possibility of fine-tuning the optoelectronic behavior of solution-cast films by selecting different solvents or hybrid solvents.[7,8] Intrinsic stiffness arising from the conjugated chain backbone, however, has rendered the polymer generally poor solubility in usual organic solvents, and hence most practically used conducting conjugated polymers involve grafting various types and amounts of flexible alkyl/alkoxy side chains to the rigid phenyl backbone. The resulting amphiphilicity with respect to various types of solvent species, in turn, gives rise to a vast swath of possible chain conformations and aggregation morphologies, first in solution and later in the quenching film. To date, the actual (microscopic and localized) polymer−solvent interactions regulating elementary chain conformations from solution to the quenching state remain elusive and are difficult to be assessed by experimental methods.

Considering a standard case with poly(2-methoxy-5-(2′-ethylhexyloxy)-1,4-phenylenevinylene) (MEH-PPV; see a sketch in Figure 1) in a novel multiscale simulation, we address in this paper two fundamental issues imperative to the upcoming applications of conducting conjugated polymers: (1) In which ways may solvent-induced chain conformations directly impact the quenching morphologies, especially in view of the formation of ordered $\pi-\pi$ stacking that is generally deemed favorable for film or device performance improvement? (2) In this context, and considering the amphiphilicity of the polymer, can the use of hybrid solvents be advantageous at all? Answers to these still debating, sometimes controversial, issues should provide in-depth insights into the highly demanded, fine morphological controls in thin films made of prevalent polymer semiconductors.

*Corresponding author. E-mail: chmcch@ccu.edu.tw.

For the two binary (aliphatic/aromatic) solvent media investigated, i.e., chloroform/chlorobenzene (CF/CB) and chloroform/toluene (CF/T), the simulation has contributed to the first revelation of anomalous solvent particle distributions within a local-phase regime of MEH-PPV, which we demonstrate to have significant impact not only on the accessible chain conformations in solution but also for the incubation of ordered $\pi-\pi$ stacking in the quenching state. Thus, the simulation helps clarify a long-standing ambiguity as to the molecular effects of specific solvents and, in particular, unveils previously unnoticed physics underlying the promising features of hybrid solvents in casting polymer thin films, as evidenced by recent experiments.[9,10] The prime results and implications are summarized in the following sections, after a brief introduction is provided to a multiscale scheme capable of capturing single MEH-PPV chains from solution to the quenching state.

Simulation Protocols

The basic ideas underlying this multiscale computation originate from a recent progress in circumventing several inherent difficulties in capturing single-chain conformations from solution to the quenching state for high-molecular-weight polymers as typically studied in experiments.[11] And the present simulation of MEH-PPV represents the first attempt to substantiate the ideas into practically interested material properties of a standard conjugated polymer. The simulation begins with the construction of a new coarse-grained (CG) polymer model for MEH-PPV that is much more efficient for investigating the solution-state chain conformations than the counterpart full-atom model. Figure 1 depicts how a (all-trans) MEH-PPV chain may be coarse-grained by introducing suitable "superatoms" to represent essential molecular units—in this case, the repeating phenyl backbone unit and two asymmetric alkoxy side-chain groups. Likewise, solvent molecules are cast into single CG "beads" of similar size. All CG particles are mapped at the mass centers and converse the full masses of the molecular units they represent. The next step is typical of prevailing CG simulations of long-chain molecules,[11−35]

 Published on Web 12/23/2010 © 2010 American Chemical Society

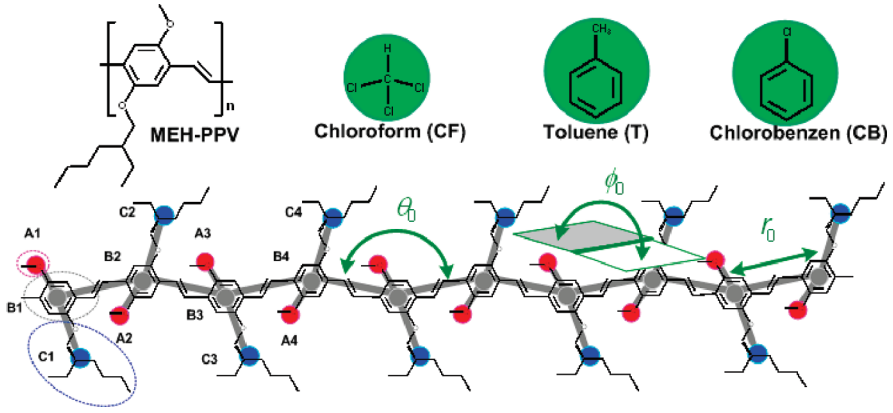


Figure 1. Specifications of a few representative bond length and angles for the CG model of MEH-PPV, where B, A, and C denote the aromatic backbone, short alkoxy, and long alkoxy side chains, respectively.

and the details can be found in previous work[11,31,35] as well as in the Supporting Information. Basically, the procedure involves the construction of self-consistent, parameter-free, intra- (bonded) or intermolecular (nonbonded) potentials governing the CG particles by using the Boltzmann inversions of essential statistical trajectories gathered from atomistic molecular dynamics (AMD) simulations of the original, atomistic models for the polymer and solvents, respectively. Additional iterative and optimization procedures are usually required in establishing the CG intermolecular potentials to account for the effect of many-body interactions. Afterward, the predicted bond-length and bond-angle (see definitions in Figure 1) distributions for a MEH-PPV oligomer from AMD and CG simulations (the latter utilizing the CG force fields already established), respectively, are checked for self-consistency and so are the predicted radial distribution functions (RDFs) for individual CG particle baths or their mixtures.

Note that the proposed CG polymer model differs from a recent one[31] in that the two side-chain groups are treated as independent CG particles rather than being lumped into the backbone unit, so as to discriminate the chemical affinities of different types of solvent molecules with respect to various parts of the polymer chain. Moreover, tetrahedral defects—a localized breakage of single/double-bond conjugation—are incorporated and assigned uniformly to every 10 repeating units on the polymer backbone in order to realistically capture the collapsed morphologies of real synthesized chains during the quenching process,[36,37] which is simulated separately by a back-mapping scheme described later. Early experiments appear to suggest that the degree of tetrahedral defects could, in general, fall below 10%,[38] yet the actual amount of defects is difficult to estimate precisely. The following results were obtained for a 300-mers MEH-PPV, close to the chain lengths of a commercial sample commonly utilized in experiment. To ensure the capability of the proposed CG system for capturing essential polymer−solvent interactions, a 10-mers MEH-PPV suspended in a binary solvent medium, i.e. CF/CB = 2:1 in number density, was first investigated in a benchmark simulation for both atomistic and CG model systems, and the predicted solvent−polymer pair distributions (see a later discussion) indicated a good agreement between the two. Both AMD and CG simulations (see Supporting Information for details) utilized the *NPT* ensemble at $T = 298$ K and $P = 1$ atm, with the same software package as described in a previous work, where the incorporated force fields were noted to lead to generally good agreement with known experimental features of MEH-PPV in solution.[31]

Results and Discussion

Solution-State Chain Conformations. Within the CG model systems described above, coarse-grained molecular dynamics (CGMD) simulations were carried out following the Newton's equations of motion for all CG particles. The results shown in Figures 2−4 were based on time (over a period of 2.5 ns) plus ensemble (for 10 independent chains) averaging for a CG model system that has been pre-equilibrated with standard Monte Carlo schemes. First, the mean radii of gyration of single MEH-PPV chain in various single- or binary-solvent media are shown in Figure 2. Note that the mean coil size often serves as a direct measure of the so-called solvent quality for the polymer in a specific solvent. Thus, the results given in Figure 2 reveal a significant feature that binary solvents of certain compositions (i.e., CF/CB = 2:1 or CF/T = 1:1) may lead to an effective solvent quality notably exceeding the ones for the two individual single solvents. The anomaly is most prominent for the case with CF/CB = 2:1, where highly extended chain conformations can frequently be noted, as partly shown by the snapshots given in Figure 4. In contrast, much collapsed chain conformations were typically noted at other mixing ratios.

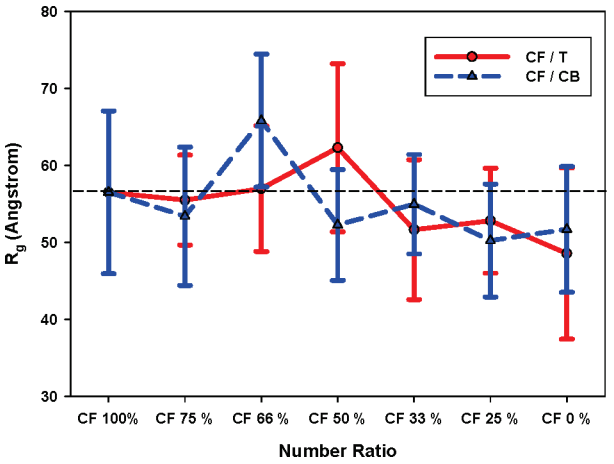


Figure 2. Predicted mean radius of gyration for single 300-mer MEH-PPV chains in single- or binary-solvent system at 298 K and 1 atm. The lines are utilized to guide the overall trend.

Given that CF arguably represents the best solvent known so far for MEH-PPV, the even surpassing solvent qualities noted in Figure 2 for two specific binary solvent media seem to be exceptional and have motivated a scrutiny into the underlying polymer−solvent interactions. An interesting general implication of the above observations with MEH-PPV is that the effective solvent quality of amphiphilic polymer solution may, to some extent, be further improved

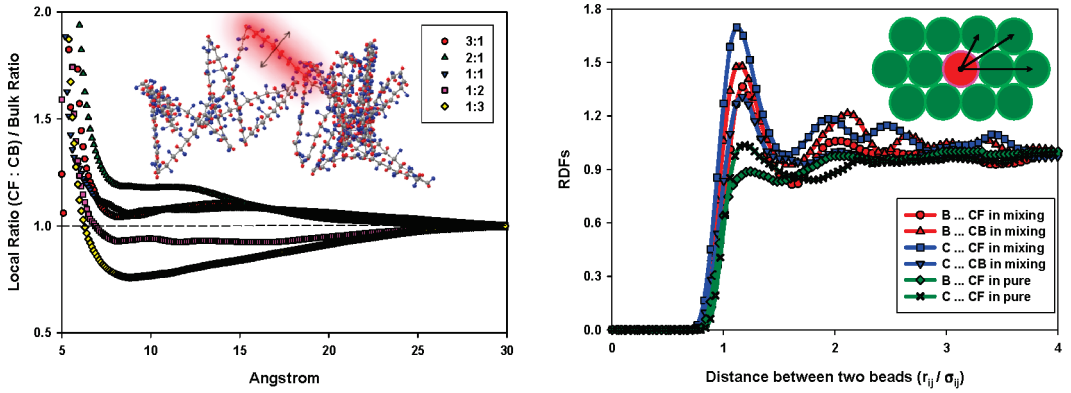


Figure 3. (a) Solvent particle distributions measured as a normal distance away from the polymer backbone in the CF/CB binary-solvent medium of MEH-PPV. (b) The RDFs (for CF/CB = 2:1) reflecting the distributions of solvent molecules with respect to the backbone (B) or the long-alkoxy side chain (C) of the polymer; the results for single-solvent CF system are also shown for comparison. The distance in (b) has been normalized using the mean van der Waals diameters of the two CG particles involved.

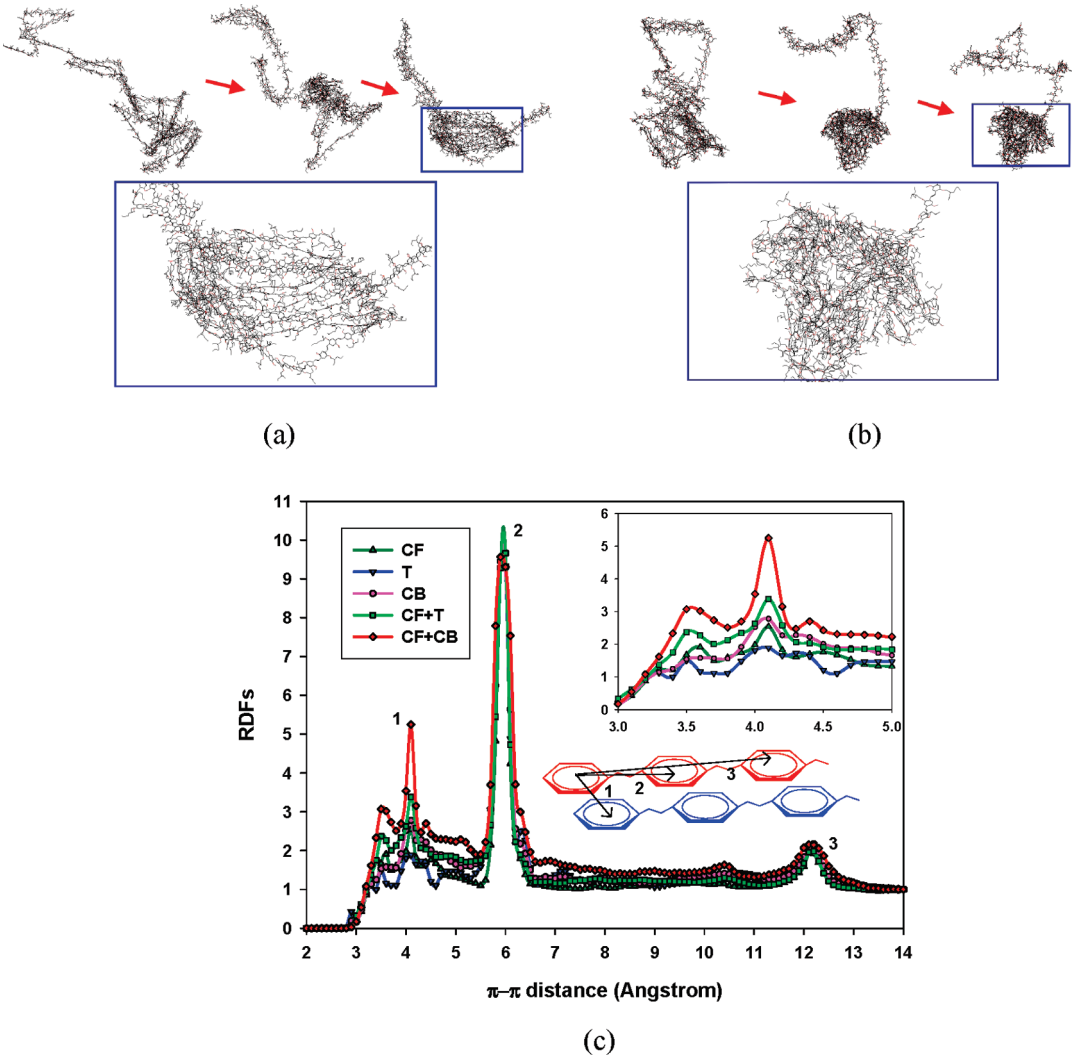


Figure 4. Snapshots of a single 300-mer MEH-PPV chain quenched from (a) a binary-solvent medium, CF/CB = 2:1, and (b) a single-solvent system, T. (c) RDFs revealing the formation of ordered $\pi-\pi$ stacking for a single MEH-PPV chain quenched from various solvent media, where the inset shows the zoomed plot that best illuminates the relative partition of $\pi-\pi$ stacking (at ca. 4.1 Å).

by exploiting hybrid solvents. In the following discussion, we focus on the case with CF/CB binary-solvent system of MEH-PPV; the general observations apply to CF/T system equally well.

Solvent Particle Distributions in Hybrid Solvent Media. To resolve the polymer−solvent interactions, we have examined the detailed solvent particle distributions in the vicinity of the MEH-PPV chain. As schematically shown in Figure 3a, the

distance has been measured in a normally outward direction of each backbone unit. It is significant to notice the ubiquity of a "boundary layer", ca. 2.5 nm in thickness, within which the ratio of the two different solvent particles derails the bulk one considerably. In particular, the (positive) deviation seems to be most prominent at a mixing ratio of CF/CB = 2:1, for which the mean coil size in Figure 2 was also suggestive of an optimal solvent quality. Similar features have been noted for the binary-solvent system with CF/T = 1:1. On the other hand, the first (and dominant) peak appearing in the RDF of Figure 3b clearly indicates that while CF molecules are considerably more attractive to the alkoxy side-chain units (C) of MEH-PPV, CB molecules are slightly more attractive to the backbone (B). An intriguing feature is that both curves (i.e., C−CF and B−CB) display conspicuous oscillations beyond the first peak, a phenomenon rarely observed with single-solvent systems. The sketch given in the same figure suggests this peculiar feature could be indicative of a somewhat ordered, lattice-like structure of solvent molecules encompassing the polymer units that are attractive to them. Another significant finding is that, as one compared the RDFs with the ones for single-solvent (pure) CF system, there is evidently a much greater partition of CF molecules enclosing the MEH-PPV chain in the CF/CB = 2:1 binary solvent medium. That is, without the presence of CB molecules, CF is normally depleted from the polymer territory, possibly to avoid the backbone molecules.

Overall, we suggest the following physical picture to accommodate the anomalous features noted above, which have intriguing consequences as we discuss momentarily on the quenched-chain morphologies. The role played by CB molecules in the CF/CB hybrid solvent system of MEH-PPV is twofold: They attract, and thus "stabilize", the MEH-PPV backbone, preventing too collapsed a chain conformation, especially with the presence of the "disliked" CF molecules that are to be avoided by the phenyl backbone. On the other hand, they help shield the "repulsions" directly between CF and MEH-PPV backbone, thus encouraging immigration of CF molecules into the "boundary layer" regime to attract the side-chain groups more effectively. Altogether, this sophisticatedly compromised, local molecular environment warrants the sustainability of exceptional, highly extended MEH-PPV chains—*which obviously require a free exposure of both the side-chain and backbone units that can only be fulfilled in a hybrid-solvent medium for an amphiphilic polymer like MEH-PPV*. Further, compared with toluene (T) molecules, the somewhat amphiphilic attribute of CB is expected to be a superior "mediator" to play the essential roles as suggested above, besides its better affinity to the CF molecule as well. Note, however, that as CF molecules progressively migrate into the boundary layer regime, they must do so against the bulk osmotic pressure, until an eventual balance between the two "phases" has been established. Thus, the peculiar features manifested by Figures 2 and 3 may be perceived as arising from a subtle balance between local-phase chemical affinities and bulk-phase osmotic pressure—the latter being basically entropic in nature.

Quenched-Chain Nanomorphology and $\pi-\pi$ Stacking. The other primary goal of this simulation is to uncover the exact pathway through which solvent-induced chain conformation might dictate the quenched-chain morphologies upon solvent evacuation. Thus, we performed a systematic backmapping to return the CG model system to full-atom representations in a way as detailed before,[11,35] so as to account for the effects of localized, anisotropic $\pi-\pi$ interactions that cannot be captured in the CG polymer model, although this specific interaction force plays only minor roles in affecting fundamental chain structures in solution, where thermal agitations of the solvent molecules significantly impede the efficacy of highly anisotropic interactions in dilute, semiflexible polymer solution.[11] In Figure 4a,b, two representative cases are examined, revealing the detailed mechanisms of chain quenching as subject to their prior solvent-induced chain conformations. Note that the quenching process simulated here, with an instant solvent evacuation, represents a considerably simplified scenario that is aimed to capture the most elementary molecular features independent of the details of a real film casting. The simulation of chain quenching was carried out in a vacuum, *NVT* environment at the same system temperature (i.e., 298 K), and the time required for a complete chain collapsing is estimated to be ca. 2.0 ns based on the time-dependent mean radius of gyration of the quenched chain. In fact, such an extremely short period compared with the time scales associated with typical film casting might, at least in part, be utilized to justify omitting the effects of solvent evaporation rate.

It is evident that a previously extended and loose chain conformation, such as that formed in the CF/CB = 2:1 medium, permits a relatively regular chain folding along the pivotal tetrahedral defects and, in turn, results in a notably higher degree of ordered $\pi-\pi$ stacking, which promotes the electronic delocalization quintessential for local charge transports. Note, in particular, that the eventual quenching structure shown in Figure 4a has been arrested by localized, anisotropic $\pi-\pi$ interactions. In contrast, for a previously compact chain conformation, such as that formed in toluene and shown in Figure 4b, the quenched chain ubiquitously becomes much collapsed and featureless due to the predominant, isotropic van der Waals segmental interactions. Quantitatively, Figure 4c (which has been created using time plus ensemble averaging as noted earlier) shows the RDFs revealing the fingerprint of ordered $\pi-\pi$ stacking, which bears a characteristic center-to-center distance about 4.1 Å—or about 3.5 Å for the vertical distance between the two phenyl planes, as is more often referred to—for MEH-PPV chains quenched from various solvent media. Clearly, the chain quenched from the CF/CB = 2:1 solvent medium accommodates the greatest amount of $\pi-\pi$ stacking, about 60% higher than the second place for CF/T = 1:1 medium and substantially surpassing the rest single-solvent systems. Moreover, a close correspondence between the mean coil size (or effective solvent quality) in solution, as revealed in Figure 2, and the degree of $\pi-\pi$ stacking in the quenching state can be observed. An interesting exception should be noted, however, with the case of single-solvent CB medium, which apparently results in a higher degree of $\pi-\pi$ stacking despite a smaller mean coil size than in the single-solvent CF medium. The disparity may be explicated by noting that the CB-induced backbone exposure—as contrasted with the CF-induced side-chain exposure—of MEH-PPV evidently serves as an advantageous precursor for the subsequent $\pi-\pi$ stacking. Thus, not only does the overall chain expansion in solution matter, the detailed solvent-induced chain conformation has an important impact on quenched-chain morphologies as well.

To this end, some recent experimental trends are worth noting. Although most experiments conducted involving the use of hybrid solvents for conjugated polymers including MEH-PPV displayed the more regular features as might be foreseen on the basis of simple mixing rules, there were a few occasions when observations evidently defy this commonplace trend. First, we mention that the systematic measurements recently conducted by Chen's group[10] have clearly indicated that the film and device performances of

MEH-PPV can be substantially improved by mixing CF with CB at a volume ratio of CF/CB = 3:1, which is close to a number ratio of CF/CB = 2:1 as simulated here. They have attributed the general improvement to the formation of spatially homogeneous distribution of ordered structures (well-packed chains and/or aggregates), with yet unknown mechanisms. For solution samples, the photoluminescence features (Figure 2 in ref 9) reported by Zhang and co-workers for MEH-PPV in the hybrid solvent medium chloroform/cyclohexane inhabited a clearly nonsystematic trend with varying compositions, resembling the phenomenon seen in Figure 2. No similar features were noted, however, for the other solution system made of chloroform and methanol, two solvents that are more alike.

Conclusions

This multiscale simulation of a standard amphiphilic conjugated polymer has unraveled an unequivocal pathway via which specific solvents or hybrid solvents may be exploited to control ordered nanostructures—the $\pi-\pi$ stacking—in the quenching state. The sophisticatedly compromised, local-phase molecular environment as has been disclosed for two representative binary (aliphatic/aromatic) solvent media of MEH-PPV not only renders in-depth insight into fine morphological controls in amphiphilic polymer solution but also points to the open opportunity of propelling the frontier performances of conjugated polymer thin films when cast from optimum hybrid solvent media.

Acknowledgment. The authors thank the reviewers for useful comments/suggestions. This work is supported by the National Science Council of ROC under Grant NSC99-2120-M007-012. Resources provided by the National Center for High-Performance Computing are also acknowledged.

Supporting Information Available: Detailed system descriptions, comparisons between the CG and AMD simulations on the predicted bond length/angle distributions (Figure S1), RDFs of individual particle baths (Figure S2), and RDFs of polymer−solvent pairs in CF/CB = 2:1 medium (Figure S3) as well as all potential functions and parameters (Table S1). This material is available free of charge via the Internet at http://pubs.acs.org.

References and Notes

(1) Burroughes, J. H.; Bradley, D. D. C.; Brown, A. R.; Marks, R. N.; Mackay, K.; Friend, R. H.; Burn, P. L.; Holmes, A. B. *Nature* **1990**, *347*, 539.
(2) Braun, D.; Heeger, A. J. *Appl. Phys. Lett.* **1991**, *58*, 1982.
(3) Friend, R. H.; Gymer, R. W.; Holmes, A. B.; Burroughes, J. H.; Mark, R. N.; Taliani, C.; Bradley, D. D. C.; Dos Santos, D. A.; Brlédas, J. L.; Löglund, M.; Salaneck, W. R. *Nature* **1999**, *397*, 121.
(4) Yu, G.; Gao, J.; Hummelen, J. C.; Wudl, F.; Heeger, A. J. *Science* **1995**, *270*, 1789.
(5) Günes, S.; Neugebauer, H.; Sariciftci, N. S. *Chem. Rev.* **2007**, *107*, 1324.
(6) Dennler, G.; Scharber, M. C.; Brabec, C. J. *Adv. Mater.* **2009**, *21*, 1323.
(7) Nguyen, T. Q.; Doan, V.; Schwartz, B. J. *J. Chem. Phys.* **1999**, *110*, 4068.
(8) Shi, Y.; Liu, J.; Yang, Y. *J. Appl. Phys.* **2000**, *87*, 4254.
(9) Zhang, H.; Lu, X.; Li, Y.; Ai, X.; Zhang, X.; Yang, G. *J. Photochem. Photobiol. A* **2002**, *116*, 143.
(10) Chen, M. C.; Hung, W. C.; Su, A. C.; Chen, S. H.; Chen, S. A. *J. Phys. Chem. B* **2009**, *113*, 11124.
(11) Lee, C. K.; Hua, C. C.; Chen, S. A. *J. Phys. Chem. B* **2009**, *113*, 15937.
(12) Tschöp, W.; Kremer, K.; Batoulis, J.; Bürger, T.; Hahn, O. *Acta Polym.* **1998**, *49*, 61.
(13) Reith, D.; Meyer, H.; Müller-Plathe, F. *Macromolecules* **2001**, *34*, 2335.
(14) Shelley, J. C.; Shelley, M. Y.; Reeder, R. C.; Bandyopadhyay, S.; Klein, M. L. *J. Phys. Chem. B* **2001**, *105*, 4464.
(15) Fukunaga, H.; Takimoto, J. I.; Doi, M. *J. Chem. Phys.* **2002**, *116*, 8183.
(16) Faller, R.; Reith, D. *Macromolecules* **2003**, *36*, 5406.
(17) Reith, D.; Pütz, M.; Müller-Plathe, F. *J. Comput. Chem.* **2003**, *24*, 1624.
(18) Clancy, T. C. *Polymer* **2004**, *45*, 7001.
(19) Faller, R. *Polymer* **2004**, *45*, 3869.
(20) Marrink, S. J.; de Vries, A. H.; Mark, A. E. *J. Phys. Chem. B* **2004**, *108*, 750.
(21) Boek, E. S.; Padding, J. T.; den Otter, W. K.; Briels, W. J. *J. Phys. Chem. B* **2005**, *109*, 19851.
(22) Li, X.; Ma, X.; Huang, L.; Liang, H. *Polymer* **2005**, *46*, 6507.
(23) Harmandaris, V. A.; Adhikari, N. P.; van der Vegt, N. F. A.; Kremer, K. *Macromolecules* **2006**, *39*, 6708.
(24) Li, X.; Kou, D.; Rao, S.; Liang, H. *J. Chem. Phys.* **2006**, *124*, 204909.
(25) Shih, A. Y.; Arkhipov, A.; Freddolino, P. L.; Schulten, K. *J. Phys. Chem. B* **2006**, *110*, 3674.
(26) Carbone, P.; Negri, F.; Müller-Plathe, F. *Macromolecules* **2007**, *40*, 7044.
(27) Santangelo, G.; Matteo, A. D.; Müller-Plathe, F.; Milano, G. *J. Phys. Chem. B* **2007**, *111*, 2765.
(28) Spyriouni, T.; Tzoumanekas, C.; Theodorou, D.; Müller-Plathe, F.; Milano, G. *Macromolecules* **2007**, *40*, 3876.
(29) Carbone, P.; Varzaneh, H. A. K.; Chen, X.; Müller-Plathe, F. *J. Chem. Phys.* **2008**, *128*, 064904.
(30) Karimi-Varzaneh, H. A.; Carbone, P.; Müller-Plathe, F. *J. Chem. Phys.* **2008**, *129*, 154904.
(31) Lee, C. K.; Hua, C. C.; Chen, S. A. *J. Phys. Chem. B* **2008**, *112*, 11479.
(32) Noid, W. G.; Chu, J. W.; Ayton, G. S.; Krishna, V.; Izvekov, S.; Voth, G. A.; Das, A.; Andersen, H. C. *J. Chem. Phys.* **2008**, *128*, 244114.
(33) Noid, W. G.; Liu, P.; Wang, Y.; Chu, J. W.; Ayton, G. S.; Izvekov, S.; Andersen, H. C.; Voth, G. A. *J. Chem. Phys.* **2008**, *128*, 244115.
(34) Peter, C.; Site, L. D.; Kremer, K. *Soft Matter* **2008**, *4*, 859.
(35) Lee, C. K.; Hua, C. C.; Chen, S. A. *J. Chem. Phys.* **2010**, *133*, 064902.
(36) Hu, D.; Yu, J.; Wong, K.; Bagchi, B.; Rossky, P. J.; Barbara, P. F. *Nature* **2000**, *405*, 1030.
(37) Sumpter, B. G.; Kumar, P.; Mehta, A.; Barnes, M. D.; Shelton, W. A.; Harrison, R. J. *J. Phys. Chem. B* **2005**, *109*, 7671.
(38) Inigo, A. R.; Chiu, H. C.; Fann, W.; Huang, Y. S.; Jeng, U. S.; Hsu, C. H.; Peng, K. Y.; Chen, S. A. *Synth. Met.* **2003**, *139*, 581.

Macromolecules
ARTICLE

Macromolecules **2011**, *44*, 325–333 **325**
DOI: 10.1021/ma101745p

Measuring Diffusion Coefficients of Nitroxide Radicals in Heterophasic Propylene−Ethylene Copolymers by Electron Spin Resonance Imaging

Krzysztof Kruczala[†,‡] **and Shulamith Schlick***[,†]

[†]*Department of Chemistry and Biochemistry, University of Detroit Mercy, 4001 West McNichols Road, Detroit, Michigan 48221, United States, and* [‡]*Faculty of Chemistry, Jagiellonian University, Ingardena 3, 30-060 Krakow, Poland*

Received July 31, 2010; Revised Manuscript Received December 17, 2010

ABSTRACT: Heterophasic propylene-ethylene copolymers (HPECs), also known as impact-modified polypropylene copolymers (IPC), are an important class of materials because of their attractive mechanical properties and low cost. Their chemical composition and phase heterogeneity have important effects on the physical and mechanical properties of these systems. Commercially used HPECs usually contain stabilizers such as hindered amines, which can be lost by diffusion (blooming). We present the measurement of the diffusion coefficient of nitroxide radicals by electron spin resonance imaging (ESRI); the radicals were obtained by oxidation of the commercial Tinuvin 770 hindered amine stabilizer (HAS) with *m*-chloroperoxybenzoic acid and consist of a mixture of mono- and biradicals. The diffusion rates were measured in two polymers, HPEC1 and HPEC2, which differed in the ethylene (E) to propylene (P) ratio, 25:75 and 10:90 wt %, respectively. One dimensional (1D) ESRI allowed the visualization of the radical distribution ("profiles") within the sample as a function of storing time at 393 K. Simulation of this distribution led to the determination of the macroscopic diffusion coefficients, *D*, of the paramagnetic tracer in HPEC1 and HPEC2. The results indicate that the main factor determining the diffusion rates in these polymers is the amount of the crystalline phase, mostly composed of isotactic polypropylene (iPP). The *D* value was the same within experimental error in both systems, 1.42×10^{-8} cm^2 s^{-1}. Comparison with literature data of the temperature variation of *D* for the same diffusant in polyethylene (PE) and polypropylene (PP) suggest that in both HPEC1 and HPEC2 the diffusion takes place in the amorphous phase restrained by the proximity of the crystalline domains. The results also indicate that ≈20% of the diffusant is lost by evaporation ("blooming"). Results of spectral-spatial 2D ESRI show that the ESR spectra of the nitroxides do not change significantly along the sample length during diffusion, suggesting that the loss of stabilizer is due to diffusion and not to chemical reactions.

Introduction

Degradation of polymers by the action of chemical agents, heat, mechanical stresses, or ultraviolet radiation in the presence of oxygen is the polymer equivalent to corrosion of metals. The term "degradation of polymers" includes all changes in the chemical structure and physical properties of the polymers as a result of external chemical or physical agents. Oxidative degradation of polymers is due to the formation of reactive free radicals such as R$^\bullet$ and ROO$^\bullet$, and of hydroperoxides ROOH.[1−4] The chemical structure can be modified due to chain scission, cross-linking, formation of double bonds, and increase or decrease of the molecular mass. The degradation chemistry is complicated because even small amounts of chromophores, free radicals, and metallic species from polymerization reactions can introduce additional reaction pathways that enhance the rate of degradation. The deleterious effects are often not detected immediately but may develop over periods of months or even years. While the time scale of structure changes may vary, the final results are degradation of the structure and collapse of the mechanical properties.

Research on the effects of radiation and thermal treatment of polymeric materials is focused on several major goals: understanding the degradation mechanism, predicting polymer lifetimes, and developing protective additives.[5−9] Hindered amine stabilizers (HAS) are often used for stabilization of polymeric materials. Nitroxides and hydroxylamines are major products of reactions involving HAS. The HAS-derived nitroxides (HAS-NO) are thermally stable, but can scavenge free radicals to yield diamagnetic species; the hydroxylamines can regenerate the original amine, thus resulting in an efficient protective effect. Some of these events are shown in Scheme 1, where >NH denotes the amine, >NO$^\bullet$ the nitroxide, and R$^\bullet$, ROO$^\bullet$, and ROOH the reactive intermediates derived from polymer chains exposed to oxygen and irradiation or heat.

The spatial distribution of polymer properties during degradation is critical for an understanding of the underlying mechanism, and methods for its determination have been developed: density profiling measures the change in density, which is expected to increase in aged samples, along the irradiation depth;[10] and modulus profiling measures the tensile modulus, which decreases during degradation.[10,11] The spatial variation of these properties is an excellent indicator of degradation, especially at advanced stages in the degradation process. Both profiling methods are *destructive*: The sample is cut into sections and each section is studied separately. However, cutting a crystalline polymer sample can lead to morphological changes; for this reason *nondestructive* methods are preferable.

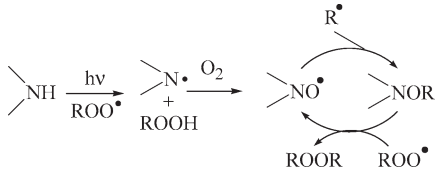
Electron spin resonance imaging (ESRI) is capable of providing spatial details on the evolution of the degradation process within sample depth in a nondestructive way.[12] Important papers

*Corresponding author. Telephone: 1-313-993-1012. Fax: 1-313-993-1144, E-mail: schlicks@udmercy.edu.

© 2010 American Chemical Society

Published on Web 12/30/2010

Scheme 1. Stabilization by Hindered Amines



on the degradation of polypropylene (PP) by one-dimensional (1D) ESRI have been published by Lucarini and co-workers[13−15] and on PP and polystyrene by Marek et al.[16]

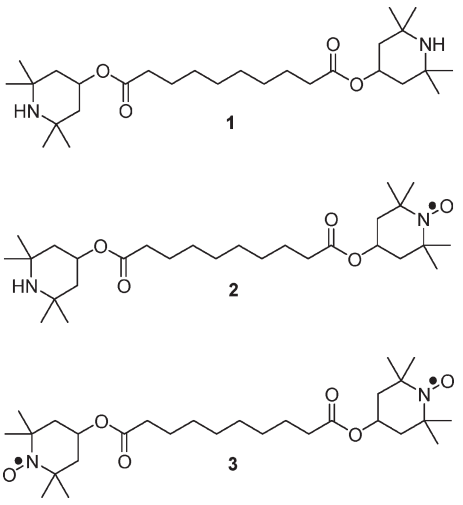
We have developed 1D and 2D spectra-spatial ESRI methods for the study of *heterophasic* systems such as poly(acrylonitrile-butadiene-styrene) (ABS)[17−23] and heterophasic propylene-ethylene copolymers (HPEC)[24−27] containing Tinuvin 770 as the HAS, when exposed to thermal treatment or UV irradiation. The major objectives were to examine polymer degradation under different conditions; to assess the effect of rubber phase (polybutadiene in ABS and ethylene-propylene rubber in HPEC) on the extent of degradation; and to evaluate the extent of stabilization by HAS. The combination of the ESRI study with the temperature variation of the ESR spectra of HAS-derived nitroxides (HAS-NO) has made possible the deduction of important morphological and structural details on the thermal- and photodegradation of these systems.

The thermal degradation of HPEC systems containing Tinuvin 770 as the HAS has been studied at 393 and 433 K.[25] Two types of HPECs were examined: HPEC1 containing 25 wt % ethylene (E), and HPEC2 containing 10 wt % E (as ethylene-propylene rubber). Spatial and temporal effects of the aging process were studied by electron spin resonance (ESR), 1D and 2D spectral spatial ESRI of HAS-NO, and FTIR of films prepared by compression molding. The spatial distribution of HAS-NO was obtained by 1D ESRI. The 2D ESRI experiments allowed the nondestructive acquisition of ESR spectra as a function of sample depth for different treatment times or other aging conditions. Much of the interpretation was based on the detection of two components in the ESR spectra of the nitroxides that differ in their dynamical properties, fast (F) and slow (S).[24−27] These two spectral components are shown in Figure 1-S in the Supporting Information for HPEC1 thermally aged at 433 K for 10 d.[27] The line shape at 340 K is typical for rotation of the nitroxide along their long axis.[17] Similar spectra were obtained for HAS-NO in HPEC2; at 300 K, however, the intensity of the F component is lower (compared to HPEC1), a result that was attributed to the lower E content.

On the basis of ESRI data and on ESR spectra of HAS-NO in the HPEC systems and in the related homopolymers (polypropylene and polyethylene), we have suggested that the F spectral component observed at 300 K represents unrestrained ethylene-propylene copolymer chains, and the S component (at the same temperature) represents amorphous polypropylene and the copolymer chains in the rigid amorphous phase (RAP).[24] RAP is the elastomer phase that is restrained by proximal crystalline domains. These studies have demonstrated the exceptional sensitivity of the ESR spectra of nitroxide radicals to polymer morphology and degree of crystallinity, and of the ESRI data to the degradation in the different polymer morphological domains.

The 1D ESRI experiments in the thermally treated HPEC systems enabled the visualization of an outer region of thickness ≈100 μm that contained a lower amount of nitroxides.[25] We have proposed that NO-depleted regions may arise from loss of stabilizer by diffusion ("blooming"), or/and in chemical reactions during aging. The mobility of the stabilizer is a very important parameter, since it has great impact on stabilizer performance: An effective stabilizer should be very soluble in the polymer,

Chart 1. Structures of Tinuvin 770 (1), the Corresponding Nitroxide Monoradical (2), and the Nitroxide Biradical (3)



and its translational mobility (diffusion and volatility) should be low.[28,29]

We present the measurement by ESRI of the diffusion coefficient of Tinuvin 770-derived nitroxide radicals (Chart1) in HPEC1 and HPEC2 at 393 K, under conditions of negligible degradation (diffusion time shorter than that necessary for the detection of carbonyls by FTIR[24]). As will be clearly seen below, the mobility of the radicals is significant, and leads to loss of stabilizer even when the extent of degradation is negligible.

Experimental Section

Materials. Two HPEC samples differing in their ethylene (E) content were a gift from the Dow Chemical Company: HPEC1 (IPC, C 708, M_n = 60,700, M_w = 227 000), and HPEC2 (IPC, C104−01, M_n = 90 400, M_w = 428 000). The polymers were prepared by polymerization of propylene in the presence of the catalyst, and sequential polymerization of the product with a propylene−ethylene mixture with the same catalyst.[30] The E content (as the ethylene−propylene copolymer) in the HPEC samples, determined as described in ref 24, was 25 wt % in HPEC1 and 10 wt % in HPEC2, within ±2%. The Tinuvin 770-derived radicals were prepared by oxidation of Tinuvin 770 from Ciba Specialty Chemicals, Chart 1, with *m*-chloroperoxybenzoic acid (*m*CPBA), and were a mixture of monoradicals (≈25%) and biradicals (≈75%).[31] These radicals are referred to as "nitroxides" or "nitroxide radicals", whereas radicals generated from HAS during polymer degradation processes are denoted as HAS-NO.

Preparation of Samples for ESR Measurements. Polymers doped with nitroxide spin probes are usually prepared by the dissolution method, which involves solubilization of the polymer and probe in the solvent, followed by solvent evaporation. This was the method used in the case of ABS polymers doped with spin probes.[32] Dissolution of HPEC1 and HPEC2 can be achieved in xylene at ≈400 K, but the process is slow and sometimes incomplete. For this reason, in this study the polymers were doped with the nitroxides by the melting method: Weighed amounts of the radical and polymer were mixed slightly above the melting point of the polymer.[24] The typical temperature for mixing of HPEC samples and nitroxide was ≈450 K. The mixtures were held at the high temperature for ≈4 min or less in most cases.

Preparation of Samples for ESRI Measurements. HPEC plaques (dimension 10 cmx10 cmx3 mm) were prepared by injection molding. The nitroxide was dissolved in toluene (10 wt %) and a layer of solution was applied to one side of the plaques, followed by drying for 10 min at 433 K. These samples were kept at 393 K, the temperature of the diffusion experiments. At selected time

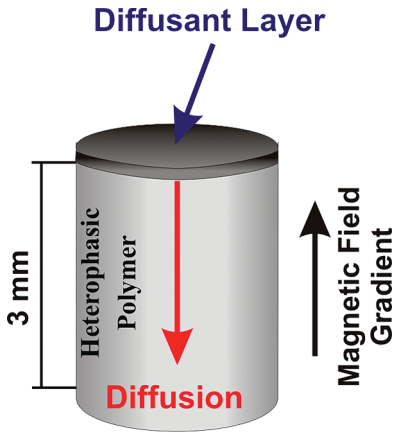


Figure 1. Configuration of the samples used in the ESRI diffusion experiments. The blue arrow points to the layer of radicals and the red arrow shows the diffusion direction ("from-top-to-bottom"). The magnetic field gradient, 200 G/cm, is along the diffusion direction. The sample height is also indicated.

intervals, cylindrical samples with diameter ≈7 mm were cut through the plaque thickness, trimmed to fit the ESRI sample tube of 5 mm od, and placed in the ESR resonator with the symmetry axis along the long (vertical) axis of the resonator and parallel to the direction of the magnetic field gradient, as shown in Figure 1.

ESR Measurements. Spectra were recorded on Bruker X-band EMX spectrometers operating at 9.7 GHz with 100 kHz magnetic field modulation and the ER 4101 STE standard resonator, and equipped with the Acquisit 32 Bit WINEPR data system version 3.01 for acquisition and manipulation, and the ER 4111 VT variable temperature units. The microwave frequency was measured with a Hewlett-Packard 5350B microwave frequency counter. The sensitivity profile of the cavity for the sample of height ≈3 mm is essentially constant. Most spectra were collected with the following parameters: sweep width 120 G, microwave power 2 mW, time constant 40.96 ms, conversion time 81.92 ms, 4−10 scans, and 1024 points. The modulation amplitude was varied in the range 0.5−1.2 G, depending on the line width. The temperature was controlled within ±1 K. All samples were allowed to equilibrate for at least 10 min after reaching the desired temperature. Additional experimental details have been described.[24]

ESR Imaging and Data Acquisition. The ESRI system is based on the EMX spectrometer equipped with two figure-eight-shaped Lewis coils connected to two regulated power supplies. Measurements were performed using vertical (perpendicular to the external magnetic field) gradients of 200 G/cm for 1D ESRI, and 250 G/cm for 2D ESRI measurements. The instrumentation has been described in detail.[17,22,25−27]

The 1D concentration profiles were determined by ESRI from two spectra: the regular ESR spectrum and the 1D image, which is the ESR spectrum measured in the presence of the magnetic field gradient. For samples less than 4 mm in height the sensitivity response of the resonator can be treated as a constant. For these conditions, the 1D image, $I(B)$, is a convolution of the ESR spectrum $S(B)$ measured in the absence of the gradient with the function $P(r)$, which describes the spatial distribution of the paramagnetic centers (the profile) along the gradient direction r, as shown in eq 1:

$$I(B) = \int_{-\infty}^{+\infty} (S(B - grad_r B)P(r))\, dr \qquad (1)$$

The convolution is legitimate if the gradient-off ESR spectrum, $\boldsymbol{S(B)}$, has no spatial dependence. In our previous ESRI study of HPEC systems we determined that the relative intensities of the F and S components vary with sample length.[25−27] For this reason all 1D ESRI measurements were performed at 340 ± 1 K; at this temperature the F and S spectral components are not distinguishable and the spatial dependence of the ESR signal is avoided.

The 1D concentration profiles were determined based on the concept of virtual components and on the genetic algorithm (GA) that enables optimization of the results.[33] In this approach the concentration profile $P(r)$ is expressed as a superposition of several Gaussian functions and two Boltzmann functions, which allow a better representation of the changes in concentration at the edges of the sample, as in eq 2. The Boltzmann (B) and Gaussian (G) functions are given in eqs 3 and 4.

$$P(r) = B(r_1, a_1, h_1) + \sum_{k=2}^{n-1} G(r_k, a_k, h_k) + B(r_n, a_n, h_n) \qquad (2)$$

$$B(r_i, a_i, h_i) = a_i/[1 + \exp(r - r_i)/h_i] \qquad (3)$$

$$G(r_i, a_i, h_i) = a_i \exp[-(r - r_i)^2/2h_i^2] \qquad (4)$$

In eqs 2−4, r is the spatial coordinate, a_i is part of a virtual stored profile, and h_i is the half-width of a virtual component. While the Fourier transform followed by the Monte Carlo optimization method leads to noisy concentration profiles, the approach based on virtual components and the genetic algorithm (VC-GA) allows the automatic determination of concentration profiles without noise and without prior knowledge about their shapes. The noiseless profiles make possible a more confident interpretation of results, as seen clearly in Figure 3, below.[26,33]

The 2D spectral−spatial ESR images were reconstructed from a complete set of projections, typically 256, obtained as a function of the magnetic field gradient, using a convoluted back-projection algorithm, as described elsewhere.[18,25] In the first reconstruction stage, the projections at the missing angles, typically 93 out of 256, were assumed to be identical to the projection measured at the largest available angle. In the second stage, the projections at the missing angles were obtained by the projection slice algorithm (PSA) with 2−10 iterations.[34] The 2D ESRI experiments were performed at 300 ± 1 K, and the two-dimensional images were saved as 256 × 256 matrices.

Determination of the Diffusion Coefficients. The translational diffusion coefficient D was determined using the program SCENARIOS,[35,36] in a Matlab environment. The program allows an automatic determination of the diffusion coefficient for different experimental settings. Figure 1 describes the "from-top-to-bottom" configuration; in this case the symmetrization procedure[35] implemented in the software was applied in order to correct for possible imperfections in the diffusant distribution perpendicular to the diffusion direction. If we assume that the diffusion is Fickian (eq 5), and the initial radical distribution can be described by a delta function, the concentration profile can be described by the Green function, eq 6.[37] Since the initial distribution of nitroxides cannot be easily predicted, a series of radical concentration profiles at different diffusion times were determined and the early profiles were taken as starting profiles for the later ones. If the diffusion follows Fick's law, combinations of several *pairs* of concentration profiles are expected to lead to the same diffusion coefficient, and the plot of $D\Delta t$ as a function of Δt for the pair ($\Delta t = t_2 - t_1$) is expected to be a straight line crossing the origin, and the slope of the line is the diffusion coefficient.

$$\frac{\partial C(x,t)}{\partial t} = D_x \frac{\partial^2 C(x,t)}{\partial x^2} \qquad (5)$$

$$C(x,t) = (1/4\pi Dt)e^{-x^2/4Dt} \qquad (6)$$

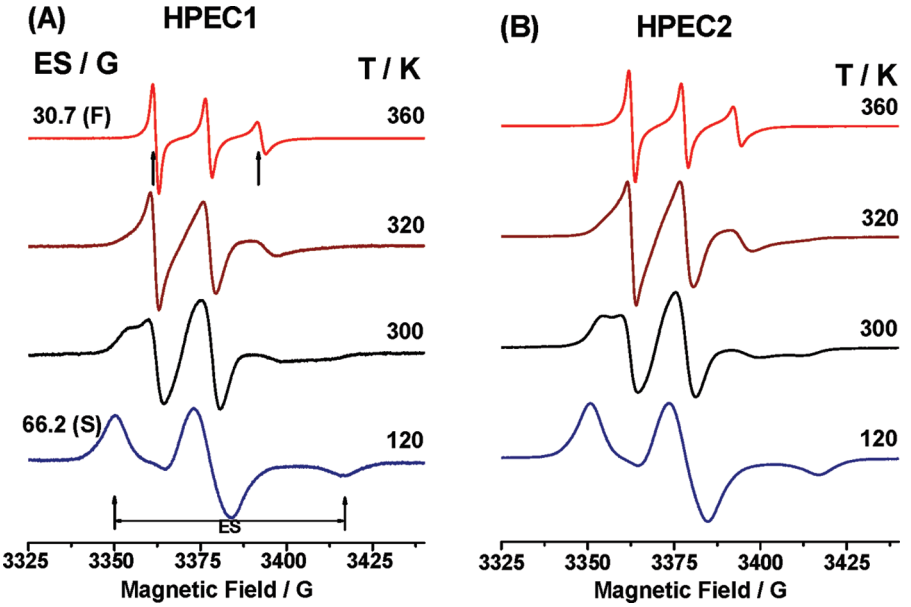


Figure 2. ESR spectra of the nitroxides at the indicated temperatures in HPEC1 (A) and HPEC2 (B). The extreme separation (ES, in G), at 300 K for the F component and at 120 K for the S component, are given in part A. Two spectral components are clearly visible in both parts A and B at 300 K. At this temperature % F is 36 in part A and 29 in part B.

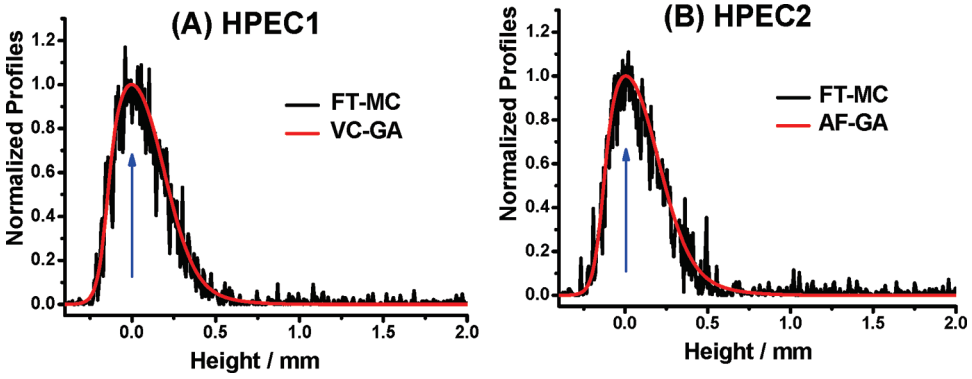


Figure 3. Concentration profiles of the nitroxide radicals in HPEC1 (A) and HPEC2 (B) obtained by Fourier transform followed by Monte Carlo optimization (black), and optimized profile calculated by the VC-GA method with 5 Gaussian and 2 Boltzmann functions. In both cases at least 100,000 iterations were necessary for profile determination. The 1D ESRI images were measured at 340 K with a magnetic field gradient of 200 G/cm. Upward arrows in parts A and B point to the maximum of the initial radical profile.

Results and Discussion

In this section we will discuss the determination of the diffusion coefficients D measured in the two HPEC systems, deduce in which phase diffusion takes place by comparing with literature D values in the corresponding homopolymers PP and PE, and comment on the implications of the present results for the degradation and stabilization of the HPECs.

Determination of the Diffusion Coefficients in HPEC1 and HPEC2. Representative ESR spectra of the nitroxide radicals in HPEC1 and HPEC2 are presented in Figure 2, parts A and B, respectively.

Spectra typical of two interacting >NO groups (a five-line spectrum) in a long molecule such as the nitroxide biradical can be expected only in fluid media and have not been detected in the present systems. Therefore, use of the biradical nitroxide will not interfere with the interpretation of the ESR spectra of the monoradical. In support of this assumption, we recall that the ESR spectrum of HAS-NO at 300 K in polybutadiene, which has a lower glass transition temperature, T_g, compared to copolymers based on P and E units, was simulated by assuming a rotation about the long axis of the HAS, indicating a rigid probe conformation.[17] The most important feature is the presence of two spectral components in the temperature range 300−320 K, with different ES values; % F is 36 in HPEC1, and 29 in HPEC2, a result that is assigned to the higher ethylene content in HPEC1. The % F is slightly lower than that detected for HAS-NO in HPEC (41 and 35% respectively) because the nitroxides are detected in the original polymers, while HAS-NO appears in the plaques prepared by injection molding and the % F is higher. Therefore, the ESR spectra shown in Figure 2 indicate that when measuring diffusion coefficients the behavior of nitroxide radicals will reflect that of the HAS-NO in the thermally degraded HPEC systems.

The concentration profiles used for calculation of the diffusion coefficient were determined by the virtual components and genetic algorithm (VC-GA) method that was described in detail elsewhere.[33] Representative profiles obtained by this approach and also by Fourier transform followed by Monte Carlo optimization are presented in Figure 3. The profiles were plotted only up to 2 mm (even though the sample height was ≈3 mm) because no radicals were detected beyond this region of the sample. We note the noiseless profiles calculated by the VC-GA method.

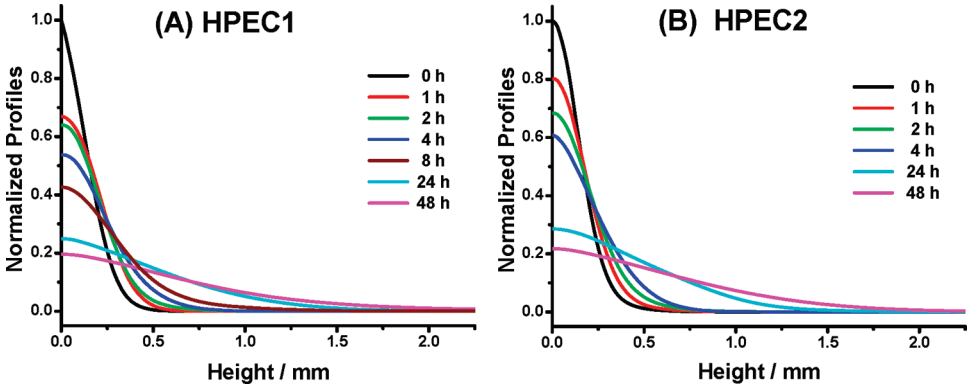


Figure 4. Concentration profiles of the nitroxide radicals in HPEC1 and HPEC2 systems calculated from the 1D ESRI experiments after diffusion at 393 K for the indicated time. For both HPEC1 and HPEC2 the profiles are normalized to the same total area, and the maximum of the profile at $t = 0$ (see arrows in Figure 3) was taken as 1, for comparison with the other profiles.

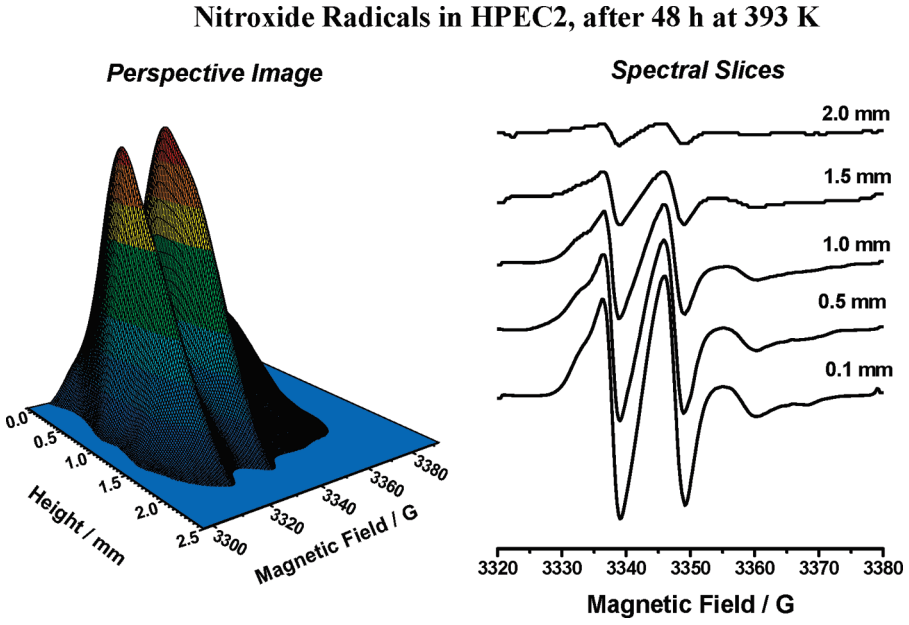


Figure 5. 2D spectral-spatial ESRI perspective image and corresponding spectral slices measured at 300 K for the nitroxide radicals in HPEC2 after 48 h of diffusion at 393 K.

Figure 4 presents the concentration profiles of radicals in HPEC1 and HPEC2, calculated from the 1D ESRI experiments and normalized to the same total area.

The first profiles (time = 0 h) for both polymers were obtained immediately after evaporation of the solvent at 433 K. The other profiles were determined after the samples were placed in the oven at 393 K for the indicated times. Changes in the profiles with time clearly indicate the diffusion of the nitroxides at 393 K.

The 2D spectral-spatial ESRI perspective plots for the radicals in HPEC2 after 48 h at 393 K, together with the spectral slices recorded nondestructively, are shown in Figure 5. The spectra were recorded at 300 K to allow visualization of the ESR spectra from the radicals, which are located in the different domains of the heterophasic polymers. The spatial profile indicates the spread of the radicals along the sample height due to diffusion, as also seen in the concentration profiles, Figure 4.

The determination of the diffusion coefficients by simulation of the distribution profiles for HPEC1 (A) and HPEC2 (B) is illustrated in Figure 6. The variation of $D \times \Delta t$ as a function of Δt together with the linear fit for radical diffusion in HPEC1 (C) and in HPEC2 (D) are also presented in Figure 6. In both cases the fit is very good, with a correlation factor R^2 better than 0.99 and an estimated error for the slope less than 4%. The determined diffusion coefficients are similar for both investigated polymers:

$$\text{HPEC1: } D_{niroxide} = (1.47 \pm 0.04) \times 10^{-8}\ \text{cm}^2\ \text{s}^{-1}$$

$$\text{HPEC2: } D_{nitroxide} = (1.38 \pm 0.02) \times 10^{-8}\ \text{cm}^2\ \text{s}^{-1}$$

Deducing in Which Phase Diffusion Takes Place. The D values given above suggest that the diffusion coefficients in the two HPEC systems are essentially the same. To understand this result in polymers containing 25 wt % E (HPEC1) and 10 wt % E (HPEC2), we go back to the description of the morphology of these systems in terms of four phases; crystalline PP, amorphous PP, crystalline part of ethylene-propylene copolymer and amorphous ethylene-propylene rubber.[24−26] These studies have provided evidence for the location of the nitroxides in a range of amorphous sites differing in their dynamical properties. As determined

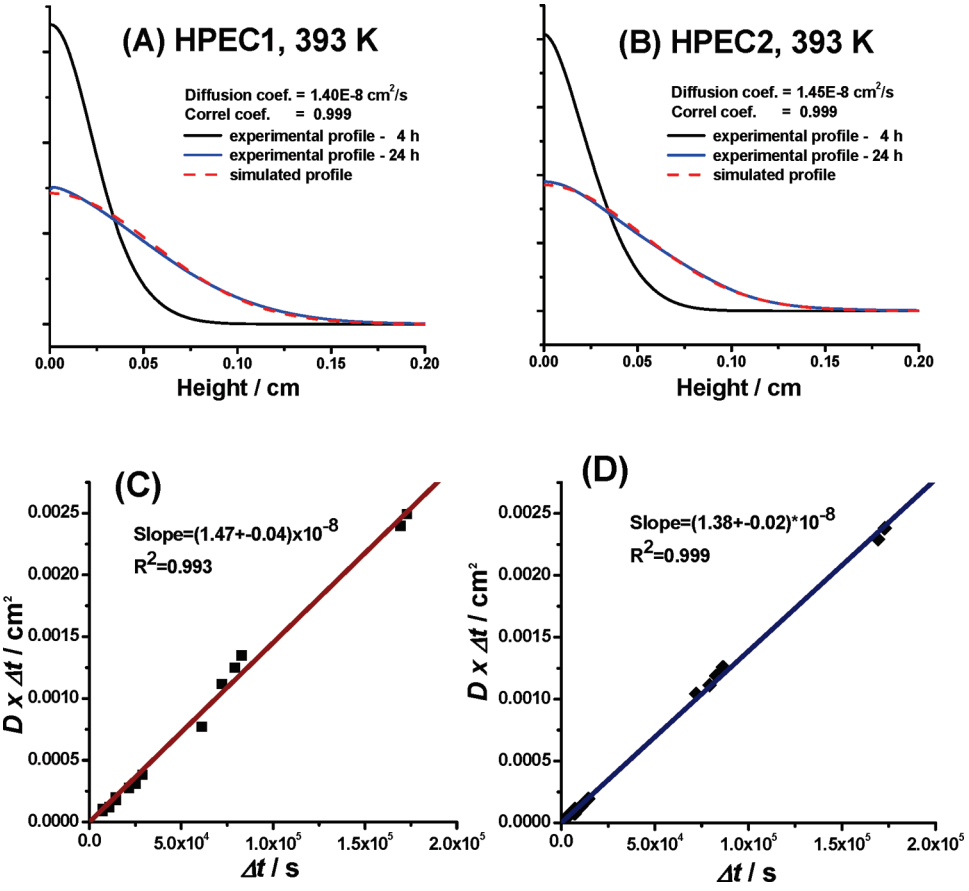


Figure 6. Pairs of profiles used for the determination of diffusion coefficients for HPEC1 (A) and HPEC2 (B). In parts A and B, the two pairs of profiles were deduced after 4 and 24 h of diffusion, and the diffusion coefficients D deduced by simulation of the profile after 24 h were 1.40×10^{-8} cm^2/s (A) and 1.45×10^{-8} cm^2/s (B). The dependence of the values $D \times \Delta t$ versus the time interval $\Delta t = t_2 - t_1$ for the indicated initial-final concentration profile pairs for HPEC1 and HPEC2 is shown in parts C and D, respectively.

Table 1. Diffusion Coefficients, D, of Tinuvin 770-Derived Nitroxide in LDPE and HDPE at the Indicated Temperatures[a]

system	T / K	D/cm^2 s^{-1}	ref
LDPE	296	*4.23 × 10^{-10}*	38
	313	2.05 × 10^{-9}	39
	323	6.49 × 10^{-9}	39
	323	*6.75 × 10^{-9}*	38
	323	*7.4 × 10^{-9}*	28a
	331	*1.95 × 10^{-8}*	38
	333	1.58 × 10^{-8}	39
	333	1.86 × 10^{-8}	28b
	338	*3.2 × 10^{-8}*	38
	340	*3.5 × 10^{-8}*	38
	343	4.75 × 10^{-9}	39
	348	*5.65 × 10^{-8}*	38
	353	1.20 × 10^{-7}	39
	393	**1.82 × 10^{-6}**	extrapolation
HDPE	333	6.79 × 10^{-10}	39
	343	2.64 × 10^{-9}	39
	353	9.85 × 10^{-9}	39
	363	1.80 × 10^{-8}	39
	373	4.16 × 10^{-8}	39
	393	**2.72 × 10^{-7}**	extrapolation

[a] Values in *italic* script are averages of different results at a given temperature measured in the original paper.

elsewhere,[24] the amorphous phase is 63% in HPEC1 and 60% in HPEC2. Therefore, the amount of the amorphous phase in both polymers is similar. Since the D values are also very close, we conclude that at 393 K the most important factor that determines the diffusion is the ratio of amorphous to crystalline domains, not the composition (PE and PP) of those amorphous domains. We note that we have assumed that the nitroxides reside only in the amorphous domains.

Since we are unable to find literature data for diffusion of Tinuvin 770-derived nitroxides in HPECs, we have compared our findings with the D values of these radicals in LDPE, HDPE and PP. The literature D values for Tinuvin 770-derived nitroxides (HAS-NO) for LDPE and HDPE are given in Table 1, and for PP in Table 2. Table 2 also contains the D values deduced in this study. In some cases two or three different literature values for D at the same temperature are given in the cited references but determined after different diffusion times; for simplicity, these multiple values were averaged and the average numbers are given in the Tables in *italic* script.

As mentioned above, the D values deduced for the nitroxide radicals in HPEC1 and HPEC2 at 393 K in this study are very similar and can be represented by average number $(1.42 \pm 0.05) \times 10^{-8}$ cm^2/s. This value is lower than the D values in both LDPE (by a factor of 125) and HDPE (by a factor of 20) at the same temperature, as calculated by extrapolation (Arrhenius relationship) of the literature data presented in Table 1.

The diffusion coefficients obtained in this work for the HPEC polymers are in the range expected for the diffusion of Tinuvin-derived radicals in PP. These D values are slightly lower than the interpolated value at 393 K. We note however that the literature data exhibit fluctuations not only between two studies,[38,39] but even for the same authors.[38] As seen in Figure 7, the value in this study, 1.42×10^{-8} cm^2 s^{-1}, can be placed in the range of predicted results for D determined on

the basis of literature data collected in Table 2. The upper and lower confidence limits in Figure 7 show the region of all possible fitted lines for a confidence level of 95%: we have 95% confidence that the best-fit line lies within the confidence limits.[40]

Table 2. Diffusion Coefficients, *D*, of Tinuvin 770-Derived Nitroxide in PP and HPEC at the Indicated Temperatures[a]

system	T / K	D/cm^2 s^{-1}	ref
PP	323	2.7×10^{-10}	28a
	330	4.50×10^{-10}	38
	333	7.36×10^{-10}	28b
	336	1.10×10^{-9}	38
	341	*1.65 × 10^{-9}*	38
	343	*1.40 × 10^{-9}*	38
	343	4.75×10^{-9}	39
	346	3.05×10^{-9}	38
	353	1.49×10^{-9}	39
	355	2.55×10^{-9}	15
	356	6.10×10^{-9}	38
	363	4.25×10^{-9}	39
	373	7.38×10^{-9}	39
	378	2.31×10^{-8}	39
	387	2.24×10^{-8}	39
	394	5.43×10^{-8}	39
	393	**3.36×10^{-8}**	interpolation
HPEC1	**393**	**1.47×10^{-8}**	this work
HPEC2	**393**	**1.38×10^{-8}**	this work

[a] Values in *italic* script are averages of different results at a given temperature measured in the cited reference.

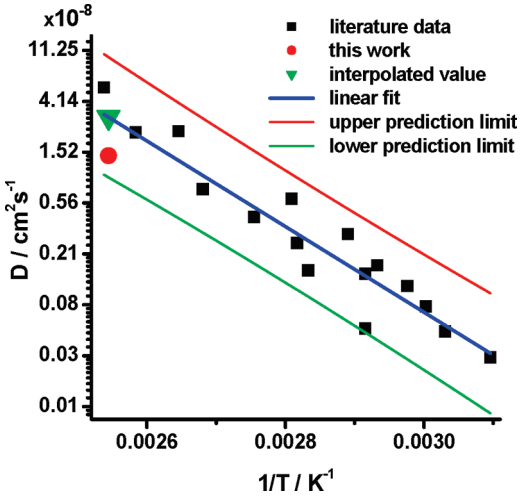


Figure 7. Arrhenius plot for the diffusion coefficients of nitroxide radicals in PP (black squares) and in HPEC (red circle). The green triangle represents the interpolated value for *D* in PP at 393 K.

Taking into account that essentially the same *D* values were determined for both HPEC polymers, and the fact that this value is characteristic for diffusion of HAS-NO radical in PP, we suggest that at 393 K the rate of diffusion for the nitroxide radicals might be related to the amount of crystalline phase, which is predominantly iPP: DSC measurements have indicated no crystalline PE in HPEC2, and a very small amount of crystalline PE in HPEC1.[24] The composition of amorphous phase (ratio PE/PP) at this temperature has no important effects.

It could be argued that the *D* value measured here represents diffusion in an E-rich region, and that the lower value compared to values given in Table 1 may be due to the presence of obstacles. We note however that, due to the method of synthesis by sequential polymerization of PP with an ethylene-propylene rubber, we do not expect PE chains in the HPEC systems. For this reason the picture of diffusion in amorphous PP-rich regions is preferable.

Implications for Polymer Stabilization. The importance of the stabilizer solubility (*S*) and diffusion coefficient (*D*) have been discussed in numerous papers, and the empirical coefficient S^2/D has been proposed as a criterion for an effective stabilizer; good agreement has been reported for HAS-stabilized LDPE films during accelerated aging and for three HAS types in LDPE and PP.[28,29,38,39] Measurement of the loss of stabilizer due to diffusion from the outer sections of a polymer sample is an important additional information on the effectivity of a stabilizer; this information for the polymer systems presented here can be visualized from Figure 8 below.

Figure 8 presents the concentration of the radicals, determined as the ESR signal intensity in the sample depth as a function of diffusion time. We note that a pronounced decrease of the total signal intensity with diffusion time is observed only for the outermost layer (■, 0 mm). For the next layer (red dot, 0.4 mm) we clearly see a slight increase of radical intensity that we assign to diffusion from the outermost layer, followed by a plateau; for the next layers we observe only slight increases in radical intensity. Also visible is a large decrease in the ESR intensity for the external layer between diffusion times $t = 0$ and $t = 0.5$ h; in the same time interval, however, the intensity increase in the next layer is much smaller. This result suggests a loss of nitroxide by evaporation of the radicals from the surface of polymer sample. The detection of a similar behavior for HPEC1 and HPEC2 suggests that the presence of the PE component does not alter the properties of the stabilizer. Quantitative determination of the loss of nitroxide due to evaporation was performed by measuring the total radical intensity (in the entire sample). The results suggest that the loss of the diffusant is on the order of 20%.

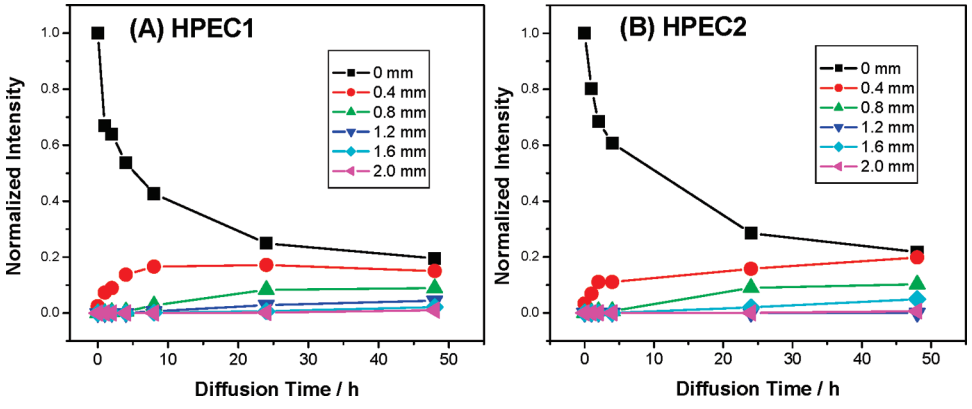


Figure 8. Variation of the normalized intensity as a function of diffusion time for the indicated heights: (A) HPEC1 and (B) HPEC2.

In our previous studies, we have proposed that the loss of the stabilizer is due either to blooming, or to chemical reactions taking place during degradation.[25] As degradation is not expected in the present samples because of the limited time the sample spent at 393 K (≤48 h), we can conclude that the loss of nitroxides is due to evaporation and not to degradation processes: Degradation was detected at 393 K for both HPEC1 and HPEC2 only after thermal treatment of 29 days or longer. Additional support for this conclusion is in Figure 5, which shows no change in the ESR spectra of the slices for conditions similar to those used in this study for the determination of the diffusion coefficient.

Conclusions

The ESR imaging (ESRI) technique was used to track the diffusion processes of nitroxide radicals derived from Tinuvin 770 as the hindered amine stabilizer in HPEC polymers and to determine their macroscopic diffusion coefficients. The ethylene (E) content in the two HPEC samples studied were different, 25 wt % E in HPEC1 and 10% wt in HPEC2.

The diffusion coefficients determined by simulation of the 1D ESR profiles as a function of diffusion time at 393 K were essentially the same for HPEC1 and HPEC2: 1.42×10^{-8} cm^2 s^{-1}. This value was considered in the context of literature data for D in LDPE, HDPE, and PP. The D value measured in this study is in the range expected for the diffusion of the nitroxides in PP, with a confidence level of 95%.

Plots of the normalized intensity of the radicals as a function of diffusion time at 393 K suggested loss of the stabilizer by evaporation from the outer layer of the sample. Moreover, we conclude that during treatment conditions (not longer than 48 h at 393 K) the loss of stabilizer is due to blooming, and not to chemical reaction.

The results deduced in this study prove that 1D ESRI is suitable for the measurement of macroscopic diffusion coefficients for paramagnetic species not only in solution or gel systems, but also in polymer plaques.

Acknowledgment. This study was supported by the Polymers Program of the National Science Foundation. We are grateful to Antonin Marek for sharing with us the SCENARIOS software for the determination of diffusion coefficients, Gian Franco Pedulli and Marco Lucarini (University of Bologna) for the gift of the radicals prepared by oxidation of Tinuvin 770, and to John L. Gerlock (Ford) for his help with plaque preparation and for numerous insightful discussions. We are grateful to the three reviewers for their careful reading of the manuscript and constructive criticism.

Supporting Information Available: Figure 1-S presenting the ESR spectra of HAS-derived onnitroxides in thermally aged HPEC1 registered at the indicated temperatures. This material is available free of charge via the Internet at http://pubs.acs.org.

References and Notes

(1) O'Donnell, J. H. Radiation Chemistry of Polymers. In *The Effects of Radiation on High-Technology Polymers*; Reichmanis, E., O'Donnell, J. H., Eds.; American Chemical Society: Washington, DC, 1989; Chapter 1, pp 1−13.
(2) *Handbook of Polymer Degradation*, Hamid, S. H., Amin, M. B., Maadhah, A. G., Eds.; Marcel Dekker: New York, 1992.
(3) *Irradiation of Polymeric Materials: Processes, Mechanisms, and Applications*; Reichmanis, E., Frank, C. W., O'Donnell, J. H., Eds.; American Chemical Society: Washington, D.C., 1993.
(4) *Polymer Durability: Degradation, Stabilization and Lifetime Prediction*; Clough, R. L.; Billingham, N. C.; Gillen, K. T., Eds.; Advances in Chemistry Series 249, American Chemical Society: Washington, DC, 1996.
(5) Rabek, J. F. *Photostabilisation of Polymers, Principles and Applications*; Elsevier: London, 1990.
(6) (a) Part I: Gerlock, J. L.; Bauer, D. R.; Briggs, L. M. *Polym. Deg. Stab*. **1986**, *14*, 53–71. (b) Part II: Gerlock, J. L.; Riley, T.; Bauer, D. R. *Polym. Deg. Stab*. **1986**, *14*, 73–84. (c) Part III: Gerlock, J. L.; Bauer, D. R. *Polym. Deg. Stab*. **1986**, *14*, 97–112.
(7) Faucitano, A.; Buttafava, A.; Martinotti, F.; Bortolus, P. *J. Phys. Chem*. **1984**, *88*, 1190–1194.
(8) Faucitano, A.; Buttafava, A.; Martinotti, F.; Greci, L. *Polym. Deg. Stab*. **1992**, *35*, 211–217and references therein .
(9) Pospisil, J. *Adv. Polym. Sci*. **1995**, *124*, 87–189.
(10) Gillen, K. T.; Clough, R. L. In *Handbook of Polymer Science and Technology*; Cheremisinoff, N. P., Ed.; M. Dekker: New York, 1989; Chapter 6, pp 167−202.
(11) Gillen, K. T.; Clough, R. L.; Quintana, C. A. *Polym. Degrad. Stab*. **1987**, *17*, 31–97.
(12) Schlick, S. ESR Imaging. In *Advanced ESR Methods in Polymer Research*, Schlick, S., Ed.; Wiley: Hoboken, NJ, 2006; Chapter 4, pp 85−98.
(13) Lucarini, M.; Pedulli, G. F.; Borzatta, V.; Lelli, N. *Res. Chem. Intermed*. **1996**, *22*, 581–591.
(14) Lucarini, M.; Pedulli, G. F. *Angew. Makromol. Chem*. **1997**, *252*, 179–193.
(15) Franchi, P.; Lucarini, M.; Pedulli, G. F.; Bonora, M.; Vitali, M. *Macromol. Chem. Phys*. **2001**, *202*, 1246–1256.
(16) Marek, A.; Kapralkova, L.; Schmidt, P.; Pfleger, J.; Humlicek, J.; Pospisil, J.; Pilar, J. *Polym. Degrad. Stab*. **2006**, *91*, 444–458.
(17) Motyakin, M. V.; Gerlock, J. L.; Schlick, S. *Macromolecules* **1999**, *32*, 5463–5467.
(18) Kruczala, K.; Motyakin, M. V.; Schlick, S. *J. Phys. Chem. B* **2000**, *104*, 3387–3392.
(19) Motyakin, M. V.; Schlick, S. *Macromolecules* **2001**, *34*, 2854–2864.
(20) Motyakin, M. V.; Schlick, S. *Macromolecules* **2002**, *35*, 3984–3992.
(21) Lucarini, M.; Pedulli, G. F.; Motyakin, M. V.; Schlick, S. *Prog. Polym. Sci*. **2003**, *28*, 331–340.
(22) Schlick, S.; Motyakin, M. V. 1D and 2D Electron Spin Resonance Imaging (ESRI) of Transport and Degradation Processes in Polymers, In *Instrumental Methods in Electron Magnetic Resonance, Biological Magnetic Resonance*; Bender, C. J., Berliner, L. J., Eds.; Kluwer Academic/Plenum Publishing Corporation: New York, 2004; Vol. *21*, pp 349−384.
(23) Schlick, S.; Motyakin, M. V. Polymer Degradation by ESR Imaging: Beyond Phantoms, In *Specialist Periodical Reports—Electron Paramagnetic Resonance*; Gilbert, B. C., Davies, M. J., Murphy, D. M., Eds.; Royal Society of Chemistry: Cambridge, U.K., 2007; Vol. *20*, pp 1−28.
(24) Kruczala, K.; Varghese, B.; Bokria, J. G.; Schlick, S. *Macromolecules* **2003**, *36*, 1899–1908.
(25) Kruczala, K.; Bokria, J. G.; Schlick, S. *Macromolecules* **2003**, *36*, 1909–1919.
(26) Kruczala, K.; Aris, W.; Schlick, S. *Macromolecules* **2005**, *38*, 6979–6987.
(27) Schlick, S.; Kruczala, K. Spatially-Resolved Degradation in Heterophasic Polymers from 1D and 2D Spectral-Spatial ESR Imaging Experiments. In *Advanced ESR Methods in Polymer Research*; Schlick, S., Ed.; Wiley: Hoboken, NJ, 2006; Chapter 9, pp 229−254.
(28) (a) Malik, J.; Hrivik, A.; Tuan, D. Q.; Alexy, P.; Danko, P.; Vucht, A. S. *Polym. Prepr*. (*Am. Chem. Soc. Div. Polym. Chem*.) **1993**, *34* (2), 170–171. (b) Malik, J.; Tuan, D. Q.; Spirk, E. *Polym. Degrad. Stab*. **1995**, *41*, 1–8.
(29) Malik, J.; Ligner, G.; Avar, L. *Polym. Degrad. Stab*. **1998**, *60*, 205–213.
(30) Albizzati, E.; Giannini, U.; Collina, G.; Noristi, L.; Resconi, L. Catalysts and Polymerizations. In *Polypropylene Handbook*; Moore, E. P. Jr., Ed.; Hanser Publishers: Munich, Germany, 1996; Chapter 2, pp 11−111.
(31) Brigati, G. University of Bologna, personal communication.
(32) Varghese, B.; Schlick, S. *J. Polym. Sci. B: Polym. Phys*. **2002**, *40*, 415–423.
(33) Spalek, T.; Kruczała, K.; Sojka, Z.; Schlick, S. *J. Magn. Reson*. **2007**, *189* (1), 139–150.
(34) Maltempo, M. M.; Eaton, S. S.; Eaton, G. R. Algorithms for Spectral-Spatial Imaging with a "Missing Angle. In *EPR Imaging and In Vivo EPR*; Eaton, S. S., Eaton, G. R., Ohno, K., Eds; CRC Press: Boca Raton, FL, 1991; Chapter 14, pp 145−152.
(35) (a) Marek, A.; Labsky, J.; Konak, C.; Pilar, J.; Schlick, S. *Macromolecules* **2002**, *35*, 5517–5528. (b) Marek, A. *ESR Study of*

Diffusion Processes in Polymer Systems. Ph.D. thesis, Charles University: Prague, 2006.
(36) Pilar, J.; Kriz, J.; Meissner, B.; Kadlec, P.; Pradny, M. *Polymer* **2009**, *50*, 4543–4551.
(37) Crank, J. *The Mathematics of Diffusion*; Clarendon Press: Oxford, U.K., 1993.
(38) Malik, J.; Hrivik, A.; Tomova, E. *Polym. Deg. Stab.* **1992**, *35*, 61–66.
(39) Dudler, V. *Polym. Degrad. Stab.* **1993**, *42*, 205–212.
(40) http://www.originlab.com/www/helponline/Origin/en/UserGuide/Confidence_and_Predicti on_Bands.html

DOI: 10.1021/ma102235r

Macromolecules
ARTICLE

Gel Formation and Interpolymer Alkyl Chain Interactions with Poly(9,9-dioctylfluorene-2,7-diyl) (PFO) in Toluene Solution: Results from NMR, SANS, DFT, and Semiempirical Calculations and Their Implications for PFO β-Phase Formation

Licínia L. G. Justino,*[,†,‡] M. Luísa Ramos,[†,‡] Matti Knaapila,*[,§] Ana T. Marques,[†,⊥] Christof J. Kudla,[⊥] Ullrich Scherf,[⊥] László Almásy,[∥,○,◆] Ralf Schweins,[#] Hugh D. Burrows,[†] and Andrew P. Monkman[▽]

[†]*Departamento de Química, Faculdade de Ciências e Tecnologia, Universidade de Coimbra, 3004-535 Coimbra, Portugal,* [‡]*Centro de Neurociências e Biologia Celular, Universidade de Coimbra, 3004-517 Coimbra, Portugal,* [§]*Physics Department, Institute for Energy Technology, NO-2027 Kjeller, Norway,* [⊥]*Makromolekulare Chemie, Bergische Universität Wuppertal, D-42097 Wuppertal, Germany,* [∥]*Laboratory for Neutron Scattering, PSI, CH-5232 Villigen, Switzerland,* [○]*Adolphe Merkle Institut, University of Fribourg, CH-1700 Fribourg, Switzerland,* [◆]*Research Institute for Solid State Physics and Optics, Budapest-1525, Hungary,* [#]*Institut Laue-Langevin, DS/LSS Group, 6 Rue Jules Horowitz, F-38042 Grenoble CEDEX 9, France, and* [▽]*OEM Research Group, Department of Physics, Durham University, Durham DH1 3LE, U.K*

Received September 28, 2010; Revised Manuscript Received November 18, 2010

ABSTRACT: Interactions between polymer chains of poly(9,9-dioctylfluorene-2,7-diyl) (PF8) have been studied in toluene solution over a wide concentration range using multinuclear NMR spectral and relaxation measurements with both the fully protonated and alkyl chain deuterated polymers, small angle neutron scattering (SANS), together with theoretical calculations using DFT and semiempirical methodologies. Full assignment of the ^{1}H and ^{13}C chemical shifts in the NMR spectra of isolated chains of PF8 has been made using DFT, and are in good agreement with spectra in chloroform and in toluene solutions. Somewhat different behavior is seen in toluene solution, where, upon increasing polymer concentration, broadening of the alkyl chain resonances is seen, consistent with interactions between the side chains. Similar behavior is seen with the ^{2}H resonance of PF8-d_{34}. In both cases, line-narrowing and restoration of the structured alkyl chain resonances is seen upon studying the spectra of concentrated solutions using the magic angle spinning (MAS) technique, in agreement with the attribution of the broadening to interchain interactions between the octyl groups. Support for this interpretation comes from ^{1}H and ^{13}C spin−lattice relaxation time measurements, which also show differences in group dynamics along the alkyl chains. Semiempirical theoretical calculations, using PM3 and PM6 Hamiltonians, add further support to the importance of interactions between the alkyl groups of separate PF8 chains. SANS measurements on PF8 in toluene solutions from very dilute to concentrated solutions, extended to ultrasmall q ranges, provide further insight. Three concentration ranges can be identified. In dilute solutions, the results suggest that PF8 is present as fully dissolved polymer coils. Upon increasing polymer concentration, an intermediate region is observed, in which there are indications of transient contacts between the polymers, which the NMR results suggest involves side chain interactions. As a consequence of interactions between the chains, gel formation occurs. On the basis of these and previous results, some general considerations are presented upon the solubility and aggregation behavior of PF8, including indications of how interactions between alkyl chains may be important in the stabilization of the so-called β-phase of PF8.

I. Introduction

Conjugated polymers (CP) are technologically important materials in the rapidly developing area of organic semiconductors. One major advantage they possess over small molecule organic systems is the possibility of using low-cost solvent-based methodologies, such as inkjet printing,[1] for preparation of thin film optoelectronic devices. This allows large-scale production of flexible systems using reel-to-reel methodologies.[2] However, the luminescence efficiency, charge transport and other properties of these devices are strongly dependent on film morphology, and it is important to be able to both understand and control the characteristics of thin films produced through such processes. There are strong indications that the properties of solution deposited films are closely related to the structures and aggregation characteristics of the polymers in the solutions used for processing.[3−5] We will address one such case.

Polyfluorenes are a particularly important CP family,[6−10] and have excellent photophysical and optoelectronic characteristics.[11] In addition, they show good solubility in many common solvents, and possess an interesting phase behavior,[12] which can lead to different morphologies and characteristics of deposited films depending on molecular weight,[13] side chain length,[14,15] and branching.[14−17] Particularly interesting behavior is observed when films of poly(9,9-dioctylfluorene) (PF8),[18,19] and some other linear side chain poly(9,9-dialkylfluorenes),[20] are obtained from poor solvents. With certain alkyl chain lengths, the so-called β-phase is formed,

*Corresponding authors. (L.L.G.J.) Telephone: +351-239-854453. Fax: +351-239-827703. E-mail: liciniaj@ci.uc.pt. (M.K.) Telephone: +47-6380-6081. Fax: +47-6381-0920. E-mail: matti.knaapila@ife.no.

 Published on Web 12/27/2010 © 2010 American Chemical Society

which shows enhanced emission in light emitting devices, in addition to increased structuring and a red shift in the photoluminescence. This is associated with conformational ordering and formation of a particularly extended chain structure.[8] This can also be induced by addition of various alkyl compounds[21] or phospholipids.[22] However, it is still not clear whether β-phase formation is a precursor to or a consequence of aggregation in solution,[23,24] and there is a clear need for more information on the nature of any supramolecular structures present. Although our knowledge of structures and aggregates in solutions of conjugated polymers is still rather limited, considerable advances have recently been made and valuable data obtained with polyfluorene systems using small-angle X-ray (SAXS)[25−27] and neutron scattering (SANS),[25,26,28−34] light scattering,[27,28,34,36−38] NMR spectroscopy,[31−33,35,39] near-field scanning optical microscopy[40] and atomic force microscopy (AFM).[17,40,41] However, there are still no clear guidelines as to the driving forces which determine the type of aggregate formed. In this work we concentrate on one case involving the important system of polymer gels with spatial inhomogeneity,[42] a materials class which can be readily studied by small-angle scattering techniques.[43] A combination of NMR and small-angle neutron scattering is used. These techniques have been shown in previous studies to provide complementary information about these systems on different length scales.[31−33] We consider the PF8/toluene system, where solution structures have been studied over a wide concentration using a variety of techniques[28,30,31,33,35,37,40,41,44,45] and where gels are formed in dense solutions.[31,37] Results are also presented of DFT and semiempirical calculations, which permit complete assignment of the NMR spectra and also provide insights on interchain association. Finally, aspects of the nature of solvents which favor particular types of aggregation with this class of hairy-rod polymers are addressed.

II. Experimental Section

Materials and Sample Preparation. Poly[9,9-di(*n*-octyl-d_{17})-fluorene-2,7-diyl] (PF8-d_{34}) with number-averaged molecular weight (M_n) of 73.1 kg/mol and weight-averaged molecular weight (M_w) o f 144 kg/mol was prepared following the microwave-assisted Yamamoto-type polymerization with $Ni(COD)_2$ as catalyst and 2,7-dibromo-9,9-dioctylfluorene monomer containing octyl-d_{17} side chains, as described previously.[8,30,46]

For NMR experiments, poly(9,9-di-*n*-octylfluorene-2,7-diyl) (PF8) was obtained from Aldrich (M_n = 15.8 kg/mol, M_w = 58.2 kg/mol). Alkyl chain deuterated and nondeuterated PF8 samples were prepared by dissolving weighed amounts of the polymers in chloroform-*d* supplied by Sigma-Aldrich (99.8% D) or toluene-d_8 (99% D). Complete dissolution of the polymers at the 2.5% and 6% (i.e., 25−60 mg/mL) concentrations was achieved by warming the samples in a water bath. The samples were kept protected from light.

For neutron scattering, PF8 (M_n = 47 kg/mol, M_w = 153 kg/mol) was mixed to deuterated toluene (toluene-d_8) that was supplied by Sigma-Aldrich (99.6% D, for low concentration samples (≤2 mg/mL)) or Armar Chemicals, Swizerland (99.5% D, high concentration samples (≥5 mg/mL)). The neutron scattering length density of PF8 is 0.702×10^{10} cm^{-2} and that of toluene-d_8 is 5.662×10^{10} cm^{-2}. The molecular weight is larger than the one of the sample studied by NMR. However, the fact that similar NMR spectral behavior was observed with this and the PF8-d_{34}, which has a comparable molecular weight to the PF8 sample used in SANS, suggests that the NMR experiments are relatively insensitive to the polymer size (vide infra).

NMR. ^{1}H, ^{2}H, and ^{13}C NMR spectra were recorded on a Varian VNMRS 600 MHz spectrometer, at 599.72, 92.06, and 150.80 MHz, respectively. The magic angle spinning (MAS) spectra were obtained using a PFG nano gHX probe at a spinning speed of 4 kHz in a 4 mm rotor. The spin−lattice relaxation times (T_1) were measured using the inversion−recovery pulse sequence, schematically represented as d_1−180°−d_2 −90°−T_a, with $d_1 + T_a \geq 5T_{1,max}$. The signals of $CDCl_3$ at δ = 7.27 ppm and of toluene at δ = 2.09 ppm, relative to TMS, were used as internal references for ^{2}H and ^{1}H, while the ^{13}C triplet of $CDCl_3$ centered at δ = 77.23 ppm and the heptet of toluene centered at δ = 20.40 ppm were used as internal references for ^{13}C. All NMR measurements were carried out at 25 °C.

Small Angle Neutron Scattering (SANS). SANS measurements of the low-concentration samples (0.2−2 mg/mL) were carried out at the LOQ beamline at ISIS Facility, Rutherford Appleton Laboratory (U.K.).[47] The LOQ instrument at ISIS uses incident wavelengths between 2.2 and 10 Å sorted by time-of-flight with a sample-to-detector distance of 4.1 m resulting in a q range between 0.006 and 0.24 Å^{-1}. The samples were in quartz cuvettes (Hellma) of 2 mm path length placed in a thermostat and kept at 25.0 ± 0.5 °C during measurements. The raw data were corrected for the transmission, D_2O background, sample cell, and detector efficiency. The 2D scattering patterns were azimuthally averaged and converted to an absolute scale. The data for each sample was collected for 1 h.

SANS measurements of the intermediate- (5−10 mg/mL) and high-concentration samples (30−70 mg/mL) were performed at the instrument D11 at the Institut Laue-Langevin (ILL, France). Scattering intensities were measured with a two-dimensional position-sensitive ^{3}He detector with an array of 128 × 128 cells of 7.5 mm × 7.5 mm size. The measurements were done using two wavelengths in order to cover a large q range. Instrument settings were as follows: a wavelength of 6 Å with sample-to-detector distances of 1.5 m, 8 and 34 m; and a wavelength of 16.5 Å with a sample-to-detector distance of 34 m. These settings provide a q range of 0.00058−0.4 Å^{-1}. All samples and backgrounds were confined in rectangular 1 mm Hellma cells of type 404−QS. The cells were placed in a high-precision temperature-controlled copper rack; measurements were performed at 25 °C. The two-dimensional scattering data obtained were radially averaged and background-corrected using the ILL standard data reduction routines. H_2O was used as secondary standard (calibrated against monodisperse polymer standards). Data were put on an absolute scale by using the known wavelength-dependent effective cross section of H_2O, determined for D11 with its current ^{3}He detector to $(d\Sigma/d\Omega)_{H_2O}$ = 0.983 cm^{-1} at 6 Å and 1.843 cm^{-1} at 16.5 Å. The incoherent background from hydrogen-containing polymer was taken into account by adding a corresponding amount of toluene to toluene-d_8 and using scattering of this mixture for background subtraction.

The scattering curves were interpreted using scaling concepts by considering scattering intensity $I(q) \sim q^{-\alpha}$. PF8 is known to be a rodlike polymer in toluene solutions.[30] When the curves show a crossover point from rodlike behavior ($\alpha \approx 1$) at $q \approx q^*$, the persistence length of the polymer, l_p, was estimated from the relation $q^* l_p \approx 1.9$. For the intermediate solutions (5−10 mg/mL) this simple interpretation was enhanced by estimating the phenomenological scatterer size using the indirect Fourier transformation program GNOM.[48] For the concentrated solutions (30−70 mg/mL), the subsequent fit of the scattering factors was adapted from Chen and co-workers[31] In this procedure, the material was expected to act as a dynamic mesh of long rodlike polymers joined together via overlapping nodes. A two-component model was employed to fit the entire scattering curve. The low q part of the curve was fitted to the Debye−Bueche equation

$$I(q) \sim \frac{1}{(1 + \xi_s{}^2 q^2)^2} \quad (1)$$

where ξ_s is the correlation length connected to the average distance between aggregate domains. The high-q part was fitted to an Ornstein−Zernike type equation

$$I(q) \sim \frac{1}{1 + \xi_d q \exp(q^2 R^2/4)} \quad (2)$$

where ξ_d represents the mesh size of the dynamic network and R is the radius of the rodlike polymer.

III. Computational Section

The geometry optimization of the PF8 monomer was performed by DFT without symmetry constraints using the GAMESS[49] code. The calculation employed the B3LYP (Becke three-parameter Lee−Yang−Parr exchange correlation functional, which combines the hybrid exchange functional of Becke,[50] with the correlation functional of Lee, Yang and Parr (LYP)[51]) and the 6-31G(d,p) basis sets for the expansion of the Kohn−Sham orbitals. At the final equilibrium geometry with minimum energy the gradient was 1×10^{-05} hartree bohr^{-1}. For the optimized structure the nuclear shieldings were computed using the NWCHEM[52] program at the B3LYP/GIAO (gauge-including atomic orbital method) level. The 6-31G(d,p) basis sets and a fine integration grid (FINE option) were used. ^{13}C and ^{1}H relative chemical shifts (δ) are given with respect to the absolute shielding values (σ) of tetramethylsilane (TMS) obtained at the same computational level ($\delta = \sigma_{ref} - \sigma$).

The aggregation behavior of PF8 was simulated using semiempirical quantum chemistry calculations for a system composed of two PF8 trimers placed with a distance of 21.5 Å separating the plans of the backbones. The system was optimized in vacuum using the PM3 and the PM6[53] Hamiltonians and the EF routine implemented in the MOPAC2007[54] system of programs. At the final equilibrium geometry, the gradient was 0.01 kcal mol^{-1} Å^{-1}.

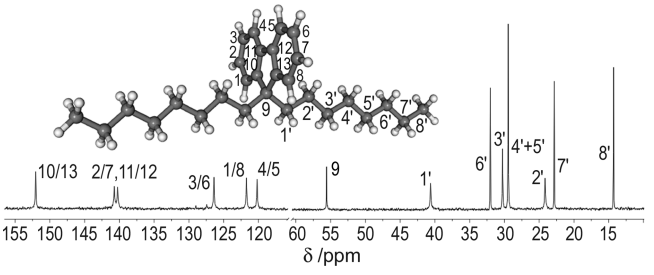


Figure 1. ^{13}C NMR spectrum of a 6% (60 mg/mL) PF8 solution in $CDCl_3$ at 25 °C. Inset: B3LYP/6-31G(d,p) optimized geometry of the PF8 monomer. Note the separate numbering of the backbone and side-chain atoms.

IV. Results and Discussion

NMR Studies on Nondeuterated PF8. Figure 1 shows a ^{13}C NMR spectrum of a 6% (or 60 mg/mL) PF8 solution in chloroform. As with our previous work with poly(9,9-bis(2-ethylhexyl)fluorene-2,7-diyl) (PF2/6),[39] in this solvent the polymer is considered to be dissolved at the molecular level to give isolated polymer chains. The assignment of the resonances was accomplished by computing, at the DFT/GIAO level, the NMR chemical shifts for the DFT-optimized geometry of the monomer. The computed values are compared in Table 1 with the experimental shifts for the polymer in chloroform and in toluene solutions. The only feature which is worthy of note is that the (4′ + 5′) resonance of the chloroform spectrum is split into two separate resonances in the toluene spectrum, with the chemical shifts indicated in Table 1.

The alkyl regions of the ^{1}H spectra in toluene and in chloroform of the same sample (Figure 2) also show some differences. The CH_2 protons 2′ to 7′ give rise to just two separate bands in chloroform, spanning the region from 1.18 to 1.25 ppm (0.07 ppm), but they present three distinct bands in toluene, ranging from 1.00 to 1.21 ppm (0.21 ppm). This result suggests much more rigid conformations for the alkyl chains of the polymer in toluene, in agreement with this solvent's poorer solubilizing properties for PF8, which will permit stronger interactions between the polymer chains. The ^{1}H assignment of the resonances was based on the computed values for the monomer, also presented in Table 1. Our assignment is in accordance with that given by Leclerc et al.[55] for the ^{13}C aromatic resonances of a low-molecular-weight PF8 in $CDCl_3$, for which spectra similar to the present ones were observed.

To analyze the dynamics of PF8 in concentrated solutions in a good solvent, where we expect very few polymer−polymer interactions, and in a poorer solvent, in which we expect some aggregation to occur, we have measured the spin−lattice relaxation times of the ^{1}H and ^{13}C atoms of the alkyl chains of PF8 in 6% solutions in chloroform and in toluene. The NMR δ and J values are interpreted in terms of the structure of each molecule, and the relaxation times T_1 and T_2 (spin−lattice and spin−spin relaxation) are affected by macroscopic dynamical properties of the nuclear

Table 1. Calculated NMR Chemical shifts for the PF8Monomer in Vacuum (B3LYP/6-31G(d,p)//B3LYP/6-31G(d,p)[a]) and Experimental Chemical Shifts (ppm) of the PF8 Polymer in $CDCl_3$

Site	$\delta(^{13}C_{calc.})$	$\delta(^{13}C_{expt.})$	$\delta(^{1}H_{calc.})$	$\delta(^{1}H_{expt.})$
		Quaternary C		
$C_{(10)}/C_{(13)}$	147.94	152.04	-	-
$C_{(11)}/C_{(12)}$	139.88	140.73 and	-	-
$C_{(2)}/C_{(7)}$	b	140.25	-	-
$C_{(9)}$	58.89	55.58	-	-
		Aromatic CH		
$C_{(3)}H/C_{(6)}H$	122.94	126.38	b	7.73; 7.71(d)[c]
$C_{(1)}H/C_{(8)}H$	117.87	121.72	b	7.71
$C_{(4)}H/C_{(5)}H$	115.46	120.18	7.84	7.88; 7.87(d)
		Alkylic region		
$C_{(1')}H_2$	45.08	40.62	2.46	2.16(b)[c]
$C_{(2')}H_2$	26.12	24.16	1.05	
$C_{(3')}H_2$	33.92	30.27	1.38	
$C_{(4')}H_2$	33.60	29.45[d]	1.22	1.25-1.18
$C_{(5')}H_2$	34.17	*29.70 and 29.62*[e]	1.34	*1.21-1.00*
$C_{(6')}H_2$	34.83	32.03	1.26	
$C_{(7')}H_2$	26.42	22.83	1.12	
$C_{(8')}H_2$	15.88	14.29	0.52	0.85

[a] The notation indicates "level of geometry calculation//level of NMR chemical shifts calculation". [b] In the PF8 polymer the 2 and 7 carbons are bonded to the adjacent monomer units, thus the calculated chemical shifts for the monomer at these positions are not suitable for comparison with the experimental shifts. [c] "d" stands for doublet and "b" stands for broad. [d] In chloroform solution, $C_{(4')}$ and $C_{(5')}$ are superimposed. [e] Chemical shifts in toluene are indicated in italics.

Table 2. ^{1}H and ^{13}C Spin−Lattice Relaxation Times Measured for the Alkylic Chains of PF8 6% (60 mg/mL) Solutions in Chloroform and in Toluene at 25 °C

	T_1 (^{1}H) /s		T_1 (^{13}C) /s	
atom	$CDCl_3$	toluene	$CDCl_3$	toluene
$C_{(1')}H_2$	0.87±0.02	0.81± 0.01	0.24±0.01	0.20±0.01
$C_{(2')}H_2$	1.19[a]	1.11[a]	0.29±0.01	0.25±0.01
$C_{(3')}H_2$			0.41±0.01	0.40±0.01
$C_{(4')}H_2$	*(1.34; 1.32; 1.25; 0.86)*	*(1.30; 1.30; 1.26; 0.90; 0.78)*	0.83[b]±0.01	0.77[a] *(0.63; 0.90)*
$C_{(5')}H_2$				
$C_{(6')}H_2$			1.60±0.02	1.44±0.08
$C_{(7')}H_2$			2.37±0.02	2.17±0.11
$C_{(8')}H_3$	1.76±0.12	1.59±0.05	3.24±0.04	3.00±0.16

[a] Average value with estimated error of 5%. [b] In chloroform solution $C_{(4')}$ and $C_{(5')}$ are superimposed.

environment. The nuclear relaxation depends on the existence of molecular motion. This generates fluctuating magnetic fields, which provide a mechanism for the loss of energy from the excited nuclear spins to the surrounding lattice. Thus, the experimental relaxation times can give valuable information on the dynamical properties both of the molecules under study and their interactions with adjacent species.[56,57] For large organic molecules having only carbon and hydrogen atoms ($I = 1/2$), dipolar relaxation is the dominant mechanism. With ^{13}C, where dipolar interactions with the directly bonded ^{1}H spins are dominant, its rate is given by eq 3, which assumes isotropic rotational diffusion of a rigid spheroid molecule:

$$T_1^{-1}(DD) = \frac{1}{10}(2\pi R)^2\tau_c\left[\frac{1}{1+(\omega_X-\omega_A)^2\tau_c^2}+\frac{3}{1+\omega_A^2\tau_c^2}+\frac{6}{1+(\omega_X+\omega_A)^2\tau_c^2}\right] \quad (3)$$

where ω is the Larmor frequency and τ_c is the correlation time, a measure of how rapidly the molecule undergoes reorientation in solution.[56] τ_c is defined as

$$\tau_c = 4\pi\eta a^3/3kT \quad (4)$$

where a is the molecular radius of a molecule, taken as a first approximation to be spherical and η is the viscosity of the medium. R is the dipolar coupling constant:

$$R = (\mu_0/4\pi)\gamma_A\gamma_X(h/4\pi^2)r_{AX}^{-3} \quad (5)$$

in which γ is the magnetogyric ratio. For relatively fast isotropic rotational motions, that is, $\omega\tau_c < 1$ (this means $\tau_c < 10^{-09}s$ for $\nu = 150.8$ MHz), $T_1^{-1}(DD)$ becomes independent of the frequency. This is termed the *extreme narrowing* condition (so-called because T_1 and T_2 become equal) and the relaxation times are given by:

$$T_1^{-1}(DD)(hetero) = T_2^{-1}(DD)(hetero) = \left(\frac{\mu_0}{4\pi}\right)^2\gamma_A^2\gamma_X^2h^2\tau_c/4\pi^2r_{AX}^6 \quad (6)$$

When there are a large number of spin pairs to be considered, the above equations must be modified to take into account the sum of all the interactions with the spin of interest.

Treatment of relaxation in polymers is further complicated[58] by the existence of multiple processes. Although formalisms[59] have been developed for the analysis of relaxation times in macromolecules, where fast internal motions are superimposed on an anisotropic overall motion, this mathematical treatment is beyond the scope of this article and for a qualitative analysis of the T_1 results with ^{13}C we will assume

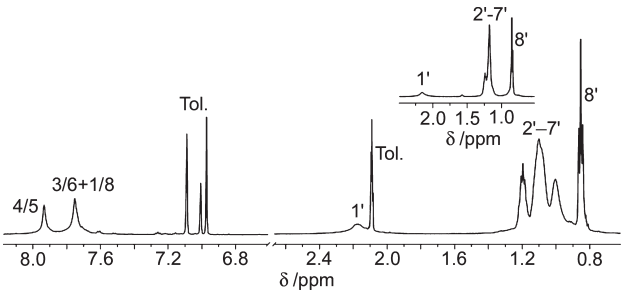


Figure 2. ^{1}H NMR spectrum of a 6% (60 mg/mL) PF8 solution in toluene at 25 °C. Inset: alkyl region of the ^{1}H NMR spectrum of the same sample in $CDCl_3$; (numbering is as defined in Figure 1).

that eqs 3 and 6, which were derived under the assumption of isotropic rotational motion of a spheroid molecule, are valid. We will also assume that the segmental motions in our systems meet the *extreme narrowing* condition, where T_1 is independent of the frequency, and we present in Table 2 the absolute ^{13}C T_1 values for the alkyl chains of PF8 in chloroform and in toluene. Results were also obtained for ^{1}H, but the treatment of the relaxation mechanism is more complicated, since for each proton there are many intramolecular and intermolecular interactions contributing to the ^{1}H T_1 values. Therefore, the ^{1}H results are only given for comparison, and no detailed analysis is attempted.

In both solvents, the ^{13}C T_1 values increase from $C_{(1')}$, to $C_{(8')}$, along the polymer alkyl chain. This is a consequence of the increasing flexibility on going from the methylene group linked to the fluorene to the terminal methyl group, and is explained in terms of the different individual correlation times for the successive internal motions in the chain, in addition to the correlation time, τ_c, defined for the overall molecular motion. A second important observation is that all the ^{13}C T_1 values decrease on going from chloroform to toluene solution, and that the T_1 values of the carbons of the end of the chain, $C_{(6')}$ and $C_{(7')}$ (the contributions to the T_1 values of $C_{(8')}$ will be discussed below), are those most affected with the change in solvent. The smaller T_1 values in toluene (in the *extreme narrowing* condition,$\omega\tau_c < 1$) indicate, through eq 6, longer correlation times in this solvent, showing a decrease in the mobility of the alkyl chains. This suggests stronger polymer−polymer interactions in toluene, conferring certain rigidity to the alkyl chains. These are expected to lead to some overlap (or interdigitation) of the alkyl chains, explaining the larger effect seen for the $C_{(6')}$ and $C_{(7')}$ carbons. Although $C_{(8')}$ is the carbon atom most markedly affected, this belongs to a methyl group, and in addition to having a different number of H atoms directly connected to it (which would decrease its $T_1(DD)$ compared to the CH_2 carbons), the spin-rotation relaxation mechanism also contributes to, and probably dominates, its relaxation. With the ^{1}H T_1 values, although, as mentioned, they are affected by

intermolecular contributions to their relaxation, they show a similar evolution on going along the polymer alkyl chains and on changing the solvent.

When handling the solutions, the 6% PF8/toluene solution was observed to be more viscous than the 6% PF8/chloroform solution, in agreement with the occurrence of stronger polymer−polymer interactions. Future rheological studies will be directed to relate viscosity with solution structure. A higher viscosity, through eq 4, at constant temperature, indicates longer τ_c values for PF8 in toluene, in agreement with the assumption that our systems meet the $\omega\tau_c < 1$ condition (for $\omega\tau_c = 1$, T_1 reaches a minimum and for $\omega\tau_c > 1$, T_1 increases with τ_c[56]). As noted above, in such systems which are very far from a spheroid geometry, we must distinguish the slow overall motion involving the PF8 backbone from the fast intramolecular motions in the alkyl lateral chains. As discussed elsewhere,[56−58,60] the processes seen in T_1 measurements in the megahertz region correspond to relaxation by fast motions such as alkyl chain segmental fluctuations.

Since the spectral line-widths at half-height can be related to the spin−spin relaxation time through equation

$$\Delta\nu_{1/2} = 1/\pi T_2^* \tag{7}$$

the small values for T_1 (which is equal to T_2 in the conditions assumed for eq 6) of carbons $C_{(1')}$, $C_{(2')}$, and $C_{(3')}$ and protons $C_{(1')}H_2$ explain the larger widths of the observed signals for these atoms. T_2^* is the effective T_2 obtained from the observed line-width, which is likely to have a contribution from the inhomogeneity of the applied magnetic field. The T_2^* values were determined for the alkyl carbon atoms of PF8 in $CDCl_3$ from the spectral line-widths, and the values are compatible with the experimental T_1 values. For example, for the $C_{(6')}$, T_2^* is 0.27 s and T_1 is 1.60 s. However, we must note that the differences between the experimental values of T_2^* and T_1 in this system can also have a contribution from the fact that the model of isotropic rotation may not be totally appropriate to these motions.

Polymer−polymer interactions in PF8 were also simulated using semiempirical calculations. A system of two F8 trimers was considered in vacuum and the input was built so that the distance between the planes of the backbones was approximately 21.5 Å. The geometry was optimized using the PM3 and the PM6 Hamiltonians and the PM3 structure is shown in Figure 3. The distance between the planes of the backbones decreased to approximately 18.5 Å, which can be attributed to the existence of van der Waals attraction between the alkyl chains. The optimized geometry shows some interdigitation of the chains. The PM6 structure shows an even higher degree of interaction and proximity between the chains, although PM6 is known to suffer from overestimation of nonbonding interactions in some molecular systems.[54] The PM6 results agree with PM3 in showing a strong tendency of PF8 to aggregate through interdigitation of the alkylic chains. This is in perfect accord with the occurrence of major changes in the above experimental T_1 values of the $C_{(6')}$ and $C_{(7')}$ carbons.

Studies on the Deuterated Polymer PF8-d_{34}. The ^{1}H NMR spectra of alkyl chain deuterated PF8 are shown in Figure 4 for a range of concentrations from 0.7% to 6% (or 7−60 mg/mL) (only the alkyl region is shown). A high-resolution magic angle spinning (MAS) spectrum is also shown for the more concentrated solution. The 0.7% solution spectrum shows the residual ^{1}H resonances of the deuterated polymer coupled with the deuterium nuclei. The relative intensities of the resonances are affected by the presence of defects from the deuteration of the individual sites. The ^{1}H spectra of the

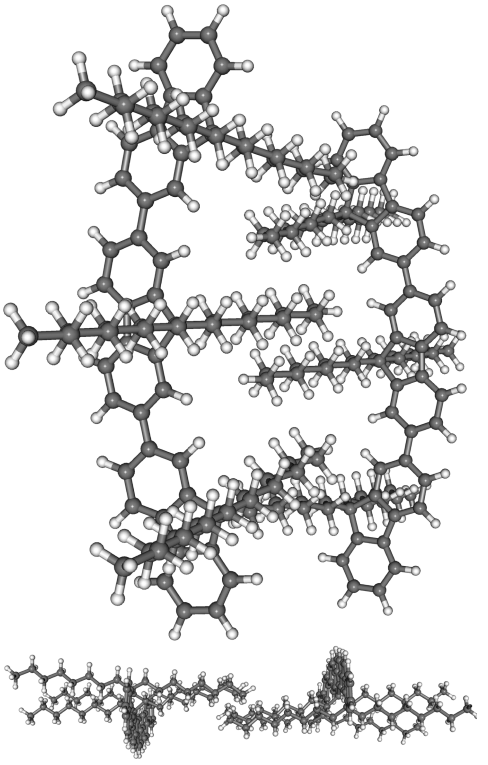


Figure 3. Two perspectives of the PM3 optimized geometry of an aggregate of two F8 trimers in vacuum.

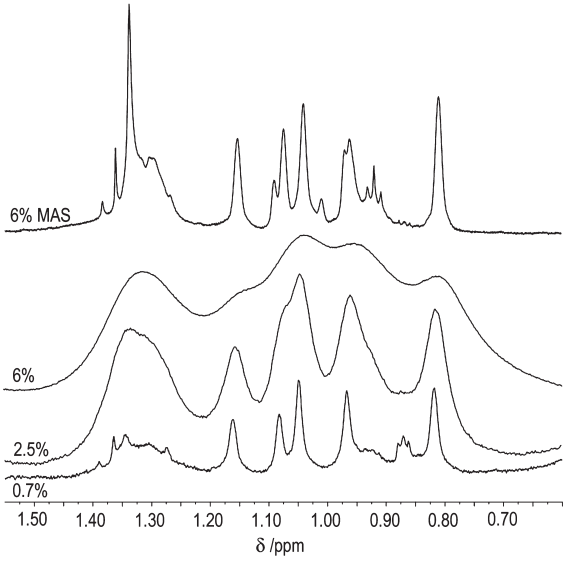


Figure 4. ^{1}H NMR spectra of residual protons of PF8-d_{34} solutions in toluene at indicated concentrations; the 6% MAS spectrum was acquired at 4 kHz spinning rate.

2.5% and 6% solutions show the same resonances as the 0.7% solution, but they are strongly broadened due to residual magnetic dipolar couplings (and possibly, although less important, residual chemical shift anisotropy). In these solutions, the increase in polymer concentration leads to stronger intermolecular interactions and the molecular motions become restricted and slower. Under these conditions, residual magnetic dipolar couplings will be present causing the signals to broaden. The MAS spectrum shown supports the assumption that the broadening arises from anisotropic interactions rather than from a direct relation with the T_2 relaxation time. The magnetic dipolar interaction depends

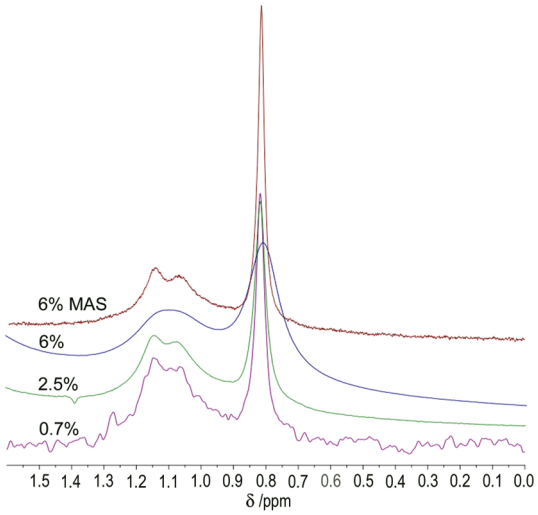


Figure 5. ^{2}H NMR spectra of PF8-d_{34} in toluene at indicated concentrations; the 6% MAS spectrum was acquired at 4 kHz spinning rate.

on the geometrical factor ($3\cos^2\theta-1$), where θ is the angle between the internuclear vector and the external magnetic field B_0. In nonviscous solutions the molecules undergo rapid and isotropic translational and rotational motion and the internuclear vectors are averaged over all orientations relative to B_0. In this situation ($3\cos^2\theta - 1$) becomes zero (the average of $\cos^2\theta$ over all directions is $^1/_3$) and the contribution of the dipolar interaction vanishes. MAS[61,62] NMR removes line broadening caused by dipolar interactions (and other anisotropic interactions such as chemical shift anisotropy and quadrupolar interaction) by averaging the orientation of all the internuclear vectors in the sample to an angle of 54.74° relative to B_0 by sample rotation at this so-called "magic" angle. This angle, $\theta = 54.74°$, is that for which ($3\cos^2\theta - 1$) becomes zero and the dipolar interaction vanishes. The line widths in the 6% MAS ^{1}H NMR spectra of PF8-d_{34} are comparable, or even narrower, than those in the 0.7% solution spectrum, showing that the line broadening is due to anisotropic interactions dependent on the ($3\cos^2\theta-1$) geometrical factor. These are due to the slower motion of the molecules in the concentrated solutions arising from the stronger polymer−polymer interactions through the alkyl side chains. The ^{2}H spectra obtained for the same solutions (Figure 5) allow the same conclusions. For the normal spectrum of the 6% solution we observe a loss of resolution which is regained in the MAS spectrum, indicating that anisotropic interactions, such as residual dipolar coupling and quadrupolar coupling, are the cause of line broadening in the concentrated solutions. Although the deuterated polymer has a higher molecular weight than the nondeuterated one, this does not seem to have any influence on the NMR spectral parameters.

Comparing the ^{1}H MAS NMR for the 6% solution and the ^{1}H spectra of the 0.7% solution, new resonances, at 0.97, 1.00, and 1.09 ppm, are detected in the former case. This finding is in agreement with the previous results in suggesting more rigid conformations of the alkyl chains in the 6% solution. A further, and as yet unattributed, broad signal is observed in the ^{1}H NMR spectrum of PF8-d_{34} around 1.35 ppm (Figure 4). Considering that we are looking at the residual proton signals for chain deuterated polymer, this may come from traces of defect or other impurity.

SANS. Polymer gels with spatial inhomogeneity are a materials class well studied by SANS, which is an ideal tool to probe the larger length scales of typical intermolecular distances, and thus complement our NMR measurements.

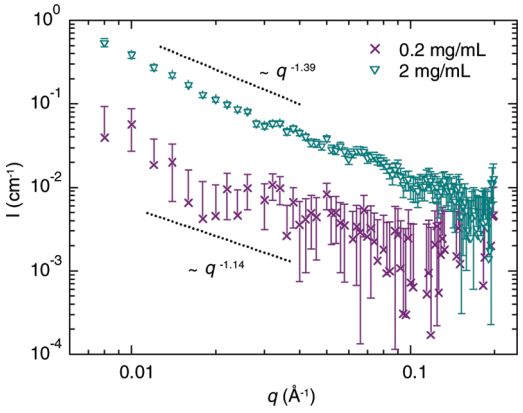


Figure 6. SANS data of PF8 in toluene-d_8 with concentrations 0.2 mg/mL (purple crosses) and 2 mg/mL (cyan down triangles). Dotted lines show the linear fits for comparison (shifted for clarity).

We have previously studied PF8 in a "good solvent", toluene, by SANS in moderate concentration (∼10 mg/mL)[30] and contrasted the results to the varying side chain length.[33] Chen and co-workers have conducted comprehensive studies of dilute (≤0.4 mg/mL)[38] PF8 toluene solutions by light scattering and dense toluene solutions (≥30 mg/mL)[31] by SANS. In the present work we extend such studies to the structural organization at larger sizes, by measuring at ultrasmall q ranges and scan over a broad range of polymer concentrations. Through this, we hope to achieve a more accurate idea of the larger length scale fluctuations unattainable by NMR.

Figure 6 plots the SANS data of PF8 in low-concentration (0.2−2 mg/mL) solution in toluene-d_8. Figure 7 plots the SANS data of the studied high-concentration samples (5−70 mg/mL) alongside the considered model fits. Structural parameters estimated from these fits are given in Table 3.

When the PF8 concentration is ≤10 mg/mL the curves decay as −1, indicative of dissolved rodlike polymers in the corresponding length scale (Figures 6 and 7). These data should be contrasted to the approximate length of the polymer that is ∼100 nm as calculated from the molecular weight and crystallographic length of the monomer (∼8.3 Å).[19] The persistence length l_p (∼10 nm) estimated from the Holtzer presentations for semidilute concentrations (Supporting Information) is consistent with the literature (8.6[18]−9.8 nm[38]) and thus corresponds to one-tenth of the polymer length. As l_p is much smaller than the polymer length, the polymer is expected to form Gaussian chains.

The overlap concentration (c^*),[63] where interpenetration of the polymer chains is assumed to begin, is approximated as $M_n/N_A(2R_g)^3 \approx 0.6$ mg/mL, where N_A is the Avogadro constant and where R_g = 249 Å is the radius of gyration measured for PF8 in dilute toluene solution at 25 °C.[38] Reference 38 gives R_g for a polymer with higher M_n than used in the present SANS measurement (128 kg/mol versus 47 kg/mol). However, c^* would not exceed 2 mg/mL if M_n was replaced by the higher value. As shown in Figure 6, both the data below (0.2 mg/mL) and above c^*(2 mg/mL) are similar except for a 10-fold difference in intensity. There seem to be a slight increase in decay from ∼−1.1 to ∼−1.4, which occurs for the samples with expected overlap of coils (∼2−10 mg/mL). The overlap becomes more apparent at very low q (∼0.006 Å^{-1}) where the data for 5−10 mg/mL samples shows few signs of leveling off, when exceeding the nominal length of individual polymers (Figure 7). An underestimation of the scatterer size is observed at the lowest q when the model of arbitrary shaped particles, expected polymer coils, is fitted to the data (orange lines in Figure 7).

When the PF8 concentration is ≥30 mg/mL, the data not only show an increase in intensity, but also a downturn at ~0.01 Å^{-1} and a significant upturn at <0.01 Å^{-1} (Figure 7), which indicates an apparent phase transition. This effect is best seen when the data are normalized to the polymer concentration (Supporting Information). When the concentration is increased up to 70 mg/mL, the data begin to show two plateaus, one at ~0.03 Å^{-1} and another at ~0.001 Å^{-1}, pointing to the structure at two levels. As proposed in ref 31, the former effect is related to the polymer overlap and the latter arises from emerging aggregation or "segmental alignment" which is responsible for the network formation and gel appearance of the dense samples. The combination of Debye−Bueche and Ornstein−Zernike type scattering functions allows an estimation of the "blob" with the size ξ_d (~20 nm) representing the length scale where polymers appear separated. Accordingly, the data do not deviate much from −1 decay for $q > 0.01$ Å^{-1} and the calculated polymer diameter (~1 nm) corresponds to a single polymer chain for the length scales below ξ_d. This fluctuation does not yet lead to gelation but the network nodes emerge above this length scale. The model includes a larger length scale fluctuation with the size ξ_s (~60 nm) that is interpreted as a distance between the network nodes. The network nodes involve parts having a few chains forming ordered elongated bundles and the gel remains transparent. These aggregates are rather different from the compact quasi-two-dimensional aggregates found for poly(2,3-diphenyl-5-decyl-1,4-phenylenevinylene) (DP10-PPV) in toluene[34] or PF8 in the poorer solvent, methylcyclohexane.[15,26,27]

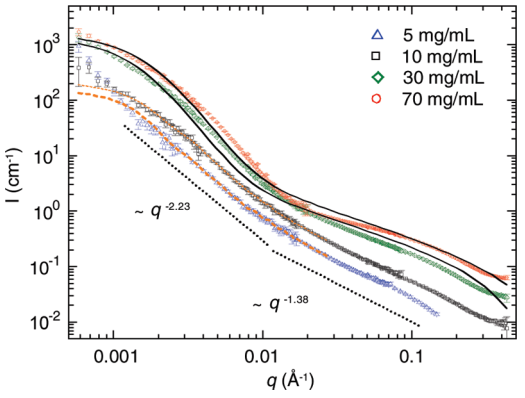


Figure 7. SANS data of PF8 in toluene-d_8 with concentrations 5 mg/mL (blue up triangles), 10 mg/mL (black squares), 30 mg/mL (green diamonds), and 70 mg/mL (red circles). Orange lines are fits to the arbitrary shaped particle "polymer coil" by software GNOM. Solid lines represent fits to the two-component model proposed in ref 31. Dotted black lines show the best linear fits for the case 10 mg/mL (shifted for clarity).

The idea of three-phase regimes and their approximate dimensions with increasing concentration are illustrated in Figure 8. At low concentrations, dissolved polymer coils with a persistence length l_p that is 1/10th of the polymer length, are observed, and may not have any contacts below c^*. The chains are forced to touch each others above c^*, and finally form a gel with the distance-ordered nodes separated by ξ_s. In this stage, the side chains are likely to be strongly interacting, in complete agreement with the NMR results in the present study. These results complement those shown by Chen and co-workers[31] for the following reasons. The low-concentration samples were not measured by SANS.[38] The previously reported q range for the high-concentration samples reached down to 0.003 Å^{-1} whereas our data extends this range down to 0.00058 Å^{-1}, showing us how the data level off at $q < 0.003$ Å^{-1} for $c \geq 30$ mg/mL. We, thus, complement these data and can be more confident with the estimated ξ_s value, while also obtaining the approximate size of scatterers corresponding to the very low q plateau (radius of gyration ~130 nm with the maximum dimension of ~300 nm). Moreover, our observation window reaches well beyond the total length of the polymer (~100 nm) and shows no clear Guinier plateau for $c \leq 10$ mg/mL (~0.001 Å^{-1}).

Some Comments on Solubility and Aggregation Behavior of PF8. In this study, both NMR and SANS show interchain interactions with PF8 upon increasing concentrations in toluene solution, and, together with semiempirical theoretical calculations, support the importance of side chain-side chain interactions in the aggregation behavior. This may help us provide more general guidelines on the aggregation of polyfluorenes in solutions. Polymer solution behavior is frequently treated by considering binary polymer−polymer, polymer−solvent and solvent−solvent interactions, through

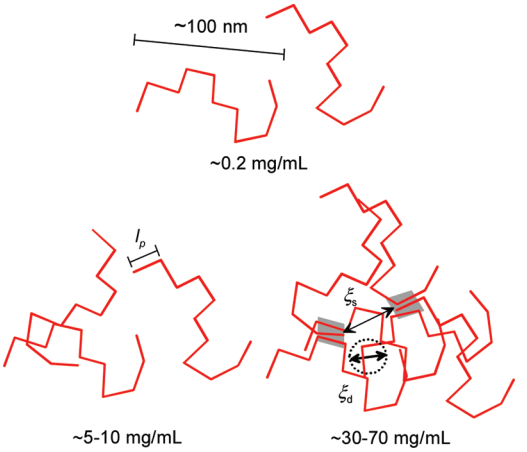


Figure 8. Idea of the intermolecular structure for PF8 in toluene-d_8 as a function of concentration. See text for details.

Table 3. Parameters Estimated from the Fits to the SANS data of PF8 in Toluene-d_8 [a]

	analyzed q range (Å^{-1})	concn = 0.2 mg/mL	concn = 2 mg/mL	concn = 5 mg/mL	concn = 10 mg/mL	concn = 30 mg/mL	concn = 70 mg/mL
α	0.00058−0.01	-	-	2.25 ± 0.02	2.21 ± 0.02	-	-
	0.0011−0.01	-	-	-	2.23 ± 0.02	-	-
	0.011−0.11	1.14 ± 0.11	1.39 ± 0.03	1.40 ± 0.01	1.38 ± 0.01	-	-
l_p (Å)	-	-	-	158 ± 26	127 ± 17	-	-
R_g (Å)	0.00058−0.027	-	-	1199 ± 36	1095 ± 34	-	-
D_{max} (Å)	-	-	-	~3250	~3250	-	-
ξ_s (Å)	0.00068−0.4	-	-	-	-	650 ± 9	550 ± 7
ξ_d (Å)	-	-	-	-	-	205 ± 30	206 ± 28
R (Å)	-	-	-	-	-	5. 0 ± 1.6	3.3 ± 1.6

[a] α and l_p stand for the scattering power for given q range and persistence length of an apparently stiff polymer. R_g and D_{max} represent radius of gyration and the maximum size of the scatterer. ξ_s, ξ_d, and R refer to the aggregate distance, mesh size and the polymer radius.

the Flory−Huggins[64−66] and Hildebrand-Scatchard[67−70] treatments. From the latter, and subsequent modifications,[70] a series of solubility parameters have been determined. Despite the simplicity of the approach, remarkable success has been achieved in predicting and interpreting various facets of the solution behavior of polymers. However, poly(9,9-dialkylfluorene)s belong to the family of "hairy-rod" polymers,[71,72] in which the relatively rigid backbone is surrounded by conformationally mobile side chains, and different interactions with solvent are anticipated for the backbone and side chains. Phenomenologically, the solution and phase behavior of polyfluorenes can be rationalized in terms of the nature of the solvent, the volume fraction of the polymer, the side chain size and shape and the molecular weight of the polymer.[13−17,30,33] In addition, experimental studies and molecular dynamics simulations on the anionic poly{1,4-phenylene-[9,9-bis(4-phenoxy-butylsulfonate)]fluorene-2,7-diyl} in mixed solvents strongly suggest specific solvent interactions with backbone, side chain and ionic regions of these systems.[73] Extension of these ideas to PF8 suggest that local solvation effects may also be important here, and that we need to consider separately the various pairwise interactions involving backbone, side chain and solvent.

Chlorinated alkanes are good solvents for polyfluorenes, and many other conjugated polymers. The fact that there is a reasonable attractive interaction with these solvents and the backbone is suggested by the monomer 2,7-dibromo-9,9-dioctylfluorene forming a solvated species on crystallization from chloroform.[74] As with interactions between many other aromatic molecules and halomethanes,[75] this probably involves an attractive contact charge transfer interaction. Since halomethanes and long-chain alkanes are generally completely miscible, there are no unfavorable solvent side-chain interactions, and polyfluorenes are dissolved in haloalkanes at the molecular level until very high polymer volume fractions.

If the solvent quality decreases, specific interactions involving the backbone or the side chains become important. One type of interaction which has frequently been invoked in aggregation behavior of aromatic molecules,[76] and applied to conjugated polymers, involves $\pi-\pi$ stacking. For example, Lazzaroni and colleagues[17] have suggested that $\pi-\pi$ stacking is responsible for formation of long fibrils of PF8 when it is deposited onto mica substrates from solution. However, from studies of the crystal structure of 9,9-di-*n*-octyl-9*H*-fluorene,[77] and other considerations,[35] the steric requirements of the alkyl groups at the 9-position strongly suggest that the backbones are prevented from coming close enough together for such $\pi-\pi$ stacking to occur in PF8. Further, a recent detailed critical analysis of the existence of $\pi-\pi$ stacking has been presented,[78] which recommends that instead of "stacking", these should be considered as $\pi-\pi$ interactions, which are only likely to be important in large unsaturated systems when they are spatially close. This is unlikely for interactions between two poly(9,9-dialkylfluorene) chains. From NMR data, there appears to be good evidence for $\pi-\pi$ interactions between the aromatic solvent toluene and polyfluorene backbones with PF8[31] and PF2/6.[35] These may involve a sandwich polymer−solvent−polymer association. However, these are still relatively weak attractions, and as we have shown in this paper from NMR spectral and relaxation data, with polymers having straight alkyl side chains, as in PF8, these are in competition with interactions between the alkyl chains, which, at high polymer concentration, may be one of the driving forces leading to gel formation. The process is dependent on van der Waals interactions between side chains on two different polymers. These increase with the chain length of the alkyl side chains.[79,80] In some cases, this may lead to β-phase formation.[40] These interactions are opposed by conformational disordering of the side chains,[80] and the observed phase behavior is a result of the subtle balance between these rather weak interactions. The differences in the phase behavior of poly(9,9-dialkylfluorene)s with different alkyl chain lengths in toluene solutions[33] are a consequence of this. With branched side chains, such as in PF2/6, van der Waals interactions between alkyl side chains are reduced, and there is little sign of β-phase formation.

In the case of poor solvents, such as tetrahydrofuran, cyclohexane, and methylcyclohexane,[24,26,40] there is little interaction between the solvent and the backbone, and the phase behavior is dominated by side chain interactions. Where straight alkyl chains are present, van der Waals interactions can favor stabilization of the β-phase. Further, for short alkyl chains these are unfavorable relative to backbone−backbone interactions, however for longer chains, the interactions are counterbalanced by alkyl chain disordering. We believe that this can explain the chain length dependence of β-phase formation,[81] with the optimum conditions occurring for the octyl side chain. In addition, because of the importance of van der Waals interactions, addition of other alkyl chain compounds, such as 1,8-diiodooctane[21] or phospholipids,[22] which can also interact with the PF8 side chains through van der Waals forces, can also stabilize the formation of the β-phase. There are suggestions that the β-phase in PF8 exists without aggregation.[23,82] In particular, single-molecule fluorescence microscopy has proved to be a powerful technique to study the conformational behavior of isolated chains of conjugated polymers,[83] and evidence has been presented for stress-induced β-phase formation in PF8 films.[82,84] Kinetic[24] and thermodynamic[40] arguments have also been presented that aggregation is not the driving force for β-phase formation. However, although β-phase formation may not require aggregation,[23,24,40] it is almost certainly stabilized by it, and we believe that the observation of interactions between the alkyl side chains of PF8 upon aggregation in toluene solutions supports the importance of their involvement in this. This is further supported from optical measurements as a function of alkyl chain length. For PF6, a spectral change with time is observed, going from a Gaussian-like absorption band to one with structure and more weighted to the red indicative of aggregation, but no beta phase can be induced, whereas for PF7 to PF9, this structured absorption band forms on thermal cycling and is also accompanied by beta phase formation. For PF10, the aggregate state does not seem to be stable but a small fraction of beta-phase formation can be induced.[81,85] In addition, for high-molecular-weight PF8, it is possible that β-phase formation for single molecules may result from backfolding of the longer chains leading to alkyl−alkyl interactions between chain ends.

V. Conclusions

NMR, SANS, and dynamic light scattering studies in this and previous works show that PF8 is present in dilute toluene solutions as isolated chains, but upon increasing polymer concentration, interchain interactions lead to association and, eventually, gel formation. As suggested by Chen and co-workers[31] this is likely to be associated, in part, with $\pi-\pi$ interactions involving toluene and the polymer backbone. However, interaction between alkyl side chains is also seen to play a major role in association and gel formation. This probably involves mainly van der Waals forces between the side chains, which will be strongly chain-length dependent. As has been suggested elsewhere based on the combination of classical molecular dynamics and DFT simulations

on model PF8 oligomers,[86] side-chain interactions play a major role in the association behavior of this class of polymers, and may be relevant to related areas, such as the stabilization of the β-phase in PF8.

Acknowledgment. The authors acknowledge the "Rede Nacional de RMN" for the spectrometer facilities, and Dr. Emeric Wasielewski for help in data acquisition. The Varian VNMRS 600 MHz spectrometer is part of the National NMR Network and was purchased in the framework of the National Programme for Scientific Re-equipment, contract REDE/1517/RMN/2005, with funds from POCI 2010 (FEDER) and "Fundação para a Ciência e a Tecnologia" (FCT). L.L.G.J. acknowledges FCT for the postdoctoral grant SFRH/BPD/26415/2006 and the "Laboratório de Computação Avançada", of the Department of Physics of the University of Coimbra, for the computing facilities (Milipeia Cluster). The experiments at ISIS (RB1010190) were supported by the European Commission under the seventh Framework Programme through the Key Action: Strengthening the European Research Area, Research Infrastructures. Contract No. CP-CSA_INFRA-2008-1.1.1 Number 226507-NMI3. We are grateful to Drs Sarah Rogers and Telma Costa for their assistance in these measurements, and to Professor Carlos F. G. C. Geraldes and a reviewer for valuable comments. M.K. and L.A. acknowledge ILL for economic support. L.A. is grateful for support from Adolphe Merkle Foundation, Fribourg.

Supporting Information Available: Figures showing SANS data of the high concentration samples normalized to the polymer concentration and the Holtzer plot of the same data. This material is available free of charge via the Internet at http://pubs.acs.org.

References and Notes

(1) Sirringhaus, H.; Kawase, T.; Friend, R. H. *MRS Bull.* **2001**, *26*, 539–543.
(2) Voigt, M. M.; Guite, A.; Chung, D. Y.; Khan, R. U. A.; Campbell, A. J.; Bradley, D. D. C.; Meng, F. S.; Steinke, J. H. G.; Tierney, S.; McCulloch, I.; Penxten, H.; Lutsen, L.; Douheret, O.; Manca, J.; Brokmann, U.; Sonnichsen, K.; Hulsenberg, D.; Bock, W.; Barron, C.; Blankaert, N.; Springer, S.; Grupp, J.; Mosley, A. *Adv. Funct. Mater.* **2010**, *20*, 239–246.
(3) Grell, M.; Bradley, D. D. C. *Adv. Mater.* **1999**, *11*, 895–905.
(4) Nguyen, T. Q.; Yee, R. Y.; Schwartz, B. J. *J. Photochem. Photobiol. A: Chemistry* **2001**, *144*, 21–30.
(5) Banach, M. J.; Friend, R. H.; Sirringhaus, H. *Macromolecules* **2004**, *37*, 6079–6085.
(6) Neher, D. *Macromol. Rapid Commun.* **2001**, *22*, 1366–1385.
(7) Leclerc, M. *J. Polym. Sci. Part A: Polym. Chem.* **2001**, *39*, 2867–2873.
(8) Scherf, U.; List, E. J. W. *Adv. Mater.* **2002**, *14*, 477–487.
(9) Grimsdale, A. C.; Müllen, K. *Adv. Polym. Sci.* **2006**, *199*, 1–82.
(10) Abbel, R.; Schenning, A. P. H. J.; Meijer, E. W. *J. Polym. Sci. Part A: Polym. Chem.* **2009**, *47*, 4215–4233.
(11) Monkman, A.; Rothe, C.; King, S.; Dias, F. *Adv. Polym. Sci.* **2008**, *212*, 187–225.
(12) Knaapila, M.; Winokur, M. J. *Adv. Polym. Sci.* **2008**, *212*, 227–272.
(13) Knaapila, M.; Stepanyan, R.; Lyons, B. P.; Torkkeli, M.; Hase, T. P. A.; Serimaa, R.; Güntner, R.; Seeck, O. H.; Scherf, U.; Monkman, A. P. *Macromolecules* **2005**, *38*, 2744–2753.
(14) Byun, H. Y.; Chung, I. J.; Shim, H.-K.; Kim, C. Y. *Macromolecules* **2004**, *37*, 6945–6953.
(15) Knaapila, M.; Stepanyan, R.; Torkkeli, M.; Garamus, V. M.; Galbrecht, F.; Nehls, B. S.; Preis, E.; Scherf, U.; Monkman, A. P. *Phys. Rev. E* **2008**, *77*, 051803.
(16) Knaapila, M.; Stepanyan, R.; Lyons, B. P.; Torkkeli, M.; Monkman, A. P. *Adv. Funct. Mater.* **2006**, *16*, 599–609.
(17) Surin, M.; Hennebicq, E.; Ego, C.; Marsitzky, D.; Grimsdale, A. C.; Müllen, K.; Brédas, J.-L.; Lazzaroni, R.; Leclère, P. *Chem. Mater.* **2004**, *16*, 994–1001.
(18) Grell, M.; Bradley, D. D. C.; Long, X.; Chamberlin, T.; Inbasekaran, M.; Woo, E. P. *Acta Polym.* **1998**, *49*, 439–444.
(19) Grell, M.; Bradley, D. D. C.; Ungar, G.; Hill, J.; Whitehead, K. S. *Macromolecules* **1999**, *32*, 5810–5817.
(20) Teetsov, J.; Fox, M. A. *J. Mater. Chem.* **1999**, *9*, 2117–2122.
(21) Peet, J.; Brocker, E.; Xu, Y.; Bazan, G. C. *Adv. Mater.* **2008**, *20*, 1882–1885.
(22) Tapia, M. J.; Monteserín, M.; Burrows, H. D. *Abstracts XXIII IUPAC Symposium on Photochemistry*; Ferrara, Italy, July 11−16, 2010; abstract P296.
(23) Chunwaschirasiri, W.; Tanto, B.; Huber, D. L.; Winokur, M. J. *Phys. Rev. Lett.* **2005**, *94*, 107402.
(24) Dias, F. B.; Morgado, J.; Maçanita, A. L.; da Costa, F. P.; Burrows, H. D.; Monkman, A. P. *Macromolecules* **2006**, *39*, 5854–5864.
(25) Hickl, P.; Ballauff, M.; Scherf, U.; Müllen, K.; Lindner, P. *Macromolecules* **1997**, *30*, 273–279.
(26) Knaapila, M.; Dias, F. B.; Garamus, V. M.; Almásy, L.; Torkkeli, M.; Leppänen, K.; Galbrecht, F.; Preis, E.; Burrows, H. D.; Scherf, U.; Monkman, A. P. *Macromolecules* **2007**, *40*, 9398–9405.
(27) Chen, C.-Y.; Chang, C.-S.; Huang, S.-W.; Chen, J.-H.; Chen, H.-L.; Sum, C.-I.; Chen, S.-A. *Macromolecules* **2010**, *43*, 4346–4356.
(28) Fytas, G.; Nothofer, H. G.; Scherf, U.; Vlassopoulos, D.; Meier, G. *Macromolecules* **2002**, *35*, 481–488.
(29) Dias, F. B.; Knaapila, M.; Monkman, A. P.; Burrows, H. D. *Macromolecules* **2006**, *39*, 1598–1606.
(30) Knaapila, M.; Garamus, V. M.; Dias, F. B.; Almásy, L.; Galbrecht, F.; Charas, A.; Morgado, J.; Burrows, H. D.; Scherf, U.; Monkman, A. P. *Macromolecules* **2006**, *39*, 6505–6512.
(31) Rahman, M. H.; Chen, C.-Y.; Liao, S.-C.; Chen, H.-L.; Tsao, C.-S.; Chen, J.-H.; Liao, J.-L.; Ivanov, V. A.; Chen, S.-A. *Macromolecules* **2007**, *40*, 6572–6578.
(32) Burrows, H. D.; Knaapila, M.; Monkman, A. P.; Tapia, M. J.; Fonseca, S. M.; Ramos, M. L.; Pyckhout-Hintzen, W.; Pradhan, S.; Scherf, U. *J. Phys.: Condensed Matter* **2008**, *20*, 104210.
(33) Knaapila, M.; Almásy, L.; Garamus, V. M.; Ramos, M. L.; Justino, L. L. G.; Galbrecht, F.; Preis, E.; Scherf, U.; Burrows, H. D.; Monkman, A. P. *Polymer* **2008**, *49*, 2033–2038.
(34) Li, Y.-C.; Chen, C.-Y.; Chang, Y.-X.; Chuang, P.-Y.; Chen, J.-H.; Chen, H.-L.; Hsu, C.-S.; Ivanov, V. A.; Khalatur, P. G.; Chen, S.-A. *Langmuir* **2009**, *25*, 4668–4677.
(35) Rahman, M. H.; Liao, S.-C.; Chen, H.-L.; Chen, J.-H.; Ivanov, V. A.; Chu, P. P. J.; Chen, S.-A. *Langmuir* **2009**, *25*, 1667–1674.
(36) Somma, E.; Loppinet, B.; Chi, C.; Wegner, G. *Phys. Chem. Chem. Phys.* **2006**, *8*, 2773–2778.
(37) Ling, J.; Fomina, N.; Rasul, G.; Hogen-Esch, T. E. *J. Phys. Chem. B* **2008**, *112*, 10116–10122.
(38) Chen, J.-H.; Chang, C.-S.; Chang, Y.-X.; Chen, C.-Y.; Chen, H.-L.; Chen, S.-A. *Macromolecules* **2009**, *42*, 1306–1314.
(39) Justino, L. L. G.; Ramos, M. L.; Abreu, P. E.; Carvalho, R.; Sobral, A. J. F. N.; Scherf, U.; Burrows, H. D. *J. Phys. Chem. B* **2009**, *113*, 11808–11821.
(40) Kitts, C. C.; Vanden Bout, D. A. *Polymer* **2007**, *48*, 2322–2330.
(41) Traiphol, R.; Charoenthai, N.; Srikhirin, T.; Perahia, D. *Synth. Met.* **2010**, *160*, 1318–1324.
(42) Panyukov, S.; Rabin, Y. *Phys. Rep.* **1996**, *269*, 1–131.
(43) Shibayama, M. *Macromol. Chem. Phys.* **1998**, *199*, 1–30.
(44) Chen, S. H.; Su, A. C.; Chen, S. A. *J. Phys. Chem. B* **2005**, *109*, 10067–10072.
(45) Chen, S.-H.; Su, A.-C.; Chen, S.-A. *Macromolecules* **2006**, *39*, 9143–9149.
(46) Galbrecht, F.; Yang, X. H.; Nehls, B. S.; Neger, D.; Farrell, T.; Scherf, U. *Chem. Commun.* **2005**, *18*, 2378–2380.
(47) Heenan, R. K.; Penfold, J.; King, S. M. *J. Appl. Crystallogr.* **1997**, *30*, 1140–1147.
(48) Svergun, D. I. *J. Appl. Crystallogr.* **1992**, *25*, 495–503.
(49) Schmidt, M. W.; Baldridge, K. K.; Boatz, J. A.; Elbert, S. T.; Gordon, M. S.; Jensen, J. H.; Koseki, S.; Matsunaga, N.; Nguyen, K. A.; Su, S. J.; Windus, T. L.; Dupuis, M.; Montgomery, J. A. *J. Comput. Chem.* **1993**, *14*, 1347–1363.
(50) Becke, A. D. *J. Chem. Phys.* **1993**, *98*, 5648–5652.
(51) Lee, C.; Yang, W.; Parr, R. G. *Phys. Rev. B* **1988**, *37*, 785–789.
(52) Bylaska, E. J.; de Jong, W. A.; Govind, N.; Kowalski, K.; Straatsma, T. P.; Valiev, M.; Wang, D.; Apra, E.; Windus, T. L.; Hammond, J.; Nichols, P.; Hirata, S.; Hackler, M. T.; Zhao, Y.; Fan, P.-D.; Harrison, R. J.; Dupuis, M.; Smith, D. M. A.; Nieplocha, J., Tipparaju, V.; Krishnan, M.; Wu, Q.; Van Voorhis, T.; Auer, A. A.; Nooijen, M.; Brown, E.; Cisneros, G.; Fann, G. I.; Fruchtl, H.; Garza, J.; Hirao, K.; Kendall, R.; Nichols, J. A.; Tsemekhman, K.; Wolinski, K.; Anchell, J.; Bernholdt, D.; Borowski, P.; Clark, T.; Clerc, D.; Dachsel, H.; Deegan, M.; Dyall, K.; Elwood, D.; Glendening, E.; Gutowski, M.; Hess, A.; Jaffe, J.; Johnson, B.; Ju,

J.; Kobayashi, R.; Kutteh, R.; Lin, Z.; Littlefield, R.; Long, X.; Meng, B.; Nakajima, T.; Niu, S.; Pollack, L.; Rosing, M.; Sandrone, G.; Stave, M.; Taylor, H.; Thomas, G.; van Lenthe, J.; Wong, A. Zhang, Z. NWChem, A Computational Chemistry Package for Parallel Computers, Version 5.1; Pacific Northwest National Laboratory: Richland, WA, 2007.High Performance Computational Chemistry: An Overview of NWChem a Distributed Parallel Application. Kendall, R. A.; Apra, E.; Bernholdt, D. E.; Bylaska, E. J.; Dupuis, M.; Fann, G. I.; Harrison, R. J.; Ju, J.; Nichols, J. A.; Nieplocha, J.; Straatsma, T. P.; Windus, T. L.; Wong, A. T. *Comput. Phys. Commun.* **2000**, *128*, 260–283.
(53) Stewart, J. J. P. *J. Mol. Modeling* **2007**, *13*, 1173–1213.
(54) MOPAC2007, James J. P. Stewart, Stewart Computational Chemistry, Version 8.087L web: HTTP://OpenMOPAC.net.
(55) Ranger, M.; Rondeau, D.; Leclerc, M. *Macromolecules* **1997**, *30*, 7686–7691.
(56) Bloembergen, N.; Purcell, E. M.; Pound, R. V. *Phys. Rev.* **1948**, *73*, 679–712.
(57) Gil, V. M. S.; Geraldes, C. F. G. C. *Ressonância Magnética Nuclear, Fundamentos, Métodos w Aplicações*, 2nd ed.; Fundação Calouste Gulbenkian: Lisbon, 2002.
(58) Heatley, F. *Prog. Nucl. Magn. Reson. Spectrosc.* **1979**, *13*, 47–85.
(59) (a) Lipari, G.; Szabo, A. *J. Am. Chem. Soc.* **1982**, *104*, 4546–4559. (b) Lipari, G.; Szabo, A. *J. Am. Chem. Soc.* **1982**, *104*, 4559–4570.
(60) Ayalur-Karunakaran, S.; Blumich, B.; Stapf, S. *Langmuir* **2009**, *25*, 12208–12216.
(61) (a) Andrew, E. R.; Bradbury, A.; Eades, R. G. *Nature* **1959**, *183*, 1802–1803. (b) Andrew, E. R.; Szczesniak, E. *Prog. Nucl. Magn. Reson. Spectrosc.* **1995**, *28*, 11–36.
(62) Lowe, I. J. *Phys. Rev. Lett.* **1959**, *2*, 285–287.
(63) Ying, Q.; Chu, B. *Macromolecules* **1987**, *20*, 362–366.
(64) Huggins, M. L. *J. Chem. Phys.* **1941**, *9*, 440.
(65) Flory, P. J. *J. Chem. Phys.* **1941**, *9*, 660–661.
(66) Flory, P. J. *Principles of Polymer Chemistry*: Cornell University Press: Ithaca, NY, 1953.
(67) Hildebrand, J. H.; Scott, R. L. *Solubility of Non-Electrolytes*, 3rd ed.; Reinhold: New York, 1950.
(68) Hildebrand, J. H.; Prausnitz, J. M.; Scott, R. L. *Regular and Related Solutions*; Van Nostrand-Reinhold: Princeton, NJ, 1970.
(69) Scatchard, G. *Chem. Rev.* **1949**, *44*, 7–35.
(70) Barton, A. F. M. *Chem. Rev.* **1975**, *75*, 731–753.
(71) Wegner, G. *Macromol. Chem. Phys.* **2003**, *204*, 347–357.
(72) Subbotin, A.; Stepanyan, R.; Knaapila, M.; Ikkala, O.; ten Brinke, G. *Eur. Phys. J. E* **2003**, *12*, 333–345.
(73) Burrows, H. D.; Fonseca, S. M.; Silva, C. L.; Pais, A. A. C. C.; Tapia, M. J.; Pradhan, S.; Scherf, U. *Phys. Chem. Chem. Phys.* **2008**, *10*, 4420–4428.
(74) Leclerc, M.; Ranger, M.; Bélanger-Gariépy, F. *Acta Crystallogr., Sect. C* **1998**, *C54*, 799–801.
(75) Davis, K. M. C.; Farmer, M. F. *J. Chem. Soc. B* **1968**, 859–862.
(76) Hunter, C. A.; Lawson, K. R.; Perkins, J.; Urch, C. J. *J. Chem. Soc., Perkin Trans. 2* **2001**, 651–669.
(77) McFarlane, S.; McDonald, R.; Veinot, J. G. C. *Acta Crystallogr. C* **2005**, *C61*, O671–O673.
(78) Grimme, S. *Angew. Chem., Int. Ed.* **2008**, *47*, 3430–3434.
(79) Nagle, J. F.; Goldstein, M. *Macromolecules* **1985**, *18*, 2643–2652.
(80) Bazuin, C. G.; Guillon, D.; Skoulios, A.; Amorim da Costa, A. M.; Burrows, H. D.; Geraldes, C. F. G. C.; Teixeira-Dias, J. J. C.; Blackmore, E.; Tiddy, G. J. T. *Liq. Cryst.* **1988**, *3*, 1655–1670.
(81) Bright, D.; Dias, F. B.; Galbrecht, F.; Scherf, U.; Monkman, A. P. *Adv. Funct. Mater.* **2009**, *19*, 67–73.
(82) Da Como, E.; Becker, K.; Lupton, J. M. *Adv. Polym. Sci.* **2008**, *212*, 293–318.
(83) Lammi, R. K.; Barbara, P. F. *Photochem. Photobiol. Sci.* **2005**, *4*, 95–99.
(84) Da Como, E.; Becker, K.; Feldman, J.; Lupton, J. M. *Nano Lett.* **2007**, *7*, 2993–2998.
(85) Bright, D. W.; Galbrecht, F.; Scherf, U.; Monkman, A. P. *Macromolecules* **2010**, *43*, 7860–7863.
(86) Kilina, S.; Batista, E. R.; Yang, P.; Tretiak, S.; Saxena, A.; Martin, R. L.; Smith, D. L. *ACS Nano* **2008**, *2*, 1381–1388.

344 *Macromolecules* **2011**, *44*, 344–348
DOI: 10.1021/ma101635q

Macromolecules
ARTICLE

Self-Organization of Liquid-Crystal and Reactive-Mesogen into 2D Surface-Stabilized Structures

Jean-Philippe Bédard-Arcand and Tigran Galstian*

Department of Physics, Engineering Physics and Optics, Laval University, Pav. d'Optique-Photonique, 2375 Rue de la Terrasse, Québec, Canada G1V 0A6

Received July 20, 2010; Revised Manuscript Received November 9, 2010

ABSTRACT: We report the experimental observation of light induced self-organization of 2D periodic structures at the liquid interface of thick nematic liquid crystal and thin reactive mesogen layers. We believe that the long scale thermal fluctuations initiate interpenetration of those two molecular species, and the geometrical asymmetry and matrix-imposed anisotropy result in very specific symmetry properties of the final blend. The photo-polymerization of the reactive mesogen is further amplifying its spatial redistribution and is fixing (stabilizing) the obtained liquid-crystal/surface-attached polymer network. The application of a strong electric field is definitely adjusting that network in terms of morphology and electro-optical response. The origin of the formation of regular and oriented periodic structures remains unclear.

Introduction

Nematic liquid crystals (NLCs) are very likely the most explored materials among anisotropic liquids.[1−3] Their applications range from large liquid crystal displays (see, e.g., ref 4) to miniature electrically variable lenses (see, e.g., the recent review in ref 5). However, the alignment of NLC's *director* (local average orientation of long molecular axes[1]) is still achieved by mechanical rubbing in a large majority of cases, which is generating undesired static charge, dust, alignment defects and damage of thin film transistors. Various alternative techniques have been explored so far to avoid the mechanical rubbing or at least to minimize the above-mentioned drawbacks. Oblique incidence SiO_x deposition,[6] plasma treatment,[7] photoalignment,[8,9] and nano structuring[10] are some examples of those explorations.

We have followed a slightly different path in our research group, by trying to use polymer networks to align the NLCs in a nonmechanical way and also to affect their electro-optical properties by the same network. It must be emphasized that, in contrast to the well-known polymer-stabilized liquid crystal (PSLC) systems[11] (where the polymer network is floating in the volume of the NLC host), we have been developing *surface-stabilized* polymer networks. Namely, the main idea here is the use of various electro-magnetic torque mechanisms to align the surface-cast reactive mesogen (RM) molecules in their liquid crystalline (nematic) phase and then to use their reactivity to cure them (e.g., by UV light exposition) to obtain a permanently aligned and surface-attached polymer network which, in turn, may affect the behavior (pretilt, electrooptics, etc.) of normal (nonreactive) NLC subsystem[12] that would be put in contact with those surfaces. Thus, one could call those systems as *surface* polymer-stabilized liquid crystals (S-PSLC).

However, it was already well established that realistically achievable torque values on individual molecules are very weak.[1] Thus, e.g., the magnetic torque $\Gamma \approx (\mu H)^2/E$ (where μ is the Bohr magneton, H is the magnetic field, and E is the electronic excitation energy) will be insufficient to align individual molecules since the corresponding energy will be well below the thermal fluctuation energy kT. However, the collective angular behavior of those molecules would multiply the torque by $\approx 10^{22}$, hence enabling the angular manipulation of the whole system by using fields of quite reasonable amplitude. To further increase the efficiency of such a torque, we have decided to create a partial interpenetration of NLC and RM molecules. Thus, the RM molecules have been cast as thin films, which were then partially cured (by UV exposure) before being used as substrates to build sandwich-like cells containing the normal NLC. This is where we have observed some unexpected formation of anisotropy "fingerprint"-like structures, we are reporting in the present work.

Materials and Methods

The RM, which we have chosen, is the photo-curable composition RMS03−001C that was commercially obtained from Merck and used without further modification. The reason for the choice of this RM is the fact that it behaves like liquid crystal in room temperature.[13] We have followed the instructions from Merck to spin coat thin films of this RM on the ITO-coated glass substrates, which were previously coated by a planar Polyimide (from Nissan) layer of approximately 50 nm thickness. Those polyimide films were rubbed prior to RM deposition. The typical thicknesses of RM films obtained were of the order of $\approx 0.6\ \mu$m. Those films were precured by using a UV lamp (Opt. Eng. Model 22-UV, 365 nm, 20 mW/cm^2) for durations ranging from 0 to 120 s. Then two such substrates were used to build (in the "drop-fill" mode) a sandwich-like structure to contain the NLC. Thus, the first substrate was horizontally disposed (with the RM film facing up) and a drop of the NLC mixture TL216 (also purchased from Merck) was disposed on the surface of RM. The periphery of the substrate was covered by a wall of UV-curable adhesive (AC A1432-Q-S2 from ADDISON) containing glass spacers (o.d. $\approx$ 50 μm) to provide the desired thickness of the cell (see next step). Then, the second RM-coated substrate (similar to the first one) was pushed on the top of the NLC (two RM films facing each other) and the peripheral adhesive was UV cured while protecting the central part of the cell by a mask. Then, after a certain delay (to allow partial interpenetration of NLC and uncured RM molecules) the same UV source was used to cure the RM film in the central part of the cell too. This last action was conducted

*Corresponding author. E-mail: galstian@phy.ulaval.ca.

 Published on Web 12/15/2010 © 2010 American Chemical Society

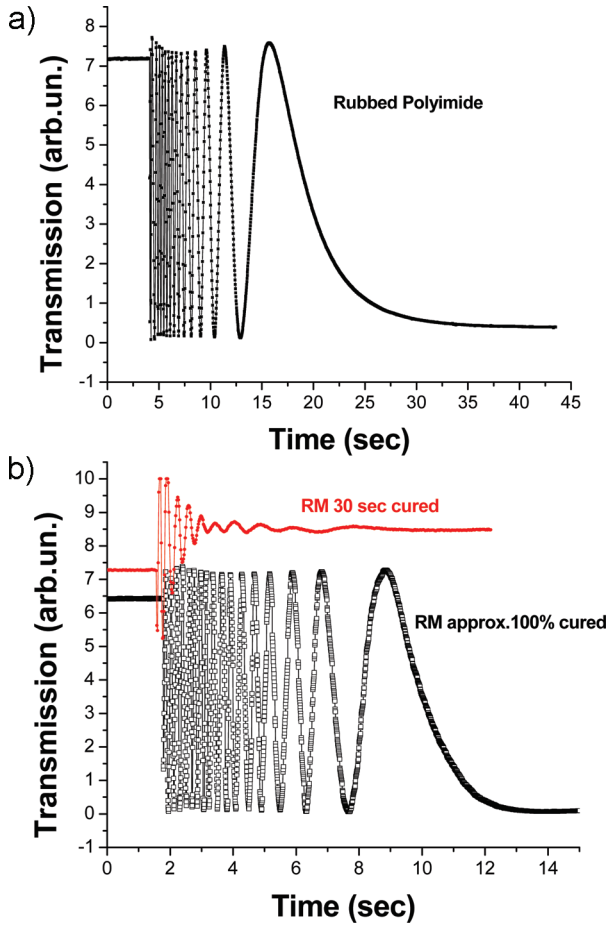


Figure 1. Dynamic polarimetric study of relaxation of the NLC cells built by using substrates of Polyimide, complete (≈100%) or partially (30 s) cured RM layers. The cell is positioned (at 45°) between two crossed polarizers, then 10 V_{rms} voltage is applied to achieve a stationary reorientation state and then the voltage is removed enabling thus the relaxation of molecules to their initial planar state; cells are built using substrates with (a) rubbed polyimide only or (b) RM films of different degree of precure (open squares, highly cured; filled circles, 30 s cured RM) spin-cast on the top of the rubbed polyimide.

with and without electrical field applied for different cells (see later). The electro optic properties of obtained cells were studied by using polarimetric and polarizing microscope techniques (with rms voltages ranging from 0 to 110 V).

Experimental Results

Cells, fabricated by using substrates with nonrubbed Polyimide, have generally shown strong light scattering. In contrast, all cells obtained by using RM films cast on rubbed Polyimide substrates initially had good uniform NLC alignment in the central part of the surface (protected during the peripheral adhesive curing). This was the case, independently if an electric field was applied or not during the final UV curing. However, different degrees of prepolymerization of the RM layers revealed different electro-optical behavior of obtained cells. Unfortunately, it was a rather difficult task to monitor the exact kinetics of polymerization of the thin RM film. For the moment, and in a very qualitative approach only, we have tested the degree of this photo-polymerization (before the cell assembly) by using mechanical scratching technique. The RM films, which were exposed for more than 2 min of UV light, were already solid, while below that exposure, they appeared like gels of different viscosity. Keeping in mind that more detailed analysis must be done to identify the exact degree of polymerization of RM films and that 100% curing would never be achieved, we shall further call the RM films "completely" or "100%" cured if they were exposed to UV for more than 2 min, for simplicity only.

Thus, in the case of cells fabricated by using completely cured RM surfaces and without the use of electrical field during UV curing ($U = 0$ V), the measured pretilt angles were rather small ≈0.3° ± 0.1°. The pretilt angles for cells with partially cured RM films (from 0 to 60 s of UV exposure) were negligible (within our experimental error). In contrast, the pretilt angles were at the order of 4.5° ± 0.1° for the reference cells built with substrates having only rubbed polyimide (cells having the same thickness and containing the same NLC, but without the RM layer).

Different durations of RM's prepolymerization have been tested. Cells built with RM films with 0 s exposure (before their contact with NLC) have shown strong light scattering after the fabrication process. This scattering was generated by irregular NLC alignment clusters, which persisted even for high voltages applied during the test. Higher curing degrees, starting from approximately 30 s, provided lower light scattering allowing thus the polarimetric characterization of obtained cells, Figure 1. The further curing of RM films resulted into an electro-optic behavior of the cell that was gradually evolving from the case of 30 s curing up to the complete curing. Thus, only those two extreme cases are shown in the Figure 1b. As we can see, the character of relaxation in the case of partially cured RM (30 s exposure) is quite different: there is a specific dynamic envelope of oscillation amplitude (that is not observed in other two cases, Figure 1, parts a and b), followed by smaller but longer amplitude oscillations.

The application of voltage to cells with completely cured RM layers has shown a normal uniform reorientation. Sometimes we have observed the appearance of irregularly shaped closed loop orientation defects or so-called disclinations, changing their form with voltage. This was expected because of relatively small pretilt angle. However, in general, the relaxation time τ_R of the obtained cells was noticeably faster (approximately by a factor 1.75, see Figure 1, parts a and b) compared to those obtained with reference cells, showing a typical relaxation time of ≈5.35 s; both being modeled by a simple exponential relaxation of unsaturated (see later) orientation angle of the director at the center of the cell as

$$\theta_{central}(t) \approx \theta_{pretilt} + \theta_{\max}\exp(-t/\tau_R) \quad (1)$$

Most unexpected results were obtained in the case of cells built with partially cured RM layers (still no voltage applied during the UV curing). Their relaxation was much faster (by a factor of 2 to 5, Figure1b) compared to the case of cells using completely cured RM. The morphology of those cells was drastically changed when relatively high electrical voltages were applied to them. In fact, Figure 2 shows the evolution of the morphology (observed in Zeiss polarizing microscope) of obtained cells when increasing the AC (at 885 Hz, sine shaped) voltage. Multiple values of voltages have been tested but only key states are shown here. As it can be seen, the uniform initial alignment (0 V, Figure 2a) was gradually transformed into a regular 2D structure with the voltage increase starting already from 6 V (Figure 2, parts b and c). Those structures may be characterized by two converging axes, each tilted with respect to the rubbing direction of the polyimide (shown by an arrow in the Figure 2c) at approximately ±15°. Other important observations follow. The distance between the walls of those structures is rather regular, being on the order of ≈35 ± 5 μm. The effective width of those walls is remarkably stable across the surface of the cell, being at the order of ≈4 μm ± 1 μm (measured at 110 V). Some preliminary experimental study shows that those parameters do not depend noticeably upon the thickness of the cell. A closer look into the lanes formed by the parallel walls shows that they contain a less

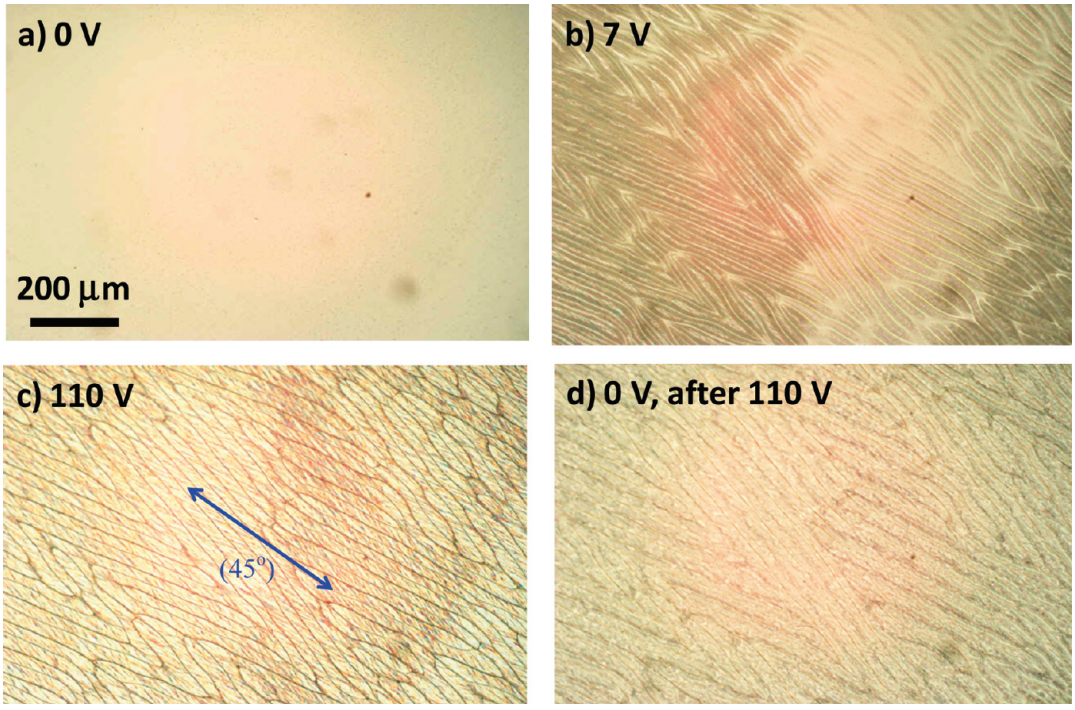


Figure 2. Microphotography (taken by a Zeiss polarizing microscope, X10 Objective) of the morphology of the NLC cell built with partially cured RMs at different stages: (a) right after the complete (≈100%) photopolymerization and at $U = 0$ V, (b) at $U = 7$ V, (c) at $U = 110$ V, and (d) at $U = 0$ V after passing by the value of 110 V. The horizontal bar (in the top left) shows 200 μm length as a reference.

regular microstructure that is tilted with respect to those walls. There is also indication of NLC being nonuniformly aligned within those walls. The 2D structuring remained when the voltage was reduced back to 0 V after passing by the value of 110 V (Figure 2d). The morphology was then stable for consecutive variations of the voltage.

The fabrication of cells using partially cured RM films and different voltages applied during UV curing is under detailed study and will be reported soon. For the moment, we can note that, at above-mentioned degrees of partial precuring (before their contact with NLC) and their final curing in the presence of NLC and with a voltage U_{cur} applied, the obtained cells show tendency for uniformization; higher is the voltage higher is the uniformity of the final alignment. We do not observe 2D structure formation already for voltages at the order of $U_{cur} =$ 20 V and more. Those cells show relaxation dynamics closer to the reference cells.

Discussion

The loss of pretilt in RM coated cells does not seem to be surprising, since, very likely, the rubbing induced alignment of Polyimide side chains is screened by the rather thick layer (≈0.6 μm) of RM. The appearance of orientation dynamic disclinations is also normal and is related to this loss of pretilt.

Concerning the relaxation times: The oscillations of the instantaneous transmission for a uniaxial layer of NLC may be described by the well-known polarimetric formula

$$I = \sin^2(2\beta)\sin^2\left(\frac{\phi}{2}\right) \qquad (2)$$

where $\phi = ((2\pi)/(\lambda))\int_0^L (n_e(z) - n_\perp)\,dz$ is the accumulated (output) phase delay between ordinary and extraordinary waves, $n_e(z)$ and $n_\perp$ are the local extraordinary and ordinary refractive indices of the NLC, respectively, β is the angle between the optical axis of the NLC and the polarizer's transmission axis (in our case $\beta = 45°$), λ is the wavelength of the probe beam in the vacuum, and L is the cell thickness. Thus, the number of oscillations during the relaxation process represents roughly the variation of the effective birefringence, while the speed of damping (of those oscillations) represents the relaxation speed. In a very rough approximation we can suppose an unsaturated sine-like reorientation profile of the director (for strong boundary conditions), which would describe the spatial distribution of the reorientation angle as $\delta\theta(z) \approx \theta_{max}\sin(\pi z/L)$. Then the local value of the extraordinary refractive index could be roughly estimated as $n_e(z) \approx n_{II}n_\perp/(n_{II}^2\sin^2\theta(z) + n_\perp^2\cos^2\theta(z))^{1/2}$, where $\theta(z) = \theta_{pretilt} + \delta\theta(z)$ is the angle between the director of the NLC and the induction vector of the probe beam.

The specific differences observed in the relaxation stage (Figure 1) could be originated by the presence of transversal (in the plane of the substrate) 2D microstructures shown in Figure 2. This observation shows the significant constraints that the polymer network is imposing on the NLC subsystem. Thus, not only the form, but also the typical duration of relaxation is very different because of these constraints. In fact, the typical relaxation times τ_R for strong anchoring conditions of a uniform NLC cell may be described (see, e.g., ref 14) as

$$\tau_R \approx \gamma L^2/(K_1\pi^2) \qquad (3)$$

where γ is the rotational viscosity and K_1 is the splay deformation's elastic constant. The rotational viscosity of the NLC used is $\gamma = 297$ mPa s (or 0.297 s N/m^2) at 20 °C. Its elasticity constant is $K_1 \approx 15.3$ pN. For a cell thickness $L = 50$ μm, we could expect to have typical free relaxation times $\tau_R \approx$ (0.297 s N/m^2) /(15.3 × 10^{-12}N) x 25 × 10^{-10} m^2/9.86 = 49.1 × 10^{-1} s ≈5 s. As it was mentioned above, the reference cells have shown typical relaxation times of ≈5.35 s (Figure 1a), which is very close to the theoretical value. The small difference could be explained by the slightly higher thickness (≈ 53−55 μm), lower anchoring energy (not infinitely high as supposed in the theory) and the lower quality of alignment in those cells.

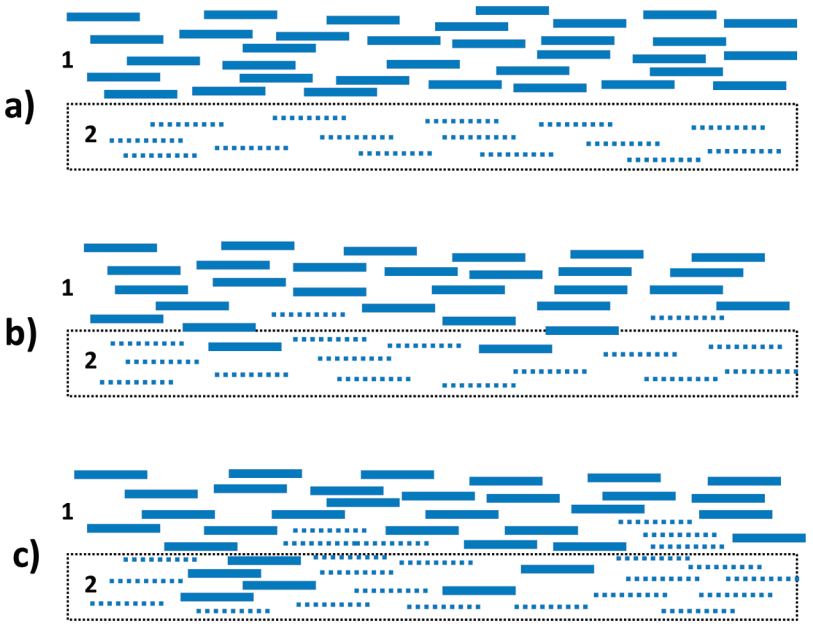


Figure 3. Schematic demonstration of the (a) initial state of the NLC-RM liquid interface, (b) spontaneous interdiffusion with long scale fluctuations, and (c) photopolymerization "amplified phase separation".

Shorter relaxation times, observed for the cells using completely cured RM (Figure 1b), could be related to some limited degree of interpenetration of NLC and RM molecules within a superficial layer due to the non 100% curing of the RM (before its contact with NLC), which could increase the anchoring energy, reduce the effective cell thickness and thus decrease the relaxation times.[14] The faster relaxation (Figure 1b), observed in the cells using partially cured RM layers (or S-PSLCs), should be related to the same (but stronger) partial interpenetration of RM and NLC, which creates significant effective cavities (proven by the morphology studies using the polarizing microscopy) with characteristic lengths smaller than the cell thickness.[15,16]

Concerning the morphological observations: so-called "fingerprint" structures have already been observed in the case of chiral LC materials or when using nonaligning surfaces for NLC.[1] However, those are nonstabilized structures, their geometrical characteristics depend upon the cell thickness and are dynamically changing, e.g., with voltage application. Our experimental conditions do not match with none of above-mentioned conditions. We believe that we could use the analogy of formation of traditional polymer dispersed liquid crystal (PDLC) and PSLC material systems[3] to understand (at least partially) the origins of formation of 2D structures reported in the present work. Thus, the initial state of the interface of two liquids (NLC and RM) is schematically shown to be uniform in the Figure 3a (media 1 and 2 representing NLC and RM, respectively). Then, in contrast to the case when only the RM layer is cast on the rubbed polyimide,[13] the addition of the layer of NLC is destabilizing the surface of the RM. Thermal fluctuations take place resulting into interdiffusion of RM molecules (shown as short horizontal *dotted* lines) and NLC molecules (shown as short horizontal *solid* lines) during the delay between the assembly and the final UV curing process (Figure 3b). Those initial fluctuations (in the dark) have long scale character with corresponding initial pattern of spontaneous interpenetration (Figure 3b). It must be emphasized here that the interpenetration taking place in the nematic phase for both liquids (RM and NLC), the molecular diffusion process is rather complicated. In fact, it is well-known[1,17] that the molecular diffusion is strongly anisotropic in those liquids (higher in the direction of the *director*). This imposes a corresponding symmetry breakdown for the above-mentioned long scale fluctuations favoring the molecular diffusion in the rubbing direction (see also ref 18 and references therein).

The further UV exposition initiates the photo-polymerization process primarily in the RM-rich regions. This process is amplifying the spatial redistribution of species (Figure 3c) since the local consumption of monomers (to build more densely packaged polymer chains) is attracting more monomers in those areas and is very likely repulsing further the NLC molecules, rather similar to the process taking place in PDLC materials. However, in contrast to PDLCs, the formation of the polymer network in our case is strongly asymmetric (because of the solid substrate, present from one side only; the second one being far away behind the thick layer of NLC), its chains are aligned and they have a spontaneously formed periodicity in the plane of the substrate. In addition, the formation of polymer chains in those conditions (anisotropy matrix and corresponding anisotropy molecular diffusion) is certainly increasing the energy and elastic constraints of the whole interpenetrated material system. That could explain the significant transformation (adjustment) of the morphology after we have applied strong electrical field. In fact, after the polymerization process is over, the NLC-RM (polymerized) material system is uniformly aligned despite of the important interpenetration and density redistribution. However, there are many areas where the NLC subsystem is "stuck" between polymer chains. That is why, the application of a strong electric field forces the reorientation of the NLC subsystem, which is rearranging also the polymer chains formed under constrains of uniform alignment and anisotropy diffusion of molecules. Let us note that similar nonreversible rearrangement of the polymer subsystem (while *nonperiodic* and in the *volume* of the cell) was observed also in traditional bulk PSLC systems (see e.g., refs 19, 20).

Summary and Conclusions

In the summary, we have described the photo-polymerization initiated self-organized formation of a *surface* polymer-stabilized liquid crystal material system. Long scale thermal fluctuations of initial material composition bring to microscopic phase separation, which is further amplified by the spatially nonuniform photopolymerization process. The asymmetry of boundary conditions (substrate/RM/NLC) and the anisotropy of the matrix impose very specific conditions on this process. This constrains result in

the formation of initially unstable self-organized 2D structures of interpenetrated polymer and NLC. The application of strong electric fields is definitively stabilizing the material system by the rearrangement of the polymer network forced by the reorientation of the NLC subsystem. The complete understanding of the origins of observed regular 2D morphology (characteristic dimensions, orientations, etc.) is still lacking and work is in progress to elucidate the underlying mechanisms.

Acknowledgment. We thank the financial support of Canadian Institute for Photonic Innovations (CIPI), Fonds Québécois de la Recherche sur la Nature et les Technologies (FQRNT) and Natural Sciences and Engineering Research Council of Canada (NSERC).

References and Notes

(1) de Gennes, P. G.; Prost, J. *The Physics of Liquid Crystals*, 2nd ed.; Oxford University Press: Oxford, U.K., 1995.
(2) Blinov, L. M.; Chigrinov, V. G. *Electrooptic Effects in Liquid Crystal Materials*; Springer: Berlin, 1994.
(3) Crawford, G. P., Zumer, S., Eds. *Liquid Crystals in Complex Geometries*; Taylor & Francis: London, 1996.
(4) Yeh, P.; Gu, C. *Optics of Liquid Crystal Displays*; Wiley: New York, 1999.
(5) Asatryan, K.; Presnyakov, V.; Tork, A.; Zohrabyan, A.; Bagramyan, A.; Galstian, T.; Optical lens with electrically variable focus using an optically hidden dielectric structure. *Opt. Express* **2010**, *18*, 13981−13992.
(6) Chaudhari, P.; Lacey, J.; Doyle, J.; Galligan, E.; Lien, S.-C. A.; Callegari, A.; Hougham, G.; Lang, N. D.; Andry, P. S.; John, R.; Yang, K.-H.; Lu, M.; Cai, C.; Speidell, J.; Purushothaman, S.; Ritsko, J.; Samant, M.; Stoehr, J.; Nakagawa, Y.; Katoh, Y.; Saitoh, Y.; Sakai, K.; Satoh, H.; Odahara, S.; Nakano, H.; Nakagaki, J.; Shiota, Y. Atomic-beam alignment of inorganic materials for liquid-crystal displays. *Nature* **2001**, *411*, 56–59.
(7) Yaroshchuk, O. V.; Kravchuk, R. M.; Dobrovolskyy, A. M.; Liu, P. C.; Lee, C. D. Plasma beam alignment for the large-area substrates: Equipment and process. *J. SID 13/4* **2005**, 289–294.
(8) Yaroshchuk, O.; Kyrychenko, V.; Tao, D.; Chigrinov, V.; Kwok, H. S.; Hasebe, H.; Takatsu, H. Stabilization of liquid crystal photoaligning layers by reactive mesogens. *Appl. Phys. Lett.* **2009**, *95*, 021902.
(9) Chigrinov, V. G.; Kozenkov, V. M.; Kwok, H. S. *Photoalignment of Liquid Crystalline Materials: Physics and Applications*; Wiley: New York, 2008.
(10) F. S.-Yan Yeung, Xie, F.-C.; Kwok, H.-S.; Wan, J.; Tsui, O.; Sheng, P. *High Pretilt Angles by Nano-Structured Surfaces and their Applications*; pp 1080−1080; SID 05 Digest.
(11) Hikmet, R. A. M. Electrically induced light scattering from anisotropic gels. *J. Appl. Phys.* **1990**, *68*, 4406; doi:10.1063/1.346190
(12) Goubert, G.; Galstian, T. Light controlled capillarity of liquid crystals on photo anisotropic surfaces. *Mol.Cryst. Liq.Cryst.* **2010**, *526*, 46–57.
(13) *Reactive Mesogens, specification sheet*; Merck KGaA: Germany, www.merck.de.
(14) Nie, X.; Lu, R.; Xianyu, H.; Wu, T. X.; Wu, S.-T.; ," Anchoring energy and cell gap effects on liquid crystal response time. *J. Appl. Phys.* **2007**, *101*, 103110−1−103110−5.
(15) Crawford, G. P.; Scharkowski, A.; Fung, Y. K.; Doane, J. W. Internal surface, orientational order, and distribution of a polymer network in a liquid crystal matrix. *Phys. Rev. E* **1995**, *52*, R1273–R1276.
(16) Zohrabyan, L.; Zohrabyan, A.; Galstian, T. Fast electro-optic switch in perfluorinated acrylate stabilized nematic liquid crystal. *Opt. Mater.* **2009**, *31*, 1189–1193.
(17) Saad, B.; Denariez-Roberge, M. M.; Galstyan, T. Diffusion of photoexcited azo dyes in liquid crystal host. *Opt. Lett.* **1998**, *23* (9), 727–729.
(18) Muzic, D. S.; Rajaram, C. V.; Chien, L. C.; Hudson, S. D. Morphology of Polymer Networks Polymerized in Highly Ordered Crystalline Phases. *Polym. Adv. Technol.* **1996**, *7*, 737−742.
(19) Presnyakov, V. V.; Galstian, T. V. Light Polarizer Based on Anisotropic Nematic Gel with Electrically Controlled Anisotropy of Scattering. *Mol.Cryst. Liq.Cryst.* **2004**, *413*, 545− 551.
(20) Zohrabyan, L.; Albu, A.-M.; Zohrabyan, A.; Galstian, T. Light induced gradient polymer stabilized liquid crystals for electrically variable focus lenses: the role of network morphology. *Proc. SPIE* **2010**, *7716*, 77160D; doi:10.1117/12.859079.

Macromolecules
ARTICLE

Macromolecules **2011**, *44*, 349–359 **349**
DOI: 10.1021/ma101765k

Relationship between Molecular Aggregation Structures and Optical Properties of Polyimide Films Analyzed by Synchrotron Wide-Angle X-ray Diffraction, Infrared Absorption, and UV/Visible Absorption Spectroscopy at Very High Pressure

Kazuhiro Takizawa, Junji Wakita, Shohei Azami, and Shinji Ando*

Department of Chemistry & Materials Science, Tokyo Institute of Technology, Ookayama 2-12-1-E4-5, Meguro-ku, Tokyo 152-8552, Japan

Received August 3, 2010; Revised Manuscript Received November 29, 2010

ABSTRACT: The relationship between the molecular aggregation structures and the optical properties of fully aromatic and semialiphatic polyimide (PI) films were analyzed by synchrotron wide-angle X-ray diffraction (WAXD), infrared absorption, and UV/visible absorption spectroscopy at very high pressures up to 8 GPa. The PIs showed significant reduction in the interchain distances in the first stage of compression up to 1 GPa, which resulted in an appreciable decrease in the interchain free volume. In addition, reduction in the C−C bond lengths of aromatic rings by ca. 0.7% was confirmed by the pressure-induced high wavenumber shift of the infrared stretching vibration of the PIs. Furthermore, pressure-induced bathochromic shifts were observed in the locally excited (LE) absorption band of PIs, which are related to the enhanced van der Waals interaction caused by the reduced interchain distances. The intensity of the charge transfer (CT) absorption band of *s*-BPDA/PDA poly(*p*-phenylene biphenyltetracarboximide) PI was reduced up to 0.3 GPa, indicating that conformational changes affect the intramolecular CT interactions. In contrast, the CT absorptions of PMDA/ODA (poly(4,4′-oxidiphenylene pyromelliticimide) and PMDA/DCHM (poly(4,4′-diaminocyclohexylmethane pyromelliticimide) PIs were enhanced by increasing the pressure, which was caused by an enhancement of intermolecular CT interactions. The significant variations observed in the LE and intermolecular CT bands below 1 GPa accord with the significant decrease in the interchain distance, as indicated by synchrotron WAXD.

1. Introduction

The fully aromatic polyimide (PI) derived from pyromellitic-dianhydride and bis(4-aminophenyl) ether (PMDA/ODA) and that from 3,3′,4,4′-biphenyltetracarboxylic dianhydride and *p*-phenylene diamine (*s*-BPDA/PDA) are known as high-performance engineering plastics exhibiting high thermal and chemical stability, flame resistance, radiation resistance, mechanical strength, and good flexibility.[1] Recently, semialiphatic PIs have attracted much interests as a new class of thermally stable electronic and optical materials.[2−5] For example, they have been applied to optical waveguides with low optical losses in the visible and near-IR regions.[4] For further development of novel thermally stable and optically functional PIs, it is mandatory to understand the relationship between the molecular aggregation structures and the optical properties of PIs at the molecular level.

It has been reported that two kinds of UV/visible absorption bands are observed for fully aromatic polyimides (Ar-PIs).[5−8] The first one is "locally excited" (LE) transition that occurs between the molecular orbitals (MOs) located around the dianhydride moiety of PIs. The second one is "charge transfer" (CT) transition originating from the CT complexes formed between the dianhydride and diamine moieties. The lowest energy CT transition generally occurs between the highest occupied MO (HOMO) located around the diamine moiety and the lowest unoccupied MO (LUMO) located around the dianhydride moiety. The energy gap of this transition is essentially determined by the electron-donating property of diamine and the electron-accepting property of dianhydride.[9] The smaller energy gaps of the CT transitions displace the absorption edges of PI films to a longer wavelength region ($\lambda > 400$ nm, visible region), which is the essential origin of the significant coloration of Ar−PI films from pale yellow to deep brown.

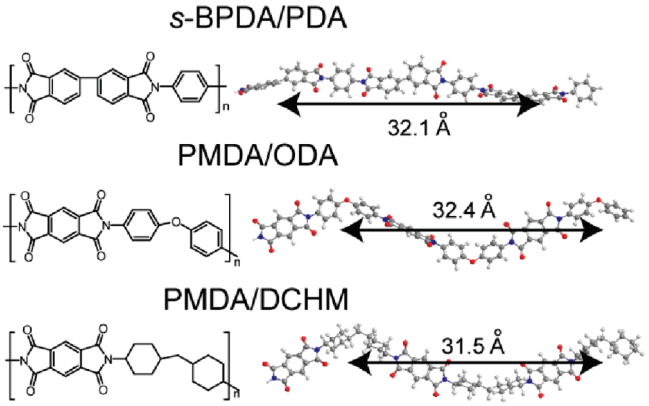
Furthermore, it was also found that intra- and intermolecular CT transitions can occur in PI films. Previously, Ishida and co-workers[6] reported that an intramolecular CT absorption band was observed near the absorption edge at around 400 nm in a thin film of PMDA/ODA PI, and the band could be assigned using the absorption spectrum of a corresponding model compound: *N*,*N*′-bis(phenoxyphenyl) pyromelliticimide. In particular, they concluded that the observed CT absorption band was attributable to an intramolecular CT transition due to the fact that the absorbance of the shoulder peak at 371 nm was linearly correlated with the concentration of the model compound. On the other hand, Hasegawa and co-workers[7,8] reported that the intensity of a fluorescent emission from an excited CT state (CT fluorescence) was enhanced by high-temperature annealing of a thin film of *s*-BPDA/PDA PI, which is due to the enhancement of intermolecular CT interactions by changes in molecular aggregation structures. The above results clearly indicate that not only the chemical and electronic structures of the repeating unit but also the intermolecular electronic interactions significantly affect the optical properties of PI films, and therefore, knowledge of the influence of aggregation structures is a prerequisite for a detailed understanding and precise control of the optical properties of PIs.

*Corresponding author. Telephone: +81-3-5734-2137. Fax: +81-3-5734-2889. E-mail: sando@polymer.titech.ac.jp.

© 2010 American Chemical Society

Published on Web 12/23/2010

Chart 1. Molecular Structure of PIs and Optimized Geometries of PI Trimers Obtained by DFT Calculations at the Level of [B3LYP/6-311G(d)]



The molecular aggregation structures of PI chains have been mainly investigated using wide-angle X-ray diffraction (WAXD).[10−19] For instance, Russell et al.[11] reported that the aggregation structures of PMDA/ODA films ranged from amorphous structures to ordered crystalline structures, depending on the film thickness and preparation conditions. In general, PI films do not exhibit definitive crystalline diffraction peaks, which indicates the absence of large domains with three-dimensional positional order. Such ordered domains with mesomorphic order between crystalline and amorphous phase in the film were formed during thermal imidization and frozen at room temperature, which can be interpreted as liquid crystalline-like (LC-like) ordered domains.[19]

Pressure is a more suitable factor than temperature in perturbing the intermolecular interactions of polymer chains in the solid state. X-ray diffraction,[20−23] infrared absorption (IR) spectra,[24−26] UV/visible absorption and the fluorescence spectra[27−31] of polymers have been measured under high pressure to examine the compression effects on their crystalline structure, and on their physical and optical properties. For instance, Lorenzen et al.[21] reported variations in the bulk compressibility of crystalline poly(tetrafluoroethylene) (PTFE) by increasing the pressure using X-ray diffraction patterns. Convington et al.[25,26] measured the pressure-induced shifts of the infrared absorption modes of poly(methyl methacrylate) (PMMA) and polycarbonate (PC), and they concluded that most of the free volume was removed after compression up to 2 and 1 GPa, respectively. Drickermer et al.[28,30,31] reported variations in the steady-state and time-dependent emission properties of neat polymer and polymer blends. Erskine et al.[29] measured pressure-induced variations in the optical transmission spectra of PMDA/ODA PI up to 12 GPa, and concluded that intermolecular CT transitions exist in the PI because a significant bathochromic shift of the absorption edges was caused by applying pressure. Very recently, we reported pressure-induced variations in the absorption spectra of aromatic and semialiphatic PIs up to 400 MPa.[32] A pressure-induced bathochromic shift was observed in the LE band, which is related to increases in the van der Waals interactions due to a decrease in interchain distances. In addition, a pressure-induced increase in absorbance was observed for the intermolecular CT absorption band of PMDA/ODA. The intensity of the CT absorption band depends on the overlap integral (S_{da}) between occupied MOs of electron-donating diamine moiety and unoccupied MOs of electron-accepting dianhydride moiety.[32] Thereby, the increase in the intermolecular CT absorption can be readily explained by an increase in S_{da} owing to a decrease in the intermolecular distance. In contrast, in the case of *s*-BPDA/PDA, in which the intramolecular CT interaction is dominant, no increase in the CT absorption band was observed at elevated pressures, which indicates that the intramolecular CT band was not enhanced. The S_{da} of intramolecular CT band could be enhanced by an increase in the coplanarity between the benzene rings of the dianhydride and diamine moieties of PIs. Hence, such a conformational change at the imide−phenyl (>N−Ph) bond was not induced in *s*-BPDA/PDA by pressure. Recently, we have reported variations in the aggregation structures of PI chains in the ordered domains up to 8 GPa as a Communication.[23] Though, the relationship between pressure-induced variations in the molecular aggregation structures and optical properties of PI films have not been examined so far. In this paper, the influence of variations in the molecular aggregation structures of PI chains to the UV/visible absorption properties, which were induced at very high pressures up to 8 GPa, are extensively examined using synchrotron-radiation WAXD, infrared absorption (IR), and UV/visible absorption spectroscopy.

2. Experimental Section

Materials. Pyromellitic dianhydride (PMDA) purchased from Kanto Chemical Co., Inc. was dried and purified by sublimation under reduced pressure. 3,4,3′,4′-Biphenyltetracarboxylic dianhydride (*s*-BPDA) from Wako Pure Chemical Industries, Ltd. was dried at 170 °C for 12 h under reduced pressure. *p*-Phenylenediamine (PDA) and 4,4-diaminodiphenyl ether (ODA) from Wako Pure Chemical Industries, Ltd. were recyrstallized from tetrahydrofuran, followed by sublimation under reduced pressure. 4,4′-Diaminocyclohexylmethane (DCHM), purchased from Tokyo Kasei Kogyo Co. Ltd. was recrystallized from *n*-hexane, followed by sublimation under reduced pressure. The content of *trans*−*trans* isomer in purified DCHM was estimated as 94% by ^{1}H NMR spectrum.[23] *N*,*O*-Bis(trimethylsilyl) trifluoroacetamide (99+%, BSTFA) and *N*,*N*-dimethylacetamide (anhydrous, DMAc), purchased from Aldrich, were used without further purification.

Preparation of Polyimide Films. The molecular structures of the PIs used in this study are shown in Chart 1. To investigate the effects of the rigidity of PI chains on their compressibility, three PI films, *s*-BPDA/PDA, having a pseudo-rigid-rod molecular structure, PMDA/ODA, having a rigid and bent molecular structure, and PMDA/DCHM, having a semiflexible structure, were studied. The precursors of aromatic PIs, poly(amic acid)s (PAAs), were prepared by mixing equimolar amounts of dianhydride and diamine in a DMAc solution under dry nitrogen. The PAA solutions were stirred at room temperature for 48 h. The precursors of PMDA/DCHM, poly(amic acid) silyleter (PASE), were prepared by the *in situ* silylation method reported by Matsumoto[33] and Oishi.[34,35] For instance, DCHM was dissolved in DMAc, stirred for a few minutes, and then a 1.05 molar amount of BSTFA was slowly added. An equimolar amount of dianhydride was then added and stirred at room temperature for 48 h to give a PASE solution. The trimethylsilylated amino groups of diamines can avoid salt formation between unreacted amino groups and the carboxyl groups of the dianhydride moieties. In general, PAA and PASE solutions become viscous after stirring for several hours, depending on the degree of polymerization and the rigidity of the molecular structures. The PI films were prepared by thermal imidization of the corresponding PAA or PASE precursors. The solutions were spin-coated onto silica substrates, followed by soft-baking at 70 °C for 1 h and subsequent thermal imidization in a one-step imidization procedure: the final curing conditions were 300 °C/1.5 h for the PMDA/DCHM thick film (thickness: ca. 20 μm) and 350 °C/1.5 h for the *s*-BPDA/PDA and PMDA/ODA thin films (thickness: ca. 1−2 μm). The heating rate was 4.6 °C/min from 70 °C to the final curing temperatures, and all curing procedures were conducted under nitrogen flow. Most PMDA/DCHM chains should have an extended *trans*−*trans* configuration due to the high *trans*−*trans* content of DCHM, as described above. The PI thick films of *s*-BPDA/PDA and PMDA/ODA

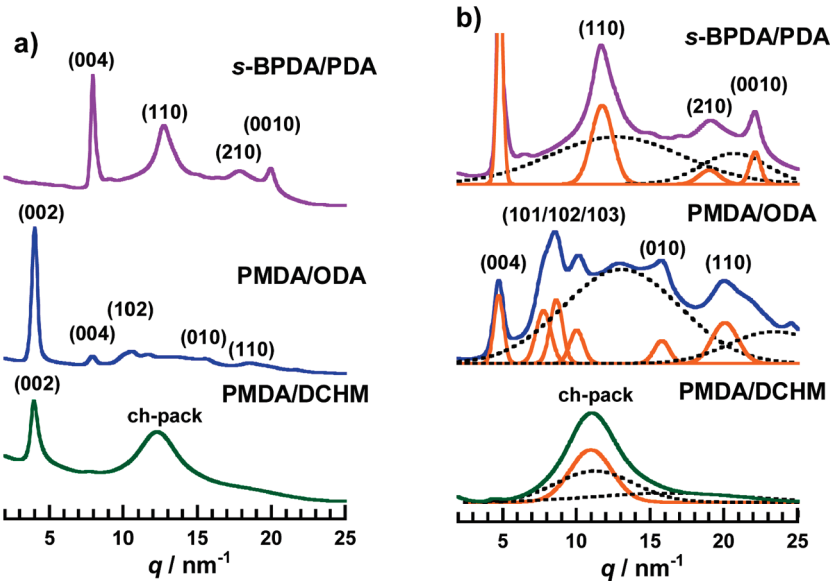


Figure 1. (a) Transmission X-ray diffraction patterns of *s*-BPDA/PDA, PMDA/ODA, and PMDA/DCHM PI thick films (thickness: ca. 20−25 μm) at atmospheric pressure. (b) Magnified representations of transmission X-ray diffraction patterns of *s*-BPDA/PDA, PMDA/ODA, and PMDA/DCHM PI thick films at atmospheric pressure. Thin solid and dotted lines respectively represent the diffraction peaks from the ordered domains and the amorphous matrix fitted by Gaussian broadening functions.

(product names: Upilex-S and Kapton-V; thickness: ca. 25 μm, Chart: 1), were kindly supplied by Ube Industries, Ltd. and DuPont-Toray Co., Ltd., respectively. The PI thin films were used for measurements of the micro-IR and the UV/visible absorption spectra, and the thick films for measurements of the transmission X-ray diffraction patterns and UV/visible absorption spectra.

Measurements. To generate pressure up to 8 GPa, the PI films were loaded into a diamond anvil cell (DAC, Syntech Co. Ltd.) equipped with 600-μm culet synthetic diamond anvils (Sumicrystal type-IIa, Sumitomo Electric Hardmetal Corp.). Type-II diamonds (Sumitomo Denko Co., Ltd.) were used because of the high transparency in the range between the ultraviolet region and the infrared region. After a 200 μm thick stainless steel gasket was indented to a thickness of 50 μm, a 230 μm diameter hole was drilled in the center of the indentation using an laser beam (JL-SP0100, DEOS., Ltd.). The standard ruby fluorescence technique was used to determine the pressure inside the sample room.[36] Ruby fluorescence spectra were measured with HR4000 spectrometer (Ocean Optics Co., Ltd.; grating, H11; slit width, 5 μm) in the range of 650−740 nm. Diode Pumped Solid State laser (Shanghai Dream Lasers Technology Co., Ltd.) was used as an excitation light source. Because the size of the sample chamber was only 230 μm in diameter, the transmission X-ray diffraction measurements were performed with a BL40B2 beamline at the Japan Synchrotron Radiation Research Institute (SPring-8) using an image-plate as the detector, and silicone oil as the pressure medium. The wavelengths of the X-ray were 0.7 Å for *s*-BPDA/PDA and 0.8 Å for PMDA/ODA and PMDA/DCHM. The diffraction peaks assignable to silicone oil and diamond anvil cell were removed from the diffraction patterns by subtracting a reference pattern measured without a sample.

The UV/visible absorption spectra of PI films at atmospheric pressure were measured by a Hitachi U-3500 spectrophotometer. The UV/visible absorption spectra of the PI films loaded in a DAC at elevated pressures were measured with a multichannel CCD spectrometer (PMA-11, Hamamatsu Photonics Co., Ltd.) in the range of 200−950 nm (C7473−36), using objective lens (cutoff wavelength: 320 nm) designed for measurement in the ultraviolet region to focus the light on the sample room, an Xe lamp (Hamamatsu Photonics Co., Ltd.) as a light source, a pinhole for adjustment to light intensity, and silicone oil as the pressure medium. Resolution of the UV/visible absorption spectra was ~0.2 nm.

The infrared absorption spectra of the PI films loaded in a DAC at elevated pressures were measured by an IRT-3000 infrared microscope (JASCO Co., Ltd.). A liquid nitrogen-cooled mercury−cadmium−tellurium (MCT) detector was used to detect the infrared radiation. The scans were performed with a nominal resolution of 2 cm^{-1} over the range of 400−4000 cm^{-1}. KBr was used as the pressure medium.

Quantum Chemical Calculation. The density functional theory (DFT) with the three-parameter Becke-style hybrid functional (B3LYP)[37−39] was adopted for the calculations of the electronic structures and spectroscopic properties of the PIs and their source materials. The 6-311G(d) basis set was utilized for the geometry optimizations and the IR spectra of the imide compounds, and the 6-311++G(d,p) basis set was used for calculating the oscillator strengths. The calculated wavenumbers were scaled down by multiplying by a single factor of 0.98 for correcting vibrational anharmonicity, basis set truncation, and the neglected part of the electron correlation. For reproducing the shapes of the experimental absorption spectra, each calculated transition was replaced by a Gaussian broadening function with a half-width at half-maximum (HWHM) of 0.3 eV. The calculated absorbance was represented by an oscillator strength divided by a van der Waals volume (nm^3) of molecules.[40−42] The van der Waals volumes were calculated based on Slonimski's method[43] using the optimized geometries, in which van der Waals radii of atoms reported by Bondi[44] were used. All calculations were performed with the Gaussian-03 D.02[45] program package installed in the Global Scientific Information and Computing Center (GSIC), Tokyo Institute of Technology.

3. Results and Discussion

3.1. Variations in the Aggregation Structure of PIs. *A. Transmission X-ray Diffraction Patterns at Atmospheric Pressure.* Figure 1a shows the transmission X-ray diffraction patterns of three kinds of 20−25 μm thick PI films measured at atmospheric pressure, and Figure 1b shows the results of peak fitting using Gaussian broadening functions. The PI film of *s*-BPDA/PDA, having a pseudo-rigid-rod molecular structure, exhibits peaks at

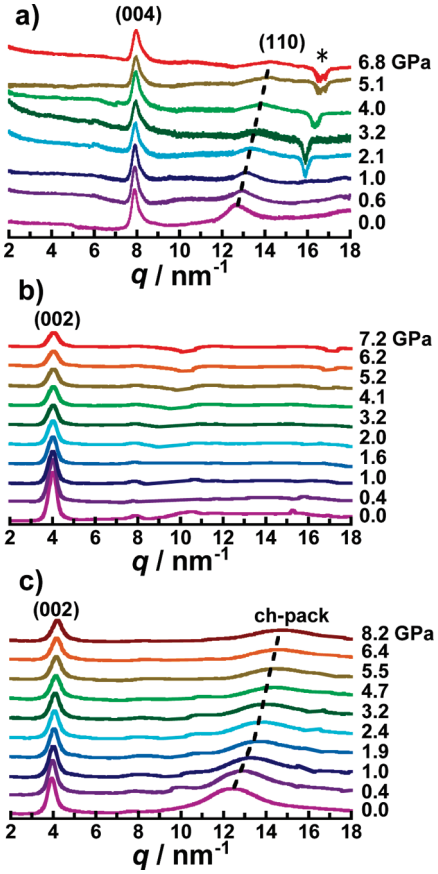


Figure 2. Variations in the X-ray diffraction patterns for (a) *s*-BPDA/PDA, (b) PMDA/ODA, and (c) PMDA/DCHM PI thick films by applying pressure. The negative peaks indicated with asterisks (∗) arise from nonperfect spectral subtraction of the pressure medium (silicone oil).

q = 7.9 nm^{-1} (d = 7.9 Å) and 19.8 nm^{-1} (3.2 Å). This PI was reported to form a crystalline structure based on an orthorhombic unit cell, and these peaks are respectively attributable to the diffractions of (004) and (0010) which represent the periodic structure along the PI main chains (c-axis).[14,16] In addition, the peaks observed at 12.7 nm^{-1} (4.9 Å) and 17.8 nm^{-1} (3.5 Å) were indexed as (110) and (210), respectively. These represent the intermolecular ordering in the directions of a- and b-axes of the PI chain packing, which are perpendicular to the PI main chains (c-axis). Because *s*-BPDA/PDA exhibited the diffraction peaks representing orderings along a-, b- and c-axes, this PI should have a highly ordered crystalline-like domain.[14,16] Also, PMDA/ODA, having a bent ether (−O−) linkage in the main chain, exhibits diffraction peaks at q = 4.0 nm^{-1} (d = 15.6 Å) and 7.9 nm^{-1} (7.9 Å). These peaks were respectively indexed as (002) and (004), in accordance with previous X-ray measurements,[10] which indicate that a curved structure consisting of two repeating units corresponds to the periodic structure along the PI chains of PMDA/ODA (see Chart 1). The peaks observed at 10.0 nm^{-1} (d = 6.3 Å), 10.7 nm^{-1} (5.9 Å), 11.6 nm^{-1} (5.4 Å), 15.6 nm^{-1} (4.0 Å), and 18.7 nm^{-1} (3.4 Å) were indexed as (101), (102), (103), (010), and (110), respectively.[10] Because PMDA/ODA exhibited the diffraction peaks which represent the ordering along a-, b-, and c-axes, this PI also should have a crystalline-like ordered domain. In addition, PMDA/DCHM exhibits a sharp peak at q = 3.9 nm^{-1} (d = 16.1 Å)

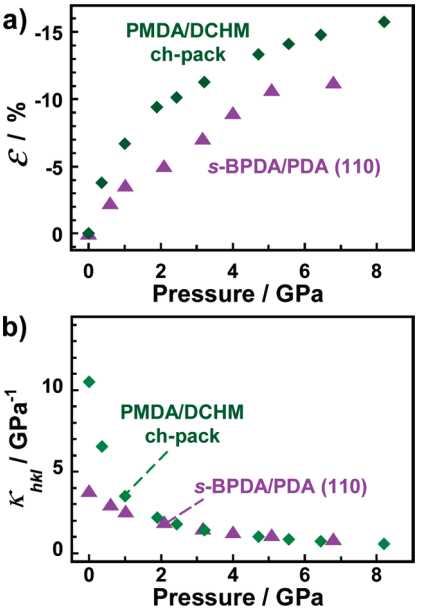


Figure 3. (a) Variations in the strains (ε) of chain packing peaks by applying pressure. (b) Variations in the linear compressibilities (κ) along the (110) peak of *s*-BPDA/PDA and the ch-pack peak of PMDA/DCHM by applying pressure.

and a broad peak at 12.4 nm^{-1} (5.1 Å). The former diffraction peak was indexed as (002),[19,23] and one pitch of the curved molecular structure consists of two repeating units similar to PMDA/ODA. Although no diffraction peaks assignable to the crystalline region were observed in PMDA/DCHM, the bandwidth of the scattering at 12.4 nm^{-1} is much narrower than those of amorphous halos.[11] Thereby, this peak can be characterized as scattering representing the PI chain packing (ch-pack) in the LC-like ordered region.[19] As shown in Figure 1b, the diffraction peaks of the three PIs are significantly overlapped by amorphous halos, as indicated by the dotted lines, which indicates the relatively low proportions of the ordered regions.

B. Variations in Interchain Distance. Figure 2 shows the pressure-induced variations in the diffraction patterns of 20−25 μm thick PI films. Figure 3a and 4a show the variations in strains (ε) of each peak observed in Figure 2, and Figure 4b shows the magnified representation of the strains of the (00l) peaks of aromatic PIs. In this study, strain is defined as $\varepsilon_{(hkl)} = \Delta d/d_{0,(hkl)}$, where $d_{0,(hkl)}$ is the d-spacing of the (hkl) plane at 0 GPa and Δd the variation in d-spacing at elevated pressures. By applying pressure up to 6 GPa, the d-spacing of the (110) peak, (d(110)), of *s*-BPDA/PDA and the d(ch-pack) of PMDA/DCHM were significantly decreased by 11 and 14%, respectively, whereas the d(004) of *s*-BPDA/PDA and the d(002) of PMDA/ODA were slightly decreased by 0.8 and 1.0%, respectively. This clearly indicates that the periodic structures perpendicular to the PI main chains are much more easily compressed than those along the PI main chains. Figure 3b depicts the variations in the linear compressibilities (κ) for the diffraction peak of (110), κ_{110} of *s*-BPDA/PDA and those for the peak of the ch-pack, $\kappa_{\text{ch-pack}}$ of PMDA/DCHM. The κ values were estimated as the numerical first derivatives of strain with respect to pressure ($\kappa = \partial\varepsilon/\partial P$). It should be noted that the $\kappa_{\text{ch-pack}}$ of PMDA/DCHM are significantly larger than those of κ_{110} of *s*-BPDA/PDA below 2 GPa. Dlubek et al.[46] reported the pressure dependence of compressibility for fluoroelastomeric copolymers of tetrafluoroethylene and perfluoro(methyl vinyl

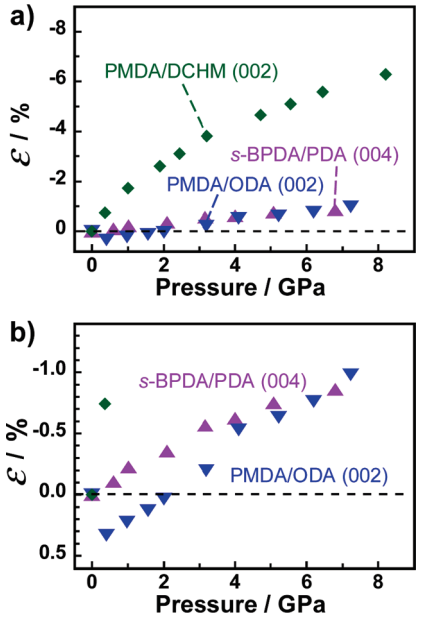


Figure 4. (a) Variations in the strains of the (00*l*) peaks of PIs by applying pressure. (b) Magnified representation of the strains of the (00*l*) peaks of aromatic PIs.

ether) as well as vinylidene fluoride and hexafluoropropylene by pressure−volume−temperature experiment (*PVT*, P = 0.1−200 MPa at 22.5 °C) and positron annihilation lifetime spectroscopy (PALS, P = 0.1−448 MPa at 22.5 °C). They reported that the compressibility of free volume is 1 order of magnitude larger than that of the total volume, and that specific occupied volume showed a definite compressibility with a value similar to that of polymer crystals. Hence, the large $\kappa_{\text{ch-pack}}$ values observed below 2 GPa indicate that semialiphatic PMDA/DCHM contains larger amounts of interchain free volume in the LC-like ordered regions, and that free volume is more compressible at lower pressures. In contrast, the much smaller κ_{110} values observed below 2 GPa indicate that fully aromatic *s*-BPDA/PDA contains a smaller amount of compressible free volume in its crystalline-like ordered region. Furthermore, the trend of significant decrease in the $\kappa_{\text{ch-pack}}$ in the former was completed at around 2 GPa, and the values of $\kappa_{\text{ch-pack}}$ and κ_{110} come close to each other above that pressure. This suggests that the easily compressible free volume in PMDA/DCHM almost disappeared at this pressure, and both the semialiphatic and aromatic PIs possess similar and dense molecular packing structures at the higher pressures. Comparable phenomena were also observed in the variations of free volume in PMMA and PC at high pressures.[25,26]

C. Variations in Periodic Length and Bond Length of PI Chains. In this section, the molecular structure dependence of pressure-induced variations in the periodic length of PI chains is investigated. As shown in Figure 4b, the d(004) value of *s*-BPDA/PDA was decreased by only 0.8% up to 6 GPa. Since *s*-BPDA/PDA has a pseudo-rigid-rod structure without bent linkages, the conformational changes should have little effect on the variation of d(004). Hence, the gradual decrease in d(004) could be mainly attributable to the shrinkage of bond lengths. For several kinds of polymers, their IR and Raman spectra have been measured at high pressures to examine the variations in intramolecular structures caused by compression.[24−26] The most noticeable changes in those spectra were the pressure-induced higher-frequency shifts of the stretching vibration peaks, and they

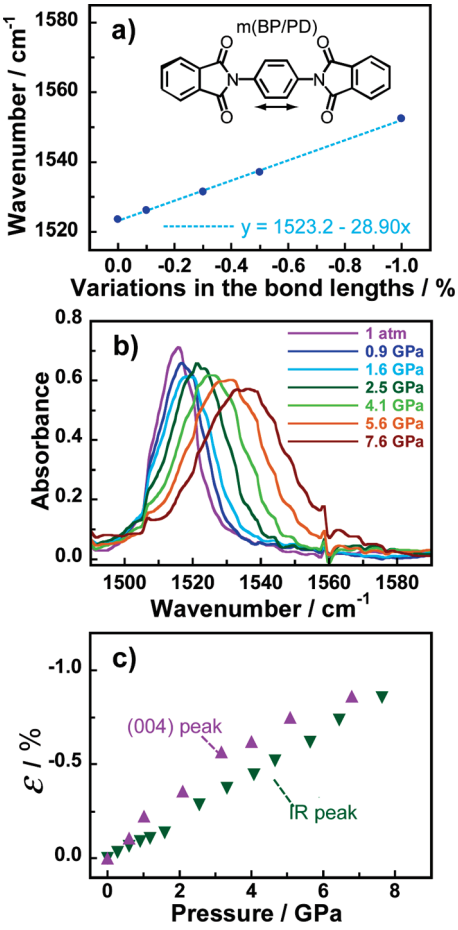


Figure 5. (a) Calculated IR peak shifts of model compound of *s*-BPDA/PDA (m(BP/PD)) for the rocking vibration of the aromatic ring of the diamine moiety as a function of reduction in bond lengths. (b) Variations in the IR spectra for the vibration of the aromatic ring of the diamine moiety at elevated pressure for *s*-BPDA/PDA thin film. (c) Comparison of the strains estimated from the peak shift of (002) for *s*-BPDA/PDA thick film (▲) and the shortening of bond lengths estimated from IR peak shift for *s*-BPDA/PDA thin film (▼) by applying pressure.

were attributed to the shrinkage of bond lengths associated with the anharmonicity of molecular vibrations. In this study, the variations in bond lengths were evaluated from the pressure-induced IR peak shifts observed for PI thin films by comparison with the IR peak shifts calculated for model compounds with shortened bond lengths. For simplicity, all the bond lengths of the model compounds were reduced at a constant proportion. The C−C stretching vibration of the benzene ring in the diamine moiety (Ph-stretch) was used for the evaluation of bond length shrinkage because of its insensitivity to variations in bond angles and dihedral angles. As shown in Figure 5a, the calculated IR peak position of Ph-stretch (ν_{cal}) of a model compound for *s*-BPDA/PDA (m(BP/PD)) is linearly shifted to higher wavenumbers with decreases in the bond lengths. The shrinkage of bond lengths by 1% induces a peak shift of 23 cm^{-1}. On the other hand, the experimental IR peak position of Ph-stretch (ν_{exp}) of a 2 μm thick film of *s*-BPDA/PDA was shifted to a higher wavenumber by 18.6 cm^{-1} by applying pressure up to 6.3 GPa (see Figure 5b). The variations in IR spectra in a wider range for *s*-BPDA/PDA are shown in Figure S1 (Supporting Information). By combining parts a and b of Figure 5, the variations in bond lengths, i.e., the strains caused by compression, ε_{IR}, were estimated by the

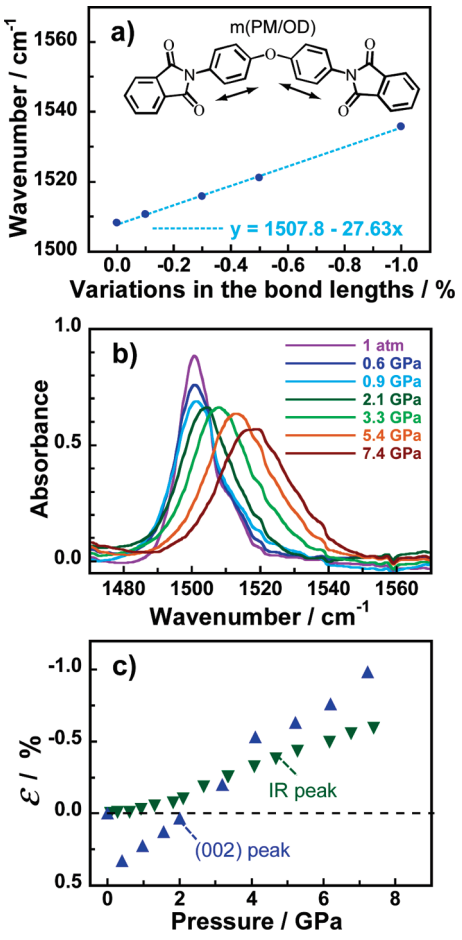


Figure 6. (a) Calculated IR peak shifts of model compound of PMDA/ODA (m(PM/OD)) for the rocking vibration of the aromatic ring of the diamine moiety as a function of reduction in bond lengths. (b) Variations in the IR spectra for the vibration of the aromatic ring of the diamine moiety at elevated pressure for PMDA/ODA thin film. (c) Comparison of strains estimated from the peak shift of (002) for PMDA/ODA thick film (▲) and the shortening of the bond lengths estimated from the IR peak shift for PMDA/ODA thin film (▼) by applying pressure.

following equation:

$$\varepsilon_{IR} = \Delta\omega/k \quad (1)$$

where $\Delta\omega$ is the pressure-induced peak shift for the Ph-stretch vibration, and k is the gradient of the fitted line depicted in Figure 5a. The k value corresponds to the peak shift (cm^{-1}) caused by variation in bond length (%). As shown in Figure 5c, the ε_{IR} value of *s*-BPDA/PDA was decreased by 0.7% by applying pressure up to 6 GPa, which coincides well with the experimental strain estimated for the d(004) peak (ε_{004} = 0.8%) of *s*-BPDA/PDA. Note that the slope of the linear pressure−ε_{IR} relation below 1 GPa (-0.072×10^{-2} GPa^{-1}) is significantly smaller than that directly estimated from the pressure−$\varepsilon_{(004)}$ relation (-0.173×10^{-2} GPa^{-1}). Hence, in the lower pressure range, the shrinkage of C−C bond lengths is smaller than that of the periodic lengths along the *c*-axis by ca. 60%, which indicates that some structural changes in the bond angles and/or dihedral angles in the pseudo rigid-rod molecular structure of *s*-BPDA/PDA were induced by pressure. Moreover, the slope of the pressure−ε_{IR} relation below 1 GPa is slightly smaller than that at above 1 GPa (-0.093×10^{-2} GPa^{-1}). This suggests that the compression stress induced on the skeletal structure of the PI could be partly released by the reduction of free volume and some structural changes in the bond angles and/or dihedral angles below 1 GPa, which could circumvent the 'stress concentration' on the phenyl C−C bonds in the PI chains. In contrast, the slopes of both the pressure-strain plots estimated from the IR band and the d(004) values are close to each other (-0.093×10^{-2} GPa^{-1} for $\varepsilon_{(004)}$ and -0.103×10^{-2} GPa^{-1} for ε_{IR}) above 2 GPa. This indicates that most of the pressured-induced structural changes along the *c*-axis are attributable to the shrinkage of the covalent bonds in *s*-BPDA/PDA. The *ab initio* all-electron periodic Hartree−Fock study for the hydrostatic compression of pentaerythritol tetranitrate indicated that the C−C bond lengths decreased by 1.12% by applying pressure up to 6.5 GPa,[47] which is close to the variation in the aromatic C−C bond length estimated from our results.

In the case of PMDA/ODA, the d(002) value was not decreased but increased by 0.3% by applying pressure up to 0.4 GPa (see Figure 4b). At a glance, the increase in the periodic length along the PI main chains looks curious, but it should be noted that this PI includes a bent diphenyl ether (−O−) linkage in the main chain. The extended chain of this PI forms not a rigid-rod structure but a zigzag structure. When the bond angle at the ether group (θ_{C-O-C}) was increased by pressure, the projected length of the repeating unit along the main chain could be elongated (see Chart: 1). In other words, when compression stress is concentrated on the ether linkage, an increase in θ_{C-O-C} led to a stretch of the pitch consisting of two repeating units. With further compression up to 6 GPa, the d(002) value was decreased by 1.0%, as expected. Figure 6a shows the calculated IR peak positions for the Ph-stretch (ν_{cal}) of a model compound for PMDA/ODA (m(PM/OD)) caused by the shortening of all the bond lengths. The ν_{cal} values are linearly shifted to higher wavenumbers by decreasing the bond lengths, the same as the case of m(BP/PD) (Figure 5a). However, as shown in Figure 6b, the experimental peak position (ν_{exp}) observed for a 2 μm thick PMDA/ODA film exhibited little changes below 1 GPa, under which the slope of the pressure−ε_{IR} is as small as -0.03×10^{-2} GPa^{-1}, whereas remarkable broadening was observed for the IR band. This indicates that the first stage of compression up to 1 GPa did not effectively shorten the average C−C bond lengths, but inhomogeneous structural and conformational changes were induced in addition to the reduction of interchain free volume. With further pressure up to 6 GPa, the IR peak was shifted to a higher wavenumber by 13.6 cm^{-1}. As shown in Figure 6c, the slope of the pressure−ε_{IR} relation above 1 GPa (-0.092×10^{-2} GPa^{-1}) is almost the same as that of the *s*-BPDA/PDA above 1 GPa (-0.093×10^{-2} GPa^{-1}), which suggests a similar amount of shrinkage for aromatic C−C bond lengths in PMDA/ODA. In contrast, the former is significantly smaller than that directly estimated from the pressure−$\varepsilon_{(002)}$ relation (-0.196×10^{-2} GPa^{-1}). This is explainable as follows. First, in contrast to the pressure range below 0.4 GPa, a narrowing of the bond angle, θ_{C-O-C}, was induced by pressure, and thus the projected length of the repeating unit was shortened up to 6 GPa. Second, the compressibility of the covalent bond varies depending on the strength of each bond, and the ether linkage in PMDA/ODA could be easily compressed compared with the aromatic rings. This is supported by the fact that the IR band of asymmetric stretching vibration of the C−O−C bond (1240 cm^{-1}) is observed at a smaller wavenumber than that of the Ph-stretch (1500 cm^{-1}), as shown in Figure S2 (Supporting Information).

In contrast to these aromatic PIs, the d(002) of semialiphatic PMDA/DCHM was significantly decreased by 5.3%

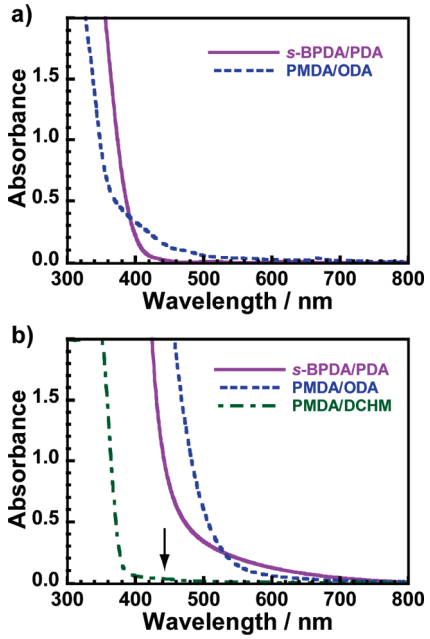


Figure 7. UV/visible absorption spectra of PIs at atmosphere pressure: (a) thin films (thickness: ca. 1 μm); (b) thick films (thickness: ca. 20−25 μm).

by increasing pressure up to 6 GPa, as shown in Figure 4a. The large slope of the variation in $\varepsilon_{(002)}$ gradually decreased above 2 GPa, but it did not become constant, even at the highest pressure of 8.2 GPa. Moreover, as shown in Figures S3 and S4 (Supporting Information), one of the C−N stretching vibration peaks at 1376 cm^{-1} of PMDA/DCHM thin film disappeared by increasing the pressure, which may indicates some structural and/or conformational changes by compression at elevated pressures. Christian et al.[48] reported that effective conversion occurs for halogenated cyclohexanes from equatorial to axial forms by applying pressure. Thereby, such a significant decrease in d(002) could be accompanied by drastic conformational changes around the $-CH_2-$ linkage and/or the six-member cyclohexane structure in the diamine moiety of PMDA/DCHM.

3.2. Variations in the UV/Visible Absorption Properties of PIs. *A. Absorptions at Atmospheric Pressure*. As stated in the introduction, the optical properties of PI films are affected not only by the chemical and electronic structures of repeating units but also by intermolecular interactions. Parts a and b of Figure 7 show the UV/visible absorption spectra of ca.1 μm thick films of *s*-BPDA/PDA and PMDA/ODA, and 20−25 μm thick films of *s*-BPDA/PDA, PMDA/ODA and PMDA/DCHM PIs measured at atmospheric pressure. The former and the latter films are called as 'thin films' and 'thick films', respectively. The absorption bands in the spectra were assigned in accordance with the previous results.[5,32] The thin film of *s*-BPDA/PDA shows a strong LE absorption at wavelengths (λ) shorter than 400 nm without apparent tailing near the absorption edge, whereas the thick film exhibits extensive tailing from 500 to 800 nm. Since the TD-DFT calculations indicate that a CT absorption band should appear at around 400 nm in *s*-BPDA/PDA,[5] the observed tailing is assignable to CT absorption. In contrast, the PMDA/ODA thin film shows a strong LE absorption at shorter wavelengths (λ < 360 nm) accompanied by extensive tailing to 500 nm, which is attributable to CT absorption. Furthermore, the PMDA/ODA thick film shows strong CT absorbance at longer wavelengths (λ > 520 nm), which should be due to apparent bathochromic effect caused by

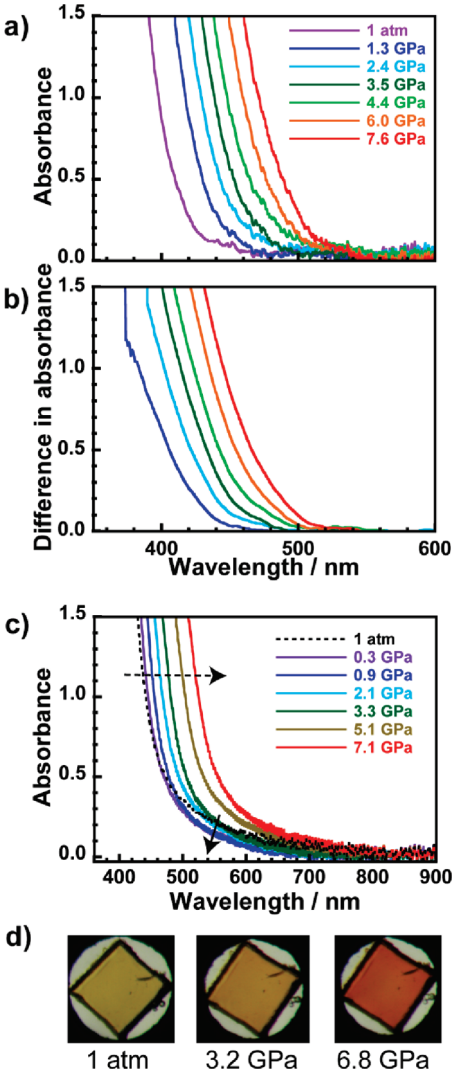


Figure 8. Pressure dependence of (a) UV/visible absorption spectra and (b) absorption differential spectra for *s*-BPDA/PDA thin film. (c) Pressure dependence of UV/visible absorption spectra for *s*-BPDA/PDA thick film. (d) Pressure-induced variations in color of *s*-BPDA/PDA thick film.

the thickening of the film. Furthermore, the semialiphatic PMDA/DCHM thick film shows strong absorption at λ < 380 nm with weak tailing to 520 nm, as indicated by the arrow in Figure 7b. Lee et al.[4] have reported that PMDA/DCHM exhibited a weak fluorescent peak at 520 nm with an excitation peak at around 410 nm, which is assignable to CT fluorescence. We have demonstrated that intramolecular CT complexes are very unlikely to be formed in this PI based on TD-DFT calculations, and the fluorescence peak observed at 495 nm with an excitation peak at 426 nm is attributable to emission from the excited intermolecular CT complexes.[5] Therefore, the tailing observed at longer wavelengths could be assignable to intermolecular CT absorption band.

B. Variations in UV/Visible Absorption Spectra at High Pressure. The influence of the variations in the aggregation structures of PI chains on their optical properties under high pressure were investigated using UV/visible absorption spectroscopy (Figures 8−10). The appearance of the thick films of *s*-BPDA/PDA, PMDA/ODA and PMDA/DCHM at elevated pressures are shown in Figures 8d, 9d, and 10c, respectively. Apparent densification in color from pale yellow through reddish brown to blackish brown was observed

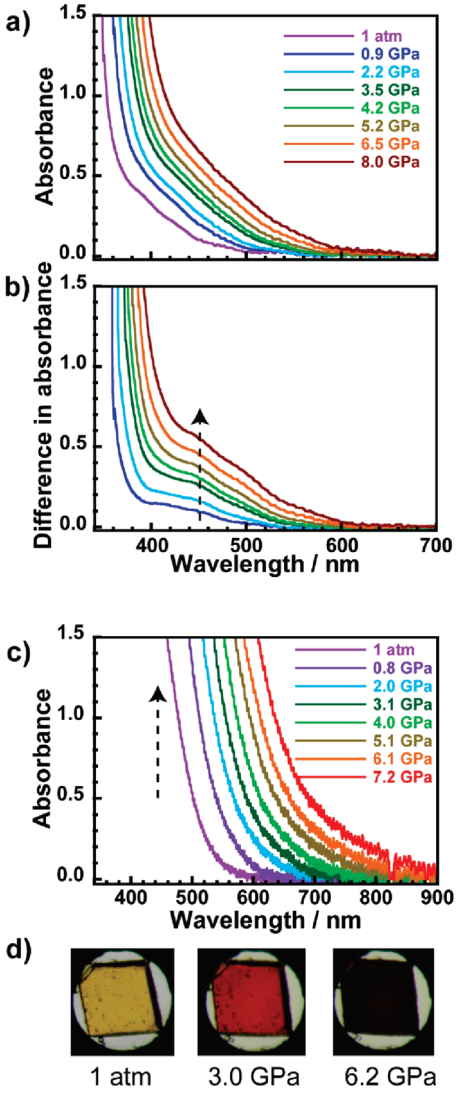


Figure 9. Pressure dependence of (a) UV/visible absorption spectra and (b) absorption differential spectra for PMDA/ODA thin film. (c) Pressure dependence of UV/visible absorption spectra for PMDA/ODA thick film. (d) Pressure-induced variations in color of PMDA/ODA thick film.

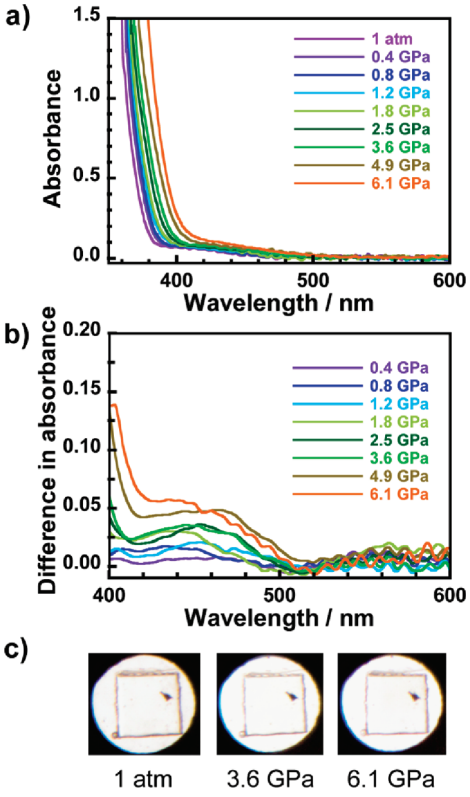


Figure 10. Pressure dependence of (a) UV/visible absorption spectra and (b) absorption differential spectra for PMDA/DCHM thick film. (c) Pressure-induced variations in color of PMDA/DCHM thick film.

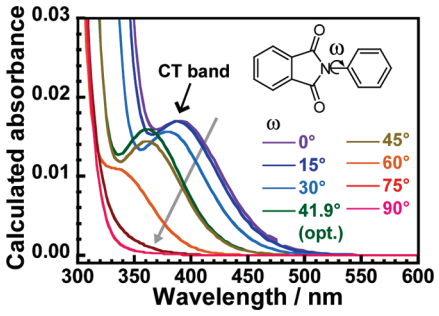


Figure 11. Calculated absorption spectra of a model compound of PI (*N*-phenyl phthalimide) as a function of the dihedral angles at the imide-phenyl bond (ω).

for fully aromatic PIs, but no apparent color changes were observed for the semialiphatic PI. Figure 8 illustrates the pressure-induced variations in (a) the absorption and (b) differential spectra of *s*-BPDA/PDA thin film and (c) the absorption spectra of *s*-BPDA/PDA thick film. The reference for the differential spectra is the spectrum measured at atmospheric pressure (0 GPa). As seen in Figure 8, pressure-induced bathochromic shifts were clearly observed in the LE absorption band of *s*-BPDA/PDA. The intercept wavelengths of the LE absorption bands at an optical density (O.D.) of 1.0 (λ_{OD1}) for the thin and thick films were respectively shifted by 67 nm (0.46 eV) and 83 nm (0.45 eV) to longer wavelengths by increasing pressure from 0 to 7 GPa. One possible cause for the bathochromic shifts is a reduction in the band gap between the ground and excited states due to enhanced van der Waals interactions.[5,32] The other cause is an apparently longer wavelength shift caused by absorption enhancement. For the thin film of *s*-BPDA/PDA, no significant enhancement of the CT absorption band at around 400 nm was observed in the differential spectra (Figure 8b). Moreover, it is interesting to note that the absorbance of the tailing of the *s*-BPDA/PDA thick film from 500 to 800 nm was decreased by applying pressure up to 0.3 GPa (Figure 8c), which indicates that the CT interactions were weakened under the pressure. We have reported that intramolecular CT interactions are dominant in this PI rather than intermolecular CT.[32] Figure 11 shows the calculated absorption spectra of *N*-phenyl-phthalimide with different dihedral angles at the imide bond (ω). By increasing ω, which apart from the coplanarity at the imide-phenyl (>N−Ph) bond, the intramolecular CT absorption band appearing at 400 nm was gradually shifted to shorter wavelengths by reducing its intensity. Hence, the intramolecular CT interaction could be weakened by conformational changes, such as an increase in the dihedral angle at the imide-phenyl bond, and thereby the decrease in CT absorption in *s*-BPDA/PDA is explainable by conformational changes caused by pressure. Furthermore, the absorption tailing exhibited only bathochromic shifts without enhancement of the absorbance above 0.3 GPa. These facts indicate

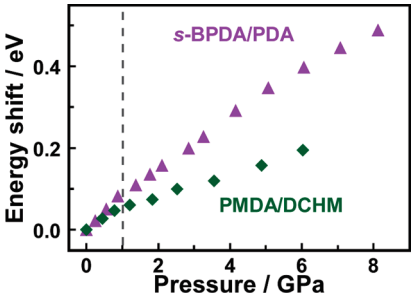


Figure 12. Pressure-induced energy shifts estimated from the intercept wavelength (optical density (O.D.) at 1.0) of the LE absorption of *s*-BPDA/PDA and PMDA/DCHM thick films.

that the pressure-induced variations in the intra- and intermolecular CT interactions had little influence on the λ_{OD1} value, and the observed bathochromic shift of λ_{OD1} is mainly due to enhancement of the van der Waals interactions.

Figure 9 illustrates the variations in (a) the absorption and (b) differential spectra of PMDA/ODA thin film, and (c) the absorption spectra of PMDA/ODA thick film by increasing pressure up to 7 GPa. The λ_{OD1} of the LE absorption of the PMDA/ODA thin film (Figure 9a) was shifted to longer wavelengths by 55 nm (0.47 eV), and the CT absorption band of the PMDA/ODA thick film was shifted by 154 nm (0.64 eV) from 0 GPa to the highest pressure (Figure 9c). In the differential spectra of the PMDA/ODA thin film (Figure 9b), a significant increase in absorbance was observed at around 450 nm, which corresponds to the enhancement of CT absorption. For PMDA/ODA, the WAXD and IR spectra demonstrated that the bond angle at the C−O−C linkage could be increased by applying pressure up to 0.4 GPa, but decreased at higher pressures. However, the calculated absorption spectra suggested that variations in the ether (C−O−C) bond angle have little effect on the intramolecular CT interactions (Figure S5, Supporting Information). Moreover, if a conformational change similar to *s*-BPDA/PDA occurred in this PI, an increase in ω should weaken the intramolecular CT interactions.[32] Thereby, the pressure-induced increase in the CT absorption appearing at around 450 nm is attributable to the enhancement of the intermolecular CT interactions.

Figure 10 illustrates the pressure-induced variations in (a) the absorption and (b) differential spectra of PMDA/DCHM thick film. The λ_{OD1} of the LE absorption band of PMDA/DCHM thick film was shifted by 21 nm (0.19 eV) by increasing pressure up to 6 GPa (Figure 10a). In the differential spectra of the same film (Figure 10b), the pressure-induced enhancement of the intermolecular CT absorption band at about 440 nm was 2 orders of magnitude smaller than that of the CT absorption of PMDA/ODA thick film. Thereby, the observed bathochromic shift of λ_{OD1} should originate from the enhancement of the van der Waals interactions in the same way as for *s*-BPDA/PDA, not by the enhancement of CT absorption like PMDA/ODA.

C. Pressure-Induced Shifts of the LE Absorption Bands at High Pressure. Figure 12 illustrates the pressure-induced energy shifts (in eV) of the λ_{OD1} values, which represent the LE absorption of *s*-BPDA/PDA and PMDA/DCHM thick films. As shown in the figure, both bands are significantly shifted to longer wavelengths up to 1 GPa, whereas the slopes of the variations slightly decrease above 1 GPa. In particular, this trend is remarkable for PMDA/DCHM. This phenomenon accords with the trend of the decrease in the interchain distance occurring in the LC-like ordered regions of PMDA/DCHM below 1−2 GPa, as observed by synchrotron

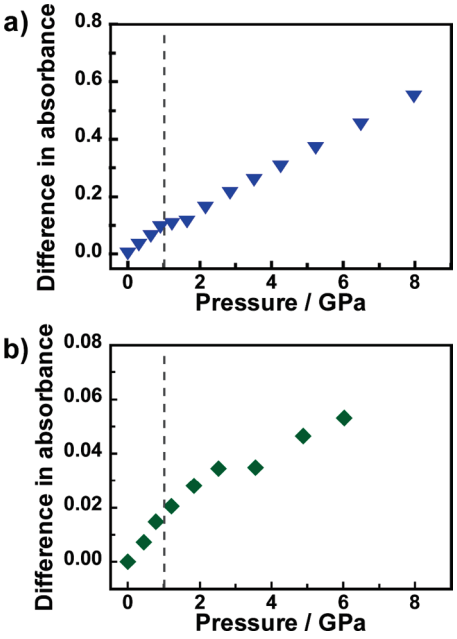


Figure 13. Pressure dependence of optical absorbance at $\lambda = 450$ nm in the differential spectra for (a) PMDA/ODA thin film and (b) PMDA/DCHM thick film.

WAXD (see Figure 3). The WAXD patterns in Figure 1b also indicate that these PIs contain significant amounts of amorphous regions having large free volumes, as represented by the amorphous halos (dotted lines). As mentioned above, Dlubek et al.[46] reported that the free volume of amorphous polymers was preferentially decreased by applying pressure, compared to the specific occupied volume. In addition, Covington et al.[25,26] reported that most of the free volumes in PMMA and PC were removed after compression up to 1 GPa. Therefore, the significant bathochromic shift of *s*-BPDA/PDA and PMDA/DCHM below 1 GPa (Figure 12) is attributable to the compression of interchain free volume in the amorphous region as well as in the LC-like ordered region. The slope of the variations in PMDA/DCHM dropped by 60% around 1 GPa, whereas that of *s*-BPDA/PDA dropped by 40%. The smaller decrease in the latter is attributable to the smaller variation in the interchain distance of the crystalline-like structure in *s*-BPDA/PDA than that of the LC-like ordered structure of PMDA/DCHM, which is characterized by smaller linear compressibility along the (110) plane of *s*-BPDA/PDA below 2 GPa (see Figure 3b).

D. Pressure-Induced Increase in CT Absorption at High Pressure. The magnitude of the increase in CT absorption at elevated pressures also depends on the decrease in interchain distances. Parts a and b of Figure 13 illustrate the pressure-induced increase in absorbance at 450 nm estimated from the differential spectra PMDA/ODA thin film (Figure 9b) and PMDA/DCHM thick film (Figure 10b), respectively. The slope values below 1 GPa are larger than those above that pressure, which is attributable to the enhancement of the intermolecular interactions via compression of interchain free volume in the amorphous and LC-like ordered regions below 1 GPa, as described above. The slopes of the increase in absorbance at 450 nm in the differential spectra go down above 1 GPa, which suggests that the easily compressible components of free volume in PMDA/ODA and PMDA/DCHM almost disappeared at 1 GPa, which is consistent with the variations in the *d*(ch-pack) of PMDA/DCHM (Figure 3).

As seen above, the pressure-induced variations in the LE absorption bands and intermolecular CT absorption bands in PI films below 1 GPa are closely related to the enhancement of the intermolecular interactions via the significant decrease in the interchain free volume, as indicated by WAXD. In consequence, the pressure-induced variations in the optical properties accord well with those in the molecular aggregation structure of PIs.

4. Conclusion

The wide-angle X-ray diffraction patterns, the infrared absorption (IR) and the UV/visible absorption spectra of three kinds of fully aromatic and semialiphatic polyimides (PIs) were measured under high pressure up to 8 GPa using a diamond anvil cell. Semialiphatic PMDA/DCHM exhibited a significant decrease in *d*(ch-pack) below 2 GPa, which is attributable to an appreciable decrease in the interchain free volume. In contrast, fully aromatic *s*-BPDA/PDA showed a much smaller decrease in the interchain distance, *d*(110), which is due to the highly ordered packing structure of the PI chains. The slope of the pressure-strain plots of *s*-BPDA/PDA, estimated from *d*(004) above 1 GPa, is almost the same as that from the C−C stretching vibration of the aromatic ring of the diamine moiety (ring C−C stretch), which indicates that the decrease in *d*(004) above 1 GPa is attributable to the reduction in bond lengths. In contrast, the *d*(002) of PMDA/ODA, having an ether linkage in the main chain, abruptly increased up to 0.4 GPa, whereas the ring C−C stretch peak exhibited no shift up to 1 GPa. This is explainable by a widening of the bond angle by concentrated compression stress at the ether linkage without significant reduction in the bond lengths. On the contrary, *d*(002) exhibited a pronounced decrease above 1 GPa as compared to the strain estimated from the ring C−C stretch peak shift of PMDA/ODA thin film. This should be due to a narrowing of the bond angle at the ether group by further compression accompanied by a slight reduction in the bond lengths. Moreover, the *d*(002) of PMDA/DCHM, having a methylene linkage and two cyclohexane rings in the main chain, significantly decreased at elevated pressures, which should be due to the structural (conformational) change in the flexible diamine moiety.

The locally excited (LE) absorption bands of fully aromatic and semialiphatic PIs shifted to longer wavelength by applying pressure, which is attributable to an enhancement of the van der Waals interactions caused by a decrease in the interchain distances. The absorbance of charge transfer (CT) band of *s*-BPDA/PDA decreased up to 0.3 GPa, which originated from a decrease in the intramolecular CT interaction caused by some structural changes, such as the decrease in the coplanarity between the dianhydride and diamine moieties. On the other hand, the CT absorption of PMDA/ODA was significantly enhanced, and the CT absorption of PMDA/DCHM was slightly enhanced by increasing pressure, both of which are caused by the enhancement of the intermolecular CT interactions. In addition, more pronounced bathochromic shifts of LE bands was observed for *s*-BPDA/PDA and PMDA/DCHM, and large enhancement of intermolecular CT absorption were observed for PMDA/ODA and PMDA/DCHM below 1 GPa, which is attributable to the significant decrease in interchain distance via compression of free volume as indicated by WAXD. Overall, it has been indicated from very high pressure experiments that the optical properties and the aggregation structure of PIs are related in a linear manner. These experimental results lead to a guiding principle to reduce the CT interactions in PIs: the incorporation of bent and/or bulky structures in the main chain, which effectively enlarge the interchain distance, and thus lower the degree of molecular aggregation. This is beneficial for developing a new class of thermally stable and highly transparent/colorless aromatic polyimides.

Acknowledgment. The synchrotron radiation experiments were performed with a BL40B2 beamline with the approval of the Japan Synchrotron Radiation Research Institute (JASRI) (Proposal No.2008B-1434, 2009A-1348, 2009B-1306). The authors thank Kei Hirose and Ryosuke Sinmyo at the Department of Earth and Planetary Sciences, Tokyo Institute of Technology, for advice on the diamond anvil cell. We also thank Kazuyuki Horie at JASRI and Masaki Kakiage at the Department of Chemistry and Materials Science, Saitama University, for helpful discussions.

Supporting Information Available: Figures showing variations in IR spectra for PI thin films by applying pressure and calculated absorption spectra of the model compound for PMDA/ODA (m(PM/OD)) with different bond angles at the C−O−C linkage, incuding text discussing the latter. This material is available free of charge via the Internet at http://pubs.acs.org.

References and Notes

(1) Sroog, C. E. *J. Polym. Sci., Part D* **1976**, *11*, 161–208.
(2) Hasegawa, M.; Shindo, Y.; Sugimura, T.; Ohshima, S.; Horie, K.; Kochi, M.; Yokota, R.; Mita, I. *J. Polym. Sci., Part B* **1993**, *31*, 1617–1625.
(3) Matsuura, T.; Ando, S.; Sasaki, S.; Yamamoto, F. *Macromolecules* **1994**, *27*, 6665–6670.
(4) Lee, S. A.; Yamashita, T.; Horie, K. *J. Polym. Sci., Part B* **1998**, *36*, 1433–1442.
(5) Wakita, S.; Sekino, H.; Sakai, K.; Urano, Y.; Ando, S. *J. Phys. Chem. B* **2009**, *113*, 15212–15224.
(6) Ishida, H.; Wellinghoff, S. T.; Baer, E.; Koenig, J. L. *Macromolecules* **1980**, *13*, 826–834.
(7) Hasegawa, M.; Kochi, M.; Mita, I.; Yokota, R. *J. Polym. Sci., Part C: Polym. Lett.* **1989**, *27*, 263–269.
(8) Hasegawa, M.; Mita, I.; Kochi, M.; Yokota, R. *Eur. Polym. J.* **1989**, *25*, 349–354.
(9) Ando, S.; Matsuura, T.; Sasaki, S. *Polym. J.* **1997**, *29*, 69–75.
(10) Kazaryan, L. G.; Tsvankin, D. Y.; Ginzburg, B. M.; Tuichiev, S.; Korzhavin, L. N.; Frenkel, S. Y. *Polym. Sci. USSR* **1972**, *14*, 1344–1354.
(11) Russell, T. P.; Toney, M. F. *Macromolecules* **1993**, *26*, 2847–2859.
(12) Wu, T. M.; Chvalun, S.; Blackwell, J.; Cheng, S. Z. D.; Wu, Z.; Harris, F. W. *Polymer* **1995**, *36*, 2123–2131.
(13) Saraf, R. F.; Dimitrakopoulos, C.; Toney, M. F.; Kowalczyk, S. P. *Langmuir* **1996**, *12*, 2802–2806.
(14) Ree, M.; Kim, K.; Woo, S. H.; Chang, H. *J. Appl. Phys.* **1997**, *81*, 698–708.
(15) Saraf, R. F. *Polym. Eng. Sci.* **1997**, *37*, 1195–1209.
(16) Ree, M.; Shin, T. J.; Lee, S. W. *Korea Polym. J.* **2001**, *9*, 1–19.
(17) Shen, Z.; Jing, A. J.; Jin, S.; Wang, H.; Harris, F. W.; Cheng, S. Z. D. *Chin. J. Polym. Sci.* **2005**, *23*, 171–174.
(18) Ruan, J.; Jin, S.; Ge, J. J.; Jeong, K.; Graham, M. J.; Zhang, D.; Harris, F. W.; Lotz, B.; Cheng, S. Z. D. *Polymer* **2006**, *47*, 4182–4193.
(19) Wakita, J.; Jin, S.; Shin, T. J.; Ree, M.; Ando, S. *Macromolecules* **2010**, *43*, 1930–1941.
(20) Samuelsen, E. J.; Mirdalen, J.; Konestabo, O. R.; Hanfland, M.; Lorenzen, M. *Synth. Met.* **1999**, *101*, 98–99.
(21) Lorenzen, M.; Hanfland, M.; Mermet, A. *Nucl. Instrum. Meth. B* **2003**, *200*, 416–420.
(22) Emmons, E. D.; Velisavljevic, N.; Schoonover, J. R.; Dattelbaum, D. M. *Appl. Spectrosc.* **2008**, *62*, 142–148.
(23) Takizawa, K.; Wakita, J.; Kakiage, M.; Masunaga, H.; Ando, S. *Macromolecules* **2010**, *43*, 2115–2117.
(24) Flores, J. J.; Chronister, E. L. *J. Raman Spectrosc.* **1996**, *27*, 149–153.
(25) Emmons, E. D.; Kraus, R. G.; Duvvuri, S. S.; Thompson, J. S.; Covington, A. M. *J. Polym. Sci., Part B* **2007**, *45*, 358–367.
(26) Kraus, R. G.; Emmons, E. D.; Thompson, J. S.; Covington, A. M. *J. Polym. Sci., Part B* **2008**, *46*, 734–742.
(27) Webster, S.; Batchelder, D. N. *Polymer* **1996**, *37*, 4961–4968.
(28) Yang, G.; Dreger, Z. A.; Drickamer, H. G. *J. Phys. Chem. B.* **1997**, *101*, 4218–4225.

(29) Erskine, D.; Yu, P. Y.; Freilich, S. C. *J. Polym. Sci., Part C* **1998**, *26*, 465–468.
(30) Yang, G.; Li, Y.; White, J. O.; Drickamer, H. G. *J. Phys. Chem. B.* **1999**, *103*, 5181–5186.
(31) Yang, G.; Li, Y.; White, J. O.; Drickamer, H. G. *J. Phys. Chem. B.* **1999**, *103*, 7853–7859.
(32) Wakita, J.; Ando, S. *J. Phys. Chem. B* **2009**, *113*, 8835–8846.
(33) Matsumoto, T. *High Perform. Polym.* **1999**, *11*, 367–377.
(34) Oishi, Y.; Ogasawara, K.; Hirahara, H.; Mori, K. *J. Photopolym. Sci. Technol.* **2001**, *14*, 37–40.
(35) Oishi, Y.; Kikuchi, N.; Mori, K.; Ando, S.; Maeda, K. *J. Photopolym. Sci. Technol.* **2002**, *15*, 213–214.
(36) Piermarini, G. J.; Block, S.; Barnett, J. D. *J. Appl. Phys.* **1973**, *44*, 5377–5382.
(37) Lee, C.; Yang, W.; Parr, R. G. *Phys. Rev.* **1988**, *B37*, 785–789.
(38) Miehlich, B.; Savin, A.; Stoll, H.; Preuss, H. *Chem. Phys. Lett.* **1989**, *157*, 200–206.
(39) Becke, A. D. *J. Chem. Phys.* **1993**, *98*, 5648–5642.
(40) Ando, S.; Fujigaya, T.; Ueda, M. *Jpn. J. Appl. Phys.* **2002**, *41* (2A), L105–L108.
(41) Ando, S.; Fujigaya, T.; Ueda, M. *J. Photopolym. Sci. Technol.* **2002**, *15*, 559–568.
(42) Ando, S.; Ueda, M. *J. Photopolym. Sci. Technol.* **2003**, *16*, 537–544.
(43) Slonimskii, G.; Askadskii, A.; Kitaigodorodskii, A. *Polym. Sci. USSR.* **1970**, *A12*, 556–557.
(44) Bondi, A. *J. Phys. Chem.* **1964**, *68*, 441–451.
(45) Frisch, M. J.; Trucks, G. W.; Schlegel, H. B.; Scuseria, G. E.; Robb, M. A.; Cheeseman, J. R.; Montgomery, J. A., Jr.; Vreven, T.; Kudin, K. N.; Burant, J. C.; Millam, J. M.; Iyengar, S. S.; Tomasi, J.; Barone, V.; Mennucci, B.; Cossi, M.; Scalmani, G.; Rega, N.; Petersson, G. A.; Nakatsuji, H.; Hada, M.; Ehara, M.; Toyota, K.; Fukuda, R.; Hasegawa, J.; Ishida, M.; Nakajima, T.; Honda, Y.; Kitao, O.; Nakai, H.; Klene, M.; Li, X.; Knox, J. E.; Hratchian, H. P.; Cross, J. B.; Bakken, V.; Adamo, C.; Jaramillo, J.; Gomperts, R.; Stratmann, R. E.; Yazyev, O.; Austin, A. J.; Cammi, R.; Pomelli, C.; Ochterski, J. W.; Ayala, P. Y.; Morokuma, K.; Voth, G. A.; Salvador, P.; Dannenberg, J. J.; Zakrzewski, V. G.; Dapprich, S.; Daniels, A. D.; Strain, M. C.; Farkas, O.; Malick, D. K.; Rabuck, A. D.; Raghavachari, K.; Foresman, J. B.; Ortiz, J. V.; Cui, Q.; Baboul, A. G.; Clifford, S.; Cioslowski, J.; Stefanov, B. B.; Liu, G.; Liashenko, A.; Piskorz, P.; Komaromi, I.; Martin, R. L.; Fox, D. J.; Keith, T.; Al-Laham, M. A.; Peng, C. Y.; Challacombe, A. M.; Gill, P. M. W.; Johnson, B.; Chen, W.; Wong, M. W.; Gonzalez, C.; Pople, J. A. *Gaussian 03*, revision D.02; Gaussian, Inc.: Wallingford, CT, 2004.
(46) Dlubek, G.; Wawryszczuk, J.; Pionteck, J.; Goworek, T.; Kaspar, H.; Lochhaas, K. H. *Macromolecules* **2005**, *38*, 429–437.
(47) Halmann, V. B. *J. Phys. Chem. B* **2005**, *109*, 13668–13675.
(48) Christian, S. D.; Grundnes, J.; Klaboe, P. *J. Am. Chem. Soc.* **1975**, *97*, 3864–3865.

360 *Macromolecules* **2011**, *44*, 360–367
DOI: 10.1021/ma1021715

Macromolecules
ARTICLE

Softening of PMMA Brushes upon Collapse/Swelling Transition. A Combined Neutron Reflectivity and Nanomechanical Cantilever Sensor Study

Sebastian Lenz,[†] Adrian Rühm,[‡] Janos Major,[‡] Rüdiger Berger,[†] and Jochen S. Gutmann*[,†]

[†]*Max Planck Institute for Polymer Research, Ackermannweg 10, D-55128 Mainz, Germany, and*
[‡]*Max Planck Institute for Metals Research, Heisenbergstrasse 3, D-70569 Stuttgart, Germany*

Received September 18, 2010; Revised Manuscript Received November 20, 2010

ABSTRACT: In this work, we establish a direct correlation between chain mechanics and structural properties of polymer brushes upon swelling. We present experimental results on poly(methyl methacrylate) (PMMA) brushes prepared via surface initiated atomic transfer radical polymerization. Neutron reflectivity studies gave insight into the brush thickness and volume fraction profiles of the brush, gradually swollen with solvent mixtures. Comparison of our experiments with scaling theory yielded specific polymer−solvent interaction parameters and gave insight into the desorption and adsorption behavior of bad and good solvents, respectively. Insight into the brush's chain mechanics was obtained from surface stress investigations using the nanomechanical cantilever sensor bending technique. It was shown that polymer brush swelling leads to a decrease in surface stress due to chain disentanglements and the related softening of the polymer brush under Θ-solvent conditions.

Introduction

Polymer brushes have been extensively investigated in terms of their structure[1−3] and physical properties, including adhesion, friction,[4,5] and lubrication.[6] In comparison to physically adsorbed brushes, surface-grafted brushes are especially interesting candidates for technical applications due to their lower susceptibility to mechanical wear. The sliding friction of two polymer brush grafted surfaces has been investigated by means of high resolution rheology[5] and molecular dynamics simulations.[7,8] These studies gave insight into the polymer brush mechanics under the influence of external shearing fields. However, for a complete understanding of the lubrication behavior of polymer brushes, the mechanics without the influence of external shearing fields has to be studied as well. This is intrinsically not possible with rheology or tribology techniques,[9] because the opposing surface will always influence the mechanics in the polymer brush.

Considerable theoretical effort was made to understand the molecular structure of high and low density polymer brushes interacting with solvents.[10] However, experimental work on polymer brush mechanics related to structural attributes is rare. Urayama et al. used a combination of results retrieved from ellipsometry and electromechanical interferometry to obtain structure/mechanical-stress relations of dry poly(methyl methacrylate) (PMMA) brushes.[11] In a previous paper we reported on the mechanical stress appearing in a grafted PMMA brush of low polydispersity, synthesized with surface initiated atomic transfer radical polymerization (ATRP), and in particular on its dependence on the solvent quality.[12] In this study the solvent quality was controlled by choosing certain mixtures of good and bad solvents for PMMA, i.e. solvents in which the free polymer would dissolve or precipitate, respectively. Stress information was obtained using brush coated nanomechanical cantilever sensor (NCS) arrays[13] which are used as tools for, e.g., biosensing[14] and material characterization.[15−19] The displacement of cantilevers with grafted PMMA brushes was measured as a function of the solvent quality by means of optical beam deflection methods similar to the ones used in atomic force microscopy (AFM) devices.[20] When the NCS sensor bends, the reflection of a laser beam focused onto the NCS changes its vertical position on the detector, and the displacement of the NCS can be calculated.[21] With the help of geometrical considerations and mechanical stress models such as Stoney's law,[22] approximate stress data can be obtained.

However, this deflection method has several limitations: First, only relative changes of the deflection can be measured, so that no information on the original stress state of the NCS before the experiment can be obtained. Second, changing the solvent mixture may alter the refractive index of the liquid environment, which also leads to a shift of the reflected laser beam (at least for laser incidence angles below 90°). In this case, the device has to be recalibrated after each solvent exchange. From these two major limitations it follows that the determination of surface stresses via laser reflection from an NCS may be difficult. In practice no stress information about polymer brushes can be obtained when the refractive index of the solvent changes upon solvent exchange. Earlier brush swelling studies using deflection methods were therefore limited to solvent combinations of matching refractive indices. To overcome these limitations we used a custom-made imaging Michelson type interferometer designed for NCS array readout in liquid applications. In this device a coherent near-infrared laser illuminates the NCS array under an incidence angle of 90°. It measures the sample's three-dimensional topography via the superposition of an optical image and the corresponding interference pattern.[23]

The obtained stress data can be interpreted in terms of a change of the free energy in the brush layer.[24] The free energy can be derived from Flory−Huggins interaction parameters, which can be estimated using simple Hildebrand Scott bulk solubility parameters.[25] However, bulk solubility estimations neglect the entropic constraints of grafted polymer chains and wetting effects. In this study, we correlate our stress data to interaction

*Corresponding author. E-mail: jochen.gutmann@uni-due.de.

 Published on Web 12/22/2010 © 2010 American Chemical Society

parameters which were derived from density profiles, where the latter were experimentally deduced from neutron reflectivity experiments (NR). It was previously shown that neutron reflectivity is a well suitable technique to understand the structure of polymer brushes[26,27] and for determining the solvent content in thin films.[28]

In conjunction with polymer brush swelling theory using scaling approaches[29] more accurate Flory−Huggins interaction parameters could be obtained from our experiments.

Samples for both types of studies (NCS bending and NR) were prepared simultaneously in order to ensure similar grafting densities and molecular weights for both PMMA brushes prepared on small NCS arrays and on large Si disks used for NR investigations.

Materials and Methods

NCS Arrays and Si Disks. Nanomechanical cantilever sensor (NCS) arrays (Octosensis, Micromotive Mikrotechnik GmbH, Mainz, Germany) were used for surface stress investigations. Each array consisted of eight individual rectangular cantilevers with an area of $500 \times 90\ \mu m^2$, a thickness of $1\ \mu m$ and a pitch of $250\ \mu m$. The NCS arrays had an overall size of $2.5\ mm \times 3.5\ mm \times 0.5\ mm$. Double sided polished Si disks (CrysTec GmbH, Berlin, Germany) for NR studies were 100 mm in diameter and 15 mm thick.

PMMA Brush Synthesis. For a reliable comparison of the results obtained from NR measurements and surface stress investigations, brushes with equal grafting densities and polymeric weights had to be synthesized for NCS and Si disk samples. Thus, all necessary reaction steps for both kinds of samples were performed simultaneously in one reaction vessel. Prior to immobilization of the ATRP initiator, the Si disk and NCS arrays were base cleaned for 20 min in a mixture of $NH_3/H_2O_2/H_2O$ (1:1:20 vol.) at 80 °C to ensure controlled oxidation of the native SiO_x surface. Half of the NCS arrays' top side and the whole backside were coated with a protecting gold film using chemical vapor deposition (deposition parameters, 30 nm, 0.1 nm/s, $p \sim 1.8 \times 10^{-5}$ mbar; deposition facility, BALTEC MED 020, BALTEC, Balzers, Lichtenstein) (first step in Figure 1). This coating procedure allowed to restrict the PMMA brush synthesis only to four cantilever sensors on one-half of the uncoated top side of the NCS array. The remaining four cantilever sensors were gold protected from both sides, so no PMMA was synthesized on these sensors. These latter sensors were used as internal reference. One side of the Si disk was protected with a 30 nm gold layer as well.

Both kinds of substrates were mounted simultaneously in special Teflon holders fitting in a suitable flat flange reaction vessel. Subsequently the surface ATRP initiator (3-(2-bromoisobutyryl)propyl)dimethylchlorosilane, synthesized as described in the literature,[30] was applied simultaneously to both types of specimens (second step in Figure 1). The reaction mixture of 400 mL of water-free toluene (Acros, 99.8%, extra dry, used as obtained), 3.3 mL of triethylamine (NEt_3) and 6.4 mL of ATRP initiator was prepared in a clean Schlenk flask under Ar atmosphere. The prepared mixture was then transferred under Ar atmosphere to the flat flange reaction vessel. Both kinds of specimens (NCS arrays and Si disks) were completely covered by the reacting mixture. The reaction was stirred for 12 h at room temperature. After silanization, the NCS arrays were thoroughly cleaned with CH_2Cl_2.

For PMMA brush synthesis the specimens were mounted in the flat flange reaction vessel as described above (third step in Figure 1). Surface initiated ATRP was performed as explained previously.[31] The apparatus was set under Ar atmosphere and the reaction mixture of 200 mL of methyl methacrylate (MMA, Acros, 99%, purified through alumina column; distilled), 300 mL of anisole (Aldrich, 99%), 513 mg of CuBr (Aldrich, 98%; purified) and 750 μL of *N*,*N*,*N*′,*N*′,*N*″-pentamethyldiethylenetrieamine (Aldrich, 99%; freshly distilled) was added to the Schlenk flask. After adding the last reactant, 530 μL of the free initiator ethyl-2-bromoisobutyrate (Aldrich, 98%; used as obtained), the Schlenk flask was immediately frozen with liquid nitrogen to prevent polymerization. After degassing of the reaction mixture through three freeze/pump/thaw cycles, the cold polymerization mixture was transferred into the reaction vessel until both kinds of specimens were totally covered by the reaction mixture. ATRP was carried out for 40 h at 30 °C under stirring and continuous Ar flow.

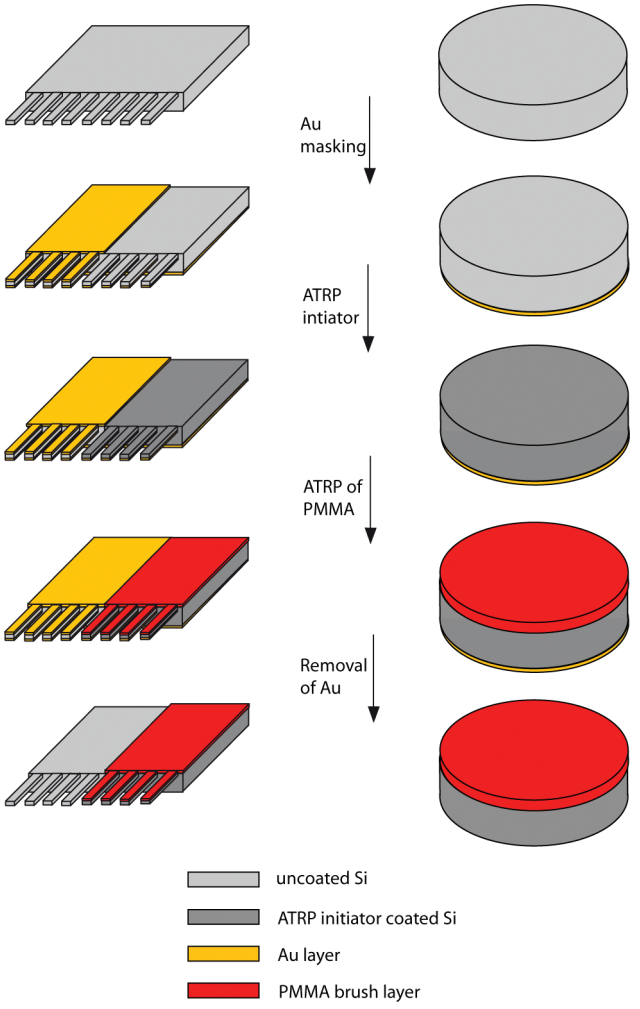


Figure 1. Scheme of the simultaneous PMMA brush synthesis on NCS arrays and Si disk specimens.

After polymerization, the PMMA-coated specimens were thoroughly cleaned from adsorbed free PMMA with CH_2Cl_2. Fractions of free PMMA from solution polymerization was precipitated under dropwise addition of the solution to an excess of methanol (MeOH). For purification, the filtered precipitate was solved again in tetrahydrofuran (THF). The precipitation process was repeated until a white precipitate was obtained. The dried precipitate was analyzed with gel permeation chromatography (GPC). For the studied sample $M_n = 23400$ g/mol with a polydispersity index (PDI) of 1.2 was obtained.

As a last step, the protecting gold layers were removed. For this purpose, the specimens were immersed in KI/I_2 solution and rinsed with Millipore water. This procedure was repeated five times in order to remove all gold residuals.

Neutron Reflectivity Experiments. Neutron reflectivity experiments on PMMA brush coated Si disks were conducted at the N-REX$^+$ reflectometer located at the Forschungsneutronenquelle Heinz Maier-Leibnitz (FRM II). The experiments were done in angle-dispersive mode at a neutron wavelength $\lambda = 4.26$ Å. The monochromator slit was set to a gap size of 20 mm horizontal×1 mm vertical. For small incidence angles α_i the

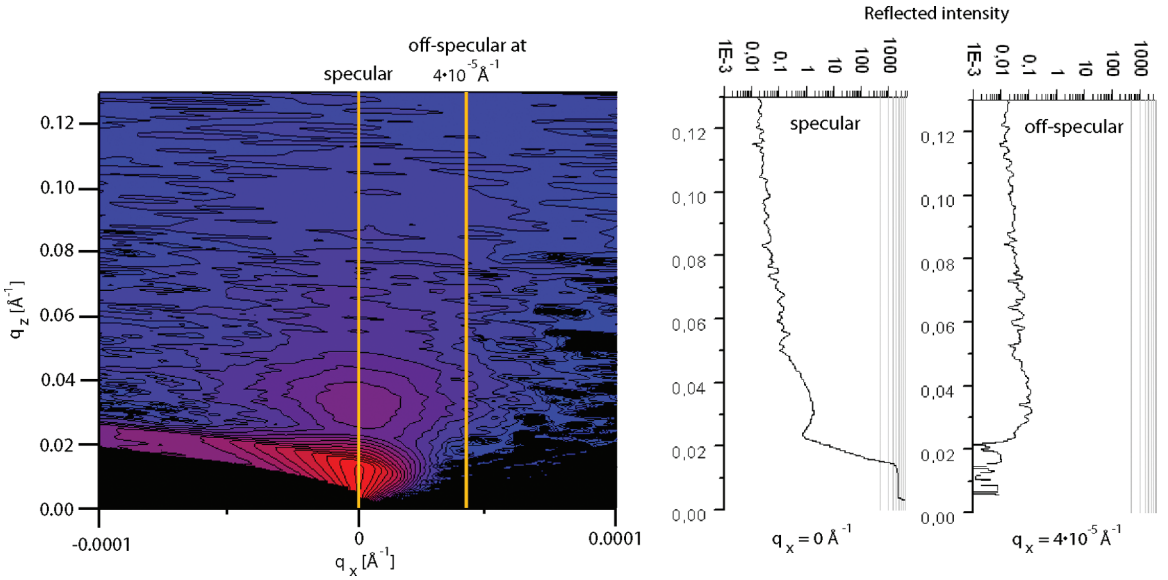


Figure 2. Left panel: Typical q_x/q_z contour plot obtained from one reflectivity scan. Right panel: Collecting linescan data along q_z from the region near the left yellow line at $q_x = 0$ Å^{-1} yields the specular reflected intensity, while the corresponding linescan data obtained from the region near the left yellow line at $q_x = 4.10^{-5}$ Å^{-1} yields the off-specular reflected intensity.

vertical gap was reduced to 0.02 mm to protect the detector. The polymer brush sample was positioned 300 mm after the sample slit (40 mm horizontal × 1 mm vertical) and mounted in a liquid cell. The neutrons were transmitted through the Si substrate and reflected at the Si/PMMA-brush/solvent interface. In order to obtain a high scattering length density (SLD) contrast, the solvent was fully deuterated, while the polymer was fully hydrogenated. The neutron flux at the sample position was estimated to be $\sim 4.1 \times 10^4$ n·cm^{-2}·s^{-1}, which includes the attenuation by the silicon disk. Reflectivity scans were performed in an incidence angle range of $0° \leq \alpha_i \leq 1.6°$ with steps of $\Delta\alpha_i = 0.02°$. For background reduction cadmium shielding was applied to the sample cell both upstream and downstream of the silicon substrate. The reflected neutrons passed a second sample slit (sample/aperture distance: ~ 300 mm) which could be optimized for background reduction (vertical gap size ~1 mm) or fully opened for the detection of off-specular scattering. Further background reduction was achieved by the application of a cadmium shielded tube between the second sample slit and the detector (sample/detector distance: 2465 mm).

For a complete reflectivity scan a series of typically 80 2D detector images were recorded. The obtained images were further processed by the reflected intensity in the direction parallel to the sample surface. Thus, a one-dimensional exit angle dependent intensity data set (α_f-profile) was obtained for each single α_i. After combining all α_f-profiles belonging to one reflectivity scan, a two-dimensional intensity data set $I(\alpha_i,\alpha_f)$ was obtained. Before plotting the data sets in the form of a q_x/q_z contour plot (where q is the neutron wavevector transfer) (Figure 2), the intensity values were corrected for the effective height of the inclined sample surface in the neutron beam with respect to the total beam height. Horizontal scans at the intensity maximum located at $q_x = 0$ yielded the specularly reflected intensity as a function of q_z. Off-specular scans along q_z at a constant q_x offset of 4.10^{-5} Å^{-1} contain information about the background level (typically 5−10% of the specularly reflected intensity) and the roughness as well as roughness correlations of the brush/solvent interface.[32] Before fitting the obtained data to a model, the specularly reflected intensities were corrected for off-specular intensities by subtraction.

In situ reflectivity experiments were performed for several mixtures of perdeuterated methanol (bad solvent) and perdeuterated tetrahydrofuran (good solvent), starting from bad solvent conditions.

Model fits to the reflectivity profiles were performed with two different brush models: The tanh expanded step function model of Alexander and de Gennes (AdG)[1,2] and the parabolic model of Milner, Witten and Cates.[33,34] The quality of the fits was not significantly different for the two models. For both models, the brush's free Helmholtz-energy F and the brush height H are proportional to each other.[33] Differences between the brush models are reflected only in higher order oscillations in the reflectivity data, which, however, were not pronounced in our experimental q_z-range. Thus, and because the subsequently used brush swelling theory[29] is based only on the AdG model, we used this model for the analysis of all reflectivity data. From the fitting results, complete parameter sets for the brush height H, the scattering length density (SLD) of the brush, and the statistical brush/solvent interface width s were obtained. Subsequently, the solvent composition was derived by a comparison of the fitted SLD values with bulk SLD values obtained with the help of a freely accessible online scattering length density calculator.[35]

NCS Bending Experiments. The Michelson type optical interferometer operating at a wavelength of $\lambda = 780$ nm was used for measuring the three-dimensional topographies of NCS arrays immersed in liquid within a custom-made liquid cell. A CCD camera recorded the images of a sample area of 1.28×0.96 mm^2. This allowed measuring all eight cantilever sensors as well as parts of the supporting chip simultaneously. The curvature of the cantilever sensors was determined via interferometric analysis of the interference fringes in the topography image, which was superposed with the optical image. For this analysis, the 3D-image processing software OPTOCAT (Breuckmann GmbH, Meersburg, Germany) was used. For a quantitative analysis of the bending state of the cantilever sensors, one-dimensional height profiles along the NCS were extracted from the topography data of each NCS. The resulting height profiles were then fitted with a parabolic function[19,36] according to

$$Z(x) = a_0 + a_1 x + \frac{\kappa}{2} x^2 \qquad (1)$$

where $z(x)$ denotes the deflection of the NCS at each position x along the NCS. If the NCS is uniformly bent, its curvature κ can be directly obtained from the fit. In order to improve the statistics, curvatures of equally coated NCS were averaged. Differential curvatures $\Delta\kappa$ were obtained by subtraction of the average curvature of reference NCS from the one of brush coated NCS. Recording a number of topographies over a period

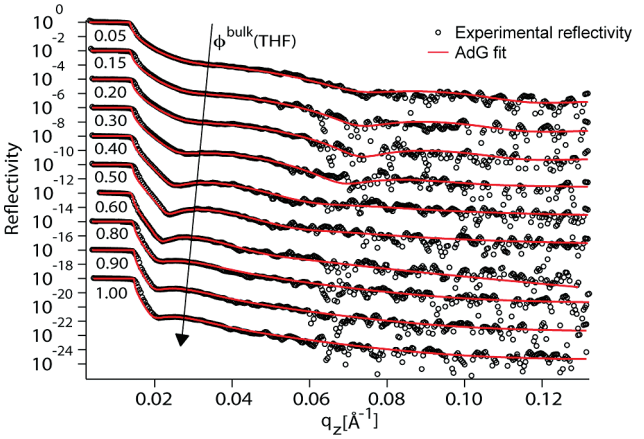


Figure 3. Reflectivity data obtained on PMMA brushes for various solvent mixtures of MeOH and THF, together with fit curves (red lines). The bulk volume fraction ϕ^{bulk} of THF is indicated at the left-hand side of each graph. For better visibility, the reflectivity scans were shifted vertically by a factor of 10^{-2} against each other with increasing volume fractions of THF.

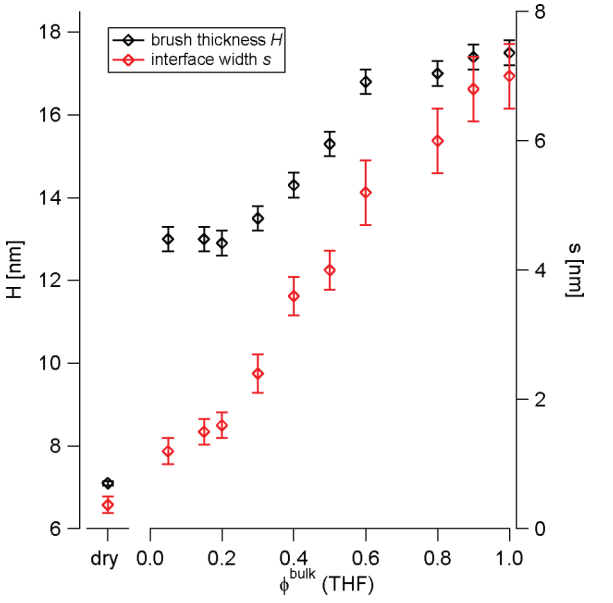


Figure 4. THF volume fraction dependence of the brush thickness H and brush/solvent interface width s as obtained from one-layer AdG fits. The sample in the dry state was measured with X-ray reflectivity using an X-ray laboratory source.

of 30 min resulted in $\Delta\kappa$ vs time spectra, which were again averaged and used for error estimation. The differential surface stress was calculated with Stoney's formula[22]

$$\Delta\sigma = \frac{E_{Si}t_{NCS}^2}{6(1-\nu_{Si})}\Delta\kappa \qquad (2)$$

where an elasticity modulus $E_{Si} = 165$ GPa with a Poisson ratio of $\nu_{Si} = 0.22$ and an NCS thickness $t_{NCS} = 1$ μm was used for our calculations.

First, the dry NCS sample was measured. Measurements in liquid environment started with pure MeOH from poor PMMA solving conditions. After recording $\Delta\kappa$ vs time spectra for 30 min, the volume fraction of good solving THF was increased by total solvent exchange.

Results and Discussion

Neutron Reflectivity Results. The neutron reflectivity results obtained on PMMA brush coated Si disks for several solvent mixtures give insight into the brush structure upon swelling. From a qualitative investigation of the obtained reflectivity curves it is directly seen that the Fresnel oscillations move toward smaller q_z for increasing THF fractions in the solvent mixture, ϕ^{bulk} (THF). This observation is a clear qualitative evidence for a gradual increase of the brush thickness. For a quantitative data analysis good fits for all measured reflectivity curves could be obtained using a one-layer model as explained in the experimental section (Figure 3). Fit results for the brush height H and the brush/solvent interface width s were obtained. The interface width accounts for the width of the concentration gradient at the brush/solvent interface. Fit results show that when immersing the brush sample from the dry state into the bad solvent methanol the brush is already swelling by 83% (Figure 4). Further swelling by gradual solvent exchange leads to a total brush thickness increase of 146% as compared to the dry state. This result gives first evidence that for the mechanism of the brush swelling enthalpic interactions play a less important role than the osmotic pressure of the liquid. This first conclusion is discussed in more detail below.

On the other hand, the steady increase of the width s of the brush/liquid interface with increasing good solvent fraction gives evidence for a less ordered brush morphology in the interface region upon swelling. In agreement with common brush models[33] a distribution between stretched and collapsed polymer chains is assumed for good solvents.

For a more detailed discussion of the interaction between the brush and the solvent mixture, we related our experimental findings to solvent−polymer interaction parameters. Birshtein and Lyatskaya[29] developed a model to calculate free energies and resulting brush heights for mixtures of good and poor solvents from Flory−Huggins parameters (also called χ-parameters). For good solvent conditions, the χ-parameter is smaller than 0.5; for bad solvent conditions, it is larger than 0.5. For $\chi = 0.5$, the polymer chain is in an intermediate Θ-solvent condition, which is characterized by Gaussian chain conformation.

Birshtein and Lyatskaya used standard Flory−Huggins theory together with scaling laws to describe the free energy of the Alexander−de Gennes brush in arbitrary solvent mixtures. Within this scaling approach, a description of the collapse/stretching mechanism was possible. Among others, they derived a system of two equations relating the volume fractions of each constituent of a binary solvent mixture in the bulk solvent, ϕ_A^{bulk} and ϕ_B^{bulk} ($= 1 - \phi_A^{bulk}$), and in the polymer brush region, $\phi_{A/Pol}^{brush}$ and $\phi_{B/Pol}^{brush}$. It was possible to relate these volume fractions to the Flory−Huggins interaction parameters χ_A, χ_B, the solvent−solvent interaction parameter χ_{AB}, and the grafting density δ . To allow an estimation of the χ-parameter, the volume fraction of total solvent in the brush was derived from the SLD profiles obtained from the neutron reflectivity data. The measured scattering length density in the brush region, SLD^{brush}, is a sum of the scattering length density of the brush molecules, SLD^{brush} (PMMA), and the scattering length density of the solvent mixture in the brush region, SLD^{brush} (MeOH + THF). The volume fraction ϕ^{brush} (MeOH + THF) is related to the measured values SLD^{brush} and SLD^{bulk} and the theoretical value $SLD^{theo} = 8.98 \times 10^{-5} \cdot Å^{-2}$ of PMMA by

$$\phi^{brush}(\mathrm{MEOH + THF}) = 1 - \frac{SLD^{brush} - SLD^{bulk}}{SLD^{theo}(\mathrm{PMMA}) - SLD^{bulk}} \qquad (3)$$

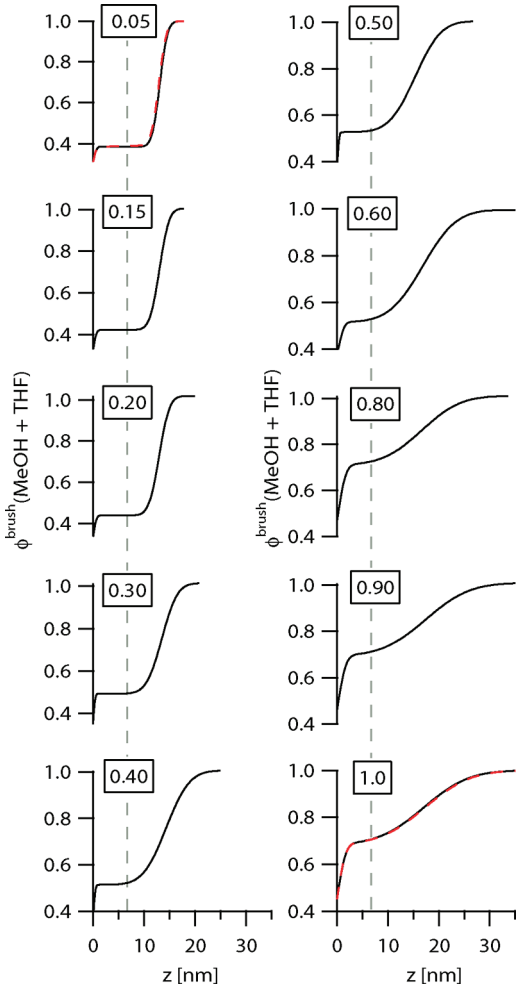


Figure 5. ϕ^{brush}(MeOH + THF) depth profiles calculated by means of eq 3 for each ϕ^{bulk} (THF) (number in box) from the AdG fittings presented in Figure 3. The gray dashed vertical lines indicate the estimated depth resolution of ~6 nm resulting from the experimental q_z-range. Dashed red lines at ϕ^{brush}(MeOH + THF) = 0.05 and ϕ^{brush}(MeOH + THF) = 1.0 were obtained from fits based on the parabolic model.

The theoretical values for the solvents are $SLD^{theo}(MeOH) = 5.80 \times 10^{-6}$ Å^{-2} and $SLD^{theo}(THF) = 6.35 \times 10^{-6}$ Å^{-2}. The thus obtained ϕ^{brush}(MeOH + THF) profiles are shown in Figure 5. Integration of these depth profiles over the depth parameter z and normalizing by the brush height H according to

$$\phi_{tot}^{brush}(\mathrm{MeOH+THF}) = \frac{1}{H}\int_0^H \phi^{brush}(\mathrm{MeOH+THF})\,\mathrm{d}z \tag{4}$$

lead to averaged ϕ_{tot}^{brush}(MeOH + THF) values.

The thus obtained averaged total solvent volume fractions ϕ_{tot}^{brush}(MeOH + THF) are plotted versus ϕ^{bulk} (THF) data and compared with a model calculation in Figure 6. The grafting density δ was first determined from X-ray reflectivity to be 0.18 chains/nm^2. Best matched model curves were then obtained for the interaction parameter set $\chi_{THF/PMMA} = -0.3$, $\chi_{MeOH/PMMA} = 0.8$, and $\chi_{THF/MeOH} = -0.6$. As seen in Figure 6 the corresponding model curve is in good agreement with our experimental data.

Compared to interaction parameter values of $\chi_{THF/PMMA} = 0.36$ and $\chi_{MeOH/PMMA} = 1.20$ obtained from Hildebrand-Scott solubility estimations,[25] the corresponding parameter

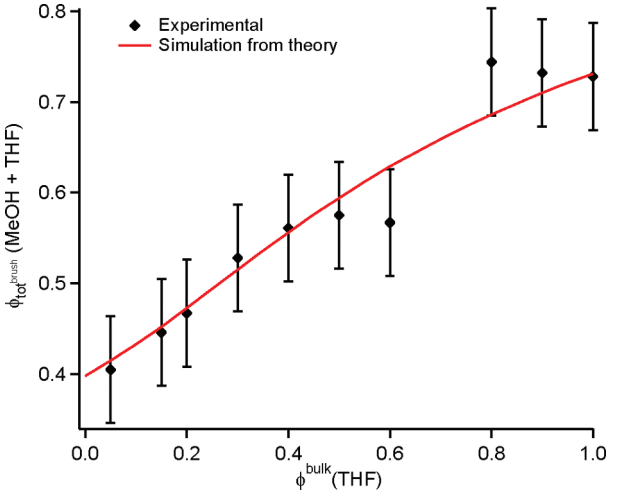


Figure 6. Plot of the deduced total solvent volume fractions in the brush region against the THF volume fraction in the bulk solvent, including estimated errors. The red line corresponds to model calculations[29] using Flory–Huggins interaction parameters of $\chi_{THF} = -0.3$, $\chi_{MeOH} = 0.8$, and $\chi_{THF/MeOH} = -0.6$.

values determined from our NR data and brush theory are remarkably low and in the case of $\chi_{THF/PMMA}$ even negative. Therefore, both solvents seem to be better solvents for the PMMA brush than expected from the bulk theory. The reason for this discrepancy may be found in the approximations made in Hildebrand–Scott theory. Within this theory χ-parameters are determined as a sum of enthalpic, χ_H, and entropic, χ_S, contributions, $\chi = \chi_H + \chi_S$. For regular polymer solutions χ_H can be estimated from solubility parameters of the respective polymer and solvent, while $\chi_S = 0.36$ was found for most systems. This theory, however, is only valid for polymer–solvent pairs with an enthalpic interaction part $\chi_H \geq 0$. Thus, interaction parameter estimations for attracting polymer/solvent pairs such as PMMA/THF are not possible within this common solubility approach. However, based on our experiments, also $\chi_{MeOH/PMMA}$ is found to be by 0.4 lower than expected from Hildebrand–Scott estimations. For both, free PMMA molecules and the PMMA brush, enthalpic contributions to the polymer/solvent interaction energies can be assumed to be equal. Thus, the physical reason for the observed difference is found in the different geometry of the PMMA brush compared to free PMMA chains. Compared to free PMMA molecules, PMMA chains in the brush are entropically constrained by their next neighbor chains and by immobilization at the substrate. Such entropic constraints lower the entropy of mixing with the surrounding solvent. Comparing the PMMA brush's entropy of mixing with the free PMMA brush's entropy of mixing one can write

$$\Delta S_{Mix}^{brush} < \Delta_{Mix}^{free} \tag{5}$$

However, reduced entropies of mixing should increase the χ-parameters instead of decreasing them. Thus, besides the enthalpic interaction energy and the entropy of mixing, there has to be at least one more energetic contribution in order to explain the observed reduced χ-parameter values. Compared to free PMMA chains, interfacial energies between the PMMA brush and the solvent have to be considered. The surface tensions of THF and MeOH are $\gamma_{lg,THF} = 27.05$ mN/m and $\gamma_{lg,MeOH} = 22.07$ mN/m.[37] Contact angle experiments with H_2O, formamide and toluene on a PMMA brush specimen yielded $\gamma_{sg,PMMA}^{brush} = (45.1 \pm 0.7)$ mN/m, which is near the literature value for bulk PMMA of $\gamma_{sg,PMMA}^{bulk} = 41.1$ mN/m.[25] Contact angle experiments with MeOH and THF on the

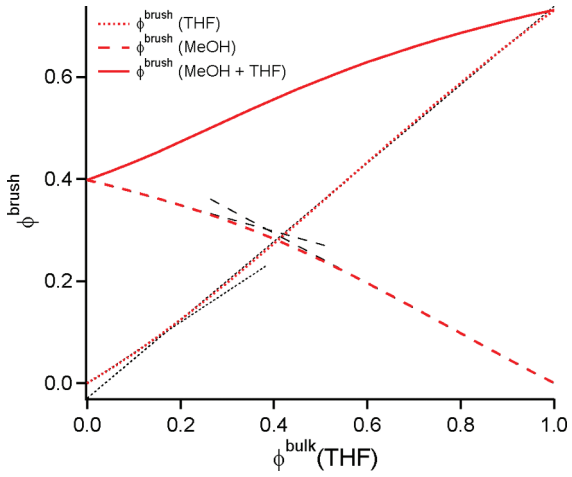


Figure 7. Simulated solvent volume fractions in the brush region for THF, ϕ^{brush}(THF) (dotted red line), MeOH, ϕ^{brush}(MeOH) (dashed red line), and total solvent ϕ^{brush}(MeOH + THF) (red line). Black lines indicate the hypothetical linear regimes for MeOH desorption and THF adsorption. The slope values mentioned in the main text refer to the slopes of these black tangential lines.

same specimen showed a complete wetting of the sample for both liquids with contact angles $\theta < 5°$, respectively. Using Young's equation

$$\cos\theta = \frac{\gamma_{sg} - \gamma_{sl}}{\gamma_{lg}} \tag{6}$$

which relates the contact angle θ and the interfacial tensions, γ, at the solid/gaseous (*sg*), solid/liquid (*sl*) and liquid/gaseous (*lg*) interfaces, we obtain $\gamma^{bulk}_{sl,PMMA/THF} = 13.7$ mN/m and $\gamma^{brush}_{sl,PMMA/THF} = 18.6$ mN/m. The definition of the free surface energy regarding only interfacial tensions

$$dG^{\sigma} = -A\, d\gamma_{s1} \tag{7}$$

shows that G^{σ} becomes negative when the brush is immersed in MeOH and THF. Since the above-reported γ_{sl} values for THF and MeOH differ only slightly (by ~5 mN/m), it is reasonable to expect that interfacial energy effects would lower the interaction parameters $\chi_{THF/PMMA}$ and $\chi_{MeOH/PMMA}$ observed in our experiment by a similar amount compared to the corresponding bulk values. This discussion shows that the better solubility of the PMMA brush compared to bulk is mainly determined by the free surface energy dG^{σ}.

NR results cannot directly give information on the specific desorption/adsorption behavior of MeOH and THF. However, using the equations derived by Birshtein and Lyatskaya,[29] it is possible to separately calculate ϕ^{brush}(THF) and ϕ^{brush}(MeOH) as a function of the THF bulk volume fraction for the interaction parameter set determined on the basis of our results (Figure 7). Considering the turning points of the obtained ϕ^{brush}(MeOH) and ϕ^{brush}(THF) model curves, the brush swelling characteristics can be divided into three regimes, as represented by the intersections of the black dotted and black dashed tangential lines in Figure 7. For ϕ^{bulk}(THF) ≤ 0.2 a constant increase of ϕ^{brush}(MeOH + THF) is observed, while the brush height $H = 13.0$ nm stays constant (see Figure 4). In this regime ϕ^{brush} (MeOH) decreases with a slope of $(\phi^{brush}(MeOH))/(\phi^{bulk}(THF)) = -0.24$, while ϕ^{brush}(THF) increases with a slope of $(\phi^{brush}(THF))/(\phi^{bulk}(THF)) = 0.60$. Since a constant brush height was observed, we conclude that THF molecules adsorb preferentially at the brush/solvent interface, by replacing small amounts of MeOH. Our conclusion is also supported by the increasing width of the brush/solvent interface.

For $0.2 < \phi^{bulk}(THF) \leq 0.5$ a flattening of the ϕ^{brush}(MeOH + THF) curve is observed, which is accompanied by an increase in H. For $\phi^{bulk}(THF) > 0.4$, brush swelling is now accompanied by an increased constant THF adsorption rate with a slope of $(\phi^{brush}(THF))/(\phi^{bulk}(THF)) = 0.77$, while the MeOH desorption is steadily increasing toward a slope of $(\phi^{brush}(MeOH))/(\phi^{bulk}(THF)) = -0.48$. Thus, MeOH exchange with THF molecules increases, while further THF adsorption in addition to this replacement effect practically ceases. It can be concluded that THF molecules are able to diffuse into the PMMA brush and replace more and more MeOH molecules, during stretching.

In the totally swollen brush regime for $\phi^{bulk}(THF) > 0.5$, the brush height stays constant at $H = 16-17$ nm while desorption of MeOH and adsorption of THF continue to increase with constant slopes of $(\phi^{brush}(MeOH))/(\phi^{bulk}(THF)) = -0.48$ and $(\phi^{brush}(THF))/(\phi^{bulk}(THF)) = 0.77$, respectively, until a theoretical total solvent exchange has occurred at $\phi^{bulk}(THF) = 1$.

NCS Bending Results. Complementary to the structural brush swelling characteristics and the solvent adsorption/desorption behavior, the mechanical properties of the polymer brush were examined in NCS bending experiments as a function of solvent quality. For a thermodynamic understanding, the surface stress results obtained from the NCS experiments were then related to effective interaction parameters calculated via the relation[29]

$$\begin{aligned}\chi_{eff} &= \chi_{THF/PMMA}\phi^{bulk}(THF) \\ &+ \chi_{MeOH/PMMA}(1-\phi^{bulk}(THF)) \\ &- \chi_{MeOH/THF}\phi^{bulk}(THF)(1-\phi^{bulk}(THF))\end{aligned} \tag{8}$$

Since the three interaction parameters in eq 8 were experimentally determined with neutron reflectivity, the only variable parameter is the volume fraction of THF in the bulk solvent, ϕ^{bulk}(THF). Since the surface stress σ was measured as a function of ϕ^{bulk}(THF), this allows a direct comparison of σ with χ_{eff}.

Surface stress results as obtained from our NCS bending experiments yield information on the laterally acting forces inside the brush phase. Attractive polymer−polymer interactions as caused by interchain entanglements lead to NCS bending toward the brush coating, corresponding to a tensile surface stress. On the contrary, lateral stresses resulting from the osmotic pressure caused by solvent incorporation into the brush lead to NCS bending away from the brush coating, corresponding to compressive stresses. In addition, the measured NCS bending can be influenced by a softening or hardening of the coated layer, as potentially caused by phase transitions of the coating. For temperature induced bending of a polystyrene coated NCS, Jung et al.[18] reported a cantilever bending away from the coating at below the glass transition temperature T_g as a consequence of a bimaterial effect. After reaching T_g the measured NCS bending stayed constant since the softened polymer was not able any more to further deflect the NCS.

Our NCS bending experiments (Figure 8) revealed positive surface stresses of the dried and collapsed brush in the bad solvent ($\chi_{eff} > 0.5$), as reflected in an NCS bending toward the PMMA brush. For Θ-solvent conditions ($\chi_{eff} \sim 0.5$), a decay of $\Delta\sigma$ toward zero was observed. Tensile stresses in polymeric bulk materials and polymer brushes can be attributed to attractive intermolecular chain interactions caused by interchain entanglements.[11,38] For our polymer brush ($M_w = 23500$ g/mol) a grafting density of $d = 0.18$ chains/nm^2 was obtained from X-ray reflectivity experiments.

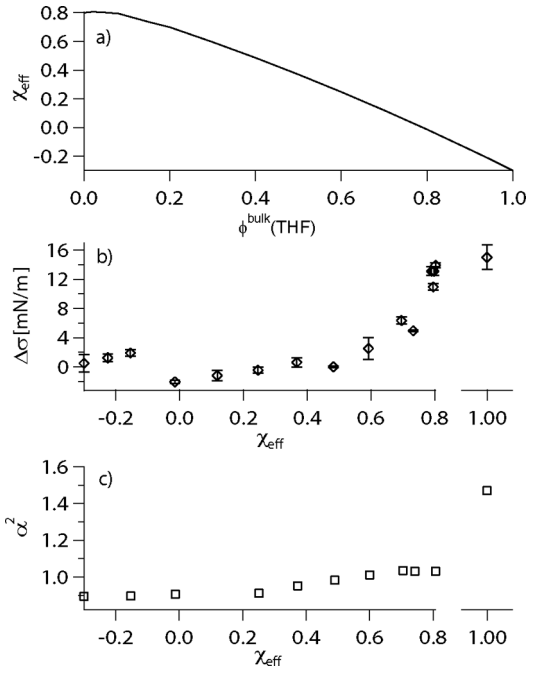


Figure 8. (a) Evolution of χ_{eff} as a function of ϕ^{bulk}(THF) according to eq 8. (b) Surface stress evolution of brush coated NCS starting (from right to left) from the dry brush over the collapsed brush in the bad solvent regime ($\chi_{eff} > 0.5$) toward the swollen brush in the good solvent regime ($\chi_{eff} < 0.5$) (eq 2). The data are presented as a function of the effective interaction parameter χ_{eff}. (c) α^2 anisotropy factor of the polymer brush as a function of χ_{eff}, eq 9.

The critical entanglement molecular weight in concentrated PMMA solutions is 11000 g/mol.[39] The criterion of lateral overlapping polymer brushes is fulfilled for $H > (1/d)^{1/2}$.[29] For the dry state our PMMA brush was $H = 7.1$ nm. Thus, the criterion of intermolecular entangled polymer chains is fulfilled. Entanglements in the compressed brush state can be also explained by assuming a simple square lattice grafting pattern. Here an interchain distance of 5 nm can be derived from this grafting density. The radius of gyration $R_{g,0}$ of the unperturbated PMMA chain is 4.1 nm. Accordingly, for a fictive ideal polymer brush there is enough lateral overlap of the polymer chains for the formation of entanglements. However, the dried polymer brush was found in a compressed state of $H = 7.1$ nm $< 2R_{g,0}$. Comparison of entanglement densities in compressed or stretched polymer brushes with an ideal Gaussian brush can be roughly estimated by the expression[11] $\alpha^2 = (R_{g,\perp}/R_{g,0})$ where $R_{g,\perp}$ for an anisotropic chain is the radius of gyration perpendicular to the stretch direction (parallel to the substrate for polymer brushes). For a polymer brush, the ratio α^2 was previously derived[11,40] as

$$\alpha^2 = \left(\frac{R_{g,\perp}}{R_{g,0}}\right)^2 = \frac{1 + (H/\langle r^2\rangle^{1/2})}{2(H/\langle r^2\rangle^{1/2})} \qquad (9)$$

with the ideal mean-square end-to-end distance $\langle r^2\rangle^{1/2}$ and the measured brush height H. Accordingly, for the dried, compressed polymer brush a value $\alpha^2 = 1.47$ was obtained, based on an end-to-end distance $\langle r^2\rangle^{1/2} = 13.8$ nm for our brush molecules (Figure 8).

We will first discuss the transition of the dried polymer brush toward the collapsed polymer brush in bad solvent conditions at $\chi_{eff} = 0.8$. Here the tensile surface stress decreases by 13% (Figure 8b), while H increases by 83% (Figure 4), which is accompanied by ϕ^{brush}(MeOH + THF) = 0.4 (Figure 6) and a change in α^2 from 1.47 to 1.03 (Figure 8c). From the high degree of brush stretching (83%) in respect to the low decrease of tensile stress (13%) it can be concluded that forces in the polymer brush caused by the osmotic pressure are mainly compensated in the direction normal to the surface. Lateral chain repulsion due to osmotic pressure in the brush can thus be regarded to be minor. The observed decrease of tensile stress can be attributed to a decrease in interchain entanglements, as reflected in the drop of α^2.

In the transition region between the bad solvent state at $\chi_{eff} = 0.8$ and Θ-solvent conditions at $\chi_{eff} = 0.5$, the tensile stress is continuously decreasing and finally dropping to zero (Figure 8b). For this transition a comparatively small further increase of the brush height H by 18% (Figure 4) and a change in α^2 from 1.03 to 0.98 Figure 8c is observed. Thus, it can be concluded that interchain entanglements do not change essentially in this regime. Similar to the dry/bad solvent transition, the osmotic pressure caused by a solvent uptake of ϕ^{brush}(MeOH + THF) = 0.52 (Figure 6, Figure 8a) is mainly compensated by brush stretching normal to the surface. However, the width s of the brush/solvent interface increases from 1.2 to 3.6 nm (Figure 4). This should be accompanied by an increased mobility of the PMMA chains near the brush/solvent interface. This prediction is consistent with the scenario of a softer brush regime, which is supported by the increasing exchange rate of MeOH with THF as discussed above. By gradual exchange of MeOH with THF the PMMA brush becomes softened and polymer−polymer interactions equalize polymer−solvent interactions. Thus, no NCS bending is detected any more in this softened brush state. In the good solvent regime for $\chi_{eff} < 0.5$, the brush phase is too soft to support distinct tensile stress due to attractive polymer−solvent interactions.

Summary

In this study, we have clarified polymer brush mechanics during the collapse swelling transition on the example of a PMMA brush. In this comparative study combining structure determinations (neutron reflectivity), mechanical analysis (NCS bending) and established scaling theories,[29] our previous findings[12] could be supported and clarified. Neutron reflectivity experiments showed that for the swelling mechanism the osmotic pressure of the liquid is dominant compared to the enthalpic polymer−solvent interactions. It was shown that Hildebrand−Scott estimations of interaction parameters are inadequate for the application in thin polymer brushes, due to dominating surface energy effects at the polymer/liquid interface. Comparison of our experimental data with brush theory yielded more adequate polymer−solvent interaction parameters, which were used to model the solvent adsorption/desorption behavior.

Surface stress investigations showed that initial tensile stresses in the dry state were only slightly reduced upon the transition into the bad solvent state. We have related this observation to a reduction in interchain entanglements. Reaching Θ-solvent conditions, tensile stresses relaxed toward zero, due to softening of the brush.

Acknowledgment. This research was supported by a focused neutron research funding of the Max Planck Society, Munich, and by the Deutsche Forschungsgemeinschaft, Bonn, (GU771/2, MU1487/5). We gratefully thank the FRM II for provision of beamtime and Jörgen Franke for technical support at the beamline N-REX$^+$. We especially thank Gunnar Kircher for his kind support during the PMMA brush synthesis.

References and Notes

(1) Alexander, S. *J. Phys.* (*Paris*) **1977**, *38*, 977–981.
(2) de Gennes, P. G. *Macromolecules* **1980**, *13*, 1069–1075.

(3) Zhao, B.; Brittain, W. J. *Prog. Polym. Sci.* **2000**, *25*, 677–710.
(4) Léger, L.; Raphaël, E.; Hervet, H. Surface-Anchored Polymer Chains: Their Role in Adhesion and Friction. In *Polymers in Confined Environments*; Springer: Berlin/Heidelberg, 1999; pp 185−225.
(5) Tadmor, R.; Janik, J.; Klein, J.; Fetters, L. J. *Phys. Rev. Lett.* **2003**, *91*, 115503/1–4.
(6) Klein, J. *Annu. Rev. Mater. Sci.* **1996**, *26*, 581–612.
(7) Kreer, T.; Muser, M. H.; Binder, K.; Klein, J. *Langmuir* **2001**, *17*, 7804–7813.
(8) Kreer, T.; Binder, K.; Muser, M. H. *Langmuir* **2003**, *19*, 7551–7559.
(9) Oulevey, F.; Gourdon, D.; Dupas, E.; Liley, M.; Duschl, C.; Kulik, A. J.; Gremaud, G.; Burnham, N. A. Micromechanics and Microtribology of Polymer Films. In *Microstructure and Microtribology of Polymer Surfaces*: American Chemical Society: Washington, DC, 1999; pp 118−123.
(10) Descas, R.; Sommer, J. U.; Blumen, A. *Macromol. Theory Simul.* **2008**, *17*, 429–453.
(11) Urayama, K.; Yamamoto, S.; Tsujii, Y.; Fukuda, T.; Neher, D. *Macromolecules* **2002**, *35*, 9459–9465.
(12) Bumbu, G. G.; Wolkenhauer, M.; Kircher, G.; Gutmann, J. S.; Berger, R. *Langmuir* **2007**, *23*, 2203–2207.
(13) Bhushan, B. *Springer Handbook of Nanotechnology*, 2nd. ed.; Springer: Berlin, 2007.
(14) McKendry, R.; Zhang, J. Y.; Arntz, Y.; Strunz, T.; Hegner, M.; Lang, H. P.; Baller, M. K.; Certa, U.; Meyer, E.; Guntherodt, H. J.; Gerber, C. *Proc. Natl. Acad. Sci. U.S.A.* **2002**, *99*, 9783–9788.
(15) Berger, R.; Gerber, C.; Lang, H. P.; Gimzewski, J. K. *Microelectron. Eng.* **1997**, *35*, 373–379.
(16) Zhou, F.; Shu, W.; Welland, M. E.; Huck, W. T. S. *J. Am. Chem. Soc.* **2006**, *128*, 5326–5327.
(17) Jung, N.; Jeon, S. *Macromolecules* **2008**, *41*, 9819–9822.
(18) Jung, N.; Seo, H.; Lee, D.; Ryu, C. Y.; Jeon, S. *Macromolecules* **2008**, *41*, 6873–6875.
(19) Lenz, S.; Nett, S. K.; Memesa, M.; Roskamp, R. F.; Timmann, A.; Roth, S. V.; Berger, R. d.; Gutmann, J. S. *Macromolecules* **2009**, *43*, 1108–1116.
(20) Lang, H. P.; Berger, R.; Andreoli, C.; Brugger, J.; Despont, M.; Vettiger, P.; Gerber, C.; Gimzewski, J. K.; Ramseyer, J. P.; Meyer, E.; Guntherodt, H. J. *Appl. Phys. Lett.* **1998**, *72*, 383–385.
(21) Butt, H. J. *J. Colloid Interface Sci.* **1996**, *180*, 251–260.
(22) Stoney, G. G. *Proc. R. Soc. London, Ser. A* **1909**, *82*, 172–175.
(23) Helm, M.; Servant, J. J.; Saurenbach, F.; Berger, R. *Appl. Phys. Lett.* **2005**, 87.
(24) Raiteri, R.; Butt, H. J. *J. Phys. Chem.* **1995**, *99*, 15728–15732.
(25) Brandrup, J.; Immergut, E. H.; Grulke, E. A., *Polymer handbook*; Wiley: New York, 1999.
(26) Auroy, P.; Auvray, L. *Macromolecules* **1992**, *25*, 4134–4141.
(27) Bunjes, N.; Paul, S.; Habicht, J.; Prucker, O.; Ruhe, J.; Knoll, W. *Colloid Polym. Sci.* **2004**, *282*, 939–945.
(28) Perlich, J.; Koì rstgens, V.; Metwalli, E.; Schulz, L.; Georgii, R.; Muì ller-Buschbaum, P. *Macromolecules* **2008**, *42*, 337–344.
(29) Birshtein, T. M.; Lyatskaya, Y. V. *Macromolecules* **1994**, *27*, 1256–1266.
(30) Ramakrishnan, A.; Dhamodharan, R.; Ruhe, J. *Macromol. Rapid Commun.* **2002**, *23*, 612–616.
(31) Bumbu, G. G.; Kircher, G.; Wolkenhauer, M.; Berger, R.; Gutmann, J. S. *Macromol. Chem. Phys.* **2004**, *205*, 1713–1720.
(32) Holy, V.; Baumbach, T. *Phys. Rev. B* **1994**, *49*, 10668–10676.
(33) Milner, S. T.; Witten, T. A.; Cates, M. E. *Macromolecules* **1988**, *21*, 2610–2619.
(34) Milner, S. T. *Europhys. Lett.* **1988**, *7*, 695–699.
(35) Scattering Length Density Calculator. http://www.ncnr.nist.gov/resources/sldcalc.html
(36) Korsunsky, A. M.; Cherian, S.; Raiteri, R.; Berger, R. *Sens. Actuators A: Phys.* **2007**, *139*, 70–77.
(37) Wohlfarth, C.; Wohlfarth, B.; Landolt, H.; Börnstein, R.; Martienssen, W.; Madelung, O., *Surface tension of pure liquids and binary liquid mixtures*; Springer: Berlin, 1997.
(38) Edwards, S. F.; Vilgis, T. *Polymer* **1986**, *27*, 483–492.
(39) Bueche, F. *J. Chem. Phys.* **1956**, *25*, 599–600.
(40) Ullman, R. *J. Chem. Phys.* **1979**, *71*, 436–449.

368 *Macromolecules* **2011**, *44*, 368–374
DOI: 10.1021/ma102032t

Macromolecules
ARTICLE

Entropic Effects on the Mechanical Behavior of Dry Polymer Brushes During Nanoindentation by Atomic Force Microscopy

Davide Tranchida,*,† Elena Sperotto,† Antoine Chateauminois,‡ and Holger Schönherr*,†

†*Department of Physical Chemistry I, University of Siegen, Adolf-Reichwein-Strasse 2, 57076 Siegen, Germany, and* ‡*Laboratoire de Physico-Chimie des Polymères et des Milieux Disperses, UMR CNRS 7615 Ecole Supérieure de Physique et Chimie Industrielles (ESPCI), 10 rue Vauquelin, 75231 Paris Cedex 05, France*

Received September 1, 2010; Revised Manuscript Received December 7, 2010

ABSTRACT: We report on the dependence of the mechanical properties of confined polymers on the film architecture. Compared to spin-coated films, grafted polymer brushes showed higher elastic moduli, which is attributed to entropy effects, and required higher loads to achieve the same residual indentation depth when compared to spin-coated samples. The contribution of entropy changes to the mechanical response of brushes was evaluated. Although qualitative, this study tries for the first time to evaluate this entropic contribution. Therefore, the role of morphology and architecture of the polymer films during mechanical deformation is highlighted, showing that the change of surface thermodynamic properties (entropy in particular) changes accordingly the nanometer scale mechanical properties.

1. Introduction

Surface-grafted polymers[1,2] allow one to design specific functional systems for various applications due to the synthetic flexibility, chemical robustness, and the high grafting densities obtained. They also offer the possibility to tune the morphology and final properties of modified surfaces, such as friction, wettability, or biocompatibility,[3−5] among others. In particular, applications to colloidal stabilization,[6,7] adhesion,[8] or lubrication[9] require a profound knowledge of surface mechanical performance.

Although nanoscale mechanical properties of polymers have been studied in detail, the peculiar morphologies obtained when considering polymer brushes pose some challenges and much less is known about their nanoscale mechanical properties.[10] The mobility of polymer chains at the interface[11] and nanoconfinement effects,[12] inherent, e.g., to ultrathin films, as well as entropic penalty contributions,[13] may give rise to unexpected and, compared to the bulk, altered behavior.

One typical example for this altered behavior is the glass transition temperature (T_g) of ultrathin free-standing or substrate-supported films.[14−16] The effect of the two interfaces, i.e. the interface of the polymer with the substrate and the interface with the air, on chain and segment mobility was shown to provide a plausible explanation for the observed depressed or elevated values of T_g.[17] Frank and co-workers addressed the relation of polymer thin film architecture and T_g in substrate supported films and concluded that the architecture had negligible influence on the T_g measured.[18] In addition, the coil configuration of the individual polymers was concluded to remain unaffected.

Apart from T_g, the confinement of polymers in ultrathin films may also significantly affect the films' mechanical properties. Previously, the surface forces apparatus (SFA)[19] and the atomic force microscope (AFM)[20] were applied to test the mechanical properties of polymer brushes swollen in good solvents. In these experiments fundamental information on the adhesion behavior and the chain conformation of polymer brushes was gained and compared to moderately dense brushes prepared by adsorption techniques. Mechanical stretching of single chains picked up by the AFM tip was also reported.[20]

Although these reports provide interesting hints on solvent-swollen systems, an exhaustive nanoscale mechanical characterization of dry polymer brushes in the glassy state, e.g., by AFM and contact mechanics, taking into account both elastic and plastic properties is still missing. In particular the interesting question of the dependence of the mechanical properties on the film architecture has remained unanswered to date.

Previously, dried poly(methyl methacrylate) (PMMA) brushes were studied on a larger scale by electromechanical interferometry, i.e., by measuring the plate compressibility of the films.[21] Urayama et al.[21] compared the mechanical behavior of spin-coated and grafted brush samples at temperatures around and above the glass-to-rubber transition temperature. These authors explained the higher resistance to compression and the considerable effect of entanglements by means of rubber elasticity theory and the Edwards−Vilgis slip-link model.[22] However, due to experimental limitations related to the low compressibility of glassy films and their limited thicknesses the anticipated differences in mechanical behavior among spin-coated and grafted PMMA films remained elusive.

In addition, surface wrinkling was used to show that the Young's modulus of poly(2-hydroxyethyl methacrylate) brush layers grafted on poly(dimethylsiloxane), PDMS are insensitive to film thickness.[23]

As a further approach to address mechanical properties of thin polymer films quantitatively, AFM nanoindentation represents often a most adequate tool for studying 3-D compressive properties, i.e., not only along the vertical direction of grafted chains.[24] Because of the ability to measure very small applied loads[25] and resulting penetration depths, AFM nanoindentation allowed in the past to link the morphology of polymers to their viscoelastic[26] and elastic[27] mechanical properties, as well as to characterize nanophases.[28] AFM based nanoindentation can be regarded as a complementary approach, since the mapping of mechanical properties of inhomogeneous samples is feasible, as well as the testing of brush films deposited on hard surfaces.

*Corresponding authors. E-mail: (H.S.) schoenherr@chemie.uni-siegen.de; (D.T.) tranchida@chemie.uni-siegen.de.

 Published on Web 12/23/2010 © 2010 American Chemical Society

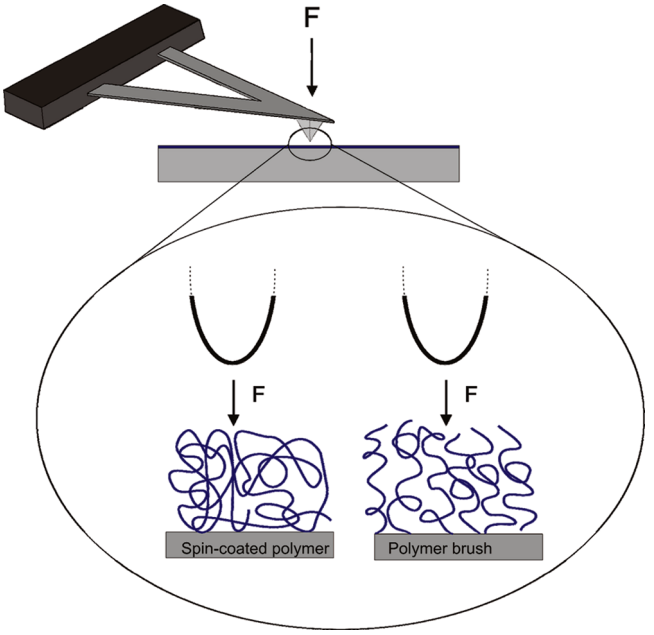


Figure 1. Schematic of AFM-based nanoindentation of ultrathin PMMA films obtained by spin-coating and SIP, respectively.

Interestingly, polymer brushes were only seldom studied in the past by AFM nanoindentation and contradictory results were reported. For example, the Young's moduli of tethered poly(styrene-*co*-2,3,4,5,6-pentafluorostyrene) (PSF) and poly(methyl acrylate) (PMA) chains were reported to be identical to the corresponding spin-coated samples.[29] By contrast, poly(styrene) brushes showed higher elastic moduli than the corresponding spin-coated samples and also better resistance to scratching in large scale scratch tests, which address a measurement of the films' plastic properties.[30]

In this article, we report on AFM nanoindentation measurements performed on grafted and spin-coated glassy PMMA films (Figure 1) to unravel qualitatively and quantitatively the effect of the polymer film architecture on the elastic and plastic properties of the films. In particular the differences among annealed spin-coated PMMA films and PMMA brushes obtained by surface-initiated polymerization (SIP) were compared. Noticeable differences in the elastic and plastic behavior on the nanometer scale[30] are explained based on a discussion of the thermodynamics of deformation.

2. Results

In this part, we will show differences in the mechanical behavior, i.e., measured Young's modulus and load required to induce the same residual depth, in order to justify the further study on the role of entropy changes to the deformation. Dealing with thin films, the effect of the substrate is unavoidable and precautions on the choice of film thicknesses, which will be discussed in the following, have been taken. The problem of identifying and minimizing substrate effects is indeed of great recent interest and a number of approaches have been proposed, both by theory, numerical simulations, and phenomenological approaches.[31−45]

The elastic and plastic properties of spin-coated and subsequently annealed PMMA films and corresponding brushes obtained by SIP were measured in AFM force-displacement curves. We compared the data of six different PMMA samples with different structure studied with different methods: (i) Macroscopic DMTA analysis (data from ref 46), AFM nanoindentations on (ii) a bulk sample (data from ref 46), (iii) a thin film on silicon obtained by spin-coating (150 nm thickness), (iv) a thin film on silicon obtained by spin-coating (70 nm thickness), and finally (v, vi) two grafted PMMA brushes on gold (similar thickness of 150 and 200 nm).

Following ref 46, a phenomenological elastic index ξ, bounded between zero and one in the ideal cases of rigid plastic behavior and elastic behavior, respectively, can be calculated as one minus the ratio of the residual indentation depth left behind the indenter and the maximum penetration depth.

In our present work, an index ξ as high as 0.80 was found for the spin-coated samples and the bulk sample. Therefore, the residual depth was 5 times smaller than the penetration under full load, giving the reader the feeling of the elastic contributions to the nanoindentation probably also related to the increase of yield stress at the high deformation rate achieved during the nanoindentation. In the case of the grafted film, the index ξ was estimated to be ~0.85. It is worth to mention that these values for ξ match the ones found for the bulk sample[46] therefore pointing at negligible substrate effects since, intuitively, when the stress field reaches the hard substrate, it causes purely elastic deformations that are completely recovered upon unloading thus increasing the ξ value with respect to nanoindentation of a bulky sample.

To quantify the force data and to model the contact mechanics, we used Sneddon's model with a parabolic indenter shape.[46,47] The tip shape was experimentally determined using blind reconstruction. This choice is motivated by previous results that highlighted the possibility to evaluate the elastic modulus of polymeric samples from AFM nanoindentations for a wide range of polymer states and morphologies, from glassy to semicrystalline to mesomorphic ones.[46] Sneddon's theory models the sample as an isotropic elastic half-space.

The evaluation of the Young's modulus of the films with Sneddon's model is in general accurate in the case of bulk polymer materials, since they can be considered as isotropic half spaces. In the case of the grafted chains and the spin coated samples, substrate effects can come into play during the course of indentation. Although the used substrate materials have different Young's moduli (79 GPa for gold substrate and 130 GPa for the silicon wafer), they can be considered as equally stiff since AFM nanoindentation cannot distinguish between them according to Tsukruk.[48] In order to compare all the indentation data and to minimize, as far as possible, the effect of the stiff gold/silicon substrate (which will be discussed further in the following section), only the results of nanoindentation experiments with a low penetration depth (roughly 10 nm) were considered for modulus measurements.[49−51]

Figure 2 shows the average values obtained from 20 nanoindentations on each sample. An elastic modulus of ~3 GPa was calculated in most of the cases, i.e., for macroscopic DMTA tests,[46] for nanoindentation on bulk PMMA[46] and for the 150 nm thick spin-coated samples (this work). An even higher modulus was observed for the 70 nm thin spin-coated sample.

By applying the same procedure used for the bulk and spin-coated samples, an equivalent nanoindentation modulus can be calculated for both the PMMA brushes in order to quantify the differences in the elastic behavior (Figure 2).

Further experimental observations confirm the enhanced elastic behavior of grafted polymer, since the plastic behavior of the grafted brush sample was found to be significantly different. The unloading curves are not shown here because the combination of viscoelastic phenomena and the sharp indenter used for AFM nanoindentations, much sharper than the indenters used for depth sensing instruments, render the AFM unloading curves poorly understood.[52] As an alternative, we analyzed the images collected on the samples after the nanoindentation. In this case, plasticity during nanoindentation manifests itself obviously with the residual imprint left behind the indenter, but also with pile-up,[53] i.e., the bulging out of the surface due to plastic flow.

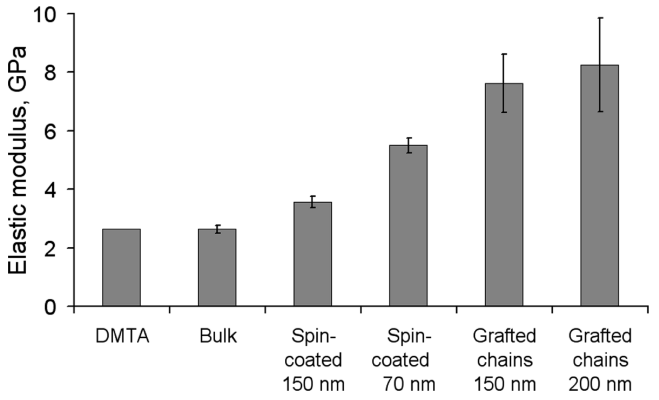


Figure 2. Comparison of the Young's moduli obtained on 5 different PMMA samples with both DMTA and AFM nanoindentations. The data for the bulk modulus determined by DMTA and by nanoindentation were taken from ref 46. Considerable stiffening was found for the thin spin-coated sample and even more dramatic increase for the grafted chains.

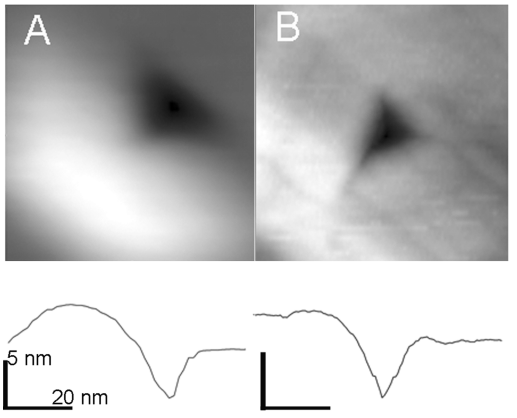


Figure 3. AFM images of the residual imprint left behind the indenter (120 nm × 120 nm), (A) for the spin-coated PMMA film (thickness 70 nm) after nanoindentations performed at 3.28 μN, and (B) the grafted PMMA brush sample after an indentation at 3.90 μN, respectively. The corresponding profiles along the direction of maximum residual depth and pile-up height are shown at the bottom.

Two representative images of the residual imprints, obtained by scanning with the same AFM tip that performed the nanoindentation, are shown in Figure 3, parts A and B, respectively, for the spin-coated and grafted brush sample. It is worth to stress that these imprints were obtained after nanoindentation that implied a penetration depth under full load in the order of 40 nm, therefore experimental conditions are completely different than the ones used for obtaining the values of Young's moduli of Figure 2. The pile-up is more pronounced on one side of the indent since the AFM tip is not symmetric, and higher stresses can be expected along the sharp edges. The respective profiles cut along the direction of maximum residual depth show that the same residual depth was obtained in this case, ~10 nm. However, this was obtained after applying a load of 3.28 μN in the case of the 70 nm thick spin-coated sample and by contrast, a higher load of 3.90 μN was required to achieve the same residual indentation depth for the brushes. In this latter case we observed an increase of 40% for the plastic load. Moreover, results not shown here indicate that a load as high as 6.0 μN is required to induce the same vertical pile-up for the grafted PMMA brushes. The increased load needed to induce the same residual depth suggests the enhanced recovery of grafted chains as compared to the entangled, spin-coated sample.

In general, a dramatic softening is observed for polymers after yield, due to the combined effect of strain and thermal softening. Arruda et al.[54] showed that the stress in stress−strain curves of

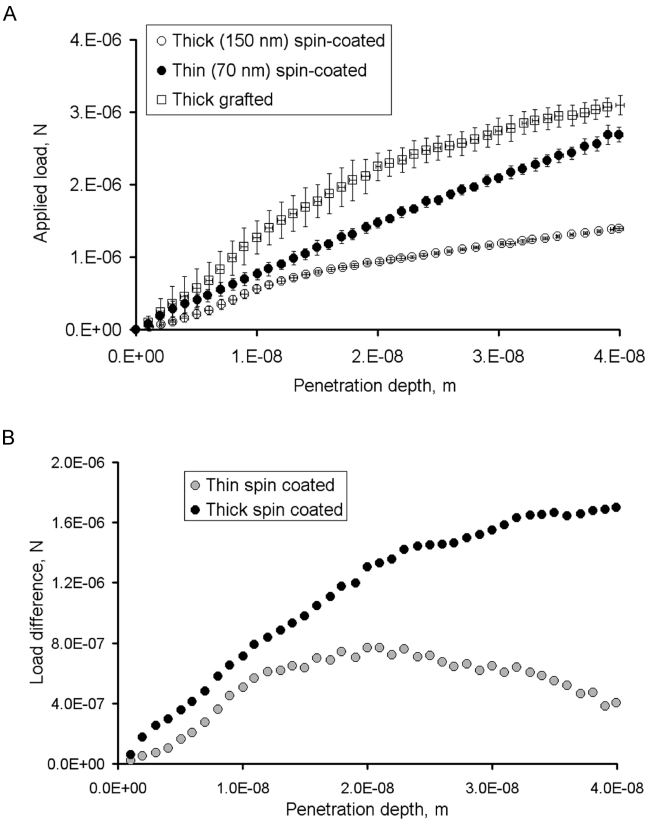


Figure 4. Averages of 20 force curves obtained from AFM nanoindentation measurements of the thin and thick spin-coated and the grafted PMMA samples (A). Compared to the spin-coated films, the raw data shows a stiffer behavior for the brush sample. Part B shows the contribution of entropy change to the stress field expressed as overall applied load, obtained as the difference between the loads of the grafted and respectively thin (gray series) or thick (black series) spin coated in part A.

PMMA in tension falls remarkably after yielding in the case of fast tests, from 140 MPa at yield to 90 MPa after it. Incidentally, the yield stress is highly enhanced as well,[54] and this finding explains the prevailing elastic constant and the high value for the elasticity parameter ξ discussed above.

Because of the anisotropically strengthened components, the grafted film is expected to require a higher load to result in the same deformation, when compared to the spin-coated one. Moreover, it is expected that the isotropic glassy polymer macromolecular structure, which forms a network by virtue of physically entangled molecular chains, evolves with the magnitude and state of strain during deformation as secondary valence interactions dissociate with plastic strains.[54]

On the other hand, for the PMMA brushes, the deformation of stretched chains is more difficult at relatively low penetration depth, while upon deformation a softer material is created as the composite of highly stretched and coiled chains.

In Figure 4A, three averaged nanoindentation curves are shown for the grafted brushes and the two spin coated samples. These curves were calculated from 20 individual force curves for each sample. Compared to the spin-coated PMMA films, the PMMA brushes were found to be stiffer. The difference in applied load needed to achieve a certain penetration depth is shown in Figure 4B.

3. Substrate Effect

As mentioned above, the method used to extract the modulus of the film from indentation data is based on a model valid for isotropic homogeneous solids. In the case of a coated substrate, a so-called "equivalent elastic modulus", E_{eq}, is obtained through

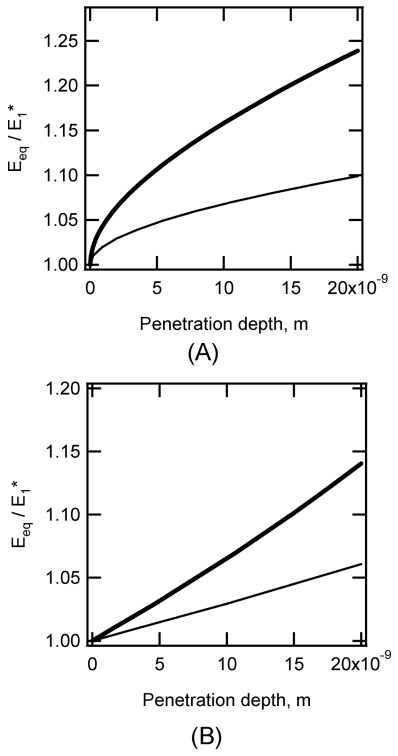


Figure 5. Calculated equivalent indentation modulus as a function of the penetration depth in the case of the elastic indentation of a frictionless coated substrate by (A) a sphere and (B) a cone. The equivalent modulus is normalized with respect to the modulus of the layer, E_1*. Bold line: 70 nm. Plain line: 150 nm. The ratio of the reduced modulus of the substrate to that of the layer, E_0*/E_1*, is set to 38 in the calculations. Penetration depths were calculated assuming a radius R = 10 nm for the sphere and a half included angle of 35 deg for the cone.

this method which is a combination of the respective moduli of the film, E_1, and of the substrate, E_0. As pointed out by Doerner and Nix,[55] the relative weight of the substrate and coating contributions to this equivalent modulus varies with penetration depth. In order to evaluate substrate effects on the measurement of the Young's modulus of spin-coated and grafted films, elastic contact mechanics calculations have been carried out along the lines of an exact semianalytical model developed for coated substrates by Perriot and Barthel.[31b] In this model, solutions are provided for the load and penetration of a frictionless coated contact indented by a cone or a sphere. Calculations were carried out using a ratio of the reduced modulus of the substrate to the reduced modulus of the film, E_0*/E_1*, equal to 38 (where E_i* = $E_i/(1-\nu_i^2)$ and ν_i are respectively the reduced modulus and the Poisson's ratio of the film (i = 1) or the substrate (i = 0). This ratio corresponds to indentation of a glassy polymer layer (E_1 = 3 GPa, ν_1 = 0.4) lying on a silicon substrate (E_0 = 130 GPa and ν_0 = 0. 2). For the low indentation depth (i.e., 10 nm) used for the determination of the modulus, the AFM tip can be assimilated to a sphere with a radius of curvature of roughly 10 nm. Figure 5a shows the changes in the normalized equivalent modulus, E_{eq}*/E_1*, as a function of the indentation depth for the two films thicknesses (70 and 150 nm) achieved with the spin coated samples. As expected, the equivalent modulus is higher for the 70 nm film than for the 150 nm film as substrate effects are more pronounced. However, it turns out that, in both cases, substrate effects induce a limited deviation of the calculated equivalent modulus from the Young's modulus of the layer. For a 10 nm indentation depth, the ratio E_{eq}*/E_1* is equal to only 1.16 for the thinnest (70 nm) film. In other words, substrate effects induce an error (16%) in the determination of the actual Young's modulus of the layer which

Table 1. Calculated Equivalent Reduced Modulus as a Function of Film Thickness in the Case of Cone and Sphere Indentation of a Coated Substrate[a]

film thickness (nm)	type	E_{eq}*/E_1*
70	cone	1.06
150	cone	1.03
70	sphere	1.16
150	sphere	1.07

[a] The equivalent modulus is calculated for a 10 nm indentation depth.

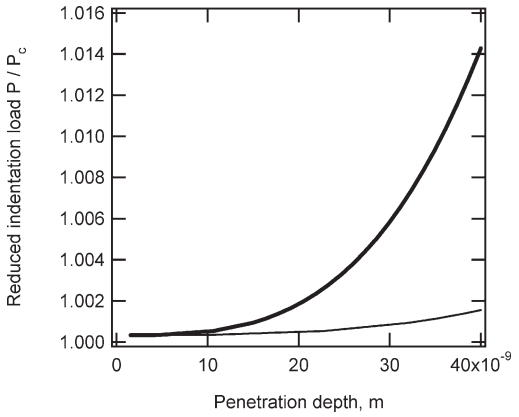


Figure 6. Calculated normalized indentation load, P/P_c, as a function of the indentation depth in the case of the elastic indentation of a coated substrate by a cone (E_0*/E_1* = 38, β = 35 deg). Bold line: 70 nm. Plain line: 150 nm.

is of the order of magnitude of experimental uncertainty (about 10−15% depending on the film specimen) and cannot justify the considerable differences of mechanical properties among the films with different morphologies observed in Figure 2. This conclusion is preserved if cone indentation is considered instead of sphere indentation (Figure 5b and Table 1). As a conclusion, it can be stated that substrate effects do not significantly affect the Young's modulus measured using Sneddon's model at the considered low penetration depth. Differences between the different spin-coated and grafted films can be therefore considered as representative of different mechanical response of these films.

Additional calculations were carried out at increased indentation depths using the cone geometry for indentation depths up to 40 nm, which correspond to the experimental data reported in Figure 4. In Figure 6, the normal load, P, normalized with respect to its value for a semi-infinite body, $P_c = \pi a^2/2E_1^* tan\beta$ (where β is the half included cone angle), is represented as a function of the penetration depth. It emerges that substrate effects induce only a minor deviation from the load, P_c, corresponding to semi-infinite substrate. Although these calculations correspond to an elastic contact situation, one does not expect substrate effects to be substantially enhanced when plastic deformation is involved. Differences in the experimental plastic indentation behaviors reported in Figure 3 can thus be considered as truly representative of the yield response of the polymer layers.

4. Discussion

Since the radius of gyration can be estimated to be in the range of 10−15 nm, it might be surprising that the two spin coated samples result in very different moduli. Tweedie et al.[51] showed that an increase in stiffness for nanoindentations at low contact depths was observed for glassy polymers, which was independent of processing, thermal history, macromolecular structural properties, and humidity. These authors argued that the increase in stiffness was related to a polymer surface stiffening mechanism, due to the creation of a mechanically unique interfacial region between the probe and the polymer surface. Confinement arising

from decreased film thickness can further boost this phenomenon, since the effect of the stiff interphase is larger for small film thickness. This effect was consistently absent for the 150 nm thick spin-coated films.

When comparing the 150 nm thick spin-coated films with the PMMA brush, a marked increase of Young's modulus of three times was observed, even though the films possess comparable thickness. The 70 nm thin spin-coated film also showed a significant decrease of roughly 30% in modulus compared to the PMMA brush sample (150 nm thick). Indeed, in this latter case, it can be intuitively understood that the deformation in the direction of the chain is more difficult when compared to lateral deformations. The 30% increase observed for the glassy brush sample at room temperature is consistent with the results reported on brush and spin-coated PMMA above the glass-to-rubber transition by Urayama et al.[23]

Thorough studies have been performed in order to explain the novel behavior and morphology of tethered polymer brushes.[56] In particular, it has been shown that macromolecules in polymer brushes exhibit deformed configurations, i.e., they are stretched, as a result of the balance between the energetic interactions and the reduction in configurational entropy.[57] Therefore, deforming stretched macromolecules in a polymer brush during nanoindentation leads to an increase of entropy. Drozdov elegantly showed that in the case of tethered chains "the conventional entropic elasticity theory may lead to conclusions that contradict our physical intuition".[58] The increase in entropy inferred from the data in Figure 4 is corroborated by data obtained by indenting along an oblique direction (12° with respect to the surface normal direction). We observed, as shown in the Supporting Information (Figure S-2), that the grafted polymer behaves softer than the spin-coated polymer. The grafting density of the polymers comprising the brush was not determined in this study since the planar substrates did not yield enough material for standard GPC analyses.

Unlike for rubbery polymer systems, for which entropy elasticity is important, PMMA is described here by concepts of energy elasticity. After Landau,[59] the change of internal energy per unit volume, $\mathcal{E}$, upon mechanical deformation can be written as the difference between the work done by external forces ($\sigma\, d\varepsilon$) and the heat per unit volume ($T\, \mathrm{d}S$):

$$d\mathcal{E}^{grafted} = T\, \mathrm{d}S^{grafted} + \sigma_{ij}^{grafted}\, \mathrm{d}\varepsilon_{ij}^{grafted} \quad (1)$$

$$\mathrm{d}\mathcal{E}^{spincoated} = \sigma_{ij}^{spincoated}\, \mathrm{d}\varepsilon_{ij}^{spincoated} \quad (2)$$

where T denotes temperature and S entropy and where σ_{ij} and ε_{ij} are the components for the stress and strain tensors, respectively. Detailed experiments on isotropic glassy PMMA below the glass-to-rubber transition showed that entropic contributions to elastic response are minor, for example in the case of hydrostatic compression.[60,61] Therefore, the entropic term for a reversible isothermal deformation of *isotropic* PMMA (compare eq 2). can be neglected. Moreover, for macroscopic tests, nearly adiabatic conditions were found when the overall deformation up to rupture took up to 10 s.[54] Fischer-Cripps showed that a negligible increase in temperature is experienced by the material during nanoindentation.[62,63]

By contrast, the polymer brushes studied here are certainly anisotropic. Since substrate effects and the oedometric nature[31] of the contact, i.e., the elastic response of the constrained material discussed in Figure 2, can be ruled out as origin for the observations, a reasonable assumption is that the different behavior among the two samples arises solely due to entropic effects. In principle, a change in Young's modulus, as shown in Figure 2, implies that the contribution of the term $\sigma d\varepsilon$ is different for the two samples. However, it can also be supposed that this change in modulus arises only because of entropic effects, therefore belonging to the term $T\, \mathrm{d}S$. This is equivalent to assuming that the stress experienced by the grafted brush sample during nanoindentation has a further entropic contribution with respect to the spin-coated sample. This contribution lowers the effective stress acting on the sample and therefore increases the apparent nanoindentation elastic modulus, when the sample is indented vertically:

$$\sigma_{ij}^{grafted} \approx \sigma_{ij}^{spincoated} - T\frac{\partial S}{\partial \varepsilon_{ij}^{grafted}} \quad (3)$$

The contributions of this "entropic" stress field expressed as overall applied load (obtained as the mere difference between the loads in Figure 4A) are reported in Figure 4B.

Unfortunately, there are no contact mechanics theories available that allow one to quantify the stress field tensor of an AFM nanoindentation with sufficiently good approximation to estimate $\partial S/\partial \varepsilon$. In order to describe the entropy change during nanoindentation, we only considered the vertical stress, where it is highest, i.e., inside the contact area at the apex of the tip ($\rho = 0$ in eq 4). These stresses indeed compress the chains vertically, not allowing them to bend and rather force them to assume a more coiled configuration, thus increasing the entropy.

After Sneddon,[47] we write the stress in the z direction in cylindrical coordinates for the case of nanoindentation with a paraboloid as follows:

$$\sigma_{zz}(\rho, 0) = -\frac{4\mu p}{\pi a^2(1-\nu^2)}\sqrt{a^2-\rho^2}, \quad \rho < a \quad (4)$$

Here a is the contact radius, p is the penetration depth, ν is the Poisson's ratio, and μ is the first Lamé coefficient, which contains the Young's modulus.

Sneddon also showed that the ratio of penetration depth and contact radius p/a in eq 4 is equal to the square root of the ratio of the penetration depth and tip radius. Following eqs 2−4 for $\rho = 0$, and assuming that the strain is proportional to the square root of the ratio of penetration depth and tip radius, while the spin-coated PMMA and the grafted one differ only in the values of Young's moduli, a qualitative change in conformational entropy per unit strain, $\partial S/\partial \varepsilon$, with increasing penetration depth was estimated.

Since only the stress at the apex of the tip, which is fairly high compared to the overall stress field, is taken into account, the values obtained are not absolute and were hence plotted in arbitrary units. By integrating $\partial S/\partial \varepsilon$, it is found that the increase in entropy is given by

$$\int_0^{\varepsilon\max} \frac{4p}{\pi a(1-\nu^2)T}\Delta\mu\, \mathrm{d}\varepsilon = \int_0^{p\max} \frac{4}{\pi(1-\nu^2)T}\sqrt{\frac{P}{R}}\Delta\mu\, \mathrm{d}\left(\sqrt{\frac{P}{R}}\right) \quad (5)$$

where R is the tip radius.

The overall entropy is found to increase with increasing penetration depth for the tethered chains (Figure 7A), both when comparing their stress field to the thick and to the thin spin coated films. These findings agree with calculations that show that the internal energy of the sample increases monotonically with strain as the isotropic material is transformed into oriented material during the deformation process.[64]

Figure 7B correctly shows that the entropy increase, because of tethered chains unstretching, causes the apparent load contribution to the force curve, to different extents whether the brush force curves are compared to the thin or to the thick sample.

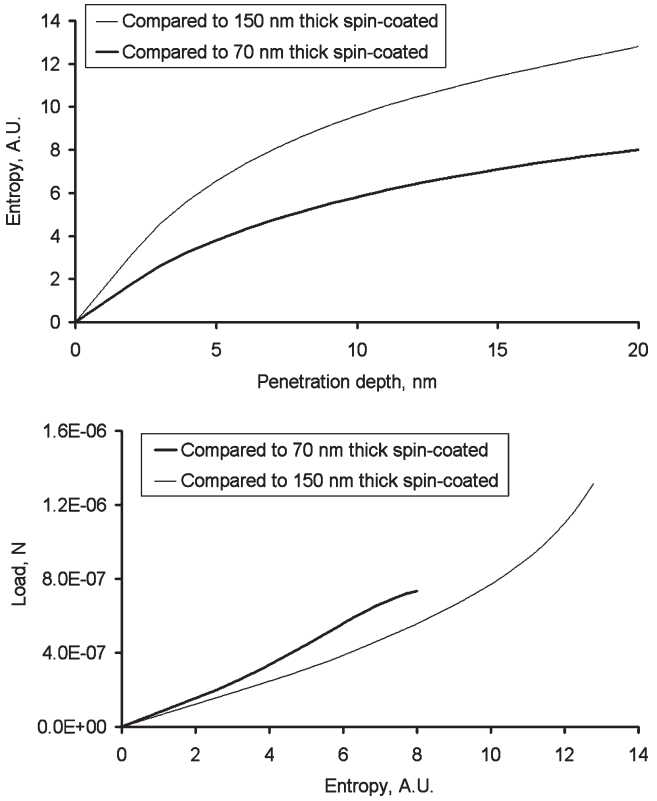


Figure 7. Entropic effects on nanoindentations of grafted chains. The overall entropy change was obtained after evaluating the stresses with Sneddon's model (details: see text).

5. Conclusions

In conclusion, grafted PMMA chains show enhanced elastic and plastic behavior, when compared to spin-coated samples. The reason can be found, according to the thermodynamics of deformation, in entropic effects that were shown to be responsible for an apparent stress contribution that lowers the stress experienced by the sample. Moreover, when the directionality is lost, e.g., by indenting along an oblique direction, the entropy-based stiffening effect disappears and the grafted polymer behaves softer. This finding is reasonable when considering that tethered chains represent a highly anisotropic system. The peculiar anisotropic deformation behavior unraveled in this current study for PMMA and the assignment of the entropic origin can very likely be generalized to account for the behavior of brushes of other amorphous polymers. Our results highlight the need of further studies of nanomechanical properties of polymeric brushes in view of applications where the deformation direction varies or is uncontrolled. Moreover, it is shown that changes of surface thermodynamic properties can be induced by deformation, which possesses very likely relevance for the unusual reactivity observed in micro- and nanoscale contacts[65,66] or for nanotribology of hydrated brushes,[67] among others.

6. Experimental Section

Spin-Coated PMMA Films. PMMA with a molar mass of 33 000 g mol^{-1} was used as received (Aldrich) and dissolved in toluene to yield solutions with concentrations of 20 and 45 mg/mL. The solutions were spin-coated at 3000 rpm on a precleaned silicon wafer using a home-built spin-coater. The films obtained were annealed for 1 h at 130 °C. The thicknesses of the films of 70 and 150 nm were estimated from AFM step height analyses of defined scratches in the films.

PMMA brushes. Methyl methacrylate (MMA, 99%), mercaptoundecanol (97%), pyridine (99%), bromoisobutyryl bromide (98%), copper(I) bromide (99.99%), and 2,2′-bipyridyl (99+%) were obtained from Aldrich. MMA was passed through an alumina column to remove the inhibitor; all other materials were used as received. ω-Mercaptoundecyl bromoisobutyrate was synthesized according to the literature.[68] Polymer brush growth was achieved by placing the substrates, modified by microcontact printing with the bromoisobutyrate-terminated initiator, in a Schlenk tube under an argon atmosphere and adding a degassed solution of MMA (10 g, 100 mmol), CuBr (143 mg, 1.0 mmol), and 2,2′-bipyridine (312 mg, 2.0 mmol), in the solvent mixture (deoxygenated Milli-Q water (2 mL) and MeOH (8 mL)) by cannulation. The polymerization was then allowed to proceed overnight at room temperature, after which removing the substrates from the reaction flask stopped the reaction. The substrates were extracted overnight with cold methanol in a Soxhlet apparatus with solvent cooling unit.

Atomic Force Microscopy. Nanoindentation was performed with a Nanoscope IIIA (Veeco, Santa Barbara, CA) under different applied loads and at tip indenting rate of 18 μm s^{-1}. Olympus OMCL-AC160TS cantilevers were used. A tip radius of 10 nm was estimated before nanoindentations by blind estimation[69] using an AFM height image $5 \times 5\ \mu m^2$ obtained on a standard calibrating sample (TGT01, NT-MDT, Moscow, Russia). The cantilever spring constant of 43 ± 1 N/m, was estimated from the resonance frequency. Moreover, standard tipless cantilevers (Applied Nanostructures, Santa Clara, CA) were used to cross-check this value. The cantilever deflection sensitivity, 51 ± 1 nm/V, was checked before and after the nanoindentation measurements on a stiff Si substrate, always giving consistent results.

Acknowledgment. D.T. acknowledges generous financial support of the Alexander von Humboldt Stiftung, Germany.

Supporting Information Available: Determination of brush thickness by AFM, AFM nanoindentation measurements for indentation in an oblique direction, values of normalized standard deviation vs number of indentations. This material is available free of charge via the Internet at http://pubs.acs.org.

References and Notes

(1) Barbey, R.; Lavanant, L.; Paripovic, D.; Schüwer, N.; Sugnaux, C.; Tugulu, S.; Klok, H.-A. *Chem. Rev.* **2009**, *109*, 5437.
(2) Bhattacharya, A.; Misra, B. N. *Prog. Polym. Sci.* **2004**, *29*, 767.
(3) Jain, P.; Baker, G. L.; Bruening, M. L. *Annu. Rev. Anal. Chem.* **2009**, *2*, 387.
(4) Ducker, R.; Garcia, A.; Zhang, J. M.; Chen, T.; Zauscher, S. *Soft Matter* **2008**, *4*, 1774.
(5) Edmondson, S.; Osborne, V. L.; Huck, W. T. S. *Chem. Soc. Rev.* **2004**, *33*, 14.
(6) Dutta, N.; Green, D. *Langmuir* **2008**, *24*, 5260.
(7) Xu, X.; Cao, D. J. *Chem. Phys.* **2009**, *130*, 164901.
(8) Zdyrko, B.; Klep, V.; Li, X.; Kang, Q.; Minko, S.; Wen, X.; Luzinov, I. *Mater. Sci. Eng., C* **2009**, *29*, 680.
(9) Vyas, M. K.; Nandan, B.; Schneider, K.; Stamm, M. *J. Colloid Interface Sci.* **2008**, *328*, 58.
(10) Zhao, B.; Brittain, W. J. *Prog. Polym. Sci.* **2000**, *25*, 677.
(11) Dimitrov, D. I.; Milchev, A.; Binder, K. *J. Chem. Phys.* **2007**, *127*, 084905.
(12) Huck, W. T. S. *Chem. Commun.* **2005**, 4143.
(13) Ohno, K.; Sakamoto, T.; Minagawa, T.; Okabe, Y. *Macromolecules* **2007**, *40*, 723.
(14) Keddie, J. L.; Jones, R. A. L.; Cory, R. A. *Europhys. Lett.* **1994**, *27*, 59.
(15) Alcoutlabi, M.; Mc Kenna, G. B. *J. Phys.: Condens. Matter* **2005**, *17*, 461.
(16) Schönherr, H.; Tocha, E.; Vancso, G. J. *Top. Curr. Chem.* **2008**, *285*, 103.
(17) Priestley, R. D.; Ellison, C. J.; Broadbelt, L. J.; Torkelson, J. M. *Science* **2005**, *309*, 456.
(18) Prucker, O.; Christian, S.; Bock, H.; Ruhe, J.; Frank, C. W.; Knoll, W. *Macromol. Chem. Phys.* **1998**, *199*, 1435.

(19) Watanabe, H.; Tirrel, M. *Macromolecules* **1993**, *26*, 6455. Taunton, H. J.; Toprakcioglu, C.; Fetters, L.; Klein, J. *Macromolecules* **1990**, *23*, 571.
(20) (a) O'Shea, S. J.; Welland, M. E.; Rayment, T. *Langmuir* **1993**, *9*, 1826. (b) Kelly, T. W.; Schorr, P. A.; Johnson, K. D.; Tirrel, M.; Frisbie, C. D. *Macromolecules* **1998**, *31*, 4297.
(21) Urayama, K.; Yamamoto, S.; Tsujii, Y.; Fukuda, T.; Neher, D. *Macromolecules* **2002**, *35*, 9459.
(22) Edwards, S. F.; Vilgis, T. A. *Polymer* **1986**, *27*, 483.
(23) Huang, H.; Young Chung, J.; Nolte, A. J.; Stafford, C. M. *Chem. Mater.* **2007**, *19*, 6555.
(24) Butt, H.-J.; Cappella, B.; Kappl, M. *Surf. Sci. Rep.* **2005**, *59*, 1.
(25) (a) Kim, M. S.; Pratt, J. R. *Measurement* **2010**, *43*, 169. (b) Kranenburg, J. M.; Tweedie, C. A.; van Vliet, K. J. *Adv. Mater.* **2009**, *21*, 3551.
(26) (a) Passeri, D.; Bettucci, A.; Biagioni, A.; Rossi, M.; Alippi, A.; Tamburri, E.; Lucci, M.; Davoli, I.; Berezina, S. *Ultramicroscopy* **2009**, *109*, 1417. (b) Cheng, Y. T.; Yang, F. Q. *J. Mater. Res.* **2009**, *24*, 3013. (c) Moeller, G. *J. Polym. Sci., B: Polym. Phys.* **2009**, *47*, 1573. (d) Gray, A.; Orecchia, D.; Beake, B. D. *J. Nanosci. Nanotechnol.* **2009**, *9*, 4514. (e) Keerthika, B.; Cao, Y. P.; Raabe, D. *CMC-Comput. Mater. Continua* **2009**, *10*, 243. (f) Bouaita, N.; Bull, S. J.; Palacio, J. F. *Polym. Eng. Sci.* **2006**, *46*, 1160. (g) Tranchida, D.; Kiflie, Z.; Piccarolo, S.; Acierno, S. *Meas. Sci. Technol.* **2009**, *20*, 095702.
(27) (a) Beayaoui, M.; Mazeran, P. E.; Arvieu, M. F. *Int. J. Mater. Res.* **2009**, *100*, 943. (b) Poon, B.; Rittel, D.; Ravichandran, G. *Int. J. Sol. Struct.* **2008**, *45*, 6399. (c) Poon, B.; Rittel, D.; Ravichandran, G. *Int. J. Sol. Struct.* **2008**, *45*, 6018. (d) Tranchida, D.; Piccarolo, S. *Polymer* **2005**, *46*, 4032. (e) Chizhik, S. A.; Huang, Z.; Gorbunov, V. V.; Myshkin, N. K.; Tsukruk, V. V. *Langmuir* **1998**, *14*, 2606.
(28) (a) Adhikari, R.; Michler, G. H. *Polym. Rev.* **2009**, *49*, 141. (b) Kranenburg, J. M.; Thijs, H. M. L.; Tweedie, C. A. *J. Mater. Chem.* **2009**, *19*, 222. (c) Bedoui, F.; Sansoz, F.; Murthy, N. S. *Acta Mater.* **2008**, *56*, 2296. (d) Jee, A. Y.; Kwon, H.; Lee, M. *J. Chem. Phys.* **2009**, *131*, 171104. (e) Tranchida, D.; Kiflie, Z.; Piccarolo, S. *Macromol. Rapid Commun.* **2006**, *27*, 1584.
(29) Lemieux, M.; Minko, S.; Usov, D.; Stamm, M.; Tsukruk, V. V. *Langmuir* **2003**, *19*, 6126.
(30) Zhao, J.; Chen, M.; An, Y.; Liu, J.; Yan, F. *Appl. Surf. Sci.* **2008**, *255*, 2295.
(31) (a) Gacoin, E.; Fretigny, C.; Chateauminois, A.; Perriot, A.; Barthel, E. *Trib. Lett.* **2006**, *21*, 245–252. (b) Perriot, A.; Barthel, E. *J. Mater. Res* **2004**, *19*, 600.
(32) Fretigny, C.; Chateauminois, A. *J. Phys. D* **2007**, *40*, 5418.
(33) Chen, S.; Liu, L.; Wang, T. *Acta Mater.* **2004**, *52*, 1089.
(34) Clifford, C. A.; Seah, M. P. *Nanotechnology* **2009**, *20*, 145708.
(35) Chen, J.; Bull, S. J. *Vacuum* **2009**, *83*, 911.
(36) Liao, Y.; Zhou, Y.; Huang, Y.; Jiang, L. *Mech. Mater.* **2009**, *41*, 308.
(37) Pelegri, A. A.; Huang, X. *Comput. Sci. Technol.* **2008**, *68*, 147.
(38) Zhao, M.; Chen, X.; Xiang, Y.; Vlassak, J.; Lee, D.; Ogasawara, N.; Chiba, N.; Gan, Y. X. *Acta Mater.* **2007**, *55*, 6260.
(39) Clifford, C. A.; Seah, M. P. *Nanotechnology* **2006**, *17*, 5283.
(40) Geng, K.; Yang, F.; Druffel, T.; Grulke, E. A. *Polymer* **2005**, *46*, 11768.
(41) Kopycinska-Müller, M.; Geiss, R. H.; Müller, J.; Hurley, D. C. *Nanotechnology* **2005**, *16*, 703.
(42) Zhao, M.; Xiang, Y.; Xu, J.; Ogasawara, N.; Chiba, N.; Chen, X. *Thin Solid Films* **2008**, *516*, 7571.
(43) Cappella, B.; Silbernagl, D. *Thin Solid Films* **2008**, *516*, 1952.
(44) Chen, S.; Liu, L.; Wang, T. *Surf. Coat. Technol.* **2005**, *191*, 25.
(45) Wang, M.; Liechti, K. M.; White, J. M.; Winter, R. M. *J. Mech. Phys. Sol.* **2004**, *52*, 2329.
(46) Tranchida, D.; Piccarolo, S.; Soliman, M. *Macromolecules* **2006**, *39*, 4547.
(47) Sneddon, I. N. *Int. J. Eng. Sci.* **1965**, *3*, 47.
(48) Tsukruk, V. V.; Gorbunov, V. V.; Huang, Z.; Chizhik, S. A. *Polym. Int.* **2000**, *49*, 441.
(49) Johnson, K. L. *Contact Mechanics*; Cambridge University Press: Cambridge, 2003.
(50) Silbernagl, D.; Sturm, H.; Cappella, B. *Langmuir* **2009**, *25*, 5091.
(51) Tweedie, C. A.; Constantinides, G.; Lehman, K. E.; Brill, D. J.; Blackman, G. S.; Van Vliet, K.J . *Adv. Mater.* **2007**, *19*, 2540.
(52) Tranchida, D.; Piccarolo, S. *Macrom. Rapid Commun.* **2005**, *26*, 1800.
(53) Tranchida, D.; Piccarolo, S.; Loos, J.; Alexeev, A. *Macromolecules* **2007**, *40*, 1259.
(54) Arruda, E. M.; Boyce, M. C.; Jayachandran, R. *Mech. Mater.* **1995**, *19*, 193.
(55) Doerner, M. F.; Nix, W. D. *J. Mater. Res.* **1986**, *1*, 601.
(56) (a) Milner, S. T.; Whitten, T. A.; Cates, M. E. *Macromolecules* **1989**, *22*, 1951. (b) Alexander, S. J. *J. Phys.* (*Paris*) **1977**, *38*, 977.
(57) Flory, P. J. *Principles of Polymer Chemistry*; Cornell University Press: Ithaca, NY, 1981.
(58) Drozdov, A. D. *Int. J. Eng. Sci.* **2005**, *43*, 1121.
(59) Landau, L. D., Lifshitz, E. M. *Theory of Elasticity*; Pergamon Press: New York, 1986.
(60) Theodorou, D. N.; Suter, U. W. *Macromolecules* **1986**, *19*, 139.
(61) Koppelmann, J.; Leder, H.; Royer, F. *Colloid Polym. Sci.* **1979**, *257*, 673.
(62) Fischer-Cripps, A. C. *J. Mater. Sci.* **2004**, *39*, 5849.
(63) Fischer-Cripps, A. C. *Nanoindentation*: Springer: Berlin, 2002.
(64) Oleinik, E. T. F.; Rudnev, S. N.; Salamatina, O. B.; Kotelyanskii, M. I. *Polym. Sci. Ser. A* **2008**, *50*, 494.
(65) Sullivan, T. P.; van Poll, M. L.; Dankers, P. Y. W.; Huck, W. T. S. *Angew. Chem., Int. Ed.* **2004**, *43*, 4190.
(66) Feng, C. L.; Embrechts, A.; Bredebusch, I.; Schnekenburger, J.; Domschke, W.; Vancso, G. J.; Schönherr, H. *Adv. Mater.* **2007**, *19*, 286.
(67) Drobek, T.; Spencer, N. D. *Langmuir* **2008**, *24*, 1484.
(68) Jones, D. M.; Brown, A. A.; Huck, W. T. S. *Langmuir* **2002**, *18*, 1265.
(69) Tranchida, D.; Piccarolo, S.; Deblieck, R. A. C. *Meas. Sci. Technol.* **2006**, *17*, 2630.

Macromolecules
ARTICLE

Macromolecules **2011**, *44*, 375–382 **375**
DOI: 10.1021/ma102456n

Formation and Characterization of Inclusion Complexes of Alkyne Functionalized Poly(ε-caprolactone) with β-Cyclodextrin. Pseudo-Polyrotaxane-Based Supramolecular Organogels.

Olga Jazkewitsch and Helmut Ritter*

Institut of Organic Chemistry and Macromolecular Chemistry II, Heinrich-Heine-University Duesseldorf, Universitätsstrasse 1, 40225 Duesseldorf, Germany

Received October 28, 2010; Revised Manuscript Received November 29, 2010

ABSTRACT: β-Cyclodextrin has been found to form pseudo-polyrotaxanes with propargyl functionalized poly(ε-caprolactone) in *N,N*-dimethylformamide. The formation of inclusion complexes was proven by ^{1}H NMR and FT-IR spectroscopy, SEC, dynamic light scattering (DLS), polarized optical microscopy and wide-angle X-ray diffraction (WAXD). Furthermore, supramolecular organogels based on the pseudo-polyratoxanes (PPR) were synthesized via 1,3-dipolar cycloaddition of propargyl functionalized poly-(ε-caprolactone) and mono-(6-azido-6-desoxy)-β-cyclodextrin. The swelling degree and rheological behavior of the PPR gels were investigated in dependence of the cross-linker content.

Introduction

Cyclodextrins (CD) are cyclic oligosaccharides and commonly consisting of 6 (α-CD), 7 (β-CD), or 8 (γ-CD) glucose units linked by α-1,4 bonds.[1] The most important characteristic is their ability to form selectively inclusion complexes (IC) with other molecules and polymers.[2] In the case of polymers the treatment of cyclodextrin as macrocyclic component onto the backbone or polymer side chain leads to the formation of so-called pseudo-polyrotaxane. Since 1990 Harada et al. reported that α-CD forms an IC with poly(ethylene glycol) in aqueous solution,[3] a great number of polymeric cyclodextrin complexes with different types of CDs were prepared and characterized.[4−9] Remarkable in these studies was the fact that the selectivity in complex formation of polymeric compounds with CDs is higher than for low molecular weight molecules. Harada and Kamachi found, for example, that β- and γ-CD form IC with poly(propylene glycol) in contrast to α-CD that does not form IC with PPGs of any molecular weight.[10] These results indicate that besides the main driving forces of the complex formation such as hydrophobic and van der Waals interactions as well as hydrogen bonding,[11] the sizes of the cyclodextrin cavities and the cross-sectional areas of the polymers are very important for the IC formation.[11] In different studies the formation of pseudo-polyrotaxane (PPR) structures between cyclodextrins and many biodegradable polyesters has been investigated, such as poly(ethylene adipate),[12] poly(lactide),[13,14] and bacterial poly(3-hydroxybutyrate).[15] The preparation and characterization of inclusion complexes from CDs with poly-(ε-caprolactone) (PEC) were also reported. The first report on complex formation of poly(ε-caprolactone) and CD by Harada et al. was investigating α-cyclodextrin.[16] In this study, they demonstrated a complex formation of α-CD with PEC not only in aqueous solutions but also in *N,N*-dimethylformamide (DMF). In a later study, the complex formation with γ- and β-CD was found. β-CD formed complexes with PECs (M_n = 2000−3000 g·mol^{-1}) in only moderate yields from aqueous solution.[17] Harada et al. suggested that the polymer chain of PEC is too slim to fit snugly in the β-CD cavity. In this work we present the formation of pseudo-polyrotaxanes of β-CD with poly((oxepan-2-one)-*co*-((3/7-prop-2-ynyl)oxepan-2-one)) that was investigated by differential scanning calorimetry, ^{1}H NMR and FT-IR spectroscopy, SEC, DLS, WAXD, and polarized optical microscopy. Furthermore, organogels based on these pseudo-polyrotaxanes were synthesized. Their swelling degree and rheological properties were examined.

*Corresponding author. E-mail: h.ritter@uni-duesseldorf.de.

Experimental Section

Materials. β-Cyclodextrin was obtained from Wacker-Chemie GmbH (Burghausen, Germany) and used after drying overnight in a vacuum oil pump over P_4O_{10}. ε-Caprolactone (ε-CL) was purchased from Acros, dried over calcium hydride, distilled under reduced pressure and stored over molecular sieves (0.4 nm) under an argon atmosphere. Cyclohexanone was purchased from Aldrich, dried over magnesium sulfate and distilled before use. Sodium ascorbate (AppliChem) and copper(II) sulfate (Carl Roth GmbH) were used as received. Commercially available reagents and solvents were used without further purification. Propargyl bromide (80 wt % solution in toluene) and lithium *N,N*-diisopropylamide solution (2.0 M in THF/heptanes/ethylbenzene) were purchased from Acros Organics and from Sigma-Aldrich, respectively. *m*-Chloroperbenzoic acid (70−75%) was purchased from Sigma-Aldrich and used as received.

Measurements. ^{1}H NMR and ^{13}C NMR spectroscopy was performed using a Bruker Advance DRX 500 spectrometer at 500.13 MHz and at 125.77 MHz in DMSO-d_6 and $CDCl_3$ as solvent, respectively. Chemical shifts were referenced to the solvent value δ = 2.5 ppm for DMSO-d_6 and δ = 7.26 ppm for $CDCl_3$. IR measurements were performed using a FT-IR spectrometer Nicolet 6700 FT-IR equipped with an ATR unit. Molecular weights and molecular weight distributions were measured by size exclusion chromatography (SEC) using a Viskotek GPCmax VE2001 system that contained a column set with one Viskotek TSK guard column HHR-H 6.0 mm (ID) × 4 cm (L) and two Viskotek TSK GMHHR-M 7.8 mm (ID) x 30 cm (L) columns at 60 °C. *N,N*-Dimethylformamide (DMF, 0.1 M LiCl) was used as eluent at a flow rate of 1 mL·min^{-1}. A Viskotek VE 3500 RI detector and a Viskotek Viscometer model

© 2010 American Chemical Society
Published on Web 12/23/2010

250 were used for detection. The system was calibrated with polystyrene standards with a molecular range from 580 D to 1186 kDa. Gas chromatography/mass spectrometry (GC/MS) measurement was accomplished on a Thermo Finnigan Trace DSQ system. The ionization occurred by means of electron impact (EI). Differential scanning calorimetry (DSC) measurements were performed using a Mettler Toledo DSC 822 controler apparatus in a temperature range between −50 and 350 °C with a heating rate of 10 °C·min^{-1}. The reported melting point (T_m) values are taken from the third heating cycle. Thermogravimetric analysis (TGA) was performed using a Perkin-Elmer STA 600 thermal analysis apparatus. The samples were heated from 30 to 800 °C under argon atmosphere with a heating rate of 10 °C·min^{-1}. The measurements were baseline corrected and analyzed by Pyris software. Wide-angle X-ray diffraction (WAXD) measurements were performed with a Huber Guinier (System 600) X-ray diffractometer with a Cu Kα radiation source (λ = 1.54 Å). The diffraction intensities were measured from 2Θ = 3° to 60° at a rate of 2Θ = 3°/min. Dynamic light scattering measurements were carried out at 25 °C using a Malvern Zetasizer Nano ZS ZEN3600 instrumentation with a laser wavelength of 633 nm and a detection angle of 173°. The polymer concentration was 0.2 mg·ml^{-1}. The solutions were filtered through 0.45 μm Chromafil Xtra syringe filters prior to measurements. The particle size distribution was derived from a deconvolution of the measured intensity autocorrelation function of the sample by the general purpose mode algorithm included in the DTS software. Elemental analysis was performed with a Perkin-Elmer 2400 CHN analyzer. Polarized optical microscopic (POM) observation was performed on an Olympus BH-2 polarizing microscope equipped with a digital camera. The dried gels were swollen in an excess of DMF for 48 h, respectively. The swelling degree was determined gravimetric and calculated according to the equation:

$$Q = (m_S - m_D)/m_D$$

m_S and m_D are the weights of the swollen and dried gels, respectively. The rheological characterization of the DMF swollen pseudo-polyrotaxane-based gels was performed using a Thermo Scientific HAAKE Mars viscosimeter in a parallel plate configuration using a MP35/S plate and a PP35/S with a diameter of 35 mm and a serrated surface. Rheological properties were studied in oscillatory experiments; mechanical spectra were recorded in the frequency range of 0.01−10 Hz. The linear viscoelastic region was assessed by amplitude sweep with a shear stress at 0.001−1 Pa.

Synthesis. *Synthesis of 2-Prop-2-ynyl-cyclohexanone* (***1***). A 250 mL round-bottom flask was purged with argon and cooled in a dry ice/acetone bath. A solution of lithium diisopropylamide (120 mmol) was added to the round-bottom flask and stirred for 30 min. An argon-purged solution of cyclohexanone (120 mmol) in 3 mL of THF was added dropwise to the LDA solution keeping the solution at −70 °C. Propargyl bromide (120 mmol) in 10 mL of THF was also added dropwise by a syringe and the solution was stirred for additional 60 min. The reaction mixture was then warmed up to room temperature and stirred overnight. The reaction was quenched with an excess of aqueous ammonium chloride, washed twice with diethyl ether, dried over $MgSO_4$ and the solvent was evaporated. The following distillation under reduced pressure (T = 45 °C, p = 0.34 mbar) afforded **1** as a colorless liquid (56% yield). ^{1}H NMR (500 MHz, $CDCl_3$, ppm): δ 2.56 (ddd, J = 17.1 Hz, 4.6 Hz, 2.7 Hz, 1H), 2.48−2.42 (m, 1H), 2.39−2.34 (m, 2H), 2.30−2.23 (m, 1H), 2.13 (ddd, J = 17.0 Hz, 8.4 Hz, 2.6 Hz, 1H), 2.07−2.03 (m, 1H), 1.92 (t, J = 2.6 Hz, 1H), 1.89−1.86 (m, 1H), 1.70−1.55 (m, 2H), 1.37 (ddd, J = 25.4 Hz, 12.7 Hz, 3.6 Hz, 1H). ^{13}C NMR (125 Hz, $CDCl_3$, ppm): δ 210.9, 82.7, 69.5, 49.6, 42.05, 33.3, 27.9, 25.2, 18.9. GC/MS (EI): m/z = 137 $[M + H]^+$, 136 $[M]^+$, 135, 108, 107, 93, 79, 77, 65, 55, 39. FT-IR (diamond): ν = 3290 (w, C−H, −C≡CH), 2930 (m, CH), 2859 (m, C−H), 1703 (s, C=O), 1450, 1424, 1129 cm^{-1}.

Synthesis of 3-/7-(Prop-2-ynyl)oxepan-2-one (***2a/b***). 2-Prop-2-ynyl-cyclohexanone (60 mmol) was added to a solution of *m*-chloroperbenzoic acid (90 mmol, 20.18 g) in 160 mL methylene chloride. The reaction mixture was refluxed for 48 h. After cooling to room temperature and filtration, the solution was washed twice with aqueous sodium sulfite and aqueous sodium hydrogen solutions. Subsequent removal of the solvent under reduced pressure and distillation under oil pump vacuum yielded 80% of the product as an isomeric mixture (3- (70%) and 7-(prop-2-ynyl)oxepan-2-one (30%)). ^{1}H NMR (500 MHz, $CDCl_3$, ppm): δ 4.35−4.16 (m, 3H), 2.77−2.72 (m, 1H), 2.66−2.52 (m, 5H), 2.43 (ddd, J = 16.7 Hz, 8.1 Hz, 2.7 Hz, 1H), 2.31 (ddd, J = 17.1 Hz, 9.2 Hz, 2.6 Hz, 1H), 2.18−2.06 (m, 2H), 2.00−1.88 (m, 5H), 1.72−1.37 (m, 6H). ^{13}C NMR (125 Hz, $CDCl_3$, ppm): δ 176.0, 174.6, 82.4, 80.02, 77.6, 71.3, 70.2, 68.5, 42.0, 34.7, 33.6, 28.9, 28.8, 28.0, 27.8, 26.1, 22.9, 21.9. FT-IR (diamond): ν = 3277 (w, −C≡CH, C−H), 2933, 2859 (m, C−H), 1723 (s, C=O), 1443, 1289, 1174, 1051 cm^{-1}. GC/MS: m/z = 153 $[M + H]^+$, 152 $[M]^+$, 135, 97, 79, 77, 65, 39. Anal. Calcd ($C_9H_{12}O_2$): C, 71.0; O, 21.0; H, 7.9. Found: C, 69.7; O, 22.1; H, 8.2.

Copolymerization of 3-/7-(Prop-2-ynyl)oxepan-2-one (***2a/b***) *and ε-CL*. To the mixture of 3-/7-(prop-2-ynyl)oxepan-2-one and ε-CL (ratio 1:9, 1:7, 1:5) in a round-bottom flask purged with argon, 0.5 mol % of $Sn(Oct)_2$ was added as a catalyst. The flask was immersed in an oil bath at 100 °C for 24 h. After cooling to room temperature the product was dissolved in CH_2Cl_2, precipitated twice in cold methanol and dried in vacuum. The yield was estimated gravimetrically (98−99%). ^{1}H NMR (500 MHz, $CDCl_3$, ppm): δ 4.9 (m, 1H), 4.03 (t, J = 6.6 Hz, 2H), 2.28 (t, J = 7.4, 2H), 1.97 (m, 2H), 1.62 (m, 4H), 1.35 (m, 2H). ^{13}C NMR (125 Hz, $CDCl_3$, ppm): δ 173.6, 173.5, 173.0, 79.6, 71.3, 70.6, 70.1, 64.2, 28.4, 25.6, 24.8, 24.6, 23.9. FT-IR (diamond): ν = 3277 (w, −C≡CH, C−H), 2943 and 2863 (m), 1723 (s, C=O), 1241, 1161 (s, C−O), 962 cm^{-1}.

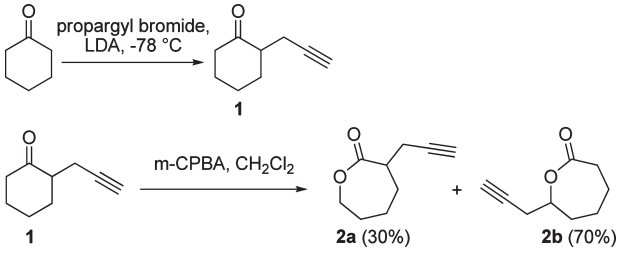
Preparation of β-Cyclodextrin Inclusion Complexes (***3a−c-β-CD***) *with Copolymers* ***3a−c***. A solution of 0.3 g polymer and β-cyclodextrine (equivalent amount relating to the alkyne group of the copolyester) dissolved in 5 mL of DMF was placed in an oil bath at 70 °C for 12 h and then stirred at 21 °C for 36 h. The reaction product was precipitated in diethyl ether and dried in vacuum. The yield was estimated gravimetrically (99%). ^{1}H NMR (500 MHz, DMSO-d_6, ppm): δ 4.9 (m, 1H), 4.03 (t, J = 6.6 Hz, 2H), 2.28 (t, J = 7.4 Hz, 2H), 1.97 (m, 2H), 1.62 (m, 4H), 1.35 (m, 2H). FT-IR (diamond): ν = 3328 (m, OH), 2937 and 2859 (m), 1723 (s, C=O), 1241, 1154 (s, C−O), 1026 cm^{-1}.

Preparation and Properties of Pseudo-Polyrotaxane-Based Gels (*PPRG*). Mono-(6-azido-6-desoxy)-β-cyclodextrin (an equivalent compared to the alkyne group of the copolyester) was added to a solution of 400 mg polyester **3a−c** in 2 mL of DMF. The solution of 10 mol % sodium ascobate and 5 mol % copper(II) sulfate pentahydrate in 0.3 mL of DMF was filtered through 0.45 μm Gelman Acrodisk syringe filters and added to the solution of the polyester and β-CD−N_3. The flask was immersed in an oil bath at 70 °C for 1 h. To examine the swelling behavior of the gels and their rheological properties, thin cylindrical shaped gels were prepared in two Teflon round molds with an internal diameter of 3 cm. For this purpose 1 mL of reaction mixture was poured into the mold and dried in a drying oven at 90 °C for 24 h. FT-IR (diamond): ν = 3356 (m, OH), 2940 and 2863 (s, CH2,CH3, C−H), 1726 (s, C=O), 1655 (w), 1154 (w), 1026 cm^{-1}.

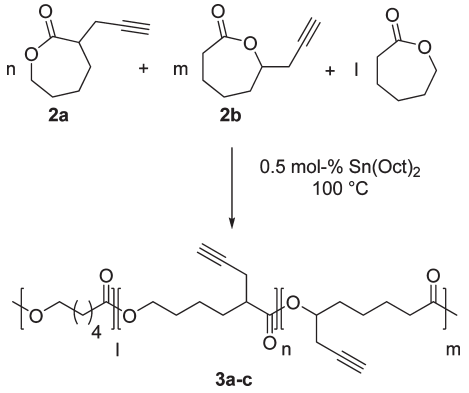
Results and Discussion

Synthesis of Alkyne-Functionalized Polyester. The strategy for the synthesis of functionalized aliphatic polyester bearing propargyl group relies on the copolymerization of ε-caprolactone and the propargyl functionalized lactone 3-/7-(prop-2-ynyl)oxepan-2-one (***2a/2b***) via $Sn(Oct)_2$-mediated ring-opening polymerization (ROP). The functionalized lactone

Scheme 1. Synthesis of Alkyne-Functionalized Lactones 2a and 2b



Scheme 2. Synthesis of Functionalized Precursor Polyester 3a−c by ROP of Lactones 2a and 2b and ε-CL



2*a*/2b was prepared in two steps. At first, 2-prop-2-ynylcyclohexanone (**1**) was obtained according to Scheme 1 from cyclohexanone by reaction with lithium *N,N*-diisopropylamide (LDA) and a toluene solution of propargyl bromide at −78 °C. The distilled product was further reacted with an excess of *m*-chloroperbenzoic acid in methylene chloride as solvent (Baeyer−Villiger oxidation). Subsequent distillation under oil pump vacuum afforded an isomeric mixture **2*a*/2b** in 80% yield. The lactone mixture was characterized by ^{1}H, ^{13}C NMR and FT-IR spectroscopy.

The FT-IR spectrum reveals an acetylene C−H stretching at 3277 cm^{-1} and a signal at 1723 cm^{-1}, corresponding to the carbonyl band of the ester group. The ^{1}H NMR-spectroscopic investigation of isomeric mixture show several overlapping signals in the region at 4.35−4.16 ppm (corresponding to CH_2OC=O and C*H*OC=O) as well as in the range of 2.75 to 1.37 ppm (corresponding to the protons of the lactone ring). From the ^{13}C NMR the ratio between **2a** and **2b** is accessible by integration of the carbonyl carbon signals at 176.03 and 174.62 ppm. It was found that the lactones mixture consists of 70% lactone **2b** and 30% lactone **2a**. For the following experiments, the isomeric mixture was used without further separation.

The copolymerization of lactones **2a/b** and ε-CL feeding different ratios of monomers was carried out using 0.5 mol % Sn(Oct)$_2$ as catalyst (Scheme 2). The polymerization was performed at 100 °C, yielding copolymers of type **3**. Table 1 summarizes some characteristic data of the obtained polymers **3a−c**.

The molar content of **2a/b** incorporated into the copolymers **3** was calculated by integration of the ^{1}H NMR spectral signals (Figure 1) at δ = 1.97 ppm (C≡C*H* from monomers **2a/b**) and at δ = 4.9 ppm (CH_2O of the polymer backbone from **2b**) compared to the signal at δ = 4.03 ppm (CH_2O of the polymer backbone from **2a** and ε-CL). The data show that the polymerizability of ε-CL is higher compared to the substituted lactones **2a** and **2b**. Anyway, the incorporation ratio differs just a little from the feed ratio, indicating a nearly complete consumption of lactone **2a/b** during the polymerization.

Table 1. Results of the Copolymerization of 2a/2b and ε-CL

entry	M_n[a] (g·mol^{-1})	PD[a]	feed ratio (**2a**/**b**: ε-CL)	incorporation ratio[b] (**2a**/**b**: ε-CL) (mol %)	T_m[c] (°C)
3a	32 700	2.6	1:9	8:92	47.5
3b	36 700	2.5	1:7	10:90	41.4
3c	28 640	3.5	1:5	13:87	36.5

[a] Determined by SEC in DMF relative to polystyrene standards. [b] Determined from ^{1}H NMR spectra. [c] DSC, determined from third heating cycle.

Table 2. Measurement Results of the Copolyesters 3a−c and Their β-CD Inclusion Complexes 3a−c-β-CD

entry	M_n[a] (g·mol^{-1})	PD[a]	*d* (nm)	T_m[c] (°C)	ΔH_m[c] (J/g)	content of CD (mol %)[b]
3a	32 700	2.6	12.2	47.5	52.2	
3a-β-CD	62 930	1.6	17.3	45.1	18.8	8.3
3b	36 700	2.5	9.2	41.4	36.2	
3b-β-CD	48 200	2.2	12.3	38.7	14.6	10.5
3c	28 640	3.5	11.7	36.5	32.8	
3c-β-CD	35 600	3.1	14.1	35.9	14.3	15.7

[a] Determined by SEC in DMF relative to polystyrene standards. [b] Determined by ^{1}H NMR spectra from signals at 3.98 ppm (O−CH_2(CH_2)$_3$ from copolymer) and 3.63−3.54 ppm (H$^{3,5,6,6'}$ from β-CD). [c] DSC, taken from the third heating cycle.

Furthermore, the thermal behavior of resulting copolymers **3a−c** was investigated by DSC measurements. As expected, the melting point of the copolymers decrease with increasing incorporation of acetylene functionalized lactones **2a/b**, because these disrupt the formation of crystalline domains, which are characteristic for poly(ε-caprolactone) and other aliphatic polyesters.[18−20] The nearly complete incorporation of ε-CL and lactones **2a/b** and the thermal properties of **3a−c** indicate that the obtained copolyesters are random copolymers.

Complex Formation of Copolyesters 3a−c with Unmodified β-CD. As mentioned above, cyclodextrins are able to include polymers as guests within their hydrophobic cavity. A large number of studies on complexes of α-, β-, γ-CDs with various polymers have been described in the literature. With this intention the copolyester **3a−c** was treated with β-CD in DMF at 80 °C, precipitated (entry **3a−c-β-CD**) and investigated by SEC, FT-IR, DLS, DSC and NMR. Table 2 lists the results of the studies.

The SEC measurements of the precursor copolymers **3a−c** and of the corresponding pseudo-polyrotaxanes **3a−c-β-CD** in DMF revealed that no free β-CD is present and that M_n of pseudo-polyrotaxanes is higher than M_n of the copolymers before the treatment with β-CD. Furthermore, the polydispersity indexes of inclusion complexes (IC) are lower than the PD of copolyesters **3a−c**. It was found that the curves differ from each other particularly in the range of low molar masses. Possible explanation for these differences is a better threading of the low molecular polymer chains into the β-CD cavity than that of the high molecular polymer chains. This process effects the narrower molecular mass distribution of the complexes **3a−c-β-CD**. The size of copolyesters **3a−c** and their complexes was also investigated in DMF solution by DLS measurements (Table 2). The hydrodynamic diameter of copolyesters increased after the complexation with β-CD. Obviously the treatment of copolyester **3a−c** with CD leads to the slight extension of the polymer chain, as would happened in the case of complex formation.

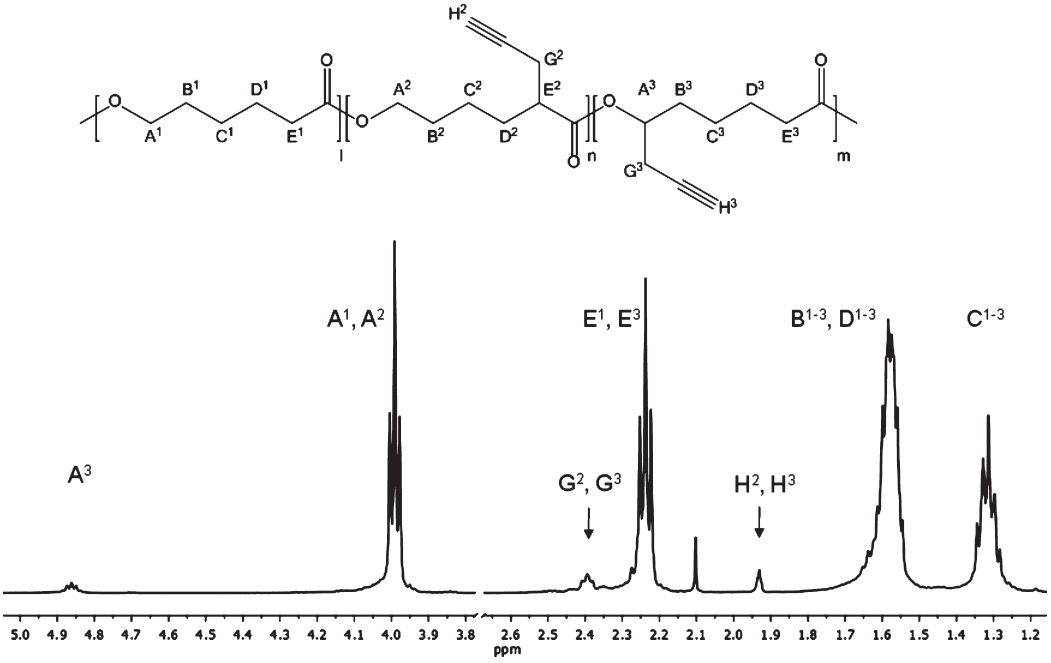


Figure 1. ^{1}H NMR (500 MHz, in $CDCl_3$) spectrum of the alkyne functionalized copolyester **3b**.

Table 3. Complexation Shifts $\Delta\delta^a$ of the Protons of β-CD and Copolyester Induced by the Inclusion of Copolyester in the CD Cavity

	β-CD							copolyester 3		
protons	H^3	H^5	$H^{6,6'}$	H^1	OH^6	$OH^{2,3}$	H^2,H^4	A^{1-2}	B^{1-3}, D^{1-3}	C^{1-3}
$\Delta\delta^a$ [ppm]	−0.02	−0.03	0	0	+0.02	+0.03, +0.01	+0.02	−0.01	−0.01	−0.01

^{a} Determined by ^{1}H NMR spectra (in DMSO-d_6) of the free compounds (f) and the inclusion complex **3a**−**c**-***β*-CD** (ic). The complexation induced shift is defined as: $\Delta\delta = \delta_f - \delta_{ic}$.

^{1}H NMR spectroscopy was used to investigate the host−guest compounds **3a**−**c**-***β*-CD** (see Figure 1 for the spectrum of **3b**). The analysis of chemical shift variations of protons provides some evidence which of them are involved in the interaction. In this connection, numerous studies indicate that the signals of the cavity protons of β-CD show a high-field shift upon complexation with a suitable guest.[21] By comparison, the protons of the guests can show as well the downfield as highfield shift.[22,23]

Hence, the formation of inclusion complexes with unmodified β-CD was studied by comparing of the ^{1}H NMR spectra of β-CD, pure copolyester **3a**−**c** and the corresponding inclusion complexes **3a**−**c**-***β*-CD** (Table 3). The comparison revealed that the β-CD protons of IC located outside the cavity show downfield shifts, whereas the peaks of H^3 and H^5 protons which are located inside the cavity move to higher fields. Furthermore, the protons of copolyester backbone also undergo highfiled shifts, indicating the interaction between the cavity of β-CD and copolyester chain in the inclusion complexes **3a**−**c**-***β*-CD**.

The DSC analysis was performed to study the influence of β-CD in the ICs on the crystallinity of the copolyester chains. The thermal properties of the pure copolyesters **3a**−**c** and their β-CD inclusion complexes were investigated in the temperature range from −30 to 350 °C. The complexes **3a**−**c**-***β*-CD** show an endothermic peak between 30 to 50 °C (Figure 2). The transition temperatures are slightly lower than the melting points of the pure precursor polymers **3a**−**c**. Generally, the complete CD−polymer ICs with channel structure[24] have no melting point, but they decompose above 310 °C.[25,26] Hence, these peaks can be attributed to the melting process of the crystalline domains of the uncovered polyester chains of the partial

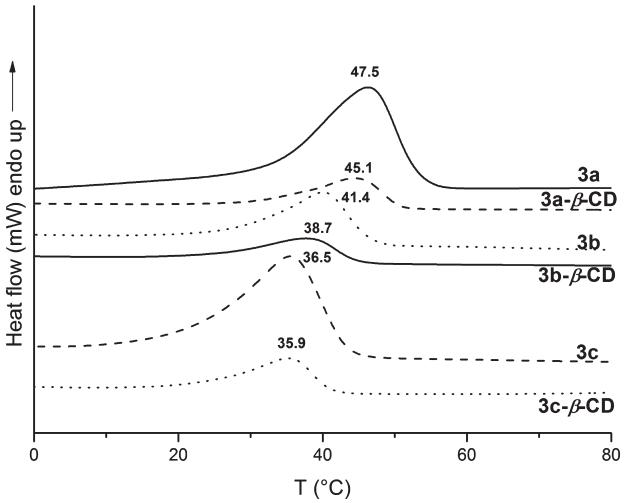


Figure 2. DSC thermogram of copolymers **3a**−**c** and of the corresponding pseudo-polyrotaxanes **3a**−**c**-***β*-CD** obtained from the third heating cycle.

inclusion complexes (Figure 3). The obtained enthalpies of fusion ΔH_m for the pseudo-polyrotaxanes **3a**−**c**-***β*-CD** deviate significant from the enthalpies of fusion for the untreated copolymers **3a**−**c** (Table 2). The ΔH_m values of pure polyesters are approximately twice as high as the ΔH_m values of the corresponding β-CD complexes. This suggests that the building of inclusion complex decreases the degree of crystallinity of the polyesters.

It may be supposed that the crystallization is restricted, because the regular chain to chain interaction of the polyesters is

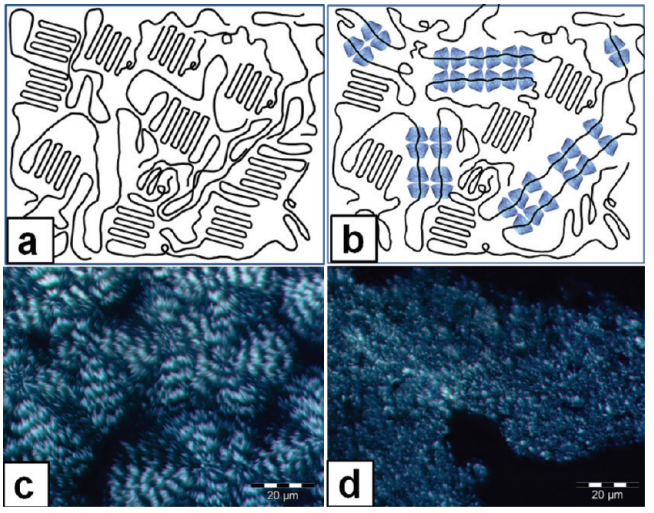


Figure 3. Schematic representation of the proposed reorganization of polymer through formation of inclusion complex (a and b). Comparison between photographs of a spherulite of **3b** and optic appearance of **3b-β-CD** obtained by polarized light microscopy (POM) (5 mg·ml^{-1} in DMF).

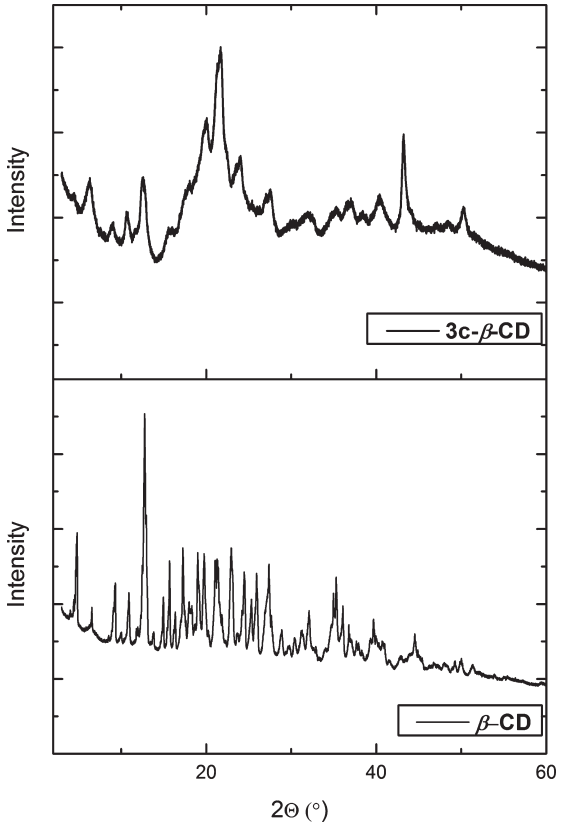


Figure 4. X-ray diffraction patterns of β-CD and partial IC **3c-β-CD** with channel structure.

disturbed by the inclusion also the mobility of the polymer segments is reduced in the pseudo rotaxane areas (Figure 3a,b). The POM photographs (Figure 3) of the copolymer **3b** and the corresponding pseudo-polyrotaxane **3b-β-CD** indicate that the formation of the relative large spherulites such as in copolyester **3b** was inhibit due to pseudo-polyrotaxane units.

The formation of partial copolyester IC with channel structure was supported by WAXD measurements. Figure 4 shows the X-ray powder patterns of the IC **3c-β-CD** in comparison with pure β-CD.

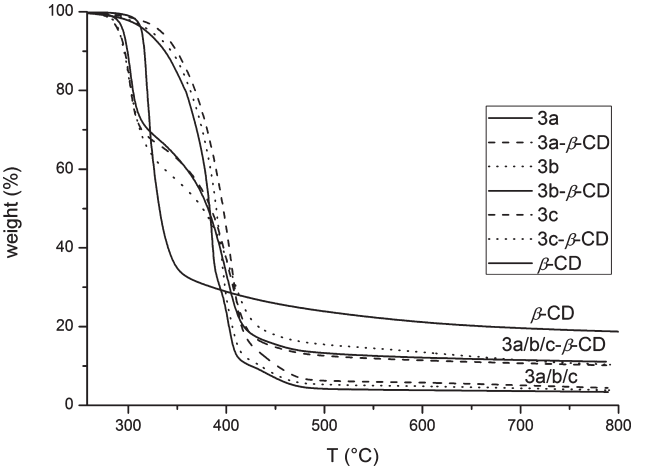


Figure 5. Thermogravimetric analysis of β-CD, copolyester **3a−c** and the corresponding inclusion complexes. The heating rate was 10 °C·min^{-1}, and the measurements were performed under argon atmosphere.

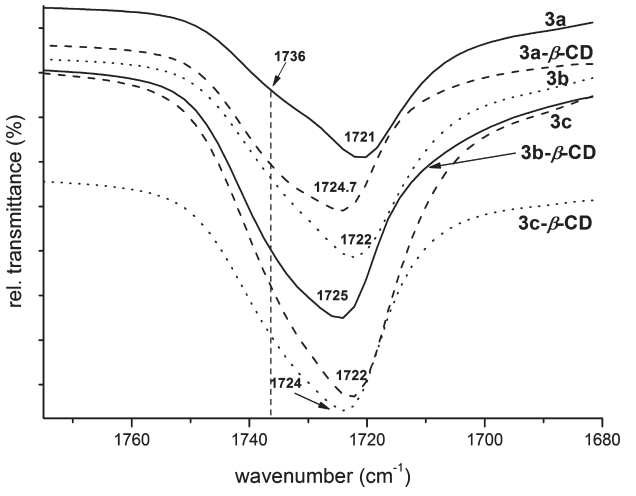


Figure 6. FT-IR spectra of copolyesters **3a−c** and the corresponding β-CD inclusion complexes.

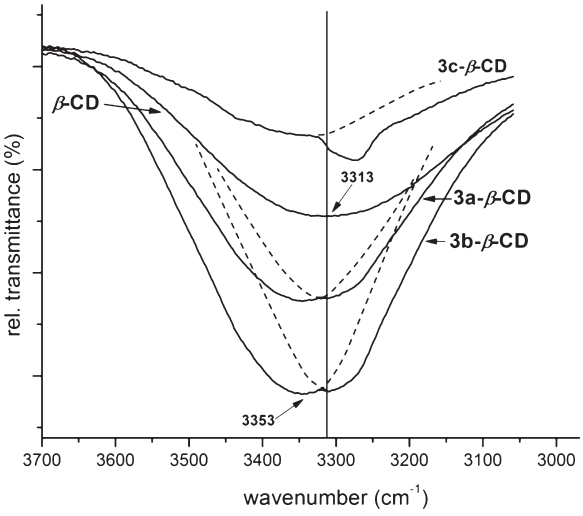
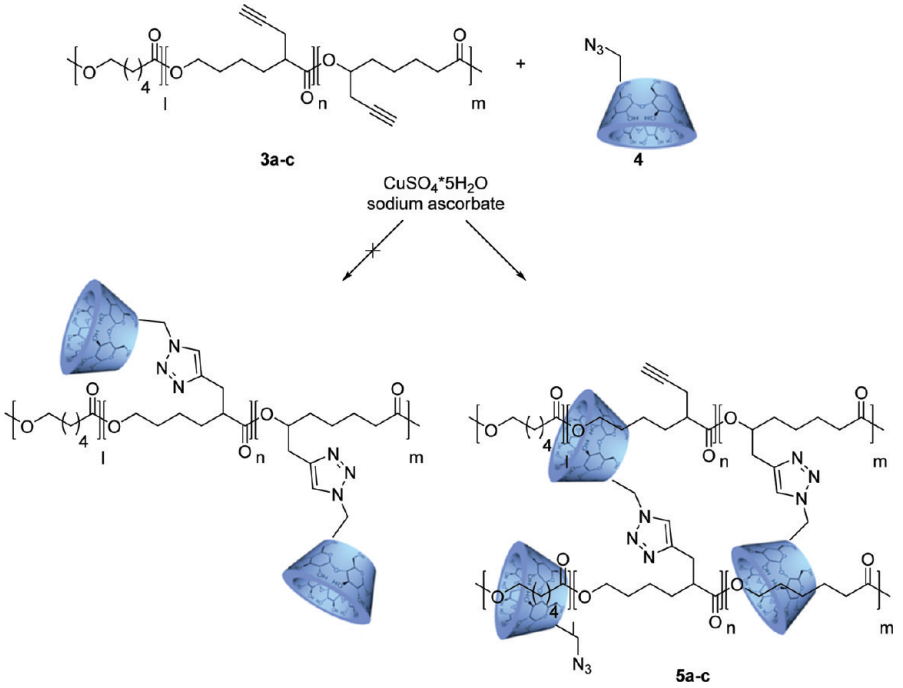


Figure 7. FT-IR spectra of the copolyesters **3a−c** and the corresponding β-CD inclusion complexes in the region from 3000 to 3700 cm^{-1}.

Scheme 3. Product of Huisgen-type 1,3-Dipolar Cycloaddition of Copolyester 3a−c and β-CD−N_3



Actually, the IC of CDs can be roughly classified as either "cage-type" or "channel-type".[27] The pattern of the inclusion complex sample (Figure 4) is different from the pattern of the pure β-CD, where CD molecules are arranged in a "cage-type" packing. The partial IC **3c-β-CD** sample shows prominent peaks at 21.6° and 23.9°, which were consistent with that of linear unmodified poly(ε-caprolactone).[28,29] Furthermore, the diffractogram of IC reveals the characteristic peaks at about 12.6° (0.7 nm) and 19.6°(0.45 nm). A similar values were observed by Li et al. in the case of polyolefin β-CD channel complexes.[30] The reflection peak at $2\theta = 6.3°$ (1.4 nm) can be attributed to the dimension of two β-CDs. This shows that, copolyesters **3a−c** formed with β-CD a partially complexes with channel type structure (Figure 3b).

The thermal stability of partial β-CD−copolyester ICs, pure copolyester and β-CD was investigated by thermogravimetric analysis (Figure 5).

The thermogravimetric curves of the pure copolyesters **3a−c** and β-CD follow a one-stage decomposition process, whereas the profiles of β-CD−copolyester ICs show a two-step thermal decomposition. The first step is attributed to decomposition of β-CD at about 255 °C and shows some lower decomposition temperature (at 278 °C) than the pure β-CD. The second degradation step is attributed to the free copolyester component. The similar behavior was observed by Bullions et al. for the ICs formed between γ-CD and poly(ethylene terephthalate).[31]

Finally, FT-IR measurements of the polymers and IC in the region from 750 to 4000 cm^{-1} were performed to receive more information concerning the formation and phase structure of the samples. The carbonyl absorption bands are shown in Figure 6. The IR spectra of pure semicrystalline polymers **3a−c** exhibit a carbonyl stretching band (s, ν C=O) at ~1722 cm^{-1} and a shoulder at ~1736 cm^{-1}, corresponding to the carbonyl absorption of the crystalline phase and of the amorphous region of the copolyester, respectively.[32−34] The FT-IR spectra of the pseudo-polyrotaxanes exhibit the peak of the amorphous band with a slightly increase of intensity according to the results of DSC measurements. Furthermore, a new peak appears at ~1724 cm^{-1}.

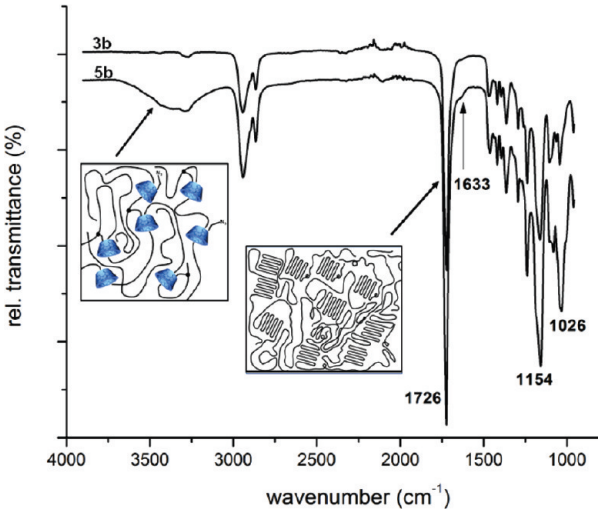


Figure 8. FT-IR spectra of the copolyesters **3b** and the pseudo-polyrotaxane-based gel **5b**.

Obviously, the shift of the carbonyl band of the copolyesters is due to the formation of hydrogen bonds with the hydroxyl groups of β-CD. According to this fact, a spectroscopic difference should be found in the region from 3100 to 3400 cm^{-1} of symmetric and asymmetric vibrations of the OH groups.[35]

As shown in Figure 7, the peak of the OH-stretching band of β-CD at 3313 cm^{-1} shifts to 3353 cm^{-1} in the case of the inclusion complex with the polyesters **3a−c**. This is shown by a dashed line in the Figure 7. It can be thus assumed that the shift mainly is due to the formation of hydrogen bonds between the carbonyl groups of polyesters and the hydroxyl groups of CDs. These studies provide evidence for the hypothesis that β-CD−N_3 should also be able to include polyester under the same conditions.

Synthesis of the Pseudo-Polyrotaxane-Based Organogels via Click Reaction. In addition, pseudo-polyrotaxane-based gels were formed in DMF solution reacting copolyester **3a−c**

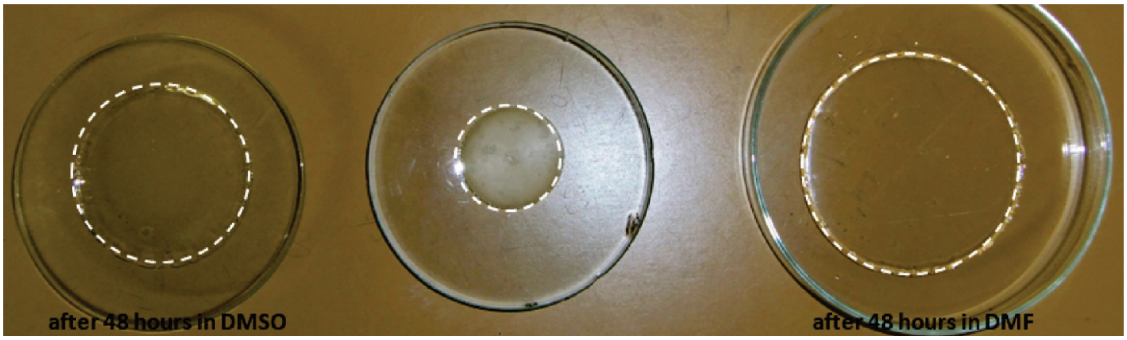


Figure 9. Photographs of a form stable pseudo rotaxane-based gels swollen for 48 h with DMSO (left), swollen for 48 h with DMF (right) and the original size after synthesis (middle).

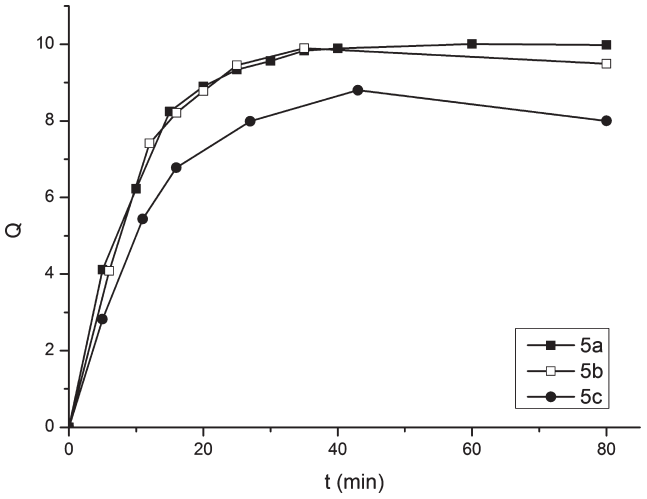


Figure 10. Swelling ratio Q of PPR-based gels **5a** (square), **5b** (circle) and **5c** (triangle) in DMF versus the swelling time at 23 °C.

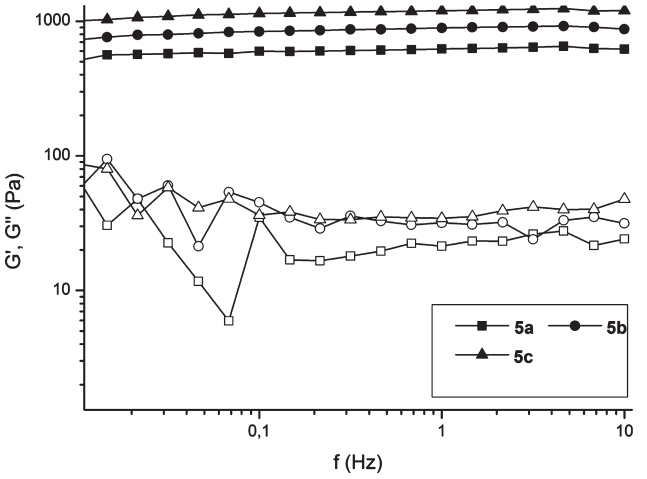


Figure 11. Frequency dependency of storage modulus G' (closed symbols) and loss modulus G'' (open symbols) for PPR-based gels containing 8.3% (square), 10.5% (circle) and 15.7% (triangle) of β-CD−N_3 swollen with DMF.

with pendant alkyne groups with mono-(6-azido-6-desoxy)-β-cyclodextrin (Scheme 3). Mono-(6-azido-6-desoxy)-β-cyclodextrin (β-CD−N_3) was synthesized according to a method described in the literature.[36] The polymer network **5a**−**c** is a result of the formation of pseudo-polyrotaxane (PPR) by incorporation of polyester chain into the cavity of β-CD−N_3 and at the same time occurring click reaction.

The FT-IR spectra of the reaction product (Figure 8) exhibit a carbonyl stretching band of polyester at 1726 cm^{-1} and the peak of the OH stretching band of β-CD at 3353 cm^{-1}. A new peak at 1655 cm^{-1}, specific for carbon−carbon double bond which, associated with the vibration of carbon−nitrogen bond at 1026 cm^{-1}, prove the formation of triazole ring by the "click" reaction. The barely visible peak at 2105 cm^{-1}, corresponding to the specific vibration of the azide group suggests that almost all of β-CD−N_3 molecules threaded onto the polyester chains were reacted during this procedure.

It was found that the obtained gels **5a**−**c** swell in DMF or in DMSO (Figure 9). To examine the swelling behaviors of the gels and their rheological properties, thin cylindrical-shaped gels were immersed in DMF.

The swelling measurements of PR-based gels **5a**−**c** were carried out by monitoring the weight change over the swelling time. Highly cross-linked gels have a tighter network structure and swell less than those with a lower cross-linking density. The equilibrium swelling state was reached after 80 min. As shown in Figure 10, the swelling ratios of the PR gels in DMF decreased with the increase in amount of "cross-linker" β-CD−N_3. Accordingly, the swelling ratio of gel **5a** comprising 8.3 mol % of β-CD−N_3 reached 10, whereas **5c** (15.7 mol % of β-CD−N_3) possessed the swelling ratio of only 8.

Figure 11 shows the frequency dependence of the storage modulus G' and loss modulus G'' of pseudo-polyrotaxane-based gels **5a**−**c** swollen in DMF. For all PPR gels swollen in DMF the values of the storage moduli were almost constant and were sufficiently higher than the corresponding values of the loss moduli in the whole frequency range, indicating that these gels behave as a viscoelastic solid. The storage modulus increased with the increase of cross-linker content.

Conclusion

A propargyl-functionalized ε-caprolactone was successful ring-opened copolymerized with ε-caprolactone yielding an aliphatic copolyester with a pendent propargyl group. It was found that the synthesized copolyesters form inclusion complexes with unmodified β-CD in DMF. These obtained pseudo-polyrotaxanes were investigated by ^{1}H NMR and FT-IR spectroscopy, DLS, SEC, and WAXD. The thermal behavior was determined by DSC and TGA. All the studies supported the formation of proposed pseudo-polyrotaxane. The alkyne group consisting copolyesters **3a**−**c** were further reacted with β-CD−N_3. The 1,3-dipolar cycloaddition led to formation of organogels, which are swellable in DMF and DMSO. In addition, the swelling degrees of the supramolecular gels depend on the degree of the supramolecular cross-linking. The rheological investigation showed a viscoelastic behavior of the synthesized organogels

which is in accordance to the behavior found in swollen polymer networks.

References and Notes

(1) Szejtli, J. *Chem. Rev.* **1998**, *98*, 1743.
(2) Wenz, G. *Angew. Chem.* **1994**, *106*, 851.
(3) Harada, A.; Kamachi, M. *Macromolecules* **1990**, *23*, 2821.
(4) Harada, A.; Li, J.; Suzuki, S.; Kamachi, M. *Macromolecules* **1993**, *26*, 5267.
(5) Harada, A.; Okada, M.; Kamachi, M. *Acta Polym.* **1995**, *46*, 453.
(6) Harada, A.; Okada, M.; Li, J.; Kamachi, M. *Macromolecules* **1995**, *28*, 8406.
(7) Steinbrunn, M. B.; Wenz, G. *Angew. Chem., Int. Ed. Engl.* **1996**, *35*, 2139.
(8) Kamitori, S.; Matsuzaka, O.; Kondo, S.; Muraoka, S.; Okuyama, K.; Noguchi, K.; Okada, M.; Harada, A. *Macromolecules* **2000**, *33*, 1500.
(9) Michishita, T.; Takashima, Y.; Harada, A. *Macromol. Rapid Commun.* **2004**, *25*, 1159.
(10) Harada, A.; Mikiharu, K. *J. Chem. Soc., Chem. Commun.* **1990**, 1322.
(11) Liu, L.; Guo, Q.-X. *J. Inclusion Phenom. Macrocyclic Chem.* **2002**, *42*, 1.
(12) Harada, A.; Toshiyuki, N.; Kawaguchi, Y.; Okada, M.; Mikiharu, K. *Macromolecules* **1997**, *30*, 7115.
(13) Rusa, C. C.; Tonelli, A. E. *Macromolecules* **2000**, *33*, 5321.
(14) Wei, M.; Shuai, X.; Tonelli, A. E. *Biomacromolecules* **2003**, *4*, 783.
(15) Shuai, X.; Porbeni, F. E.; Wei, M.; Bullions, T.; Tonelli, A. E. *Macromolecules* **2002**, *35*, 3778.
(16) Harada, A.; Kawaguchi, Y.; Nishiyama, T.; Kamachi, M. *Macromol. Rapid Commun.* **1997**, *18*, 535.
(17) Kawaguchi, Y.; Nishiyama, T.; Okada, M.; Kamachi, M.; Harada, A. *Macromolecules* **2000**, *33*, 4472.
(18) Chatani, Y.; Yasuo, O.; Tadokoro, H.; Yamashita, Y. *Polym. J.* **1970**, *1*, 555.
(19) Kanamoto, T.; Tanaka, K.; Nagai, H. *J. Polym. Sci., Part A-2: Polym. Phys.* **1971**, *9*, 2043.
(20) Holland-Moritz, K.; Hummel, D. O. *J. Mol. Struct.* **1973**, *19*, 289.
(21) Jiang, H.; Hongjie, S.; Zhang, S.; Hua, R.; Xu, Y.; Jin, S.; Gong, H.; Li, L. *J. Inclusion Phenom. Macrocyclic Chem.* **2007**, *58*, 133.
(22) Salvadori, P.; Gloria, U.-B.; Balzano, F.; Bertucci, C.; Chiavacci, C. *Chirality* **1996**, *8*, 423.
(23) Bernini, A.; Ottavia, S.; Ciutti, A.; Scarselli, M.; Bottoni, G.; Mascagni, P.; Niccolai, N. *Eur. J. Pharm. Sci.* **2004**, *22*, 445.
(24) McMullan, R. K.; Saenger, W.; Fayos, J.; Mootz, D. *Carbohydr. Res.* **1973**, *31*, 37.
(25) Harada, A.; Li, J.; Kamachi, M. *Macromolecules* **1993**, *26*, 5698.
(26) Li, J.; Ni, X.; Zhou, Z.; Leong, K. W. *J. Am. Chem. Soc.* **2003**, *125*, 1788.
(27) Saenger, W. *J. Inclusion Phenom. Macrocyclic Chem.* **1984**, *2*, 445.
(28) Luo, H.; Liu, Y.; Yu, Z.; Zhang, S.; Li, B. *Biomacromolecules* **2008**, *9*, 2573.
(29) Vazquez-Torres, H.; C.-R., C. A. *J. Appl. Polym. Sci.* **1994**, *54*, 1141.
(30) Li, C.; Naoe, I.; Saito, H.; Kohno, K.; Toyota, A. *Polym. Bull.* **2009**, *63*, 779.
(31) Bullions, T. A.; Wei, M.; Porbeni, F. E.; Gerber, M. J.; Peet, J.; Balik, M.; White, J. L.; Tonelli, A. E. *J. Polym. Sci., Part B: Polym. Phys.* **2002**, *40*, 992.
(32) Coleman, M. M.; Zarian, J. *J. Polym. Sci., Polym. Phys. Ed.* **1979**, *17*, 837.
(33) Sanchis, A.; Prolongo, M. G.; Salom, C.; Masegosa, R. M. *J. Polym. Sci., Part B: Polym. Phys.* **1998**, *36*, 95.
(34) He, Y.; Yoshio, I. *Polym. Int.* **2000**, *49*, 623.
(35) Dong, T.; Yong, H.; Shin, K.; Inoue, Y. *Macromol. Biosci.* **2004**, *4*, 1084.
(36) Kretschmann, O. Assoziative Hydrogele und thermosensitive Polymer-Einschlussverbindungen auf Basis von adamantylhaltigen Polymeren und Cyclodextrinen, Heinrich-Heine University: Duesseldorf, Germany, 2006.

Macromolecules
ARTICLE

Macromolecules **2011**, *44*, 383–392 **383**
DOI: 10.1021/ma1020837

Simulating the Relaxation of Stretched DNA in Slitlike Confinement

Daniel W. Trahan and Patrick S. Doyle*

Department of Chemical Engineering, Massachusetts Institute of Technology, Cambridge, Massachusetts 02139, United States

Received September 8, 2010; Revised Manuscript Received November 27, 2010

ABSTRACT: Brownian dynamics simulations of bead−spring chains were used to study the relaxation of an initially stretched DNA molecule in slitlike confinement. Taking into account excluded volume effects but neglecting hydrodynamic interactions, the simulations are able to reproduce the two relaxation times in the linear force regime that our group has experimentally studied and recently reported. The relaxation dynamics of the transverse dimensions are extensively studied, and a theoretical model is developed to describe them. The interplay between the longitudinal and the transverse dynamics is investigated and used to corroborate a physical model previously proposed to describe polymer relaxation in a slit.

1. Introduction

1.1. Motivation. The emergence of micro- and nanofluidic devices has led to many new and exciting developments in the field of single-molecule manipulations. For example, DNA separations[1,2] and genomic mapping[3,4] have benefited greatly from the precise control offered by so-called "lab-on-a-chip" devices. More generally, these microscopic systems have provided an important new platform to study fundamental problems in polymer physics.[5−11]

One recent problem that has received a considerable amount of attention is the relaxation dynamics of DNA in different types of confined environments.[6,10,12,13] This is particularly important for many single-molecule mapping devices that rely upon collisions[14] and field gradients[3,14] to deform DNA for subsequent analysis. This deformation process is highly dependent upon the balance between the stretching rate of the device and the relaxation of the polymer. Therefore, understanding how confinement affects the relaxation process of confined polymers is critical both to optimizing current technologies and to developing novel device designs.

Additionally, many important biological molecules are polymeric in nature (e.g., DNA, actin, and microtubules, although only DNA is typically flexible enough and of sufficient length to observe the sort of relaxation processes we shall study), and most cellular environments are highly confined. For example, 3 m of human DNA is packed into a nucleus of around 5 μm in diameter. Study of the dynamics of confined DNA molecules is critical to understanding how the cell stores, accesses, and replicates its genetic information. In vivo relaxation of chromosomal DNA has even been used to probe the intracellular environment.[15]

1.2. Past Work. Over the last two decades, the relaxation of unconfined polymers has been studied comprehensively both experimentally[5] and via simulations.[16−18] They have confirmed the theoretical prediction that unconfined single molecule relaxation is well-described by a single longest relaxation time τ_I over all extensions within the chain's linear force regime[19] (from equilibrium to ∼30% fractional extension[5]). However, relaxation in slitlike confinement has been studied much less extensively, with several studies offering contradictory findings.[6,13,20−23] It is only recently that these results have begun to be reconciled by suggesting the existence of two relaxation times in the linear force regime.[10]

The dynamics of polymers in slitlike confinement were first treated theoretically by Brochard[24] using blob theory. The first direct observation of such confined relaxation, by Bakajin and co-workers,[6] was of molecules relaxing after having been highly stretched by collisions with microfabricated posts. The results produced scalings for the relaxation time that were more in line with the unconfined case.[10] Nearly a decade later, new experiments from our group obtained the confined relaxation time by measuring the rotational autocorrelation function of chains at equilibrium.[13] This study found good agreement with the blob theory predictions, contradicting the previous work of Bakajin et al.[6] Interestingly, several simulation studies found evidence to support the findings of both of the aforementioned experimental works. Simulating the relaxation of initially stretched chains[22,23] reproduced the un-confined-like results of Bakajin et al.,[6] while Monte Carlo simulations of chains at equilibrium[20,21] corroborated the blob theory scalings seen by our group.[13]

Although seemingly contradictory, taken together these studies hint at the cause of the discrepancies. All the work where chains were perturbed from equilibrium agree with each other and demonstrate un-confined-like behavior. On the other hand, agreement was also seen among the studies of chains at equilibrium which exhibited blob scalings. To explain this, our group suggested that two distinct relaxation times existed in the linear force regime.[10] When the molecule is stretched, the width of the chain in the transverse dimension is smaller that the height of the channel, and the confining walls do not significantly affect the conformation of the molecule. Therefore, the chain is governed by an un-confined-like relaxation time τ_I. However, at or near equilibrium, the polymer feels the full steric effects of the confining walls, and its dynamics slow as a consequence. A second relaxation time τ_{II} emerges which is longer than τ_I and which follows the predictions of blob theory.

Our group has shown that both of these relaxation times can be seen and measured by observing the longitudinal relaxation of initially stretched molecules over time scales

*To whom correspondence should be addressed. E-mail: pdoyle@mit.edu.

© 2010 American Chemical Society

Published on Web 12/21/2010

long enough for the chain to reach equilibrium.[10,25] A physical model based upon blob theory has also been proposed that assumes this extension-dependence of the relaxation time is due entirely to excluded volume effects (EV) and not hydrodynamic interactions (HI). Although there is some experimental evidence that this model is correct, experiments are greatly hampered by the fact that the dynamics cannot be accurately measured on small time and length scales, especially in the dimension transverse to the plane of the channel.

1.3. Problem Statement. In this paper, we study the relaxation of a bead−spring chain in slitlike confinement from a stretched configuration that is initially straight using a combination of simulations and theory. Because simulations allow us to set which physics will be included, we can conclusively determine if excluded volume effects are sufficient to reproduce the qualitative features observed in experiments (e.g., two relaxation times). In addition, simulations can probe dynamics of the relaxation process on length and time scales that are inaccessible to experiments, particularly in the confined dimension. This allows us to consider the interplay between the dynamics in the direction of initial stretch and the confined dimension, enabling us to assess the validity of the current physical model for confined relaxation and its underlying assumptions.

2. Background

We now describe the theory of polymer relaxation both unconfined and in slitlike confinement. We start by considering the equilibrium size of a polymer chain and the basics of blob theory. We then use these results to develop scalings for the relaxation times of these chains. We also explain the current physical model of relaxation in slitlike confinement and some of its consequences.

In particular, we concern ourselves with the expected theoretical scalings based upon the physics included in our simulations. Therefore, we take EV into account, but we neglect the effects of HI. The chains are assumed to be free-draining so that

$$\zeta = N_K \zeta_K \tag{1}$$

where ζ and ζ_K are the chain and Kuhn length drag coefficients, respectively. Additionally, HI with the channel walls is neglected, and changes in the chain diffusivity due to confinement are ignored. Intramolecular HI decreases the relaxation time and affects the scaling of the relaxation time with chain length for an unconfined chain, while HI with channel walls increases the relaxation time and affects its scaling with channel height. However, we are unconcerned with these physics in this work and wish to isolate the effects of EV on the relaxation time in confinement.

2.1. Equilibrium Chain Size. The polymer is modeled as a chain composed of N_K Kuhn steps each of length b_K. When unconfined, the equilibrium radius of gyration $R_{g,0}$ of the chain can be determined from the statistics of random walks

$$\frac{R_{g,0}}{b_K} \sim {N_K}^{\nu_{3D}} \tag{2}$$

where ν_{3D} is the scaling exponent for the equilibrium chain size in a 3D environment. If the chain is ideal and intramolecular excluded volume effects are neglected, then $\nu_{3D} = 1/2$. The inclusion of EV causes the chain to swell and increases the scaling exponent to $\nu_{3D} \approx 3/5$.

In slitlike confinement, the polymer is squashed like a pancake, and due to EV, it swells in size even further. Blob theory is often used to describe confined polymers.[26] In this framework, the polymer is represented by a string of N_K/g blobs, where g is the number of Kuhn segments per blob

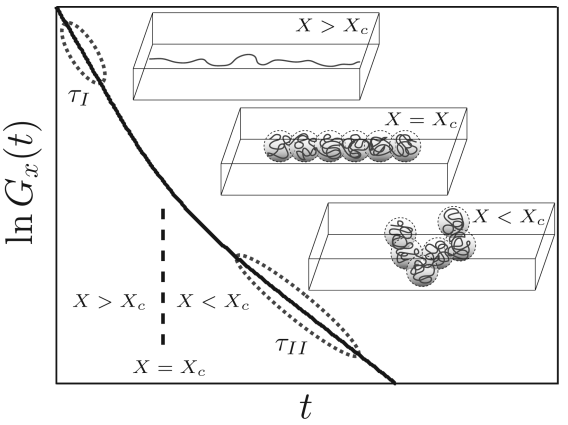


Figure 1. A cartoon depicting the physical model of confined relaxation based upon tension-blobs and how it relates to the longitudinal relaxation function $G_x(t) = \langle X(t)^2 \rangle - \langle X_{eq}{}^2 \rangle$, where $X(t)$ is the fractional extension in the longitudinal direction and X_{eq} is its average equilibrium value. Above a certain crossover extension X_c, the chain is not sterically confined and relaxes as if it were unconfined. Below X_c, the confining walls become important, and the chain relaxes by rearranging its self-avoiding blobs.

(see Figure 1). The size of a blob is set by the height of the channel, h.

On length scales smaller than h (i.e., within a blob), the polymer retains its un-confined-like behavior. So using eq 2, we can say that $h \sim g^{\nu_{3D}} b_K$, and upon rearrangement, the number of Kuhn segments g in a blob is given by

$$g \sim \left(\frac{h}{b_K}\right)^{1/\nu_{3D}} \tag{3}$$

On scales larger than h, the blobs, which repel each other due to EV, obey the scalings of a 2D self-avoiding walk (2D-SAW). So in slitlike confinement, the size of the chain is given by

$$\frac{R_{g,0}}{b_K} \sim \left(\frac{N_K}{g}\right)^{\nu_{2D}} \frac{h}{b_K} \sim {N_K}^{\nu_{2D}} \left(\frac{h}{b_K}\right)^{1-\nu_{2D}/\nu_{3D}} \tag{4}$$

where $\nu_{2D} = 3/4$.

2.2. Relaxation Times. *2.2.1. Unconfined.* First, we consider the relaxation of an unconfined linear polymer. Scalings for the longest relaxation time of the chain can be derived by considering a force balance between the elastic spring force F_E of the chain and the drag force F_D that opposes it. The force required to stretch a chain away from its equilibrium size R_0 by an amount δR is given by

$$F_E \sim -\frac{k_B T}{{R_0}^2} \delta R \tag{5}$$

where k_B is the Boltzmann constant and T is the temperature. Note that, from a scaling perspective, R_0 can be any measure of the equilibrium size of the coil, including the radius of gyration $R_{g,0}$ or the end-to-end distance $R_{ee,0}$. The drag force felt by the chain is

$$F_D \sim -\zeta \dot{R} \tag{6}$$

where $\dot{R}$ is the rate of change of the size of the chain. Balancing these forces gives the longest relaxation time τ_I for the chain

$$\tau_I \sim -\frac{\delta R}{\dot{R}} \sim \frac{\zeta {R_0}^2}{k_B T} \tag{7}$$

Introducing the results from eqs 1 and 2 and noting that $\zeta_K = k_B T/D_K$, we arrive at

$$\frac{\tau_I}{{b_K}^2/D_K} \sim {N_K}^{1+2\nu_{3D}} \tag{8}$$

where D_K is the diffusivity of a Kuhn segment.

2.2.2. Slitlike Confinement. When a molecule in a slit is stretched strongly enough, it is not sterically confined by the walls of the channel (see Figure 1). Therefore, the initial relaxation process is unaffected by the presence of the confining walls, and the molecule relaxes with the un-confined-like time constant τ_I given by eq 8. However, as the molecule relaxes, its lateral dimensions grow in size, and the confining effects of the wall become significant. This slows down the relaxation process, and a new, longer relaxation time τ_{II} emerges that governs the remaining relaxation to equilibrium.

A simple physical model based upon a quasi-steady tension-blob framework was proposed by Balducci and co-workers[10] to describe the transition between these two relaxation times. The stretched molecule can be represented by a string of N_K/g tension-blobs[27] of size ξ, where g is again the number of Kuhn segments per blob. Unconfined scalings hold within each blob so $g \sim (\xi/b_K)^{1/\nu 3D}$. The fractional extension of the chain X is then given by $X = \xi/gb_K \sim (\xi/b_K)^{1-1/\nu_{3D}}$. If the crossover from τ_I to τ_{II} occurs when the tension-blob size reaches the height of the channel (i.e., $\xi = h$), then the critical fractional extension X_c at which this crossover occurs is given by

$$X_c \sim (h/b_K)^{1-1/\nu_{3D}} \tag{9}$$

Above X_c, the molecule relaxes by growing the size of the tension blobs. But below X_c, tension-blob growth is restricted by the confining walls, and the molecule relaxes by rearranging the blobs. An interesting consequence of this model is that X_c is independent of chain length.

To determine τ_{II}, we employ eq 7 which is valid near equilibrium. We simply use the blob scalings for $R_{g,0}$ as given in eq 4. At or near equilibrium, the relaxation time of a confined molecule is given by

$$\frac{\tau_{II}}{{b_K}^2/D_K} \sim {N_K}^{1+2\nu_{2D}} \left(\frac{h}{b_K}\right)^{2(1-\nu_{2D}/\nu_{3D})} \tag{10}$$

3. Simulation Method

We simulated the relaxation of DNA using a model developed by Kim and Doyle.[28] This method is based upon Brownian dynamics and is well-suited for studying the dynamics of DNA in microfludic devices. A brief description of the numerical model is presented here.

3.1. Brownian Dynamics. DNA molecules are modeled as chains of N_b beads connected by $N_s = (N_b - 1)$ springs. The equation of motion for the position r_i of the ith bead is

$$\frac{d\boldsymbol{r}_i}{dt} = \frac{1}{\zeta_b}\left[\boldsymbol{F}_i^B(t) + \boldsymbol{F}_i^S(t) + \boldsymbol{F}_i^{EV}(t) + \boldsymbol{F}_i^{EV,\,wall}(t)\right] \tag{11}$$

where ζ_b is the bead drag coefficient, $\boldsymbol{F}_i^B$ is the Brownian force, $\boldsymbol{F}_i^S$ is the total spring force felt by the bead, $\boldsymbol{F}_i^{EV}$ is the intrachain excluded volume force due to nearby beads, and $\boldsymbol{F}_i^{EV,wall}$ represents the interaction of the bead with the wall of the device.

We nondimensionalize the variables as follows:

$$\hat{\boldsymbol{r}} \equiv \frac{\boldsymbol{r}}{l_s},\ \hat{t} \equiv \frac{t}{{l_s}^2/D_b} \tag{12}$$

where $\boldsymbol{r}$ is position, l_s is the maximum extension of a single spring ($l_s \equiv L/N_s$), t is time, and $D_b = k_B T/\zeta_b$ is the diffusivity of a bead.

We nondimensionalize the forces $\boldsymbol{F}$ as follows:

$$\hat{\boldsymbol{F}}(\hat{\boldsymbol{r}}) \equiv \frac{\boldsymbol{F}}{k_B T/l_s} \tag{13}$$

This leads to the nondimensional form of eq 11:

$$\frac{d\hat{\boldsymbol{r}}_i}{d\hat{t}} = \hat{\boldsymbol{F}}_i^B + \hat{\boldsymbol{F}}_i^S + \hat{\boldsymbol{F}}_i^{EV} + \hat{\boldsymbol{F}}_i^{EV,\,wall} \tag{14}$$

The nondimensional Brownian force is given by:

$$\hat{\boldsymbol{F}}_i^B = \sqrt{\frac{24}{\Delta\hat{t}}}\,(\boldsymbol{r}_n)_i \tag{15}$$

where $\Delta\hat{t}$ is the dimensionless time step and $(\boldsymbol{r}_n)_i$ are uniform random numbers such that each component $(\boldsymbol{r}_n)_i^j \in [-1/2, 1/2]$, where j denotes the coordinate x, y, or z. The net nondimensional spring force on the ith bead is

$$\hat{\boldsymbol{F}}_i^S = \begin{cases} \hat{\boldsymbol{f}}_{i,2}^s, & i = 1 \\ \hat{\boldsymbol{f}}_{i,i+1}^s + \hat{\boldsymbol{f}}_{i,i-1}^s, & 1 < i < N_b \\ \hat{\boldsymbol{f}}_{i,N_b-1}^s, & i = N_b \end{cases} \tag{16}$$

where the spring force $\hat{\boldsymbol{f}}_{i,j}^s$ is given by a spring law developed by Underhill and Doyle[29] to correctly reproduce the Marko-Siggia spring force law for a wormlike chain[30] at varying degrees of coarse-graining:[31]

$$\hat{\boldsymbol{f}}_{i,j}^s = v\left[\frac{1}{(1-\hat{r}_{j,i}^2)^2} - \frac{7}{v(1-\hat{r}_{j,i}^2)} + C + B(1-\hat{r}_{j,i}^2)\right]\hat{\boldsymbol{r}}_j - \hat{\boldsymbol{r}}_i \tag{17}$$

where v is the number of persistence lengths represented by each spring ($v \equiv l_s/A_p$), $\hat{r}_{j,i}$ represents the distance between $\hat{\boldsymbol{r}}_j$ and $\hat{\boldsymbol{r}}_i$, $C = 3/32 - 3/4v - 6/v^2$, and $B = (13/32 + 0.8172/v - 14.79/v^2)/(1 - 4.225/v + 4.87/v^2)$. The intrachain excluded volume force $\hat{\boldsymbol{F}}_i^{EV}$ is modeled with the soft potential used by Jendrejack et al.[32]

$$\hat{\boldsymbol{F}}_i^{EV} = -\sum_{j=1(j\neq i)}^{N_b} \frac{9}{2}\hat{\nu}^{ev,p}\left(\frac{3}{4\sqrt{\pi}}\right)^3 v^{9/2}\exp\left[-\frac{9}{4}v\hat{r}_{i,j}^2\right]\hat{\boldsymbol{r}}_{j,i} \tag{18}$$

where $\hat{\nu}^{ev,p} \equiv \nu^{ev,p}/{l_s}^3$ is the dimensionless form of the excluded volume parameter $\nu^{ev,p}$.

The interactions between a bead and the walls represented by $\hat{\boldsymbol{F}}_i^{EV,wall}$ are resolved using a modified Heyes−Melrose algorithm.[28,33] Whenever a bead moves outside the domain during a time step, it is moved to the nearest point on the domain boundary before commencing the next time step:

$$\Delta\hat{\boldsymbol{r}}_i^{HM} = \Delta\boldsymbol{p}_i H(\Delta p_i) \tag{19}$$

where $\Delta\hat{\boldsymbol{r}}_i^{HM}$ is the displacement vector due to the Heyes−Melrose algorithm, $\Delta\boldsymbol{p}_i$ is the vector pointing from the bead outside the domain to the nearest boundary point, and the Heaviside step function $H(\Delta p_i)$ restricts the application of the algorithm to only the beads that have penetrated the domain boundaries.

3.2. Parameters. Many different lengths of DNA were simulated in this study, ranging from $N_s = 10$ to $N_s = 300$. The chosen discretization of DNA was $v = 5.571$, which, assuming a persistence length of $A_p = 53$ nm, corresponds to DNA contour lengths of $L \approx 3$−90 μm. The excluded volume parameter was set to $\nu^{ev,p} = 3.71 \times 10^{-4}\,\mu m^3$ to accurately reproduce the unconfined radius of gyration of a T4-DNA molecule ($N_s = 254$ and $L = 75$ μm).

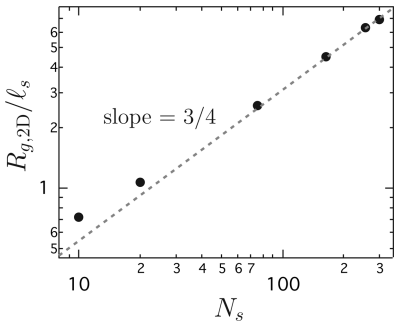


Figure 2. Plot of the 2D, in-plane radius of gyration $R_{g,2D}$ of chains at equilibrium in a 300 nm channel vs the chain length N_s. The predicted blob theory scaling $R_{g,2D} \sim N_s^{3/4}$ is also shown.

For the relaxation of initially extended molecules, the chains were uniformly stretched to the desired fractional extension (typically $X = 75\%$) along the x-direction and placed in the center of a 300 nm slit where the z-direction was transverse to the plane of the channel. The chains were then allowed to relax, and their configurations were saved for later analysis. Two different time steps were used. To obtain the short time behavior, a time step of $\Delta\hat{t} = 2 \times 10^{-5}$ was employed, and the chains were observed for a time of $\approx \tau_{II}$. For the long time behavior, a time step of $\Delta\hat{t} = 5 \times 10^{-4}$ was used, and the chains run for $\approx 10\tau_{II}$. For all measurements, at least 100 individual chains were simulated and averaged together for each chain length.

The equilibrium properties were obtained by initially placing the chains in the channel in a Gaussian manner and allowing them to equilibrate for $\approx 50\tau_{II}$. Configurations were then saved at specified time intervals for subsequent analysis. At least $\approx 300\tau_{II}$ worth of data was obtained.

4. Results

Before we begin analyzing the relaxation dynamics of confined chains, we would like to ascertain that we are using chains of adequate length for blob theory scalings to be valid. To do this, we look at the 2D, in-plane radius of gyration $R_{g,2D}$ of the chains at equilibrium. These results are shown in Figure 2, along with the predicted scaling of $R_{g,2D} \sim N_s^{3/4}$. It is clear that blob theory scalings are valid for chains with $N_s \geq 75$, and in our future analysis, we often only present results for these chain lengths.

In our study of the relaxation dynamics of confined chains, we first consider experimentally accessible measurables such as the relaxation of the longitudinal stretch at long times both at equilibrium and when initially perturbed away from equilibrium. This allows us to compare our findings to experimental results and validate our simulation model. We then look at the relaxation process in the transverse dimensions and attempt to build simple models based on Rouse-like chains to describe the observed dynamics. Finally, we consider how adding in additional physics, like intramolecular excluded volume and nonlinear springs, affects the relaxation dynamics.

4.1. Experimental Measurables. Typical measurables that are experimentally accessible are usually restricted to those involving the in-plane stretch of the molecule's major axis. We start by looking at the scaled longitudinal relaxation function $G_x(t) = \langle X(t)^2 \rangle - \langle X_{eq}{}^2 \rangle$, where $X(t)$ is the fractional extension in the longitudinal direction and X_{eq} is its average equilibrium value. Figure 3A shows a characteristic curve for $G_x(t)$ when the number of springs is $N_s = 164$. As seen in experiments, there are two distinct regions that are well-approximated by a single decaying exponential, each with a different time constant. The first region, with time constant τ_I, occurs at fractional extensions near $X = 30\%$ and represents the un-confined-like relaxation process where the chain

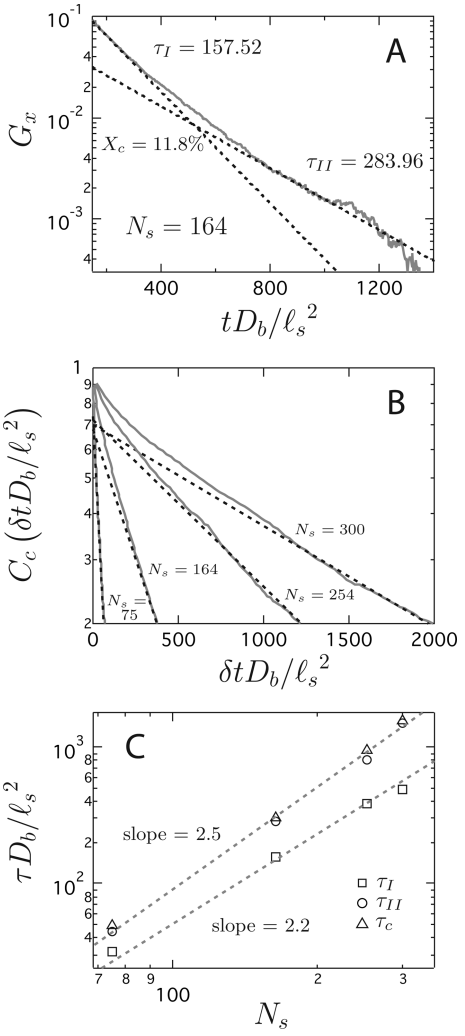


Figure 3. (A) Characteristic plot of the scaled longitudinal relaxation function $G_x(t) = \langle X(t)^2 \rangle - \langle X_{eq}{}^2 \rangle$ for chain length $N_s = 164$. The fittings for the two linear regions are also shown along with their respective time constants (τ_I and τ_{II}) and the predicted crossover extension X_c. (B) Plot of the equilibrium conformational autocorrelation function $C_c(\delta t)$ vs the lag time δt (see eq 20) for several chain lengths ($N_s = 75$, 164, 254, 300). The linear fittings for each curve are also shown. (C) Plot of various measured relaxation times vs chain length N_s. Included are the un-confined-like relaxation time τ_I, the near-equilibrium relaxation time τ_{II}, and the conformational relaxation time τ_c. Also shown are the predicted scalings $\tau_I \sim N_s^{2.2}$ and $\tau_{II} \sim \tau_c \sim N_s^{2.5}$.

is not sterically constrained. The second region occurs very near the chain's equilibrium size and, in agreement with experiments, has a longer time constant τ_{II} than the un-confined-like relaxation time ($\tau_{II} > \tau_I$). This second linear relaxation process is governed by the rearrangement of the blobs that compose the sterically confined chain. Finally, these two linear relaxation periods are connected by a non-linear transition region.

In Figure 3C, we have plotted both τ_I and τ_{II} as a function of chain length along with their predicted blob theory scalings. The simulation results for τ_{II} clearly follow the predicted scaling of $\tau_{II} \sim N_s^{2.5}$, while the results for τ_I appear to fall slightly below the theoretical scaling of $\tau_I \sim N_s^{2.2}$. The apparent discrepancy between the simulations and theory for τ_I is not unexpected and can be explained by noting that when eq 18 is used to account for EV, moderately extended chains are only mildly affected by the EV force. Because the un-confined-like relaxation time τ_I is seen near fractional extensions of $X \approx 30\%$, EV effects are not as significant as

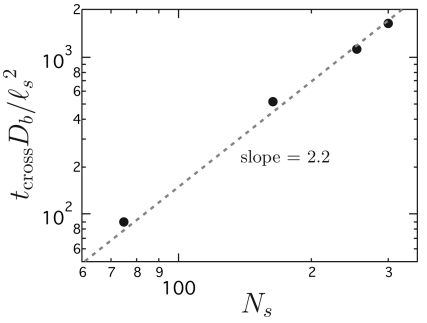


Figure 4. Plot of the computed crossover time t_{cross} vs chain length N_s. Also shown is the predicted scaling $t_{cross} \sim N_s^{2.2}$.

they are near the equilibrium extension. Therefore, the observed scaling for τ_I falls somewhere between the ideal chain scaling of $\sim N_s^2$ and the real chain scaling of $\sim N_s^{2.2}$.

Experiments have shown that relaxation processes measured when a confined molecule is at equilibrium should correspond to the second relaxation region where steric confinement is important. To confirm that our simulations can reproduce this finding, we considered the conformational relaxation time of a chain at equilibrium τ_c. The conformational autocorrelation function is defined as

$$C_c(\delta t) = \langle R_{ee}(t) \cdot R_{ee}(t+\delta t)\rangle / R_{ee,0}^2 \qquad (20)$$

where $R_{ee}(t)$ is the 2D, in-plane end-to-end vector of the chain, $R_{ee,0}$ is the equilibrium in-plane end-to-end distance, and δt is the lag time. The conformational autocorrelation functions for several different chain lengths are shown in Figure 3B along with their respective linear fittings, and the measured conformational relaxation times τ_c are plotted in Figure 3C. τ_c is very near the value of τ_{II} and follows the same predicted scaling $\tau_c \sim \tau_{II} \sim N_s^{2.5}$, in agreement with experiments.

We have clearly shown that our simulation model can reproduce the qualitative features seen in experiments. These include two distinct linear relaxation times for $G_x(t)$ with $\tau_{II} > \tau_I$, the proper scaling for τ_{II} with chain length, very near the predicted scaling for τ_I, and finally that near-equilibrium relaxation processes are associated with τ_{II}, as demonstrated by the fact that $\tau_c \sim \tau_{II}$.

One final experimentally accessible measurement we obtained is the time t_{cross} at which the crossover extension occurs. This is defined as the time where the two linear fittings for $G_x(t)$ intersect (see Figure 3A). Although t_{cross} can be found from experiments, to date this analysis has not been performed. t_{cross} is a measure of the when the transition between un-confined-like relaxation and near-equilibrium, sterically confined relaxation occurs. Based upon the current mechanisitic model of confined relaxation, the approach to this transition should be driven by the un-confined-like relaxation process leading up to it. Therefore, it is expected that t_{cross} should scale as $t_{cross} \sim \tau_I \sim N_s^{2.2}$. Indeed, this is clearly seen in Figure 4.

4.2. Transverse Dynamics. We now turn to the relaxation dynamics in the two transverse directions (y and z), which cannot currently be determined by experiments. Studying the of the out-of-plane behavior of these chains is particularly important because it can shed light on the physics of relaxation in confinement and help assess the validity of the current physical model.

4.2.1. General Features and Characteristics. We measured the 1D radius of gyration squared $R_{g,i}^2$ in the direction of each of the three coordinates (i can be either x, y, or z).

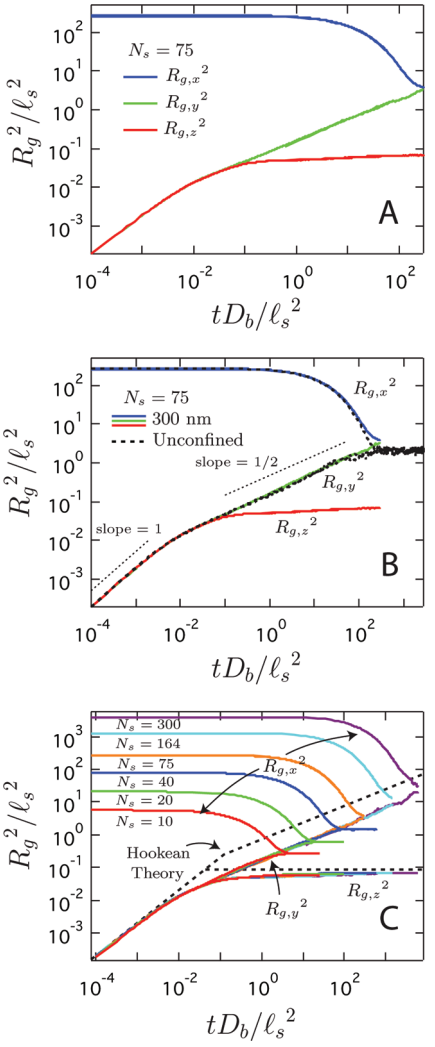


Figure 5. (A) Characteristic plot of the 1D radius of gyration squared in all three directions for a confined chain ($N_s = 75$ and $h = 300$ nm). (B) Plot of the 1D radius of gyration squared in all three directions for a single chain length ($N_s = 75$) both unconfined and in a 300 nm channel. The observed power law regions and their approximate scalings with time are also shown. (C) Plot of the 1D radius of gyration squared in all three directions for several chain lengths in a 300 nm channel. Also shown are the predicted values for each of the power law regimes as determined from the Hookean, Rouse-like theory given in eq 30.

Characteristic relaxation curves for all $R_{g,i}^2$ are shown in Figure 5A for a confined chain. In the longitudinal, or x-direction, $R_{g,x}^2$ remains fairly constant and slowly relaxes to its equilibrium value in an exponential manner only at long times. The behavior for the transverse directions is richer. $R_{g,y}^2$ and $R_{g,z}^2$, initially, are equal and grow together. However, at some point, the size of the chain in the confined dimension $R_{g,z}^2$ is restricted by the presence of the walls, and it peels off from the $R_{g,y}^2$ curve and quickly plateaus at its equilibrium value. On the other hand, the unconfined, transverse direction $R_{g,y}^2$ continues to grow even after $R_{g,z}^2$ has plateaued, and it finally reaches the same equilibrium value as the longitudinal direction so that at long times $R_{g,y}^2 = R_{g,x}^2$.

In Figure 5B, characteristic curves for unconfined relaxation have been added for comparison to the curves shown in Figure 5A for confined relaxation. In the unconfined case, $R_{g,y}^2$ and $R_{g,z}^2$ are always equivalent, all the way to their equilibrium. Additionally, at equilibrium all three directions have the same value so that $R_{g,x}^2 = R_{g,y}^2 = R_{g,z}^2 = R_{g,0}^2/3$. It is clear that, at short times, relaxation in all directions is the

same in both the confined and the unconfined cases. At intermediate times, $R_{g,z}^2$ plateaus for the confined case, while in the unconfined case it continues to grow, but the other two dimensions $R_{g,x}^2$ and $R_{g,y}^2$ continue to remain the same in both the confined and the unconfined cases. It is only at long times near equilibrium that $R_{g,x}^2$ and $R_{g,y}^2$ differ between the two cases. The unconfined chain has a smaller equilibrium value and it reaches this equilibrium sooner than the confined case. Lastly, two power law regimes are clearly see in the growth of the transverse directions $R_{g,y}^2$ and $R_{g,z}^2$ at short and intermediate times. The first regime is linear in time, while the second appears to follow a scaling close to $\sim t^{1/2}$. We will derive these scalings for a Rouse chain shortly.

Now that we have commented on the general features of the relaxation for a single chain, we look at the effect of chain length on the relaxation dynamics. In Figure 5C, we show the three 1D radii of gyration squared for several different chain lengths. As expected, $R_{g,x}^2$ is highly length dependent since its initial value is proportional to the chain length squared. Additionally, the relaxation times for the exponential decay and the final equilibrium values of $R_{g,x}^2$ are length dependent and have already been studied in section 4.1. On the other hand, the relaxation of the two transverse dimensions appears to change little based upon the length of the chain. $R_{g,z}^2$ nearly falls on a universal curve for all time and chain lengths, with only slight deviations which will be discussed later. $R_{g,y}^2$ also falls on a universal curve until it nears its equilibrium value, at which point it stops growing and plateaus at its length dependent final size.

Now that we have identified the general features of the relaxation process in the transverse dimensions, we turn to understanding the mechanisms behind the observed behavior. In particular, we would like to identify the important physics governing each of the observed power law regimes. And, with this in hand, we can study how the dynamics in the confined dimension affect, and are affected by, the longitudinal stretch.

4.2.2. Unconfined, Ideal Hookean Chain. Before we consider the relaxation dynamics in the confined dimension, we will look at the much simpler case of the transverse relaxation of an unconfined, Hookean chain. Because all three directions act independently for a linear chain, we only need to consider a 1D bead−spring chain with N_s springs each with a Hookean spring constant of H_s. Initially, the chain starts with all of the beads at the same point or, alternatively, with all of the springs having an initial stretch of zero. In this case, three different regimes arise during the relaxation process. We start by considering each of these from a scaling perspective and then use a continuous 1D Rouse model to prove some of our scalings and develop more quantitative expressions for the chain's size as a function of time.

At very short times, the bead movement is dominated by thermal forces. The springs are not yet extended enough to exert any significant force on the beads, so the beads act independently like an ideal gas. Therefore, the chain size initially grows in a diffusive manner such that $R_g^2 \sim D_b t$.

This growth continues until the spring forces are large enough to compete with the thermal forces. If this occurs when the spring lengths are of order l^*, then the spring forces are approximately $H_s l^*$ and the thermal forces are $k_B T/l^*$. Balancing these forces gives $l^* \sim (k_B T/H_s)^{1/2}$. At this point, the scaling of the chain size with time changes to a new power law $R_g^2 \sim At^\alpha$, where A and α will be determined below. Due to the influence of the significant spring forces, which impede the advancement of individual beads, the chain begins to grow subdiffusively so that $\alpha < 1$. We will refer to this new regime as the tension-dominated regime. The transition from the diffusive regime to the tension-dominated regime begins when R_g^2 is approximately $k_B T/H_s$, which occurs at $t \sim k_B T/H_s D_b$.

The third regime, which we call the equilibrium regime, occurs when the chain reaches its final size of $R_g^2 \sim N_s k_B T/H_s$. This should occur at times on the order of the longest Rouse relaxation time of the chain or $t \sim N_s^2 k_B T/H_s$. We can determine the power law exponent α and the scaling of the prefactor A for the tension-dominated regime by matching the end of the diffusive regime and the beginning of the equilibrium regime to the beginning and the end of the tension-dominated regime, respectively. Matching to the diffusive regime gives the expression $R_g^2 \sim k_B T/H_s \sim A(k_B T/H_s D_b)^\alpha$, and matching to the equilibrium regime gives $R_g^2 \sim N_s k_B T/H_s \sim A(N_s^2 k_B T/H_s D_b)^\alpha$. This only holds valid for $\alpha = 1/2$ and $A \sim (kBTD_b/H_s)^{1/2}$. Combining all of our results, we finally arrive at a scaling for the chain size in all three regimes as a function of time

$$R_g^2 \sim \begin{cases} D_b t, & t \ll \dfrac{k_B T}{H_s D_b} \\ \left(\dfrac{k_B T D_b}{H_s}\, t\right)^{1/2}, & \dfrac{k_B T}{H_s D_b} \ll t \ll \dfrac{N_s^2 k_B T}{H_s D_b} \\ \dfrac{N_s k_B T}{H_s}, & t \gg \dfrac{N_s^2 k_B T}{H_s D_b} \end{cases} \quad (21)$$

To more rigorously confirm our scalings, particularly in the tension-dominated regime, we now briefly develop a continuous 1D Rouse model for the transverse relaxation of an initially straight chain. Lengthier more detailed derivations are available elsewhere.[19,34] We start with a discrete bead−spring chain with N_b beads connected by $N_s = N_b - 1$ Hookean springs with spring constant H_s. If we allow the nth bead position to be a continuous variable, we can recast the discrete bead−spring model as a continuous chain obeying the partial differential equation

$$\zeta_b \frac{\partial r_n}{\partial t} = H_s \frac{\partial^2 r_n}{\partial n^2} + F_n^B \quad (22)$$

where the second moment of the Brownian force is

$$\langle F_n^B(t) \rangle = 0$$
$$\langle F_n^B(t) F_m^B(t') \rangle = 2k_B T \zeta_b \delta(n-m)\delta(t-t') \quad (23)$$

The initial condition and boundary conditions are given by

$$r_n|_{t=0} = \left.\frac{\partial r_n}{\partial n}\right|_{n=0} = \left.\frac{\partial r_n}{\partial n}\right|_{n=N_b} = 0 \quad (24)$$

The normal coordinates of the system can be found by solving the eigenvalue problem.

We are interested in the chain's ensemble-averaged radius of gyration squared

$$\langle R_g^2(t) \rangle = \left\langle \frac{1}{N_b} \int_0^{N_b} dn [r_n(t) - R_{c.m.}(t)]^2 \right\rangle \quad (25)$$

where $R_{c.m.}(t)$ is the center of mass of the chain. Using normal coordinates and linear response theory, it can be shown that

$$\langle R_g^2(t) \rangle = \frac{N_b k_B T}{\pi^2 H_s} \sum_{p=1}^{\infty} p^{-2} \left[1 - \exp\left(\frac{-2\pi^2 H_s p^2}{N_b^2 \zeta_b} t\right)\right] \quad (26)$$

At long times, the exponential dies off, and only the sum $\sum_{p=1}^{\infty} p^{-2} = \pi^2/6$ remains. This gives an equilibrium value of

$\langle R_g{}^2(t)\rangle = N_b k_B T/6H_s$, which is exactly the expected theoretical result.

If we transform the summation $\sum_{p=1}^{\infty}$ in eq 26 to an integral $\int_{6/\pi}^{\infty} dp$ (the lower bound has been chosen so that the equilibrium value remains the same) then our expression becomes

$$\langle R_g{}^2(t)\rangle = \frac{N_b k_B T}{6H_s}\left[1 - \exp\left(\frac{-72H_s}{\pi^2 N_b{}^2 \zeta_b} t\right) + \sqrt{\frac{72H_s}{\pi N_b{}^2 \zeta_b} t}\,\mathrm{erfc}\left(\sqrt{\frac{72H_s}{\pi^2 N_s{}^2 \zeta_b} t}\right)\right] \quad (27)$$

Finally, since we are interested in short times (i.e., $t \ll \pi^2 N_b{}^2 \zeta_b/72H_s$), we can expand this expression into a power series and keep only the leading order term

$$\langle R_g{}^2(t)\rangle = \sqrt{\frac{2k_B T D_b}{\pi H_s} t} \quad (28)$$

As predicted by our previous scaling arguments, in the tension-dominated regime $R_g{}^2 \sim t^{1/2}$.

For the diffusion-dominated regime, $R_g{}^2$ is simply the mean-squared displacement of a gas of beads that all initially start at the same point. This gives the well-known result $R_g{}^2 = 2D_b t$.

If we take all of our results, we can determine the locations of the regime transitions from the intersections of the expressions. Finally, combining all of our findings, we find

$$R_g{}^2 \approx \begin{cases} 2D_b t, & t \ll \dfrac{k_B T}{H_s D_b} \\ \left(\dfrac{2k_B T D_b}{\pi H_s} t\right)^{1/2}, & \dfrac{k_B T}{H_s D_b} \ll t \ll \dfrac{N_s{}^2 k_B T}{H_s D_b} \\ \dfrac{N_s k_B T}{6H_s}, & t \gg \dfrac{N_s{}^2 k_B T}{H_s D_b} \end{cases} \quad (29)$$

Comparing this to eq 21, we find that our predicted scalings are, indeed, correct.

Our theoretical predictions for the two power law regimes of the unconfined case are plotted in Figure 5C to be compared to $R_{g,y}{}^2$. It is clear that our expression catches the qualitative behavior seen in the simulations. It quantitatively predicts the value in the diffusive regime at short times, but it overestimates the time at which the transition to the tension-dominated regime occurs. This leads to an overprediction of $R_{g,y}{}^2$ in the tension-dominated regime. These discrepancies are due to the nonlinearities in the spring law used in the simulations when the chain is initially stretched beyond its linear regime. Effectively, this increases the spring constant H_s felt by the beads which, according to eq 29, should decrease the time of the transition to the tension-dominated regime as well as the value of $R_{g,y}{}^2$ in this regime. So incorporating the spring law nonlinearities into the above Hookean analysis should bring the theoretical prediction more in line with the simulation results. The effects of these nonlinearities will be discussed in greater detail later.

4.2.3. Confined, Ideal Hookean Chain. When a Hookean chain relaxes in a channel of height $h \ll (N_s k_B T/H_s)^{1/2}$, the equilibrium size of the chain in the confined dimension decreases to $R_g{}^2 \sim h^2$. Going further, if we assume that the bead distribution across the channel height is uniform, then $R_g{}^2 = h^2/12$. This is actually an overprediction of $R_g{}^2$ because the bead distribution is not truly uniform and has a Gaussian quality to it.

Assuming that $h \gg (k_B T/H_s)^{1/2}$, the effect of confinement is both to limit the chain size and to truncate the width of the tension-dominated regime so that

$$R_g{}^2 \approx \begin{cases} 2D_b t, & t \ll \dfrac{k_B T}{H_s D_b} \\ \left(\dfrac{2k_B T D_b}{\pi H_s} t\right)^{1/2}, & \dfrac{k_B T}{H_s D_b} \ll t \ll \dfrac{\pi H_s h^4}{288 k_B T D_b} \\ \dfrac{h^2}{12}, & t \gg \dfrac{\pi H_s h^4}{288 k_B T D_b} \end{cases} \quad (30)$$

A similar expression can be written if $h \ll (k_B T/H_s)^{1/2}$, but in that case, the diffusive regime is truncated and the tension-dominated regime is eliminated entirely.

This prediction for the confined case is also plotted in Figure 5C to be compared to $R_{g,z}{}^2$. Again, fairly good qualitative agreement exists between theory and simulations except that the tension-dominated regime is not seen in the theoretical prediction, as $h \ll (k_B T/H_s)^{1/2}$, but it is present in the simulation results. As in the unconfined case, this is due to the nonlinearities in the spring law.

4.2.4. Excluded Volume. As mentioned in section 4.1, the EV forces are not significant for moderately stretched chains. This means that the effects of EV will not be seen until the chain has relaxed significantly in the longitudinal direction, which only occurs on time scales on the order of τ_I or longer. This can clearly be seen in Figure 6 where the curves for the chain with EV do not deviate from those without EV until very near equilibrium. Therefore, the effects of EV on the transverse dynamics are minimal except at very long times.

We can demonstrate this by considering a scaling analysis to estimate the fractional extension X_{ev} at which EV becomes important. We accomplish this using a Flory-type approach where an estimate of the energy gain due to excluded volume interactions F_I is obtained using a mean field approach (see Chapter 3 of Rubinstein and Colby[27] for more details concerning the following analysis). We begin by viewing the chain as a series of tension blobs whose in-plane dimensions are ξ_y and whose transverse dimensions are h (i.e., they are small disks). Therefore, the pervaded volume of a tension blob scales as $\sim h\xi_y{}^2$. If there are g_y Kuhn lengths in a blob, then the chain interaction parameter[27] of a blob is given by

$$z \sim \frac{F_I}{k_B T} \sim \nu^{ev,p}\frac{g_y{}^2}{h\xi_y{}^2} \sim \frac{\nu^{ev,p}}{hb_K{}^2} g_y \quad (31)$$

where here F_I is the energy gain for a blob and $\nu^{ev,p}$ is the excluded volume parameter for a Kuhn length. The last scaling comes from assuming ideal chain statistics within a blob, as Flory did (i.e., $\xi_y \sim g_y{}^{1/2} b_K$). The chain interaction parameter simply compares the energy gain due to excluded volume interactions to the thermal energy, so the point at which EV becomes important is when $z \approx 1$. Therefore, the critical number of Kuhn lengths in a tension blob $g_{y,ev}$, where EV becomes important is

$$g_{y,ev} \sim \frac{hb_K{}^2}{\nu^{ev,p}} \quad (32)$$

which corresponds to a fractional extension of

$$X_{ev} \sim \frac{(N_K/g_{y,ev})\xi_{y,ev}}{N_K b_K} \sim g_{y,ev}{}^{-1/2} \sim \sqrt{\frac{\nu^{ev,p}}{hb_K{}^2}} \quad (33)$$

For our choice of parameters, in a 300 nm channel, this corresponds to a fractional extension of $X_{ev} \approx 0.3$. Of course,

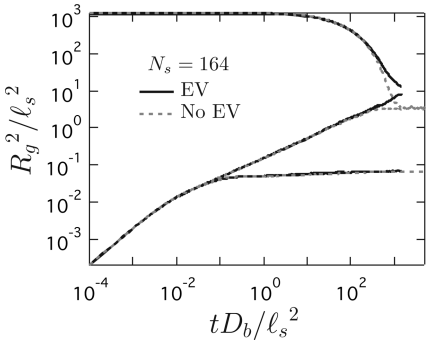


Figure 6. Plot of the 1D radius of gyration squared in all three directions for a single chain length of $N_s = 164$ both with and without EV. The initial stretch of the chain was 75% in a 300 nm channel.

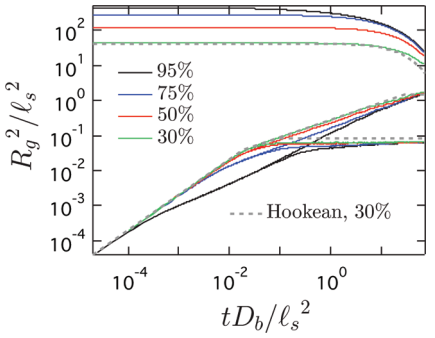


Figure 7. Plot of the 1D radius of gyration squared in all three directions for a single chain length of $N_s = 75$ in a 300 nm channel. The results for various values of the initial fractional extension are shown. Also included is the Hookean theory given by eqs 29 and 30.

this is a scaling analysis, so order unity prefactors have been ignored. But this suggests that a chain must relax significantly in the longitudinal direction before EV effects become important, and this only occurs at very long times. This means that examining chain growth across multiple time scales by plotting the chain size against a logarithmic scale of time is inappropriate for the study of the effects of EV. To see these effects, a linear time scale must be used, which is precisely the sort of analysis performed in section 4.1.

EV does not directly affect the dynamics of the confined dimension, even at long time scales, as will be shown in the following section. However, we will show that under certain conditions spring nonlinearities can lead to coupling between the confined and longitudinal dimensions that affects the relaxation of $R_{g,z}^2$ to its true equilibrium value at long times. Therefore, $R_{g,z}^2$ is sensitive to EV insofar as the longitudinal dimension is affected by EV at long times. On the other hand, the unconfined, transverse dimension certainly feels the effects of EV as it nears the equilibrium value it shares with the longitudinal dimension, but at this point, these two unconfined dimensions are governed by the same linear relaxation processes which have already been studied in significant detail in section 4.1. So no further analysis is required.

4.2.5. Nonlinearities. Finally, we consider the effects of the spring nonlinearities, which are most evident at the beginning of the relaxation process when the springs are highly stretched. One consequence of these nonlinearities is that the spring force is no longer independent for each dimension. This means that the strong stretching in the longitudinal direction leads to an increased effective spring constant in both of the transverse directions. As already pointed out in sections 4.2.2 and 4.2.3, this can lead to deviations from the

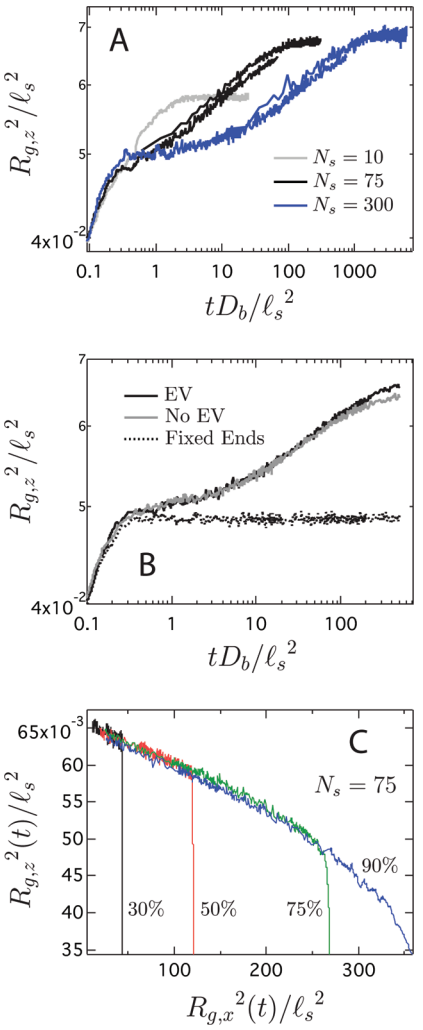


Figure 8. (A) Plot of 1D radius of gyration squared in the confined, transverse dimension $R_{g,z}^2$ for several different chain lengths in a 300 nm channel with an initial fractional extension of 75%. Only the equilibrium regime is shown (see Figure 5C for the entire relaxation process). Two curves are seen for $N_s = 75$ and 300 because the data from both the short time and long time simulations are plotted. (B) Plot of 1D radius of gyration squared in the confined, transverse dimension $R_{g,z}^2$ for a single chain length of $N_s = 75$ in a 300 nm channel with an initial fractional extension of 75%. The results for three different cases are shown: with EV, without EV, and the longitudinal stretch held fixed. Only the equilibrium regime is shown. (C) Plot of 1D radius of gyration squared in the confined, transverse dimension $R_{g,z}^2$ vs the 1D radius of gyration squared in the longitudinal dimension $R_{g,x}^2$ for a single chain length of $N_s = 75$ in a 300 nm channel. The results for several different initial fractional extensions is shown.

Hookean theory and retards the growth of the transverse dimensions during the tension-dominated regime.

To clearly demonstrate this effect, we simulated the relaxation of a chain from several different initial fractional extensions. The results are shown in Figure 7. It has been observed that chains behave in a Hookean manner up to fractional extensions around 30%. In accordance with this, excellent agreement is seen between the Hookean theory and the chain initially stretched to 30%. As the initial extension is increased, the size in the transverse dimensions falls farther below that of the theory. This is precisely the expected effect of the strong nonlinearities in the springs at high extensions.

The nonlinearities also affect the equilibrium regime of the confined, transverse dimension. Figure 8A shows a zoomed in view of $R_{g,z}^2$ from Figure 5C for several different chain

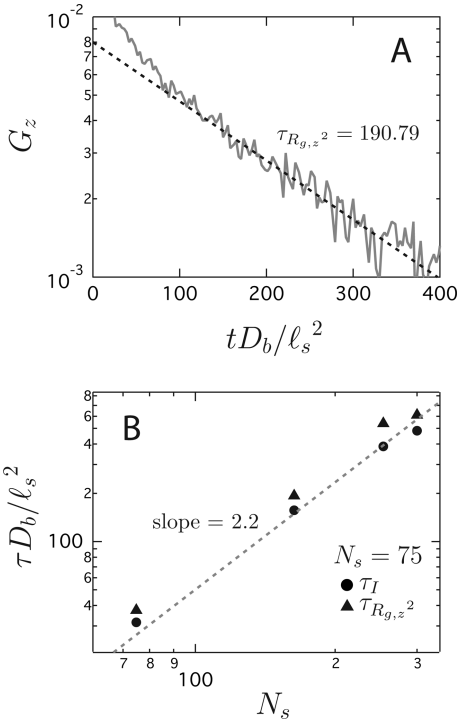


Figure 9. (A) Characteristic plot of the confined transverse relaxation function $G_z(t) = [R_{g,z,0}^2 - R_{g,z,0}^2]/l_s^2$ for chain length $N_s = 164$. The fitting for the linear region is shown. (B) Plot of the un-confined-like relaxation times τ_I and $\tau_{R_{g,z}^2}$ vs chain length N_s. Also shown is the predicted scaling $\tau_{R_{g,z}^2} \sim \tau_I \sim N_s^{2.2}$.

lengths. We have zoomed in on the region that looks like a plateau in Figure 5C, which we have been referring to as the equilibrium regime. In Figure 8A, $R_{g,z}^2$ is the same for all three chain lengths through the diffusive and tension-dominated regimes, but they behave somewhat differently once they reach the equilibrium regime. (Note that the two curves seen for both $N_s = 75$ and 300 are due to the inclusion of both the short time and long time simulations.) The Hookean theory of section 4.2.3 predicts that $R_{g,z}^2$ should immediately plateau to its final equilibrium value after the tension-dominated regime, but clearly the dynamics are richer for real chains. All three chain lengths exit the tension-dominated regime by temporarily pausing their growth of $R_{g,z}^2$ at an intermediate value slightly below their final equilibrium. The duration of this pause is dependent upon the chain length. For $N_s = 10$, the pause is only barely evident, while it is quite significant for $N_s = 300$. After this interruption in its growth, $R_{g,z}^2$ slowly approaches its final value.

To prove that this behavior is due to the spring nonlinearities, we ran a simulation where an initially stretched chain was allowed to relax in the transverse directions, but its initial longitudinal stretch was held fixed for all time. The result is shown in Figure 8B along with the results for chains with and without EV that are allowed to relax in the longitudinal direction. The two chains that are allowed to relax in all dimensions are nearly identical except that the chain with EV has a slightly higher final equilibrium value at long times. Therefore, EV cannot account for this behavior. On the other hand, the chain whose stretch is held fixed plateaus at its final value precisely where the other chains temporarily pause. Clearly, this temporary arrest in the growth is due to the nonlinearities of the springs, and the subsequent slow approach to equilibrium is due to the relaxation of the longitudinal stretch which reduces the tension in the springs.

To demonstrate that relaxation of the longitudinal stretch is responsible for the slow approach to equilibrium after the pause, we have taken the data from Figure 7 and plotted $R_{g,z}^2$ against $R_{g,x}^2$. This is shown in Figure 8C for different initial chain extensions. Initially, $R_{g,z}^2$ grows during the diffusive and tension-dominated regimes without much change in $R_{g,x}^2$, which relaxes on much longer time scales. But once the equilibrium regime is reached, all the curves fall on the same universal curve. This reveals that a quasi-steady equilibrium exists for $R_{g,z}^2$ during the equilibrium regime and it is slaved to the relaxation of the longitudinal stretch. This also verifies the quasi-steady assumption made in the tension-blob physical model for the relaxation, as discussed in section 2.2.2.

A consequence of this quasi-steady equilibrium is that during the equilibrium regime, $R_{g,z}^2$ is a measure of the relaxation of the longitudinal stretch. This means analyzing $R_{g,z}^2$ provides another way of studying the relaxation times of the chain. We can do this by defining a relaxation function $G_z(t) = [R_{g,z,0}^2 - R_{g,z,0}^2]/l_s^2$ for the confined dimension. A characteristic curve for $G_z(t)$ is shown in Figure 9A. An obvious linear region is seen, indicative of a single exponential decay with the time constant $\tau_{R_{g,z}^2}$. Because this approach to equilibrium is due the nonlinearities in the spring law when the longitudinal direction is extended beyond 30%, it is expected that $\tau_{R_{g,z}^2}$ should provide an estimate of the un-confined-like relaxation time τ_I. Indeed, good agreement is found between the two as seen in Figure 9B, and it is clear that they follow the same scaling $\tau_{R_{g,z}^2} \sim \tau_I \sim N_s^{2.2}$.

5. Conclusions

We have used Brownian dynamics simulations to study the relaxation of initially stretched chains in slitlike confinement. We have shown that our simulation technique is capable of reproducing the qualitative findings of recent experimental studies. In particular, our simulations clearly show the existence of two distinct relaxation times in the linear force regime: one that scales similar to an un-confined-like relaxation time and another that follows the scalings predicted by blob theory. We have conclusively demonstrated that the emergence of the second relaxation time is due to excluded volume effects and not hydrodynamic interactions.

We developed a Rouse-like theory to describe the confined relaxation of the transverse dimensions of an initially straight bead−spring chain and find good agreement between our theory and the simulations. The effects of excluded volume and spring nonlinearities on the dynamics were also explored. It was found that these nonlinearities lead to a quasi-steady equilibrium between the size of the chain in the confined dimension and in the longitudinal dimension. This corroborates one of the underlying assumptions of the physical model for confined relaxation proposed by Balducci and co-workers.[10]

Our results are important to developing a clear mechanistic understanding of the relaxation of polymers in slitlike confinement. Not only is this a problem of fundamental importance in polymer physics, it also has practical interest for the development of microfluidic devices that exploit confinement to manipulate DNA molecules. This work only considered the scalings of the relaxation times with chain length, and the height of the channel was not varied. Future studies should examine the predicted scalings of the relaxation times with channel height. Additionally, hydrodynamics interactions were not included in the simulation model, and their effects should be explored at a later date.

Acknowledgment. The authors are indebted to Jing Tang and Will Uspal for their numerous insightful discussions. Additionally, the authors thank the Singapore-MIT Alliance for Research

and Technology (SMART) for funding, and the National Science Foundation Grant CBET-0852235.

References and Notes

(1) Doyle, P. S.; Bibette, J.; Bancaud, A.; Viovy, J.-L. *Science* **2002**, *295*, 2237.
(2) Han, J.; Craighead, H. G. *Science* **2000**, *288*, 1026.
(3) Chan, E. Y.; Goncalves, N. M.; Haeusler, R. A.; Hatch, A. J.; Larson, J. W.; Maletta, A. M.; Yantz, G. R.; Carstea, E. D.; Fuchs, M.; Wong, G. G.; Gullans, S. R.; Gilmanshin, R. *Genome Res.* **2004**, *14*, 1137.
(4) Jo, K.; Dhingra, D. M.; Odijk, T.; de Pablo, J. J.; Graham, M. D.; Runnheim, R.; Forrest, D.; Schwartz, D. C. *Proc. Natl. Acad. Sci. U.S.A.* **2007**, *104*, 2673.
(5) Perkins, T. T.; Quake, S. R.; Smith, D. E.; Chu, S. *Science* **1994**, *264*, 822.
(6) Bakajin, O. B.; Duke, T. A. J.; Chou, C. F.; Chan, S. S.; Austin, R. H.; Cox, E. C. *Phys. Rev. Lett.* **1998**, *80*, 2737.
(7) Turner, S.; Cabodi, M.; Craighead, H. *Phys. Rev. Lett.* **2002**, *88*, 128103.
(8) Schroeder, C. M.; Babcock, H. P.; Shaqfeh, E. S. G.; Chu, S. *Science* **2003**, *301*, 1515.
(9) Reisner, W.; Morton, K. J.; Riehn, R.; Wang, Y. M.; Yu, Z.; Rosen, M.; Sturm, J. C.; Chou, S. Y.; Frey, E.; Austin, R. H. *Phys. Rev. Lett.* **2005**, *94*, 196101.
(10) Balducci, A.; Hsieh, C.-C.; Doyle, P. S. *Phys. Rev. Lett.* **2007**, *99*, 238102.
(11) Bonthuis, D. J.; Meyer, C.; Stein, D.; Dekker, C. *Phys. Rev. Lett.* **2008**, *101*, 108303.
(12) Reccius, C. H.; Mannion, J. T.; Cross, J. D.; Craighead, H. G. *Phys. Rev. Lett.* **2005**, *95*, 268101.
(13) Hsieh, C.-C.; Balducci, A.; Doyle, P. S. *Macromolecules* **2007**, *40*, 5196.
(14) Balducci, A.; Doyle, P. S. *Macromolecules* **2008**, *41*, 5485.
(15) Fisher, J. K.; Ballenger, M.; O'Brien, E. T.; Haase, J.; Superfine, R.; Bloom, K. *Proc. Natl. Acad. Sci. U.S.A.* **2009**, *106*, 9250.
(16) Grassia, P.; Hinch, E. J. *J. Fluid Mech.* **1996**, *308*, 255.
(17) Doyle, P. S.; Shaqfeh, E. S. G.; McKinley, G. H.; Spiegelberg, S. H. *J. Non-Newtonian Fluid Mech.* **1998**, *76*, 94.
(18) Dimitrakopoulos, P. *J. Fluid Mech.* **2004**, *513*, 265.
(19) Doi, M.; Edwards, S. *The Theory of Polymer Dynamics*; Oxford University Press: New York, 1986.
(20) Milchev, A.; Binder, K. *J. Phys. II* (*France*) **1996**, *6*, 21.
(21) Hagita, K.; Koseki, S.; Takano, H. *J. Phys. Soc. Jpn.* **1999**, *68*, 2144.
(22) Stigter, D. *Biophys. Chem.* **2002**, *101*, 447.
(23) Woo, N. J.; Shaqfeh, E. S. G.; Khomami, B. *J. Rheol.* **2004**, *48*, 281.
(24) Brochard, F. *J. Phys.* (*Paris*) **1977**, *38*, 1285.
(25) Tang, J.; Trahan, D. W.; Doyle, P. S. *Macromolecules* **2010**, *43*, 3081.
(26) Daoud, M.; de Gennes, P. G. *J. Phys.* (*Paris*) **1977**, *38*, 85.
(27) Rubinstein, M.; Colby, R. H. *Polymer Physics*; Oxford University Press: New York, 2003.
(28) Kim, J. M.; Doyle, P. S. *J. Chem. Phys.* **2006**, *125*, 074906.
(29) Underhill, P. T.; Doyle, P. S. *J. Rheol.* **2006**, *50*, 513.
(30) Marko, J. F.; Siggia, E. D. *Macromolecules* **1995**, *28*, 8759.
(31) Underhill, P. T.; Doyle, P. S. *J. Non-Newtonian Fluid Mech.* **2004**, *122*, 3.
(32) Jendrejack, R. M.; de Pablo, J. J.; Graham, M. D. *J. Chem. Phys.* **2002**, *116*, 7752.
(33) Heyes, D.; Melrose, J. *J. Non-Newtonian Fluid Mech.* **1993**, *46*, 1.
(34) Trahan, D. W. Simulating DNA Behavior in Microfluidic Devices. *Ph.D. Thesis*, Massachusetts Institute of Technology, 2010.

Macromolecules
ARTICLE

Macromolecules **2011**, *44*, 393–402 **393**
DOI: 10.1021/ma102179b

Temperature and Pressure Dependence of Polystyrene Dynamics through Molecular Dynamics Simulations and Experiments

Vagelis A. Harmandaris,*,†,‡,∥ George Floudas,*,§,⊥ and Kurt Kremer∥

†*Department of Applied Mathematics, University of Crete, GR-71110 Heraklion, Greece,* ‡*IACM FORTH, GR-71110 Heraklion, Greece,* §*Department of Physics, University of Ioannina, GR-45110, Ioannina, Greece,* ⊥*Foundation for Research and Technology-Biomedical Research Institute, Ioannina, Greece, and* ∥*Max Planck Institute for Polymer Research, D-55128 Mainz, Germany*

Received September 21, 2010; Revised Manuscript Received December 9, 2010

ABSTRACT: We present a detailed comparison of the segmental and chain dynamics of an atactic monodisperse polystyrene (molecular weight 1800 g/mol) (a-PS) studied by hierarchical multiscale molecular dynamics (MD) simulations, with an atactic polystyrene (M_n = 1644 g/mol, polydispersity index 1.14) investigated by dielectric spectroscopy, rheology and differential scanning calorimetry. The MD simulations, performed at three temperatures (403, 433, and 463 K), can capture the temperature dependence of the segmental and terminal relaxations in good quantitative agreement with experiment, taking into account the uncertainties in the development of the atomistic force field. In addition, ring and backbone segmental dynamics are studied by analyzing time-correlation functions for various bond vectors in the monomer level. MD simulations at elevated pressures (40 and 60 MPa) were also in good agreement with experiments probing the pressure-dependent glass temperature.

1. Introduction

Accurate knowledge of the local and global polymer dynamics[1,2] as a function of temperature and pressure is important for technological applications, since they dictate the processability and the final mechanical and electrical properties of polymers. Therefore, efforts to obtain and ultimately predict these properties, either through experimental methods or theoretical and simulation approaches, have attracted considerable interest over the years.[1−5]

Recent experimental efforts have addressed the origin of the freezing of the dynamics at the liquid-to-glass temperature by decreasing temperature or increasing pressure. One such approach emphasized the importance of monomer volume and local packing[6] whereas other approaches proposed[7−11] a thermodynamic scaling of the dynamics on temperature and density. Of central importance in these experimental efforts has been the application of pressure, since it can be applied isothermally, thus affecting only the density.

In addition to experiments molecular dynamics (MD) simulations provide an excellent tool for investigating polymer dynamics as a function of temperature and pressure at various length scales. Thus, over the past years, several attempts have been made to exploit MD trajectories for simplified generic, coarse grained or even atomistic models and calculate relaxation times both at the segmental and at the end-to-end distance level.[12−31] In MD the segmental dynamics is usually studied through the time-decay of autocorrelation functions of various quantities, such as dihedral angles, dipolar moments, C−H bond vectors which then can be directly compared with experimental probes (NMR, dielectric spectroscopy (DS)).

Boyd and collaborators[12,13] were the first to report simulation results for the effect of pressure, and temperature, on the thermodynamic and structural properties of polyethylene (PE) by performing MD runs. They studied a single PE chain, which folded back into the original box via periodic boundary conditions in order to reach melt density. Other simulation studies of pressure effects on the dynamics of amorphous polymers include the MD works of Hotston et al.[14] and Smith and co-workers[15,16] on the segmental relaxation of PE and 1,4-polybutadiene (PB) respectively, and of Yang et al.[17] on the glass transition of a model polymer through isobaric or isochoric cooling. Segmental dynamics at ambient atmospheric pressure of different polymers have also been exploited through atomistic MD simulations. These studies include the local structure and the local reorientation dynamics of C−H bonds in *trans*-polyisoprene oligomers,[25] the local dynamics of a miscible blend of *cis*-1,4-PI with 1,2-PB,[24] and the dynamics of atactic polypropylene.[21] In addition to temperature, pressure effects on the structure and dynamics were studied in *cis*-1−4 PB.[22]

Atactic polystyrene has also been investigated by simulations. The segmental dynamics in atactic polystyrene with molecular weight of 2200 g/mol was recently studied by MD simulations at three temperatures and the results were compared with NMR spin−lattice relaxation experiments.[17] The simulated segmental relaxation times were slower by a factor of 1.8, however the comparison indicated a qualitative agreement of the shape of the $P_2(t)$ orientation autocorrelation function as probed by MD and experiments. In addition, united atom MD simulations have addressed the segmental dynamics and the issue of dynamic heterogeneity near the glass transition temperature for short atactic polystyrene chains.[26,27]

With MD simulations usually only oligomeric systems (i.e., low molecular weight polymers) can be investigated in all-atom detail and, even then, for a rather limited range of temperatures and pressures. The reason are difficulties arising from the wide spectrum of time- and length-scales characterizing their structure and associated dynamics. To overcome these difficulties, coarse grained (CG) dynamic simulations have been developed. Such CG MD simulations are capable of exploiting a broader range of

*Corresponding authors. E-mail: (V.A.H.) vagelis@tem.uoc.gr; (G.F.) gfloudas@cc.uoi.gr.

© 2010 American Chemical Society

Published on Web 12/27/2010

time- and length-scales due to the simpler models and bead interactions as compared to the more detailed all-atom ones. For this purpose various coarse-grained models have been used in studying the dynamics of bulk polymers, varying from simple bead−spring models[29−31] to more detailed, systematically obtained CG models, that allow a quantitative study of the structure and dynamics of specific polymeric systems (see, for example, refs 4, 5, 29, and 32−35 and references within).

Despite recent progress made with the aid of various MD simulation methods and experiments, an in-depth understanding of the molecular mechanisms governing the (multiple) relaxation processes of polymers, is still lacking. In particular, a comparison of the local segmental and chain dynamics as deduced from simulations and experiments at temperatures and pressures that are typically encountered during processing is a necessity for understanding—and ultimately predicting—properties of polymers. Multiscale simulation approaches combined with experimental methods with the capability of probing the dynamics at the molecular level are best suited for this purpose.

Here we present such a methodology that combines systematic multiscale simulation methods and experimental techniques for understanding the dynamics of atactic polystyrene (a-PS). The polymer dynamics is examined both at the submonomer and end-to-end distance level. At the same time the temperature and the pressure dependence of the segmental dynamics is studied and compared with the results from dielectric spectroscopy, rheology and differential scanning calorimetry made on the very same sample. In addition, the results of the equation-of-state, obtained from pressure-volume-temperature measurements, are employed as a guide for the MD simulations. Overall the main goal of the present work is to provide a direct comparison of the segmental and terminal dynamics from simulation and experiments (DS, rheology) at atmospheric pressure and, for the first time, of the segmental dynamics at elevated pressures. The paper is organized as follows. In the first two sections, a brief overview of the experimental techniques as well as of the atomistic and the coarse-grained simulations is given. Results on the relevant thermodynamic properties and comparison of the dynamics as probed by MD simulations and experiments are presented in section 4. Finally, our findings and conclusions are summarized in section 5.

2. Experimental Methods

2.1. Sample. The PS sample, synthesized by J. Thiel in Mainz, had $M_w = 1870$ g/mol, $M_n = 1644$ g/mol giving a polydispesrity of $M_w/M_n = 1.14$. The glass temperature was at 334 K as determined by differential scanning calorimetry (DSC) at a heating rate of 10 K/min (from the second heating circle) with a heat capacity step, Δc_p, of $\Delta c_p = 0.32$ J/gK.

2.2. Pressure−Volume−Temperature (*PVT*). Pressure−volume−temperature measurements were made using a fully automated GNOMIX high-pressure dilatometer. About 1 g was used in the measurements. First, we performed runs by changing pressures from 10 to 200 MPa in steps of 10 MPa at constant temperatures (i.e., under "isothermal" conditions) from 293 to 433 K. Subsequently, measurements were made by heating/cooling experiments with a rate of 1 K/min at different fixed pressures (i.e., under "isobaric" conditions) in the range from 10 to 200 MPa. The 0.1 MPa data were obtained by extrapolation from the higher pressures. The data from the "isothermal" measurements are shown in Figure 1 for the different pressures. The $V(P,T)$ data can be parametrized according to the Tait equation

$$V(P,T) = V(0,T)\left\{1 - 0.0894 \ln\left[1 + \frac{P}{B(T)}\right]\right\} \qquad (1)$$

where, $V(0,T) = (0.8165 + 4.5 \times 10^{-4}T)$ (V in cm^3/g, T in K) is the specific volume at atmospheric pressure and $B(T) = (446\ \text{MPa})\exp(-0.00029T)$ (T in K) are the parameters in the liquid melt state. In the glassy state, the following parameters were employed: $V(0,T) = (0.9486 + 5 \times 10^{-5}T)$ (V in cm^3/g, T in K) and $B(T) = (212.5\ \text{MPa})\exp(0.00046T)$ (T in K). The glass temperature, at each pressure, was determined by extrapolating the $V(P)$ dependencies below and above the "transition" and the resulted glass temperatures (T_g) are plotted as an inset to Figure 1.

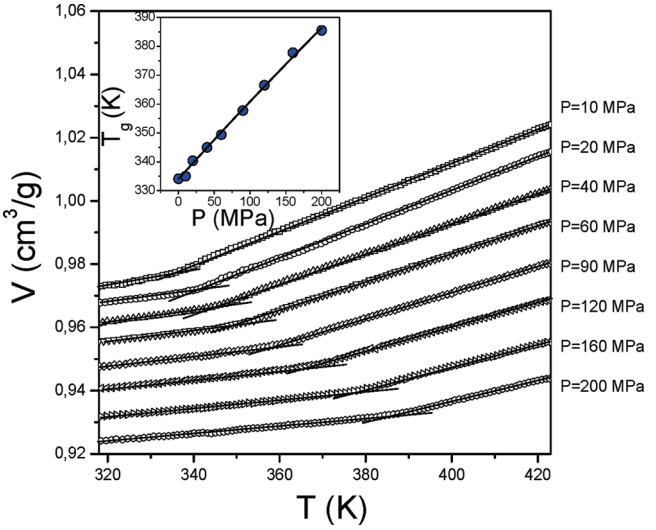


Figure 1. Specific volume as a function of temperature for different pressures in the range from 10 to 200 MPa, obtained from *PVT* measurements. The lines represent linear fits to temperatures below and above the liquid-to-glass temperature and the latter is obtained from their intersection. Inset: Glass temperature as a function of pressure. The line is a fit to eq 5.

2.3. Dielectric Spectroscopy (DS). Dielectric measurements were made under isobaric (atmospheric pressure) conditions as a function of temperature at different temperatures in the range 123.15−423.15 K and for frequencies in the range from 10^{-2} to 10^6 Hz. The complex dielectric permittivity $\varepsilon^* = \varepsilon' - i\varepsilon''$, where ε' is the real and ε'' is the imaginary part, was obtained as a function of frequency ω and temperature T, i.e., $\varepsilon^*(T,\omega)$.[36] The analysis of the T- dependent experiments was made using the empirical equation of Havriliak and Negami (HN):

$$\varepsilon^*(T,P,\omega) = \varepsilon_\infty(T,P) + \frac{\Delta\varepsilon(T,P)}{[1 + (i\omega\tau_{HN}(T,P))^m]^n} + \frac{\sigma_0(T,P)}{i\varepsilon_f\omega} \qquad (2)$$

where $\varepsilon_\infty(T)$ is the high frequency permittivity, $\tau_{HN}(T)$ is the characteristic relaxation time in this equation, $\Delta\varepsilon(T) = \varepsilon_o(T) - \varepsilon_\infty(T)$ is the relaxation strength, m, n (with limits $0 < m, mn \le 1$) describe, respectively, the symmetrical and asymmetrical broadening of the distribution of relaxation times, σ_o is the dc-conductivity and ε_f is the permittivity of free space. From τ_{HN}, the relaxation time at maximum loss, τ_{max}, is obtained analytically following

$$\tau_{max} = \tau_{HN}\left[\frac{\sin\left(\frac{\pi m}{2+2n}\right)}{\sin\left(\frac{\pi mn}{2+2n}\right)}\right]^{-1/m} \qquad (3)$$

Some representative dielectric loss spectra are shown in Figure S1 of the Supporting Information. In DS, the quantity that is probed is the fluctuation of the weak dipole moment associated with styrene (∼0.12 D) with a direction perpendicular to the backbone.[36] Subsequently, the DS spectra (Figure S1, Supporting Information) were analyzed using eq 2 and the relaxation times at maximum loss were extracted. From the

shape parameters m and n, the single Kohlrausch−Williams−Watts (KWW) exponent β was obtained following[37] $\beta = [mn]^{1/1.23}$, that is based on the following constraint on m and n: $n = 1 - 0.812(1 - m)^{0.387}$.

2.4. Rheology. An advanced rheometric expansion system (ARES) equipped with a force-rebalanced transducer was used in the oscillatory mode. Depending on the temperature range two transducers were used with 2000, 2 g·cm and 200, 0.2 g·cm upper and lower sensitivity, respectively. The sample was prepared on the lower plate of the 10 mm diameter parallel plate geometry setup and heated under a nitrogen atmosphere until it could flow. Subsequently, the upper plate was brought into contact, the gap thickness was adjusted to 1 mm, and the sample was slowly cooled to the desired starting temperature. For the lower temperatures investigated (near the glass temperature) plates with 6 mm diameter were employed. The storage (G′) and loss (G″) shear moduli were monitored in different types of experiments. These experiments involved isothermal frequency scans for temperatures in the range 329−373 K and for frequencies $10^{-1} < \omega < 10^{2}$ rad/s. In Figure S2 of the Supporting Information, a master-curve of the storage and loss moduli is shown. According to the principle of time−temperature superposition (tTs), the frequency (ω) dependence of the complex shear modulus G^* at any temperature can be obtained from a master curve at a reference temperature (T_r) according to $G^*(\omega,T) = G^*(a_T\omega; T_r)$. According to t$T$s, at each temperature a single frequency-scale shift factor a_T allows superposition of all modulus data at temperature T to the corresponding data at T_r. The horizontal shift factors can be described by the Williams−Landel−Ferry (WLF) equation[1]

$$\log_{10} a_T = -\frac{c_1{}^r(T - T_r)}{c_2{}^r + (T - T_r)} \quad (4)$$

where $c_1{}^r$ (=14.8) and $c_2{}^r$ (=69.4 K) are the WLF parameters at the reference temperature (T_r = 332.15 K). These values, when calculated at T_g (=334 K), result to $c_1{}^g$ = 14.4 and $c_2{}^g$ = 71.4 K. When these shift factors apply to the segmental and terminal relaxations, they provide us with the full T-dependence.

3. Molecular Simulations

The hierarchical simulation approach presented here involves detailed all-atom (AA) and coarse-grained (CG) MD simulations of an atactic PS melt with M = 1800 g/mol, i.e., with a molecular weight close to the experimental conditions.

3.1. Atomistic Simulations. An important goal of the present work is the investigation of segmental and chain dynamics of PS, at the all-atom detail, as a function of both temperature and pressure aiming at a comparison with the experimental results from dielectric spectroscopy (DS), differential scanning calorimetry (DSC) and PVT measurements, the latter performed on the same sample. To achieve this, all-atom MD simulations of short PS chains were performed using a model, where hydrogens and carbons are treated explicitly.[38] All bond lengths were kept rigid whereas a harmonic potential was used to describe bond angle bending. Standard torsional potentials were used to describe rotations along bonds in the aliphatic backbone. Parameters of the barriers for the rotation of polystyrene backbone dihedral angles were calculated from ab initio calculations on polystyrene fragments. Nonbonded interactions were described by pairwise-additive Lennard-Jones potentials. Furthermore, the AA model included partial charges on the carbon and hydrogen atoms of the phenyl groups that reproduce the electric quadropole moment of the benzene molecule. For more details of the model see ref 38.

Using this AA model, atomistic MD simulations of an atactic PS melt of 36 chains with molecular weight, M = 1800 g/mol (18mer), were performed for a range of temperatures and pressures. The molecular dynamics package

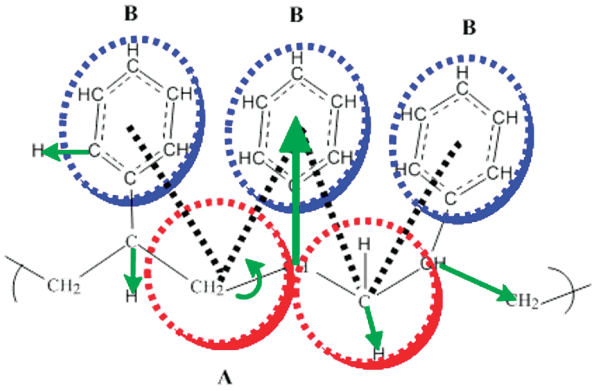


Figure 2. Atomistic and coarse grained model of PS chain. In the CG model one monomer is mapped to two different CG beads (σ_A = 4.1 Å, m_A = 27 amu; σ_B = 5.2 Å, m_B = 77 amu). Dashed lines show CG bonds between CG beads A and B. The arrows indicate the different vectors where the time−autocorrelation functions were calculated.

GROMACS[39] was employed for the atomistic MD simulations. Initial well-equilibrated atomistic configurations were obtained by back-mapping of the CG melts.[32,33] All-atom MD simulations were conducted under constant temperature and volume NVT conditions using the Berendsen thermostat (coupling time 0.1ps).[39] As a guide for the densities of the simulated melt we employed the experimental PVT data depicted in Figure 1. We should also note here, that pressure in the atomistic simulations is slightly negative (by about 10−20 MPa) since the density predicted by the AA force-field is about 3−4% larger than the experimental ones. A negative pressure, induced by the constant volume constraint, is unphysical and would lead to inhomogeneities in the system. However, this is not the case here because the fluctuations of instantaneous pressure due to the small system size are about 5−10 times larger than the average (negative) pressure. In addition, runs at higher than atmospheric pressure were made under NVT conditions at densities corresponding to the experimental densities at the specific pressure (Figure 1). In all cases the pressure of the atomistic simulations is slightly smaller than the experimental one. Nonbonded interactions were cutoff beyond 1.2 nm. Tail corrections for the energy and pressure were applied. The integration time step was 1 fs. Finally, the overall atomistic simulation time of the production runs ranged from 0.5 to 2 μs depending on the actual temperature and pressure. All segmental relaxation times, reported in the present work, were calculated by analyzing these all-atom MD simulations.

3.2. Coarse-Grained Simulations of Polystyrene. The CG MD simulations have been performed using a model where one PS monomer is mapped onto two effective coarse-grained beads.[33] In this model a CG bead "A" includes information from 3 consequent CH_x groups along the backbone (see Figure 2). In more detail, CG bead "A" corresponds to the CH_2 of a PS monomer plus the half mass of each of the two neighboring CH groups along the chain backbone, whereas CG bead "B" is just the phenyl ring. This model has the advantage of capturing tacticity without introducing side groups. More details about the CG model and the procedure to obtain the CG force-field can be found elsewhere.[32−35,40]

All coarse-grained MD simulations were performed using the ESPResSO package.[41] PS melts of 100 chains were simulated. The size of the box is fixed such that the density of the PS melt is equal to that of the experimental density. Periodic boundary conditions were used. Also, CG MD simulations have been performed in dimensionless LJ units using m_A to

scale all masses, σ_{AV} [$\sigma_{AV} = (\sigma_A + \sigma_B)/2$] to scale all lengths and ε ($\varepsilon = kT$) to scale all energies. The time step used in the MD simulations was $dt = 0.01\tau$, where τ is defined as $\tau = (m\sigma^2/\varepsilon)^{1/2}$. In order to control the temperature in the system a Langevin thermostat was employed with friction coefficient $\Gamma = 1.0\tau^{-1}$. MD simulations were performed for times 1×10^4 to $1 \times 10^5\tau$ depending upon the actual temperature and pressure. Note that even though τ has the unit of time, it is the physical time of the coarse grained model, rather than that of the underlying polymer with its specific chemical structure and has to be scaled accordingly.[32,34] The main reason for that is the softer interaction in the CG models compared to the all atom models. Calibration of the CG time scale with respect to the atomistic simulations will be discussed below. Note that the CG model used here has been parametrized at $T = 463$ K. However, various tests have shown that it can be used in a $\pm 15-20\%$ range of temperatures without any loss of accuracy.[33,35]

Finally, we should state that, as mentioned above, the CG MD simulations in this work were used: (a) for equilibrating the PS melts in the CG description, thus providing, through a back-mapping procedure, initial well-equilibrated all-atom configurations, and (b) for probing chain (end-to-end distance) relaxation of PS melts, which cannot be calculated from the all-atom MD simulations because of the very long relaxation times.

4. Results and Discussion

4.1. Thermodynamics. First we present $V(P,T)$ data from PVT measurements in Figure 1. From these data the glass temperature was extracted at each pressure and the resulting $T_g(P)$ can be described by the following empirical equation

$$T_g(P) = T_g(0)\left(1 + \frac{\kappa}{\lambda} P\right)^{1/\kappa} \quad (5)$$

where $T_g(0)$ is the glass temperature at 0.1 MPa (334 K) and κ and λ are system-specific parameters that amount to 1.72 ± 0.8 and 1210 ± 60 MPa, respectively. The initial slope, $(dT_g/dP)_{P\to 0}$ amounts to 0.277 K/MPa, i.e., similar to earlier reports for PS.[11,42] Equation 5 was first proposed for the melting of solidified gases under pressure,[43] and subsequently, it was employed by others to describe the pressure dependence of the glass temperature in glass-forming systems.[44,45]

4.2. Analysis of the MD Simulations. In the following, we will first discuss the experimental and MD results for the segmental and chain dynamics at *atmospheric pressure*. We examine the segmental dynamics of the atactic PS melt, as predicted from all-atom MD simulations, by analyzing autocorrelation functions of different vectors that include the C−CM ring and C−H bond vectors as shown in Figure 2. To examine the difference between the relaxation along the backbone and in the ring we also distinguish the C−H vectors along the backbone and in the ring.

In MD simulations different measures of the segmental dynamics of polymer melts can be employed. For example, a very common measure is by calculating time-correlation functions of a vector, $\mathbf{v}_b$, representing a chemical bond. The reorientation of such a vector can be studied by considering ensemble-averaged Legendre polynomial of order l, $P_l(t)$, of the inner product of the unit vector parallel to $\mathbf{v}_b$ at time $t = t$ and $t = 0$. A common choice for the vector $\mathbf{v}_b$, if someone is interested to compare with NMR data, is the C−H vector. The reason is that for ^{2}H nuclei, spin−lattice relaxation is dominated by electric quadrupole coupling and the spin relaxation time can be directly related to the reorientation of the C−^{2}H bond. In this case, the second Legendre polynomial: $P_2(t) = {}^3/_2\langle\cos^2(\theta(t))\rangle - {}^1/_2$, where $\theta(t)$ is the angle of $\mathbf{v}_b$ bond at time t relative to its original position is employed as a measure of the polymer segmental dynamics, and $\langle ... \rangle$ denotes the ensemble average over all chains in the system. If, on the other hand, a comparison with DS is sought (as in the present case), then a more suitable vector $\mathbf{v}_b$, is one starting from the backbone CH to the center of mass (CM) of the phenyl ring (shown by a thick arrow in Figure 2). In this case the quantity of interest is the first Legendre polynomial: $P_1(t) = \langle\cos(\theta(t))\rangle$. In addition, MD can provide the correlation functions of various other vectors, such as the C−C backbone vector, the α C−H, the β C−H, and the ring C−H as well as the dihedral angle (see Figure 2). All these correlation times can, in principle, be compared to the experimentally obtained ones. Simulations also offer the opportunity to study cross-correlations. However, there we do not know of currently available experimental data to compare to.

As an example, Figure 3a compares the $P_2(t)$ autocorrelation curves of various C−H bond vectors as well as the C−CM ring vector at the same temperature and pressure conditions ($T = 433$ K, $P = 0.1$ MPa). $P_2(t)$ exhibits a rapid decay at short times (shorter than about 10−100 ps) followed by a rather slow decorrelation at later times. The short-time regime (not shown here) corresponds to a primitive (bond vibrations and angle librations) relaxation, whereas the long-time regime corresponds to the segmental (α-) relaxation. All curves, for the range of temperatures and pressures studied here, show the same structure that is typical for amorphous polymer.[13,16,22] At a first glance, clearly the slower decay corresponds to the C−C backbone vector followed by the C−CM ring whereas the ring C−H is the fastest. This is not surprising given that C−H bonds on the phenyl ring can relax due to the motion of the backbone but also due to the faster rotational dynamics (reorientation) of the ring. Similar conclusion has been reported in the past by Vorselaars et al. in a detailed analysis of the phenyl-ring motions of PS near T_g using united-atom MD simulations.[27]

Another important aspect is related to the relaxation of the PS backbone at the monomer level and the effect of the side group. To examine this we further distinguish C−H bonds along the backbone, i.e., C−H bonds at the α C (where the phenyl group is attached) and the two C−H bonds at the β C (see Figure 2). The corresponding $P_2(t)$ curves are shown in Figure 3a with half-filled triangles. It can be seen that the relaxation of the C−H bond of the α C is slightly slower than that of the C−H bonds of the β C, and this is attributed to the bulky side group (phenyl ring). However, as we can see from Figure 3a, the difference between the two $P_2(t)$ curves for the C−H bond vectors is very small, leading to almost indistinguishable values for the relaxation times. Therefore, from here on we analyze all C−H bonds of the backbone as a single group. Inspecting the curve, however, it is not at all clear whether this hierarchy of relaxations, which is also found in experiment, only is due to initial fluctuations of different amplitude, leading to lower values of the correlation functions at short times around 100 ps. As mentioned above, the fast initial drop of the C−H vectors is related with very fast local fluctuations of the primitive relaxation at short times. To further explore the slow relaxation process we normalize all the curves of the various bond vectors, shown in Figure 3a, to 1 at 100 ps (see Figure 3b). The question is if the normalized data form a master curve with the same stretching exponent. As we can see from Figure 3b there are still differences, however almost indistinguishable,

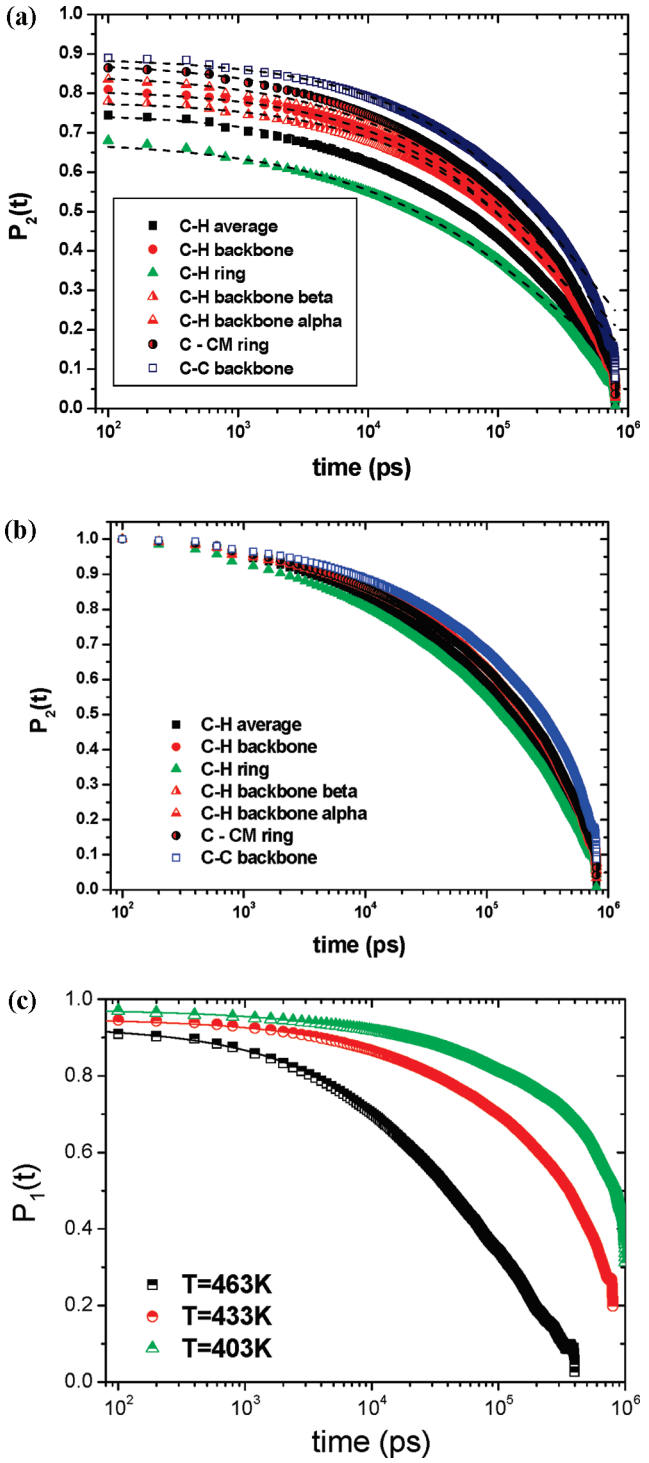


Figure 3. (a) $P_2(t)$ Time-autocorrelation function of various C−H bond vectors, the backbone C−C bond, and the C−CM ring vector at T = 433 K, obtained from the atomistic MD simulations (P = 0.1 MPa). Lines show best KWW fits. (b) $P_2(t)$ Time-autocorrelation function of various C−H bond vectors, the backbone C−C vector, and the C−CM ring bond at T = 433 K, obtained from the atomistic MD simulations (P = 0.1 MPa). Data are scaled in order to start from 1 at t = 100 ps. (c) $P_1(t)$ time-autocorrelation functions of the C−CM ring vector for different temperatures as indicated (P = 0.1 MPa). Lines show best KWW fits.

in the slow relaxation of the different C−H vectors as well as in the stretching exponent (discussed below in Figure 6); thus indicating that the long time decay is governed by the very same structural relaxation processes.

Figure 3c shows the effect of temperature variation (at P = 0.1 MPa) on the P_1 autocorrelation function corresponding to the C−CM ring vector. This quantity is of particular interest here as it is the one that is probed experimentally with DS. $P_1(t)$ exhibits a similar rapid decay at short times as $P_2(t)$, followed by a rather slow decorrelation at later times. Again the short- and long-time regime corresponds to a primitive and to the segmental relaxations, respectively. As expected, the relaxation of the C−CM bonds takes longer with decreasing temperature and at the same time the fast initial decay is smaller due to reduced fluctuations.

It is quite common to fit the long-time regime of such autocorrelation functions by a KWW stretched-exponential function:

$$P_i(t) = A \exp\left[-\left(\frac{t}{\tau_{KWW}}\right)^{\beta}\right], \quad i = 1, 2 \qquad (6)$$

where τ_{KWW} is a characteristic relaxation time, β the stretch exponent, and A a pre-exponential factor that takes into account relaxation processes at very short time scales. The segmental correlation time, τ_s, is defined as the integral of the above equation, which can be numerically calculated. We should also point out here that, in order to examine the fitting procedure, we have used different fitting ranges or even an additional fitting function, including an exponential term for the short-time (up to 10−100 ps) regime. In all cases the differences between the obtained correlation times are 5−10%, i.e., within the error bars. Finally, note that the difference in the calculated relaxation times between the original and the scaled data, shown in Figure 3, parts a and b, respectively, vary only 10−20% due to the difference in the prefactor A. Keeping this in mind, we in the following calculate the segmental relaxation times from the original data, shown in Figure 3a in order to be more consistent with the experimentally available results.

In the next step we compare the segmental relaxation times of the various autocorrelation curves shown in Figure 3,parts a and c. On the basis of the discussion above for the presence of two different modes of decay (a rapid and a slow one), we describe the second regime (times longer than about 10−100 ps) with eq 6. Lines in Figure 3, parts a and c, show the best KWW fits for the $P_2(t)$ and $P_1(t)$ curves, respectively. Values of the pre-exponential factor A were chosen properly to take into account the fast relaxation for the specific T- and P-conditions. Then the relaxation times were calculated from the time integral of $P_1(t)$ or $P_2(t)$. The thus extracted relaxation times are compared in parts a and b of Figure 4. In Figure 4a, the segmental relaxation times of the average C−H bond vector, calculated from the analysis of the $P_1(t)$ and $P_2(t)$ curves as a function of temperature, are shown at atmospheric pressure. At all temperatures, $\tau_1/\tau_2 \cong 2.2-2.7$ (this factor is also similar, within the error bars, for the segmental correlation times of the other vectors studied in this work). Note that according to the Debye theory of rotational relaxation, based upon a simple rotational diffusion coefficient, the ratio of the relaxation times calculated from $P_1(t)$ and $P_2(t)$ curves is $\tau_1/\tau_2 = 3$.[46] Deviations from this theoretical value are associated with the much more complex translational and rotational diffusion of polymeric segments as compared with a simple rotational diffusion.

In Figure 4b segmental relaxation times corresponding to the average C−H bond vector, i.e., all C−H bonds in a PS chain, as well as of individual backbone C−H bonds, ring C−H bonds, the C−CM ring vector, and the terminal relaxation for the three temperatures investigated, are included. Note that the relaxation time of the backbone C−H bonds is consistently

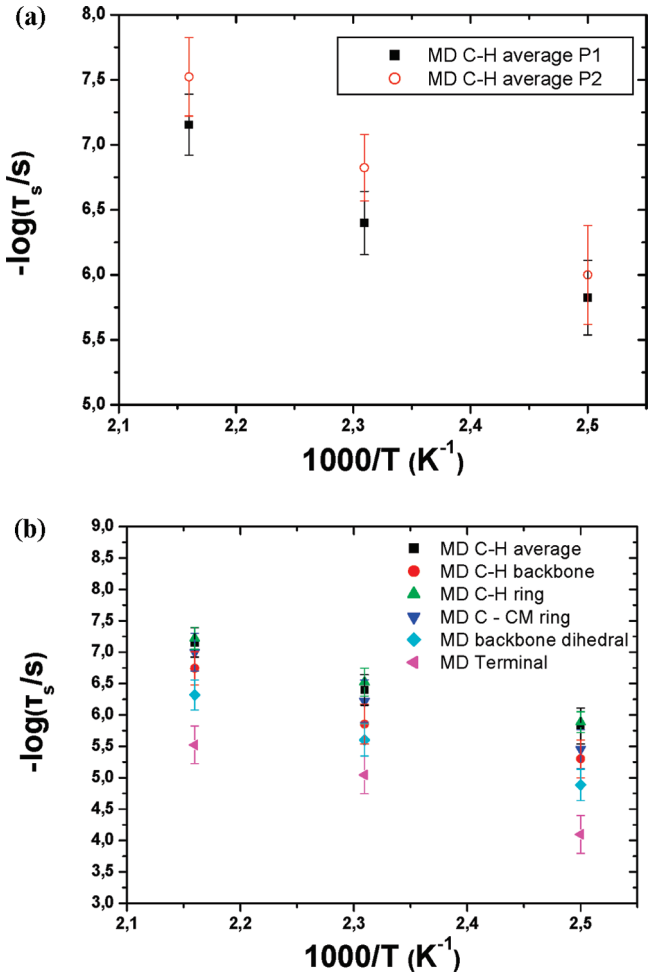


Figure 4. (a) Temperature dependence of the segmental relaxation time obtained through analysis of $P_1(t)$ and $P_2(t)$ curves of the average C−H bond vectors of MD simulation data. (b) Temperature dependence of the different characteristic times obtained through analysis of P_l(t) Legendre polynomials of various vectors of MD simulation data. Data about backbone dihedral relaxation times from the AA MD as well as the maximum (terminal) relaxation time from the CG MD simulations are also shown.

larger than for the ring C−H bonds; their ratio being in the range from 1.5 to 2.

In addition to these local bonds, the local-segmental dynamics of the backbone of PS chains can be also analyzed in the level of the dihedral angle, defined through four consecutive C atoms along the backbone. Dihedral dynamics can be quantified in terms of the torsional autocorrelation function, defined as

$$P(\phi(t)) = \frac{\langle \cos\phi(t)\cos\phi(0)\rangle - \langle\cos\phi(0)\rangle^2}{\langle\cos\phi(0)\cos\phi(0)\rangle - \langle\cos\phi(0)\rangle^2} \qquad (7)$$

where $\phi(t)$ is the dihedral angle at time t. Characteristic dihedral relaxation times can be obtained by fitting P($\phi(t)$) curves with a KWW function and calculating the integral below the curve. Dihedral relaxation times, τ_d, are included in Figure 4b for the different temperatures investigated. Two important conclusions can be derived from these data. First, that the dihedral relaxation times are longer than the C−H ones, at the same temperature and pressure. Indeed, dihedral angles along the backbone decorrelate much slower (about 10 times) than the C−H bonds along the backbone. This is not surprising given that a dihedral angle involves the motion

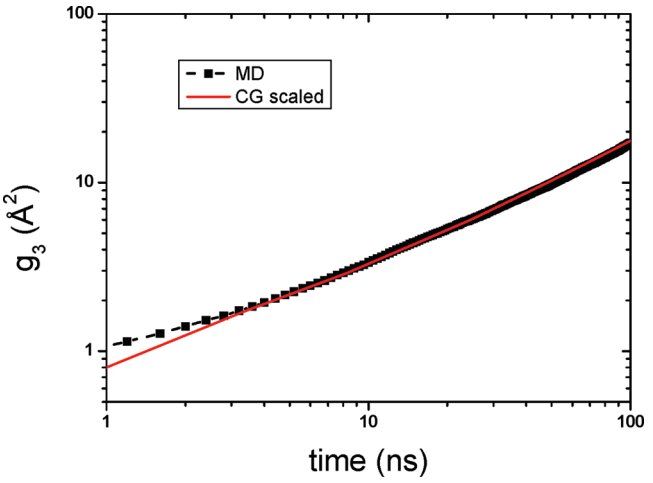


Figure 5. Time scaling of the CG simulations using all-atom data for a PS melt (T = 463 K, P = 1 atm) based on the motion of the center of mass.

of four consecutive carbon atoms. Second, the dihedral relaxation times follow similar temperature dependence as with the relaxation of the C−H bond vectors. This is also the expectation borne out by the fact that all these probes are coupled to the same structural relaxation process.

4.3. Comparison between Simulations and Experiments. In a next step, the chain relaxation of PS has been studied by MD to facilitate a one-to-one comparison with the experimentally measured one (DS and rheology). The long-time chain relaxation of PS chains precludes a prediction through brute force all-atom MD simulations because of the very long relaxation times, especially at the lower temperatures. Therefore, for the chain dynamics we have used a hierarchical scheme that combines atomistic and CG MD simulations. As discussed before, CG MD simulations are much faster than atomistic ones, and the CG time-scale has to be calibrated by all atom simulations or experiment. Through such a time-mapping of CG dynamics on the atomistic one, CG data can be directly compared to experimental or atomistic simulation data.[34] We have followed the above-described procedure in order to calculate the longest relaxation time for the PS chain. Specifically, we determine the time-mapping factor based on mean-square displacement, MSD, of center-of-mass (or of segments) on the atomistic level compared to the CG level. In Figure 5 we show a typical MSD plot for the motion of center-of-mass, $g_3(t) = \langle (R_{cm}(t) - R_{cm}(0))^2 \rangle$, with $\langle\ \rangle$ denoting ensemble average, from atomistic (squares) and CG scaled (line) data, for a specific PS melt (T = 463 K, P = 1 atm). As we can see, the agreement between the two sets of data is excellent for all times above about 300 ps and lengths of a few Å. Next, all CG dynamic quantities for this specific system are scaled to this factor. Qualitatively similar is the situation for different T, P conditions. Note that as we show elsewhere the scaling factor is the same if the MSD of center-of-mass or of the individual beads is used.[34]

Subsequently, the autocorrelation factor of the first normal mode is described by the KWW function that provides with the maximum (Rouse) relaxation time, τ_R, for the PS chain.[2,20] The thus obtained, τ_R, from the CG MD simulations are included in Figure 4b. Within the investigated temperature range, τ_R has a similar temperature dependence with the segmental relaxation times. Furthermore, τ_R is, as expected, larger than the dihedral relaxation time by a factor of 3−5. The reason is the rather short chain length, i.e., a 18mer PS consists of only 36 backbone atoms.

The thus obtained MD relaxation times can now be compared to the experimental ones. On the experimental

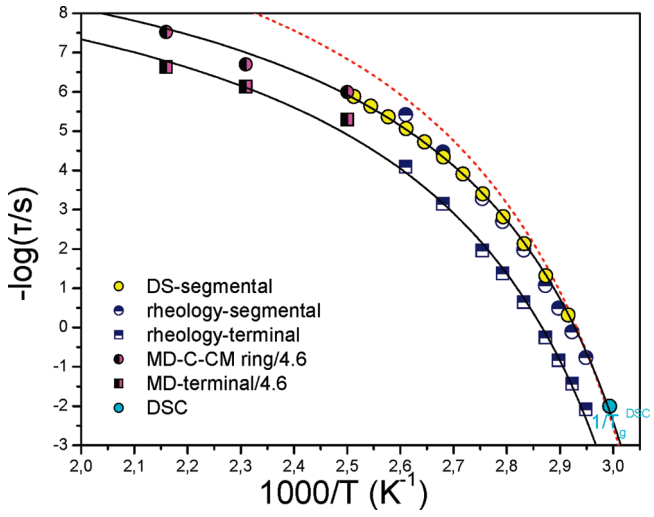


Figure 6. Compilation of the relaxation times through MD corresponding to the C−CM ring vector (vertical half-filled symbols), DS (filled circles in yellow), DSC at τ = 100 s (filled circle in blue) and rheology (horizontal half-filled symbols) at the different temperatures investigated. The latter times were scaled to the DS and DSC T_g (see text). The MD and DS times correspond to the $P_1(t)$ time-autocorrelation functions (see text). Only the segmental (circles) and the terminal (squares) relaxation times are shown. The solid lines are the result of the fit to the VFT equation. The dashed line is the T_g-scaled VFT obtained by NMR.

side, rheology provides with both the segmental and terminal times. The frequency scale shift factor, a_T, was applied to the master-curve (Figure S2, Supporting Information), resulting to the T-dependence of the two characteristic frequencies, ω_S and ω_c, corresponding to the segmental and chain dynamics, respectively. These frequencies correspond to the crossing of the storage and loss moduli (ω_S) and to the crossing of lines with slopes 2 and 1, respectively (ω_c) corresponding to the terminal regime. The dynamics extracted from rheology is compared to the one from DS and the simulations in Figure 6. First, in comparing the rheology and dielectric times we find that the crossing of the storage and loss moduli for the segmental relaxation process (Figure S2, Supporting Information) occurs at lower frequencies as compared to the dielectric loss maximum. Parenthetically, the electric modulus representation, $M^*(\omega) = 1/\varepsilon^*(\omega)$, is more suitable when comparing rheology with DS relaxation times, however, the low dielectric activity of PS makes the peak frequency in ε'' and M'' nearly indistinguishable. Thus, the reason for the faster segmental dynamics as probed by rheology is not the different representation. This suggests that for PS, dynamic mechanical and dielectric spectroscopies, performed on the same sample, are sensitive to different kinds of motion. Indeed, dielectric relaxation is probing the response of the dipolar units to the external electric field whereas rheology is affected by the way the underlying molecular motion couples to the applied stress. Thus, the two times need not be the same.

Since the purpose of the present investigation is to make a one-to-one comparison of the dipolar relaxation being perpendicular to the backbone with the relaxation of the C−CM vector obtained in MD, in Figure 6 the rheology times have been scaled to the DS and DSC T_g. This facilitates the comparison with the terminal dynamics as studied by MD (the latter for the C−CM ring autocorrelation function) and rheology. The Figure includes the DSC glass temperature (assuming isochronal at $\tau\sim$100 s). We found that the MD relaxation times, using the $P_1(t)$ curves, follow qualitatively very well the temperature dependence found by DS (again $P_1(t)$) but a quantitative comparison reveals that MD relaxation times are slower than DS by a factor of about 4.6. This discrepancy can have different origins. First, the molecular weights of the sample used in MD and DS are not identical. An 18mer has a somewhat larger molecular weight that the one investigated experimentally, and to the extent that the segmental dynamics are influenced by the mobile chain-ends this can result in faster experimental dynamics. The Rouse times (relaxation time of the first normal mode) would deviate by a factor of about almost 1.4. In addition the natural abundance of very short fragments in polydisperse samples leads to larger local mobilities. The effect of the different molecular weight and of polydispersity will be a subject of a future work. Second, the all-atom model, used in this work, has been developed[38] through parametrization of (a) quantum calculations of very small fragments (the intramolecular bonded interactions) and (b) fittings of the intermolecular nonbonded interactions in order to reproduce the experimental density (at 1 atm) and heat of vaporization of liquid benzene. If we consider the difference between the density values of the *NPT* MD PS simulations and experimental data (density by the AA force field is about 3−4% larger than the experimental one) then it seems that the latter procedure, i.e. the extension of the benzene nonbonded interaction parameters to PS melts, is the most problematic one. In order to test this hypothesis we have performed a few test atomistic NPT MD runs, with a modified all-atom model in which the minimum of the cohesive intermolecular energy between all atoms (the corresponding ε_C, and ε_H in the Lennard-Jones parameters) were decreased about 15%, in order the density of the NPT MD simulations of the PS 18mer system to match the experimental density (at 1 atm). This result, as expected, into faster segmental relaxation times of about 3 times, thus the new MD relaxation times, are slower than the DS with a factor of only 1.5, which compares well to the one expected from the different chain lengths. However, since we do not have any solid basis on the physical reason for the modified all-atom model and the goal of the present work is not to develop a new all-atom PS force field, we decide here to report data from the original atomistic model. In overall, taken into account the approximations of such parametrizations in atomistic force fields, and also that there is no adjustment of the model to any dynamical quantity, it is not surprising that the MD relaxation times are somewhat larger than the experimental times and the agreement, and here especially the temperature dependence is very good. Lastly, the experimental times are influenced by the strong ionic conductivity, due to impurities—a dynamic process that is not affecting MD—and thus cause also some uncertainty to the experiment (about the symbol size). Nevertheless, this factor seems to be independent of temperature and pressure. Therefore, we present the MD data here scaled by this factor. This facilitates the comparison of terminal relaxation times obtained from rheology with the longest Rouse time obtained from MD simulations. The nonscaled MD data can be found in the Supporting Information (Figure S3).

The temperature dependence of both time-scales can also be described by the Vogel−Fulcher−Tammann (VFT) equation:

$$\tau_c = \tau_o \exp\left(\frac{B}{T - T_0}\right) \tag{8}$$

where τ_0 is the relaxation time calibration constant in the limit of very high temperatures, B is a generalized activation energy and T_0 is the Vogel temperature known as the "ideal" glass temperature "zero temperature" where all relaxation times diverge. The combined DSC, DS, rheology and MD data for the segmental process result to $\tau_0 = (5 \pm 2)\text{x}10^{-11}$s, B = 1040 ± 80 K and T_0 = 298 ± 2 K. These parameters are somewhat different than the ones obtained earlier for the segmental relaxation of atactic PS (M = 2100g/mol) through various NMR experiments and MD simulations covering a broad T-range from 390 to 510 K[17]

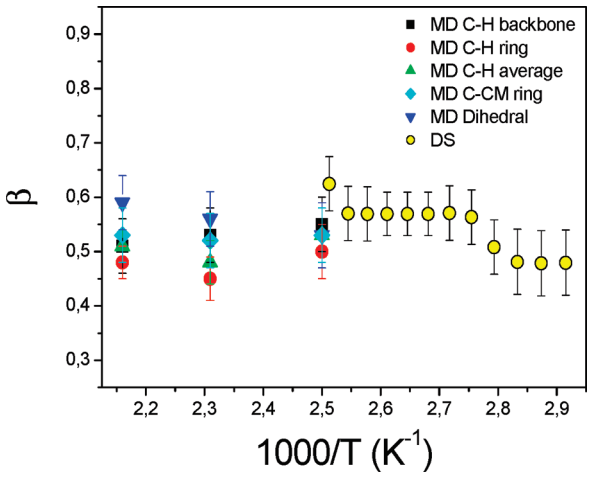


Figure 7. KWW stretch exponent, β, obtained through the different $P_1(t)$ curves (MD) and calculated in DS plotted as a function of temperature.

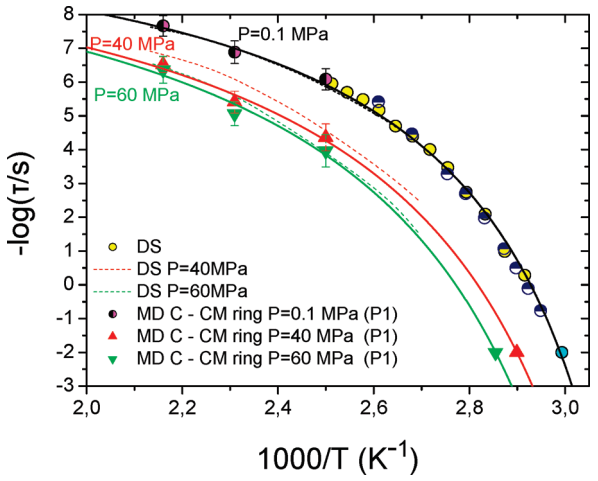


Figure 8. Pressure dependence of the segmental relaxation times obtained from MD (C−CM ring vector) at 0.1, 40, and 60 MPa. The different symbols for the relaxation times at 0.1 MPa are the same as in Figure 6. The points at τ = 100s are obtained through *PVT* (by assuming that the glass temperature is isochronal). The solid lines are the result of the fit to the VFT equation. The dashed black, red and green lines are literature[42] T_g-scaled dielectric relaxation times measured at 0.1 MPa and calculated at 40 and 60 MPa, respectively.

(shown by the dotted line in Figure 6). The latter times are faster on the high temperature side (the NMR times were scaled to the current T_g), but this is not surprising given that they present $P_2(t)$ correlation times ($\tau_2 \sim \tau_1/3$). On the other hand, the combined data for the terminal relaxation (rheology, MD) result to very similar values: $\tau_0 = (2 \pm 1) \times 10^{-10}$ s, $B = 1150 \pm 20$ K, and $T_0 = 298 \pm 2$ K. We are aware that higher molecular weight polymers, show different T-dependencies for the segmental and terminal relaxations in the vicinity of T_g.[47−50] This is not evident here, probably because of the low molecular weight.

In Figure 7, the KWW exponent, β, of the different autocorrelation functions is plotted as a function of temperature and compared with the one obtained experimentally (DS). In all cases, β is considerably lower than 1, thus indicating a broad distribution of relaxation times. The KWW exponent of the autocorrelation function for the C−H bonds, β_{C-H}, varies between 0.45 to 0.55. The stretching exponent is independent of temperature. The C−CM ring values are also in very good agreement with β_{DS}, the latter extracted from the HN shape parameters as described earlier. The β_{C-H} values depend only slightly on the position of the C−H bonds, being somewhat the β_{C-H} values for the backbone C−H bonds. The latter could be attributed to the additional relaxation mechanism of the C−H bonds in the phenyl ring, related with the orientational motion of the ring. Values for the KWW exponent of the dihedral autocorrelation function, β_d, vary between 0.5 and 0.6, being higher than the β_{C-H} ones. This is not surprising, since for the C−H bonds additional relaxation mechanisms (such as bond vibrations, angle librations, phenyl ring motions) play a more significant role than for the relaxation of the backbone dihedral leading to a broader distribution of relaxation times. Furthermore, there seems to be a weak dependence of β_d on temperature; i.e., β_d decreases with decreasing temperature. Note also the large error bars of the β values, especially at lower temperatures, due to limited time-window available. Finally it should be stated, that values of both β_{C-H} and β_d presented here are typical for amorphous polymers and in agreement with data reported in the literature by other MD simulations of polystyrene[15,26,27] and other polymers like polyethylene[12,20] and polybutadiene.[22]

4.4. Pressure Dependence of Segmental Dynamics. In this section we present the first results on the effect of pressure on the segmental dynamics of PS by means of MD simulations, performed at experimental density (see Figure 1) at two elevated pressures (40 and 60 MPa). Computationally, this is not a trivial task since at elevated pressures the segmental dynamics are slowed-down as a result of densification. In addition, the presence of higher conductivity makes pressure-dependent DS measurements a difficult task for this sample. To overcome these problems we use a combination of experimental *PVT* $T_g(P)$ dependencies (Figure 1) together with the simulation data at two pressures, 40 and 60 MPa.

As mentioned above the $P_2(t)$ autocorrelation curves of various C−H bond vectors as well as the C−CM ring vector at elevated pressures show the same structure as the curves at the atmospheric pressure, discussed in section 4.2. In Figure S4 (Supporting Information), we present such curves for the C−CM ring vector at T = 463 K. From these curves the relaxation times at elevated pressures can be calculated following the analysis presented before (see section 4.2). In Figure 8 the segmental relaxation times obtained through the all-atom MD simulations are shown together with the *PVT* times (the assumption here is that T_g is "isochronal" at 100 s). As expected, increasing pressure slows-down the segmental dynamics and increases the glass temperature. Despite the few experimental points, the MD and *PVT* $\tau(T)$ data span more than 8 orders of magnitude.

The combined $\tau(T)$ times at elevated pressures are described by the same VFT equation for the different isobars (shown in Figure 8 with the solid lines). In addition, we display literature[42] DS segmental relaxation times at elevated pressures from a PS with M_w = 780 g/mol. Following a T_g-scaling of the dynamics to account for the difference in molecular weights the interpolated segmental relaxation times at the investigated pressures are also shown in Figure 8 with the dashed lines. Note that there is a near quantitative agreement between the MD simulation and DS results.

Segmental relaxation times calculated from the VFT parameters at different temperatures and pressures are shown in Figure 9. Intrinsic to the pressure dependence of segmental relaxation times is information that relates to the apparent activation volume.[51] The latter quantity, $\Delta V^{\ddagger} = 2.303RT(\partial[\log \tau]/\partial P)_T$), represents the pressure sensitivity of the segmental relaxation times and was originally interpreted as reflecting the difference in molar volumes of activated and nonactivated species.[52,53,54] $\Delta V^{\ddagger}$ can be extracted from the slopes of the "isothermal"

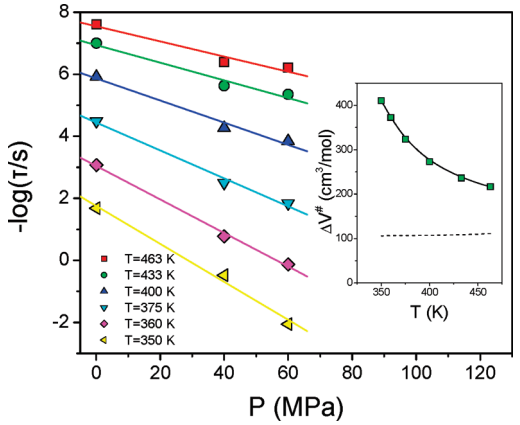


Figure 9. Pressure dependence of the segmental relaxation times calculated from the VFT parameters at different temperatures as indicated. In the inset, the apparent activation volume is obtained and plotted as a function of temperature. The dashed line is the monomer volume.

representation (inset to Figure 9). Several experimental studies[45,47,55,56] on glass-forming systems probed the temperature dependence of the apparent activation volume; $\Delta V^{\ddagger}$ has a strong T-dependence, increasing by decreasing temperature toward the glass temperature. At the same time the high temperature values of $\Delta V^{\ddagger}$ approach the monomer volume at some 70−100 K above the glass temperature. In the inset of Figure 9 the monomer volume, in cm^3/mol (calculated from the PVT density data of Figure 1), is shown with dash line for all temperatures studied here (at P = 0.1 MPa). Herein the obtained values do show the expected increase at lower temperatures, but the limiting values at higher temperatures are still above the monomer volume, probably because of the limited accuracy of the VFT parameters.

5. Conclusions

The segmental and terminal dynamics of a-PS have been investigated by hierarchical simulation methodologies and experiments at atmospheric and, for the first time, at elevated pressures. We have examined the polymer dynamics both at the submonomer and end-to-end distance level using a multiscale simulation approach that combines atomistic and coarse-grained dynamic simulations. We have also presented, for the first time, an investigation of the atactic PS dynamics as a function of pressure.

The detailed, all-atom MD simulations at atmospheric pressure, revealed that the various characteristic times corresponding to the decay of time-autocorrelation functions for various C−H bond vectors as well as of the C−CM ring bond can be different by nearly one decade but all share the same temperature dependence and have nearly the same distribution of relaxation times that is in agreement with the one obtained through dielectric spectroscopy. When the $P_1(t)$ times for the relevant C−CM ring bond were compared to the dipolar dynamics obtained though dielectric spectroscopy they were found to be slower by a factor of about 4.6. That could be accounted for by various factors, involving differences between PS model systems and experimental samples as well as approximations in the parametrization of the atomistic force field. When the MD data were scaled by this factor toward the DS times, the predicted terminal dynamics were in excellent agreement with the ones obtained by rheology.

MD simulations were also performed at elevated pressures using the experimental equation-of-state as a guide. As expected, as the pressure increases the segmental dynamics slows-down and the glass temperature increases. The obtained temperature dependence of relaxation times and the associated glass temperatures at the two elevated pressures investigated were also found to be in good agreement with the experimentally measured glass temperature and allowed extracting the apparent activation volume as a function of temperature.

Acknowledgment. We thank H. W. Spiess, B. Dünweg and D. Fritz for helpful discussions. We thank A. Best and A. Hanewald for the PVT and rheology measurement, respectively.

Supporting Information Available: Plots of dielectric loss spectra, storage and loss shear moduli, compilation of the relaxation times, and $P_2(t)$ time-autocorrelation functions. This material is available free of charge via the Internet at http://pubs.acs.org.

References and Notes

(1) Ferry, J. D. *Viscoelastic Properties of Polymers*; John Wiley and Sons: New York, 1980.
(2) Doi, M.; Edwards, S. F. *The Theory of Polymer Dynamics*; Claredon Press: Oxford, England, 1986.
(3) *Simulation Methods for Polymers*; Theodorou, D. N., Kotelyanski, M., Eds.; Marcel Dekker: New York, 2004.
(4) Baschnagel, J.; Binder, K.; Doruker, P.; Gusev, A. A.; Hahn, O.; Kremer, K.; Mattice, W. L.; Müller-Plathe, F.; Murat, M.; Paul, W.; Santos, S.; Suter, U. W.; Tries, V. *Adv. Polym. Sci.* **2000**, *152*, 41.
(5) Kremer, K.; Peter, C. *Faraday Discuss.* **2010**, *144*, 9.
(6) Floudas, G.; Mpoukouvalas, K.; Papadopoulos, P. *J. Chem. Phys.* **2006**, *124*, 074905.
(7) Tölle, A.; Schober, H.; Wuttke, J.; Randl, O. G.; Fujara, F. *Phys. Rev. Lett.* **1998**, *80*, 2374.
(8) Dreyfus, C.; Aouadi, A.; Gapinski, J.; Matos-Lopes, M.; Steffen, W.; Patkowski, A.; Pick, R. M. *Phys. Rev. E* **2003**, *68*, 011204.
(9) Casalini, R.; Roland, C. M. *Phys. Rev. E* **2004**, *69*, 062501.
(10) Alba-Simionseco, C.; Cailliaux, A.; Alegria, A.; Tarjus, G. *Europhys. Lett.* **2004**, *68*, 58.
(11) Roland, C. M.; Hensel-Bielowka, S.; Paluch, M.; Casalini, R. *Rep. Prog. Phys.* **2005**, *68*, 1405.
(12) Pant, P. V. K.; Han, J.; Smith, G. D.; Boyd, R. H. *J. Chem. Phys.* **1993**, *99*, 597.
(13) Bharadwaj, R. K.; Boyd, R. H. *Macromolecules* **2000**, *33*, 5897.
(14) Hotston, S. D.; Adolf, D. B.; Karatasos, K. *J. Chem. Phys.* **2001**, *115*, 2359.
(15) Smith, G. D.; Borodin, O.; Bedrov, D.; Paul, W.; Qiu, X. H.; Ediger, M. D. *Macromolecules* **2001**, *34*, 5192.
(16) Smith, G. D.; Borodin, O.; Paul, W. *J. Chem. Phys.* **2002**, *117*, 10350.
(17) He, Y.; Lutz, T. R.; Ediger, M. D.; Ayyagari, C.; Bedrov, D.; Smith, G. D. *Macromolecules* **2004**, *37*, 5032.
(18) Yang, L.; Srolovitz, D. J.; Yee, A. F. *J. Chem. Phys.* **1999**, *110*, 7058.
(19) Qiu, X.; Ediger, M. D. *Macromolecules* **2000**, 490.
(20) Harmandaris, V. A.; Mavrantzas, V. G.; Theodorou, D. N. *Macromolecules* **1998**, *31*, 7934. Harmandaris, V. A.; Mavrantzas, V. G.; Theodorou, D. N.; Kroeger, M.; Ramirej, J. O.; Oettinger, H. C.; Vlassopoulos, D. *Macromolecules* **2003**, *36*, 1376.
(21) Ahumada, O.; Theodorou, D. N.; Triolo, A.; Arrighi, V.; Karatasos, C.; Ryckaert, J. P. *Macromolecules* **2002**, *35*, 7110.
(22) Tsolou, G.; Harmandaris, V. A.; Mavrantzas, V. G. *J. Chem. Phys.* **2006**, *124*, 084906. Tsolou, G.; Harmandaris, V. A.; Mavrantzas, V. G. *Macromol. Theor. Simul.* **2006**, *15*, 381. Tsolou, G.; Harmandaris, V. A.; Mavrantzas, V. G. *J. Non-Newtonian Fluid Dyn.* **2008**, *152*, 184.
(23) Kirpatch, A.; Adolf, D. B. *Macromolecules* **2004**, *37*, 1576.
(24) Faller, R.; Müller-Plathe, F.; Doxastakis, M.; Theodorou, D. *Macromolecules* **2001**, *34*, 1436.
(25) Doxastakis, M.; Theodorou, D. N.; Fytas, G.; Kremer, F.; Faller, R.; Müller-Plathe, F.; Hadjichristidis, N. *J. Chem. Phys.* **2003**, *119*, 6883.
(26) Lyulin, A. V.; Michels, M. A. *J. Comput. Phys. Commun.* **2002**, *147*, 298. *Macromolecules* **2002**, *35*, 1463.
(27) Vorselaars, B.; Lyulin, A. V.; Michels, M. A. *Macromolecules* **2007**, *40*, 6001.
(28) Liu, J.; Wu, S.; Cao, D.; Zhang, L. *J. Chem. Phys.* **2008**, *129*, 154905.
(29) Kremer, K.; Grest, G. *J. Chem. Phys.* **1990**, *92*, 5097. León, S.; Van der Vegt, N.; Delle Site, L.; Kremer, K. *Macromolecules* **2005**, *38*, 8078.

(30) Bennemann, C.; Paul, W.; Baschnagel, J.; Binder, K. *J. Phys.: Condens. Matter* **1999**, *11*, 2179.
(31) Barbieri, A.; Prevosto, D.; Lucchesi, M.; Leporini, D. *J. Phys.: Condens. Matter* **2004**, *16*, 6609.
(32) Tschöp, W.; Kremer, K.; Batoulis, J.; Buerger, T.; Hahn, O. *Acta Polym.* **1998**, *49*, 61. **1998**, *49*, 75.
(33) Harmandaris, V. A.; Reith, D.; Van der Vegt, N. F. A.; Kremer, K. *Macromol. Chem. Phys.* **2007**, *208*, 2109. Harmandaris, V. A.; Adhikari, N. P.; Van der Vegt, N. F. A.; Kremer, K.; Mann, B. A.; Voelkel, R.; Weiss, H.; Liew, CheeChin. *Macromolecules* **2007**, *40*, 7026.
(34) Harmandaris, V. A.; Kremer, K. *Macromolecules* **2009**, *42*, 791. Harmandaris, V. A.; Kremer, K. *Soft Matter* **2009**, *5*, 3920.
(35) Fritz, D.; Harmandaris, V. A.; Kremer, K.; Van der Vegt, N. F. A. *Macromolecules* **2009**, *42*, 7579.
(36) *Broadband Dielectric Spectroscopy*; Kremer, F., Schönhals, A., Eds; Spinger: Berlin, 2002.
(37) Alvarez, F.; Alegria, A.; Colmenero, J. *Phys. Rev. B.* **1991**, *44*, 7306.
(38) Müller-Plathe, F. *Macromolecules* **1996**, *29*, 4782.
(39) Hess, B.; Kutzner, C.; van der Spoel, D.; Lindahl, E. *J. Chem. Theor. Comput.* **2008**, *4*, 435–447.
(40) Baig, C.; Harmandaris, V. A. *Macromolecules* **2010**, *43*, 3156.
(41) Limbach, H. J.; Arnold, A.; Mann, B. A.; Holm, C. *Comput. Phys. Commun.* **2006**, *174*, 704; see also: http://www.espresso.mpg.de/.
(42) Schwartz, G. A.; Colmenero, J.; Alegria, A. *J. Non-Cryst. Solids* **2007**, *353*, 4298.
(43) Simon, F. E.; Glatzel, Z. *Z. Anorg. Allg. Chem.* **1929**, *178*, 309.
(44) Andresson, S. P.; Andersson, O. *Macromolecules* **1998**, *31*, 2992.
(45) Gitsas, A.; Floudas, G. *Macromolecules* **2008**, *41*, 9423.
(46) McQuarie, D. A. *Statistical Mechanics*; University Science Books: New York, 2000.
(47) Mpoukouvalas, K.; Gomopoulos, N.; Floudas, G.; Herrmann, C.; Hanewald, A.; Best, A. *Polymer* **2006**, *47*, 7170.
(48) Plazek, D. J.; Schlosser, E.; Schönhals, A.; Ngai, K. L. *J. Chem. Phys.* **1993**, *98*, 6488.
(49) Schönhals, A. *Macromolecules* **1993**, *26*, 1309.
(50) Nicolai, T.; Floudas, G. *Macromolecules* **1998**, *31*, 2578.
(51) Floudas, G.; Reisinger, T. *J. Chem. Phys.* **1999**, *111*, 5201.
(52) Floudas, G. In *Broadband Dielectric Spectroscopy*; Kremer, F., Schönhals, A.; Eds.; Springer: Berlin, 2002.
(53) Glasstone, S. T., Leidler, K. J., Eyring, H. *Theory of rate process* McGraw-Hill: New York, 1941.
(54) Williams, G. *Trans. Faraday Soc.* **1964**, *60*, 1548.
(55) Floudas, G.; Gravalides, C.; Reisinger, T.; Wegner, G. *J. Chem. Phys.* **1999**, *111*, 9847.
(56) Mpoukouvalas, K.; Floudas, G.; Williams, G. *Macromolecules* **2009**, *42*, 4690.

Macromolecules
ARTICLE

Macromolecules **2011**, *44*, 403–412 **403**
DOI: 10.1021/ma102308q

Mean Span Dimensions of Ideal Polymer Chains Containing Branches and Rings

Yanwei Wang,*,† Iwao Teraoka,‡ Flemming Y. Hansen,§ Günther H. Peters,§,∥ and Ole Hassager†

†*Danish Polymer Center, Department of Chemical and Biochemical Engineering, Technical University of Denmark, DK-2800 Kgs. Lyngby, Denmark,* ‡*Department of Chemical and Biological Sciences, Polytechnic Institute of New York University, 333 Jay Street, Brooklyn, New York 11201, United States,* §*Department of Chemistry, Technical University of Denmark, DK-2800 Kgs. Lyngby, Denmark, and* ∥*MEMPHYS-Center for Biomembrane Physics, DK-2800 Kgs. Lyngby, Denmark*

Received October 8, 2010; Revised Manuscript Received December 10, 2010

ABSTRACT: We present a general method for calculating the mean span dimension of various branched and ringed polymers under the assumption of Gaussian chain statistics. The method allows a routine construction of an integral expression of the mean span dimension based on three base functions, determined for a connector, an arm and a loop, respectively. Applications of our method are shown to a variety of polymer architectures including star, two-branch-point, comb and various cyclic chains (eight-shaped, Θ-shaped and several semicyclic chains). Comparing the mean span dimension with other commonly used molecular size parameters—the radius of gyration and the hydrodynamic radius, it is found that both the mean span dimension and the hydrodynamic radius shrink less than does the radius of gyration when comparing averaged sizes of a branched chain with its linear analogue. Finally, possible use of the mean span dimension in size exclusion chromatography (SEC) experiments is discussed.

1. Introduction

Size is an important parameter in our understanding and prediction of physical properties and behavior of polymers. For instance, size exclusion chromatography (SEC), a major tool in polymer characterization, separates macromolecules by their size in dilute solution.[1] To predict the elution order of topologically different polymers, it is essential to know their respective sizes.[2] Furthermore, as there exist different measures for the size of a polymer chain, it is necessary to know which size parameter is relevant to SEC.[3−12]

The focus of this paper is on the mean span dimension. It is defined as the mean maximum projection of the outlines of a polymer molecule on an axis. Interest in the mean span dimension as a size parameter for polymer chains, or random walks, arises from various sources including an equilibrium theory of SEC,[4−8] the range of entropic depletion of polymers near a hard wall,[13−15] as well as general random walk theory,[16,17] multiparticle Brownian motion,[18,19] and extrema statistics.[20,21] In particular, it is known, at least from an equilibrium theory,[4] that the mean span dimension is more relevant than the radius of gyration or the hydrodynamic radius to the equilibrium partitioning of topologically different polymer chains in small pores.[7,8] In the case of polymer depletion near a flat surface, the range of the depletion zone caused by steric exclusion (i.e., the depletion layer thickness) is found to be one-half of the mean span dimension.[15] Those findings underlie the importance of the mean span dimension as a size parameter for polymers.

Since the pioneering work of Daniels[16] and Kuhn[22] in the 1940s, considerable effort has been made to estimate the mean span dimensions of polymer chains. Assuming ideal Gaussian chain statistics, results have been obtained for several different polymer architectures including linear,[16,22−24] symmetric star,[5,6,25] ring,[26] and other cyclic topologies.[27,28] The existing method for calculating the mean span dimension is mostly from the limiting universal behavior of the equilibrium partition coefficient in wide pores,[8,27,28] which may be elaborate for topologically complex architectures. This situation motivates us to present a new, simple approach.

This paper is organized as follows. Section 2 presents our method, which is applied in section 3 to a variety of polymer architectures. In section 4, we compare the mean span dimension with other size parameter in terms of the branching indices and also discuss possible use of the mean span dimension in SEC experiments. As our method gives the mean (first moment) of the span without finding its distribution function, we provide in Appendix A an approach to obtain the distribution function of the span dimension.

2. Methodology

2.1. Preliminary. For a polymer chain in free solution, statistical properties of the span dimension are equal in all directions. Therefore, one may concentrate only on one direction, for instance, the x direction in an XYZ Cartesian coordinate system. Let x_i (i = 1, 2, ...) denote the x component of the position vector of the i-th segment in the chain. The span dimension in the x direction, denoted by X, is defined as

$$X = \max_i(x_i) - \min_i(x_i) \tag{1}$$

where $\max_i(...)$ and $\min_i(...)$ are respectively the maximum and minimum of x_i with i being the running index. The span dimension can be separated into two one-sided span components, α_o and β_o, corresponding to the $-x$ and x directions

*Corresponding author. E-mail: wangyanwei@gmail.com.

© 2010 American Chemical Society

Published on Web 12/27/2010

from the oth segment, a reference, in the chain. α_o and β_o are given by

$$\alpha_o = x_o - \min_i(x_i) \tag{2}$$

$$\beta_o = \max_i(x_i) - x_o \tag{3}$$

It follows from the isotropy argument that

$$\langle\alpha_o\rangle = \langle\beta_o\rangle = \frac{1}{2}\overline{X} \tag{4}$$

where the angular bracket $\langle ...\rangle$ represents the ensemble average over the configuration space of a chain molecule. Following Kuhn's notation,[22] the symbol $\overline{X}$ ($\equiv\langle X\rangle$) is used for the mean span dimension. It is evident from eq 4 that the mean one-sided span dimension, $\langle\alpha_o\rangle$, or $\langle\beta_o\rangle$ does not depend on a specific choice of the reference segment.[15]

Suppose that a chain, of an arbitrary architecture, is placed with its o-th segment at distance x ($x > 0$) from the confining wall at $x = 0$. The chain would take many different configurations in the absence of the wall. However, with the wall present, some configurations may be intersected by the wall. Those being intersected need to be excluded from the configuration space of the bulk chain. Let $\rho_o(x)$ be the fraction of polymer configurations that are not intersected by the wall. From a simple geometric argument, we obtained[15]

$$\rho_o(x) = \langle H(x - \alpha_o)\rangle \tag{5}$$

where $H(x)$ is the Heaviside function. The $\rho_o(x)$ may be called "the probability of success in generating a chain with its o-th segment located at distance x from an absorbing wall", or "the depletion profile (equilibrium density relative to bulk) of the oth segment of the chain". It is also the cumulative distribution function of the one-sided span α_o for a polymer chain in free space.

The depletion layer thickness, δ, which describes the range of a step function such that it excludes exactly the same amount of polymer as the true density profile, is given by

$$\delta = \int_0^\infty [1 - \rho_o(x)]\,dx \tag{6}$$

Inserting eq 5 into 6 leads to[15]

$$\delta = \langle\alpha_o\rangle \tag{7}$$

We emphasize that both eqs 4 and 7 hold for an arbitrary choice of the reference segment o, regardless of details in chain architecture and configuration statistics.

Assuming ideal Gaussian chain statistics for any linear part of the polymer molecule, the depletion profile can be obtained by solving the diffusion equation subject to an absorbing boundary.[4,29] This method may be useful for some simple chain architectures[13,14] but not for more complex structures. Alternatively, since $\rho_o(x)$ is a probability, we consider the multiplication rule as is done in the following.

2.2. Multiplication Rule and Base Functions. In general, a chain molecule consists of three types of fundamental subchains (FSCs), namely, a connector, an arm and a loop. For example, Figure 1 shows a chain molecule consisting of a connector, two arms and a loop. By definition, an FSC does not contain any branch unit (i.e., a chain segment with more than two neighboring segments). Both a connector and an arm are linear paths; the difference is that a connector does not contain chain ends (i.e., segments with only one neighbor) while an arm does. A loop does not contain any end segment, and its path is closed.

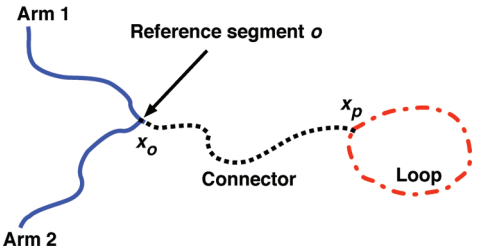


Figure 1. Complex chain consisting of two arms (Arm 1, Arm 2), a connector, and a loop. The chain contains two branch units located at x_o and x_p, respectively. The linestyles are solid for an arm, dotted for a connector and dash-dotted for a loop.

For ideal chains, the probability of success in generating one FSC in the presence of a wall is independent of other FSCs, and the success probability of generating a full chain is simply the product of success probabilities for each individual FSCs (the multiplication rule for independent events). Suppose we choose for the chain in Figure 1 the branch unit located at x_o ($x_o > 0$) as a reference segment. The success probability for generating such a chain configuration in the presence of an absorbing wall at $x = 0$ can be written as

$$\rho_o(x_o) = P_{\mathrm{Arm1}}(x_o, n_{a1})P_{\mathrm{Arm2}}(x_o, n_{a2}) \int_0^{+\infty} P_{\mathrm{Connector}}(x_o, x_p, n_c)P_{\mathrm{Loop}}(x_p, n_l)\,dx_p \tag{8}$$

Here, $P_{\mathrm{Arm1}}(x_o,n_{a1})$ and $P_{\mathrm{Arm2}}(x_o,n_{a2})$ are the success probabilities in generating Arm1 and Arm2 with n_{a1} and n_{a2} segments, respectively, from the reference point at x_o; $P_{\mathrm{Connector}}(x_o,x_p,n_c)\,dx_p$ is the success probability for generating a connector of n_c segments that starts from x_o and ends between x_p and $x_p + dx_p$; $P_{\mathrm{Loop}}(x_p,n_l)$ is the success probability of generating the loop of n_l segments starting from x_p.

In the following, we determine the success probability for each of the three FSCs. As in eq 8, they are base functions that constitute the success probability of the entire chain. For simplicity, we consider throughout this paper polymer chains consisting of identical segments of root-mean-square segment length b. A parameter p is introduced as

$$p \equiv p(n) = \sqrt{\frac{3}{2nb^2}} \tag{9}$$

2.2.1. Connector. The success probability of a connector can be obtained using the method of mirror images.[30] It is well-known that the success probability in generating a random walk in an infinite space that begins at x and ends at a point between x' and $x' + dx'$ after n steps of size b is given as[31]

$$P_{\mathrm{Free\ Space}}(x, x', n)\,dx' = \frac{p}{\pi^{1/2}}\exp[-p^2(x' - x)^2]\,dx' \tag{10}$$

Consider the problem in a semi-infinite domain ($x > 0$) with an absorbing plane boundary at $x = 0$. To find the success probability, we place hypothetically a negative source of unit strength at $-x$, which gives

$$P_{\mathrm{Mirror\ Image}}(x, x', n)\,dx' = -\frac{p}{\pi^{1/2}}\exp[-p^2(x' + x)^2]\,dx' \tag{11}$$

The true solution that satisfies the absorbing boundary condition is the sum of the real and image solutions. Thus, one finds the success probability of generating a connector, that begins at x and ends between x' and $x' + dx'$ after n steps in the presence of the absorbing boundary, to be[14]

$$P_{\text{Connector}}(x,x',n)\,\mathrm{d}x' = \frac{p}{\pi^{1/2}} H(x')\{\exp[-p^2(x'-x)^2] - \exp[-p^2(x'+x)^2]\}\,\mathrm{d}x' \quad (12)$$

where the Heaviside function $H(x')$ guarantees that $P_{\text{Connector}}(x, x',n) = 0$ for $x' < 0$.

2.2.2. Arm. Integrating $P_{\text{Connector}}(x,x',n)\,\mathrm{d}x'$ over all possible destinations x', one obtains the success probability for generating an arm of n segments beginning at distance x from the absorbing boundary at $x = 0$:

$$P_{\text{Arm}}(x,n) = \int_{-\infty}^{\infty} P_{\text{Connector}}(x,x',n)\,\mathrm{d}x' = \mathrm{erf}(px) \quad (13)$$

2.2.3. Loop. The probability of successfully generating a loop of n segments, starting from a point at a distance x from the boundary, without touching the boundary can be obtained using the conditional probability:

$$P_{\text{Loop}}(x,n) = \frac{\int_{-\infty}^{\infty} P_{\text{Connector}}(x,x',n)\delta(x'-x)\,\mathrm{d}x'}{\int_{-\infty}^{\infty} P_{\text{Free Space}}(x,x',n)\delta(x'-x)\,\mathrm{d}x'} \quad (14)$$

where the numerator and the denominator are the success probabilities in generating a connector that ends where it starts (i.e., a loop) in the presence of the boundary and in an infinite space, respectively. Inserting eq 10 and 12 into 14 leads to

$$P_{\text{Loop}}(x,n) = 1 - \exp[-4p^2x^2] \quad (15)$$

To summarize, we start with choosing a reference segment in a chain that divides the span dimension into two one-sided spans of equal statistical properties. The cumulative distribution function of any one-sided span, $\rho_o(x)$, can be constructed from the three base functions, $P_{\text{Connector}}(x,x',n)\,\mathrm{d}x'$, $P_{\text{Arm}}(x,n)$, and $P_{\text{Loop}}(x,n)$, determined for a connector, an arm and a loop, respectively. Detailed form of $\rho_o(x)$ and computational efforts may vary, depending on the choice of o, but the mean span dimension, given by

$$\overline{X} = 2\int_0^{\infty} [1 - \rho_o(x)]\,\mathrm{d}x \quad (16)$$

remains unchanged. A similar expression appeared in the work of Casassa and Tagami,[5] but was not generalized to arbitrary chain architectures. Using integration by parts, we may rewrite eq 16 as

$$\overline{X} = 2\int_0^{\infty} x\rho'_o(x)\,\mathrm{d}x \quad (17)$$

where $\rho_o'(x) \equiv \mathrm{d}\rho_o(x)/\mathrm{d}x$ is the probability density function of the one-sided span from the chosen reference.

3. Applications

We now apply the method to two categories of polymer topology, chains without a loop and cyclic polymers, as shown in Figure 2. Recent progress in polymer synthesis has unleashed different architectures of polymer chains having complex topological structures, and the architectures considered in this work have been realized.[32−34]

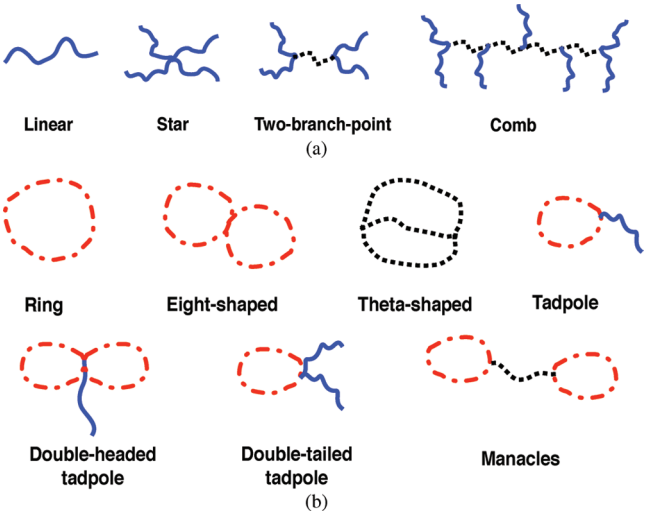


Figure 2. Polymer architectures considered in this work: (a) chains without a loop; (b) cyclic chains. See Figure 1 for linestyles.

3.1. Chains without a Loop. *3.1.1. A Linear Chain.* Consider a linear chain of N segments. The whole chain can be regarded as one arm if we choose one of the ends as the reference segment. Then,

$$\rho_o(x) = P_{\text{Arm}}(x,N) = \mathrm{erf}(px) \quad (18)$$

with $p = p(N)$, defined in eq 9. Inserting eq 18 into 16 leads to the mean span dimension for a linear chain

$$\overline{X} = \frac{2}{\pi^{1/2}p} = \sqrt{\frac{8Nb^2}{3\pi}} \quad (19)$$

This result was first obtained by Daniels in 1941.[16] Had the middle segment been chosen as the reference segment, $\rho_o(x) = P_{\text{Arm}}(x,N/2)^2$, and one obtains the same $\overline{X}$, but the derivation is more involved.

Comparing the mean span dimension to other commonly used molecular size parameters obtained for a linear ideal chain,[35] one obtains

$$\frac{\overline{X}}{2R_g} = \frac{2}{\sqrt{\pi}} \approx 1.1284, \qquad \frac{\overline{X}}{2R_H} = \frac{16}{3\pi} \approx 1.6976 \quad (20)$$

where R_g and R_H are the root-mean-square radius of gyration and the hydrodynamic radius, respectively.

3.1.2. Star Polymers. Consider a star polymer of f arms. Figure 2a shows a case of $f = 4$. Asymmetry may be allowed by assigning a different number of chain segments, N_i, to each of the f arms ($i = 1, 2, ..., f$). We choose the branch unit as our reference so that all the FSCs are arms. Then,

$$\rho_o(x) = \prod_i^f P_{\text{Arm}}(x,N_i) = \prod_i^f \mathrm{erf}(p_i x) \quad (21)$$

where we use p_i for the short-hand notation of $p(N_i)$. Differentiating $\rho_o(x)$ with respect to x gives

$$\rho_o'(x) = \frac{2}{\pi^{1/2}} \sum_{i=1}^{f} p_i \exp(-p_i^2x^2) \prod_{j\neq i}^{f} \mathrm{erf}(p_j x) \quad (22)$$

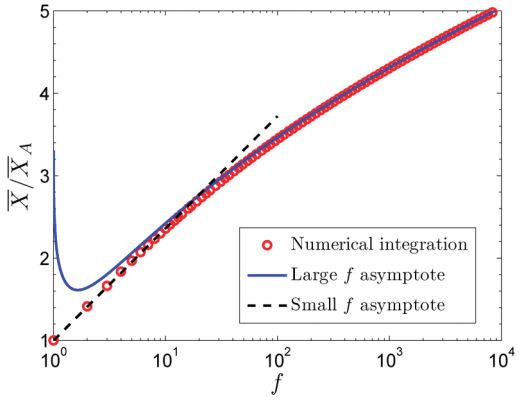


Figure 3. The mean span dimension, $\overline{X}$, of a symmetric star relative to that of a single arm, $\overline{X}_A$, is shown as a function of the total number of arms, f. The symbols represent results from numerical integration of eq 24. The large f and small f asymptotes are shown as solid and dashed lines, respectively.

According to eq 17, we have

$$\overline{X} = \frac{4}{\pi^{1/2}} \sum_{i=1}^{f} \left[p_i \int_0^\infty x \exp(-p_i^2 x^2) \prod_{j \neq i}^{f} \mathrm{erf}(p_j x)\, \mathrm{d}x \right] \quad (23)$$

For a symmetric star, $p_1 = p_2 = \ldots = p_f = p$, and eq 23 reduces to

$$\overline{X} = \frac{2f}{p\pi^{1/2}} \int_0^\infty [\exp(-t)\, \mathrm{erf}(t^{1/2})]^{f-1}\, \mathrm{d}t \quad (24)$$

where $t = p^2x^2$. This result was first obtained by Casassa and Tagami.[5,6] The integral in eq 24 may be easily evaluated by numerical integration. For large f, Sastry and Agmon obtained an approximation:[19]

$$\overline{X} \approx 2p^{-1} \sqrt{\ln f - \ln \sqrt{\kappa \ln f}} \quad (25)$$

where $\kappa = \pi[\mathrm{erf}(\pi^{-1/2})]^2 \approx 1.0$. Equation 25 contains a finite-f correction to the leading p^{-1} $(\ln f)^{1/2}$ dependence found earlier by Larralde et al.[36] It is interesting to compare eq 25 with the root-mean-square radius of gyration of a symmetric star polymer:[37]

$$R_g = (3 - 2/f)^{1/2} R_{g,A} \quad (26)$$

where $R_{g,A}$ $(= p^{-1}/2)$ is the radius of gyration of an arm. As $f \to \infty$, R_g converges to $3^{1/2}R_{g,A}$, while the mean span dimension keeps increasing as $\sim(\ln f)^{1/2}$.

Figure 3 compares eq 25 with the exact numerical integration, eq 24. Clearly, the approximation agrees well with the exact result when f is large (the difference is less than 3% for $f \geq 10$). Interestingly, Figure 3 shows that the mean span dimension depends linearly on In f for small f. We found that the following equation

$$\overline{X} \approx \frac{2}{p}\left(\frac{1}{3}\ln f + \frac{1}{\sqrt{\pi}}\right) \quad (27)$$

provides a good agreement with the exact numerical integration for $f \leq 10$.

To calculate $\overline{X}$ for $f = 3$ and 4, one can apply the integrals solved by Prudnikov et al.[38] In the case of symmetric stars,

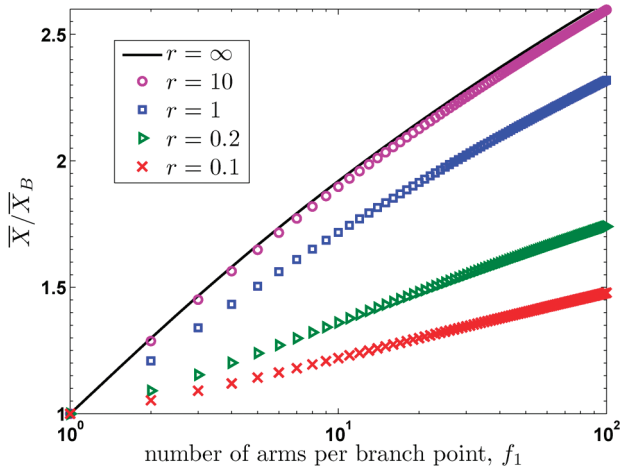


Figure 4. Mean span dimension, $\overline{X}$ of a symmetric two-branch-point polymer, relative to that of its backbone (consisting of $N_c + 2N_a$ segments), $\overline{X}_B$, is shown as a function of the number of arms per branch point, f_1. The symbols represent results from numerical integration with $r = N_a/N_c = 10$, 1, 0.2, and 0.1, respectively. The line denotes numerical results for symmetric stars (corresponding to $r = \infty$) of $2f_1$ arms.

we obtain for $f = 3$

$$\overline{X} = \frac{12\sqrt{2}}{\pi^{3/2}p} \arctan(2^{-1/2}) \quad (28)$$

and

$$\overline{X} = \frac{24\sqrt{2}}{\pi^{3/2}p} \arctan(2^{-3/2}) \quad (29)$$

for $f = 4$. Results for asymmetric 3- and 4-arm stars are provided in Appendix B. To the best of our knowledge, these results have not been derived earlier.

3.1.3. Two-Branch-Point Polymers. Consider a two-branch-point chain that has f_1 and f_2 arms from the two branch units 1 and 2, respectively, of a connector. Figure 2a shows a two-branch-point chain with $f_1 = f_2 = 2$, also known as an "H polymer". We assign a different number of segments, $N_{1,i}$ $(i = 1, 2, \ldots, f_1)$ and $N_{2,j}$ $(j = 1, 2, \ldots, f_2)$ to each of the $f_1 + f_2$ arms. The connector has N_c segments. Placing branch unit 1 at distance x_1 from the wall at $x = 0$ as the reference segment, the success probability of generating such a chain is given by

$$\rho_o(x_1) = \prod_{i=1}^{f_1} P_{\mathrm{Arm}}(x_1, N_{1,i}) \int_0^\infty P_{\mathrm{Connector}}(x_1, x_2, N_c) \prod_{j=1}^{f_2} P_{\mathrm{Arm}}(x_2, N_{2,j})\, \mathrm{d}x_2 \quad (30)$$

Once $\rho_o(x_1)$ is calculated, eq 16 gives $\overline{X}$.

As an example, we consider a symmetric case where $f_2 = f_1$, $N_{1,i} = N_{2,j} = N_a$ for all i and j. Let r be the ratio of the total number of segments of an arm to that of the connector, $r \equiv N_a/N_c$. For $r \to \infty$, the mean span dimension approaches that of a symmetric star with $2f_1$ arms, whereas for $r \to 0$, it approaches that of a linear chain with $N_c + 2N_a$ segments. These features are confirmed in Figure 4. Notice that as r decreases, the linear dependence of $\overline{X}$ on In f_1 extends to a larger value of f_1.

3.1.4. Comb Polymers. A comb polymer consists of a linear backbone to which linear side chains (branches) are attached

Table 1. Mean Span Dimension, $\overline{X}$, of Symmetric Comb Polymers with a Different Number of Branch Units, f[a]

f	$\overline{X}/p^{-1}$	$\overline{X}/\overline{X}_B$	g_s	g_H	g	$(g^{0.85})^{2/3}$
1	1.88	1.18	0.92	0.90	0.78	0.87
2	2.36	1.21	0.88	0.85	0.71	0.82
3	2.74	1.21	0.84	0.82	0.67	0.80
4	3.06	1.21	0.82	0.79	0.64	0.78
5	3.34	1.21	0.80	0.77	0.62	0.76
6	3.59	1.20	0.78	0.75	0.60	0.75
7	3.82	1.20	0.76	0.74	0.59	0.74
8	4.03	1.19	0.75	0.72	0.58	0.73
9	4.23	1.18	0.74	0.71	0.57	0.73

[a] $\overline{X}_B$ refers to the mean span dimension of the backbone, $\overline{X}_B = 2(f+1)^{1/2}/(\pi^{1/2}p)$ and $p = (3/(2Nb^2))^{1/2}$. g_s, g_H, and g are the branching indices defined for the mean span dimension, the hydrodynamic radius, and the radius of gyration, respectively.

by one end at various positions along the backbone. Figure 2a shows a comb with five branches.

It is straightforward to obtain integral expressions of the mean span dimension for comb polymers. However, due to the presence of many branch units, one needs to calculate multiple integral in order to obtain the value of $\overline{X}$. Such integrals may be solved effectively by Monte Carlo integration method, which we have not investigated further here. We limit ourselves to a regular case where all the arms and connectors contain the same number of segments, N. All the branch units are numbered consecutively from 1 to f with a total number of f branch units. We take the middle segment along the backbone (which is a linear path containing $(f+1)N$ segments) as our reference. For an odd f, the reference segment coincides with the No. $(f+1)/2$ branch unit. Then,

$$\rho_o(x_{(f+1)/2}) = P_{\mathrm{Arm}}(x_{(f+1)/2}, N)\left[\int_0^\infty \cdots \int_0^\infty P_{\mathrm{Connector}}(x_{(f+1)/2}, x_{(f-1)/2}, N) P_{\mathrm{Arm}}(x_{(f-1)/2}, N) \cdots P_{\mathrm{Connector}}(x_2, x_1, N) P_{\mathrm{Arm}}(x_1, N)^2 \, \mathrm{d}x_{(f-1)/2} \cdots \mathrm{d}x_1\right]^2 \quad (31)$$

For an even f, we have

$$\rho_o(x_o) = \left[\int_0^\infty \cdots \int_0^\infty P_{\mathrm{Connector}}(x_o, x_{f/2}, N/2) P_{\mathrm{Arm}}(x_{f/2}, N) P_{\mathrm{Connector}}(x_{f/2}, x_{f/2-1}, N) P_{\mathrm{Arm}}(x_{f/2-1}, N) \cdots P_{\mathrm{Connector}}(x_2, x_1, N) P_{\mathrm{Arm}}(x_1, N)^2 \, \mathrm{d}x_{f/2} \cdots \mathrm{d}x_1\right]^2 \quad (32)$$

Inserting the above two equations into 16 leads to the mean span dimension. Table 1 presents our numerical results for f up to 9. Also shown are the branching indices to be discussed in section 4. Although $\overline{X}$ increases as f increases, the ratio of the mean span dimension of the comb to that of the backbone, $\overline{X}_B$, remains nearly unchanged ($\approx$1.2), showing the bulkiness of the comb polymer around its backbone. This is an interesting result which largely simplifies the calculation of $\overline{X}$ for combs. However, as this ratio depends on the contour length of the backbone relative to that of an arm, further investigations are necessary to obtain useful approximations.

It is noteworthy that considerable progress has been made regarding conformational properties of comb polymers.[39−47] Of particular interest to this work are the studies by Lipson,[45,46] where it was shown that the Gaussian chain model is not as effective in modeling the metric properties of combs as it is with stars and H-polymers. Compared to available experimental data in both good and Θ solvent conditions,[10,48] the Zimm−Stockmayer branching index g and also the branch index for the hydrodynamic radius are notably underestimated by the Gaussian chain model, whereas results from Monte Carlo simulations of excluded volume chains show an excellent agreement.[45] The poor performance of the Gaussian chain model was attributed to its inadequacy in dealing with the effects of a branch unit which is magnified in the case of comb molecules by the presence of many of them. Furthermore, while the overall dimensions of the comb are reduced relative to that of a linear chain of the same number of segments, the backbone is expanded when the self-avoiding condition is incorporated.[46] Those results suggest the need to explore the span dimensions of self-avoiding combs and other branched architectures including stars and two-branch-point polymers of many arms. We will return to this discussion in section 4.

3.2. Cyclic Polymers. Loop-containing polymers are fascinating topological objects that can exist as single rings but also in the form of more complex structures. Examples considered here are shown in Figure 2b.

3.2.1. A Single Ring. Consider a single ring of N segments. For any choice of the reference segment o, we have

$$\rho_o(x) = P_{\mathrm{Loop}}(x, N) \quad (33)$$

With eq 15, we obtain

$$\overline{X} = 2\int_0^\infty \exp[-4p^2x^2] \, \mathrm{d}x = \frac{\pi^{1/2}}{2p} = \sqrt{\frac{\pi N b^2}{6}} \quad (34)$$

This result was first obtained by Rubin et al.,[26] but our derivation is much simpler.

Comparing the mean span dimension to other commonly used molecular size parameters obtained for an ideal ring,[49] one finds

$$\frac{\overline{X}}{2R_g} = \left(\frac{\pi}{2}\right)^{1/2} \approx 1.2533, \quad \frac{\overline{X}}{2R_H} = \frac{\pi}{2} \approx 1.5708 \quad (35)$$

Relative to the values obtained for a linear chain (cf. eq 20), the first ratio increases whereas the second one decreases.

3.2.2. Eight-Shaped Cyclic Chains. Consider an eight-shaped chain as shown in Figure 2(b). There are N_1 and N_2 segments on each of the two loops. Choosing the branch unit as our reference gives

$$\rho_o(x) = P_{\mathrm{Loop}}(x, N_1) P_{\mathrm{Loop}}(x, N_2) \quad (36)$$

Inserting eq 36 into 16 leads to

$$\overline{X} = \frac{\pi^{1/2}}{2}\left(\frac{1}{p_1} + \frac{1}{p_2} - \frac{1}{\sqrt{p_1^2 + p_2^2}}\right) \quad (37)$$

In the general case with f loop fragments (the so-called daisy-like polymer[27]), we have

$$\rho_o(x) = \prod_{i=1}^{f} P_{\mathrm{Loop}}(x, N_i) = \prod_{i=1}^{f} [1 - \exp(-4{p_i}^2x^2)] \quad (38)$$

Consider a symmetric case where $p_1 = p_2 = \ldots = p_f = p$. According to the binomial theorem, eq 38 reduces to

$$\rho_o(x) = \sum_{m=0}^{f} C_f^m (-1)^m \exp(-4mp^2x^2) \quad (39)$$

where $C_f^m = f!/[m!(f-m)!]$ is the binomial coefficient. Substituting eq 39 into 16 leads to

$$\overline{X} = \frac{\pi^{1/2}}{2}\left[\sum_{m=1}^{f}(-1)^{m-1}\frac{C_f^m}{\sqrt{m}}\right]\frac{1}{p} \tag{40}$$

This result was also obtained by Gorbunov and Vakhrushev from the universal behavior of the equilibrium partition coefficient in wide pores.[27] As a partial check, one finds that for $f = 1$, eq 40 reduces to eq 34, and for $f = 2$, eq 40 reduces to eq 37 with $p_1 = p_2 = p$.

An eight-shaped polymer of f loops may be obtained by closing every two ends of a symmetric $2f$-arm star polymer (each arm is half the length of the loop). Comparing the mean span dimension of an eight-shaped polymer of f loops of n segments to that of a symmetric star of $2f$ arms of $n/2$ segments (cf. Equations 40 and 24), we found that the ratio $\overline{X}_{\text{eight}}(f,n)/\overline{X}_{\text{star}}(2f,n/2)$ is exactly $\pi/4$ for $f = 1$ and barely changes as f increases.

3.2.3. Θ-Shaped Cyclic Chains. Consider a symmetric Θ-polymer, as shown in Figure 2b), with two branch units connecting three identical linear fragments of N segments. Choosing one of the branch units as a reference segment, we have

$$\rho_o(x_1) = C\int_{-\infty}^{\infty}[P_{\text{Connector}}(x_1, x_2, N)]^3\,dx_2 \tag{41}$$

$$= C\frac{p^2}{\sqrt{3}\pi}\left[\text{erf}(\sqrt{3}px_1) - 3\exp\left(-\frac{8}{3}p^2{x_1}^2\right)\text{erf}\left(\frac{px_1}{\sqrt{3}}\right)\right] \tag{42}$$

The prefactor C is determined from the normalization condition $\rho_o(\infty) = 1$. This gives

$$\rho_o(x_1) = \text{erf}(\sqrt{3}px_1) - 3\exp\left(-\frac{8}{3}p^2{x_1}^2\right)\text{erf}\left(\frac{px_1}{\sqrt{3}}\right) \tag{43}$$

Inserting eq 43 into 16 leads to

$$\overline{X} = \frac{2}{p\sqrt{3\pi}}\left[1 + \frac{9\sqrt{2}}{4}\arctan\left(\frac{\sqrt{2}}{4}\right)\right] \tag{44}$$

This result is in agreement with that obtained by Vakhrushev et al. from the universal behavior of the equilibrium partition coefficient in wide pores.[28] In the general case where the two branch units connect f identical linear fragments, we obtain for an even f:

$$\overline{X} = \frac{\sqrt{f}}{4p\sqrt{\pi}}\sum_{m=1}^{f-1}\frac{C_f^m(-1)^{m-1}}{\sqrt{(f-m)m}}\left[\pi + 2\arctan\left(\frac{f-2m}{2\sqrt{(f-m)m}}\right)\right] \tag{45}$$

and for an odd f:

$$\overline{X} = \frac{2}{p\sqrt{f\pi}}\left\{1 + \frac{f}{8}\sum_{m=1}^{f-1}\frac{C_f^m(-1)^{m-1}}{\sqrt{(f-m)m}}\left[\pi + 2\arctan\left(\frac{f-2m}{2\sqrt{(f-m)m}}\right)\right]\right\} \tag{46}$$

Figure 5 compares the mean span dimensions of Θ-shaped chains of f connectors (cf. eqs 45 and 46), eight-shaped chains of f loops (cf. eq 40) and symmetric stars of f arms (cf. eq 24). All the arms, connectors and loops consist of the same number of segments, n. As one may expect, the increase in $\overline{X}$ of both Θ- and eight-shaped chains with an increase of f is much slower compared to that for symmetric stars. When f is large, results for Θ-shaped chains coincide with those for eight-shaped chains. The reason is as follows. The distance between the two branch units in a Θ-shaped chain, $x_2 - x_1$, follows a Gaussian distribution with zero mean and variance $\sigma^2 \sim 1/f$. In the limit of large f, $\sigma \to 0$, and the distribution of $x_2 - x_1$ approaches a Dirac delta function $\delta(x_2 - x_1)$. Thus, a Θ-shaped chain resembles essentially an eight-shaped chain.

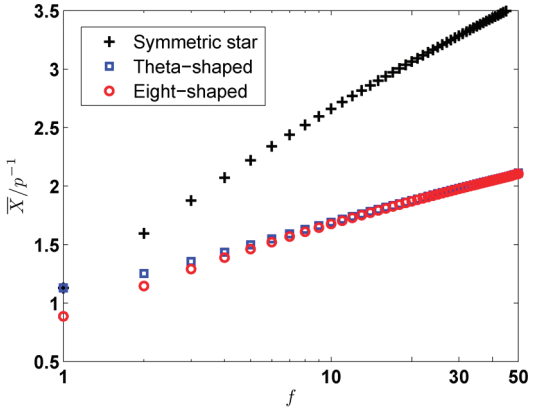


Figure 5. Mean span dimension, in units of p^{-1}, of symmetric stars of f arms, Θ-shaped cyclic chains of f connectors, and eight-shaped cyclic chains of f loops.

Table 2. Results of the Mean Span Dimension, $\overline{X}$, and the Corresponding Branching Index, g_s, for Several Topologically Different Chains[a]

architecture	$(\pi)^{1/2}p\overline{X}$	g_s
3-arm sym. star, cf. eq 28	$(12(2)^{1/2}/\pi)\arctan((2)^{1/2}/2)$	0.9212
double-tailed tadpole	$2(2)^{1/2} + \arctan((6)^{1/2}/12)$	0.7650
tadpole	$2 + \arctan(1/2)$	0.7587
manacles	$2 + 2\arctan(1/2) - (1/(6)^{1/2})\,\text{arccot}(2(6)^{1/2})$	0.6745
ring, cf. eq 34	$\pi/2$	0.6168
double-headed tadpole	$2 + 2\arctan(1/2) - ((2)^{1/2}/2)\arctan((2)^{1/2}/4)$	0.6017
eight, cf. eq 37	$\pi(1 - (2)^{1/2}/4)$	0.5156
Θ, cf. eq 44	$2/(3)^{1/2} + (3(6)^{1/2}/2)\arctan((2)^{1/2}/4)$	0.4813

[a] Chain architectures are arranged in decreasing order of g_s. All the FSCs composing the molecule are assumed to have the same number of segments, n.

3.2.4. Some Semicyclic Chains. Figure 2b shows the semicyclic chains considered in this work, namely, tadpole, double-headed tadpole, double-tailed tadpole, and manacles. Our choices are motivated by an ongoing interest in separating those topologically different polymers by liquid chromatography.[27,28,50] For simplicity, all the FSCs are considered to contain the same number of segments. As listed in Table 2, results of the mean span dimension can be expressed using elementary functions.

4. Branching Indices

4.1. A Branching Index, g_s, Based on the Mean Span Dimension. Branching indices are useful parameters in characterizing chain architectures. Ideally, a set of branching indices provide an "fingerprint" specifying uniquely the branching architecture.[51] A classical branching index is the Zimm−Stockmayer

branching index, g, defined based on the radius of gyration[37]

$$g = R_{g,\mathrm{br}}{}^2/R_{g,\mathrm{lin}}{}^2 \quad (47)$$

where $R_{g,\mathrm{br}}{}^2$ and $R_{g,\mathrm{lin}}{}^2$ are respectively the mean square radii of gyration of the branched polymer and the linear polymer that consist of the same repeating units and have the same total number of repeating units. Likewise, we introduce the branching index based on the mean span dimension, g_s, as

$$g_s = \overline{X}_{\mathrm{br}}{}^2/\overline{X}_{\mathrm{lin}}{}^2 \quad (48)$$

where $\overline{X}_{\mathrm{br}}$ and $\overline{X}_{\mathrm{lin}}$ are the mean span dimensions of the branched polymer and the otherwise identical linear polymer, respectively. Other commonly employed branched indices include g_η ($=V_{H,\mathrm{br}}/V_{H,\mathrm{lin}} = [\eta]_{\mathrm{br}}/[\eta]_{\mathrm{lin}}$) and h ($=R_{H,\mathrm{br}}/R_{H,\mathrm{lin}}$), defined as the ratios of the hydrodynamic volume V_H ($\sim M[\eta]$, where $[\eta]$ is the intrinsic viscosity) and the hydrodynamic radius R_H for the branched to the linear polymer species, respectively. Since both g and g_s are ratios of squared dimensions, we take the square of h, denoted by g_H, i.e., $g_H = h^2 = R_{H,\mathrm{br}}{}^2/R_{H,\mathrm{lin}}{}^2$.

4.2. Comparison of g_s to Other Branching Indices. There has been much progress in calculating g, g_H and g_η for more realistic polymer models by taking into account, for instance, excluded volume interactions, ternary interactions and finite hydrodynamic interactions based on the renormalization group theory, path-integral methods, and computer simulations.[45−47,51−53] Such calculations generally provide better agreement with available experiment data.[45,46] However, since we have only calculated g_s for ideal chains, the comparison is limited here to results based on the Gaussian chain model and the classical treatment of hydrodynamic interactions (the preaveraged Kirkwood−Riseman and Zimm theories).[35,52] In this limit, the hydrodynamic radius is essentially the harmonic mean of pair distances between chain segments:

$$R_H{}^{-1} = N^{-2}\left\langle \sum_{i=1}^{N}\sum_{j=1(j\neq i)}^{N} |\mathbf{r}_{ij}|^{-1} \right\rangle \quad (49)$$

where $\mathbf{r}_{ij}$ is the vector connecting segments i and j.

Figure 6 compares different branching indices for symmetric stars. Results of g, g_H, g_η and g_s were derived by Zimm and Stockmayer,[37] Stockmayer and Fixman,[54] Zimm and Kilb,[55] and this work, respectively. For a fair comparison, $g_\eta{}^{2/3}$ is shown. It is obvious that the branching index based on the radius of gyration, g, decreases more rapidly than those based on other size parameters as the number of arms increases. We have also calculated g and g_H for the two-branch-point and the comb architectures using expressions in ref11. and found the same trend that g decreases more rapidly than g_s and g_H. The results are shown in Figure 6b and Table 1, respectively. We did not calculate g_η directly for those two architectures since there are no reference available. Instead, we estimated g_η for the comb architecture based on an empirical relation,[55] $g_\eta = g^\varepsilon$, with $\varepsilon = 0.85$ suggested by experiments.[10] The estimated values of $g_\eta{}^{2/3}$ are close to g_H and g_s (see Table 1). Little is known about the value of ε for the two-branched architectures. However, trials of both $\varepsilon = 0.5$ (theoretical value for symmetric stars[55]) and 0.85 suggest a slower decrease of $g_\eta{}^{2/3}$ than g with an increasing f.

To understand why for the same branched chain g is smaller than g_s and g_H, let us consider differences in the set of pair distances, $\mathbf{r}_{ij}$, between that branched chain and its homologous linear chain. Among other possible differences, two are apparent: namely, (1) the branched chain has a smaller population of large $|r_{ij}|$ values (on the order of $\sqrt{N}^{1/2}b$) than the linear one, but (2) it also has a larger population of small $|r_{ij}|$ values (on the order of b and mostly around branch units) than its linear analogue.

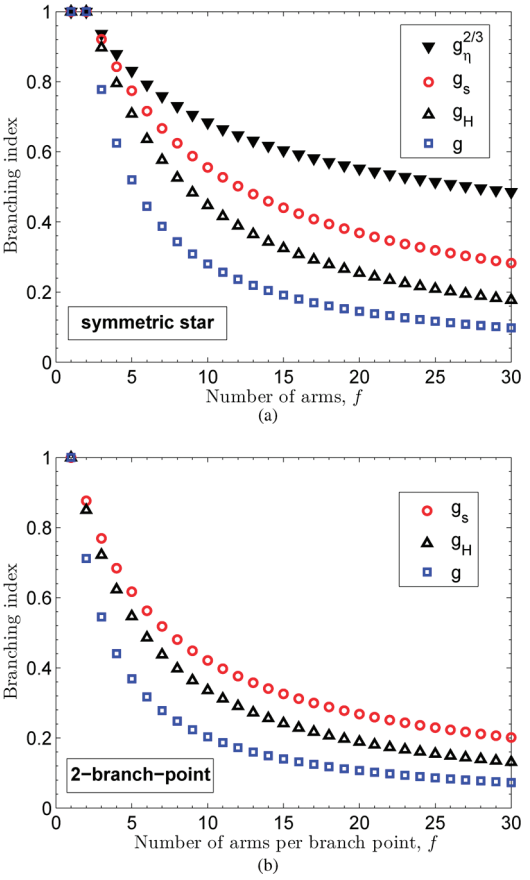


Figure 6. Branching indices for (a) star polymers of f identical arms and (b) two-branch-point polymers of f identical arms per branch point. The connector contains the same number of segments as an arm.

Both aspects (1 and 2) cause a decrease of R_g and R_H of the branched chain relative to its linear analogue, but $\overline{X}$ is reduced only by the former; even the effect of point 1 is expected to be stronger with regard to R_g than to $\overline{X}$, because R_g is the root-mean-square average whereas $\overline{X}$ is an arithmetic mean. This may explain why g_s decreases more slowly than does g with an increasing degree of branching, and the trend is expected to hold for more realistic polymer models as our argument here does not rely on the assumption of ideal chains. Different from R_g and $\overline{X}$, the hydrodynamic radius is mostly affected by a change in small distances according to eq 49. Since the population of small $|r_{ij}|$ values is large even in the case of a linear chain, the effect of point 2 on R_H is expected to be more moderate than that of point 1 on R_g. Thus, g_H should also decrease more slowly than does g. It is difficult to argue the relative difference between g_s and g_H. Although we found the decrease of g_s is slower than that of g_H for the star, the two-branch-point and the comb architectures, an exception is also found: in the case of a ring polymer,[49] $g = {}^1/_2$, $g_H = 0.720506$ and is larger than g_s ($=0.61685$), possibly because the increase in the population of small $|r_{ij}|$ values is limited in the case of a ring as it has no branch units.

4.3. Possible Use of g_s in SEC Experiments. The branching index for the mean span dimension, g_s, may be applied to the interpretation of SEC data. The idea is as follows. Consider a branched chain with molecular weight M_{br} and a linear chain with molecular weight M_L, both of the same chemical composition, have the same equilibrium partition coefficient and thus the same elution volume. According to an equilibrium theory,[6,8] they would have also the same mean span dimension: $\overline{X}_{\mathrm{br}}(M_{\mathrm{br}}) = \overline{X}_{\mathrm{lin}}(M_{\mathrm{lin}})$. The mean span dimension of the branched chain, $\overline{X}_{br}(M_{br})$, can be expressed in

terms of the branching index introduced in eq 48. Then,

$$g_s^{1/2}\overline{X}_{\rm lin}(M_{\rm br}) = \overline{X}_{\rm lin}(M_{\rm lin}) \quad (50)$$

The mean span dimension of a linear chain, like other averaged size parameters, is expected to follow a power law relationship with its molecular weight in the long chain limit[56]

$$\overline{X}_{\rm lin}(M) = AM^{\nu} \quad (51)$$

Here, ν is the Flory exponent; the prefactor A is not universal but depends on molecular details. Inserting eq 51 into eq 50 leads to

$$g_s = (M_{\rm lin}/M_{\rm br})^{2\nu} \quad (52)$$

Thus, by measuring molecular weights (M_L and M_{br}) of linear and branched chains staying in the same elution volume with an inline light scattering detector, g_s can be estimated. It would be interesting to compare experimental estimates of g_s to our calculations.

The idea behind eq 52 is essentially the same as the traditional universal SEC calibration except that we use the mean span dimension instead of the hydrodynamic volume. In the traditional approach, a branched chain with molecular weight M_{br} and a linear one with molecular weight M_L, having the same elution volume, would have the same hydrodynamic volume.[1,3] Using the definition of g_η and the Mark−Houwink equation for the intrinsic viscosity of a linear chain, one finds

$$g_\eta = (M_{\rm lin}/M_{\rm br})^{1+a} \quad (53)$$

For a polymer coil in the asymptotic nondraining limit, $a = 3\nu - 1$.[56,57] Hence, g_s and $g_\eta^{2/3}$ estimated by eqs 52 and 53 are identical. Experimentally, however, the exponent in the Mark−Houwink equation, a, is often slightly smaller than $3\nu - 1$, which was attributed to the des Cloizeaux-Weill effect.[56,57]

As an example, we consider the SEC experiments of Sun et al.[10] on nearly monodisperse samples of linear, 3-arm star, 2-branch-point and comb polyethylenes. For the same data, it was demonstrated that the elution volume shows a good correlation with the hydrodynamic volume,[10] the hydrodynamic radius[11] and the mean span dimension[8] of the polymers. In the present work, we estimated g_s and g_η using eqs 52 and 53; the values of g_s and $g_\eta^{2/3}$ are nearly identical for each of the polymer.[58] In Figure 7a, we plot experimental estimates of g_s with our calculations based on the target architecture. For comparison, we plot in Figure 7b estimated values of $g_\eta^{2/3}$ with those measured by an inline viscometer. Both figures show a reasonably good match between the two axes for the 3-arm star and the 2-branch-point architectures, indicating a comparable performance of the mean span dimension and the hydrodynamic volume as a predictor of elution volume. However, although the Gaussian chain model appears to be acceptable for those two architectures, it seems rather systematic that our calculations underestimate g_s as compared to those estimated from SEC experiments. In contrast, an excellent match is found between the two axes in Figure 7b.

Our calculations of g_s are based on the target architectures (molecular weights of arms and backbones). Possible differences between target and real architectures may account for some of the deviations in Figure 7a. On the other hand, as mentioned earlier, previous studies on combs have revealed that values of g and g_H obtained from experiments[10,48] and Monte Carlo simulations[45] of excluded volume chains are considerably bigger than those predicted by the idealized Gaussian chain models. If this is also true for g_s, a better agreement with experiments may be obtained by calculations of g_s that take into account excluded volume interactions.

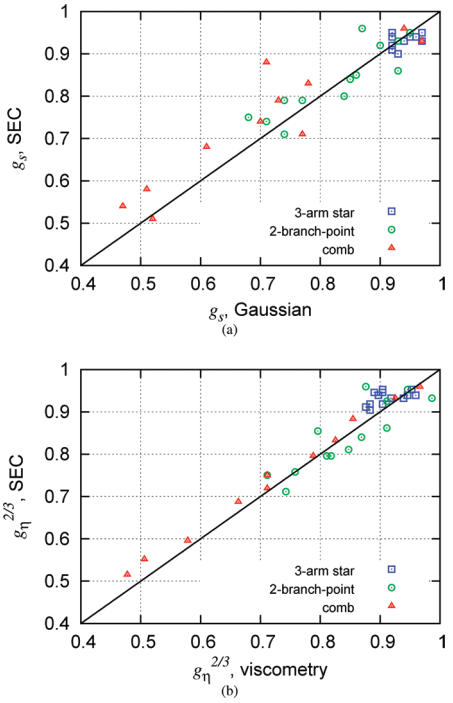


Figure 7. (a) g_s estimated from SEC experiments versus that obtained from our Gaussian chain calculations. (b) $g_\eta^{2/3}$ estimated from SEC experiments versus data measured by an inline viscometer. The original experimental data were obtained by Sun et al.[10]

5. Conclusion

Assuming ideal chain statistics, it is now possible to obtain the mean span dimensions of any complicated chain architectures. The method presented in this work allows one to construct integral expressions of the mean span dimension routinely. Such integrals may be solved analytically for some simple cases, or they have to be solved by numerical integration techniques. As examples, we obtained results of the mean span dimensions of linear, star, two-branch-point polymer, comb and various cyclic chains, and our deviations are generally simpler than using other existing method.

When comparing averaged sizes of a branched chain with its linear analogue, we observed that both the mean span dimension and the hydrodynamic radius decrease more slowly with the increase of degree of branching than does the radius of gyration. An explanation to this observation was provided. We also introduced a branching index based on the mean span dimension in the same way as the classical Zimm−Stockmayer branching index. Possible use of this new branching index in SEC experiments was discussed.

Our method is not applicable to excluded volume chains, in which case the probabilities of success in generating different subchains are coupled. In addition, the Gaussian chain model also fails to account for effects like topological constraints and chain rigidity. The former is crucial to cyclic polymers,[35] and the latter is important for low molecular weight polymers. We have noticed from simulations of discrete random walks[7] and Gaussian bead−spring polymers[15] that the mean span dimension obtained from simulations is smaller than the continuum result (cf. eq 19) for the same number of segments, and the convergence to the continuum result is rather slow compared to that of the radius of gyration.

Acknowledgment. Y.W. acknowledges financial support by the Danish Research Council for Technology and Production Sciences under Grant No. 274-08-0051. G.H.P. acknowledges financial support from the Danish National Research Foundation via a grant to MEMPHYS-Center for Biomembrane Physics.

Appendix A: Distribution Function of the Span Dimension

Let f_X be the probability density function of the span dimension, X. For a polymer chain in a slit of width W, the equilibrium partition coefficient can be expressed in the form[7]

$$K(W) = \int_0^W \left(1 - \frac{s}{W}\right) f_X(s)\,\mathrm{d}s = \int_0^W f_X(s)\,\mathrm{d}s - \frac{1}{W}\int_0^W s f_X(s)\,\mathrm{d}s \tag{54}$$

Multiplying both sides by W gives

$$WK(W) = W\int_0^W f_X(s)\,\mathrm{d}s - \int_0^W s f_X(s)\,\mathrm{d}s \equiv \psi(W) \tag{55}$$

Differentiating $\psi(W)$ by W, we have

$$\frac{\mathrm{d}}{\mathrm{d}W}\psi(W) = \int_0^W f_X(s)\,\mathrm{d}s + W f_X(W) - W f_X(W) = \int_0^W f_X(s)\,\mathrm{d}s \equiv F_X(W) \tag{56}$$

which is the cumulative distribution function of the span dimension. Thus, differentiating $F_X(W)$ by W gives the probability density function:

$$f_X(W) = \frac{\mathrm{d}}{\mathrm{d}W} F_X(W) = \frac{\mathrm{d}^2}{\mathrm{d}W^2}\psi(W) \tag{57}$$

Using a Green function approach, Teraoka[11] derived $K(W)$ for several branched architectures. Once $K(W)$ is obtained, $\psi(W)$ is also known, and its second derivative with respect to the slit width gives the probability density of the span dimension. Note that eq 57 is equivalent to those used to determine f_X of linear[16,23,24] and symmetric star[25] polymers.

Appendix B: The Mean Span Dimensions of Asymmetric Stars with Three and Four Arms

We take asymmetry into account by assigning a different number of chain segments, N_i, to each of the f arms (i = 1, 2, ..., f). The mean span dimension of the asymmetric 3-arm star is

$$\overline{X} = \frac{4}{\pi^{3/2}}\left[\frac{p_1/p_2 + p_2/p_1}{\sqrt{{p_1}^2 + {p_2}^2}}\arctan\left(\frac{p_3}{\sqrt{{p_1}^2 + {p_2}^2}}\right) + \frac{p_2/p_3 + p_3/p_2}{\sqrt{{p_2}^2 + {p_3}^2}}\arctan\left(\frac{p_1}{\sqrt{{p_2}^2 + {p_3}^2}}\right) + \frac{p_3/p_1 + p_1/p_3}{\sqrt{{p_1}^2 + {p_3}^2}}\arctan\left(\frac{p_2}{\sqrt{{p_1}^2 + {p_3}^2}}\right)\right] \tag{58}$$

and for the asymmetric 4-arm star,

$$\overline{X} = \frac{4}{\pi^{3/2}}\left[\frac{p_1/p_2 + p_2/p_1}{\sqrt{{p_1}^2 + {p_2}^2}}\arctan\left(\frac{p_3 p_4}{\Delta\sqrt{{p_1}^2 + {p_2}^2}}\right) + \frac{p_2/p_3 + p_3/p_2}{\sqrt{{p_2}^2 + {p_3}^2}}\arctan\left(\frac{p_1 p_4}{\Delta\sqrt{{p_2}^2 + {p_3}^2}}\right) + \frac{p_3/p_4 + p_4/p_3}{\sqrt{{p_3}^2 + {p_4}^2}}\arctan\left(\frac{p_1 p_2}{\Delta\sqrt{{p_3}^2 + {p_4}^2}}\right) + \frac{p_4/p_1 + p_1/p_4}{\sqrt{{p_1}^2 + {p_4}^2}}\arctan\left(\frac{p_2 p_3}{\Delta\sqrt{{p_1}^2 + {p_4}^2}}\right) + \frac{p_1/p_3 + p_3/p_1}{\sqrt{{p_1}^2 + {p_3}^2}}\arctan\left(\frac{p_2 p_4}{\Delta\sqrt{{p_1}^2 + {p_3}^2}}\right) + \frac{p_2/p_4 + p_4/p_2}{\sqrt{{p_2}^2 + {p_4}^2}}\arctan\left(\frac{p_1 p_3}{\Delta\sqrt{{p_2}^2 + {p_4}^2}}\right)\right] \tag{59}$$

with $\Delta = ({p_1}^2 + {p_2}^2 + {p_3}^2 + {p_4}^2)^{1/2}$.

References and Notes

(1) *Handbook of Size Exclusion Chromatography and Related Techniques*, 2nd ed.; Wu, C.-S., Ed.; Marcel Dekker: New York, 2004.
(2) (a) Tobita, H.; Saito, S. *Macromol. Theory Simul.* **1999**, *8*, 513–519. (b) Tobita, H.; Hamashima, N. *Macromol. Theory Simul.* **2000**, *9*, 453–462. (c) Tobita, H.; Hamashima, N. J. *Polym. Sci., Polym. Phys.* **2000**, *38*, 2009–2018.
(3) Grubisic, Z.; Rempp, P.; Benoit, H. J. *Polym. Sci., Polym. Lett.* **1967**, *5*, 753–759.
(4) Casassa, E. F. *J. Polym. Sci., Polym. Lett.* **1967**, *5*, 773–778.
(5) Casassa, E. F.; Tagami, Y. *Macromolecules* **1969**, *2*, 14–26.
(6) Casassa, E. F. *Macromolecules* **1976**, *9*, 182–185.
(7) Wang, Y.; Peters, G. H.; Hansen, F. Y.; Hassager, O. *J. Chem. Phys.* **2008**, *128*, 124904.
(8) Wang, Y.; Teroaka, I.; Hansen, F. Y.; Peters, G. H.; Hassager, O. *Macromolecules* **2010**, *43*, 1651–1659.
(9) Degoulet, C.; Busnel, J.-P.; Tassin, J.-F. *Polymer* **1994**, *35*, 1957–1962.
(10) Sun, T.; Chance, R. R.; Graessley, W. W.; Lohse, D. J. *Macromolecules* **2004**, *37*, 4304–4312.
(11) Teraoka, I. *Macromolecules* **2004**, *37*, 6632–6639.
(12) (a) Radke, W. *Macromol. Theory Simul.* **2001**, *10*, 668–675. (b) Radke, W. J. Chromatogr., A. **2004**, *1028*, 211−218.
(13) Casassa, E. F. *Macromolecules* **1984**, *17*, 601–604.
(14) Casassa, E. F. *Macromolecules* **1995**, *28*, 7756–7763.
(15) Wang, Y.; Hansen, F. Y.; Peters, G. H.; Hassager, O. *J. Chem. Phys.* **2008**, *129*, 074904.
(16) Daniels, H. E. *Proc. Cambr. Philos. Soc.* **1941**, *37*, 244–251.
(17) Weiss, G. H.; Rubin, R. J. *Adv. Chem. Phys.* **1983**, *52*, 363–505.
(18) Makhnovskii, Y. A.; Maslova, M. E.; Berezhkovskii, A. M. *Physica A* **1996**, *225*, 221–234.
(19) Sastry, G. M.; Agmon, N. *J. Chem. Phys.* **1996**, *104*, 3022–3025.
(20) Feller, W. *Ann. Math. Stat.* **1951**, *22*, 427–432.
(21) Seshadri, V.; Lindenberg, K. *J. Stat. Phys.* **1980**, *22*, 69–79.
(22) (a) Kuhn, H. *Experientia* **1945**, *1*, 28–29. (b) Kuhn, H. *Helv. Chim. Acta* **1948**, *31*, 1677–1690.
(23) Weidmann, J. J.; Kuhn, H.; Kuhn, W. *J. Chim. Phys., Phys.-Chim. Biol.* **1953**, *50*, 226–235.
(24) Rubin, R. J. *J. Chem. Phys.* **1972**, *56*, 5747–5757.
(25) Rubin, R. J.; Weiss, G. H. *Macromolecules* **1977**, *10*, 332–334.
(26) Rubin, R. J.; Mazur, J.; Weiss, G. H. *Pure Appl. Chem.* **1976**, *46*, 143–148.
(27) Gorbunov, A. A.; Vakhrushev, A. V. *Polymer* **2004**, *45*, 6761–6770.
(28) Vakhrushev, A. V.; Gorbunov, A. A.; Tezuka, Y.; Tsuchitani, A.; Oike, H. *Anal. Chem.* **2008**, *80*, 8153–8162.
(29) DiMarzio, E. A. *J. Chem. Phys.* **1965**, *42*, 2101–2106.
(30) Carslaw, H. S.; Jaeger, J. C. *Conduction of Heat in Solids*, 2nd ed.; Oxford University Press: London, 1959; p 58.

(31) Teraoka, I. *Polymer Solutions: An Introduction to Physical Properties*; John Wiley & Sons: New York, 2002; p 24.
(32) Matyjaszewski, K.; Xia, J. *Chem. Rev*. **2001**, *101*, 2921–2990.
(33) Hadjichristidisa, N.; Iatroua, H.; Pitsikalisa, M.; Mays, J. *Prog. Polym. Sci*. **2006**, *27*, 1068–1132.
(34) (a) Tezuka, Y.; Oike, H. *Prog. Polym. Sci*. **2002**, *27*, 1069–1122. (b) Tezuka, Y.; Taka-hashi, N.; Satoh, T.; Adachi, K. *Macromolecules* **2007**, *40*, 7910–7918.
(35) Grosberg, A. Y.; Khokhlov, A. R. *Statistical Physics of Macromolecules*; American Institute of Physics: New York, 1994.
(36) Larralde, H.; Trunfio, P.; Havlin, S.; Stanley, H. E.; Weiss, G. H. *Nature* **1992**, *355*, 423–426.
(37) Zimm, B. H.; Stockmayer, W. H. *J. Chem. Phys*. **1949**, *17*, 1301–1314.
(38) Prudnikov, A. P.; Brychkov, Y.; Marichev, O. I. *Integrals and Series, Vol. 2: Special Functions*; Gordon and Breach: New York, 1990; p 123, Eqs. (2.8.19.8) and (2.8.19.11).
(39) (a) Casassa, E. F.; Berry, G. C. *J. Polym. Sci., Polym. Phys*. **1966**, *4*, 881–897. (b) Berry, G. C. *J. Polym. Sci., Polym. Phys*. **1968**, *6*, 1551–1554. (c) Berry, G. C. *J. Polym. Sci., Polym. Phys*. **1971**, *9*, 687–715.
(40) Kurata, M.; Fukatsu, M. *J. Chem. Phys*. **1964**, *41*, 2934–2944.
(41) Šolc, K. *Macromolecules* **1973**, *6*, 378–385.
(42) Galina, H. *Macromolecules* **1983**, *16*, 1479–1483.
(43) Zhulina, E. B.; Vilgis, T. A. *Macromolecules* **1995**, *28*, 1008–1015.
(44) Rouault, Y.; Borisov, O. V. *Macromolecules* **1996**, *29*, 2605–2611.
(45) Lipson, J. E. G. *Macromolecules* **1991**, *24*, 1327–1333.
(46) Lipson, J. E. G. *Macromolecules* **1993**, *26*, 203–207.
(47) (a) Freire, J. J. Conformational properties of branched polymers: Theory and simulations. In *Branched Polymers II*; Springer-Verlag: Berlin, 1999; Vol. *143*, pp 35−112. (b) Burchard,W. Solution properties of branched macromolecules. In *Branched Polymers II*; Springer-Verlag: Berlin, 1999; Vol. *143*, pp 113−194.
(48) (a) Roovers, J. *Polymer* **1979**, *20*, 843–849. (b) Roovers, J.; Toporowski, P. M. *J. Polym. Sci., Polym. Phys*. **1980**, *18*, 1907–1917.
(49) Benmounaa, M.; Maschkeb, U. In *Cyclic Polymers*, 2nd ed.; Semlyen, J. A., Ed.; Kluwer Academic Publishers: Dordrecht, The Netherlands, 2000; *Chapter Theoretical Aspects of Cyclic Polymers: Effects of Excluded Vol. Interactions*, page 776.
(50) Gorbunov, A. A.; Vakhrushev, A. V. *Proc. Chem*. **2010**, *2*, 140–151.
(51) Douglas, J. F.; Roovers, J.; Freed, K. F. *Macromolecules* **1990**, *23*, 4168–4180.
(52) Yamakawa, H. *Modern Theory of Polymer Solutions*; Harper & Row: New York, 1971.
(53) (a) Mansfield, M. L.; Douglas, J. F.; Irfan, S.; Kang, E.-H. *Macromolecules* **2007**, *40*, 2575–2589. (b) Mansfield, M. L.; Douglas, J. F. *J. Chem. Phys*. **2010**, *133*, 044903. (c) Mans-field, M. L.; Douglas, J. F. *J. Chem. Phys*. **2010**, *133*, 044904.
(54) Stockmayer, W. H.; Fixman, M. *Ann. N.Y. Acad. Sci*. **1953**, *57*, 334–352.
(55) Zimm, B. H.; Kilb, R. W. *J. Polym. Sci*. **1959**, *37*, 19–42.
(56) de Gennes, P. G. *Scaling Concepts in Polymer Physics*; Cornell Univ. Press: Ithaca, 1979; p 183.
(57) Weill, G.; des Cloizeaux, J. *J. Phys*. (*Paris*) **1979**, *40*, 99–105.
(58) To estimate g_s and g_η, we used $\nu = 0.585$, $a = 0.705$ and molecular weights of the 37 branched chains for M_{br} measured by an inline multiangle laser light scattering (MALLS) detector as reported in ref 10; the corresponding M_L values were estimated from the elution volumes based on a calibration curve constructed for the linear polyethylene data (we discarded two data points with elution volumes larger than 21.5 mL as they are irrelevant; the rest were fitted to a quadratic polynomial on a plot of $\log_{10}M$ versus elution volume). To calculate g_s, we used the reported target architectures in accordance with our work in ref 8.

Macromolecules
NOTE

Macromolecules **2011**, *44*, 413–415 **413**
DOI: 10.1021/ma102677k

Well-Defined Uncharged Polymers with a Sharp UCST in Water and in Physiological Milieu

Stefan Glatzel,[†] André Laschewsky,[†,‡] and Jean-François Lutz*[,†,§]

[†]*Fraunhofer Institute for Applied Polymer Research, Geiselbergstrasse 69, Potsdam 14476, Germany, and* [‡]*Department of Chemistry, University of Potsdam, Potsdam, Germany.* [§]*New address: Institut Charles Sadron, UPR-22 CNRS, 23 rue du Loess, BP 84047, 67034 Strasbourg cedex 2, France.*

Received November 24, 2010; Revised Manuscript Received December 13, 2010

Thermoresponsive macromolecules have become very important in academic and applied polymer science during the past two decades.[1] In particular, water-soluble polymers capable of changing their solution properties at useful temperatures (e.g., room temperature, body temperature, fever temperature) are broadly studied for applications in nanomedicine, surface science, and cosmetics.[1] There are typically two basic types of thermoresponsive behaviors in aqueous medium: polymers with a lower critical solution temperature (LCST) precipitate upon heating, whereas polymers with an upper critical solution temperature (UCST) dissolve upon heating.[1] However, LCST polymers have been by far the most studied ones. Indeed, their aqueous behavior is rather peculiar (i.e., heat does not favor dissolution but phase separation) and useful. Yet, although counterintuitive, the LCST behavior is actually quite common. In fact, virtually all uncharged water-soluble macromolecules seem to exhibit a LCST in water. The explanation of this behavior is, after all, quite simple. A polymer dissolves in water because it forms favorable interactions with the solvent. In the case of uncharged macromolecules, polymer−water interactions are mostly hydrogen bonds. At elevated temperatures, these weak polymer−solvent interactions are easily disrupted, thus resulting in phase separation. Hence, LCST behavior has been observed for a wide variety of water-soluble nonionic polymers, including poly(ethylene oxide), poly(vinyl alcohol), and poly(hydroxyethyl methacrylate).[2,3] However, only some polymers exhibit LCST values in a convenient range of temperature. So far, poly(*N*-substituted acrylamide)s such as poly(*N*-isopropylacrylamide),[4] polymers with short oligo(ethylene glycol) side chains,[5] poly(alkyloxazolines),[6] and elastin-like polypeptides[7] are the most studied thermoresponsive polymers for practical applications.[8]

On the other hand, there are only a few known polymers exhibiting a controllable UCST in aqueous medium. The UCST behavior is more commonly observed in organic solvents or in water/organic solvent mixtures.[9] In pure water, this behavior is rather atypical. The reason for that is simple to understand: UCST in water implies that strong polymer−polymer interactions are formed in aqueous medium but that these interactions are weak enough to be disrupted by temperature. In a sense, the heat treatment of biopolymer solutions (e.g., protein thermal denaturation and DNA melting) follows this scheme. However, these events occur at relatively high temperatures and generally do not result in observable and controllable phase transitions. The UCST behavior is even more unlikely in the case of synthetic macromolecules. Indeed, typical polymer−polymer interactions such as hydrophobic aggregation (e.g., hydrophobic polymers or macrosurfactants) or electrostatic interactions (e.g., polyampholites or polyelectrolyte complexes) are generally not affected by temperature. Hence, UCST behavior in water has been only reported for some specific homopolymers,[3,10,11] copolymers,[12] cross-linked networks,[13] and polymer complexes.[14] In the latter case, Kataoka and co-workers described an interesting series of hydrogen-bonding polymer complexes.[14] It was shown that complementary homopolymers containing either H-bond donor or H-bond acceptor functions exhibit a UCST behavior in water. Such bicomponent systems require relatively concentrated polymer solutions and are therefore difficult to exploit for applications in materials science and life science. In fact, the most studied UCST polymers to date are sulfobetaine-based (meth)acrylic polymers.[10] These zwitterionic homopolymers usually exhibit a UCST in water. Moreover, they can be polymerized using controlled radical polymerization (CRP) techniques such as atom transfer radical polymerization (ATRP)[15] or reversible addition−fragmentation chain transfer (RAFT) polymerization[16] and can therefore be exploited for macromolecular engineering (e.g., synthesis of block copolymers or modification of surfaces).[17] Still, these polymers bear ionic groups and are therefore relatively sensitive to ionic strength and specific ion−ion interactions.[18]

In this context, the synthesis of well-defined uncharged macromolecules exhibiting a defined UCST in water is a pertinent topic. Ohnishi and co-workers[19] reported that some (co)polymers based on *N*-acryloylglycinamide (NAGAM) may exhibit a UCST in water, as more recently extended by Agarwal and co-workers.[20] In these studies, the polymers were prepared by conventional free radical polymerization (RP). We studied lately the RAFT homopolymerization of NAGAM in water and demonstrated that well-defined polymers with a controlled chain-length and a narrow molecular weight distribution can be synthesized.[21] However, poly(NAGAM) polymers prepared by RAFT polymerization did not exhibit a UCST behavior in aqueous medium. Instead, these polymers exhibit gel−sol thermogelation in water and in physiological media.[21,22] The UCST behavior described for RP polymers was not obvious for the RAFT samples. Only weak turbidities were observed for dilute solutions of low molecular weight samples (i.e., $DP_n \sim 100$). Generally speaking, poly(NAGAM) polymers led to transparent physical gels in aqueous medium.

In this Note, we describe the RAFT homopolymerization of *N*-acryloylasparaginamide (NAAAM, **1**). The molecular structure of this monomer resembles that of NAGAM as it also possesses both H-bond donor and acceptor amide sites.[19] However, NAAAM contains two primary amide functions instead of one in the case of NAGAM. NAAAM was synthesized in one step by reacting acryloyl chloride with L-asparaginamide

*Corresponding author. E-mail: jflutz@unistra.fr.

© 2010 American Chemical Society
Published on Web 12/30/2010

hydrochloride. Because of its particular molecular structure, NAAAM is not soluble in most of the conventional organic solvents but can be dissolved in DMSO and water. Interestingly, this monomer starts to dissolve only above 22 °C in pure water (Figure S1). Thus, NAAAM was an attractive option for exploring the synthesis of well-defined polymers with a UCST behavior in aqueous medium.

A series of NAAAM homopolymers of variable chain length were synthesized by RAFT polymerization (Table 1). Because of the limited solubility of the monomer in organic solvents, the polymerization was conducted in deionized water. The water-soluble chain transfer agent **2** (Scheme 1) and the water-soluble radical initiator VA-044 were used to generate a controlled RAFT process. We previously reported that this combination allows a good control of the radical polymerization of NAGAM in water.[21] In the present study, homogeneous NAAAM polymerizations were observed at 60 °C in all cases. The formed polymers were purified by dialysis against pure deionized water, lyophilized, and analyzed by ^{1}H NMR and size exclusion chromatography (SEC) (Table 1 and Figure 1). These characterizations showed that well-defined poly(NAAAM) samples with controlled chain lengths, chain ends, and molecular weight distributions were synthesized in all cases. For instance, Figure 1A shows the SEC traces obtained in DMSO for this series of polymers. For all samples, monomodal chromatograms with a narrow molecular weight distribution (i.e., $M_w/M_n \sim 1.25$) were obtained. We previously reported that poly(NAGAM) homopolymers prepared by RAFT have a tendency to aggregate in DMSO and that therefore bimodal SEC chromatograms can be observed in some cases in this solvent.[21] The RAFT homopolymers of **1** obviously behave differently in DMSO, thus suggesting different modes of self-association for poly(NAAAM) and poly(NAGAM) in polar solvents. Besides SEC analysis, ^{1}H NMR measurements confirmed that the homopolymers of **1** are prepared via a controlled RAFT mechanism. Typical chain-end signals due to the initiating (i.e., R-group) and transfer (i.e., Z-group) moieties of the RAFT chain transfer agent are visible in the spectra of the purified polymers (Figure 1). The integration of these signals confirmed that the polymers have a controlled degree of polymerization (Table 1).

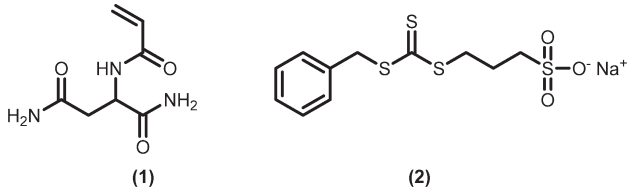
Additionally, the properties of the formed homopolymers in dilute aqueous solutions were studied by turbidimetry. These measurements evidenced an obvious UCST behavior for all samples (Table 1). Yet, this phase transition was found to depend on chain length (Figure S2). Short poly(NAAAM) samples (i.e., $DP_{n,th} < 300$) exhibited UCSTs below room temperature, whereas longer chains (i.e., $DP_{n,th} > 300$) exhibited higher, and therefore more practical, values. Besides, the phase transition was also found to be dependent on concentration for a given homopolymer. For instance, Figure 1 and Figure S3 show the cloud-point measurements obtained for a homopolymer with a $DP_{n,th}$ of 500 at different concentrations in water. In dilute conditions (i.e., polymer concentration below 1 wt %), the UCST behavior was found to depend on concentration. In addition, small hystereses of about 0.5−0.8 °C were noticed in this range of concentration. These particular aspects should be taken into account for potential applications. However, at higher concentrations (i.e., above 2 wt %), the UCST behavior was found to be less sensitive to concentration. In addition, no significant hysteresis was observed for more concentrated solutions (Figure 1). Furthermore, it is important to specify that below UCST a macroscopic phase separation can be observed. At concentrations around 2−3 wt %, the polymer solutions appear as stable milky colloidal dispersions at first, but after some hours, they typically flocculate into filterable or centrifugable polymer-rich

Table 1. Properties of the Homopolymers Prepared by RAFT Polymerization

$DP_{n,th}$[a]	M_n[b] [g mol^{-1}]	M_w/M_n[c]	DP_n	cloud point[f] [°C]
100	17 300	1.26	79[d]	4.3[f]
200	27 800	1.26	161[d]	10.6[g]
300	60 800	1.27	326[e]	18.9[g]
400	100 400	1.22	540[e]	26.2[g]
500	118 700	1.26	639[e]	24.3[g]

[a] Theoretical average chain-length $DP_{n,th}$ = [**1**]/[**2**]. [b] Number-average molecular weight measured by SEC in DMSO. [c] Molecular weight distribution measured by SEC in DMSO. [d] Estimated from 300 MHz ^{1}H NMR spectra in D_2O. [e] Not measurable in D_2O at room temperature. [f] Cloud point of a 1 wt % solution measured visually. [g] Cloud point of a 1 wt % solution measured by turbidimetry.

Scheme 1. Molecular Structures of the Monomer and the Chain-Transfer Agent Used



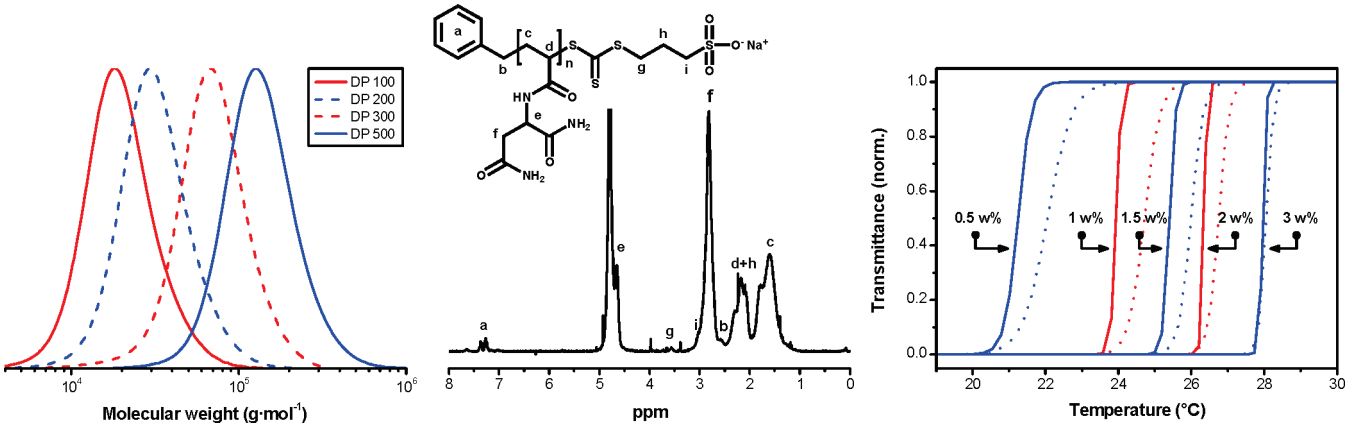


Figure 1. Molecular characterization of homopolymers of **1** prepared by RAFT polymerization: (left) SEC chromatograms recorded at 70 °C in DMSO for samples of different DP_n. From left to right: $DP_{n,th}$ = 100, 200, 300, and 500; (middle) ^{1}H NMR spectrum recorded in D_2O for a homopolymer with an average degree of polymerization of 100; (right) turbidimetry measurements recorded for a homopolymer with an average degree of polymerization of 500 in pure deionized water at different concentrations. From left to right: concentration = 0.5, 1, 1.5, 2, and 3 wt %. Solid lines: cooling curves; dotted lines: heating curves. The raw experimental data were smoothened for clarity.

phases. Thus, above a critical DP_n, poly(NAAAM) homopolymers seem very interesting macromolecules for applications in materials science and biosciences. For instance, samples with $DP_{n,th}$ in the range 400−500 exhibited optimal UCST values in between room and body temperature. This interesting behavior was also observed in physiological medium, e.g., in phosphate buffered saline (PBS) solutions. The phase transitions measured in PBS were roughly similar to those observed in pure water (Figure S4).

In conclusion, we demonstrated that RAFT polymerization allows a successful control of the radical polymerization of NAAAM in aqueous medium. The formed polymers exhibit a well-defined molecular structure and unprecedented UCST properties in water and in physiological milieu. These thermoresponsive macromolecules devoid of any ionic groups open new avenues for the design of waterborne stimuli-responsive materials.

Acknowledgment. This research was supported by the Fraunhofer Society (Bioactive Surfaces Project) and the German Federal Ministry of Education and Research (BMBF, IZIB project 03IS2201B). Additionally, the authors thank Dr. Michael Päch (Fraunhofer IAP) for providing the RAFT CTA and Dr. Helmut Schlaad and Marlies Gräwert (MPI-KGF) for SEC measurements in DMSO.

Supporting Information Available: Full experimental part and Figures S1−S4. This material is available free of charge via the Internet at http://pubs.acs.org.

References and Notes

(1) (a) Gil, E. S.; Hudson, S. M. *Prog. Polym. Sci.* **2004**, *29*, 1173–1222. (b) Nath, N.; Chilkoti, A. *Adv. Mater.* **2002**, *14* (17), 1243–1247. (c) de las Heras Alarcón, C.; Pennadam, S.; Alexander, C. *Chem. Soc. Rev.* **2005**, No. 3, 276–285. (d) Wischerhoff, E.; Badi, N.; Lutz, J.-F.; Laschewsky, A. *Soft Matter* **2010**, *6* (4), 705–713.

(2) (a) Bailey, F. E.; Callard, R. W. *J. Appl. Polym. Sci.* **1959**, *1* (1), 56–62. (b) Weaver, J. V. M.; Bannister, I.; Robinson, K. L.; Bories-Azeau, X.; Armes, S. P.; Smallridge, M.; McKenna, P. *Macromolecules* **2004**, *37* (7), 2395–2403.

(3) Briscoe, B.; Luckham, P.; Zhu, S. *Proc. R. Soc. London, A* **1999**, *455* (1982), 737–756.

(4) (a) Winnik, F. M.; Ringsdorf, H.; Venzmer, J. *Langmuir* **1991**, *7* (5), 905–911. (b) Schild, H. G. *Prog. Polym. Sci.* **1992**, *17* (2), 163–249. (c) Laschewsky, A.; Rekai, E. D.; Wischerhoff, E. *Macromol. Chem. Phys.* **2001**, *202* (2), 276–286. (d) Vogt, A. P.; Sumerlin, B. S. *Macromolecules* **2008**, *41* (20), 7368–7373. (e) Jochum, F. D.; Theato, P. *Macromolecules* **2009**, *42* (16), 5941–5945.

(5) (a) Han, S.; Hagiwara, M.; Ishizone, T. *Macromolecules* **2003**, *26* (22), 8312–8319. (b) Lutz, J.-F.; Akdemir, O.; Hoth, A. *J. Am. Chem. Soc.* **2006**, *128* (40), 13046–13047. (c) Lutz, J.-F.; Hoth, A. *Macromolecules* **2006**, *39* (2), 893–896. (d) Magnusson, J. P.; Khan, A.; Pasparakis, G.; Saeed, A. O.; Wang, W.; Alexander, C. *J. Am. Chem. Soc.* **2008**, *130* (33), 10852–10853. (e) Lutz, J.-F. *J. Polym. Sci., Part A: Polym. Chem.* **2008**, *46*, 3459–3470. (f) Holder, S. J.; Durand, G. G.; Yeoh, C.-T.; Illi, E.; Hardy, N. J.; Richardson, T. H. *J. Polym Sci., Part A: Polym. Chem.* **2008**, *46* (23), 7739–7756.

(6) (a) Park, J.-S.; Kataoka, K. *Macromolecules* **2006**, *39* (19), 6622–6630. (b) Hoogenboom, R.; Thijs, H. M. L.; Jochems, M. J. H. C.; van Lankvelt, B. M.; Fijten, M. W. M.; Schubert, U. S. *Chem. Commun.* **2008**, 5758–5760. (c) Diehl, C.; Schlaad, H. *Macromol. Biosci.* **2009**, *9* (2), 157–161.

(7) (a) Ayres, L.; Koch, K.; Adams, P. J. H. M.; van Hest, J. C. M. *Macromolecules* **2005**, *38* (5), 1699–1704. (b) Mart, R. J.; Osborne, R. D.; Stevens, M. M.; Ulijn, R. V. *Soft Matter* **2006**, *2*, 822–835.

(8) (a) McCormick, C. L.; Sumerlin, B. S.; Lokitz, B. S.; Stempka, J. E. *Soft Matter* **2008**, *4*, 1760–1773. (b) Okano, T.; Yamada, N.; Sakai, H.; Sakurai, Y. *J. Biomed. Mater. Res.* **1993**, *27* (10), 1243–1251. (c) Stayton, P. S.; Shimoboji, T.; Long, C.; Chilkoti, A.; Ghen, G.; Harris, J. M.; Hoffman, A. S. *Nature* **1995**, *378*, 472–474. (d) Meyer, D. E.; Chilkoti, A. *Nature Biotechnol.* **1999**, *17* (11), 1112–1115. (e) Berndt, I.; Pedersen, J. S.; Richtering, W. *J. Am. Chem. Soc.* **2005**, *127* (26), 9372–9373. (f) Quinn, J. F.; Caruso, F. *Langmuir* **2004**, *20* (1), 20–22. (g) Wischerhoff, E.; Uhlig, K.; Lankenau, A.; Börner, H. G.; Laschewsky, A.; Duschl, C.; Lutz, J.-F. *Angew. Chem., Int. Ed.* **2008**, *47* (30), 5666–5668. (h) Etika, K. C.; Jochum, F. D.; Theato, P.; Grunlan, J. C. *J. Am. Chem. Soc.* **2009**, *131* (38), 13598–13599.

(9) (a) Costa, R. O. R.; Freitas, R. F. S. *Polymer* **2002**, *43* (22), 5879–5885. (b) Boyko, V.; Lu, Y.; Richter, A.; Pich, A. *Macromol. Chem. Phys.* **2003**, *204* (16), 2031–2039. (c) Gelbrich, T.; Feyen, M.; Schmidt, A. M. *Macromolecules* **2006**, *39* (9), 3469–3472. (d) Yamauchi, H.; Maeda, Y. *J. Phys. Chem. B* **2007**, *111* (45), 12964–12968. (e) Hoogenboom, R.; Lambermont-Thijs, H. M. L.; Jochems, M.; Hoeppener, S.; Guerlain, C.; Fustin, C. A.; Gohy, J. F.; Schubert, U. S. *Soft Matter* **2009**, *5* (19), 3590–3592. (f) Ueki, T.; Watanabe, M.; Lodge, T. P. *Macromolecules* **2009**, *42* (4), 1315–1320.

(10) (a) Soto, V. M. M.; Galin, J. C. *Polymer* **1984**, *25* (2), 254–262. (b) Schulz, D. N.; Peiffer, D. G.; Agarwal, P. K.; Larabee, J.; Kaladas, J. J.; Soni, L.; Handwerker, B.; Garner, R. T. *Polymer* **1986**, *27* (11), 1734–1742.

(11) Aoki, T.; Nakamura, K.; Sanui, K.; Kikuchi, A.; Okano, T.; Sakurai, Y.; Ogata, N. *Polym. J.* **1999**, *31* (11), 1185–1188.

(12) (a) Zhou, X. J.; Weng, L. H.; Chen, Q.; Zhang, J. M.; Shen, D. Y.; Li, Z. C.; Shao, M. J.; Xu, J. *Polym. Int.* **2003**, *52* (7), 1153–1157. (b) Mori, H.; Kato, I.; Saito, S.; Endo, T. *Macromolecules* **2010**, *43* (3), 1289–1298.

(13) (a) Katono, H.; Maruyama, A.; Sanui, K.; Ogata, N.; Okano, T.; Sakurai, Y. *J. Controlled Release* **1991**, *16* (1−2), 215–227. (b) Sasase, H.; Aoki, T.; Katono, H.; Sanui, K.; Ogata, N.; Ohta, R.; Kondo, T.; Okano, T.; Sakurai, Y. *Makromol. Chem., Rapid Commun.* **1992**, *13* (12), 577–581.

(14) Ohnishi, N.; Furukawa, H.; Kataoka, K.; Ueno, K. US2003156618, Natl. Inst. Adv. Ind. Sci. Technol., Chisso Corp., 2005.

(15) Matyjaszewski, K.; Tsarevsky, N. V. *Nature Chem.* **2009**, *1* (4), 276–288.

(16) Moad, G.; Rizzardo, E.; Thang, S. H. *Polymer* **2008**, *49* (5), 1079–1131.

(17) (a) Arotçaréna, M.; Heise, B.; Ishaya, S.; Laschewsky, A. J. *Am. Chem. Soc.* **2002**, *124* (14), 3787–3793. (b) Maeda, Y.; Mochiduki, H.; Ikeda, I. *Macromol. Rapid Commun.* **2004**, *25* (14), 1330–1334. (c) Heinz, B. S.; Laschewsky, A.; Rekai, E. D.; Wischerhoff, E.; Zacher, T. Grafting of Functionalized Water Soluble Polymers on Gold Surfaces. In *ACS Symposium Series*; McCormick, C. L., Ed.; American Chemical Society: Washington, DC, 2001; Vol. *780*.(d) Azzaroni, O.; Brown, A. A.; Huck, W. T. S. *Angew. Chem., Int. Ed.* **2006**, *45* (11), 1770–1774.

(18) (a) Koberle, P.; Laschewsky, A.; Lomax, T. D. *Makromol. Chem., Rapid Commun.* **1991**, *12* (7), 427–433. (b) Mertoglu, M.; Laschewsky, A.; Skrabania, K.; Wieland, C. *Macromolecules* **2005**, *38* (9), 3601–3614. (c) Mary, P.; Bendejacq, D. D.; Labeau, M. P.; Dupuis, P. *J. Phys. Chem. B* **2007**, *111* (27), 7767–7777.

(19) (a) Nagaoka, H.; Ohnishi, N.; Eguchi, M. US2007203313, A1 Chisso Corp., 2007. (b) Eguchi, M.; Ohnishi, N. EP2009044, Chisso Corp., 2008.

(20) Seuring, J.; Agarwal, S. *Macromol. Chem. Phys.* **2010**, *211* (19), 2109–2117.

(21) Glatzel, S.; Badi, N.; Pach, M.; Laschewsky, A.; Lutz, J.-F. *Chem. Commun.* **2010**, *46* (25), 4517–4519.

(22) (a) Haas, H. C.; Schuler, N. W. *J. Polym. Sci., Part B: Polym. Lett.* **1964**, *2* (12), 1095–1096. (b) Haas, H. C.; Moreau, R. D.; Schuler, N. W. *J. Polym. Sci., Part A-2: Polym. Phys.* **1967**, *5* (5), 915–927.

Macromolecules
ADDITIONS AND CORRECTIONS

Segmental Dynamics in PMMA-Grafted Nanoparticle Composites
[*Macromolecules* **2010** , *43*, 8275]. Pinar Akcora,* Shane E. Harton, Sanat K. Kumar,* Victoria Garcia Sakai, Yu Li, Brian C. Benicewicz, and Linda S. Schadler

Page 8275. In the original submission of this article, one coauthor, Shane E. Harton, was inadvertently omitted.

Page 8277. The Figure 1 caption and Figure 1C image have been corrected. For the bare silica/PMMA nanocomposite, atactic PMMA (Scientific Polymer Products) was used at a filler loading of 20 mass %. However, the underlying conclusions drawn from the data are unchanged.

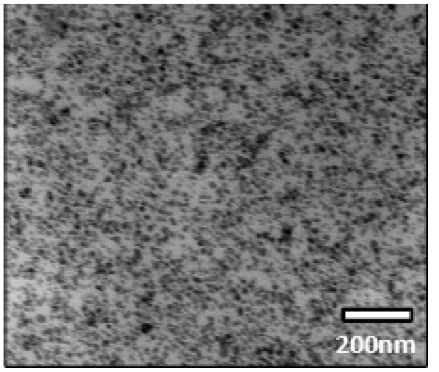


Figure 1. Transmission electron micrographs show the dispersion of PMMA grafted particles in immiscible composite A (part A) and in miscible composite B (part B). Images on the left were taken after 2 days of annealing and on the right after 30 days of annealing. Particle loadings are 15 mass % in parts A and B. Scale bars are 0.2 μm. For reference, we also show the dispersion of 20 mass % bare silica particles in atactic PMMA ($T_g \sim 110$ °C, $M_w \sim 75$ kg/mol) after annealing for 3 days at 160 °C. Clearly, good dispersion is seen in the last case.

DOI: 10.1021/ma102771k
Published on Web 12/31/2010